Dong Dai
Cheng Zhang
Zhi Fang
Xinpei Lu   *Editors*

Proceedings of the 4th International Symposium on Plasma and Energy Conversion

ISPEC 2022, 14–16 Oct, Foshan, China

Springer

Springer Proceedings in Physics   **391**

Dong Dai · Cheng Zhang · Zhi Fang · Xinpei Lu
Editors

Proceedings of the 4th International Symposium on Plasma and Energy Conversion

ISPEC 2022, 14–16 Oct, Foshan, China

Springer

Editors
Dong Dai
South China University of Technology
Guangzhou, China

Zhi Fang
Xi'an Jiaotong University
Xi'an, China

Cheng Zhang
Institute of Electrical Engineering
Beijing, China

Xinpei Lu
Huazhong University of Science
and Technology
Wuhan, China

Preface

This proceedings highlights the fundamental research and up-to-date developments on energy conversion and high-voltage application by means of low temperature and atmospheric pressure plasma. In recent years, plasma-assisted energy conversion gains increasing attention as an alternative to thermal catalysis or electro-catalysis. This proceedings discusses and exchanges cutting-edge scientific innovations and technological advances in fields like plasma-enabled synthesis of chemicals and fuels, plasma-enabled environmental clean-up, plasma-enabled catalysis treatment, in situ probing of plasma-catalyst interactions and its high-voltage applications, which show great potentials in industrial demands like CO_2 hydrogenation, CH_4 reforming and nitrogen fixation, plasma deposition, chemical synthesis, VOC abatement and high-voltage insulation.

This collection of papers presents the main applications of plasma-induced energy conversion and high-voltage discharge in the form of separate chapters, including cutting-edge studies on conversion technology, complex mechanism simulation, in situ detection and converged applications by artificial intelligence.

This proceedings is suitable for researchers engaged in fields like plasma catalysis, discharge diagnosis and modelling, chemical modelling and high-voltage applications.

The major topics covered in the conference proceedings are

1) Advanced plasma catalysis conversion technology;
2) Advanced in situ discharge diagnosis technology;
3) Advanced in situ plasma catalysis characterization;
4) Multi-scale or innovative modelling technology;
5) High-voltage discharge and applications

Contents

High-Voltage Discharge and Application

Basic Process, Diagnosis and Simulation in Plasmas

High Voltage Insulation

Plasma Assisted Processing

Rapid Recovery of Hydrophobicity of Silicone Rubber by Pulsed Discharge Plasma: Impact of Treatment Atmosphere and Underlying Mechanism

Jiachuan Yu[1], Yiheng Xia[1], Jianben Liu[2], Bangdou Huang[1(✉)] , Cheng Zhang[1,3] , and Tao Shao[1,3]

[1] Beijing International S&T Cooperation Base for Plasma Science and Energy Conversion, Institute of Electrical Engineering, Chinese Academy of Sciences, Beijing 100190, China
huangbangdou@mail.iee.ac.cn

[2] State Key Laboratory of Power Grid Environmental Protection, China Electric Power Research Institute, Wuhan 430074, Hubei, China

[3] University of Chinese Academy of Sciences, Beijing 100049, China

Abstract. Atmospheric pressure plasma treatment has been proved to be an efficient method to recover the hydrophobicity of contaminated silicone rubber (SR) for electrical insulators, while the underlying mechanism still needs to be explored. In this work, microsecond pulsed gliding arc plasma at atmospheric pressure is used to treat artificially contaminated SR and different kinds of discharge gases, i.e., Air, N_2, O_2, and Ar, are employed. It is found that with Air, N_2, and O_2 as the discharge gas, the originally hydrophilic SR due to contamination can turn to be hydrophobic and the recovery efficiency is ordered as N_2 > Air ~ O_2. However, Ar plasma can slightly increase the hydrophobicity with a very short plasma treatment time and then the hydrophobicity is totally lost. Based on optical emission spectroscopy from plasma and Fourier transform infrared analysis of contamination, it is demonstrated that plasma with different discharge gases can generate low molecular weight (LMW) silane chains and accelerates their transfer to the surface of contaminated layer. Furthermore, it is inferred that excited N_2 species may be positive for the hydrophobicity recovery, while the excessive activity of Ar plasma may destroy the hydrophobicity of LMW components.

Keywords: Pulsed Discharge · Surface Treatment · Hydrophobicity

1 Introduction

Silicone rubber (SR), with good dielectric characteristics and temperature tolerance, is widely used for insulators in transmission lines of power system. The hydrophobicity of SR is very important for its flashover property, especially under conditions with rain, fog, ice, or pollution [1]. Generally, a clean SR surface of a newly produced insulator is well hydrophobic. However, when the SR surface gets contaminated or the insulator is aged for a long term under high-voltage (HV) condition, the hydrophobicity can be

lost and the potential of flashover accidents increases [2, 3]. Therefore, it is desirable to recover the hydrophobicity of SR with an on-line method (without power interruption), which should also be rapid and cheap as a luge amount of SR insulators are used in power system.

Even though different physical or chemical methods have been tried to build hydrophobic SR surface [4], atmospheric pressure plasma treatment has been proved to be an efficient strategy to recover hydrophobicity of SR especially under contaminated condition [5, 6], which is due to the unique advantage of plasma surface treatment [7]. Recently, gliding arc (GA) plasma source driven by microsecond HV pulses has been developed, combining the advantage of both high reactivity and low power consumption, and used for hydrophobicity recovery of SR [8]. However, the underlying mechanism for hydrophobicity recovery of SR by plasma treatment is yet to be clarified.

In this work, different kinds of discharge gases are employed to generated GA plasma and their effect on hydrophobicity recovery of SR is compared. Combining analysis of both contamination samples and GA plasma, the possible mechanism for hydrophobicity recovery of SR by plasma treatment is proposed.

2   Experimental Setup

Figure 1 shows a schematic diagram of the experimental setup used in this work. A microsecond pulsed bi-polar HV generator developed in our previous work is used to generate atmospheric pressure GA plasma with two diverging blade electrodes. The breakdown voltage is ~5 kV, the peak discharge current is ~0.6 A, and the discharge energy per pulse is ~0.6 mJ. The discharge frequency is ~15 kHz. In particular, different kinds of discharge gases including Air, N_2, O_2, and Ar are employed with a gas flow rate of 10 standard liter per second (SLM).

In this work, artificially contaminated SR samples are prepared according to standard IEC 60507, using Kaolin and NaCl solution as the contaminating suspension. The contaminating suspension is smeared uniformly on the SR surface, with a non-soluble deposit density (NSDD) of 1 mg/cm^2, which represents heavily contaminated condition. And then the samples are dried at room temperature for 5 h. The SR samples are treated by the GA plasma with a distance of ~2 mm for different time periods. The surface temperature of SR samples with GA treatment is measured using an infrared camera (Fluke, TiS20 + MAX).

The static water contact angle (WCA) is measured using an optical microscope (JGW-360A) after a 4 µL droplet of distilled water imposed on the SR surface. The contamination before and after GA plasma treatment is scraped gently from the SR surface, mixed with KBr, and squashed into thin samples, which are analyzed by a Fourier transform infrared (FTIR) spectrometer (Nicolet-iS50) using transmission method. Note that the transmission FTIR has a better sensitivity than the reflection FTIR. In addition, optical emission spectroscopy (OES) from the GA plasma is collected with a fiber and measured with a spectrometer (Ocean Optics, QE 65000).
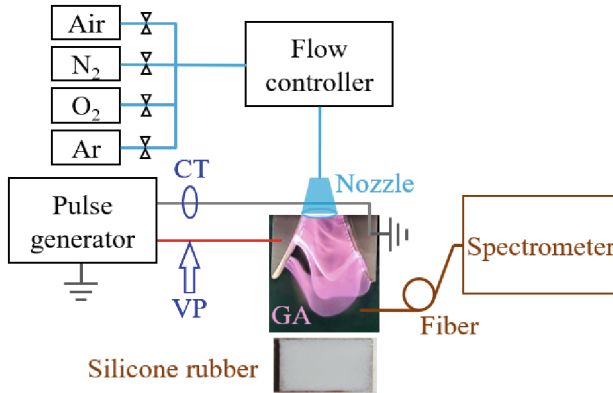
Fig. 1. A schematic diagram of the experimental setup used in this work.

3   Results and Discussion

Figure 2 shows the WCA evolution of artificially contaminated SR with plasma treatment time using different kinds of discharge gases. It can be seen that N_2 is the mostly efficient discharge gas for recovering hydrophobicity of artificially contaminated SR, i.e., after only 20 s treatment, the WCA increases from a very low value to ~131° and then increases to ~141° after 40 s treatment. When Air and O_2 are used, the rise rate of WCA with treatment time is slower and longer time is needed to recover the WCA of artificially contaminated SR to a hydrophobic level. However, when Ar is used, the WCA of SR sample increases to ~83° after 10 s treatment and the decreases drastically to a very low value after longer treatment time.
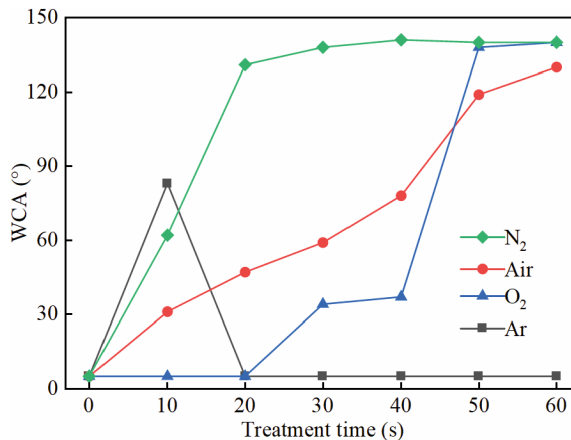
Fig. 2. The WCA evolution of artificially contaminated SR with GA plasma treatment time using different kinds of discharge gases.

In order to explore the mechanism of hydrophobicity recovery with plasma treatment, contamination from the SR surface is analyzed using transmission FTIR, as shown in Fig. 2. It can be seen that the dominant FTIR peak is from anti-symmetrical stretching of Si-O-Si at around 1100 cm^{-1}. After GA plasma treatment, a weak but distinguished peak appears around 1385 cm^{-1}, which is from the symmetrical stretching of CH$_3$. This indicates that the plasma treatment breaks the long chain of polydimethylsiloxane (PDMS) from the SR matrix into low molecular weight (LMW) silane chains and accelerates the transfer of LMW silane chains to the surface of contaminated layer.

Even so, CH$_3$ peak appears after plasma treatment with all different kinds of discharge gases, this means that it is not the specific reason for hydrophobicity recovery of artificially contaminated SR. Further investigation is needed to distinguish the unique effect of different discharge gases.
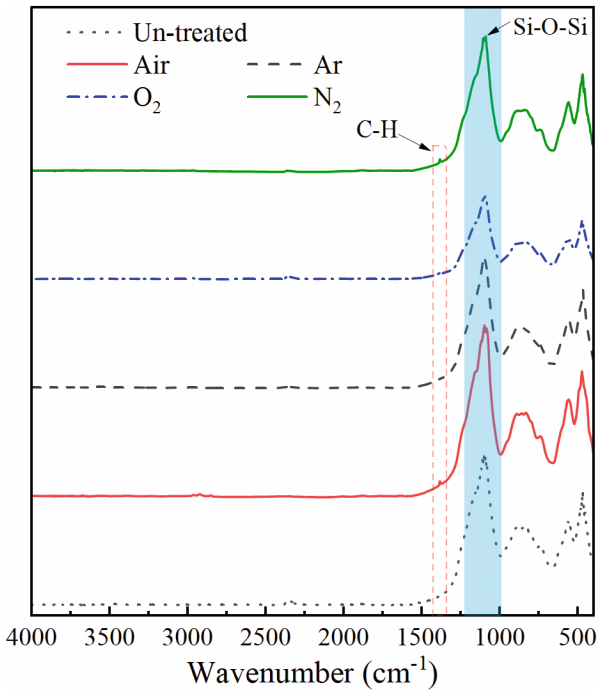
Fig. 3. FTIR of contamination from the SR surface before and after GA plasma treatment.

For this purpose, OES from GA plasma with different discharge gases is measured and analyzed, as shown in Fig. 4. It can be seen that GA plasma with a given discharge gas has its unique OES components. With N$_2$ as discharge gas, the dominant OES components include N$_2$ C $\rightarrow$ B band around 290–410 nm, NO A $\rightarrow$ X band around 220–280 nm, and O I lines at ~777 and 844.6 nm. The appearance of NO band and O I lines with N$_2$ as the discharge gas is due to that the GA plasma is operated in ambient atmosphere and there are reactions between excited N$_2$ species with surrounding O$_2$ molecules. With Air as the discharge gas, the dominant OES components are similar as

those with N_2. However, emission from N_2 and NO is much suppressed with Air, while that from O I maintains similar. With O_2 as the discharge gas, the emission intensity from O I is much enhanced, while that from N_2 and NO is further suppressed.

As for the case with Ar as the discharge gas, the dominant OES components are from Ar I 2p → 1s group (in Paschen's notation) around 696–965 nm. There also exists N_2 C → B band with Ar, due to reactions between excited Ar species and N_2 molecules, whose intensity is lower than the case with N_2 as the discharge gas, but much higher than the cases with Air and O_2. Note that the y-scale with Ar is different from those with other gases and the emission intensity from Ar I is much stronger.
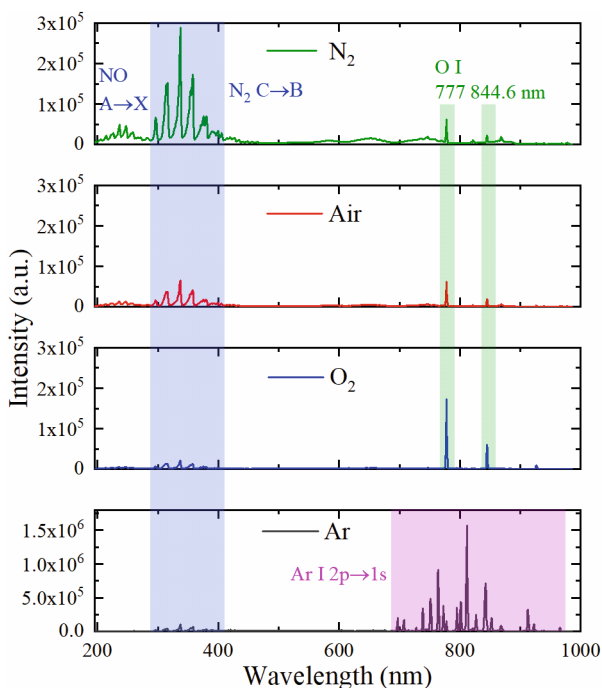
Fig. 4. OES from GA plasma with different kinds of discharge gases.

The generation of active species in GA plasma is analyzed based on OES and threshold energy (ε_{thr}) for certain reactions. For GA plasma with N_2, Air, and O_2, ε_{thr} for exciting N_2 C is ~11.03 eV, ε_{thr} for dissociating O_2 is ~5.12 eV, and ε_{thr} for exciting O is ~10.74 for 3p ^{5}P level (777 nm) and ~10.99 eV for 3p ^{3}P level (844.6 nm). Note that there can be stepwise reactions which need much lower ε_{thr} (several eV). However, for Ar as rare gas, its minimum ε_{thr} to generate excited state is as high as ~11.55 eV.

Combining the WCA evolution with treatment time shown in Fig. 2 and FTIR shown in Fig. 3, it is demonstrated that GA plasma with all different gases can generate LMW silane chains and accelerate their transfer. As N_2 plasma is mostly efficient in hydrophobicity recovery and has the highest N_2 C band intensity, it can be inferred that the excited N_2 species may have a positive effect on the hydrophobicity recovery process. However,
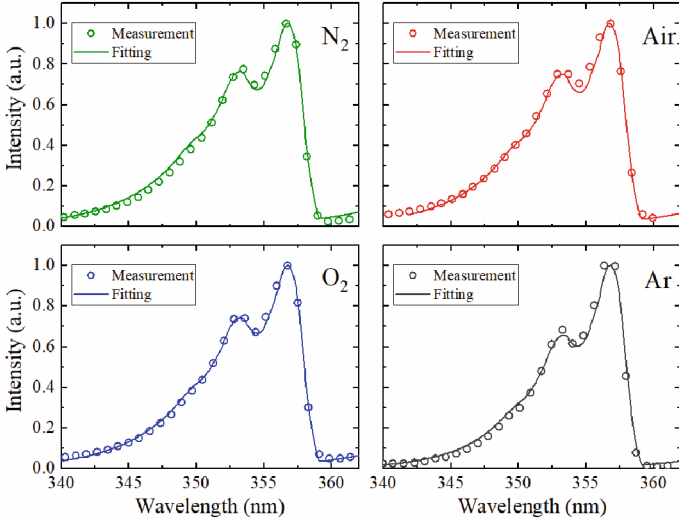
Fig. 5. N_2 C → B band from measurement and fitting with different kinds of discharge gases.

Ar plasma can initially increase the hydrophobicity of SR, but will further destroy the structure of LMW silane chains due to the excessive reactivity as Ar excited states have a high ε_{thr} and result in loss of hydrophobicity.

Temperature can also be an important factor when performing plasma treatment. The surface temperature of SR samples with different discharge gases is summarized in Table 1. It can be seen that the surface temperature in all cases is below 100 °C and the case with Ar has the lowest temperature. Such a low surface temperature cannot breakdown the chemical band of SR due to thermal effect.

The rotational and vibrational temperature (T_r and T_v) of GA plasma with different gases can be obtained by fitting the measured N_2 C → B band, which are also listed in Table 1 with fitting results shown in Fig. 5. It can be seen that T_r and T_v of GA plasma can reach more than 3000 K, indicating its high reaction activity and non-equilibrium characteristic. GA plasma with Ar has slightly lower T_r and T_v compared with other

Table 1. Surface temperature of SR when performing plasma treatment and rotational and vibrational temperature of GA plasma with different kinds of discharge gases.

Discharge gas	Surface temperature (°C)	Rotational temperature (K)	Vibrational temperature (K)
N_2	97 ± 5	3700 ± 500	4200 ± 500
Air	95 ± 5	3500 ± 500	4300 ± 500
O_2	82 ± 5	3600 ± 500	4000 ± 500
Ar	47 ± 5	3000 ± 500	3500 ± 500

cases. Therefore, T_r and T_v should not be the specific reason for the different performance of hydrophobicity recovery with different gases.

4   Summary and Conclusion

In this work, microsecond pulsed GA plasma is used to treat the artificially contaminated SR with a NSDD of 1 mg/cm^2. Different kinds of discharge gases, i.e., Air, N$_2$, O$_2$, and Ar, are used and their effect on the hydrophobicity recovery of contaminated SR is compared. It is found that when Air, N$_2$, and O$_2$ are used as the discharge gas, the originally hydrophilic SR due to contamination can turn to be hydrophobic with treatment time within 1 min and the recovery efficiency is ordered as N$_2$ > Air ~ O$_2$. However, when Ar is used as the discharge gas, the hydrophobicity of SR increases slightly with very short treatment time (10 s) and then the hydrophobicity is totally lost. Based on FTIR analysis of contamination on the SR surface before and after plasma treatment, it is demonstrated that pulsed GA plasma with different discharge gases can generate low LMW silane chains and accelerates their transfer to the surface of contaminated layer. Combined with OES from plasma, it is inferred that excited N$_2$ species may be positive for the hydrophobicity recovery, whose emission intensity is highest with N$_2$ as the discharge gas, while the excessive activity of Ar plasma may destroy the hydrophobicity of LMW components.

References

1. Wang, S., Lei, S., Zhou, J., Ding, Y.: Experimental study on bird streamer flashover for V-type insulators of DC transmission line in high altitude area. IEEE Trans. Power Deliv. **38**(2), 812–820 (2023)
2. Liu, Y., et al.: Pollution morphology characteristics on a superhydrophobic surface and its pollution flashover voltage in DC electric field. High Volt. **7**(3), 564–574 (2022)
3. Zeng, L., et al.: Aging state evaluation methods for silicone rubber sheds of composite insulators. Insulators and Surge Arresters **306**, 139–152 (2022)
4. Wang, G., et al.: A review on fabrication methods and research progress of superhydrophobic silicone rubber materials. Adv. Mater. Interfaces **8**, 2001460 (2020)
5. Vazirinasab, E., Jafari, R., G. Momen, G.: Evaluation of atmospheric-pressure plasma parameters to achieve superhydrophobic and self-cleaning HTV silicone rubber surfaces via a single-step, eco-friendly approach. Surf. Coatings Tech. **375**, 100–111 (2019)
6. Li, S., Li, J., Fu, Y., Zhang, R.: Interaction between plasma jet and silicone rubber covered by porous inorganic contaminants: Surface hydrophobicity or hydrophilicity? High Volt. **7**(6), 1023–1033 (2022)
7. Kong, F., Zhao, M., Zhang, C., Ren, C., Ostrikov, K., Shao, T.: Two-phase-interfaced, graded-permittivity titania electrical insulation by atmospheric pressure plasmas. ACS Appl. Mater. Interfaces **14**(1), 1900–1909 (2022)
8. Huang, B., Liu, J., Liu, Y., Yu, J., Zhang, C., Shao, T.: Rapid Treatment with Pulsed Gliding Arc Plasma in Ambient Air to Increase the Hydrophobicity of Silicone Rubber for Electrical Insulators. In: Proceedings of 2022 IEEE 5th International Electrical and Energy Conference, CIEEC 2022, 4353–4356 (2022)

Discharge Characteristics of Ar/Alkoxysilane Atmospheric Pressure Plasma Jet and Its Application in Surface Treatment

Jiazhen Duan[(✉)], Ruxin Shi, Hongtao Liu, and Xianming Ren

State Grid Changzhou Power Supply Company, Changzhou 213004, Jiangsu, China
`61113256@qq.com`

Abstract. Polymer insulation materials, widely used in electric power systems, are inevitably aging and cracking due to long-term work in the natural environment, causing the degradation in hydrophobicity and insulating properties. Currently, the main method for repairing surface cracks of the insulation material is physical coating, but it introduces a new interface and affects insulation properties. Therefore, in this paper, an Ar/alkoxysilane/H_2O atmospheric pressure plasma jet (APPJ) driven by microsecond pulsed power supply was established to treat the damaged silicon rubber (SiR) materials. The experimental results show that the addition of water and alkoxysilane promotes the discharge intensity with higher discharge current and enhanced spectral intensity. However, the excessive addition of reaction medium inhibited the discharge. Furthermore, under an optimal APPJ experiment condition (1 L/min Ar, 13 ml/min alkoxysilane and 3 ml/min H_2O), the flashover voltage of damaged SiR is increased by 19.1% after plasma treatment, and it returns to 89.9% of the intact SiR. Moreover, the mechanical stress of the damaged SiR is also recovered, where the maximum mechanical stress increases from 2.94 to 11.76 N. It is demonstrated that the plasma repair achieves a significant improvement in the electrical and mechanical properties of damaged SiR.

Keywords: Plasma jet · Surface treatment · Discharge characteristics · Electrical properties · Mechanical properties

1 Introduction

Electrical insulation materials are of great importance for the reliable operation of transmission circuits and power systems, which are divided into organic insulating materials, inorganic insulating materials and composite insulating materials. Compared with inorganic and organic insulating materials, silicone rubber (SiR) composite insulating materials have significant advantages such as lightweight, excellent surface hydrophobicity and less pollution flashover. However, outdoor SiR insulating materials are exposed to harsh climatic conditions and corona discharge for a long time, such as extreme changes in temperature, heavy sandstorm and acid rain, which breaks the chemical bonds and causes a series of physicochemical reactions, eventually leads to small holes and crack

defects on the surface [1−3]. These defects may change the macro-micro shape of insulation and affect material properties of SIR insulation, such as mechanical and electrical strength. Therefore, it is of great significance to process the SIR material and recover the damaged electrical insulation.

Currently, physical coating techniques are applied to repair the damages or defects on these insulation surfaces. It is noted that the hydrophobicity of aged insulation materials is effectively improved by RTV (room temperature vulcanized) coating and reinforcing. However, the coating method constructs the independent layers on SIR surface, where the molecular structure of the coating and the SIR substrate is different. It may introduce a weak interface and lead to the potential failures. Chemical self-repair technology is an emerging technology in recent years, which is a novel attempt to treat the aging problem of insulation materials precisely and repair the target defects autonomously [4, 5]. However, repair agents used in self-repair technology require certain physicochemical conditions to restore the insulating materials, which is not suitable for the outdoor SIR insulation.

Plasma treatment is a processing method that uses electrified non-polymeric inorganic gases (Ar, H_2, N_2, O_2, etc.) for surface reaction, which contains a high concentration of excited and free radical particles and triggers multi-level physicochemical reactions on material surface. For example, high-energy particles in plasma bombard the material and trigger etching on surface, which changes surface physical morphology and opens the surface chemical bonds to promote active particle grafting, polymerization and further crosslinking. In recent years, plasma has been widely applied in surface modification and enhancement of insulation properties. Kirk et al. applied the plasma with F_2 and CF_4 to treat the polypropylene films, and studied the changes in chemical composites. It showed that the hydrophobicity of the material could be enhanced by introducing fluorine atoms ($C-F_n$) to the surface of the material [6]. Moreover, some researchers found that the fluorine-containing groups on material surface would introduce the shallow traps and improve the flashover voltage [7, 8]. However, there are few studies on plasma treatment for surface crack healing and insulation recovery. Researchers at Nanjing Tech University have proposed a crack repairing method for SIR insulation based on plasma jet [9], but the effect of plasma experimental parameters on surface repair is unclear.

In this paper, a plasma jet repair device consisting of microsecond pulse power supply, gas path, flow rate control meter, jet reactor, mechanical arm and experimental platform was designed. Discharge characteristics under different experimental conditions were studied, and the effect of reaction medium addition on the plasma discharge characteristics was analyzed. Moreover, the plasma jet was applied to treat the damaged SIR surface to study the insulating material properties under different experimental conditions, and the physicochemical reaction mechanism of plasma repair on SIR was investigated.

2 Experiment

2.1 Materials Preparation

Square SIR insulation materials of 1 cm in length, 1 cm in width and 1 mm in thickness are prepared as a sample, and a 5 mm long and 1 mm deep crack is introduced on sample

surface with a knife to simulate crack aging. The samples are treated continuously for 10 min under different plasma reaction conditions.

2.2 Set up of APPJ System

A plasma jet system applied to the surface treatment of SIR insulation is shown in Fig. 1. A 140 mm long (6 mm inner diameter and 8 mm outer diameter) glass tube is used as the barrier medium, a 3 mm diameter copper needle as the high voltage electrode, and a 10 mm wide copper foil as the ground electrode for the jet reactor. A microsecond pulsed power supply with adjustable frequency and amplitude is applied to excite the plasma jet with an output voltage range of 0–30 kV and an output frequency of 1–5 kHz. A flow meter is used to control the concentration of the working gas Ar, the reaction medium (alkoxysilane) and the additive water. In this study, the flow rate of Ar is kept at 1 L/min, that of reaction medium is controlled from10 to 16 mL/min and that of water is controlled from 0 to 9 mL/min. The voltage and discharge current waveforms are obtained by a high-voltage probe and a current coil, respectively, and recorded by an oscilloscope. The emission spectra of the APPJ plume are obtained by a spectrometer to analyze the reaction characteristics of the active particles in the plasma.
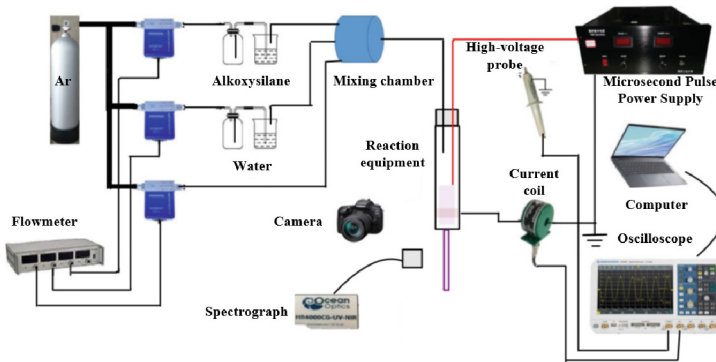
Fig. 1. Diagram of APPJ system and discharge diagnosis

2.3 Characterization of Insulting Materials

(1) Flashover test

A flashover voltage test equipment is illustrated in Fig. 2. It consists of a high voltage DC source, high voltage probe, current coil, oscilloscope and a sample platform. The platform is constructed by two finger electrodes with a diameter of 10 mm and a distance of 5 mm. The voltage increases at a rate of 500 V/s until flashover occurs, and the flashover voltage is recorded.
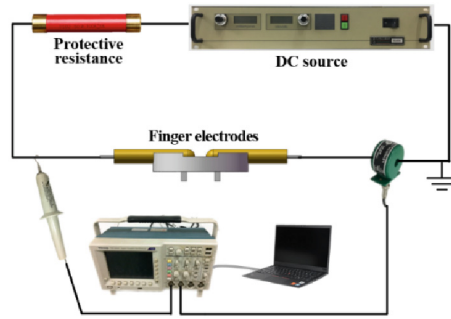
Fig.2. The setup of flashover test

(2) Mechanical test

The mechanical properties of the insulation material are evaluated by weight tension, as shown in Fig. 3. A simple vertical stretching device is made by hooks, dovetail clamps, tray and weights. During the mechanical test, the weights gradually increase at 50 g/time until the cracks completely reappear, and the weights are recorded as the typical parameter for evaluating the mechanical properties of the SIR materials.
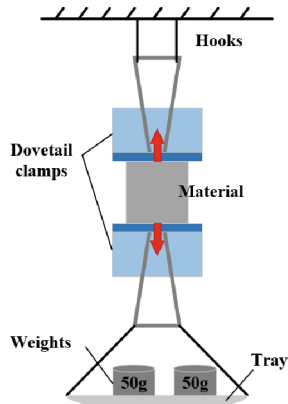
Fig. 3. The setup of mechanical test

3 Plasma Jet Discharge Characteristics

Diagnosis of discharge characteristics and optical properties is the key means to analyze the discharge level. Through the pre-experimental investigation, it is found that the microsecond pulse power supply produces the longest jet plume, highest luminescence intensity and continuous discharge without obvious interruptions under the voltage of

15 kV and frequency of 3 kHz. Therefore, in this chapter, the variation of APPJ discharge characteristics under different combinations of the repair agent and water at 15 kV/3 kHz is analyzed to find the optimal addition content of reaction medium.

3.1 Discharge Characteristics Analysis

The symbols of different experiments are shown in Table 1, and the voltage and discharge current waveforms of plasma under different experiments are shown in Fig. 4. It can be seen that, compared with the discharge current under the experimental conditions of $0 + 0$, the addition of repair agent and water increases the peak discharge current to a certain extent. The peak current is 0.13 A under the condition of $0 + 0$; as the reaction medium remains 13 ml/min and the water flow rate increases from 0 to 3 ml/min, the peak current increases from 0.28 to 0.5A, and the addition of water promotes the discharge to a certain extent. By contrast, as the water further increases to 9 mL/min, the discharge current is weakened. It can be seen that the promotion effect of water addition on plasma discharge has a tendency to increase first and then decrease, and the best discharge intensity reaches as the water flow rate is 3 ml/min. When the water flow rate is kept at 3 mL/min and the flow rates of reaction medium are 10, 13 and 16 mL/min, the peak discharge currents are 0.32, 0.5 and 0.18 A, respectively. It can be seen that the addition of the reaction medium also has a tendency to increase and then decrease the plasma discharge effect, and the best discharge effect obtains as the flow rate of reaction medium is 13 mL/min.

Table 1. Symbols of different experiments

Symbols	Flow rate (mL/min)		
	Ar	Alkoxysilane	Water
$0 + 0$	1000	0	0
$13 + 0$	1000	13	0
$13 + 3$	1000	13	3
$13 + 9$	1000	13	9
$10 + 3$	1000	10	3
$16 + 3$	1000	16	3

3.2 Emission Spectral Characteristics

The emission spectra images under different experimental conditions are shown in Fig. 5. Since different active particles locate at different wavelengths in the spectral images, the type and the concentration of active particles can be characterized by wavelength and intensity, respectively. The spectral images show that the excited particles are mainly OH (A $\rightarrow$ X), N_2 (C $\rightarrow$ B) and Ar (4p $\rightarrow$ 4s), and the reaction equations are shown below. After adding alkoxysilane and water, the number of active particles increases

(a) 0+0

(b) 13+0

(c) 13+3

(d) 13+9

(e) 16+3

(f) 10+3
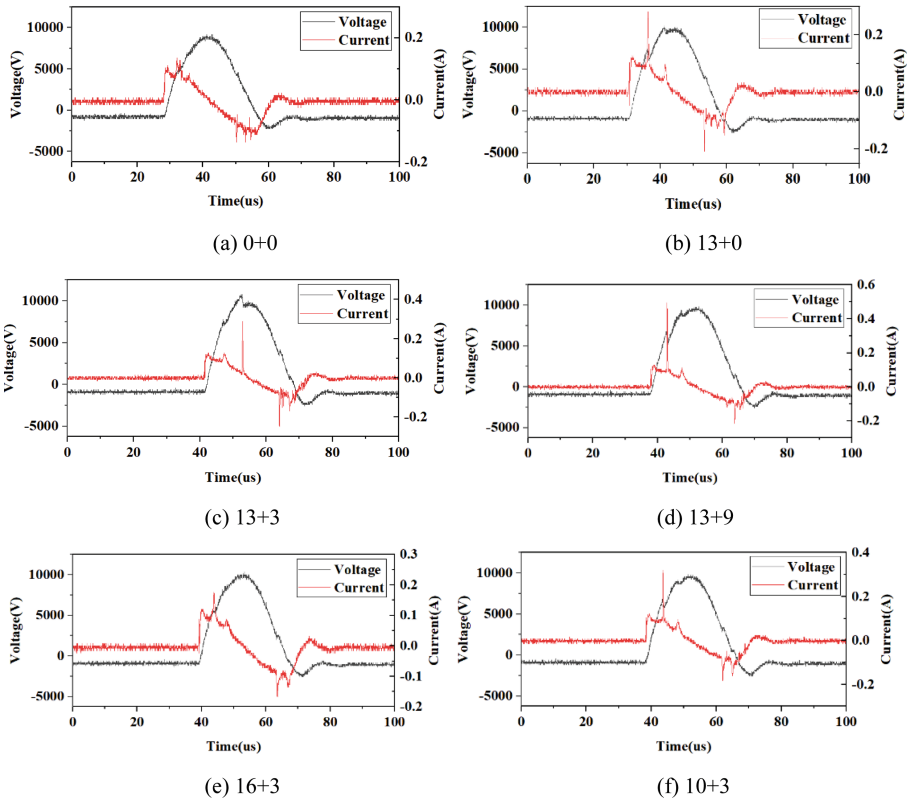
Fig. 4. Discharge voltage and current waveforms under different experimental conditions

due to the Penning ionization of these medium reacting with e* and Ar*; on the other hand, water and alkoxysilane macromolecules will adsorb e* and Ar* and decrease the number of active particles, inhibiting the discharge to some extent. Therefore, it can be seen that the intensity of the excited particles under $13 + 3$, $13 + 9$, $10 + 3$, $0 + 0$, and $13 + 0$ are all higher, and the intensities of the excited particles under the experimental conditions of $13 + 3$ and $10 + 3$ reach at the best level. By contrast, under the condition of $16 + 3$, the content of OH particles and N* is significantly lower, which is consistent with the results of the discharge current. The moderate addition of alkoxysilane and water can promote the ionization reaction and thus enhance the APPJ intensity, which increases the peak discharge current and promotes the content of excited state particles; while as excessive water and alkoxysilane is added, these macromolecules will adsorb a certain amount of excited particles and inhibit the discharge, leading to the decrease

of discharge current and the spectral intensity.

$$\begin{cases} Ar + e^* \rightarrow Ar^* + e \\ H_2O + e^* \rightarrow H + OH^* + e \\ H_2O + Ar^* \rightarrow H + OH^* + Ar \\ N_2 + e^* \rightarrow N_2^* + e \\ N_2 + Ar^* \rightarrow N_2^* + Ar \end{cases}$$

(a)   0+0

(b) 13+0

(c) 13+3

(d) 13+9

(e) 16+3

(f) 10+3
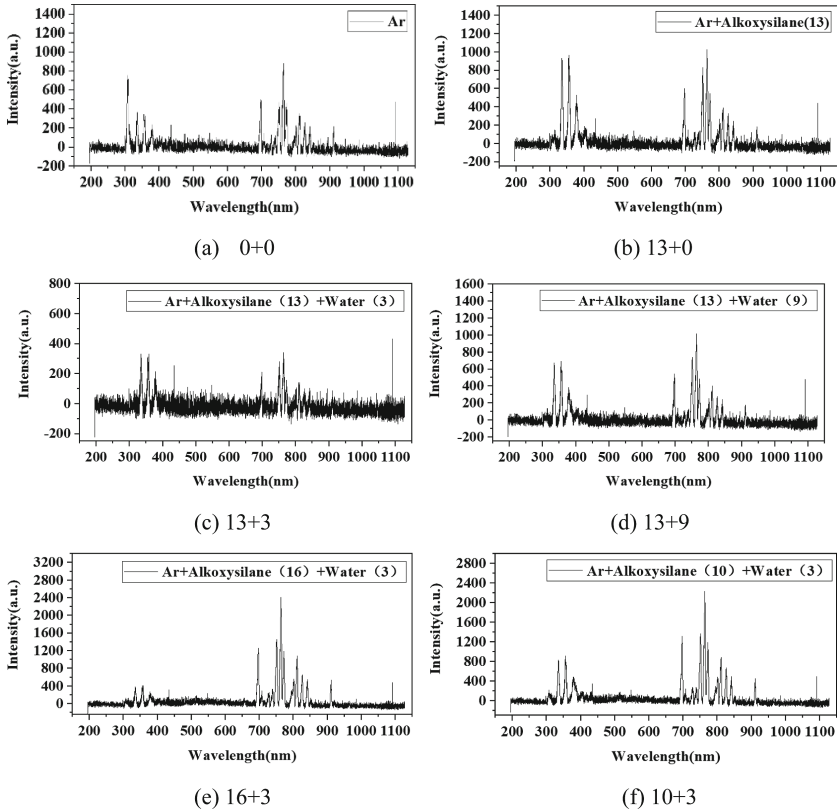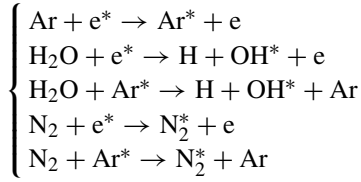
Fig. 5. Images of discharge spectra under different experimental conditions

4   Insulation Material Repair Based on APPJ

4.1   Flashover Voltage

The flashover voltages on the SIR surface under different experimental conditions are shown in Fig. 6. It can be seen that the introduction of cracks significantly reduces the flashover voltage from 12 kV to 8.48 kV, while the plasma treatment effectively

improves the electrical properties of the damaged insulating material. Although pure plasma treatment $(0 + 0)$ does not deposit a thin film on the insulating material surface, the plasma etching increases the surface roughness of the material, which promotes the flashover voltage. The electrical insulating properties of SIR are further enhanced by the addition of reaction medium, which heals the cracks under plasma action and deposits a silicone-containing film at the same time. It can be seen that the flashover voltage increases from 8.48 to 10.76 kV in $13 + 3$ experimental condition, increased by 89.9%. Although both $13 + 0$ and excess water addition $(13 + 9)$ reduce the recovery effect, such as 8.48 kV under $13 + 0$ and 9.54 kV under $13 + 9$, the electrical insulating properties are still recovered to some extent compared to the damaged SIR insulation.
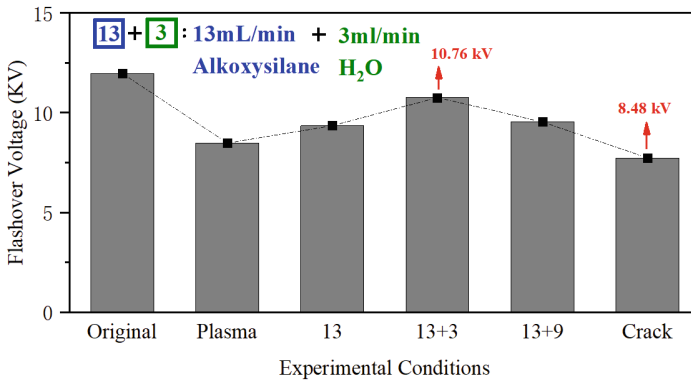
Fig. 6. Flashover voltage under different experiment conditions

4.2 Mechanical Properties

The effects of mechanical properties recovery of SIR insulation under different treatment experimental conditions are shown in Fig. 7. It can be seen that the introduction of cracks has a significant damage to the mechanical properties of the SIR material, causing a decrease in tensile strength (2.94 N). After the plasma treatment, the mechanical properties of the damaged SIR insulation are enhanced to a certain extent regardless of the experimental conditions. The optimal repair effect is achieved under $13 + 3$, which withstands a maximum mechanical stress (11.76 N, increased by 300% compared to the damaged insulation material). Close to the trend of flashover voltage, water-free $(13 + 0)$ and excess water addition $(13 + 9)$ both reduce the repair effect of plasma on the mechanical properties, e.g., the maximum mechanical stress is 8.82 N under $13 + 0$ and that is 9.80 N under $13 + 9$. However, pure Ar treatment $(0 + 0)$ has limited repair effect on the mechanical properties of damaged SIR materials, which may be caused by the small effect of plasma etching on the mechanical strength of the material. By contrast, the plasma-assisted silicone deposition completely fills the crack gaps, thus effectively enhancing the mechanical strength of the insulation material.
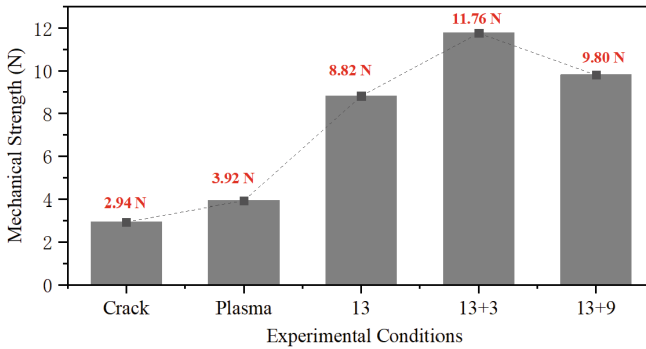
Fig. 7. Mechanical properties of damaged SIR under different experimental conditions

5   Conclusion

This paper proposed a repair method for damaged SIR insulating materials based on APPJ with alkoxysilane and water. By regulating the additive concentration of reaction medium, the discharge characteristics of APPJ and its repair effect on the damaged SIR insulating materials were studied.

(1)   A plasma repair equipment based on APPJ is established, which consists of jet reactor, gas-liquid mixing device, microsecond pulse power supply and gas flow rate controller. It is demonstrated that the plasma repair achieves a significant improvement in the electrical and mechanical properties of damaged SIR.

(2)   Under the conditions of 1 L/min Ar, 13 mL/min alkoxysilane and 3 mL/min water, a plasma jet with good discharge intensity, long plume length and high concentration of active particles is obtained. The moderate addition of reaction medium increases the active particle through Penning ionization effect, thus enhancing the plasma discharge.

(3)   After treated by the optimal plasma conditions, the flashover voltage of SIR increases to 10.76 kV compared with the damaged material (8.48 kV), which returns to 89.9% of the intact SIR (11.97 kV). In addition, the mechanical stress of the damaged SIR is also recovered, where the maximum mechanical stress increases from 2.94 to 11.76 N.

References

1. Gao, Y., Liang, X., Lu, Y., et al.: Comparative investigation on fracture of suspension high voltage composite insulators: a review—Part I: fracture morphology characteristics. IEEE Electr. Insul. Mag. **37**(3), 7–17 (2021)

2. Wang, X., Hong, X., Wang, H., et al.: Analysis of the silicone polymer surface aging profile with laser-induced breakdown spectroscopy. J. Phys. D Appl. Phys. **50**, 415601 (2017)
3. Ma, J., Wang, X., Zhang, R., et al.: Influence of sheath radial crack on flashover arc and leakage current of roof silicon rubber insulator for high-speed train. IEEE Access **10**, 19720–19731 (2022)
4. Pelissou, S., Lessard, G.: Underground medium-voltage cable rejuvenation—Part I: laboratory tests on cables. IEEE Trans. Power Delivery **26**, 2324–2332 (2011)
5. Sima, W., Liang, C., Sun, P., et al.: Novel smart insulating materials achieving targeting self-healing of electrical trees: high performance, low cost, and eco-friendliness. ACS Appl. Mater. Interfaces. **13**(28), 33485–33495 (2021)
6. Kirk, S., Strobel, M., Lee, C., et al.: Fluorine plasma treatments of polypropylene films, 1–surface characterization. Plasma Processes Polym. **7**(2), 107–122 (2010)
7. Yang, Y., Strobel, M., Kirk, S., et al.: Fluorine plasma treatments of poly (propylene) films, 2–Modeling reaction mechanisms and scaling. Plasma Processes Polym. **7**(2), 123–150 (2010)
8. Shao, T., Yang, W., Zhang, C., et al.: Enhanced surface flashover strength in vacuum of polymethylmethacrylate by surface modification using atmospheric-pressure dielectric barrier discharge. Appl. Phys. Lett. **105**(7), 071607 (2014)
9. Zhu, X., Xu, J., Cui, X., et al.: Plasma-electrified repair of damaged polymer composites for surface crack healing and insulation recovery. Chem. Eng. J. **449**(1), 137754 (2022)

Study on the De-NOx Performance by Dielectric Barrier Discharge with NaCl Solution Grounded Electrode

Wei Zhang[1], Mengfei Yang[1], Zongyu Wang[2,3](✉), Jifeng Zhang[1,2], Hai Zhang[3], and Yulong Ji[1]

[1] Dalian Maritime University, Liaoning 116026, CN, China
[2] Yangtze Delta Region Institute of Tsinghua University Zhejiang, Zhejiang 314006, CN, China
wangzongyu09@163.com
[3] Tsinghua University, Beijing 100084, CN, China

Abstract. The traditional dielectric barrier discharge reactors with metal-grounded electrodes have the disadvantages of electrode ablation, short lifetime and poor stability, which limit the practical application of non-thermal plasma de-NOx technology. In order to solve this problem, a coaxial cylindrical DBD reactor with the NaCl solution grounded electrode was constructed. The effects of simulated exhaust gas flow rate, O_2 concentration and NO concentration on the de-NOx performance were studied. The results show that the specific energy density for de-NOx gradually decreases with the exhaust gas flow rate. The NOx transformation trend with the increasing O_2 volume fraction by plasma treatment is shown as NOx removal mode (de-NOx efficiency >90%) → NOx stable mode → NOx growth mode. The energy consumption of removing NO per unit volume gradually decreases with the initial NO concentration. In addition, the reactor with liquid-grounded electrode shows excellent performance of de-NOx efficiency and energy consumption. This work provides novel idea for the optimization of the dielectric barrier discharge reactor structure and the practical application of de-NOx process.

Keywords: NaCl solution grounded electrode · Dielectric barrier discharge · NOx removal

1 Introduction

The exhaust gas emitted by the combustion of fossil fuels and biomass fuels has a big bad impact on regional development, ecological environment and human health [1, 2]. Nitrogen Oxides (NOx) are considered as one of the major atmospheric pollutants and the main source of greenhouse effect, acid rain, photochemical smog, and PM2.5 [3]. Many governments have issued increasingly stringent policies and regulations to control NOx emissions in response to the serious harm caused by NOx.

Nitric Oxide (NO), the main component of NOx, has stable chemical properties. While the components of industrial exhaust gas are often complicated, it is difficult to achieve efficient NOx removal by simple absorption and chemical separation. The DBD

technology has the advantages of simple reactor structures, ambient operation conditions and abundant active free radicals [4, 5]. It has a wide range of application prospects in the field of exhaust gases NOx treatment [6–8]. The main principle of DBD de-NOx technology is that gas molecules generate high-energy electrons, active radicals, ions and other particles under high-voltage excitation. These particles collide with the exhaust gas molecules to produce chain chemical reactions, so that the exhaust gas harmful substances crack, compound, and convert into harmless product N_2. The structure of DBD reactor is the key factor to determining the discharge and de-NOx performance [9–12]. For the coaxial DBD reactors. The grounded electrode is arranged outside the insulating dielectric layer to directly contact with the external environment. The design is more diverse, which is an important factor affecting the discharge performance. Shao et al. [13] studied the effects of metal-grounded electrode materials, electrode lengths, and electrode structures on reactant conversions, product selectivity and energy conversion efficiencies by a micro-second pulsed power supply. The results show that the copper foil electrode with higher conductivity, longer discharge length and larger coverage area has better performance. Niu et al. [12] investigated the effects of a multi-stage metal grounded electrode on the electrical property, discharge mode, and energy consumption of plasma discharge. It was found that the multi-stage grounded electrode structure can obtain a lower pulse current peak, more locally homogenous and stronger filamentary micro-discharge channels, and lower energy consumption. Lee et al. [14] further analyzed the effects of increasing segmented grounded electrode structure on discharge characteristics. The results show that the discharge power, current density and current intensity gradually increase with the number of segments of the grounded electrode under the same applied voltage. Although scholars have made some progress in the research of traditional metal-grounded electrodes. However, there are still many shortcomings in the practical application of metal-grounded electrodes. For example, the metal electrodes often form electrode edge effects at local spikes and outside edges [15, 16], which enhances the charge memory effect at the edges and weakens the homogeneity of the entire discharge area [17]. In addition, the metal-grounded electrodes exposed to the environment are prone to ablative oxidation during long-term operation, affecting the operating lifetime and discharge stability of the electrodes.

To overcome the drawbacks of the traditional metal-grounded electrode structures, a novel grounded electrode with liquid solution was proposed. A NaCl solution grounded electrode reactor was used in this work. The effects of simulated exhaust gas flow rate, O_2 concentration and NOx concentration on the de-NOx performances were studied further. This work is helpful to promote the development of DBD technology with the liquid-grounded electrode and reveal the plasma de-NOx mechanism.

2 Experimental Sections

2.1 Experimental System

Figure 1 shows the experimental system diagram of the DBD de-NOx with the liquid grounded electrode. The de-NOx experimental devices of the DBD reactor mainly include the plasma generation system, the control system of simulated gas, and the diagnosis system of characteristic parameter. The plasma generation system includes

a high-voltage AC power supply (CTP-2000K), a self-designed DBD reactor with the liquid-grounded electrode. Detailed parameters of the DBD reactor can be found in our previous study [18]. The NaCl (Analytical Purity $\geq$ 99.5%) solution was pumped into the reaction chamber for circulation. The solution conductivity was determined by a portable conductivity meter (DDS-11A). The simulated exhaust gas was mixed by N_2, O_2, NO, NO_2. The simulated exhaust gas flow rates and composition fractions were controlled by mass flow meters (CS200AD). The diagnostic system of feature parameters consisted an exhaust gas analyzer (Model 3080UV), a digital oscilloscope and an eight-channel fiber spectrometer (MX2500+). The discharge image was taken by the digital camera Canon DS126201. Finally, the treated exhaust gas was washed by a chemical washing bottle.
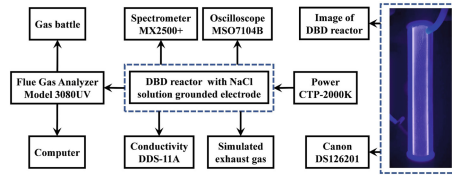
Fig. 1. Experimental system diagram of the DBD de-NOx with liquid grounded electrode.

2.2 Experimental Conditions

The temperature of the NaCl solution and the initial exhaust gas NOx were kept at 300 K. The discharge frequency and conductivity of NaCl solution were 8 kHz and 32 mS/cm, respectively [18]. The effects of simulated exhaust gas flow rate, O_2 concentration, NO concentration, NO_2 concentration on de-NOx performances were studied in this paper. The parameters of exhaust gas NOx are shown in Table 1.

Table 1. Specific parameters of simulated exhaust gas NO*x*.

Parameters	Value
Exhaust gas flow rate (L/min)	0.4, 0.8, 1.2, 1.6, 2.0
O_2 concentration (%)	0, 2, 4, 6, 8, 10, 12, 14, 16
NO concentration (ppm)	0, 100, 300, 500, 700, 900
NO_2 concentration (ppm)	0, 500

2.3 Data Analysis

Specific energy density (SED) is used to characterize the energy consumption of exhaust gas per unit volume during plasma de-NOx, as shown in Eq. (1).

$$SED = \frac{60 * P_{in}}{1000 * Q} \tag{1}$$

where P_{in} is the input power (W), Q is the simulated exhaust gas flow rate (L/min).

The NOx removal efficiency is shown in Eq. (2).

$$\eta_{NOx} = \frac{C_{NOx-in} - C_{NOx-out}}{C_{NOx-in}} \times 100\% \tag{2}$$

where $C_{NOx\text{-}in}$ is the initial concentration of NOx, $C_{NOx\text{-}out}$ is the concentration of NOx after plasma treatment.

3 Results and Analysis

3.1 Influence of Exhaust Gas Flow Rate on De-NOx Performance

The effect of exhaust gas flow rate on de-NOx performance was studied at the constant molar ratio of exhaust gas NOx (4% O_2, NO 500 ppm, NO_2 0 ppm). Figure 2(a-b) show the variation of NOx removal efficiency versus the exhaust gas flow rate. The NOx removal efficiency decreases as the exhaust gas flow rate at the same input power. The NOx removal efficiency reaches highest 97.67% when the exhaust gas flow rate is 0.4 L/min and the power is 44 W. This is because the SED decreases with the gas flow rate, which resulting in the reduction of the dissociation reaction rate and the active particles. In addition, the residence time of exhaust gas in the reaction zone decreases [19, 20]. However, to achieve the same de-NOx efficiency, the larger the exhaust gas flow rate, the smaller the SED is required. When the de-NOx efficiency is 92.71%, the SED required for the exhaust gas system with a flow rate of 2.0 L/min is the minimum, which is 3.15 kJ/L. It is found that the bigger flow rate can make the distribution of charged particles more dispersed [16]. A large flow rate can improve the uniformity of DBD discharge, but excessive flow rate will lead to insufficient de- NOx reactions. So, there is an optimal flow rate value. This pattern has also been confirmed by relevant reports [21, 22].
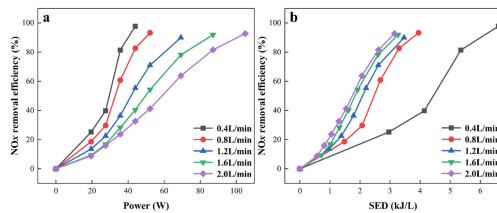
Fig. 2. Influence of exhaust gas flow rate on de-NOx performance.

3.2 Effect of O_2 Concentration on De-NOx Performance

Effect of NOx Components on de-NOx Performance Without O_2

The exhaust gas flow rate of 2.0 L/min was selected, and the NOx concentration was set

at 500 ppm. The effect of NOx components on de-NOx performance was studied in the absence of oxygen, as shown in Fig. 3. When the initial NOx component is only NO, the NO concentration first decreases rapidly with the SED, and then slowly decreases to 0 ppm. The NO_2 concentration increases slightly during the initial discharge phase, reaching a maximum of 17 ppm at 0.65 kJ/L, and then gradually decreasing to 0 ppm. This is because O atoms, which can easily recombine with NO to form low concentration NO_2, is one of the yields of NO reduction. When the initial NOx component is only NO_2, the change trend of the NO_2 concentration is similar with that of NO alone. However, the NO concentration increases obviously in the initial discharge phase, reaching the maximum value of 94ppm at 0.65 kJ/L, and then gradually decreases to 0ppm. It is pointed out that NO_2 removal process can be divided into two phases. NO_2 is reduced to NO and then NO is reduced to N_2, as shown in Fig. 3a. Figure 3b shows the effect of NOx components on removal efficiency. The NOx can be basically removed in the absence of oxygen. And the discharge process is close to dispersion uniform discharge [23]. Furthermore, the removal efficiency of NO is higher than that of NO_2 due to NO removal only needs one stage. The difference of between the two can reach 15.85% at 0.65 kJ/L.
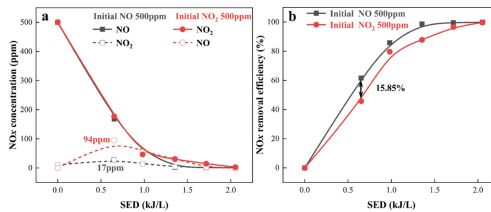
Fig. 3. Effect of NOx components on de-NOx performance without O_2.

Effect of Oxygen Concentration on De-NOx Performance

The N_2/O_2/NOx (NO 500 ppm, NO_2 0 ppm) system with a total flow rate of 2 L/min was built. The effects of different O_2 concentrations (2%–16%) on the de-NOx perfor- mance were studied, as shown in Fig. 4. Figure 4 (a-c) show the variation curves of NO, NO_2 and O_3 versus SED at different oxygen concentrations. In order to facilitate the analysis, O_2 concentrations were divided into three levels: oxygen-poor condition (2%–4%), oxygen-medium condition (6%–10%), and oxygen-enriched condition (12%– 16%). Under oxygen-poor condition, the NO concentration decreases rapidly to close to 0 ppm as SED increases, while the NO_2 concentration reaches the maximum and is accompanied by the production of O_3. With the further increase of SED, the NO_2 concentration gradually decreases, and the O_3 concentration increases rapidly and then flattens. It is pointed out that NOx reduction pathway dominates. Moreover, the transition from NOx mode to O_3 mode occurs during the NOx removal process (NOx decreases, O_3 increases). This is because the fact that NO accelerates the quenching of O_3 [24]. O_3 shows a rapid and then slow growth trend after NO is removed. This is because the temperature of the reaction zone rises with the increase of SED, accelerating the decomposition of O_3 [25]. Under oxygen-medium condition, The NO first decreases

rapidly with SED, and then stabilizes. The NO_2 concentration first rises rapidly and then maintains at a stable trend. And the increase of NO_2 is basically close to the decreases of NO. It can be seen that the NO oxidation pathway dominates, and O_3-free is produced due to the residues of NO. Under oxygen-enriched condition, the NO concentration first decreases with SED and then gradually rises. The NO_2 concentration remains stable after rapid increases. And the NO_2 growth was higher than the reduction of NO. Figure 4d shows the removal efficiency of NOx at different O_2 concentrations. Under the conditions of oxygen-poor, oxygen-medium and oxygen-enriched, the NOx removal efficiency is greater than 90%, less than 40% and negative, respectively. This is because the reaction rate of $N(2D) + O_2 \rightarrow NO + O$ increases with the O_2 concentration, generating extra NO. Thus, the exhaust gas system shows a NOx growth pattern [26], and only part of NO is removed.
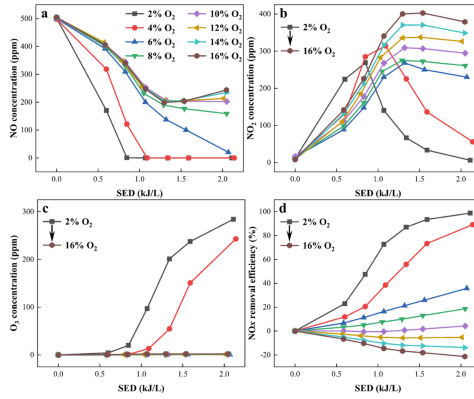
Fig. 4. Effect of oxygen concentration on de-NOx performance.

Diagnosis of Plasma Optical Emission Spectroscopy

The optical emission spectroscopy (OES) is a non-invasive plasma diagnostic technique, which is usually used to characterize the discharge collision processes of species excitation and ionization [27]. Figure 5 shows the OES for N_2 and simulated exhaust gas with oxygen-poor. Firstly, the OES of N_2 mainly includes spectrum bands such as the NOγ, the second positive system (SPS), the first negative system (FNS), the first positive system (FPS), and a series of N atoms spectrum lines (742.4 nm, 744.2 nm, 746.8 nm, 868.0 nm, etc.). It is noticeable that there is a NOγ spectrum band at N_2 discharge. It is because the N_2 used in the experiment contains trace amounts of water vapor. This phenomenon is also supported by relevant literature [28]. In addition, the intensity of N atoms spectrum lines is relatively weak. However, The N atoms is an important active radical for exhaust gas NOx to achieve high N_2 selectivity [29]. Secondly, the OES of simulated exhaust gas with oxygen-poor shows that the NOγ spectrum bond basically disappears. It is confirmed that NO has been basically removed. In addition, the O atoms spectrum lines are observed at the wavelength of 777.4 nm and 844.6 nm. The O atoms are a kind of reactive radical with strong oxidation, which can be combined with

background gas to produce O_3. The O atoms and O_3 molecules cooperate to create an oxidizing atmosphere [30].
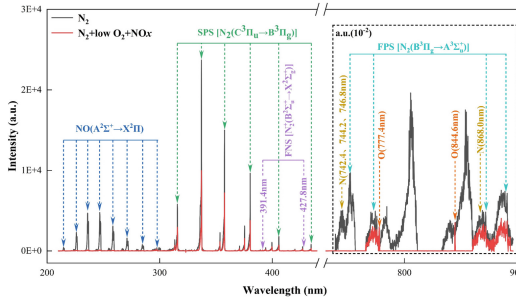
Fig. 5. Plasma optical emission spectroscopy of N_2 and oxygen-poor simulated exhaust gas.

3.3   Effect of NO Concentration on de-NOx Performance

Figure 6 shows the effect of NO concentration on de-NOx performance. The variation of NOx removal efficiency with the SED at different initial NO concentration is shown in Fig. 6a. The NOx removal efficiency is the highest at an initial NO concentration of 100 ppm, reaching a maximum of 97% at 2.1 kJ/L. The NOx removal efficiency decreases with the NO concentration which accompanied by the increase of energy consumption. This phenomenon is also confirmed in the literature [21]. The variation of SED with NO concentration at the same de-NOx efficiency is further analyzed as shown in Fig. 6b. The initial NO concentration of 100 ppm is normalized to unit volume fraction, and the required SED is considered as the calculation basis. The theoretical SED values required for other NO concentrations at the same removal efficiency are calculated by the law of equal proportional increase, and compared with the experimental results. The results show that the SED required for the experiment increase proportionally at first and then tends to slow down gradually with the increase of the initial NO concentration. And the experimental value is lower than the theoretical value at the higher NO concentration. In addition, the difference between experimental and theoretical value of SED increases with the improvement of removal efficiency. The SED required for the experiment is 1.8 times lower than the theoretical value when the de-NOx efficiency is 75% and the initial NO concentration is 900 ppm. It is found that increasing the NO concentration of the reactant can increase the number of activated molecules, the number of effective collisions and the reaction rate. Therefore, increasing the NO concentration can reduce the energy consumption of NO removal per unit volume fraction.
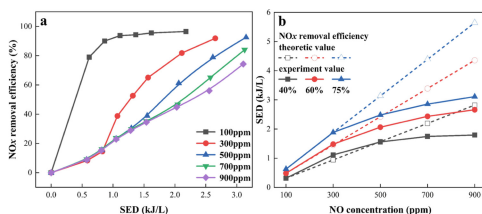
Fig. 6. Effect of initial NO concentration on de-NOx performance.

4   Conclusions

In this paper, the effects of simulated exhaust gas NOx flow rate, O_2 concentration and NO concentration on de-NOx performance were studied based on a DBD reactor of NaCl solution grounded electrode. Firstly, it is revealed that the de-NOx efficiency is higher under the low exhaust gas flow rate. While the energy consumption per unit volume exhaust gas is lower at high exhaust gas flow rate. Secondly, the influence of O_2 concentration on NOx removal was elaborated. At the oxygen-free condition, NOx removal efficiency is close to100%. It is noticeable that NO can be reduced by only one step, while NO_2 removal requires two-steps. At the oxygen-poor condition, the plasma discharge area of simulated exhaust gas NOx is a reducing environment, and the de-NOx efficiency is high. Under the oxygen-medium condition, the de-NOx efficiency is low. Under oxygen-enriched condition, the simulated exhaust NOx shows a growth mode. Finally, it is pointed out that higher NO concentration can reduce the energy consumption of NO per unit volume fraction. In this work, it is confirmed that the DBD reactor with liquid-grounded electrode has better discharge characteristics and de-NOx performances than the traditional DBD reactor.

References

1. Richter, A., Burrows, J.P., Nüß, H., Granier, C., Niemeier, U.: Increase in tropospheric nitrogen dioxide over China observed from space. Nature **437**(7055), 129–132 (2005)
2. Carr, E.W., Corbett, J.: Ship compliance in emission control areas: technology costs and policy instruments. Environ. Sci. Technol. **49**(16) (2015)
3. Paolucci, C., et al.: Dynamic multinuclear sites formed by mobilized copper ions in NOx selective catalytic reduction. Science **357**(6354), 898–903 (2017)
4. Veerapandian, S.K.P.: Regeneration of Hopcalite used for the adsorption plasma catalytic removal of toluene by non-thermal plasma. J. Hazard. Mater. **402**, 123877 (2021)
5. Wang, H., Yuan, B., Hao, R., Zhao, Y., Wang, X.: A critical review on the method of simultaneous removal of multi-air-pollutant in flue gas. Chem. Eng. J. **378**, 122155 (2019). https://doi.org/10.1016/j.cej.2019.122155
6. Tendero, C., Tixier, C., Tristant, P., Desmaison, J., Leprince, P.: Atmospheric pressure plasmas: a review. Spectrochim. Acta, Part B **61**(1), 2–30 (2006)
7. Obradović, B.M., Sretenović, G.B., Kuraica, M.M.: A dual-use of DBD plasma for simultaneous NOx and SO2 removal from coal-combustion flue gas. J. Hazard. Mater. **185**(2–3), 1280–1286 (2011)
8. Stasiulaitiene, I.: Comparative life cycle assessment of plasma-based and traditional exhaust gas treatment technologies. J. Clean. Prod. **112**, 1804–1812 (2016)

9. Jiang, B., et al.: Plasma-enhanced low temperature NH3-SCR of NOx over a Cu-Mn/SAPO-34 catalyst under oxygen-rich conditions. Appl. Catal. B: Environ. **286**, 119886 (2021). https://doi.org/10.1016/j.apcatb.2021.119886

10. Okubo, M.: Recent development of technology in scale-up of plasma reactors for environmental and energy applications. Plasma Chem. Plasma Process. **42**(1), 3–33 (2021). https://doi.org/10.1007/s11090-021-10201-7

11. Chen, S., Feng, W., Wang, H., Zhongbiao, W.: Synergistic degradation of NO and ethyl acetate by plasma activated "pseudo photocatalysis" on Ce/ZnGa2O4/NH2-UiO-66 catalyst: restrictive relation and reaction pathways exploration. Chem. Eng. J. **421**, 129725 (2021). https://doi.org/10.1016/j.cej.2021.129725

12. Niu, G.: Design and electrical analysis of multi-electrode cylindrical dielectric barrier discharge plasma reactor. IEEE Trans. Plasma Sci. **47**(1), 419–426 (2019)

13. Zhang, S., Gao, Y., Sun, H., Fan, Z., Shao, T.: Dry reforming of methane by microsecond pulsed dielectric barrier discharge plasma: Optimizing the reactor structures. High Voltage **7**(4), 718–729 (2022). https://doi.org/10.1049/hve2.12201

14. Lee, B., Kim, D.-W., Park, D.-W.: Dielectric barrier discharge reactor with the segmented electrodes for decomposition of toluene adsorbed on bare-zeolite. Chem. Eng. J. **357**, 188–197 (2019)

15. Pavon, S., Dorier, J.L., Hollenstein, C., Ott, P., Leyland, P.: Effects of high-speed airflows on a surface dielectric barrier discharge. J. Phys. D Appl. Phys. **40**(6), 1733–1741 (2007)

16. Guo, H., Yan, H., Liu, Y., Fan, Z., Wang, Y., Ren, C.: Experimental study on uniformity of dielectric barrier discharge generated by nanosecond pulse in atmospheric air. Phys. Plasmas **25**(9), 093505 (2018). https://doi.org/10.1063/1.5038943

17. Viegas, P., et al.: Quantification of surface charging memory effect in ionization wave dynamics. Sci. Rep. **12**(1), 1181 (2022)

18. Zhang, W., et al.: Experimental and mechanism research on the NOx removal by a novel liquid electrode dielectric barrier discharge reactor. Chem. Eng. J. **443**, 136375 (2022)

19. Srinivasan, A., Rajagopala, R., Jagadisha, N., Bharghavi, A.: A laboratory investigation of pulsed discharged based techniques for engine exhaust treatment—Effect of exhaust nature and operating conditions. Int. J. Plasma Environ. Sci. Technol **6**(3), 215–221 (2012)

20. Mohapatro, S., Rajanikanth, B.S.: Studies on NOx removal from diesel engine exhaust using duct-type DBD reactor. IEEE Trans. Ind. Appl. **51**(3), 2489–2496 (2014)

21. Cui, S., Hao, R., Fu, D.: Integrated method of non-thermal plasma combined with catalytical oxidation for simultaneous removal of SO2 and NO. Fuel **246**, 365–374 (2019)

22. Yamasaki, H., Koizumi, Y., Kuroki, T., Okubo, M.: Plasma–chemical hybrid NOx removal in flue gas from semiconductor manufacturing industries using a blade-dielectric barrier-type plasma reactor. Energies **12**(14), 2717 (2019). https://doi.org/10.3390/en12142717

23. Luo, H., Liang, Z., Wang, X., Guan, Z., Wang, L.: Homogeneous dielectric barrier discharge in nitrogen at atmospheric pressure. J. Phys. D Appl. Phys. **43**(15), 155201 (2010)

24. Shimizu, T., Sakiyama, Y., Graves, D.B., Zimmermann, J.L., Morfill, G.E.: The dynamics of ozone generation and mode transition in air surface micro-discharge plasma at atmospheric pressure. New J. Phys. **14**(10), 103028 (2012). https://doi.org/10.1088/1367-2630/14/10/103028

25. Yuan, D.: Ozone production with dielectric barrier discharge from: air the influence of pulse polarity. Ozone Sci. Eng. **40**(6), 494–502 (2018)

26. Park, S., Choe, W., Jo, C.: Interplay among ozone and nitrogen oxides in air plasmas: Rapid change in plasma chemistry. Chem. Eng. J. **352**, 1014–1021 (2018)

27. Šimek, M.: Optical diagnostics of streamer discharges in atmospheric gases. J. Phys. D Appl. Phys. **47**(46), 463001 (2014)

28. Lamichhane, P., et al.: Sustainable nitrogen fixation from synergistic effect of photo-electrochemical water splitting and atmospheric pressure N2 plasma. Plasma Sources Sci. Technol. **29**(4), 045026 (2020). https://doi.org/10.1088/1361-6595/ab7f4d
29. Chen, S., Wang, T., Wang, H., Wu, Z.: Insights into the reaction pathways and mechanism of NO removal by SDBD plasma via FT-IR measurements. Fuel Process. Technol. **186**, 125–136 (2019)
30. Jōgi, I., Erme, K., Levoll, E., Raud, J., Stamate, E.: Plasma and catalyst for the oxidation of NOx. Plasma Sources Sci. Technol. **27**(3), 035001 (2018)

Study on the Effect of Release Agent on the Surface Flashover of Plasma Modified Epoxy Resin

Ke Xie[1], Senwei Lu[1], Chun Shao[1], Jun Xie[2], Zihao Xie[2], Yujin Zhang[2], Jiang Liu[2], and Yanze Song[2(✉)]

[1] Guizhou Power Grid Co., Ltd., Anshun 561000, Guizhou, China
[2] North China Electric Power University (Baoding), Baoding 071000, Hebei, China
`songyanze@ncepu.edu.cn`

Abstract. Micron alumina epoxy resin is easy to accumulate a large number of charges under a DC electric field, which leads to flashover along the surface and threatens the operation of the power system. In the paper, we used four common release agents to prepare micron alumina epoxy resin samples, and modified the surface of each sample by plasma technology. We explored the effect of release agent on the physicochemical properties of plasma modified epoxy resin by SEM and XPS. Finally, we tested the flashover voltage, charge dissipation rate, and trap distribution, and analyzed the influence of release agent and plasma etching on the electrical properties of epoxy resin. The results show that the four release agents have different effects on the flashover voltage of epoxy resin; Plasma etching introduces the physical traps and chemical shallow traps, and increases the charge dissipation rate of epoxy resin. The flashover voltage of epoxy resin increases first and then decreases with etching time of plasma. The various test methods and test results used in this paper will help to reveal the intrinsic connection between the gas-solid interface properties of epoxy materials and DC flashover, and provide a possible scheme to improve the DC flashover performance of insulating materials.

Keywords: Release Agent · Plasma Etching · Epoxy Resin · Surface Flashover

1 Introduction

With the rapid development of the HVDC transmission system, the power system has put forward higher requirements for the insulation performance of electrical equipment [1]. HVDC is suitable for long-distance and large-capacity power transmission, which is convenient to realize the allocation of resources in a wide range. For areas where overhead lines are difficult to erect, we often use gas-insulated transmission lines (GIL) to realize HVDC [2]. At present, alumina epoxy resin is commonly used as insulation supports for DC transmission equipment such as gas-insulated transmission lines. However, epoxy resin tends to accumulate a large number of charges under the DC electric field, which leads to surface flashover and seriously threatens the operation of the power system [3].

The results show that the surface flashover of epoxy resin is closely related to the accumulation and dispersion of surface charge at the gas-solid interface. The movement characteristics of surface charge are affected by the surface morphology, chemical composition, and electrical parameters of the material, and it specifically includes surface roughness, functional group content, surface conductivity, and volume conductivity, traps energy level distribution, etc. [4, 5]. Low-temperature plasma etching technology has the characteristics of high reaction efficiency, simple operation, energy saving, and environmental protection, and it can achieve surface modification safely and efficiently [6]. Therefore, many scholars use the plasma etching effect to improve the surface flashover performance of insulating materials. Seok et al. used DBD (Dielectric Barrier Discharge) to modulate the etching depth of the SiC surface by varying the power supply parameters and gas occupancy in an NF3/He gas atmosphere [7]. Dai et al. used a plasma jet device to etch the material in a He/O2 gas mixture and etched different microporous properties in the material by controlling the distance between the nozzle and the material, the oxygen content and the etching time [8]. Luan et al. achieved the surface etching of polystyrene, polymethyl methacrylate and polyvinyl alcohol in Ar/O2 mixed gas by using radio frequency plasma jet device [9]. Shao et al. found that plasma etching increases the flashover voltage of the epoxy resin and changes the surface chemical composition of the epoxy resin, which in turn affects the surface charge dissipation rate and trap level distribution [10]. Zhang Caiqin et al. used DBD and atmospheric pressure plasma jet devices to physically etch the surface of epoxy resin, and found that the surface roughness, surface conductivity, flasticity voltage and charge dissipation rate of the sample increased after etching [11].

To sum up, although scholars at home and abroad have carried out much research on plasma etching modification and improvement of surface flashover performance of composite materials, most of them only focus on the improvement of composite materials by plasma treatment while ignoring the influence of process parameters in material preparation [12, 13]. The epoxy insulator used in the actual GIL is produced in a standardized and large-scale way by a specific process flow. As a thermosetting resin, epoxy material is mainly produced by high-temperature curing molding [14]. To ensure that the epoxy insulator can be separated from the metal mold after molding, it is necessary to apply the mold release agent when the mold is installed and the release agent directly contacts the insulator surface, so it will have a certain impact on the interface characteristics and surface flashover performance of epoxy materials [15]. Therefore, studying the process parameters of epoxy resin will be helpful to further reveal its gas-solid interface characteristics and improve the effect of plasma surface modification.

In this paper, we used four common release agents to prepare micron alumina epoxy resin samples, and we modified the surface of each sample by plasma technology. And we investigated the effects of mold release agents on the physical and chemical properties of plasma-modified epoxy resin interface by various testing methods. Finally, we tested the flashover voltage, charge dissipation rate, and trap distribution, and analyzed the influence of release agent and plasma etching on the electrical properties of epoxy resin.

2   Experimental Device and Test Platform

2.1   Sample Preparation

The sample materials used in this paper were epoxy resin samples doped with micron alumina particles, which were made by our research team. The micron alumina epoxy resin sample was based on bisphenol A diglycidyl ether (DGEBA, RD518) produced by Shanghai Resin Factory Co., Ltd., with methyl tetrahydro phthalic anhydride (MTHPA,504) as curing agent,2,4,6- tris (dimethylaminomethyl) phenol (DMP30) as an accelerator, and 10 u m Al:O produced by Shanghai Chaowei Nanotechnology Co., Ltd. The ratio of epoxy resin, curing agent, alumina filler, and accelerator in the sample was 100:80:300:1. The preparation experimental process is shown in Fig. 1.
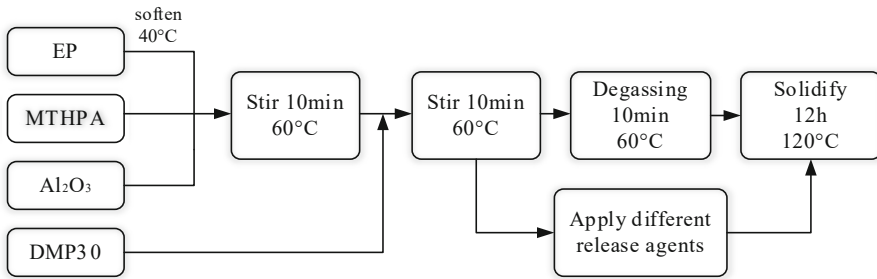
Fig. 1. Alumina epoxy resin sample preparation process

2.2   Plasma Etching

In this paper, we used DBD to achieve uniform etching on the sample surface, as shown in Fig. 2. The plasma DBD device consisted of two parts: a circuit and a gas path. The circuit part mainly included a high-frequency power supply, DBD reactor and oscilloscope. The gas path part mainly included an argon gas bottle, exhaust gas processor and mass flow controller.

After the sample was prepared, we first clean the surface of the sample with anhydrous ethanol. Then we put the sample into a drying oven for 2 h. Finally, we conducted plasma surface etching experiments in a constant temperature laboratory with a temperature of 25 °C and a humidity of 40%. The etching time of plasma surface was set as 1 min, 2 min, 3 min, 4 min and 5 min, and the samples were labeled according to the different release agents. If marked 95-DBD-1, it meant that the sample prepared with release agent 95 had been physically etched for 1 min.

2.3   Sample Characterization and Testing

This paper tested the surface morphology, chemical composition, and surface electrical properties of micron alumina epoxy resin before and after physical etching on the plasma
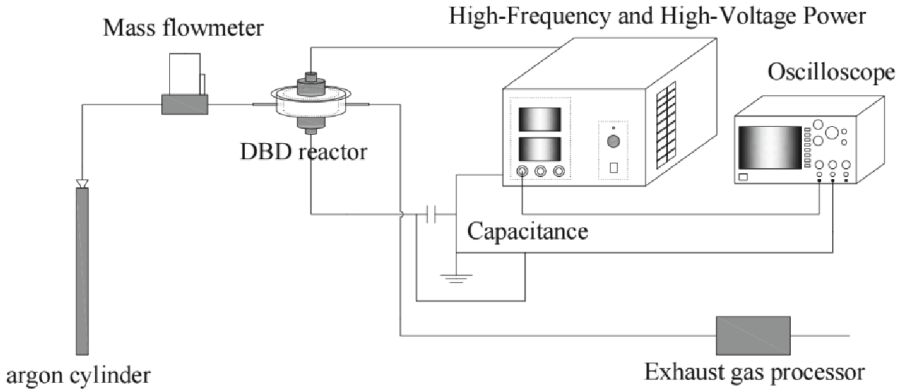
Fig. 2. Plasma dielectric barrier discharge modified platform

surface. Scanning Electron Microscope (SEM) observed the surface morphology of the filler. X-ray Photoelectron Spectroscopy (XPS) was used to obtain surface element composition and relative content.

The negative polarity flashover test along the surface was carried out on the samples with different release agents and different treatment times, as shown in Fig. 3. The electrode spacing was 7 mm and the radius of the finger electrode was 7.5 mm. A negative polarity DC source is applied to ramp up the electrode at a uniform rate of 50 V/s until a flashover occurs along the face. For each type of release agent, 4 samples were tested for 15 times at each treatment time, with each test interval of 1 h. We used Weibull distribution to analyze the absolute value of negative flashover voltage and determine the final flashover voltage.
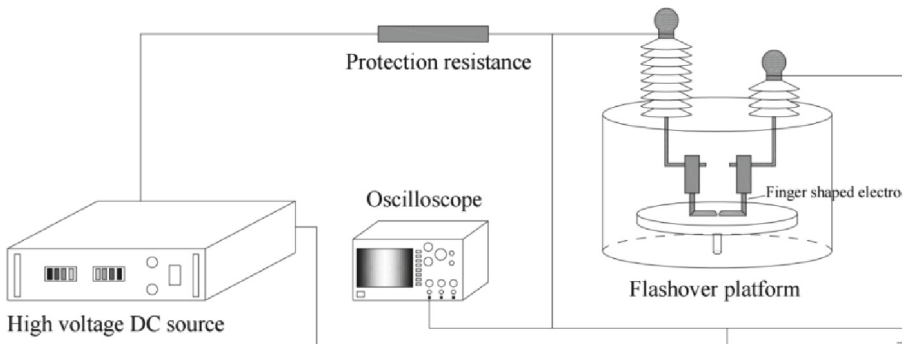
Fig. 3. Flashover experiment platform

To investigate the surface charge and trap distribution characteristics of micron alumina epoxy resin with different release agents at different treatment times, the experimental facility shown in Fig. 4 was applied to test the decay rate of the surface potential of sample. A needle with a length of 10 cm and a curvature of 0.5 mm was suspended
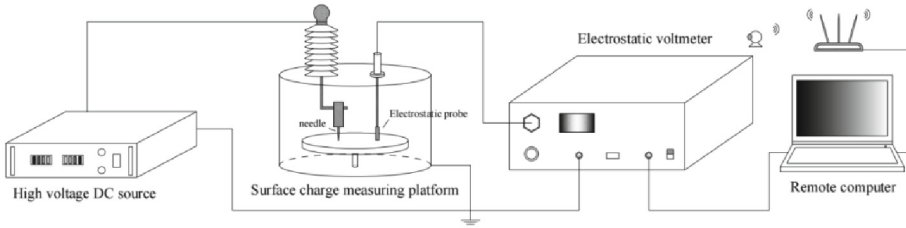
Fig. 4. Surface charge measuring platform

5 mm above the specimen and charged the surface of the specimen for 1 min. An probe was suspended 2 mm above the specimen for single-point potential dissipation measurement with a sampling frequency of 0.01 kHz, and the surface potential decay data were recorded within 30 min.

3   Experimental Result

3.1   Sample Surface Morphology and Elemental Changes

Since the processing means of the samples prepared by different release agents were the same, and the processing time was 0–5 min, SEM was used to observe the microscopic morphology of the filler surface of the treated alumina epoxy resin samples according to the different processing times of different release agents, and the SEM images of the selected 95-DBD 0–5 min samples are shown in Fig. 5. It can be found that the surface of the untreated sample is relatively flat except for a small number of burrs, and after 1 min of plasma physical etching on the surface of the sample, protrusions and grooves begin to appear on the surface of the sample, and part of the Al_2O_3 filler is exposed. After 5 min of plasma etching, the protrusions and grooves on the surface of the sample further increased, which not only aggravated the exposure of the filler, but also many fillers were etched, and the surface flatness was affected. A similar pattern can be obtained by comparing the SEM images of the epoxy resin samples under different release agents, which are not listed here.

All samples etched for 5 min were selected for XPS testing, and the C 1s peaks of all samples were separated into peaks, and the results are shown in Fig. 6(a)–(e). The samples with fluorine-based release agents had obvious F 1 s peaks at 688–689 eV, which were attributed to the organic fluoride in the release agent. The epoxy resin used in this paper contains Si elements, and all five samples show Si 2s peaks and Si 2p peaks at 150.5 eV and 102 eV, respectively. The peaks at 284.8 eV and 286 eV corresponded to C-C and C-O bonds, respectively, peaks corresponding to C=O bonds were present at 288.5 eV for the unused release agent sample, the fluorinated release agent sample and the release wax sample.

In addition, the changes of chemical elements on the sample surface before and after modification can be known by XPS, and the XPS plots of selected 95-DBD-0 and 95-DBD-5 samples are shown in Fig. 6(f). It was found that with the increase of etching time, the relative content of carbon elements on the surface of the samples gradually

(a) untreated   (b) 1 min etching   (c) 2 min etching

(d) 3 min etching   (e) 4 min etching   (f) 5 min etching
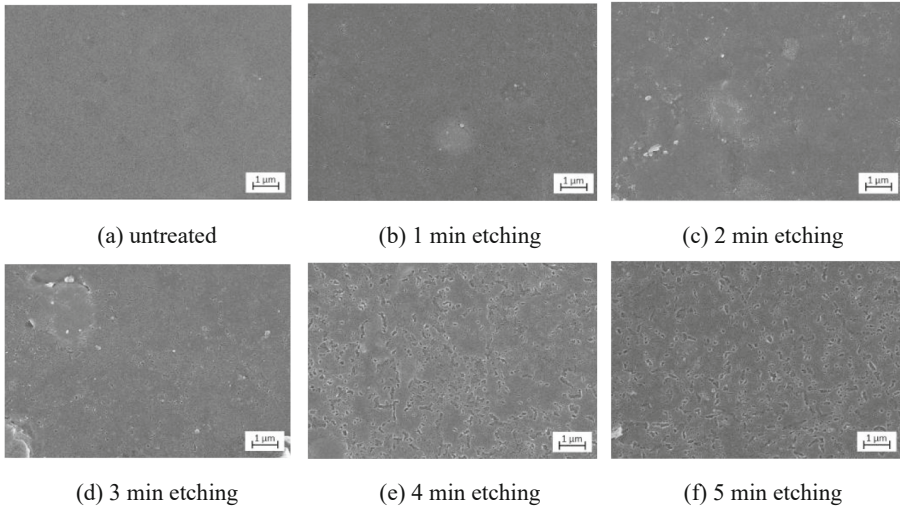
Fig. 5. SEM image of epoxy resin surface before and after plasma fluorination

decreased, while the relative content of oxygen elements gradually increased. The C 1s peaks of the samples with different etching times were divided into peaks, and it was found that the C-O bond and C=O bond contents on the surface of the plasma-etched samples increased.

In summary, the analysis suggests that this is because after the sample is moved out of the reactor after the argon plasma DBD treatment is completed, the high-energy groups on the surface come into contact with air, generating oxygen-containing functional groups such as hydroxyl groups, and reorganize with the chemical bonds on the surface of the sample that are also broken by high energy, thus grafting oxygen elements onto the sample.

Figure 7 shows the relative elemental contents of the five types of samples after etching for 5 min. Among them, the relative elemental content of F is the most in the sample prepared by the fluorine release agent, and the relative elemental content of F is less in the sample prepared by other release agents. After the plasma etching process was completed, the samples were removed from the reactor, and the high-energy groups on the surface came into contact with air and formed C-O bonds and C=O double bonds, so the samples had the highest relative elemental content of O. The silicon release agent has a layer of oil film on the surface, which hinders the etching, and the release wax will also leave more wax on the surface of the sample, so the C-O bond and C=O bond are not formed on the surface of both.

3.2   Results of Flashover Along the Surface

The variation of flashover voltage along the surface of micron alumina epoxy resin samples with different release agents at different treatment times is shown in Fig. 8. The horizontal coordinate of the graph is the plasma physical etching treatment time, and the different release agents are replaced by different colors, where the 11 kV horizontal

(a) Original

(b) Silicon release agent

(c) Fluorine release agent

(d) Aliphatic hydrocarbon release agent

(e)Epoxy resin release wax

(f)XPS images before and after plasma modification
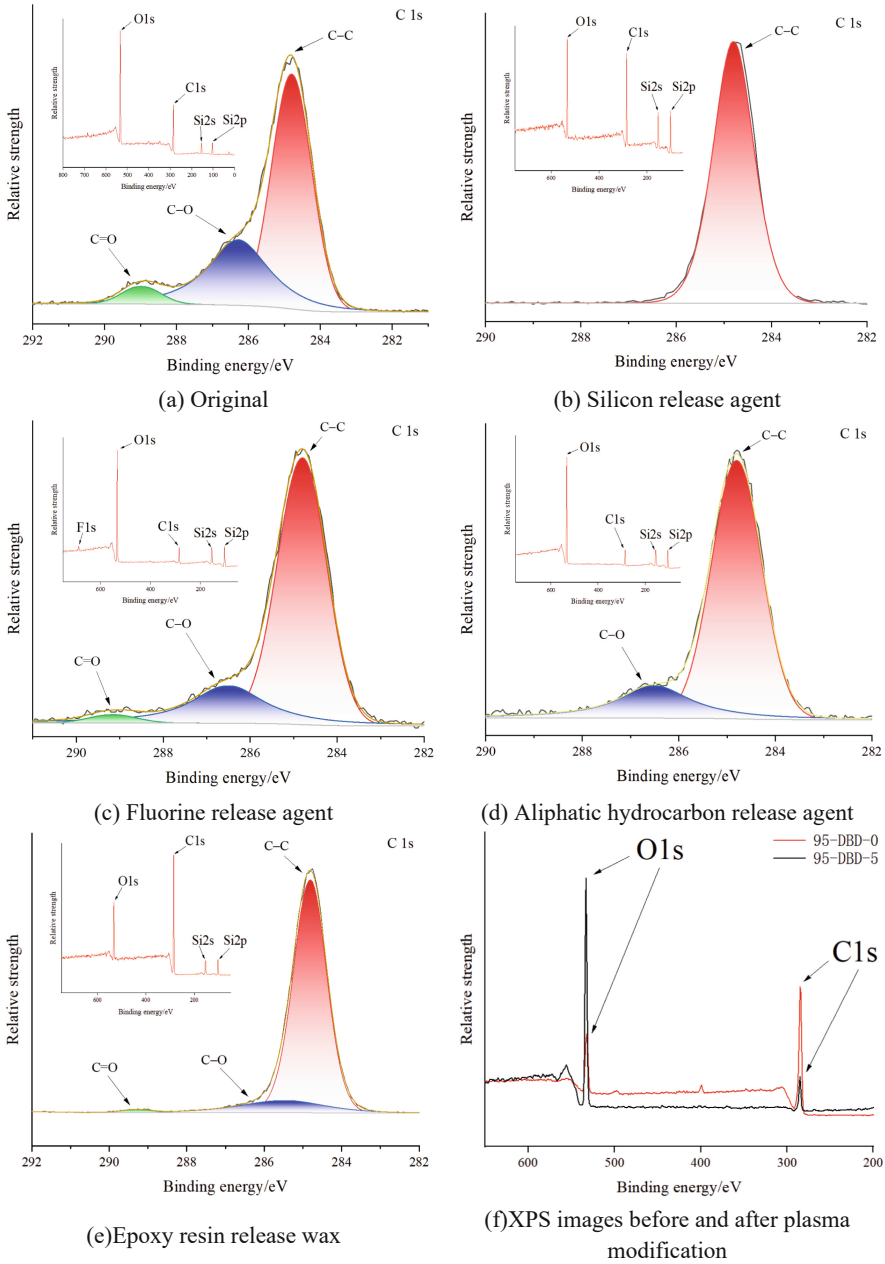
Fig. 6. XPS images of all samples

line represents the flashover voltage of the original sample without the release agent. From the figure, it can be seen that the plasma physical etching of epoxy resin samples with different release agents can increase the flashover voltage along the surface of the
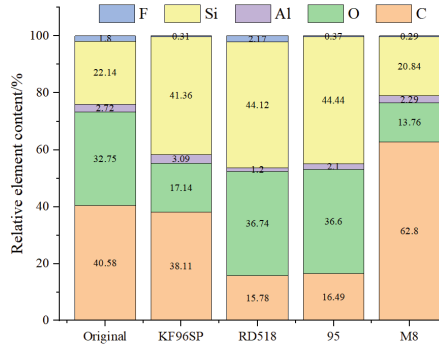
Fig. 7. Relative element content of all samples
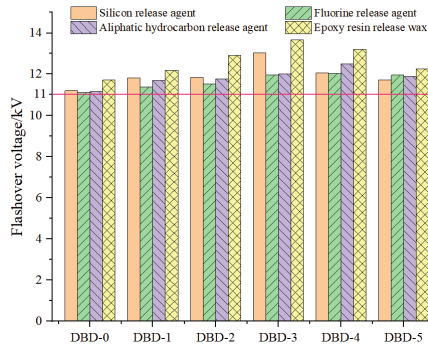
Fig. 8. Flashover voltage before and after plasma modification

samples, but the increase is different, among which the epoxy resin release wax has the best increase effect, reaching 13.67 kV after 3 min of etching, with an increasing effect of 16.7%. Taking the plasma physical etching treatment time as the variable, it was found that the overall flashover voltage of the samples showed a trend of increasing and then gradually decreasing with the increase in treatment time. The highest flashover voltage was achieved at 3 min of etching for the samples prepared with silicone release agent and epoxy resin release wax. The sample prepared by the fluorine release agent and aliphatic hydrocarbon release agent reached the highest flash voltage at 4 min of etching. It indicates that different release agents have certain effects on the flashing along the DC surface of the plasma-modified epoxy resin, but the modification trend is basically the same.

3.3 Surface Charge Dissipation and Trap Distribution

In this paper, the single-point surface potential decay of the sample was measured before and after the modification for 30 min, and the surface potential decay curve of the sample was obtained by normalization, as shown in Fig. 9. It is found that plasma surface etching can enhance the surface potential decay rate, and it gradually accelerates with the increase of the time of physical etching on the plasma surface.

Isothermal Surface Potential Decay (ISPD) uses DC charging to deposit a certain amount of charge on the material surface, and the internal charge transport characteristics and trap distribution characteristics are explored by measuring the charge variation law with time [16]. The ISPD theory is further used to calculate the distribution of trap energy levels for different slices. The trap energy level of the insulating material and the trap energy level density satisfies the following relationship.

$$E_t = kT \ln(\gamma t) \tag{1}$$

$$N(E_t) = \frac{\varepsilon_0 \varepsilon_r t}{kTf_0(E_t)\delta L} \frac{dV(t)}{dt} \tag{2}$$

where $V(t)$ is the surface potential decay function, k is the Boltzmann constant, T is the ambient test temperature, γ is the electron escape frequency, ε_0 and ε_r are the vacuum permittivity and relative permittivity, respectively. The surface potential decay curve in Fig. 9 satisfies the double exponential function distribution, and $V(t)$ can be expressed as:

$$V(t) = ae^{-t/c} + be^{-t/d} \tag{3}$$

where a, b, c, and d are the fitting parameters of the double exponential function. The calculated trap curves can be used to analyze the flash performance of the composite from both deep and shallow trap perspectives, as shown in Fig. 10.

It was found that the trap energy levels of the four samples after modification gradually became shallower and the content of shallow traps gradually increased. Combining the changes in surface morphology and chemical elements in Sect. 2.1, it is clear that plasma etching improves the surface roughness and increases the physical traps on the surface, thus shallowing the surface trap energy levels. On the other hand, plasma etching causes oxygen-containing groups such as hydroxyl groups to graft on the material surface, leading to the introduction of some shallow traps. The combined effect of the two factors accelerates the rate of surface charge dissipation.

(a) silicon release agent

(b) fluorine release agent

(c) aliphatic hydrocarbon release agent

(d) epoxy resin release wax
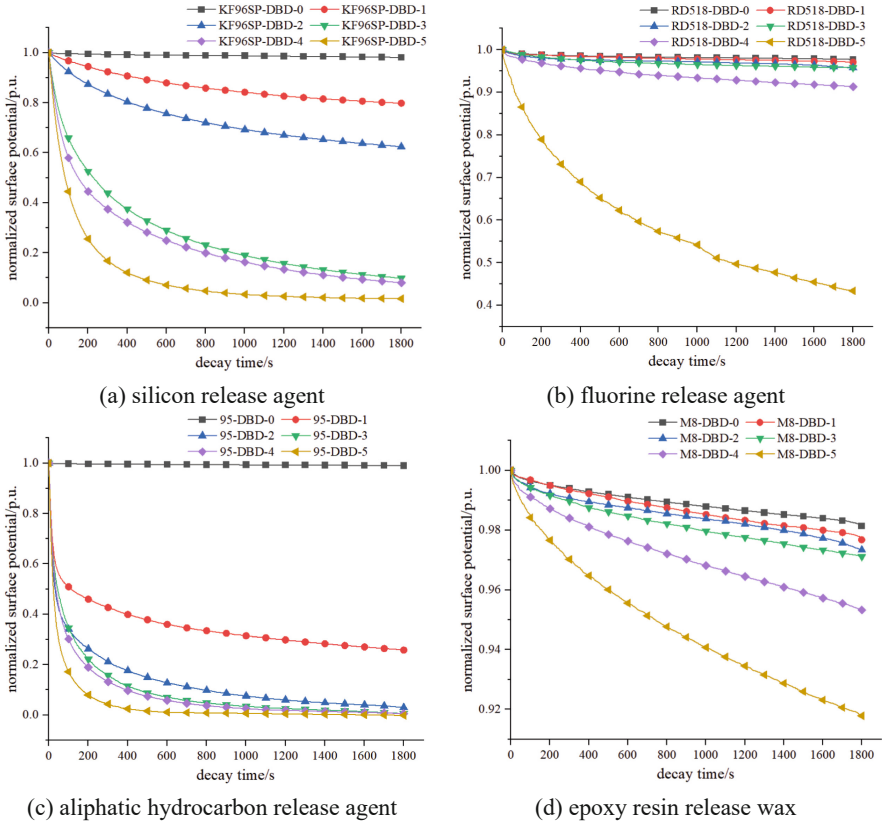
Fig. 9. Surface charge dissipation curves before and after plasma modification

4 Analysis and Discussion

4.1 Effect and Analysis of Different Release Agents on the Electrical Properties of Epoxy Resin

It can be seen from Sect. 2.2 that there are differences in the flashover voltage along the surface of samples by plasma physical etching with different release agents. Due to the different transfer rates of release agents, the release agent will be left on the surface of the sample to varying degrees when the sample is peeled off the mold. According to the release effects of different release agents, the roughness of the contact surface will also be affected [17]. In the process of sample preparation, we find that different release agents can release the mold easily. After demoulding, the surface roughness of the original sample is relatively consistent, but the residual amount of the release agent is different. Therefore, this paper argues that different release agents affect the electrical properties of epoxy resin mainly through the chemical composition remaining on the surface of the sample.

Among the untreated samples prepared by four kinds of release agents, the flashover voltage of samples prepared with silicon release agent, fluorine release agent, and

(a) silicon release agent

(b) fluorine release agent

(c) aliphatic hydrocarbon release agent

(d) epoxy resin release wax
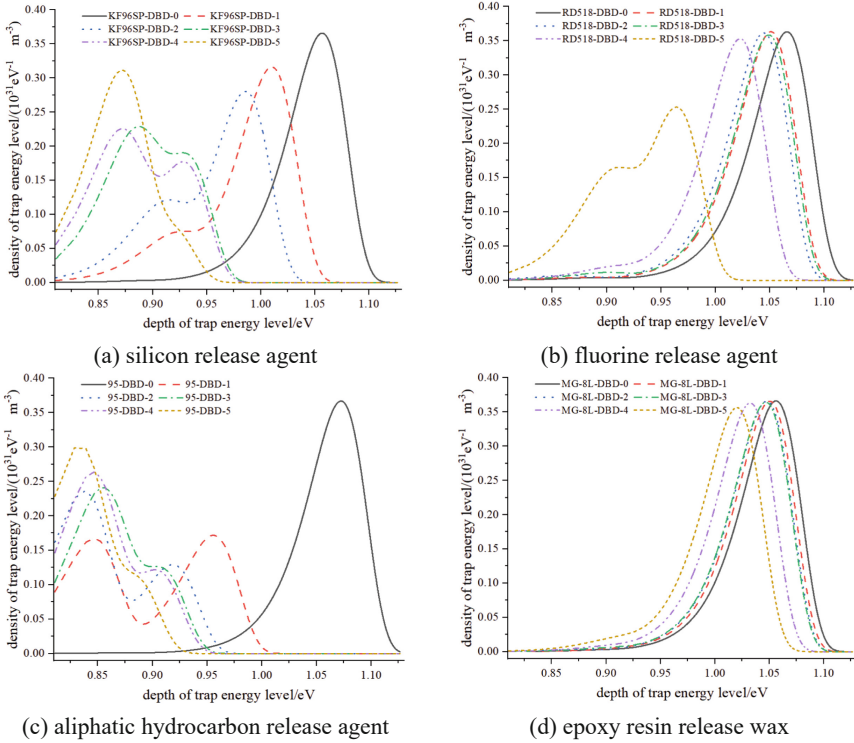
Fig. 10. Curve of trap before and after plasma modification

aliphatic hydrocarbon release agent is relatively low, which is 11.2 kV, 11.11 kV, and 11.15 kV respectively; the flashover voltage of samples prepared with epoxy resin release wax is relatively high, which is 11.71 kV. Organic silicon is a low surface energy material, so the stripping force of release agent made of organic silicon polymer is relatively small. At the same time, there will be more silicone oil remaining on the surface of the sample [18]. Silicone oil is mainly presented with siloxane (polydimethylsiloxane), and siloxane has good chemical stability and electrical insulation. The four valence electrons in the outermost layer of silicon make the silicon atoms in a metastable structure. These valence electrons make the silicon atoms bond with each other in a covalent bond, which makes the covalent bond relatively strong and does not affect the dielectric properties of the sample surface. Fluorine release agent inherits the characteristics of fluorine-containing materials, which can significantly reduce the surface energy of solids and well solve the adhesion problem between finished products and abrasive tools [19]. However, when the release agent is configured, the amount of organic fluoride is very small. Therefore, although fluorine has a strong electron affinity and can absorb electrons, it has little influence on the electrical properties of the sample surface. Aliphatic hydrocarbon release agent mainly uses liquid aliphatic hydrocarbon as a solvent. The highest temperature in the experiment is 120 °C, under which the carbon chain will not break and the chemical properties are stable. At the same time, there is no residue on

the sample surface after the release, so it has little influence on the electrical properties of the sample surface. The release wax is a solid coating agent. Compared with other release agents, the uniformity of the wax is lower. When the sample is peeled off from the mold after curing, the residual amount of the wax is the most. At the same time, in the four kinds of samples, due to the uneven distribution of the residual wax on the surface [20], the surface is also the most uneven. The undulating structure formed increases the creepage distance of the electron, which makes it more able to suppress the movement of the electron compared with the samples prepared by other release agents. Therefore, the flashover voltage of the sample is higher.

4.2 Effect and Analysis of Plasma Physical Etching on the Electrical Properties of Epoxy Resin

Plasma physical etching can change the physical morphology, chemical elements and electrical properties of the sample surface. Due to the limitation of preparation technology and mold accuracy, there are a few burrs and defects on the surface of the unetched sample, which will distort the nearby electric field, generate local corona, accumulate a large amount of charge, and seriously affect the flashover voltage of the sample [21]. After plasma physical etching, the wavy structure formed increases the creepage distance of electrons emitted by the cathode in the electric field, which makes the sample after plasma etching more able to suppress the motion process of electrons. With the increase in etching time, there is a larger undulating structure on the sample surface, which further inhibits the movement of electrons on the sample surface, thus further improving the flashover voltage of the sample. And plasma etching can introduce oxygen-containing functional groups on the surface of the material, thus improving the surface conductivity of the sample. In addition, the introduction of oxygen-containing functional groups can increase the physical trap and chemical shallow trap of the material, so that the surface charge dissipates faster and the distortion ability of the surface charge to the external electric field is inhibited. The combined action of the two factors makes the plasma etching method can effectively improve the surface flashover performance of the sample.

At the same time, a large amount of surface charge accumulates around the three junction points of the finger electrode, which distorts the field intensity extremely. Long-term plasma physical etching in this area can significantly promote the dissipation of surface charge and inhibit the accumulation of surface charge at the three junction points. Therefore, a certain time of plasma physical etching treatment can significantly increase the flashover voltage of the sample. However, the rapid dissipation of surface charge will introduce the seed charge to the development of surface discharge, and provide conditions for the formation of conductive channels. Therefore, long-time plasma etching will reduce the flashover voltage along the surface. In conclusion, plasma physical etching modification can specifically regulate the surface charge characteristics of the sample, and improve the surface flashover performance of the sample.

5 Conclusion

The paper used the argon plasma DBD method to modify micron alumina epoxy resin samples with different release agents. We studied the changes of surface morphology, chemical elements, surface flashover voltage, surface charge dissipation rate, and trap distribution before and after etching. Finally we analyzed the mechanism of improving the surface flashover performance of samples by the release agent and plasma gradient etching modification. The main conclusions are as follows:

(1) The plasma physical etching of epoxy resin samples with different release agents can improve the flashover voltage along the surface, but the increased amplitude is different. Among them, the release wax of epoxy resin has the best improvement, reaching 13.67 kV 3min after etching, and the improvement effect is 16.7%.
(2) By increasing the surface roughness of the sample and grafting oxygen-containing functional groups, the plasma physical etching method introduced the physical traps and the chemical shallow traps on the surface of the sample, accelerated the dissipation of surface charges, and increased the surface flashover voltage of the sample.
(3) The slow dissipation of surface charge will distort the surrounding electric field, but the excessively high dissipation rate will provide favorable conditions for discharge development. Therefore, Accelerating the surface charge dissipation rate at the air-electrode-sample triple junction and controlling the charge transfer rate between the electrodes are helpful to maximize the overall flashover performance of the sample.

References

1. Ma, W.M., Wang, L., Li, M., et al.: SLCC converter technology of UHVDC transmission in new power system. High Voltage Eng. **48**(12), 4941–4948 (2022)
2. Li, P., Yan, X.L., Wang, H., et al.: Research and application of UHVAC gas-insulated transmission line. Power Syst. Technol. **41**(10), 3161–3167 (2017)
3. Sun, Q.Q., Luo, C.J., Wang, F., et al.: Overview on the surface flashover of basin-type insulator in UHV GIS. High Voltage Apparatus **54**(05), 17–25+32 (2018)
4. Ran, H.J., Song, Y.Z., Yan, J.Y., et al.: Improving the surface insulation of epoxy resin by plasma etching. Plasma Sci. Technol **23**(09), 148–157 (2021)
5. Zhan, Z.Y., Ruan, H.O., Lv, F.C., et al.: Plasma fluorinated epoxy resin and its insulation properties in C_4F_7N/CO_2 mixed gas. Trans. China Electrotech. Soc. **35**(08), 1787–1798 (2020)
6. Yan, H.O., Wu, X.: Surface fluorination of epoxy resin by plasma and its surface flashover characteristics. Insulating Mater. **54**(12), 52–57 (2021)
7. Seok, D.C., Yoo, S.R., Lee, K.I., et al.: Relation between etching profile and voltage–current shape of sintered SiC etching by atmospheric pressure plasma. Plasma Sci. Technol **21**(4), 045504 (2019)
8. Dai, Y.C., Zhang, M., Li, Q., et al.: Separated type atmospheric pressure plasma microjets array for maskless microscale etching. Micromachines **8**(6), 173 (2017)
9. Luan, P., Knoll, A.J., Wang, H., et al.: Model polymer etching and surface modification by a time modulated RF plasma jet: role of atomic oxygen and water vapor. J. Phys. D: Appl. Phys. **50**(3), 03LT02 (2016). https://doi.org/10.1088/1361-6463/aa4e97

10. Shao, T., Liu, F., Hai, B., et al.: Surface modification of epoxy using an atmospheric pressure dielectric barrier discharge to accelerate surface charge dissipation. IEEE Trans. Dielectr. Electr. Insul. **24**(3), 1557–1565 (2017)
11. Zhang, C.Q.: The Surface Plasma Treatment and its Study on Electrical Properties of Epoxy Resin. North China Electric Power University (2020)
12. Liang, M., Su, L.P., Chou, Z.M., et al.: Effects of DMP-30 on curing kinetics and mechanical properties of epoxy resin/anhydride system. J. China Univ. Pet. (Ed. Nat. Sci.) **45**(06), 175–181 (2021)
13. Wu, Y.Q.Q.G., Ma, L.Y., Li, F., et al.: Study on properties of high temperature cured epoxy aramid fiber composites. Hi-Tech Fiber Appl. **45**(06), 17–22 (2020)
14. Liu, Y.Q., Wu, G.N., Gao, G.Q., et al.: Surface charge accumulation behavior and its influence on surface flashover performance of Al_2O_3-filled epoxy resin insulators under DC voltages. Plasma Sci. Technol **21**(05), 134–143 (2019)
15. Lin, C.J., Gao, W.H., Li, Q., et al.: Correlation between epoxy resin process parameters and AC flashover. High Voltage Eng. **45**(09), 2732–2739 (2019)
16. Liu, M.J., Zhou, F.S., Chen, Z.Z., et al.: Characterizing trap distribution in LDPE and HDPE based on isothermal surface potential decay measurement. Proc. CSEE **36**(01), 285–291 (2016)
17. Dang, Z.P., Wu, Y.M.: Influence of mold releasing agent used in production of composite insulator core on quality of composite insulators. Power Syst. Technol. **12**, 106–108 (2006)
18. Huang, D.S., Wu, J.: Influence of waxes on the properties of EMC. Electron. Packag. **9**(10), 4–9 (2009)
19. Cao, Y.G., Zhang, Y.C.: The reseach progress and prospects of fluorochemical releasing agent. Plast. Packag. **21**(06), 29–32+28 (2011)
20. Li, Z.L., Liu, Y.M., Wang, D.N., et al.: Study on the effect of mold release agent(wax) on the adherence of EMC/Adhesives system. Electron. Packag. **21**(03), 40–45 (2021)
21. Yan, J.Y., Liang, G.S., Kang, Y.C., et al.: Effect of plasma surface gradient etching on surface flashover performance of epoxy resin. High Power Laser Part. Beams **33**(6), 134–142 (2021)

Effect of Deposition Power on DLC Structure on Alumina in RF-Biased Inductively Coupled Plasma

Zhijun Ai[1], Zhicheng Wu[1], Qiaogen Zhang[1(✉)], Zehao Zhang[1], and Zhengyong Hu[2]

[1] Xi'an Jiaotong University, Xi'an 710049, China
hvzhang@mail.xjtu.edu.cn
[2] State Grid Shanghai Electric Power Company, Shanghai 200125, China

Abstract. Diamond-like carbon (DLC) coating can improve the material surface's friction performance and interfacial compatibility. The current process for DLC deposition on alumina is inadequate, and the effect of deposition power on DLC structure is still unclear. In this paper, the RF-biased inductively coupled plasma (ICP) was introduced to enhance DLC deposition on alumina. By studying the morphology and bonding structure of films under different power conditions, the effects of total power and bias power fraction on DLC structure were decoupled, and the dominant mechanism determining the behavior of the sp^2 phase in the films was investigated. The results show that the increase of total power and bias power fraction led to a decrease in the fraction of sp^3 hybridized carbon in films, and partition phenomena with increasing internal stress. As the total power increased from 90 W to 180 W, the variation trend of sp^2 clusters and CH groups with the bias power fraction reversed, which reflected that the dominant effect factor for deposition changed from implanted ion energy to thermal spike accumulation. The study deepened the understanding of the DLC formation process under plasma action.

Keywords: DLC · Film structure · ICP · PECVD

1 Introduction

Improving the surface properties of alumina by depositing coating is a widely concerned research. Diamond-like carbon (DLC) is an attractive amorphous carbon coating because of its unique surface modification ability in friction, electricity, and biocompatibility [1, 2]. The modification effect is closely linked with the coating structure. For example, the friction properties of the material are related to the DLC morphology and sp^3 sites, and the electrical properties and biocompatibility are determined by the sp^2 sites and CH groups, respectively [3, 4]. Plasma-enhanced chemical vapor deposition (PECVD) provides a wide range of process parameters for DLC deposition, which leads to difficulties in the selection of process parameters for target properties [5]. In RF-biased inductively coupled plasma (ICP), the inductively coupled power and bias power are the

key parameters affecting DLC deposition [6]. This paper aims to clarify the effect of deposition power on DLC structure in RF-biased ICP.

The effect of a single power condition on DLC structure has been extensively studied with silicon as the substrate. Phillips and Thorpe proposed that DLC was a fully constrained random network formed by sp^3 and sp^2 hybridized carbon [7]. The subplantation model by Robertson has explained the phenomenon that the sp^3 fraction first increased and then decreased with increasing bias [3]. The ion energy was considered the key factor for DLC structure in the model and was usually adjusted by a DC bias below substrates. The DC bias caused positive charge accumulation and inhibited film growth, a characteristic that distinguished insulating substrates from doped silicon [8]. To deposit DLC on insulating substrates such as alumina, RF bias was used to neutralize the charge [9]. The bimodal ion energy distribution at RF bias increased the difficulty to adjust film structure, especially when the characteristic time for the ion crossing sheath was much less than the RF period [10].

The ion flux is determined by both inductively coupled power and bias power, while the ion energy is only controlled by the bias condition [11]. To decouple the role of ion flux and energy, we investigated the effect of power conditions with total power and the fraction of bias power as variables. The effects of individual variables on DLC morphology and sp^3 fraction were examined, and the coupling effect of both variables on the behavior of the sp^2 phase and CH groups was further found.

The purpose of this paper is to elucidate the effect of deposition power on DLC structure in RF-biased ICP. The RF-biased ICP enhanced DLC deposition method and the characterization method of DLC structure were described in Sect. 2. The individual effects of total power and bias power fraction on DLC morphology and sp^3 fraction were analyzed in Sect. 3. The coupling effect of power variables on the sp^2 phase and CH groups was found, and the dominant effect mechanism was discussed in Sect. 4. The study deepened the understanding of the DLC formation process under plasma action.

2 Experiments and Methods

2.1 RF-Biased ICP-Enhanced DLC Deposition

An RF-biased ICP-enhanced DLC deposition device was established, as shown in Fig. 1. To increase the nucleation density and deposition rate, high-density ICP was used as the particle source for deposition. RF bias was employed to avoid the inhibition of DLC growth caused by charge accumulation on the highly insulating alumina. The ICP was generated by 40.68 MHz power and the bias condition was adjusted by 13.56 MHz power. Matching networks were connected between power sources and loads for reducing the power reflection. Thanks to the plasma driven by RF power, the electrodes were set outside the reaction chamber to avoid metal contamination. CH_4 passed continuously into the reaction chamber and provided carbon atoms for DLC deposition. The air pressure in the reaction chamber was maintained at 20 Pa by a vacuum pump and measured by a pressure transducer.

It is of primary importance to select the variables of deposition power. The sum of inductively coupled power and bias power ($P_I + P_B$) was used as a variable to describe the ion flux. The fraction of bias power ($P_B/P_I + P_B$) was used as the other variable to
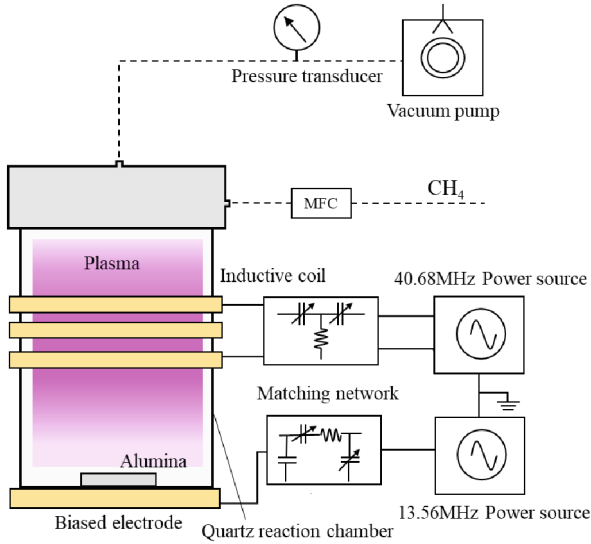
Fig.1. Schematic diagram of RF-biased ICP enhanced DLC deposition device

describe the ion energy. The lower limit of total power is constrained by the deposition threshold, and the upper limit is constrained by the etching effect. The range of total power in experiments was from 90 to 180 W, specifically 90, 120, 150, and 180 W. The bias power fraction included 1/6, 2/6, 3/6, 4/6, and 5/6.

The samples were 2 mm thick alumina discs, which were cleaned with anhydrous ethanol before experiments. In addition, the sample was etched by Ar plasma for 5 min to avoid interference from residual impurities. The deposition process in RF-biased ICP took 10 min.

2.2 DLC Structure Characterization

The morphology and sp^3 fraction were critical to the mechanical properties of films [12]. The microscopic morphology of DLC was observed by field emission scanning electron microscopy (Sigma 300, Carl Zeiss AG, Oberkochen, Germany)). Considering the insulating nature of the samples, the platinum was sputtered on samples before observation. The acceleration voltage was chosen to be 10 kV to avoid excessive charge accumulation. The atomic structure of C was characterized by X-ray photoelectron spectroscopy (ESCALAB Xi+, Thermo Fisher Scientific, Waltham, USA)) and the fraction of sp^3 was obtained by fitting the C1s peak.

The hundreds-fold sensitivity of Raman spectroscopy to sp^2 sites compared to sp^3 sites provides the basis for a more detailed study of sp^2 phase behavior [13]. The Raman spectra were tested by confocal Raman microscopy (LabRAM HR Evolution, Horiba Ltd., Kyoto, Japan) in the range of 800–2000 cm^{-1}, which covered the Raman characteristic of DLC. The laser power was kept below 1.5 mW during tests to avoid sample ablation.

The H bound to C provided the breakpoint for the amorphous carbon network, and the formed CH groups could be characterized by infrared absorption spectroscopy [14]. The infrared absorption spectra of films were tested using an infrared spectrometer (Vertex 70, Bruker Corporation, Billerica, USA). The tests were performed in diffuse reflection mode due to the uneven surface of sintered alumina. The test range was from 2700 to 3200 cm^{-1}, which was the typical absorption band of the CH group.

3 Individual Effects of Power Conditions

3.1 Effect of Total Power

The individual effect of total power on DLC structure was first examined, here focusing on the morphology and sp^3 fraction. The microscopic images of DLC on alumina at different total power are shown in Fig. 2. A large number of submicron particles were observed on the sample without DLC and distributed on the surface or in the interstices of micron particles. The submicron particles were covered by films after DLC deposition and became difficult to be observed with increasing total power. As the total power increased, some wrinkles started to appear in DLC, and divided the film into partitions. The wrinkles were an indication of internal stress release at weak points in films. At 180 W total power, the situation was even more severe, with localized fragmentation in films.
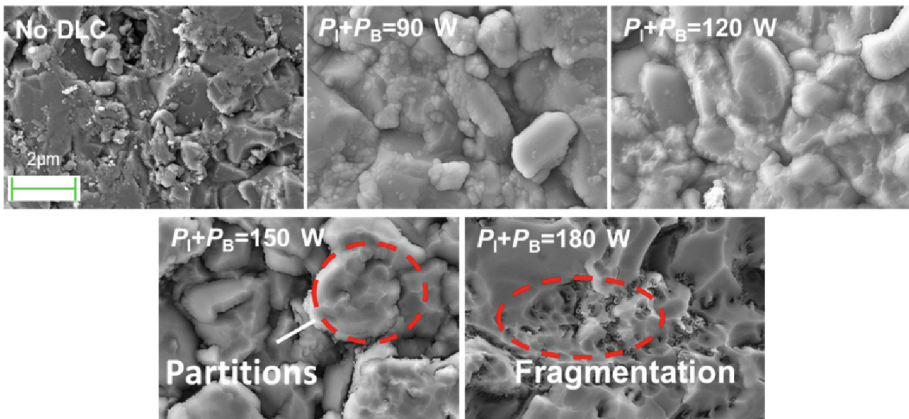
Fig. 2. The microscopic images of DLC on alumina at different total power $P_I + P_B$, bias power fraction $P_B/(P_I + P_B) = 1/6$.

Further attention was paid to the sp^3 fraction, which is directly related to the hardness and density of DLC. The split peak fitting of the C1s peak in X-ray photoelectron spectroscopy (XPS) is shown in Fig. 3a. The peak shapes were assumed to be 80% Gaussian and 20% Lorentzian. The separation of the electron binding energy between the sp^2 peak and sp^3 peak was fixed at 0.5 eV, based on the comparison of C1s and O1s in diamond and graphite [15]. The C1s peak is broadened by the separated peaks, sp^3 and

sp^2, and the full width at half maximum (FWHM) reached 3.0 eV (Fig. 3b). In addition, there is a peak near 286.5 eV corresponding to C-O bonds formed by oxidation of the carbon on the surface. As the total power increased, the FWHM of C1s peak gradually decreased, which implied a possible change in sp^2/sp^3. To quantitatively examine the changing of the sp^3 fraction, we calculated the sp^3 fraction based on the peak area in C1s (Fig. 3b). The results show that the sp^3 fraction decreased from 63.4% to 25.9% as the power increased from 90 W to 180 W.
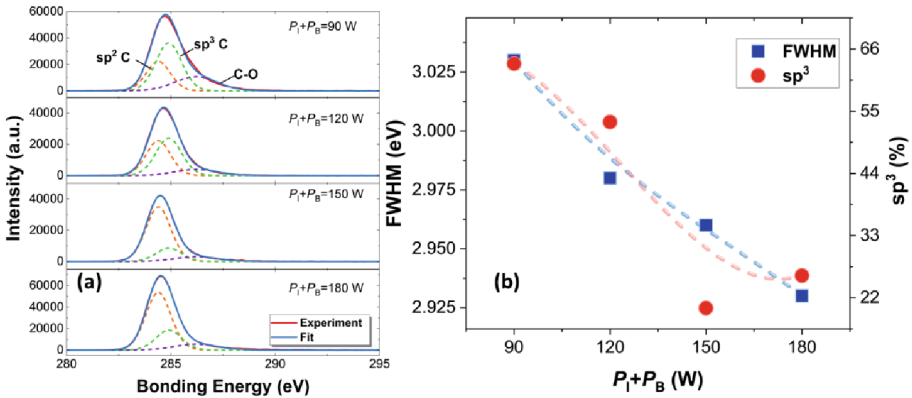
Fig.3. (a)The split peak fitting, (b) FWHM and sp^3 fractions of C1s peaks in XPS at different total power $P_I + P_B$, bias power fraction $P_B/(P_I + P_B) = 1/6$.

3.2 Effect of Bias Power Fraction

The effect of bias power fraction on DLC structure could not be neglected after grasping the effect of total power. The microscopic images of DLC on alumina at different bias power fractions are shown in Fig. 4. At low bias power fraction, the films on different alumina particles were relatively continuous and the film layer could be considered as a single unit. As the bias power fraction increased, the films at gaps were disrupted by high-energy ion bombardment, and the film layer separated. In addition, the partition phenomenon was also observed and intensified with increasing bias power fraction.

To grasp the effect of the bias condition on the sp^3 fraction, the XPS of DLC deposited with different bias power fractions were investigated. The FWHM and sp^3 fractions were obtained by the fitting of C1s peaks in XPS (Fig. 5). The results show that the FWHM decreased with increasing bias power fraction, and the decreasing trend leveled off. At the same time, the sp^3 fraction of DLC decreased from 56.1% to 18.5%, which is similar to that when the total power increased.

3.3 Discussion and Analysis

The increase in total power resulted in more frequent ion bombardment, which can lead to an increase in internal stress in films [16]. The increase of single bombardment
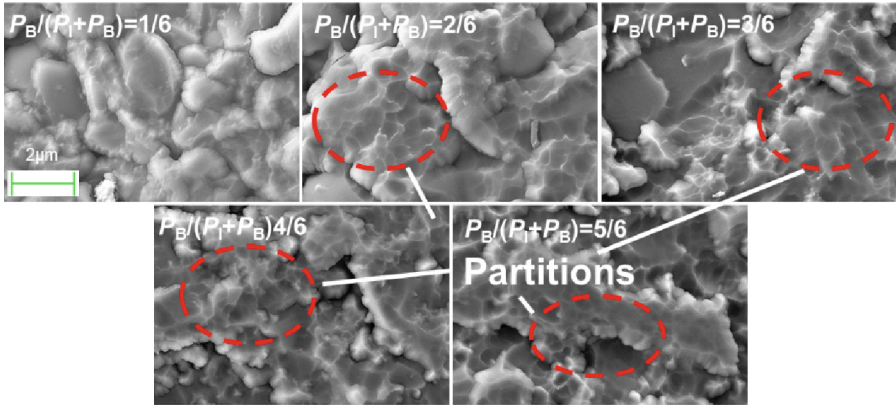
Fig. 4. The microscopic images of DLC on alumina at different bias power fractions $P_B/(P_I + P_B)$, total power $P_I + P_B = 120$ W.
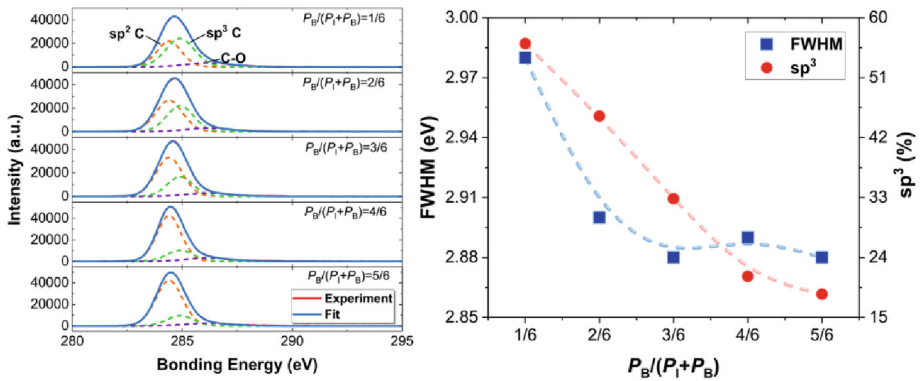
Fig. 5. (a)The split peak fitting, (b) FWHM and sp^3 fractions of C1s peaks in XPS at different bias power fraction $P_B/(P_I + P_B)$, total power $P_I + P_B = 120$ W.

energy with bias condition also contributed to the internal stress [17]. The stress release phenomenon occurred if the internal stress reached a threshold, such as the partitioning of films. The internal stress would be effectively released once the partition occurred.

The formation of the sp^3 site in DLC required a high-pressure environment, which can be provided by internal stresses [18]. The film had a high sp^3 fraction before the stress was released. However, as the internal stress exceeded the threshold and was released, the pressure became unfavorable for the stable presence of the sp^3 site. Therefore, the sp^3 fraction decreased as the total power and bias power fraction increased.

4   Coupling Effect of Power Conditions

4.1 Sp^2 Phase Behavior

The morphology and sp^3 fraction were overall properties of the fully constrained random network and were not sensitive to the differences in effects of total power and bias power fraction [19]. The behavior of the sp^2 phase was studied using Raman spectroscopy to explore the coupling effect between power variables in more detail. The Raman spectrum of DLC has a broad asymmetric peak in the range of 1000 to 1800 cm^{-1} (Fig. 6). The broad peak was composed of D and G peaks, which correspond to the breathing vibration of sp^2 rings and the bond-stretching motion of sp^2 pairs, respectively [20]. A combination of BWF (G peak) and Lorentzian (D peak) line shapes were used to improve the fitting for low-frequency tails. The key characteristic parameters, D and G intensity ratio I(D)/I(G) and G peak position G POS, were used to describe the size of sp^2 clusters and the bond angle disorder of the sp^2 phase, respectively [13].
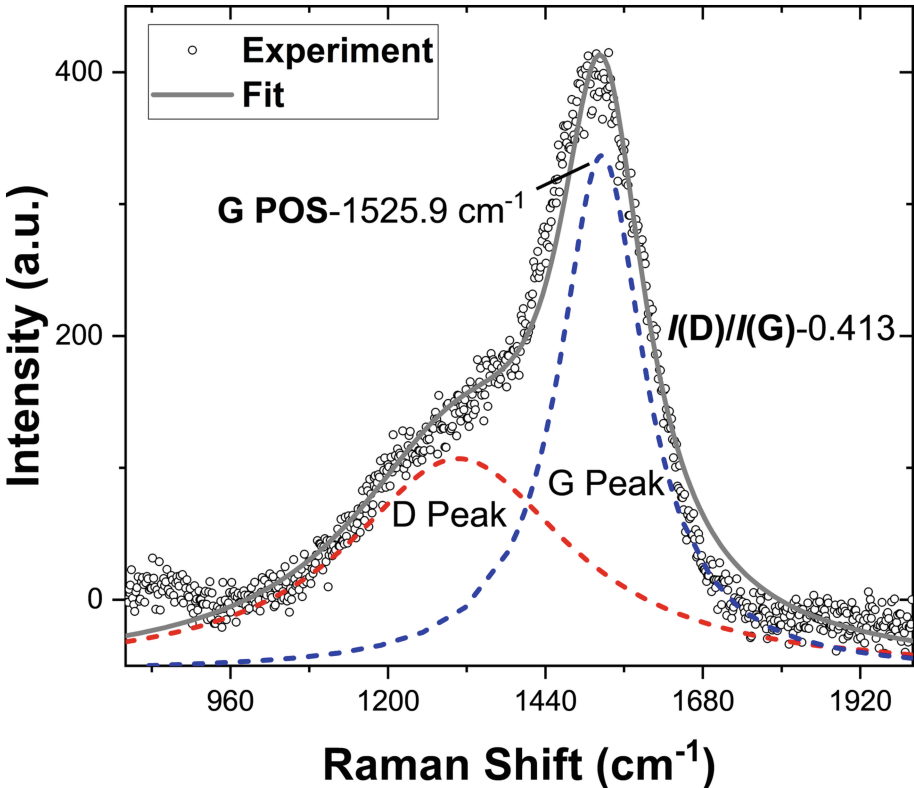
Fig. 6. Typical fitting and characteristic parameters for Raman spectrum of DLC

The Raman characteristics as a function of the bias power fraction at different total power are shown in Fig. 7. At 90 W total power, I(D)/I(G) decreased from 0.40 to

0.33, and G position shifted down from 1530.7 cm^{-1} to 1517.8 cm^{-1} as the bias power fraction increased. The downward shift of the G position implies an increase in the bond angle disorder of the sp^2 phase, and the decrease in $I(D)/I(G)$ implies a decrease in the sp^2 cluster size [21]. At total power above 150 W, the changing trend of Raman characteristics reversed. The bond angle became ordered and the cluster size increased as the bias power fraction increased.
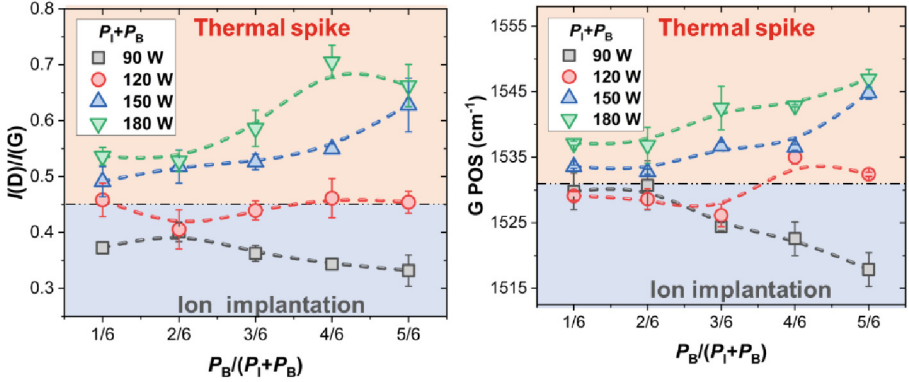
Fig. 7. The Raman characteristics as a function of the bias power fraction $P_B/(P_I + P_B)$ at different total power $P_I + P_B$. The red and blue regions represent the deposition dominant mechanisms are thermal spike accumulation and ion injection, respectively.

The variation in sp^2 phase behavior at different total power showed the coupling effect of power variables. This phenomenon can be explained by the change in the effect mechanism of ion energy on deposition. The ion energy in the deposition area increased with the bias condition [22]. On one hand, the implanted high-energy ions broke the disordered sp^2 rings and reduced the size of sp^2 clusters at low total power. On the other hand, the ion bombardment produced localized thermal spikes, and the relaxation process facilitated sp^2 clustering. As the total power increased, frequent ion bombardment caused severe thermal spike accumulation and the enhancement of sp^2 clustering behavior was observed.

In conclusion, sp^2 clustering was suppressed or enhanced with increasing bias conditions at low and high total power, respectively. The phenomenon was explained by the change of the dominant mechanism from ion implantation to thermal spike accumulation.

4.2 CH Group Behavior

After recognizing the change in the dominant mechanism for DLC deposition, we examined another structure that was sensitive to the action of the thermal spike, CH group. The asymmetric C-H structure was detected by infrared absorption spectroscopy, and typical C-H stretching vibrational modes were in the range of 2800–3100 cm^{-1} [23], as shown in Fig. 8. The absorption peak was divided into two parts, sp^3 CH and sp^2 CH, according to the distribution of vibrational modes. We evaluated the sum and ratio of peak areas, corresponding to the total number of CH groups and the sp^3 CH/sp^2 CH.
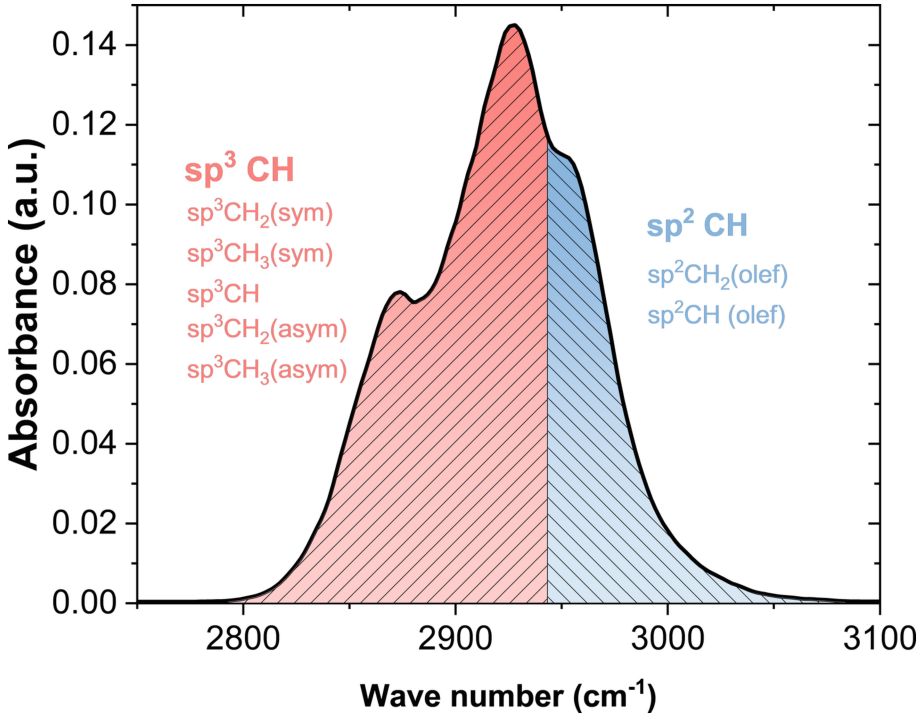
Fig. 8. Infrared absorption spectrum and C-H stretching vibration mode of DLC. (sym-symmetrical, asym-asymmetrical, olef-olefin)

Figure 9 shows the number of CH groups and sp^3 CH/sp^2 CH as a function of bias power fraction at different total power. As the total power increased, the variation
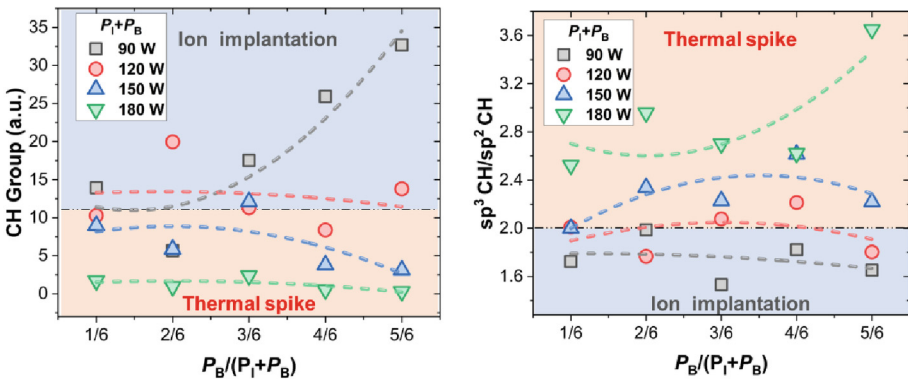
Fig. 9. The number of CH groups and sp^3 CH/sp^2 CH as a function of bias power fraction $P_B/(P_I + P_B)$ at different total power $P_I + P_B$.

law of CH groups on the bias power fraction changed. At low total power, the number of CH groups increased and sp^3 CH/sp^2 CH decreased as the bias power fraction increased. However, at high total power, the total number of CH groups decreased and the sp^3 CH/sp^2 CH increased. This phenomenon was also attributed to the change in the dominant mechanism of DLC deposition.

5 Conclusions

The paper investigates the effect of deposition power on DLC structure on alumina in RF-biased ICP, with total power and bias power fraction as power variables. The conclusions were:

a) At low total power and bias power fraction, alumina particles were covered with continuous films and the sp^3 fraction in DLC reached 63.4%. As the total power or bias power fraction increased, the film wrinkled and partitioned and the sp^3 fraction decreased. The release of internal stress was inferred to be the reason for the reduction of sp^3 phase.

b) The behavior of sp^2 phase and CH groups under different power conditions exhibited the coupling effect of power variables. At 90 W total power, sp^2 phase clustering was suppressed and CH groups and the ratio of sp^2CH increased with the bias power fraction. However, the trends reversed at total power above 150 W. It was attributed to the change in the dominant mechanism from ion implantation to thermal spike accumulation.

References

1. Rajak, D.K., Kumar, A., Behera, A., et al.: Diamond-like carbon (DLC) coatings: classification, properties, and applications. Appl. Sci. **11**(10), 4445 (2021)
2. Erdemir, A., Martin, J.M.: Superior wear resistance of diamond and DLC coatings. Curr. Opin. Solid State Mater. Sci. **22**(6), 243–254 (2018)
3. Robertson, J.: Diamond-like amorphous carbon. Mater. Sci. Eng. R. Rep. **37**(4–6), 129–281 (2002)
4. Castellino, M., Stolojan, V., Virga, A., et al.: Chemico-physical characterisation and in vivo biocompatibility assessment of DLC-coated coronary stents. Anal. Bioanal. Chem. **405**(1), 321–329 (2013)
5. Vetter, J.: 60 years of DLC coatings: historical highlights and technical review of cathodic arc processes to synthesize various DLC types, and their evolution for industrial applications. Surf. Coat. Technol. **257**, 213–240 (2014)
6. Oleszkiewicz, W., Markowski, J., Srnanek, R., et al.: Influence of RF ICP PECVD process parameters of diamond-like carbon films on DC bias and optical emission spectra. Opt. Appl. **43**(1), 109–115 (2013)

7. Phillips, J.C., Thorpe, M.F.: Constraint theory, vector percolation and glass formation. Solid State Commun. **53**(8), 699–702 (1985)

8. Bendavid, A., Martin, P.J., Preston, E.W.: The effect of pulsed direct current substrate bias on the properties of titanium dioxide thin films deposited by filtered cathodic vacuum arc deposition. Thin Solid Films **517**(2), 494–499 (2008)

9. Azhan, N.H., Su, K., Okimura, K., et al.: Radio frequency substrate biasing effects on the insulator-metal transition behavior of reactively sputtered VO2 films on sapphire (001). J. Appl. Phys. **117**(18), 185307 (2015)

10. Cortázar, O.D., Megía-Macías, A.: Bimodal ion energy distribution functions in a hydrogen magnetized plasma. Plasma Sources Sci. Technol. **28**(2), 025010 (2019)

11. Hoekstra, R.J., Kushner, M.J.: Predictions of ion energy distributions and radical fluxes in radio frequency biased inductively coupled plasma etching reactors. J. Appl. Phys. **79**(5), 2275–2286 (1996)

12. Shahsavari, F., Ehteshamzadeh, M., Amin, M.H., et al.: A comparative study of surface morphology, mechanical and tribological properties of DLC films deposited on Cr and Ni nanolayers. Ceram. Int. **46**(4), 5077–5085 (2020)

13. Ferrari, A.C., Robertson, J.: Interpretation of Raman spectra of disordered and amorphous carbon. Phys. Rev. B **61**(20), 14095 (2000)

14. Lemoine, P., Quinn, J.P., Maguire, P.D., McLaughlin, J.A.: Mechanical characterisation and properties of DLC films. In: Donnet, C., Erdemir, A. (eds.) Tribology of Diamond-Like Carbon Films, pp. 83–101. Springer US, Boston, MA (2008). https://doi.org/10.1007/978-0-387-49891-1_3

15. Leung, T.Y., Man, W.F., Lim, P.K., et al.: Determination of the sp3/sp2 ratio of aC: H by XPS and XAES. J. Non-Cryst. Solids **254**(1–3), 156–160 (1999)

16. Aijaz, A., Kubart, T.: Ion induced stress relaxation in dense sputter-deposited DLC thin films. Appl. Phys. Lett. **111**(5), 051902 (2017)

17. Damasceno, J.C., Camargo, S.S., Jr., Freire, F.L., Jr., et al.: Deposition of Si-DLC films with high hardness, low stress and high deposition rates. Surf. Coat. Technol. **133**, 247–252 (2000)

18. Ferrari, A.C., Kleinsorge, B., Morrison, N.A., et al.: Stress reduction and bond stability during thermal annealing of tetrahedral amorphous carbon. J. Appl. Phys. **85**(10), 7191–7197 (1999)

19. Dwivedi, N., Kumar, S., Malik, H.K., et al.: Correlation of sp3 and sp2 fraction of carbon with electrical, optical and nano-mechanical properties of argon-diluted diamond-like carbon films. Appl. Surf. Sci. **257**(15), 6804–6810 (2011)

20. Lubwama, M., Corcoran, B., Rajani, K.V., et al.: Raman analysis of DLC and Si-DLC films deposited on nitrile rubber. Surf. Coat. Technol. **232**, 521–527 (2013)

21. Casiraghi, C., Piazza, F., Ferrari, A.C., et al.: Bonding in hydrogenated diamond-like carbon by Raman spectroscopy. Diam. Relat. Mater. **14**(3–7), 1098–1102 (2005)

22. Gahan, D., Dolinaj, B., Hopkins, M.B.: Retarding field analyzer for ion energy distribution measurements at a radio-frequency biased electrode. Rev. Sci. Instrum. **79**(3), 033502 (2008)

23. Ţucureanu, V., Matei, A., Avram, A.M.: FTIR spectroscopy for carbon family study. Crit. Rev. Anal. Chem. **46**(6), 502–520 (2016)

Dynamic Behavior of Graphite Electrode Under the Thermal Shock of the Pulsed Arc

Hongyu Dai[1(✉)], Jingrun Guo[2], Lee Li[2], Junfeng Chen[1], Meng Yang[1], Long Xiao[1], and Jingxian Yang[1]

[1] China Ship Development and Design Center, Science and Technology on Electromagnetic Compatibility Laboratory, Wuhan 430000, China
`139866430@qq.com`
[2] State Key Laboratory of Advanced Electromagnetic Engineering and Technology, Key Laboratory of Pulsed Power Technology (Ministry of Education), Huazhong University of Science and Technology, Wuhan 430074, China

Abstract. The thermal shock of the arc is the main cause of electrode damage in the spark gap switch, reducing the reliability of the switch. In this paper, we investigate the erosion characteristics of high-current pulsed arc on the graphite electrode based on the energy coupling model between the switching arc and graphite electrode. The magneto-hydrodynamic (MHD) theory is adopted to calculate the current density and temperature distribution of the pulsed arc, and the arc is considered as energy source on the electrodes. The transient energy flux intensity and the response of the electrodes are calculated with several typical pulsed discharge, and the energy state of the graphite is achieved. The sublimation characteristics of graphite electrode are studied under transient heating condition. The paper reveals the mass-loss mechanism of the graphite electrode and verifies the effect of reducing the energy flux to achieve anti-ablation of the electrodes.

Keywords: Graphite electrode · Magneto-hydrodynamic · thermal shock · Pulsed arc

1 Introduction

The spark gap switch is a key component of the high-power electromagnetic energy equipment, which can converge pulse current and determine the conducting state of the power supply. The energy is transferred through the arc, which is generated between the electrodes, and the switching arc could be considered as fully ionized gas in the arcing duration [1]. The arc root directly connects to the electrode, due to the high temperature characteristics of the arc, there are strong melting, evaporation, and splashing processes on the electrode surface, changing the surface morphology of the electrode [2]. Electrode erosion is one of the research hotspots in the field of high-power energy transmission [3].

There is high power density on the surface of the electrode. The material types has a great impact on the service life of the electrode [4]. Donaldson's experimental

research also confirmed that the mass-loss rate of graphite was lower than that of copper and tungsten-copper under high-current discharge conditions. As the temperature keeps rising, for metal electrode, the first phase transition is from solid to liquid phase, where the molten pool is formed on the surface of the electrode. Then, the metal will vaporize and diffuse to the plasma arc in the form of metal vapor. The advantage of graphite material is that it does not exist in the form of liquid in the rated pressure in the switch, and it will not escape from the electrode in the form of viscous liquid. The electrode surface is smoother after being shocked by arc. After multiple discharges, the uniformity of the electric field is better, and the static withstand voltage is higher when the graphite electrode is used [5].

Still, the problem of electrode erosion has not been solved properly, but it promoted the progress of theoretical research. Tanaka et al. photographed the process of polymer ablation and intuitively described the evolution process of polymer [6]. Xiang et al. developed a combined diffusion coefficient model to calculate the movement of the electrode vapor [7], and he found that ordinary diffusion was the main driving force for upward vapor diffusion away from the anode. The change of arc energy determines the phase state of the electrode, and the arc strength has a significant impact on the service life of the electrode. Based on the phase change characteristics of the graphite, it is necessary to study the transient thermodynamic response of the graphite electrode with a high-current switching arc, explore the escape mechanism of graphite.

2   Experimental Setup and Simulation Model

2.1   Thermodynamic Model of Switching Arc

The switching arc is assumed to be in local thermodynamic equilibrium condition, which can be described by electromagnetic thermo-fluid equations. The MHD equations are adopted to calculate the thermodynamic state of the arc, and the energy exchange of the arc-electrode interface is calculated without considering the non-equilibrium phenomena at the sheath region of the arc plasma. Under pulsed discharge condition, the plasma flow is assumed to be turbulence, and the k-ε turbulence model is adopted. The effect of graphite vapor on the physical parameters of discharge gas is not considered. Assuming that all the sublimation of the electrode enters the gas region, no re-condensation occurs during arcing time, and no energy is consumed or released by chemical reactions (Fig. 1).

The MHD equations consists of mass conservation equation, momentum conservation equation, and energy conservation equation, as shown in (1)–(3)

$$\frac{\partial \rho}{\partial t} + \nabla \cdot (\rho \vec{v}) = S_g \tag{1}$$

$$\frac{\partial (\rho \vec{v})}{\partial t} + \nabla \cdot (\rho \vec{v} \vec{v}) = -\nabla P + \nabla \cdot \overline{\overline{\tau}} + \vec{J} \times \vec{B} \tag{2}$$

$$\frac{\partial (\rho h)}{\partial t} + \nabla \cdot (\rho \vec{v} h) = -\nabla \cdot \left(\frac{k}{c_p} \nabla h\right) - U + \frac{1}{\sigma} \vec{J}^2 + \frac{5 k_B}{2 e c_p} \vec{J} \cdot \nabla h - S_h \tag{3}$$

In the mass conservation equation, S_g is the mass source term, which represents the mass of graphite vapor produced from the electrodes [kg/m³/s]. ρ is the gas density
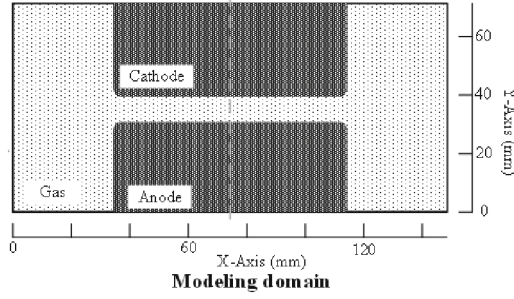
Fig. 1. The modeling domain in the switch, according to actual size of the switch

[kg/m^3], t is the time [s], $\vec{v}$ is the velocity of the gas [m/s], P is the pressure [Pa], and $\overline{\overline{\tau}}$ is the viscous stress tensor [Pa]. $\overrightarrow{J}$ is the current density [A/m^3] and $\overrightarrow{B}$ is the magnetic field strength [T], which is induced by the current. In the energy conservation equation, h is the enthalpy [J/kg], k is the thermal conductivity [W/m/K], c_p is the specific heat [J/kg/K], U is the net radiative coefficient [W/m^3], and the value is the result of the radiation strength at 1.5 mm from the arc. σ is the electrical conductivity [S/m], k_B is the Boltzmann constant. Joule heat, radiation loss, and electron flow heat generated by current are the additional source terms of the energy conservation equation. S_h is the latent heat of evaporation of graphite, which is only considered in the electrode area.

2.2   Calculation of Heat Flux at the Arc-Electrode Interface

The template is used to format your paper and style the text. All margins, column widths, line spaces, and text fonts are prescribed; please do not alter them. You may note peculiarities. For example, the head margin in this template measures proportionately more than is customary. This measurement and others are deliberate, using specifications that anticipate your paper as one part of the entire proceedings, and not as an independent document. Please do not revise any of the current designations.

Near the arc region, the heat flux on the cathode surface is produced by the arc's thermal conduction, and ion impact. At the same time, the electron emission and the thermal radiation of the electrode will cool the electrode[8]. Heating of the electrodes by radiation from the arc is neglected. On the arc-electrode interface, it is stipulated that the energy from the arc to the electrode is positive and the energy dissipated from the electrode is negative. The cathode heat flux can be expressed as [9]

$$S_{\text{cathode}} = -\varepsilon\alpha T^4 - j_e\phi_{\text{graphite}} + |j_\mathrm{i}|V_\mathrm{i} + k\frac{\partial T}{\partial z} \tag{4}$$

where $\varepsilon\alpha T^4$ is the thermal radiation effect of the electrode, ε refers to the radiation emission coefficient of the graphite material, and α is the Stefan-Boltzmann constant. The radiation energy on the electrode is substantially less than the thermal conduction and ion bombardment heat. ϕ_{graphite} is the work function of graphite, and V_i is the ionization potential of the plasma. The total current density of the arc is the sum of the electron current density and the ion current density, that is $|J| = |j_i| + |j_e|$, and the electron

current j_e is derived from the thermionic emission of the cathode material, which can be calculated by the Richardson-Dushman expression.

$$j_e = AT^2 \exp\left(-\frac{e\phi_{\text{graphite}}}{k_B T}\right) \tag{5}$$

The thermionic emission intensity of electrons is mainly related to temperature. Where A is the thermionic emission constant.

The anode heat flux S_{anode} mainly considers the electrons impact heat and the thermal conduction from the arc, and the heat flux can be expressed as

$$S_{\text{anode}} = j_e \phi_{\text{graphite}} + k\frac{\partial T}{\partial z} - \varepsilon\alpha T^4 \tag{6}$$

2.3 Graphite Evaporation Model

There is a transport process of the graphite vapor, from the electrode surface to the arc region, and the transfer of the vapor satisfies the equation of mass conservation equation, which can be expressed as

$$\frac{\partial(\rho Y)}{\partial t} + \nabla \cdot (\rho\vec{v}Y) = \nabla \cdot \left(\rho D_{graphite}\nabla Y\right) + S_g \tag{7}$$

where Y is the mass fraction of graphite vapor in the mixed gases, and $D_{graphite}$ is the diffusion coefficient of graphite vapor in the discharge gas. $S_{graphite}$ is related to the mass flux J_{evp} of graphite vapor. J_{evp} can be calculated according to the Hertz-Knudsen-Langmuir equation given by (9), which is mainly related to the vapor pressure in different regions. The evaporation coefficient $\sigma_{evaporation}$ is set at 18/25 and use the following approximate expression.

$$S_{graphite} = J_{evp} \times \Delta A_{evp}/\Delta V_{evp} \tag{8}$$

$$J_{evp} = \sqrt{\frac{m_{\text{graphite}}}{2\pi k_B T}}\left(\frac{16\sigma_{evaporation}}{16-7\sigma_{evaporation}}\right) \times p_{wall}\left(\frac{p_{wall} - p_{switch}}{p_{wall}}\right) \tag{9}$$

where m_{graphite} is the mass of carbon atom [kg]. The vapor pressure p_{switch} is set as the switch working pressure [Pa]

3 Experimental Research

The graphite electrode is experimented on the discharge platform with pulse power supply. The platform mainly includes the energy storage module and load module, the current waveform is shown in Fig. 2.

The electrode surface is polished with 3000-grit sandpaper, and two electrodes with the same shape are fixed in the sealed cavity. The cathode is above the anode. To guarantee measuring precision of the experimental apparatus, the same discharges are repeated 5 times. The mass-loss of the electrode is measured by an electronic balance with an accuracy of 0.0001 g, and the mass difference of the electrode under different discharge conditions are recorded.
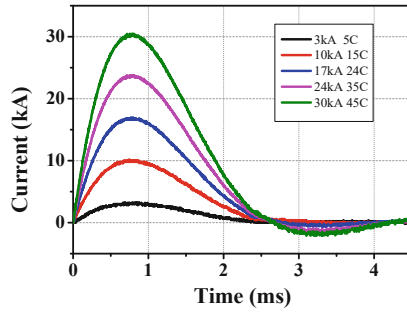
Fig. 2. Current waveform of five different conditions in the experiment

4   Result and Discussion

4.1   Energy Analysis of Electrode Surface

Since the switch is broken down by a nanosecond pulse voltage trigger, there is an initial spark discharge channel. Assume that the radius of the initial channel is 0.1 mm and the temperature is 10,000 K. In the current rising phase, the arc starts to expand from the center position. The thermal erosion surface area of the electrode expands with the increase of the arc current. Typical calculation time points are shown in the Fig. 3.
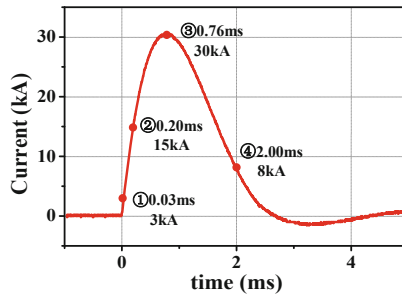
Fig. 3. Current waveform and calculation data at four different times

Arc's heat conduction is the main source of heat flux on the electrode surface. The impact of electrons and ions also has a great influence on the energy state of the electrode surface. Although the electron emission has a cooling effect on cathode surface, the heat from the impact of ions exceeds the emission cooling intensity of electrons, and the heat flux intensity on the cathode surface is much higher than that on the anode, as shown in Fig. 4. Especially at the maximum current of 0.76 ms, the arc is concentrated in the center part due to the influence of the Lorentz force. The maximum temperature of the arc is up to 17,000 K, and the heat flux intensity of the electrode center reaches 10^9 W/m^2, which is much higher than that of the boundary region. When the current drops, the current density decreases, but the radius continues to rise. With the increase of the total energy in arc region, the ionization gas continues to diffuse. During the current drop phase, the

overall temperature of the arc decreases from 16,000–17,000 K to 7,000–8,000 K, and the heat flux mainly comes from the heat conduction.
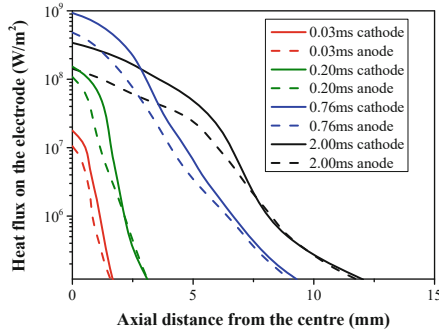
Fig. 4. Heat flux intensity on the cathode and the anode at four different times

The surface input energy of the electrode is obtained by integrating the heat flux of the electrode surface, as shown in Fig. 5. The results show that in the case of 30 kA/2.3 ms pulse arc, the electrode heat flux is mainly concentrated in the area within the radius of 3 mm, and electrodes are damaged by the arc energy within the radius of 12 mm. In contrast, the energy accumulated on the cathode is much higher than that on the anode, and the cathode is theoretically suffered more thermal damage.
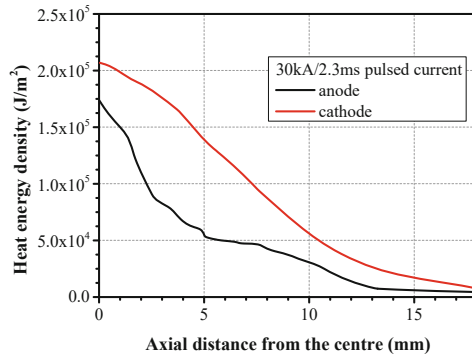
Fig. 5. Energy density distribution of cathode and anode by integrating the heat flux in the case of 30 kA/2.3 ms pulse arc

4.2 Analysis of Sublimation Characteristics of Graphite Electrode

The thermal coupling analysis is adopted at the arc-electrode interface, the temperature distribution in the graphite electrode at different discharge times is obtained. In Fig. 6, the calculation results of anode temperature are given. Affected by the thermal conduction

from the arc and electron impact, the partial area of graphite electrode reaches the phase transition temperature at the initial discharge. Especially in the central area, the arc temperature and the electrode temperature rise almost synchronously. It only takes a few microseconds to change from the initial temperature to the phase transition temperature, and the specific time varies with the discharge conditions.

With the increase of discharge current, a critical point of phase transition occurs in a larger area. In the radial direction, with the increase of the arc radius, the thermal shock area of the electrode expands, and the radius increases from 2 mm to 8 mm. In the axial direction, due to the continuous energy input, the heat conduction of the graphite is low, and the temperature of the local surface area continues to rise. However, the temperature of the electrode in most areas remains below the phase transition temperature.

Based on the energy balance theory on the arc-electrode interface, the energy input from the arc to the electrode is consumed by heating and sublimation. Part of the energy absorbed by electrode is used to heat it, and the temperature will rise immediately. Once the energy absorbed locally reaches the critical point of sublimation, the electrode changes rapidly to gas phase. The heat accumulated on the surface of graphite electrode can be taken away by phase change, which effectively prevents the transmission of arc energy to deeper areas and protects the electrode surface.
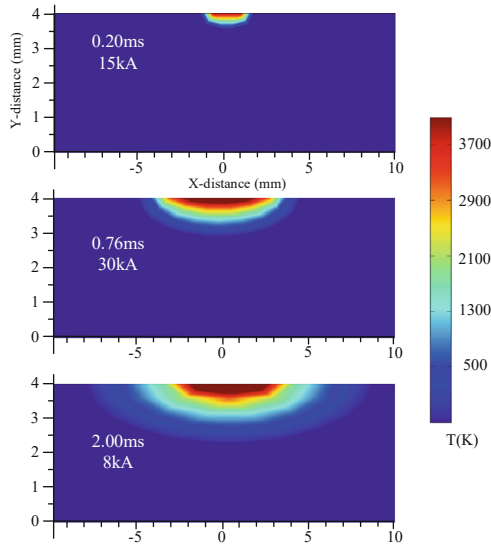
Fig. 6. The anode temperature varies with discharge time

The generation of graphite vapor is related to the arc intensity. The vapor is concentrated in the central area of the electrode, and the vapor concentration decreases with the radius. At the time of 0.03 ms, the heat conduction power of the arc on the electrode is low, and the evaporation area focus on a 1 mm radius, meanwhile the maximum concentration only accounts for 0.005 mass fraction. The evaporation rate and evaporation radius of graphite gradually increase with the increase of current. At the peak current, the

mass fraction of graphite on the electrode surface is close to 0.05, and the electrode radius involved in evaporation also increases to nearly 10 mm. In the decreasing stage of current, the energy intensity on the electrode decreases, and the evaporation rate of graphite decreases accordingly. Since the electrode surface temperature is already near the sublimation point under the heat effect of the pulse arc, once there is an energy excitation oriented to the electrode direction at the electrode interface, the graphite immediately transforms into a sublimation state (Fig. 7).
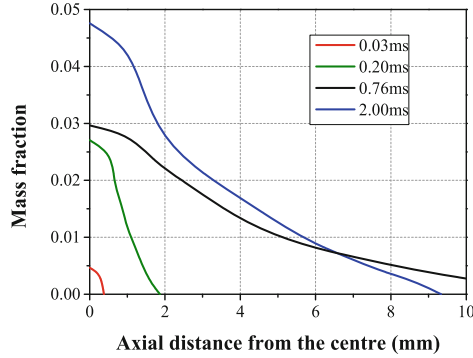
Fig. 7. The anode temperature varies with discharge time

5   Conclusions

In this paper, a transient axisymmetric model of the switching arc is built, and the sublimation characteristics of graphite electrode are discussed. The heat flux intensity and the energy accumulation characteristics of electrode-arc interface are calculated with a typical pulsed current. The temperature distribution on graphite electrode surface is obtained, and the erosion characteristics and the mass loss of graphite are verified by experiments. The conclusions of the current research and the content that needs further research can be summarized as:

(1) The size of the electrode erosion area is closely related to the radius of the arc. Under the pulse current of 30 kA/2.3 ms, the maximum arc radius is around 10 mm, and the corresponding radius of erosion area is approximate to it.

(2) The erosion of graphite is mainly determined by the thermodynamic accumulation of the arc. During the discharge process, the heat flux intensity on the electrode surface severely changes with time. However, the energy transmitted by the arc to the electrode increases continuously, and the graphite changes from heated state to sublimation state rapidly. Especially in the current drop phase, sublimation still exists there.

(3) The calculation model considers the influence of electrode surface energy on the sublimation rate of the electrode, but the non-equilibrium effect of the arc sheath is not considered in the model. The electron density near the cathode is less than the actual electron density, and the energy density of the calculation may be smaller.

References

1. Boulos, M.I., Fauchais, P., Pfender, E.: The plasma state. In: Boulos, M.I., Fauchais, P., Pfender, E. (eds.) Thermal Plasmas, pp. 1–47. Springer US, Boston, MA (1994). https://doi.org/10.1007/978-1-4899-1337-1_1

2. Donaldson, A., Kristiansen, M., Watson, A., Zinsmeyer, K., Kristiansen, E., Dethlefsen, R.: Electrode erosion in high current, high energy transient arcs. IEEE Trans. Magn. **22**(6), 1441–1447 (1986)

3. Wu, Y., et al.: Visualization and mechanisms of splashing erosion of electrodes in a DC air arc. J. Phys. D: Appl. Phys. **50**(47), 47LT01 (2017)

4. Wu, G., Gao, G., Wei, W., Yang, Z.: The Electrical Contact of the Pantograph-Catenary System: Theory and Application. The Electrical Contact of the Pantograph-Catenary System: Theory and Application (2019)

5. Li, L., Li, C., Feng, Y., Jing, N., Zheng-Yang, Z., Fu-Chang, L.: Analysis of electrical contact temperature rise in spark gap switches with graphite electrodes. IEEE Trans. Dielectr. Electr. Insul. **18**(4), 1307–1313 (2011)

6. Tanaka, Y., Shinsei, N., Amitani, K., Uesugi, Y., Wada, J., Okabe, S.: Spallation particle ejection from polymer surface irradiated by thermal plasmas. IEEE Trans. Plasma Sci. **39**(11), 2776–2777 (2011)

7. Xiang, J., Tanaka, K., Chen, F.F., Shigeta, M., Tanaka, M., Murphy, A.B.: Modelling and measurements of gas tungsten arc welding in argon–helium mixtures with metal vapour. Weld. World **65**(4), 767–783 (2021). https://doi.org/10.1007/s40194-020-01053-4

8. Zhu, P., Lowke, J.J., Morrow, R.: A unified theory of free burning arcs, cathode sheaths and cathodes. J. Phys. D-Appl. Phys. **25**(8), 1221–1230 (1992)

9. Murphy, A.B.: Thermal plasmas in gas mixtures. J. Phys. D-Appl. Phys. **34**, R151 (2001)

Effect of Discharge Properties of the Oxide High Barrier Film Deposited by Roll-to-Roll MF-PECVD

Maojin Dong[(✉)], Yudong Feng, Jizhou Wang, Lili Qin, Yi Wang, Xianhu Han, Yuhong Cai, Erpeng Feng, Guan Wang, and Fengying Ma

Key Laboratory of Vacuum Technology and Physics, Lanzhou Institute of Physics, Lanzhou 730000, China

`klmdmj@126.com`

Abstract. In accordance with the application of magnetically enhanced plasma discharge in high barrier film, the discharge parameters of roll-to-roll medium-frequency magnetic enhanced chemical vapor deposition (MF-PECVD) were studied. We discuss the discharge parameters, such as voltage, current, with the different vacuum pressure, and barrier property change rule by the parameters change. The results show that with the increase of discharge current, the voltage increases, and the deposition rate increases. The optimize vacuum pressure is 3 Pa, the water permeability decreases significantly with the increase of thickness, and the 300 nm films show high barrier properties, as low as 1×10^{-2} g/(m^2·day). The film thickness reached 500 nm, and the water permeability value was less than 5×10^{-3} g/(m^2·day), and the water permeability changed little with the increase of the thickness. And the average transmittance is 88.6%@380 nm–760 nm, film has good optical properties for display devices.

Keywords: Discharge Parameters · High Barrier Film · MF-PECVD · Vacuum Pressure

1 Introduction

Flexible electronic devices have the characteristics of miniaturization and deformability, and are widely applied. Typical applications include organic light-emitting devices (OLEDs), organic photovoltaic devices, thin-film transistors (TFT) array, and quantum dot TVs. The barrier property of flexible polymer materials is relatively weaker than the glass or metal encapsulating materials. The shelf-life and working lifetime of encapsulated flexible organic electronic devices are closely related to the barrier property against small molecules such as oxygen (O$_2$) or water vapor. We need coating barrier film to prevent the penetration of these molecules into the working device, which is called high barrier film [1–5].

Magnetic-enhanced chemical vapor deposition (PECVD) technology has been widely used due to its high vacuum environment, high quality, few impurities, and good performance of the deposited films. Meanwhile, it is generated by the dielectric barrier

discharges (DBD) structure with medium-frequency power [6–11]. In this paper, an MF-PECVD system with a pair of rollers was used to deposit transparent siloxane films with a high barrier property on the polymer substrate. In the MF-PECVD process, the chemical reaction species generated in the plasma may help to obtain higher deposition rate at relatively low process temperature, while in the conventional thermal CVD process, thermally stable precursors are needed. The coating depositions have been intensively investigated due to the high growth rate and the good uniformity. This method can be continuously winding, and has the characteristics of the transparent visible spectrum and high barrier. It has great application potential in the development of the barrier film industry [12–14].

To obtain accurate information about the problems encountered in the glow discharge coating process, one of the main purposes of this study is to measure the electrical parameters of the PECVD process and further understand the influence of parameters on the depositing process. Understanding the basic principles of these reactive plasmas is important for optimizing the coating function, as well as process and quality control [15–19].

2 Experimental Procedure

2.1 Structure of System

A schematic diagram of discharge PECVD apparatus is shown in Fig. 1. The system uses the opposite electrode dual rollers to tighten the substrate film on the roller surface for continuous winding and coating. One of the important features of this coating device is the application of a medium-frequency power supply to the dual rollers, where a non-rotating magnet system is assembled to produce an oval magnetic enhanced discharge area on the surface of the pair rollers. The inside of the electrode roller is a completely symmetrical magnetic system, the magnetic system of the two rollers is relative, the plasma is confined between the rollers by the magnetic field, and the AC magnetically controlled discharge helps to excite the plasma. The surface of the deposition roll is covered with an insulating organic substrate film, but the medium-frequency discharge is sufficient to penetrate the polymer substrate film and achieve glow discharge. At the same time, the process gas used for deposition is distributed to the area between the rollers, and the source gas is decomposed, dissociated, and excited by plasma, adsorbed on the organic substrate film on the surface of the electrode roller to grow the high barrier oxide film.

The source gas is O_2/HMDSO mixture supplied by a gas distribution system located at the top of the deposit to keep the pressure within 0.5–10 Pa range.

2.2 Experimental Parameters

The vacuum system is composed of mechanical pump, roots pump group and a molecular pump. The power type is TruPlasma Bipolar 4010, using full-waveform mode control. The vacuum is measured by Inficon thin film vacuum gauge, and the gas flow is adjusted by gas mass flowmeter. The gas flow and experimental parameters in this experiment are shown in Table 1.
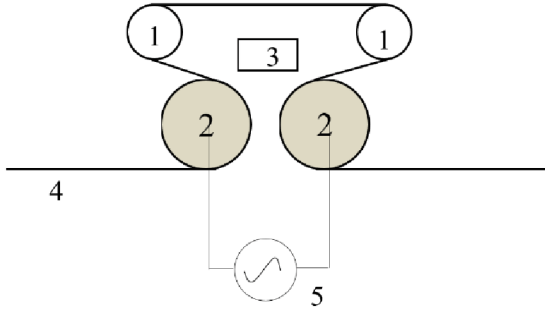
Fig. 1. Diagram of magnetic field distribution of electrode ① guide roller, ② magnet, ③ air distribution plate, ④ substrate film, ⑤medium-frequency power supply

Table 1. Experimental parameters

content	range
vacuum/Pa	0.5–10
HMDSO/sccm	80 (99.99%)
O_2/sccm	600 (99.999%)
power/w	0–2000
voltage/V	0–800
background vacuum/Pa	5×10^{-3}
winding speed	600 mm/min

The KEITHLEY DAQ6510 multimeter was used to test the electrical parameters during the discharge, which were collected and recorded by the computer. Film Thickness Mapping with an Astigmatic Optical Profilometer, the water permeability was tested by MOCON AQUATRAN MODEL 2. The spectrum of thin film was tested by Perkin Elmer LAMBDA 900 UV-Vis Spectrophotometer.

3   Results and Discussion

3.1   Medium Frequency Discharge

Plasma discharge is an important step in the study of MF-PECVD. According to the characteristics of plasma power, voltage, and power density, the deposition rate, compactness, and thickness uniformity of the coating can be analyzed. We get the change rules of the plasma discharge parameters to deposition rate [20, 21].

In the synthetic insulation film process, in order to effectively neutralize the charge accumulation on the edge target surface, a negative pulse bias of about 400–600 V is usually applied to the target surface. In order to characterize the variation of voltage with time during discharge, a rectangular wave medium frequency discharge is used with a

duty cycle of 50%. The discharge characteristic was test by The KEITHLEY DAQ6510 multimeter (Fig. 2).
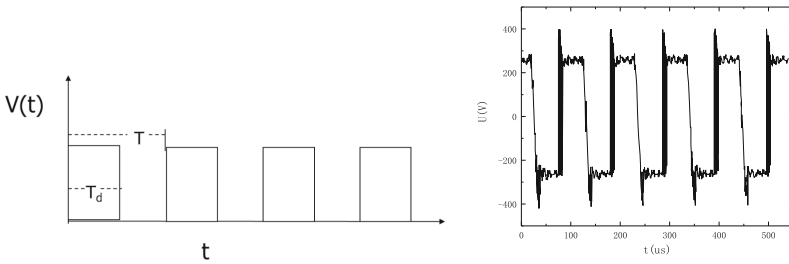
Fig. 2. Comparison of model voltage (left) and measured voltage (right)

The discharge of medium-frequency PECVD state is a periodic breakdown, discharge and extinction process. Firstly, with the increase of the power supply voltage, the voltage between the two rollers increases, and then the breakdown and discharge cause the voltage at both ends of the roller to decrease and the first spike appears. As the supply voltage continues to rise, the voltage between the roller's rebounds and a second downward spike appears. Then discharge tends to be stable appear relatively straight line. As the power supply voltage of the cycle decreases, the voltage at the roller end also decreases. However, where the discharge is extinguished cannot be determined from the diagram. So, it can be seen as a periodic DC discharge.

After averaging the discharge voltage by filtering, the relationship between power and voltage is discussed. As the discharge power increases, the voltage increases, but it is not completely linear. It increases sharply first and then slowly. At the same time, the sputtering effect of plasma has a certain influence on the base film. The higher the discharge voltage is, the more easily the thin substrate will wrinkle.

Power supply drive and test voltage characteristics. To meet the stable glow, discharge characteristics appear a voltage peak each cycle. Can see composite pulse power waveform takes on the form of high and low pulse superposition, is a high peak voltage pulse beginning but shorter pulse width of the pulse, with the rising of an ignition pulse voltage, the corresponding time is proportional to the test current is also rising, ignition pulse voltage of vacuum indoor gas discharge has an important influence.

3.2 Electrical Characteristics

Figure 3 shows the normal coating discharge state. The curve results are the same as the DC magnetron sputtering V-I curve. The discharge current can be freely adjusted in this section. This is also the curve segment interval we usually use for anti-IF pecvd. The film prepared in this state is a transparent insulator. Although the values measured under different pressures are slightly different, they can be basically regarded as a linear relationship. The voltage increases with the increase of the current to the positive resistance region, that is, the resistance R = dv/dI; is a positive value. Compared with the
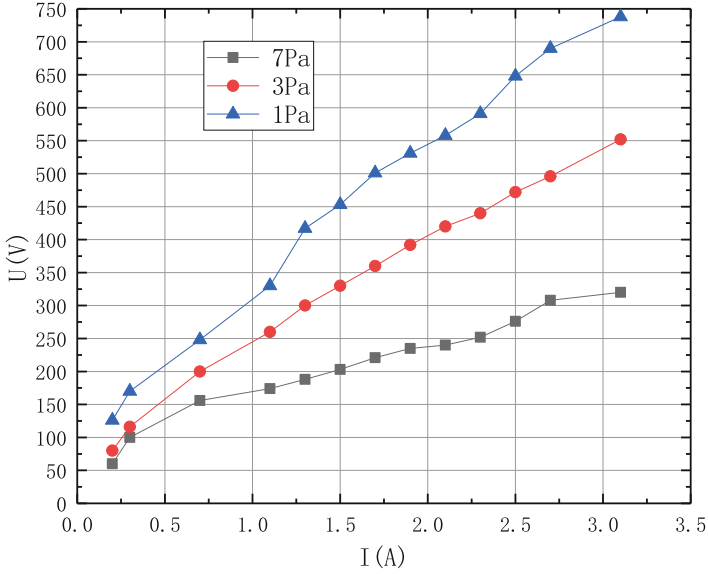
Fig. 3. Volt-ampere characteristics at different vacuum pressures

standard gas discharge voltammetry, this section conforms to the characteristics of the abnormal glow discharge section. The average current density varies from 24 mA/cm^2 to 250 mA/cm^2 with the average voltage, which is similar to the relationship between the current density of magnetron sputtering and the target voltage (Fig. 4).
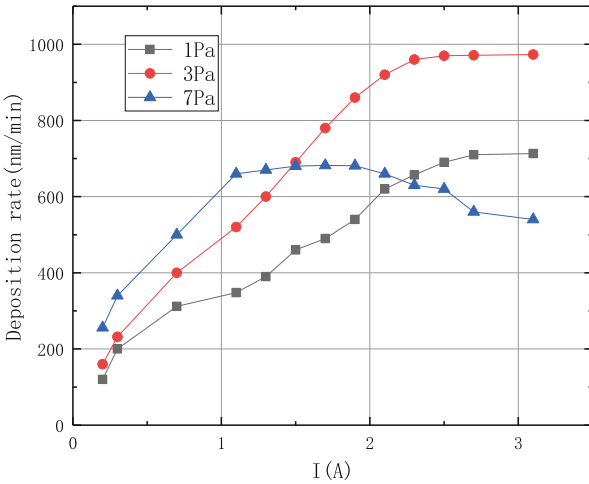
Fig. 4. Deposition rate and current characteristics under different vacuum pressures

The film deposition rate increases with the increase of plasma discharge current at 1 Pa vacuum pressure, the deposition rate increases faster than that at 3 Pa vacuum pressure. For 7 Pa vacuum pressure, in the initial stage, the deposition rate increases rapidly with the increase of current, but it quickly becomes gentle, and the deposition rate does not increase but decreases. Combined with Fig. 3, it can be seen that the discharge voltage also increases sharply with the increase of current. After 600 V, the sputtering effect of voltage increase exceeds the influence of current increase on the deposition rate. A higher deposition rate is achieved at 3 Pa vacuum pressure.

3.3 WVTR and Spectrum with Plasma Discharge Characteristics

The winding speed is constant 600 mm/min. The relationship between water permeability and discharge current under different vacuum pressure is discussed. For 1 Pa vacuum pressure, with the increase of plasma discharge current, the permeability has been reduced. When the vacuum pressure is 3 Pa, compared with 1 Pa condition, the permeability decreases faster with the increase of current, and better water vapor barrier is obtained. When the vacuum pressure is 7 Pa, in the initial stage, the permeability decreases faster with the increase of current, but it soon becomes gentle, and the permeability no longer decreases. The water permeability of oxide barrier film is closely related to the film thickness. Generally speaking, the thicker the film prepared under the same vacuum pressure, the better the barrier property (Fig. 5).
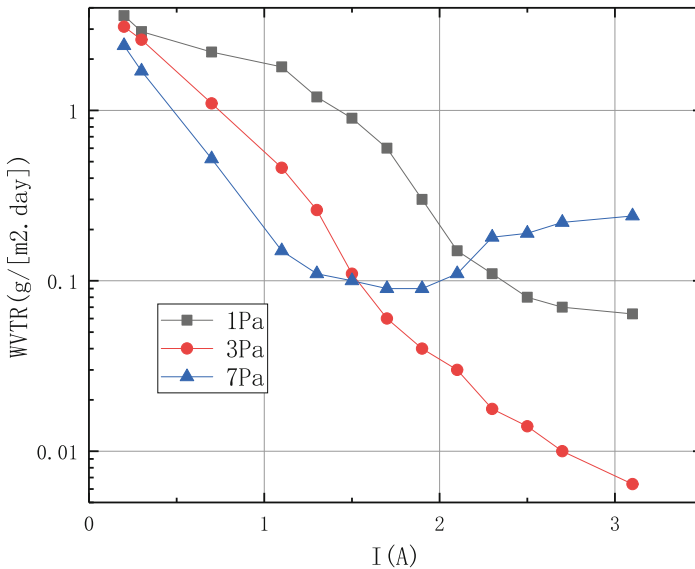
Fig. 5. Permeability and current characteristics under different vacuum pressures

Figure 6 shows the water permeability (WVTR) of different thickness. As can be seen from the figure, the water permeability decreases significantly with the increase of thickness, and the 300 nm films show high barrier properties, as low as 1×10^{-2} g/(m^2·day).

The film thickness reached 500 nm, and the water permeability value was less than 5×10^{-3} g/(m²·day), and the water permeability changed little with the increase of the thickness.
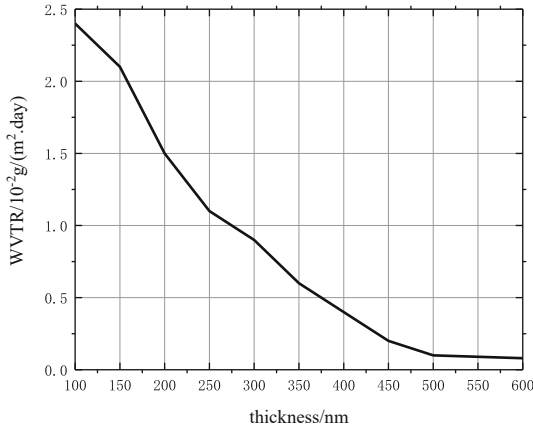
Fig. 6. The water permeability varies with the thickness of the film

We believe that there are two reasons for this result: one is that the film plated contains organic components, has good flexibility, and fewer cracks appear with the increase of film thickness, as shown in the figure; Second, there are a small number of large-size particles on the surface of the base film. With the increase of film thickness, these particles are gradually completely covered and the water permeability decreases.
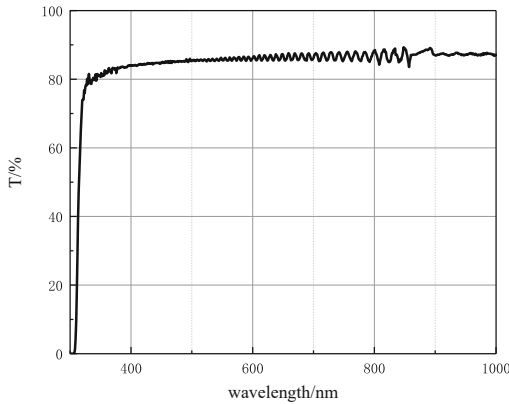
Fig. 7. Light transmittance spectrum of siloxane film

The optical transmission of 500 nm thin film is shown in Fig. 7. The average transmittance of 300–600 nm band is more than 86%, and above 600 nm band is more than 90%, and the change is gentle. It is proved that the siloxane film prepared by MF-PECVD has

good optical properties for display devices. When the transmittance @380 nm–760 nm is 88.6%, it can have good barrier performance at the same time. The ripples in the spectrum are due to interference by thin film and base film, but does not affect the overall transmittance.

4   Conclusions

A roll-to-roll PECVD system was developed for the deposition of transparent and high barrier films on organic substrates. Transparent oxide barrier film was prepared by using O_2/ HMDSO mixture as process gas. we discuss the discharge and deposition parameters with different vacuum pressure The main parameters, such as magnetic field distribution, discharge characteristics, were obtained by testing different discharge parameters and characteristics. The results show that the deposition rate increase with the increase of discharge current. The optimize vacuum pressure is 3 Pa, the water permeability decreases significantly with the increase of thickness, and the 300 nm films show high barrier properties, as low as 1×10^{-2} g/(m^2·day). The film thickness reached 500 nm, and the water permeability value was less than 5×10^{-3} g/(m^2·day), and the water permeability changed little with the increase of the thickness. And the average transmittance is 88.6%@380 nm–760 nm, film has good optical properties for display devices.

References

1. Lee, S., Han, J.-H., Lee, S.-H., Baek, G.-H., Park, J.-S.: Review of organic/inorganic thin film encapsulation by atomic layer deposition for a flexible OLED display. JOM **71**(1), 197–211 (2018)
2. Park, K.W., et al.: High-performance thin H:SiON OLED encapsulation layer deposited by PECVD at low temperature. RSC Adv. **9**(1), 58–64 (2018)
3. Shin, S., Yoon, H.W., Jang, Y., Hong, M.: Stoichiometric silicon nitride thin films for gas barrier, with applications to flexible and stretchable OLED encapsulation. Appl. Phys. Lett. **118**(18), 181901 (2021)
4. Wu, J., et al.: Efficient multi-barrier thin film encapsulation of OLED using alternating Al2O3 and polymer layers. RSC Adv. **8**(11), 5721–5727 (2018)
5. Bari, G.A.K.M.R., Kim, H.: High-barrier polymeric multilayer film with organic and interactive materials. Prog. Org. Coat. **147**, 105814 (2020)
6. Banerjee, D., Mukherjee, S., Chattopadhyay, K.K.: Synthesis of amorphous carbon nanowalls by DC-PECVD on different substrates and study of its field emission properties. Appl. Surf. Sci. **257**(8), 3717–3722 (2011)
7. Gosar, Ž, et al.: PECVD of Hexamethyldisiloxane coatings using extremely asymmetric capacitive RF discharge. Materials **13**(9), 2147 (2020)
8. Gosar, Ž, Kovač, J., Mozetič, M., Primc, G., Vesel, A., Zaplotnik, R.: Deposition of SiOxCyHz protective coatings on polymer substrates in an industrial-scale PECVD reactor. Coatings **9**(4), 234 (2019)
9. Hegemann, D., Bülbül, E., Hanselmann, B., Schütz, U., Amberg, M., Gaiser, S.: Plasma polymerization of hexamethyldisiloxane: Revisited. Plasma Processes Polym. **18**(2), 2000176 (2020)
10. Liehr, M., Dieguez-Campo, M.: Microwave PECVD for large area coating. Surf. Coat. Technol. **200**(1–4), 21–25 (2005)

11. Top, M., et al.: Hollow-cathode activated PECVD for the high-rate deposition of permeation barrier films. Surf. Coat. Technol. **314**, 155–159 (2017)
12. Kwon, S., et al.: Effect of plasma power on properties of hydrogenated amorphous silicon carbide hardmask films deposited by PECVD. Vacuum **174**, 109187 (2020)
13. Lukianov, A.N., et al.: Effect of discharge power and silicon content on optical and mechanical properties of carbon-rich amorphous silicon carbide films obtained by PECVD. J. Alloy. Compd. **801**, 285–294 (2019)
14. Zajíčková, L., et al.: Comparative Study of Films Deposited from HMDSO/O2 in Continuous Wave and Pulsed rf Discharges. Plasma Processes Polym. **4**(S1), S287–S293 (2007)
15. Grüniger, A., Bieder, A., Sonnenfeld, A., von Rohr, P.R., Müller, U., Hauert, R.: Influence of film structure and composition on diffusion barrier performance of SiOx thin films deposited by PECVD. Surf. Coat. Technol. **200**(14–15), 4564–4571 (2006)
16. Israel, D., Riemann, K.U., Tsendin, L.: Relaxation of a collisionless ion matrix sheath. J. Appl. Phys. **95**(9), 4565–4574 (2004)
17. Lee, S.H., Lee, D.C.: Preparation and characterization of thin films by plasma polymerization of hexamethyldisiloxane. Thin Solid Films **325**(1), 83–86 (1998)
18. Lin, H., et al.: Moisture-resistant properties of SiNx films prepared by PECVD. Thin Solid Films **333**(1), 71–76 (1998)
19. Sansonnens, L., Bondkowski, J., Mousel, S., Schmitt, J.P.M., Cassagne, V.: Development of a numerical simulation tool to study uniformity of large area PECVD film processing. Thin Solid Films **427**(1–2), 21–26 (2003)
20. Xiao, W., et al.: A flexible transparent gas barrier film employing the method of mixing ALD/MLD-grown Al2O3 and alucone layers. Nanoscale Res Lett **10**, 130 (2015)
21. Zhang, H., Sang, L., Wang, Z., Liu, Z., Yang, L., Chen, Q.: Recent progress on non-thermal plasma technology for high barrier layer fabrication. Plasma Sci. Technol. **20**(6), 063001 (2018)

Portable Cold Plasma Sterilization Device Based on Dielectric Barrier Discharge and Its Characteristics

Xiuyun Lian, Feng He, Jianxiong Yao, Jiaxin Li, Juan Feng, Chengzhi Deng, and Jiting Ouyang(✉)

School of Physics, Beijing Institute of Technology, Beijing 100081, China
jtouyang@bit.edu.cn

Abstract. For handling the drawbacks of large volume, complex operation and high cost of circuit realization of existing cold plasma sterilization equipment, a portable cold plasma sterilization device incorporating the micro electric power supply technology with surface dielectric barrier discharge (SDBD) structure was proposed in this paper. The discharge characteristics, emission spectrum, active particles and O_3 concentration of plasma generator were studied, and the sterilization experiment was conducted with the sterilization device. The results show that the discharge filament around the SDBD linear electrode are uniform, the discharge power is no more than 5 W. The emission spectrum are mainly composed of N I, N_2 SPS, N_2^+ FNS, O I and OH radical lines. The O_3 concentration within 3 mm from the discharge electrode reached 70 ppm, but O_3 concentration beyond 5 cm is very low. The sterilization device which moves with a homogeneously speed can completely kill *Escherichia coli* (*E.coli*) and *Staphylococcus aureus* (*S.aureus*) in the petri dish (diameter 90 mm) within 15 s; The applied voltage and action distance have a significant effect on the sterilization effect, with the best applied voltage of 4.5 kV and action distance of 3 mm. This device has a lot of advantages, such as simple operation, high sterilization efficiency, low concentration of by-products (say, residual O_3, nitrogen oxide, etc.) and low noise.

Keywords: Cold Plasma · SDBD · active substances · Sterilization

1 Introduction

The widespread of bacteria has threatened public health in recent years. Also, the situation of microbial resistance is increasingly serious. Exploring sterilization technology becomes the primary task at present [1–3]. However, Traditional physical sterilization method has many drawbacks such as low efficiency, high cost, incomplete disinfection, dead ends, etc. Traditional chemical sterilization method has by-product residues and is prone to ecological risks. Nowadays, as a promising alternative technology, cold plasma sterilization has the superiorities of green, fast and efficient [4–6]. The discharge plasma is accompanied by the electric field, UV photons, charged particle, reactive oxygen

species (ROS), reactive nitrogen species (RNS) and chemicals. These substances can quickly destroy biological structures and inactivate cells [7, 8]. Many researchers have studied O_3 as the main ROS has an oxidation potential of 2.07 V, it plays an important role in the sterilization process [9, 10].

Early plasma generators mostly use low-pressure conditions, in contrast, atmospheric pressure cold plasma without vacuum equipment, simple operation process, more practical value [11, 12]. In atmospheric pressure environment, cold plasma can be generated in various ways, such as dielectric barrier discharge, corona discharge, microwave discharge and plasma jet. Among them, dielectric barrier discharge shows brilliant application prospects for its characteristics of low temperature, low noise, high efficiency and rapidity, such as biomedicine [13, 14], food safety [15, 16], environmental protection [17], material surface modification [18], mutagenesis breeding [19], flow control [20], etc. In recent years, sterilization devices based on dielectric barrier discharge have also received much attention [21]. But, existing sterilization equipment is large in size and complex in structure. Thus, it is especially important to optimize the generator to make it be a portable one.

In this paper, we designed a novel SDBD sterilization device, investigated its discharge characteristics, O_3 concentration and sterilization efficiency. Furthermore, we simply examined its by-products and noise.

2 Material and Methods

2.1 Microorganism and Culture Conditions

E.coli (ATCC 23922) and *S.aureus* (ATCC 22004) were used for the sterilization study [22, 23]. These two species are commonly employed as the reference microorganisms in the development of new sterilization techniques, representing Gram-negative and Gram-positive bacteria, respectively. A small amount of *E. Coli* and *S.aureus* stored on solid medium were added to the centrifuge tubes and shaken well. The centrifuge tubes were placed in a constant temperature shaker for 12 h and kept at 37 °C. The shaker oscillated at a frequency of $200\,r\,min^{-1}$ to produce bacterial suspensions. The bacterial suspensions with different dilution concentrations were determined by the enzyme marker (M200 Pro, Tecan, Switzerland). The bacterial concentration was estimated by optical density (OD) measurements at 450 nm (OD450), corresponding to 10^8 CFU mL^{-1} of bacterial cells. The Petri dishes were divided into the control groups and the experimental groups. The experimental group Petri plate was placed at $d = 3, 6, 9, 12$ and 15 mm below the discharge electrode for different treatment time, while the control group was not treated. The viable count method was adopted for counting.

2.2 Experimental Setup

The experimental setup is schematically shown in Fig. 1. The discharge electrode (high voltage electrode) is a wire made of tungsten, with 35 mm in length and 0.1 mm in diameter. It connects to a high voltage sinusoidal AC power supply (Coronalab CTP-2000K) with the frequency of 22 kHz and the voltage amplitude in the range of 0–15 kV through a current limiting resistor R_1 of 2000 Ω. The ground electrode is a round

aluminum plate with 35 mm in diameter. The dielectric barriers is a 0.63 mm ceramic plate. The following experiment is conducted in ambient air with a temperature of 25 °C and the relative humidity of 30% – 40%.
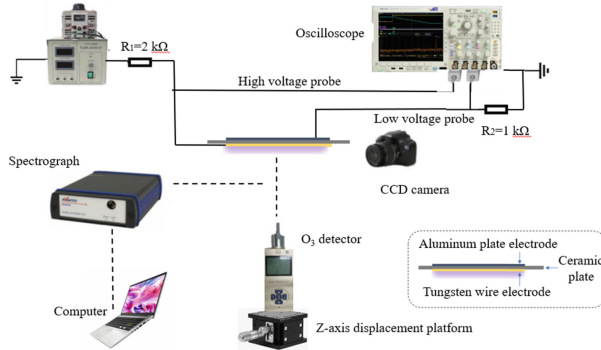
Fig. 1. Experimental setup

The applied voltage was measured by an oscilloscope (Tektronix DPO4104B) through a high voltage probe (Tektronix P6105A). The discharge current was recorded by measuring the voltage across a resistor R_2 of 1000 Ω connected in series with the ground electrode ($I = U/R$). The discharge power was obtained by calulating the area of Lissajous figure. The discharge images were taken by a CCD camera (Canon-EOS-550D). The emission spectrum (OES) generated by the discharge was measured by a spectrometer (Zolix Omni λ-5008); The concentration of O_3 produced by the discharge is measured by an O_3 detector (XLA-B X-03); The NO concentration generated by the discharge is measured by a portable NO gas analyzer (SKY-6000-NO-XY); The noise generated by the discharg is measured by a noise meter.

3   Results and Discussion

3.1   Discharge Characteristics

SDBD Current, Power and Discharge Image
The discharge begins and the current pulse appears when the applied voltage is higher than the breakdown voltage. Figure 2 shows The voltage and current waveforms of 3–5 kV. The current is composed of a series of small pulses. The number and amplitude of current pulses increase with the applied voltage, and the amplitude of current pulses in the positive voltage phase are significantly higher than that in the negative voltage phase.
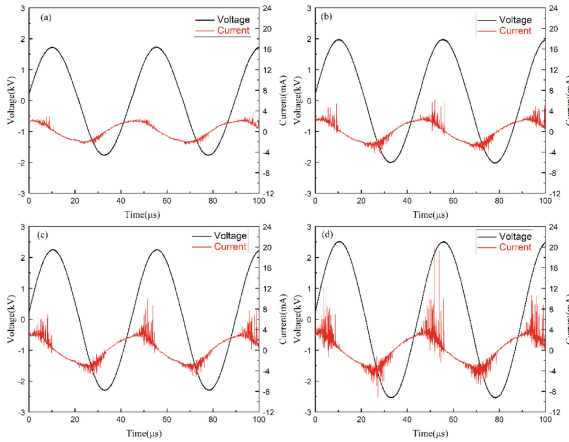
Fig. 2. *U-I* waveform of surface DBD: (a) peak-peak voltage = 3.5 kV; (b) peak-peak voltage = 4 kV; (c) peak-peak voltage = 4.5 kV; (d) peak-peak voltage = 5 kV

As shown in Fig. 3, from the Q–V Lissajous figure the discharge power is calculated using the standard method based on the figure's area [24]:

$$P = \frac{1}{T} \int_0^T u(t)i(t)dt = \frac{1}{T} \int_0^T u(t)C_M \frac{du_M(t)}{dt}dt = fC_M \oint u(t)du_M(t)$$

where f is the power supply frequency. The discharge power increases with the applied voltage, and in the experimental voltage range (3–5 kV), the power is about 1–5 W.
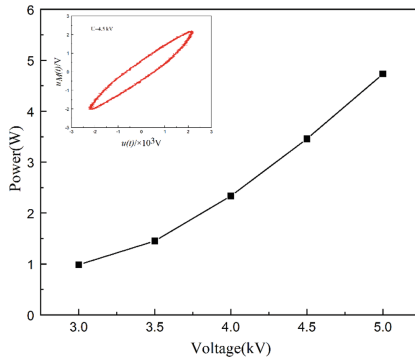
Fig. 3. Discharge power versus peak-peak voltage

Figure 4 shows the variation of SDBD images with the discharge voltage. The CCD exposure times are all 200 ms. At lower voltage, the electrode boundary is distributed with weak discharge filaments, which is a typical corona discharge morphology. As the voltage rises, the discharge filaments become denser and increase in strength, almost uniformly covering the entire edge of the electrode and expanding outward. However,

the discharge may be unstable when the voltage is too high, the highest voltage in this experiment is about 5 kV.
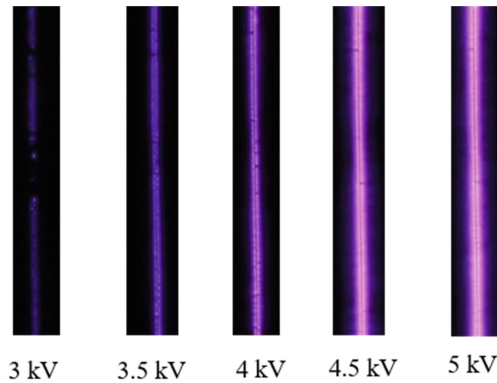
Fig. 4. Image of SDBD

Emission Spectrum, Active Substances and Rotation Temperature

The emission spectrum contains rich information on the plasma parameters, through the analysis of emission spectrum, various active substances generated by SDBD were preliminarily determined. Figure 5 reveals the emission spectrum of SDBD collected at $d = 15$ mm below the discharge electrode, under voltage of 4.5 kV.
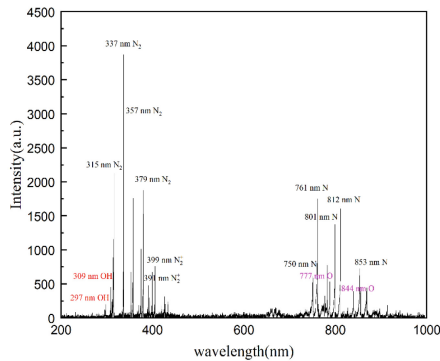
Fig. 5. Emission spectrum of surface DBD

The emission spectrum is mainly dominated by the spectral lines of N I, N_2 SPS, N_2^+ FNS, O I and OH radicals. The highest intensity occurs at 337.1nm, which corresponds to the radiation in the second positive band system of the nitrogen. Due to the presence of water vapor in the air, the OH radical of 309 nm can also be observed with an intensity of about 456 a.u. Important sources of various reactive particles (e.g. O_3, NO_X) can also

be observed in the spectrum: e.g. the spectral lines of oxygen atoms (O-777.2 nm, O: 844.6 nm) corresponding to the atomic transition from the $O(3p^5P)$ state to the $O(3s^5S)$ state and from the $O(3p^3P_{0,1,2})$ state to the $O(3s^3S)$ state, respectively.

O_3 has been selected as an indicator of ROS, which can destroy the cell walls and membranes of bacteria. In Fig. 6, the O_3 concentration decreases with the distance from the discharge electrode and increases with the applied voltage. Precisely because of the rising voltage, the discharge intensity increases, and the high-energy electrons produced rapidly, which greatly increases the probability of inelastic collision between high-energy electrons and oxygen, that accelerates the synthesis of O_3. However, the growth rate decreases at higher voltages, as in the case from 4.5 kV to 5 KV. This may be related to the increased thermal decomposition of O_3 at higher temperatures $(3O_2 \Leftrightarrow 2O_3)$. The highest O_3 concentration under the conditions is about 70 ppm.
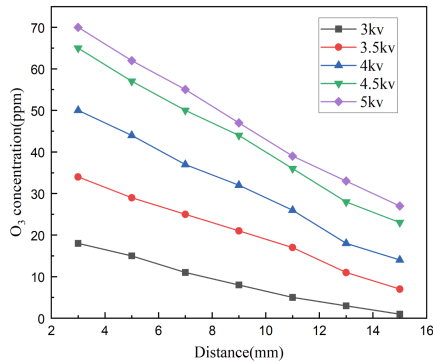
Fig. 6. Ozone concentration versus distance

Considering that the gas temperature in specific disinfection scenarios (e.g. surface processing) is not easily too high, we approximated the plasma temperature using the rotation temperature of gas molecules such as N_2, N_2^+, OH, O_2, CH [25]. Figure 7 shows the variation of the N_2^+ FNS rotation temperature with the discharge voltage, obtained by fitting the spectral line of N_2^+ FNS with the LIFBASE Spectroscopy Tool (SRI International).
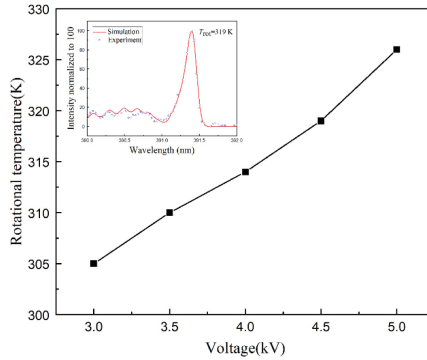
Fig. 7. Rotation temperature as a function of peak-peak voltage

The plasma temperature of SDBD increases with the discharge voltage from 305 K (32 °C) at 3 kV to 326 K (53 °C) at 5 kV. The temperature can be controlled by adjusting the voltage in practical applications.

3.2 Design of Portable Cold Plasma Sterilization Device

Based on the above experiments, we designed a portable cold plasma sterilization device, including a SDBD structure and a power supply, which includes a battery and a high-voltage generator, is shown in Fig. 8.

Side view   Top view
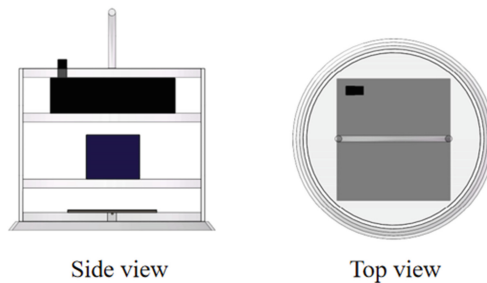
Fig. 8. Schematic diagram of cold plasma sterilization device

With variable sinusoidal AC high voltage (3–5 kV, 22 kHz), we tested its performances of sterilization, by-products, and noise.

3.3 Sterilization Device Performances

Sterilization Efficiency
Plasma sterilization effect is related to many factors, the inactivated effect of *E. coli* and

S. aureus under different treatment time, applied voltage and action distance (distance between the plasma and the bacteria to be treated) was studied in this section.

The Impact of Treatment Time on Sterilization Effect

Figure 9 shows the variation of the sterilization efficiency with the treatment time for different device moving speeds *v*, under the voltage of 4.5 kV and action distance of 3 mm.
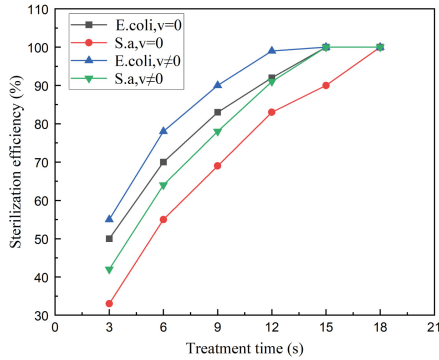
Fig. 9. Sterilization efficiency as a function of treatment time

The sterilization efficiency increases with the treatment time. *E. coli* and *S. aureus* in the Petri dish were completely killed after 18 s at $v = 0$ and 15 s at $v \neq 0$. Relatively speaking, the sterilization efficiency is higher for $v \neq 0$ than for $v = 0$. In addition, it takes longer to kill *S.aureus*, which is related to the structure of the cell. *E. coli* is Gram-negative bacterium with a thin cell wall of about 10–15 nm and a lax strength; While *S.aureus* belongs to Gram-positive bacterium, the cell wall is thicker, about 20–80 nm, and the strength is tougher.

The Impact of Applied Voltage on Sterilization Effect

The variation of the sterilization efficiency with the applied voltage under the treatment time of 6 s, action distance of 3 mm and a moving speed $v \neq 0$ is shown in Fig. 10. It can be seen that the sterilization efficiency increases with the applied voltage. Plasma treatment at 3 kV for 6 s caused only 12% and 23% inactivation of *E. coli* and *S.aureus*; when the voltage was rised to 4.5 kV, the sterilization efficiency reached 78% and 63%. As the applied voltage rises, the active component in the plasma increases and the inactivated effect of bacteria is enhanced. However, the growth rate of the sterilization efficiency decreases at higher voltages, e.g., from 4.5 kV to 5 kV by only about 4%.
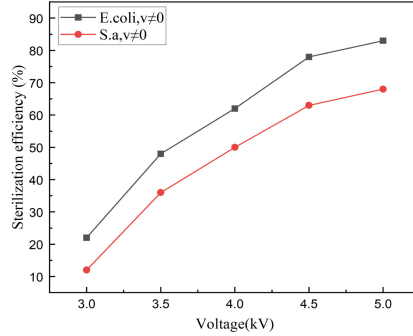
Fig. 10. Sterilization efficiency as a function of peak-peak voltage

The Impact of Action Distance on Sterilization Effect

The variation of the sterilization efficiency with the action distance under the treatment time of 6 s, voltage of 4.5 kV and a moving speed $v \neq 0$, as shown in Fig. 11 with the rise of action distance, the bactericidal effect gradually decreases. Inactivation efficiencies of 78% and 64% for E. coli and S. a at an action distance of 3 mm. When the action distance was adjusted to 15 mm, the inactivation efficiency of *E. coli* and *S.aureus* was only 33% and 21%. It depends on the lifetime of the particles produced by the discharge. The short-lived active particles include N, HO_2, OH, etc. While long-lived active particles contain O_3, HNO_2, etc. At a close distance, the presence of short-lived active particles near the Petri dishes makes the bactericidal efficiency higher than elsewhere. But at a long distance, because of the disappearance of short-lived active particles, the sterilization efficiency decreases. On the other hand, the concentrations of long-lived active particles also affect bacteria with a certain efficiency.
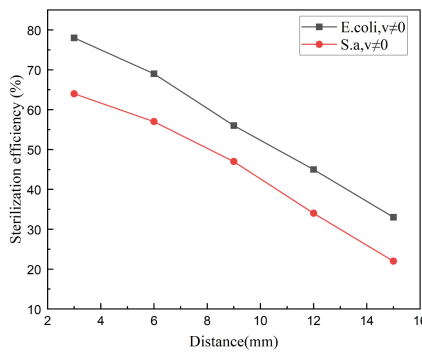
Fig. 11. Sterilization efficiency as a function of operating distance

By-Products-O_3 and NO_X

O_3 and NO_X are not just bactericidal actives or harmful by-products. We tested the

residual O_3 and NO_x concentrations at the voltage of 4.5 kV and the distance of 5 cm from the discharge electrode.

Higher concentration of O_3 are found only close to the discharge electrode (e.g. Figure 7). However, due to the rapid decomposition of O_3, the O_3 concentration was only 1.6 ppm of continuous discharge for 0.5 h. After the end of discharge for 2 min, the O_3 concentration was only 0.05 ppm, which is lower than the O_3 safety concentration (0.1 ppm). In addition, the NO, NO_2, and NO_X produced were all less than 0.1 ppm (48.8 μg/m3), which is lower than the Class I limit value of NOx < 250 μg/m^3 in GB 3095–2012.

Discharge Noise

This sterilization device is free of mechanical rotating component, so it produces very little noise. Figure 12 shows the variation of the detection noise with the discharge voltage at $d = 50$ mm below the discharge electrode, which contains the background noise in the room of about 32 dB(A). At the discharge voltage lower than 3.3 kV, Due to the background noise is higher than the discharge noise, the noise from the discharge is almost undetectable. At the voltage greater than 3.3 kV, the detection noise increases with the voltage, and in the range of the investigation, the total noise are less than 40 dB (A), in line with the requirement that machine noise should be less than 55 dB (A) in GB/T18801–2015.
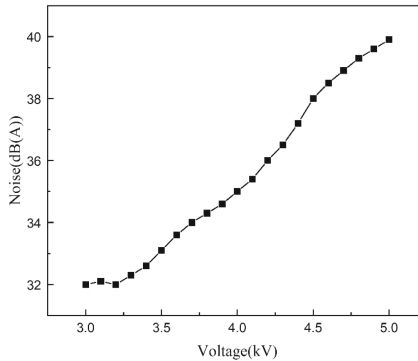
Fig. 12. Variation of surface DBD noise with peak-peak voltage

4   Conclusion

In summary, a sterilization device based on SDBD is designed. We have studied the optical and electrical characteristics of this device. Choosing *E.coli* and *S. aureus* as the experimental bacteria for plasma treatment and calculating the sterilization efficiency. The main conclusions are as follows:

1) The current amplitude of SDBD is in the order of mA, and the discharge power is less than 5W. The emission spectrum indicate that a variety of active substances are

produced by SDBD, which is dominated by the spectral lines of N I, N_2 SPS, N_2^+ FNS, O I and OH radicals. The concentration of O_3 can reach up to 70 ppm under the experimental conditions.

2) Sterilization efficiency increases with the treatment time and applied voltage, and decreases with the action distance. The uniformly moving sterilization device can completely kill *E.coli* and *S. aureus* in the petri dishes within 15 s, and it takes longer to kill *S.aureus*.

3) The performances of the sterilization device are excellent. Due to the free of mechanical rotating component, its noise is very little. Due to the rapid O_3 decomposition and diffusion, the O_3 concentration was only 1.6 ppm of continuous discharge for 0.5 h and only 0.05 ppm after the end of discharge for 2 min at about $d = 5$ cm below the discharge electrode; the NOx concentration was less than 0.1 ppm, indicating that the by-products produced by the device comply with the relevant quality standards.

References

1. Carrillo, I.O., Valverde, C.M., Tingle, T.N., et al.: Immediate use steam sterilization (IUSS) sterilizes n95 masks Without mask damage. Infect. Controland Hosp. Epidemiol. **41**(9), 1–5 (2020)
2. Wolf, C., Vongunten, U., Kohn, T.: Kinetics of inactivation of water borne enteric viruses by O_3. Environ. Sci. Technol. **52**(4), 2170–2177 (2018)
3. Wang, H., Zhang, L.Y., Luo, H.Y., et al.: Sterilizing processes and mechanisms for processing of Escherichia coli with dielectric-barrier discharge plasma. Appl. Environ. Microbiol. **86**(1), e01907-e1919 (2020)
4. Feldmann, F., Shupert, W.L., Haddock, E., et al.: Gamma irradiation as an effective method for inactivation of Emerging viral pathogens. Am. J. Trop. Med. Hyg. **100**(5), 1275–1277 (2019)
5. Li, D., Sangion, A., Li, L.: Evaluating consumer exposure to disinfecting chemicals against coronavirus disease 2019 (COVID-19) and associated health risks. Env. Int. **145**, 106108 (2020)
6. Filipic, A., Gutierrez-Aguirre, I., Primc, G., et al.: Cold plasma, a new hope in the field of virus inactivation. Trends Biotechnol. **38**(11), 1278–1291 (2020)
7. Moisan, M., Barbeau, J., Pelletier, J.: Plasma sterilization methods and mechanisms. Pure Appl. Chem. **74**(3), 349–358 (2013)
8. Guo, J., Huang, K., Wang, J.P.: Bactericidal effect of various non-thermal plasma agents and the influence of experimental conditions in microbial inactivation: a review. Food Control **50**, 482–490 (2015)
9. von Gunten, U.: Ozonation of drinking water: Part I. Oxidation kinetics and product formation. Water Res. **37**(7), 1443–1467 (2003)
10. Sharma, M., Hudson, J.B.: O_3 gas is an effective and practical antibacterial agent. Am. J. Infect. Control **36**(8), 559–563 (2008)
11. Xu, X.J., Zhu, D.C.: Gas Discharge Physics. Fudan University Press, Shanghai (1996)
12. Wu, Y., Liang, Y.D., Wei, K., et al.: Rapid allergen inactivation using atmospheric pressure cold plasma. Environ. Sci. Technol. **48**(5), 2901–2909 (2014)
13. Weltmann, K.-D., von Woedtke, Th.: Plasma medicine—current state of research and medical application. Plasma Phys. Control. Fusion **59**(1), 014031 (2017)

14. Fridman, G., Friedman, G., Gutsol, A., et al.: Applied plasma medicine. Plasma Processes Polym. **5**(6), 503–533 (2010)
15. Olatunde, O.O., Benjakul, S.: Dielectric barrier discharge cold atmospheric plasma: Bacterial inactivation mechanism. J. Food Saf. **39**(6), e12705 (2019)
16. Feizollahi, E., Misra, N.N., Roopesh, M.S.: Factors influencing the antimicrobial efficacy of Dielectric Barrier Discharge (DBD) Atmospheric Cold Plasma (ACP) in food processing applications. Crit. Rev. Food Sci. Nutr. **4**, 1–24 (2020)
17. Shi, M.C.: Research on the application of plasma technology in environ mental protection. Env. Dev. **31**(1), 78 (2019)
18. Šira, M., Trunec, D., Stahel, P., et al.: modification of polycarbonate in homogeneous atmospheric pressure discharge. J. Phys. D Appl. Phys. **41**(1), 015205 (2007)
19. Li, H., Wang, L., Li, G., et al.: Manipulation of lipase activity by the Helium radio-frequency, atmospheric-pressure glow discharge plasma jet. Plasma Processes Polym. **8**(3), 224–229 (2011)
20. Li, Y., Wang, J., Wang, C., et al.: Properties of surface arc discharge in a supersonic airflow. Plasma Sources Sci. Technol. **19**(2), 025016 (2010)
21. Lee, J., Bong, C., Lim, W., et al.: Fast and easy disinfection of coronavirus-contaminated face masks using O3 gas produced by a dielectric barrier discharge plasma generator. Env. Sci. Technol. Lett. **8**, 339–344 (2021)
22. Timoshkin, I.V., et al.: Bactericidal effect of corona discharges in atmospheric air. IEEE Trans. Plasma Sci. **40**(10), 2322–2333 (2012)
23. Li, Q., Xie, R.C., Liy, W., et al.: Enhanced visible-light-induced photocata lytic disinfection of E. coli by carbon-sensitized Nitrogen-dopedtitanium oxide. Env. Sci. Technol. **41**(14), 5050–5056 (2016)
24. Tang, X.L., Qiu, G., Reng, Z.F., et al.: Partial electrical parameters of dielectric barrier discharge at atmospheric pressure. High Voltage Eng. **30**(9), 55–57 (2004)
25. Raud, J., Laan, M., Jogi, I.: Rotational temperatures of N_2(C,0) and OH(A,0) as gas temperature estimates in the middle pressure Ar/O_2 discharge. J. Phys. D Appl. Phys. **44**(34), 345201 (2011)
26. GB 3095–2012: Ambient Air Quality Standards. China Standards Press, Beijing (2012)

High-Voltage Discharge and Application

Study on the Time Characteristics of Polarization/Depolarization Currents in High Voltage Cables

Ji Wu[1], Shihu Yu[1], Jianping Huang[1], Zijian Wan[2], Haozhou Wang[2], Cheng Zhang[2] (ID),
and Chengyan Ren[2(✉)] (ID)

[1] Guangdong Key Laboratory of Electric Power Equipment Reliability, Electric Power Research
Institute of Guangdong Power Grid Co., Ltd., Guangzhou 510080, China

[2] Beijing International S&T Cooperation Base for Plasma Science and Energy Conversion,
Institute of Electrical Engineering Chinese Academy of Sciences, Beijing 100190, China

rcy@mail.iee.ac.cn

Abstract. To study the effect of polarization/depolarization time on the
isothermal relaxation current (IRC) of high-voltage cables, the polariza-
tion/depolarization currents of 110 kV high-voltage cross-linked polyethylene
(XLPE) cables were tested under different experimental conditions. A third order
exponential function was used to fit the depolarization current to calculate the
aging factor and the resulting depolarization current curve was used to observe
the steady state current and the time constant. The results show that with the
increase of depolarization time, the fitted curve time constant and aging factor
A gradually stabilize. When the depolarization time is greater than 1200 s, the
stability of the time constant and aging factor A can be effectively improved. The
polarization/depolarization current gradually increases with increasing polariza-
tion time, and the steady state polarization current stabilizes after 1200 s. More
accurate polarization current test results can be obtained at polarization time
of 1500–1800 s. The results of this paper are useful for the selection of polar-
ization/depolarization time in IRC tests for the field application of isothermal
relaxation currents to assess the aging state of cables.

Keywords: High voltage cables · Polarization/depolarization currents ·
Temporal characteristics

1 Introduction

Since the 1950s, China has been transformed from an agricultural to an industrial country,
and its industrial economy has a rapid grown these years, which increases the demand
for power generation and power quality [1]. Compared to traditional oil-impregnated
paper-insulated cables, XLPE cables have better electrical and mechanical properties
[2].

There are currently three main methods for diagnosing the condition of cable insula-
tion, namely online monitoring, offline monitoring and powered testing methods [3, 4].

Most of the above diagnostic methods require testing the electrical parameters associated with the cable in operation and assessing the cable insulation condition by the measured parameters.

The polarization/depolarization current method used in this paper is a new method based on the theory of dielectric response [5, 6], which has the advantages of non-destructive, rich diagnostic information, simple test circuit, low power consumption, etc. It is suitable for insulation diagnosis of cables in engineering sites. The subject of this paper is a section of 110 kV retired XLPE cable, with the length of 0.5 m, the type of ZC-YJLW02-64/110 V-1 × 800 m^2, and service life of 12 years.

2　Effect of Different Depolarization Time on the Results of Depolarization Current Fitting

The polarization voltage was set to 1 kV and the depolarization time was varied from 300 s to 3000 s. A third-order exponential function was fitted every 300 s and the fitted results were observed.

As can be seen from Fig. 1, the high voltage DC source is responsible for charging the high voltage cable and the circuit is equipped with a 1 MΩ current limiting resistor to prevent excessive circuit current from damaging the weak current test set Keithley 6517B. A high voltage relay enables switching of the polarization/depolarization current test circuit and the host computer is responsible for the collection of experimental data.
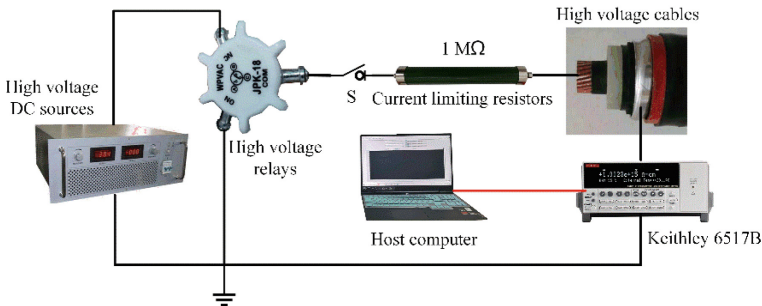
Fig. 1. Polarization/Depolarization current test loop

According to the theory of isothermal relaxation currents proposed by J.G. Simmons and M.C. Tam [7], a third order exponential function can be fitted to the depolarization current with the following equation:

$$I_d(t) = I_0 + \sum_{i=1}^{3} \alpha_i e^{(-t/\tau_i)} \tag{1}$$

where $I_d(t)$ is the depolarization current, t is the depolarization time, I_0 is the current value when the depolarization current is at steady state, α_i and τ_i reflect the trap density and trap level depth respectively. The third order indices represent the bulk polarization

Table 1. Results of current fitting for different depolarization time.

t_d	I_0	α_1	τ_1	α_2	τ_2	α_3	τ_3	A
300 s	−17.33	−126.81	1.46	−151.29	5.69	−77.12	77.43	4.19
600 s	−15.58	−138.49	1.55	−142.74	6.26	−75.25	85.93	4.21
900 s	−2.61	−244.51	3.41	−77.88	55.47	−25.98	626.60	3.12
1200 s	−5.20	−242.78	3.30	−74.94	47.85	−29.67	396.51	2.68
1500 s	−3.13	−243.62	3.35	−76.84	51.53	−28.30	519.88	2.75
1800 s	−5.20	−242.82	3.31	−74.94	47.98	−29.59	397.17	2.68
2100 s	−4.86	−242.99	3.32	−75.36	48.70	−29.22	417.28	2.73
2400 s	−5.73	−242.40	3.29	−74.03	46.31	−30.70	361.72	2.62
2700 s	−5.38	−242.67	3.30	−74.63	47.36	−30.00	384.08	2.66
3000 s	−5.29	−242.75	3.30	−74.80	47.72	−29.76	391.16	2.67

of the cable insulation, the interfacial polarization of the crystalline and amorphous regions and the interfacial polarization of salt and hydrated ions due to aging [8, 9].

According to the German aging factor criterion, when the aging factor A is greater than 2.10, the cable insulation state is seriously deteriorated, which is in line with its 12 years of operation. The aging state of the cable can be initially determined by testing the polarization/depolarization current.

An increase in depolarization time does not change the dielectric response of the insulation, but has an effect on the third order exponential fit of the depolarization current data. In terms of the mechanism of isothermal relaxation currents, the longer the depolarization time, the wider the distribution of trap level that can be reflected. So the characterization of deep traps requires longer depolarization measurement time. As can be seen from Table 1, the time constants are more stable at depolarization time of 1200–3000 s. Therefore, the depolarization time of 1200–3000 s can effectively improve the accuracy of the isothermal relaxation current measurement results and the stability of the time constant, thus improving the reliability of the isothermal relaxation current method in cable insulation condition assessment.

3 Effect of Different Polarization Time on the Results of Depolarization Current Fitting

The depolarization current decreases when the polarization time increases from 300 s to 600 s from the Fig. 2, which may be due to the fact that the charge fully fills the trap at 300 s of polarization, but some of the charges are not completely released during the depolarization process. When polarized again, the charge remaining near the cable core may weaken the electric field at the core to a certain extent, affecting the charge injection at the electrode and the charge migration inside the material, resulting in a reduction in the trap charge, making the depolarization current for a polarization time of 600 s decrease compared to that for a polarization time of 300 s.
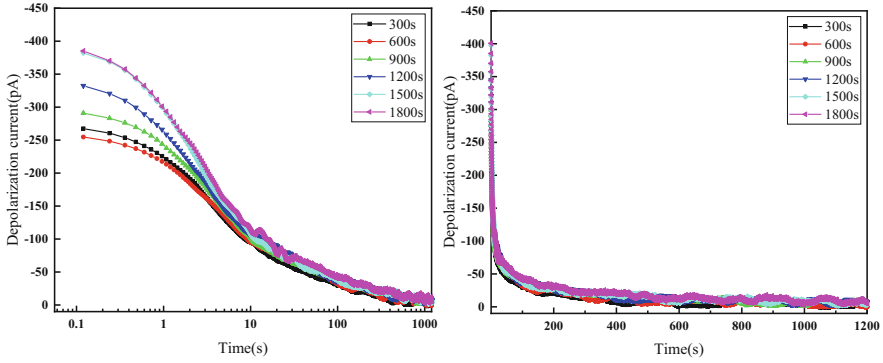
Fig. 2. Depolarization current curves at different polarization time

When the polarization time increases from 600 s to 1800 s, the depolarization current tends to increase, and the increase is more obvious. The depolarization currents obtained at 1500 s and 1800 s are almost identical, probably because the increase in polarization time overcomes the influence of residual charge on charge injection and migration, and to a certain extent drives more charges into the trap, thus causing the depolarization current to increase. However, the charge trapping process has basically reached a steady state, so the depolarization current values obtained at different polarization times are close. In the later stages of the depolarization current test, the polarization time has no effect on the depolarization current, as the difference between the depolarization currents in the cables becomes smaller after a longer discharge time.

4   Conclusions

The steady-state depolarization current, time constant and aging factor A obtained after fitting are gradually stabilized as the depolarization time increases. When the depolarization time is greater than 1200 s, the depolarization current test results are more accurate at this point. A shorter polarization time will produce a smaller depolarization current, extending the polarization time will improve the reliability of the measurement results. A polarization time of not less than 1200 s will give more accurate results.

References

1. Andritsch, T., Vaughan, A., Stevens, G.C.: Novel insulation materials for high voltage cable systems. IEEE Electr. Insul. Mag. **33**(4), 27–33 (2017)
2. Habib, M.A., Nasart, L.S., Sharkawy, R.M.: Improvement the electrical performance of cross-linked polyethylene high voltage cables. In: Abdalla, O.H. (eds.) 18th International Middle-East Power Systems Conference 2016, MEPCON, pp. 21–25. Egypt, Cairo (2016)

3. Dakka, M., Bulinski, A., Bamji, S.: On-site diagnostics of medium-voltage underground cross-linked polyethylene cables. IEEE Electr. Insul. Mag. **27**(4), 34–44 (2011)
4. Zhang, Y., Li, M., Xu, Z., et al.: Cable incipient fault identification based on trajectory image and convolutional neural network. Guangdong Electr. Power **35**(8), 86–94 (2022). (in Chinese)
5. Mitroi, M.R., Ilies, C.: Analysis of insulation system of power transformers by polarization/depolarization currents method. Univ. Politehnica Bucharest Sci. Bull.-Ser. A-Appl. Math. Phys. **73**(3), 163–172 (2011)
6. Baral, A., Chakravorti, S.A.: Modified maxwell model for characterization of relaxation processes within insulation system having non-uniform aging due to temperature gradient. IEEE Trans. Dielectr. Electr. Insul. **20**(2), 524–534 (2013)
7. Simmons, J.G., Tam, M.C.: Theory of isothermal currents and the direct determination of trap parameters in semiconductors and insulators containing arbitrary trap distributions. Phys. Rev. B **7**(8), 3706–3713 (1973)
8. Tiandi, L., Cheng, Z., Hao, L., et al.: Insulation state evaluation of 110 kV cable based on isothermal relaxation current. Adv. Technol. Electr. Eng. Energy **39**(04), 43–52 (2020). (in Chinese)
9. Chen, J., Zhao, Y., Fan, X., et al.: Effect of electrothermal combined aging on dielectric spectrum properties on high voltage AC XLPE cable insulation. Guangdong Electr. Power **35**(9), 117–126 (2022). (in Chinese)

A Novel Electrical Life Model of Crosslinked Polyethylene Based on AC Breakdown Time Statistical Analysis

Linru Ning, Dangguo Xu$^{(\boxtimes)}$, Shiyang Huang, Zhaowei Peng, and Yi Lu

Electric Power Research Institute of State Grid Jibei Electric Power Company Limited, Beijing, China
derzinit@126.com

Abstract. To propose a more accurate electrical life model of crosslinked polyethylene (XLPE) under AC voltage, breakdown experiments of XLPE samples were carried out. The distribution of breakdown time varied with electric field strength within the sample were statistically analyzed, based on which the traditional inverse-power-law related electrical life model was thoroughly improved. The results showed that, under the same electric field strength, the breakdown time of XLPE could still be very dispersive, which mainly distributed in three time intervals. Different time intervals corresponded to different insulation failure processes, where the dominant failure process was determined by the electric field strength. By replacing the whole electrical life of the XLPE samples with only the breakdown time component of the dominant failure process, an improved electrical life model of XLPE was obtained. Compared with the traditional life model, the lifetime index n obtained by the improved model was more precise to evaluate the aging time of XLPE samples, especially those under long electrical aging process.

Keywords: Cross-linked Polyethylene · Failure time · Weibull Distribution · Statistic Characteristics · Inverse Power Law

1 Introduction

Cross-linked polyethylene (XLPE) is a semi-crystalline polymer formed by physical or chemical cross-linking of polyethylene (PE), and is widely used as an insulating material for power cables due to its outstanding electrical, thermal and mechanical properties [1]. XLPE cable has been applied in urban power systems in China for more than 40 years since the 1980s [2]. However, concerning problem rises as the insulation performance of XLPE cable decreases gradually due to the influence of electrical, thermal, moisture and other factors in long-term operation, which threatens the stability of power system [3]. According to statistics, cable failures due to insulation aging account for 21.1% of transmission line failures, ranking second among all other factors. With the further increase of cable service life, insulation aging of cables tends to be more serious, which will inevitably increase the frequency of cable transmission failure [4]. Therefore, it is

of great significance to analyze the failure characteristics of XLPE, and make intensive studies of XLPE life assessment to improve the reliability of power grid operation.

For cables that are put into operation at early years, or those operates under low voltage levels, thermal aging is the main form of the insulating aging. However, with the continuous increase of cable transmission voltage level, electrical aging begins to play an increasingly important role in the failure process of XLPE insulation. Therefore, attention has been drawn to the electrical aging process of XLPE [5]. Due to the difference between the external environment and the internal structure of materials, there are different forms of electrical aging in insulating materials. For different aging forms, scholars have proposed different electrical aging theories, including charge injection and extraction theory, photodegradation theory, hot electron theory, and partial discharge theory, etc. [8, 9]. Under long-term electric stress, the molecular structure of XLPE is destroyed, and its insulation performance is gradually reduced. If there are defects such as air gaps or micropores in the insulation, the electric field distortion will also occur at the defects, thus accelerating the electrical aging process. To evaluate the electrical life of XLPE, scholars have conducted further researches. Liu carried out the AC withstand test and DC withstand test on XLPE cable slices respectively, and found that the AC breakdown field strength of XLPE decreases, whereas the DC breakdown field strength of XLPE increases, with the increase of voltage application time. Wang studied the DC electrical life of XLPE under different temperature, and adopted the traditional inverse power law model to quantify results. Conclusion indicates that the life exponent n of XLPE decreases with the increase of temperature. Yang obtained the XLPE insulation aging life index by changing the test parameters in the step-boost withstand test, and proved that the life model accuracy can be improved by prolonging the voltage duration. Despite of all the above researches, the electrical life model of XLPE is still within laboratory and being not adopted to industry. The reason is that the effect of electric stress on the performance of insulation material is of probability distribution. Even under the same experimental conditions, the insulation failure time of the sample also has a large dispersion [6–9]. However, the existed researches often ignore the statistical characteristics of the electrical life of XLPE.

In order to improve the accuracy of electrical life assessment of cable insulation materials, it is necessary to strengthen the research on the statistical characteristics of failure time of XLPE materials, but little attention has been paid to this point. In this paper, the voltage withstand test of XLPE samples is carried out; the distribution characteristics of XLPE failure time under different field strengths are counted; and the traditional XLPE electrical life model based on the inverse power law is modified based on statistical characteristics of failure time accordingly.

2   Experimental Setup

The setup of voltage withstand test platform is shown in Fig. 1. The platform mainly consists of a transformer, a voltage regulator, a water resistor and a high voltage oil cup. The transformer and the voltage regulator provide the high voltage required for the test. The water resistor has a resistance value of 30 kΩ, which limits the short-circuit current once the sample is broken down. High voltage generated by the transformer is applied

to the XLPE sheet sample through the oil cup. Inside the oil cup are two disc-shaped copper electrodes with a diameter of 25 mm and a thickness of 4 mm, the edges of which are rounded into a semicircle with a radius of 2.5 mm. Place the XLPE sheet between the two electrodes and rotate the adjusting nut on the oil cup to clamp the sample, then measure the thickness of the three-layer structure of "electrode-XLPE sample-electrode" with a vernier caliper. The thickness should be within 9 ± 0.01 mm to ensure that each sample bears the same pressure during the test. In order to avoid surface flashover and partial discharge during the experiment, the electrodes and samples were immersed in Kunlun 25 transformer oil. The experimental temperature was controlled between 15 °C and 20 °C.
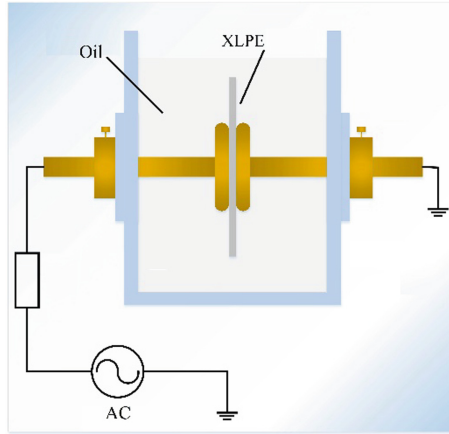
Fig. 1. Voltage withstand test platform for XLPE sheet samples

XLPE samples used in the study were 200 mm × 200 mm × 1 mm sheets provided by Sunway Co., Ltd. The thickness of different samples and different parts of the same sample is measured by a thickness meter, the results show that the thickness of the sample is 1 ± 0.01 mm. Before the experiment, the sample was cut into 55 mm × 55 mm × 1 mm. The surface of each sample was wiped with absolute ethanol to eliminate the influence of surface impurities on the experimental results.

To determine the testing voltage of the voltage withstand test, the breakdown strength of 10 XLPE samples were first measured based on GB/T 1408.1. The test was carried out with an equal diameter electrode with a diameter of 25 mm and the edges rounded to an arc with a radius of 2.5 mm. The size of the tested sample was 55 mm × 55 mm × 1 mm. During the test, the voltage was continuously increased at a rate of 0.5 kV/s until the breakdown. To avoid flashover, the sample and electrodes were immersed in Kunlun 25 transformer oil.

According to the test results, the breakdown strength E_0 of the XLPE sheet sample is 42.49 kV/mm, which meets the specified value of JB/T 10437 on XLPE insulation breakdown strength. Referring to GB/T 29311, the initial field strength applied on the XLPE samples during the voltage withstand test should be between $0.8E_0$ and $0.9E_0$, therefore, $E = 36$ kV/mm is selected as the initial field strength of the test. The field

strengths of the other four groups were set to 28 kV/mm, 30 kV/mm, 32 kV/mm and 33 kV/mm. The thickness of the XLPE samples is 1 mm, therefore, voltages applied on the samples are 28 kV, 30 kV, 32 kV, 33kV and 36 kV, respectively.

In order to study the effect of the internal structure of XLPE on its electrical life, the microstructure of the cross section of XLPE sheet sample was observed by JSM7500F scanning electron microscopy (SEM). The magnification was 2000 times. Before the test, the XLPE was cooled in liquid nitrogen for 30 min for brittle fracture, and the fracture surface was treated by metal spraying.

3   Experimental Results

3.1   Breakdown Strength Rest Results

The breakdown strength test results of the XLPE sheet samples are shown in Fig. 2. According to the standard GB/T 29310, the sample breakdown data can be analyzed by using the two-parameter Weibull distribution.
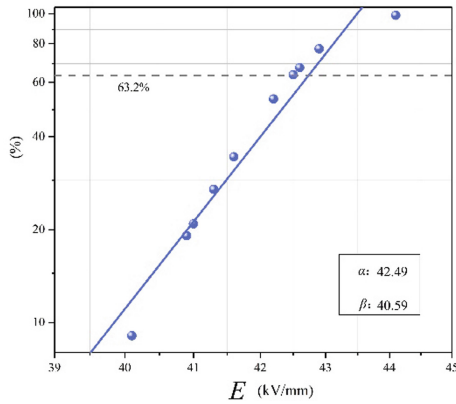
Fig. 2. The breakdown strength test result of samples

The Weibull distribution can be expressed as following:

$$F(x) = 1 - \exp(-(\frac{x}{\alpha})^{\beta}) \tag{1}$$

In formula (1), $F(x)$ is the cumulative failure probability of the sample; x is the independent variable, which can represent the breakdown time or breakdown field strength of the sample in this paper; β is the shape parameter, and the larger the value of β, the smaller the data dispersion is; α is the scale parameter. When x represents the failure time of the sample under constant electrical stress, α represents the failure time corresponding to the cumulative failure probability of 63.2% of the sample. When x represents the short-term breakdown strength of the sample, α represents the electric field strength corresponding to the cumulative failure probability of 63.2% of the samples. Generally,

α is used to represent the characteristic failure time or breakdown strength of the sampled
。

It can be seen from Fig. 2 that the characteristic breakdown strength of the XLPE
sheet sample is $E_0 = 42.49$ kV/mm. The shape parameter $\beta = 40.59$, which indicates
that the dispersion of the breakdown strength of XLPE is small.

3.2 Voltage Withstand Test Results

5 set of experiments were conducted to investigate the *E-t* characteristics of XLPE
samples at different electric field strengths, with 12 sample in each set.

Figure 3 is the schematic diagram of the distribution of breakdown points of the
sample, in which the "pressurized area" is the part of the sample in close contact with
the electrode. In order to avoid the influence of the edge effect on the experimental
results, the failure time of the samples whose breakdown points are located in the edge
area is not included in the statistics.
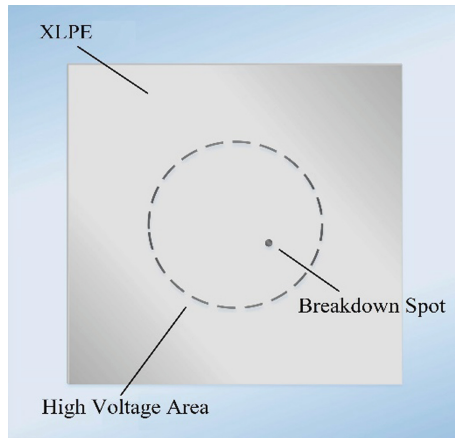
Fig. 3. Breakdown point distribution diagram

The Weibull distribution of the failure time of samples under different electric field
strengths is shown in Fig. 4. According to the results, failure time of the XLPE sample
increase with the decrease of the applied field strength. At the same time, it can be found
that the shape parameter β is always lower than 1 regardless of the field strength, which
indicates that the failure time dispersion of the samples is large.

4   Electrical Life Model and Its Modification

4.1   XLPE Electrical Life Model Based on Statistical Characteristics of Failure Time

The relationship between the electrical lifetime of XLPE and the applied electric field
follows the inverse power law:

$$t = CE^{-n} \tag{2}$$
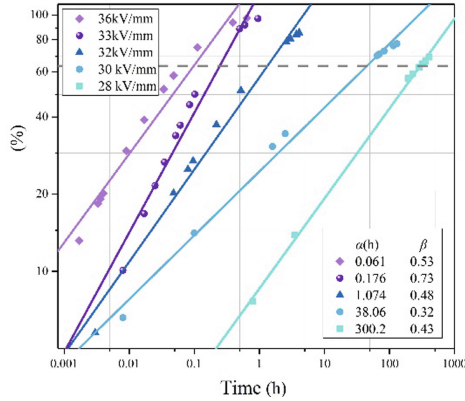
Fig. 4. Weibull distribution of failure time of XLPE samples under different electric field intensities

In formula (2), t represents the sample failure time; E represents the electric field strength, and C is a constant. When the life index n is a constant, the E-t characteristic curve of the material is a straight line on the log-log coordinate axis. The E-t characteristic curve of XLPE sheet samples can be drawn from the voltage withstand test results, and then the XLPE electrical life model can be established.

In the course of the study, it was found that some samples were not broken down in the limited experimental time, although the electrical life of the samples should be prolonged with the decrease of electric field strength according to the inverse power law, the proportion of the number of samples that were not broken down to the total number of samples in the same group was still increasing. On the other hand, through the statistics of the breakdown time of the breakdown samples, it is known that the failure time of XLPE sheet samples has a large dispersion, even under the same field strength. The maximum failure time of the samples is more than a hundred times of the minimum failure time. Therefore, it is not appropriate to draw the E-t characteristic curve of XLPE sheet samples directly according to the statistical results of failure time.

According to Fig. 4, failure time of samples under same electric field strength has a large dispersion, and can be divided into several time intervals, each of which may correspond to different failure processes of XLPE. Therefore, it is necessary to classify and discuss different failure processes when establishing a new electrical life model.

In order to reduce the influence of subjective factors on the classification results, a noisy spatial clustering method based on Density (Density-Based Spatial Clustering of Applications with Noise) is used. The DBSCAN algorithm divides the failure time of the broken down samples according to the distribution concentration of data points. Firstly, the algorithm traverses each data point, calculates the local density of each point and the distance between each data point, and then finds out the point with the maximum local density as the clustering center, and completes the data clustering analysis according to the distance between each point and the clustering center. The clustering results are shown in Fig. 5.
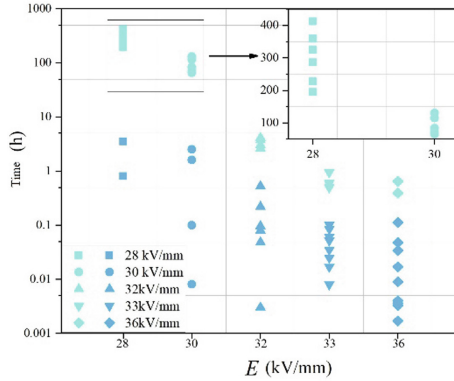
Fig. 5. Clustering result of failure time of the breakdown samples

According to Fig. 6, the failure time of the punctured samples can also be divided into two categories. Considering the availability of unbroken samples, the failure time of XLPE insulation is distributed in three time intervals.

According to the classification results of DBSCAN algorithm, the XLPE insulation failure is divided into three failure processes: failure process 1 (samples with short time breakdown), failure process 2 (samples with long time breakdown) and failure process 3 (samples without breakdown in the experiment). The failure time of samples in different failure processes is processed by Weber distribution, and the statistical results are shown in Table 2.

Table 2. Statistical results of failure time of different failure processes of XLPE samples

E (kV/mm)	Scale parameter α/H		The shape parameter β	
	Failure process 1	Failure process 2	Failure process 1	Failure process 2
36	0.022	0.609	0.74	2.87
33	0.056	0.790	1.35	3.01
32	0.174	3.674	0.63	5.21
30	0.958	104.8	0.40	3.46
28	2.941	335.8	0.96	3.98

In the experiment, it is found that the number of unbroken samples (corresponding to failure process 3) increases with the decrease of applied field strength, and the number of samples in failure process 1 and failure process 2 also changes with the change of field strength by analyzing the breakdown time data of broken samples. In order to study the relationship between XLPE failure process and electric field strength, the proportion of samples in each failure process to the total number of samples in the same group under different field intensities is calculated, and the calculation results are shown in Fig. 6.
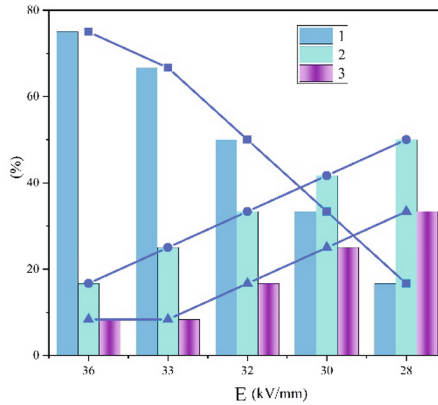
Fig. 6. The relationship between the proportion of different failure processes and the electric field strength

It can be seen from Fig. 6 that when the electric field strength is high, the failure process 1 accounts for the highest proportion, followed by the failure process 2, and the failure process 3 accounts for the lowest proportion. With the decrease of electric field strength, the proportion of failure process 1 decreases, while the proportion of failure process 2 and failure process 3 increases. When the electric field strength $E = 30$ kV/mm, the proportion of failure process 2 exceeds that of failure process 1, which is the highest among the three failure processes. When the field strength E = 28 kV/mm, the proportion of failure process 1 decreases further, and it is the lowest among the three failure processes. The above results show that different failure processes are affected by different electric field strengths, and the three failure processes may correspond to different insulation failure mechanisms.

The relationship between failure probability and time of power equipment meets the "bathtub curve", that is, the failure rate of equipment is higher in the early stage of operation, and the "early failure" of equipment often occurs at this time. When the equipment runs stably, the failure probability decreases and tends to be stable, and the failure of the equipment is mostly "random failure". With the increase of the operation life of the equipment, the failure probability of the equipment also increases. At this time, the failure of the equipment is mostly caused by "aging failure", and the failure time of different failure processes is quite different.

In the manufacturing process, there are inevitably defects such as cracks or micropores in XLPE. Due to the distortion of the electric field near the cracks or micropores, the defects bear higher electric stress, which further develops the defects in the material and eventually leads to insulation failure [6].

Figure 7 is the microtopography of two different XLPE sheet samples, in which the convex part is the brittle fracture crack generated in the brittle fracture process. It can be seen that the internal structure of XLPE is not exactly the same even if it is produced by the same manufacturer in the same batch. There are micropore defects in the samples shown in Fig. (A) and Fig. (B), in which the micropores in sample 1# are small and the defects are sparsely distributed, and there are more micropores in sample 2# and

the defects are densely distributed. Under electric field, the internal defects of XLPE develop gradually. When the internal defects of XLPE are densely distributed, the fine defects close to each other are easy to merge into larger defects in the development process, and the size of the merged defects is higher than that of the original defects, which leads to more serious electric field distortion at the defects and accelerates the material deterioration rate until breakdown. This process takes less time and corresponds to the "early failure" process described above.

When the internal defects of the material are sparsely distributed, due to the long distance, the defects are not easy to merge into larger defects in the growth process, but keep relatively independent development, eventually leading to the insulation failure of the sample, which takes a long time, corresponding to the above "random failure" process.

The above analysis shows the influence of the sparseness of defects in the material on its electrical life. When there are no obvious defects, the internal electric field is more uniform. Under the action of electrical stress, the material is gradually aged and the insulation performance is continuously decreased. When the breakdown strength of the sample is lower than the applied field strength, the sample will be broken down under the action of high field strength, and this process takes the longest time, which corresponds to the "aging failure" process mentioned above.

(A) 1 # sample   (B) 2 # sample
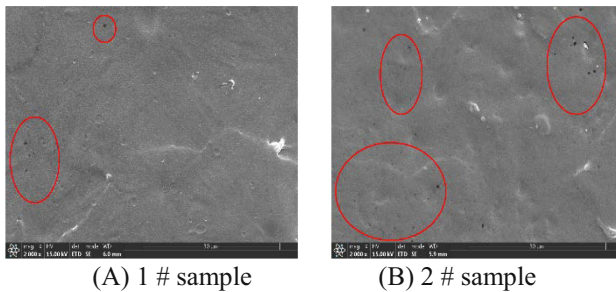
Fig. 7. SEM images of XLPE samples

Figure 8 is an *E-t* characteristic curve for different failure processes of XLPE sheet samples plotted from the data in Table 2. Because that failure time of the sample in the aging failure process is not observed in the experiment, only the *E-t* characteristics of the samples in the early failure and random failure processes are analyzed. It can be seen from Fig. 8 that the early failure process life index n_1 of XLPE is 20.73, and the random failure process life index n_2 is 28.45. Observing Fig. 6, when the electric field strength $E \geq 32$ kV/mm, the early failure (failure process 1) accounts for the highest proportion among the three failure processes, and the breakdown time of the sample in the early failure process represents the electrical life of the XLPE sheet sample; When the field strength $E \leq 32$ kV/mm, the random failure (failure process 2) dominates the three failure processes, and the breakdown time of the sample in the random failure process is used to represent the electrical life of the XLPE sheet sample, so the modified

XLPE electrical life model is obtained as follows:

$$\lg t = \begin{cases} 30.46 - 20.73 \times \lg E & E \in [32, 42.49) \\ 43.65 - 28.45 \times \lg E & E \in (0, 32) \end{cases} \tag{3}$$

where $E = 42.49$ kV/mm is the power frequency breakdown strength of the XLPE sheet sample. When the electric field strength exceeds this value, the E-t characteristic of XLPE will no longer satisfy the relationship described in formula (3).
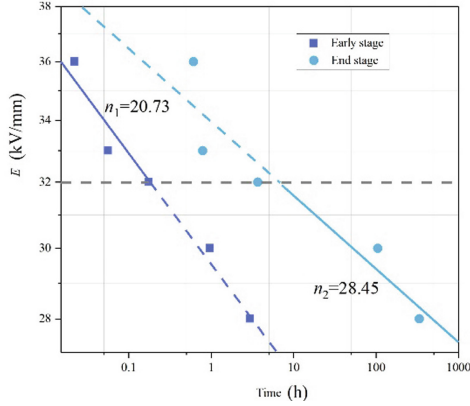
Fig. 8. E-t characteristic curve of different failure process of XLPE sheet sample

According to formula (3), when the electric field strength $E \geq 32$ kV/mm, the lifetime index n_1 of XLPE is 20.73, and when the electric field strength $E < 32$ kV/mm, the lifetime index n_2 of XLPE is 28.45. The point corresponding to $E = 32$ kV/mm is the "inflection point" in the E-t characteristic curve.

It should be pointed out that the proportion of samples in the aging failure process increases with the decrease of the applied field strength, so it can be determined that there is a certain field strength E_c, when the field strength $E < E_c$, the aging failure will occupy the dominant position in the XLPE failure process. The electrical life of XLPE will be much larger than that calculated by formula (3), that is, the electrical life model of XLPE obtained is conservative at lower field strength.

4.2   Traditional XLPE Electrical Life Model

The E-t characteristic curve of the XLPE sheet sample can be drawn from the data in Fig. 4, and then the traditional XLPE electrical life model based on the inverse power law is established as shown in Formula (4).

The slope of the E-t curve is related to the life index n. The failure process of XLPE under high and low electric field strength is different, and the corresponding life index n is also different. Generally, the E-t characteristic curve of XLPE can be approximately regarded as a broken line composed of different straight line segments, and the position of the inflection point of the curve determines the shape of the curve. At present, the

selection of curve inflection point is mostly from the mathematical point of view. In the process of curve fitting, the appropriate inflection point is selected to make the fitting curve have the highest fitting degree. Compared with the traditional method, the method proposed in this paper gives more consideration to the physical meaning when determining the position of the inflection point of the curve, so that the modified model has more application value. The comparison between the traditional XLPE electrical life model and the modified model is shown in Fig. 9.

$$\lg t = \begin{cases} 32.47 - 21.69 \times \lg E & E \in [32,\, 42.49) \\ 63.44 - 42.04 \times \lg E & E \in (0,\, 32) \end{cases} \tag{4}$$
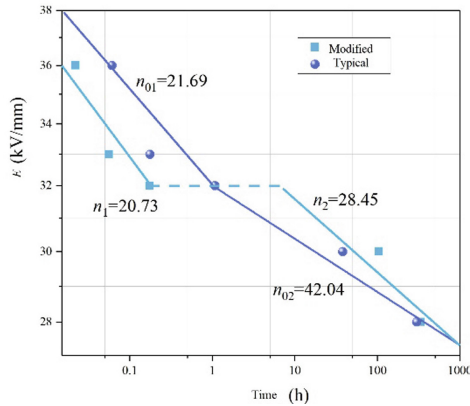
Fig. 9. Comparison of traditional XLPE electrical life model and modified model

5   Conclusion

In this paper, that statistical characteristics of XLPE failure time under different electric field strengths are studied by voltage endurance experiment on thin XLPE samples, and the traditional XLPE electrical life model base on inverse power law is improved. The following conclusions are drawn:

1) in this pap, that failure time of XLPE, which is in the dominant failure process, is use to express the electrical life of the material under the same field strength without waiting for the breakdown of all samples, which can improve the efficiency of voltage durability experiment.

   And 2) determine that position of an inflection point in an *E-t* characteristic curve of the XLPE through the statistical characteristics of the XLPE failure time under the action of different electric field strengths, and correcting a traditional XLPE electric life model based on an inverse pow law according to the position. According to the modified model, when the electric field strength $E \geq 32$ kV/mm, the lifetime index n_1 of XLPE is 20.73; When the electric field strength $E < 32$ kV/mm, the lifetime index of XLPE $n_2 = 28.45$.

3) The results show that the difference of breakdown strength between different XLPE samples is small, and the difference of failure time of XLPE under the same field strength is significant, so the voltage durability test can better reflect the insulation state of the material.

References

1. Yin, Y., Zhou, K., Li, S., et al.: Interface polarization characteristics of water tree aged XLPE cables based on polarization and depolarization current method. Trans. China Electrotech. Soc. **35**(12), 2643–2651 (2020)
2. Liu, Y., Jiang, H., Cao, X.: Comparison of AC and DC voltage endurance properties of insulation sheet samples spirally-cut from existing AC XLPE cables. High Voltage Eng. **43**(11), 3559–3567 (2017)
3. Yang, L., Li, Z., Yao, R., et al.: Selection of step-stress test parameters for obtaining DC voltage endurance coefficient of XLPE insulation. Trans. China Electrotech. Soc. **34**(24), 5244–5251 (2019)
4. Su, P., Wu, J., Zhu, X., et al.: Effect of degassing treatment on breakdown strength in direct current cable insulation. Proc. CSEE **40**(02), 663–672 (2020)
5. Li, B., Qin, F., Wu, Y., et al.: Short-term daily load curve forecasting based on fuzzy information granulation and multi-strategy sensitivity. Trans. China Electrotech. Soc. **32**(09), 149–159 (2017)
6. Montanari, G.C., Seri, P., Dissado, L.A.: Aging mechanisms of polymeric materials under DC electrical stress: a new approach and similarities to mechanical aging. IEEE Trans. Dielectr. Electr. Insul. **26**(2), 634–641 (2019)
7. Liu, X., Yu, Q., Zhong, L., et al.: Review on research of V-t characteristics of HV XLPE cables. Southern Power Syst. Technol. **9**(10), 57–63 (2015)
8. Chen, X., Meng, F., Xia, F., et al.: Effect of degassing treatment on 500 kV XLPE insulation characteristics and aggregation structure. Proc. CSEE **41**(10), 3645–3656+3688 (2021)
9. Bamji, S.S., Bulinski, A.T.: Degradation of polymeric insulation due to photoemission caused by high electric fields. IEEE Trans. Electr. Insul. **24**(1), 91–98 (1989)
10. Li, Y., Zhang, Q.G., Wang, T.L., Li, J.Z., Guo, C., Ni, H.L.: Degradation characteristics of oil-immersed pressboard samples induced by partial discharges under DC voltage. IEEE Trans. Dielectr. Electr. Insul. **24**(2), 1110–1117 (2017)
11. Chen, Q.G., Wang, J.L., Lin, L., Chi, M.H., Wei, X.L.: Influence of operation conditions on flow electrification characteristics of oil-paper insulation in converter transformer. High Volt. Eng. **44**(12), 3880–3887 (2018)
12. Tobazeon, R., Filippini, J.C., Marteau, C.: On the measurement of the conductivity of highly insulating liquids. IEEE Trans. Dielectr. Electr. Insul. **1**(6), 1000–1004 (1994)

Negative Corona Discharge Characteristics in Atmospheric Pressure and the Influence of Detachment on It

Jinghan Fu, Haoyu Zhan, Yanze Zhang, Xiaoyue Chen[✉], and Yu Wang

School of Electrical Engineering and Automation, Wuhan University, Wuhan 430072, China
chenxiaoyue@whu.edu.cn

Abstract. Detachment refers to the process in which negative ions react with neutral particles to produce electrons. The theory of negative glow corona is reviewed by probing the influence of detachment. In this paper, a numerical simulation model of fluid dynamics for atmospheric coaxial cylindrical corona discharge is established. We simulate the negative corona discharge in two cases: considering detachment and not considering detachment. By comparing the results, we show the importance of detachment to the corona discharge. The results show that if the influence of detachment is ignored, the generation rate of electrons in the ionization region will be underestimated, resulting in the underestimation of the peak value of positive and negative ions and electron density. And the amplitude of the electric field and current peak value of the wire surface will be smaller. Meanwhile, the consumption rate of negative ions will be underestimated, resulting in a longer pulse period and deviation from the real results. Therefore, it is necessary to consider the detachment in the simulation of atmospheric corona discharge for the accuracy of the simulation.

Keywords: Negative corona discharge · Detachment · The Trichel pulse · Electric field distribution

1 Introduction

Corona discharge is a common form of discharge in industry, which has a broad impact on social production. On the one hand, Corona discharge produces plasma [1], which has good applications in the fields of plasma medicine [2] and environmental governance [3–5] due to its stability and convenience. For example, in the disposal of oil pollution, the active material produced by corona discharge plasma attaches to petroleum hydrocarbons, which will promote their degradation. On the other hand, Corona discharge causes power loss and a series of electromagnetic environmental problems, such as radio interference, audible noise and the surge of reduced electric field [6].

The regular current pulses that occur during negative corona discharge is known as the Trichel pulse, whose periodicity is caused by the generation and disappearance of space charge in discharge. The discharge process can be simulated macroscopically with a fluid model. There are many scholars who have obtained the Trichel pulse by fluid

model simulation. Zhuang et al. proposed a fluid model simulation of the wire plate electrode for negative discharge to obtain the Trichel pulse. The results were in good agreement with a designed experiment in the laboratory, which provided a reference for analyzing the transient process of corona on transmission lines [7]; He et al. proposed a coaxial cylindrical electrode fluid model and discussed the change of electric field, electron density and negative ion density during the pulse, illustrating the effect of space charge on the synthesized field [8]. However, these traditional fluid models only considered ionization, attachment, and recombination. The effect of detachment was neglected.

Detachment refers to the process in which negative ions react with neutral particles to produce electrons. It will have an effect on the space charge density in the discharge area. Consideration for detachment was first proposed by Morrow. He proposed that the seed electrons required for continuous pulses were mainly provided by detachment of metastable oxygen molecules with negative ions [9]. Then, Liu et al. used a coaxial cylindrical electrode structure and mainly considered the detachment of O2−, extending Morrow's proposed model to two dimensions. It was found that the discharge current suddenly increased by more than two orders of magnitude when streamers with filamentary structures appeared [10]. Furthermore, He et al. proposed a chemical-fluid model and compared it with the model built by Liu Lipeng. The results showed that the model with the averaged kinetic scheme (AKS) underestimated the detachment that played an important role in the positive glow corona discharge.

The above studies are all for the positive glow corona model. However, little research has been done for detachment in the negative corona. Compared to positive corona, negative corona discharge is dominated by negative ions, since positive ions will disappear rapidly from the electrode surface after being generated. Therefore, detachment in a negative corona mainly affects the generation and disappearance of space charges, which differs from its primary role in maintaining discharge in positive corona. In this paper, we proposed a fluid model that considers positive and negative ions and electrons. An infinitely long coaxial cylindrical electrode corona discharge model was developed to simulate separately with and without detachment. The effect of detachment on the negative corona discharge is illustrated by comparing the electric field strength at the wire surface, current, and particle distribution.

2 Model Description

2.1 Circuit Structure and Environment Setting

The corona discharge model is shown in Fig. 1, where the discharge area is an infinitely long coaxial cylindrical electrode with an internal solid wire radius of 0.5 mm. The applied voltage is −24 kV, and the radius of the ground outer electrode is 20 cm. Since it is symmetrical, the one-dimensional model is used to simplify the discharge model. In order to simplify the calculation, we set the artificial boundary at 1 cm [15]. The discharge occurs at ambient temperature and atmospheric pressure. The gas in the gap is air.
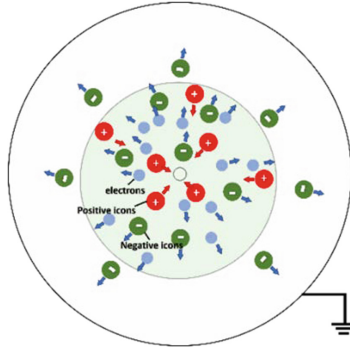
Fig. 1. Schematic diagram of circuit structure

2.2 Governing Equations

In this study, a fluid model was constructed with the consideration of detachment. The Poisson equation is solved to describe the effect of space charge on the electric field intensity. The continuity equation is solved to describe the generation, disappearance and transport of positive ions, negative ions and electrons. By coupling the Poisson equation with the continuity equation, the discharge process of coaxial cylindrical electrode can be numerically simulated [10].

$$\nabla^2 \varphi = -e(N_p - N_n - N_e)/\varepsilon \tag{1}$$

$$\nabla \varphi = -E \tag{2}$$

The Poisson equation is shown above. Where ε is the permittivity of air. e is the charge of an electron. φ is the electric potential. E is the electric field vector. The potential distribution can be calculated from the charge distribution. Then, the electric field strength distribution can be obtained from the potential distribution.

The continuity equation of each particle is solved according to the reaction source term and transport in the discharge process. It involves the ionization and attachment of electrons and neutral particles, the combination of electrons and positive ions, and the detachment of negative ions and neutral particles. For positive ions, ionization and recombination are considered. For negative ions, attachment, recombination, and detachment are considered.

$$\partial N_e/\partial t = (\alpha - \eta)N_e|W_e| - \beta N_e W_e + K_d N_n - \nabla(N_e W_e) \tag{3}$$

$$\partial N_n/\partial t = \eta N_e|W_e| - \beta N_n W_p - K_d N_n - \nabla(N_n W_n) \tag{4}$$

$$\partial N_p/\partial t = \alpha N_e|W_e|| - \beta(N_n + N_e)N_p - \nabla(N_p W_p) \tag{5}$$

Ne, *Np*, and *Nn* are the densities of electrons, positive ions, and negative ions, respectively. α is the ionization coefficient and η is the attachment coefficient. They are used to

describe the intensity of ionization and attachment under different electric field strengths. β is the recombination coefficient, which is independent of the electric field strength. Kd is the detachment rate coefficient. Since negative ions mostly react with stable background gas to generate electrons, the detachment rate coefficient characterizes the ability of negative ions to detach electrons. Wi is the velocity vector of the corresponding substance, determined by the mobility and the electric field strength of the spatial location. The specific calculation of the relevant parameters is shown below [13].

$$W_i = E\mu_i \tag{6}$$

$$\beta = 2.2 \times 10^{-12} \tag{7}$$

$$\eta = 9.865 \times 10^2 - 5.41 \times 10^{-4}|E| + 1.145 \times 10^{-10}|E|^2 \tag{8}$$

$$\alpha = \begin{cases} 3.632 \times 10^5 \times e^{-1.68 \times 10^7 / E} & |E| \leq 4.56 \times 10^6 V/m \\ 7.356 \times 10^5 \times e^{-2.01 \times 10^7 / E} & |E| \geq 4.56 \times 10^6 V/m \end{cases} \tag{9}$$

According to values for the detachment rate coefficient taken by previous scholars, we take the Kd value as 1×10^5 orders of magnitude [14, 15]. The finite element method is applied to solve the fluid model. The simulation stops after obtaining the regular pulse.

3   Simulation Results and Analysis

3.1   Characteristics of Trichel Pulse

Figure 2 shows the variation of simulated current and simulated electric field on the wire surface. The results show that the current pulse has a relatively short rising edge and duration, and it occurs again after a long dead time. The amplitude of each current pulse is almost the same, which seems relatively regular, exhibiting the typical characteristics of Trichel pulse. Analyzing the features of the current pulse, we can observe that the simulation results conform to the characteristics of negative corona discharge. The pulse period of the electric field on the wire surface is consistent with the current pulse period. The value of electric field accumulates continuously during the dead time of the current pulse, and then drops sharply in the meantime when the current falling edge occurs. Since the discharge near the wire surface is intense, the variation of the electric field on the wire surface can basically represent the overall electric field in the ionization region. Therefore, the pulse discharge can be represented by the electric field on the wire surface.

The pulse discharge period studied in this paper starts when the electric field on the wire surface reaches the trough. In a period, the electric field on the wire surface rises slowly and then drops sharply before the next period begins. The electric field on the wire surface is affected by the space charge. After the collision ionization and attachment in the ionization zone, a large number of positive and negative ions are generated, which will distort the electric field near the cathode. Whereas the positive ions are closer to the cathode surface and have higher density, they tend to have a stronger impact on the

electric field distortion on the cathode surface, which leads to a sharp increase on the electric field; When the positive ions collide with the cathode surface and disappear, the electric field on the conductor surface will also drop sharply. However, when the reactions of the ionization zone become weak, the influence of positive ions on the surface field strength of the conductor becomes little. The electric field strength of the wire surface is mainly affected by the inhibition of the negative ions that are gradually away and run out. As negative ions lose inhibition gradually, the electric field strength presents a slowly rising trend.

The detachment mainly affects the distribution of negative ions. When the detachment is considered in the simulation, the current amplitude will increase and the period will be shortened, corresponding to the increase in the amplitude and decrease of the period length of the electric field on the wire surface.

(a) Model without detachment   (b) Model with detachment
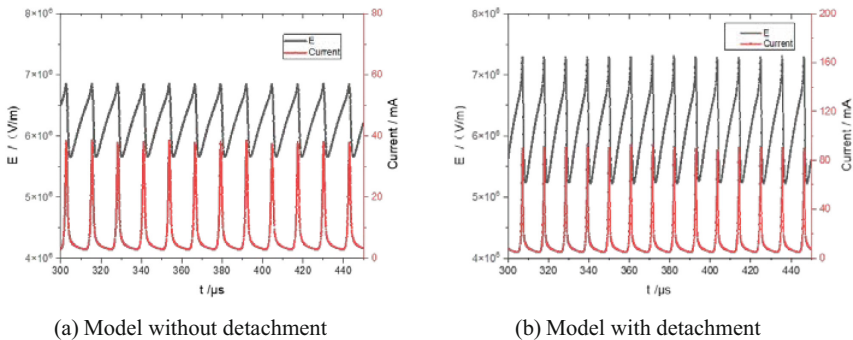
Fig. 2. Trichel pulse characteristics

3.2 The Distribution of Particles in a Single Period and the Effect of Detachment

The period of the discharge model without detachment starts at 355.9 μs and ends at 368.7 μs. While the period of the model with detachment starts at 362.3 μs and ends at 373.1 μs. Select five moments with typical characteristics to describe the changes of positive and negative ions and electrons in a period discharge process. These moments will be further illustrated in the next section.

Figure 3 shows the changes of the radial number density distribution of each particle in a period in the model without detachment. After the field strength trough arrives, each reaction stagnates. Since a large number of electrons come from the ionization zone, the electron density reaches a peak near the ionization zone, but the value of density is diminutive; Positive ions collide with the cathode and they gradually run out; Negative ions mainly accumulate outside the ionization zone. There are almost no negative ions in the ionization zone. Then, the negative ions gradually move away from the cathode, decreasing with the progress of recombination. When the electric field strength in the ionization zone reaches a certain value, the electron ionization rate increases sharply. Due to the different migration directions of positive ions and electrons, the peak of

positive ion density appears near the cathode in the ionization zone. These positive ions distort the electric field near the cathode, resulting in a sharp increase on the surface field strength of the cathode; Whereas the peak of electron density appears in the outer region of the ionization zone, a large number of negative ions are generated by attachment at the same position. At this stage, the density of positive and negative ions and electrons and the surface field strength of the wire reach their peak value almost simultaneously. As the positive ions begin to collide with the cathode, the field strength in the ionization zone drops rapidly, and all reactions come to a standstill. Due to the large specific charge, the electrons rapidly migrated away from the ionization region under the effect of the electric field force. Due to the concentration of the positive ions, they quickly collide with the cathode and run out. There are almost only negative ions left in the space. They slowly move away from the cathode, and gradually depleted.
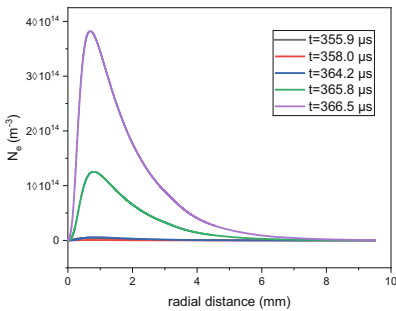
(a) Electron distribution
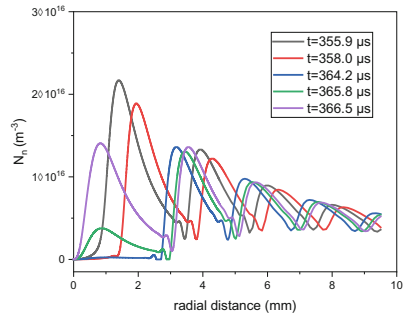
(b) Negative ion distribution
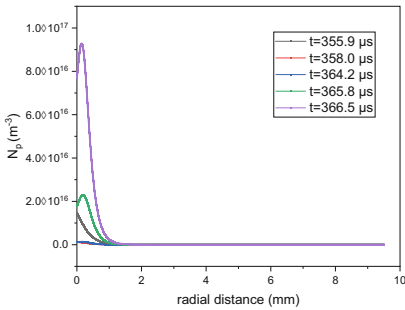
(c) Positive ion distribution(complete)
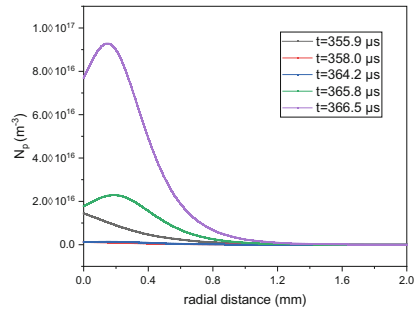
(d) Positive ion distribution(detailed)

Fig. 3. Spatial distribution of positive and negative ions and electron densities (the model without detachment)

Figure 4 shows how positive and negative ions and electrons change in a period in the model with detachment. After the field strength trough arrives, each reaction stagnates. Since the detachment greatly accelerates the loss of negative ions, the negative ions rapidly come to a lower level not far from the ionization zone. Compared with the model without detachment, the electric field intensity in the ionization zone reaches a

higher level in advance, shortening the period length. When the ionization zone gets into the active state, the electrons generated by the detachment are positive feedback to the collision ionization to generate a large number of electrons. More positive ions are generated at the same time, which will make the electric field strength near the cathode greater. As a result of great electric field strength, the generation of positive and negative ions is more intense, thus accelerating the reaction rate, which makes the peaks of positive and negative ions and electrons higher.

Compared with the model without detachment, the peak of positive ion density increased to 3.10 times, the peak of negative ion density increased to 2.78 times, and that of electron density increased to 2.65 times.

(a) Electron distribution

(b) Negative ion distribution

(c) Positive ion distribution(complete)

(d) Positive ion distribution(detailed)
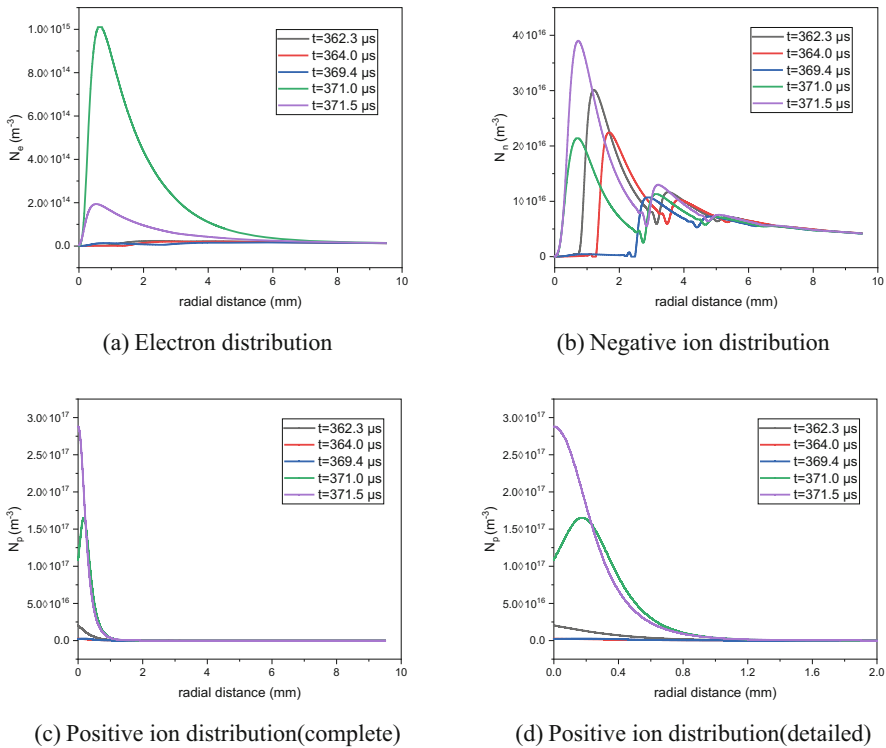
Fig. 4. Spatial distribution of positive and negative ions and electron densities (the model with detachment)

3.3 Cathode Surface Field Strength Change in a Single Period and the Effect of Detachment

Given the discharge process is closely related to the wire surface field strength, the following analysis of the discharge process will be based on the fluctuation period of the wire surface field strength as a complete stage to explore the relationship between the

positive, negative ions and the electron density and the cathode surface field strength, so as to illustrate the impact of the detachment.

Figure 5 shows the change of the electric field intensity on the cathode surface in a period in the discharge model without detachment. At $355.9\,\mu s$, the electric field intensity reaches the valley, and only a small number of positive ions remain in the ionization zone, which hasn't collided with the cathode. The negative ions gradually move away from the cathode and the electric field strength begins to rise. Since the electric field intensity is too low, all reactions will stagnate. Almost no new particles are produced in the ionization zone. At $358.0\,\mu s$, the positive ions in the ionization zone run out. Since then, the negative ions gradually move away from the cathode and slowly recombine with a small number of positive ions. The electric field strength gradually increases. At $364.2\,\mu s$, the electric field strength reaches a certain level, and the collision ionization rate of electrons begins to increase sharply, producing a large number of electrons and positive ions. At the same time, due to the increase in electron density, the attachment rate of electrons and neutral particles increases, A large number of negative ions begin to be generated outside the ionization zone. In contrast, the reaction rate of electron collision ionization is higher than the level of negative ion density, which makes the positive ion density rise faster. At the same time, due to the closer distance to the ionization region, the distortion of the electric field in the ionization region is greater. At $365.8\,\mu s$, the electron density is relatively high. The gain of positive ions on the electric field strength in the ionization region also reaches a higher level. The collision ionization reaction is further accelerated and continues to promote the attachment, producing more positive and negative ions and electrons. The electric field strength shows a trend of sharp increase. At $366.5\,\mu s$, some positive ions collide with the cathode surface and emit electrons. Due to the violent and short-lived collision process of high-density positive ions, the electric field intensity in the ionization region begins to drop rapidly. At $368.7\,\mu s$, only a small number of positive ions haven't collided with the cathode, which makes the electric field intensity reaches the trough again.
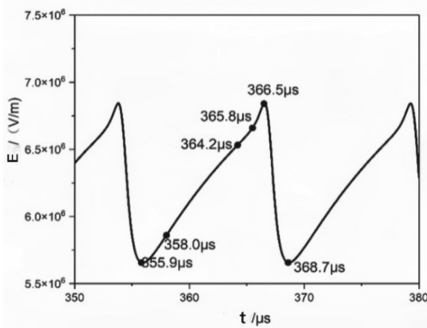
Fig. 5. Cathode surface electric field strength (the model without detachment)
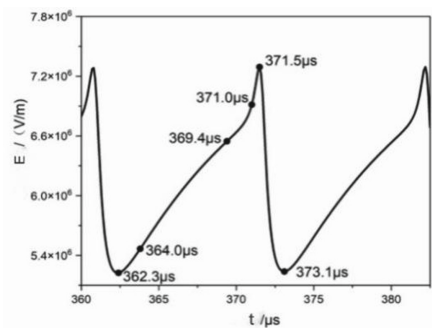
Fig. 6. Cathode surface electric field strength(the model with detachment)

Figure 6 shows the change of the electric field intensity on the cathode surface in a period in the discharge model with detachment. At $362.3\,\mu s$, the electric field strength

reaches the valley value. Since more negative ions were generated in the previous period, the electric field strength will be lower than that without the detachment. At 364.0 μs, the positive ions run out. After that, in addition to gradually moving away from the cathode and slowly recombining with a small number of positive ions, the electrons will also detach from the negative ions. It greatly increases the loss rate of the negative ion density while improving the electron density. Therefore, the electric field strength will increase at a higher rate, which will advance the stage of violent reaction. At 369.4 μs, positive and negative ions and electrons begin to generate in large quantities. At 371.0 μs, the electric field strength begins to rise sharply. At this time, the electric field intensity has been high. The collision ionization rate of electrons has reached a high level, producing a large number of electrons and positive ions. As the electron density increases, the attachment rate of electrons and neutral particles increases. A large number of negative ions are generated in the area with high electron density. The generated large number of negative ions will have a violent detachment with the neutral ions, which will consume part of the negative ion density and continuously increase the electron density. This process will positively feedback on the collisional ionization of electrons, significantly increasing the electron density and positive ion density. Due to the further increase of electron density, the attachment between electrons and neutral particles is intensified, resulting in a large number of negative ions. On the other hand, due to the higher density of positive ions, the distortion effect on electric field intensity is also stronger, and greater electric field intensity is generated in the ionization region. The great electric field intensity also helps to improve the rate of various reactions and increase the density of positive, negative ions and electrons. Therefore, in the ionization region with large field strength, the gain of negative ion density brought by the detachment will be greater than the loss of negative ion density in the detachment. After considering the detachment, the reaction rates will be improved, the positive and negative ions and electron densities will be higher, and a higher maximum density will be generated at the same time. At 371.5 μs, a large number of positive ions collided with the cathode, and the electric field strength began to decline. The electric field intensity has a higher peak due to the higher density of positive ions after detachment. At 373.1 μs, only a small number of positive ions have not yet collided with the cathode, and the electric field strength quickly reaches the valley. Since the negative ion density is higher after considering the detachment, the valley value of the electric field strength is also lower.

After considering the detachment, the discharge period is reduced from 12.8 μs to 10.8 μs. The period is only 84.4% of the previous one.

3.4   The Current Change in a Single Period and the Effect of Detachment

Figure 7 shows the changes of current in the two models. The pulse period of the electric field on the wire surface is consistent with the current pulse period. Considering detachment, the period of the current is shortened. In addition, the peak value of the current will increase significantly. Since the directional movement of positive and negative ions and electrons generates the current, the significant increase in their peak density will cause a significant increase in the peak current.

Compared to the model that does not consider detachment, the peak current in this model is 2.4 times higher. Additionally, the gain factor of the current peak is close to the density gain of each particle, which justifies the model.
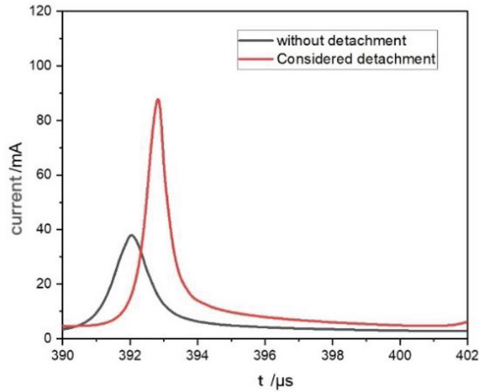
Fig. 7. Comparison of currents in a single period between the two models

4 Conclusion

For negative corona discharge with coaxial cylindrical electrode structure, a fluid model was constructed to analyze the discharge process and the influence of detachment. Compared with the traditional fluid model without the detachment, the model considering the detachment shows differences in the spatial distribution of particles, the electric field intensity waveform on the wire surface and the current waveform.

In the process of negative Trichel pulse discharge, the negative ions mainly have an inhibitory effect on the electric field. The consideration of detachment makes the negative ions not only move away from the cathode surface under the action of the electric field, but also makes their density continuously depleted in the process of migration. Some of the negative ions are detached into neutral particles and electrons. As a result, the density of negative ions outside the ionization region is lower in the model with detachment. Therefore, compared with the traditional model, when negative ions leave, the inhibition on the electric field intensity strengthens, the pulse period shortens. Apart from this, due to the addition of the electron source, the particle activity in the ionization region becomes more intense. During this period, the positive and negative ions together with electron production are higher than that in the traditional model. As a consequence, the peak value of the field intensity on the wire surface is increased, while the peak value of the current within the period is also greater. Compared with the traditional model, more residual negative ions also make the trough of the electric field on the wire surface lower, which makes the electric field peak on the wire surface larger.

It can be seen that if the influence of detachment is ignored, the generation rate of electrons in the ionization region during the period of high field intensity will be

underestimated. This could lead to our underestimation of the peak number of particles. Additionally, the amplitude of the field intensity as well as the peak current of the wire surface will be smaller. As a result, the consumption rate of negative ions will be underestimated, and the pulse period will be longer. All of this will deviate from the real results.

References

1. Li, H.: State-of-the-art of atmospheric discharge plasmas. High Volt. Eng. **42**(12), 3697–3727 (2016). (in Chinese)
2. Weltmann, K.D.: Plasma medicine – current state of research and medical application. Plasma Phys. Control. Fusion **59**(1), 014031 (2017)
3. Magureanu, M.: Pulsed corona discharge for degradation of methylene blue in water. Plasma Chem. Plasma Process. **33**(1), 51–64 (2013)
4. Chung, W.: Removal of VOCs from gas streams via plasma and catalysis. Catal. Rev. Sci. Eng. **61**(2), 270–331 (2019)
5. Wang, Q.: Investigation of NO removal using a pulse-assisted RF discharge. Plasma Sci. Technol. **19**(6), 064013 (2017)
6. Liu, Y.: Analysis of the positive corona onset characteristic of the bundle conductors in the UHV corona cage. Trans. China Electrotech. Soc. **28**(1), 73–79 (2013). (in Chinese)
7. Yin, H.: Modeling of Trichel pulses in the negative corona on a line-to-plane geometry. IEEE Trans. Magn. **50**(2), 473–476 (2014)
8. He, W.: Characteristics of negative corona Trichel pulses in a coaxial electrode system. Trans. China Electrotech. Soc. **31**(11), 211–218 (2016). (in Chinese)
9. Morrow, R.: The theory of positive glow corona. J. Phys. D: Appl. Phys. **30**(22), 3099–3114 (1997)
10. Liu, L.: On the transition from stable positive glow corona to streamers. J. Phys. D: Appl. Phys. **49**(22), 225202–225214 (2016)
11. Xiao, M.: Revisiting the theory of positive glow corona with a comprehensive kinetic scheme. J. Phys. D: Appl. Phys. **55**(9), 095203 (2022)
12. Tran, T.N.: Numerical modelling of negative discharges in air with experimental validation. J. Phys. D: Appl. Phys. **44**(1), 015203 (2011)
13. Yin, H.: The Conversion Relationship Between High-Frequency Corona Current in DC Transmission Lines and Radio Interference. Tsinghua University, Beijing (2014). (in Chinese)
14. Barni, R.: Chemical kinetics simulations of an atmospheric pressure plasma device in air. Surf. Coat. Technol. **200**(1–4), 924–927 (2005)
15. Sakiyama, Y.: Plasma chemistry model of surface microdischarge in humid air and dynamics of reactive neutral species. Journal of Physics D: Applied Physics **45**(42), 42520 (2012)

Finite Element Analysis Regarding Electric Field Distribution Effect on Corona Discharge Due to Various Electrode Shapes and Applied Voltage

Khalid Hussain[✉] and Tiebing Lu

School of Electrical and Electronics Engineering, North China Electric Power University, Beijing, China
Engr.khalid125@gmail.com

Abstract. This research presents a simulation analysis of D.C. corona characteristics to investigate the effects of electric field distribution on corona discharge caused by different electrode geometries. A model setup with various electrode shapes is designed to evaluate the corona discharge characteristics. This model solves the electron and ion continuity and momentum equations with a drift-diffusion approximation that is coherently coupled with the Poisson equation. To explore the impact of the electric field (E.F.) on corona discharges caused by various electrode geometries (sharp, flat, and spherical) and applied voltages, the electric field dispersal was analyzed using finite element analysis (FEA). The simulation software models corona discharges with different electrode shapes (sharp, flat, spherical) and undergoing discrete applied voltages. The bi-dimensional (2D) model was constructed to investigate the distribution of the electrical field and its impact on corona discharge. Due to these simulations based on Finite Element Analysis (FEA), the dispersion of the electric field's impact on corona discharge of various electrode geometries and applied voltage will be investigated. To elaborate on the influence of variation in applied voltage and the varied shape of electrode geometries on corona discharge, the dispersion of the electric field, electron current density, and electron density will be evaluated.

.

Keywords: D.C. Corona · Electric Field Distribution · HVDC · Displacement Current Density · Electron Density · Finite Element Analysis (FEA)

1 Introduction

High Voltage Direct Current (HVDC) transmission automation offers various technical, cost-effective, and atmospheric advantages for traditional A.C. transmission when bulk electrical energy is delivered over distance or in the case of asynchronous interconnections. It is anticipated that HVDC transmission will play an increasingly important role in subsequent power systems, presenting new provocation for electrical engineers. Besides its well-known advantages, HVDC systems show better corona performance than conventional A.C. transmission. Corona discharge is the most undesirable phenomenon in H.V. insolation systems.

This causes equipment insolation to deteriorate, resulting in system failure. [1]. Electrical breakdown refers to the process by which a non-conductive material is transformed into a conductive material when a sufficiently strong electric field is applied, a series of transients such as the collisions of electrons, ions, photons with gas molecules and electrode processes which Occurs at or near the electrode surface [2]. When an electric field accelerates certain elementary seed electrons in cascade ionization, it invariably leads to the start of electrical breakdown. After the first phase, the subsequent growth of the discharge process is influenced by a number of factors, including the gas composition, pressure, electrode spacing, intensity of the applied field, and electrode shape [3]. Special circumstances of electrical breakdown comprise corona, breakdown of non-uniform fields, lightning discharges, and laser-induced faults in prolonged discharge spaces [4]. Most studies emphasize investigating corona discharge plasmas' generation mechanism and development process in different weather conditions and other related parameters [5].

A phenomenon known as a corona discharge occurs when power conductors ionize the air around them at a voltage higher than the threshold breakdown voltage [6]. A hissing noise, a blue discharge, the production of ozone fumes, and a flashover are often the characteristics of this process. Corona discharge brings many hazards, so it is necessary to determine influencing factors and prediction methods for corona discharge [7]. Liang studied the corona discharge properties of HVDC conductors at various heights from the ground. However, he primarily concentrated on the correlation between the corona inception voltage, conductor structure, and height [8]. Mosch investigated the corona properties of HVDC transmission lines' shaped and stranded wires [9]. Most of the Electric energy consumed in forming the corona discharge plasma is directed preferentially to produce energetic electrons instead of heating the gas components [10]. Plasma breakdown is a fundamental process, and A frequent source of plasma known as a glow discharge may be created by the avalanche-like ionization of gas neutrals under certain gas pressure and voltage circumstances [11]. Gas discharges and related plasmas are used in many application fields and are primarily recognized as promising tools in the search for new materials [12].

This work studies D.C. corona discharge in dry air at specific temperatures and pressure but with different voltage levels and electrode geometries. The electric field distribution (E.F.) was simulated by finite element analysis (FEA) to investigate the effect of E.F. on corona discharge due to distinct electrode geometries and different voltage levels. I have designed a simulation model to investigate the effect of various electrode geometries (sharp, flat, and spherical) on the electric field, electron density, and electron current density. The designed model will also elaborate on the effect of various applied voltages on electric field distribution, electron density, and electron current density. The temperature of the gas is maintained at 600 K, and simulation can be done at any convenient temperature. This model solves the continuity and momentum equations for electrons and ions with a drift-diffusion approximation that is coherently coupled with the Poisson equation. Surrounding field correspondence is employed, which implies that the assumption is that the source and transport coefficients are accurately specified by the

reduced electric field (E/N). In the local-field approximation, the mean-electron-energy-fluid equations are not significantly involved in reducing the complexity of numerical problems.

2 Simulation Model Setup

A model has been designed to demonstrate the impact of the electric field distribution of various electrode geometries on corona discharging characteristics. The applied voltage for the developed model is 100 V, and after this, the parametric sweep function is used to apply the various levels of voltages, e.g., 500–1000 V. All The parameters were kept constant and the same for multiple shapes of electrodes. A cut-line 2D is drawn in-between ground, and the electrode is defined to evaluate the electric field distribution, electron density, and electronic current density.

The primary objective of the simulation model is to analyze the density profiles of charged particles and currents. R1, R3, and R3 are chemical reactions. Instead, the prevalent species M is used for background gas. M is ionized to form positive ion p, and M combines electrons to form negative ion n. The process of generating and destroying electrons in the contained area is explained by ionization, Townsend coefficient and rate constant for triple-body attachments and electron-ion recombination. The Townsend coefficients are derived as a function of the average energy of electrons by appropriately averaging the electron energy distributions calculated using the Boltzmann solver using a consistent set of electron dispersing collision cross sections for nitrogen and oxygen.

$$e + M \rightarrow p + 2e \qquad \text{Ionization} \quad \text{(R1)}$$
$$e + M \rightarrow n \qquad \text{Attachment} \quad \text{(R2)}$$
$$e + 2M \rightarrow n + M \qquad \text{Attachment} \quad \text{(R3)}$$
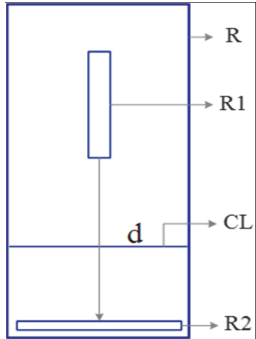
At a steady state, the predominant charged species in plasma are ions. Therefore, in the initial conditions, the densities of cations and anions are equal, and electrons are less dense. Charge neutrality is preserved under these preliminary conditions, which is crucial for numerical reasons. The electrodes' geometry and applied voltage level play a critical role in the discharge produced and the overall breakdown voltage. This study uses software simulation to model the corona discharge under various applied voltage levels and electrode shapes (sharp, flat, and spherical).

Bi-dimensional (2D) models have been designed to analyze the electric field orientation and its impact on corona discharge. The dispersion of the electric field between high-voltage electrodes and the ground was examined using electric current physics. Extremely fine element sizes have been used in a physics-governed mesh to achieve more precise results. To compute the electric field distribution, time-based analysis is employed to resolve the model. With the help of these simulations, It will investigate the effect of variation of applied voltage and the various shape of electrode geometry on the distribution of electric field, electron current density, and electron density.

To evaluate the distribution of electric field, electron current density, and electron density, I have defined a cut-line 2D(CL) with coordinate {(0 1.375), (2.5 1.375)} in-between ground and electrode. Dimensions of the simulation model geometry of various shapes of electrodes are given in Table 1. In the table, L is for length, and W is for width.

Table 1. Dimensions of Simulation Model Geometry.

Expression	Dimensions (mm)	Description	
R	L; 5 W; 2.5	Corona Cage	
R1	L; 1.5 W; 0.3	Electrode	
R2	L; 0.25 W; 2.25	Ground	
CL	{(0 1.375),(2.5 1.375)}	Cut-Line 2D	
d	2	Distance Between Electrode and Ground	

The applied voltage level and the other designing parameters are given in Table 2. According to the model design, I have used the parametric sweep to apply the two different voltage levels (500–1000 V) for the same electrode but with different geometry.

Table 2. Table of Simulation Model Parameters.

Name	Expression			Units	Description
Vapp	V0	$-V_0$*ramp	100	V	Applied Voltage
P0	760[torr]			Pa	Pressure of Gass
T0	600[K]			K	Temperature of Gas

The model governing equations to calculate the relevant parameters are given below. The density of electrons is calculated by resolving the equation of drift-diffusion for the electron density.

$$\frac{\partial}{\partial t}(n_e) + \nabla \Gamma_e = R_e - (\mathbf{u} \cdot \nabla)n_e \tag{1}$$

where $\mathbf{u}$ is the neutral fluid velocity vector, R_e is either a source or a sink of electrons, and Γ_e is electron flux. n_e denotes the electron density.

$$\Gamma_e = -(\mu \cdot \mathbf{E})n_e - \mathbf{D}_e - \nabla n_e \tag{2}$$

$\mathbf{D}_e$ is electron diffusivity, E represents the electric field, while μ_e is either a scalar or tensor representing the electron mobility. Electron convection due to fluid motion is spurned. The transport and source coefficients are still presented as the mean electron energy function when utilizing the local energy estimate or the localized field. However,

when using the localized-field approximation, we need to provide procedures for the average of the decreased electric field and electron energy.

$$\varepsilon = F(E/N) \tag{3}$$

ε is the mean electron energy. The rate of change of the scalar potential V with distance is what constitutes the electric field.

$$\mathbf{E} = -\nabla V \tag{4}$$

In the aforementioned equations, $\mathbf{E}$ is the electric field, F is a constant, ∇ V is the potential gradient, and $\mathbf{N}$ is a number density. The following equation is used to calculate the electrostatic field.

$$-\nabla \cdot (\varepsilon_o \varepsilon_r \mathbf{E}) = \rho_q \tag{5}$$

The formula is used to simultaneously calculate the space charge density ρ appertaining to the model-specified plasma dynamics.

$$\rho = q\left[\sum_{k=1}^{N} Z_k n_k - n_e\right] \tag{6}$$

In the above equation, n_k is a number density for specie k, n_e is electronic number density, q is the unit charge, and Z_k is the charge species k.

Boundary conditions for the designed corona model to evaluate the influence of various electrode geometries are specified. Electrons are demolished to the wall due to random mobility within a few accessible paths and acquired due to subsequent emission effects, resulting in the boundary condition for the electron flux.

$$\mathbf{n} \cdot \Gamma_e = \left(\frac{1}{2}V_{e.th}n_e\right) - \sum_p \gamma_p(\Gamma_p \cdot \mathbf{n}) \tag{7}$$

The gain of electrons due to secondary emission phenomena is represented by the second component on the right-hand side of Eq. 7, where γ_p is the secondary emission coefficient. Ions are dispersed to the wall due to surface interactions in heavier species, and the electric field is deflected towards the wall.

$$\mathbf{n} \cdot \mathbf{J}_k = M_w R_k + M_w c_k Z \mu_k(\mathbf{E} \cdot \mathbf{n})[Z_k \mu_k(\mathbf{E} \cdot \mathbf{n}) > 0] \tag{8}$$

In Eq. 8, $\mathbf{J}_k$ is the Diffusive flux vector of species k, c_k is a molar concentration of species k, R_k Rate expression, species k, and μ_k averaged mobility of species k. A D.C. electric potential (V_0) is provided with the inside conductor of the various geometries, triggering the discharge. A step function modulates V_0 with the transient applied potential, assuming the form, to assist the initiation of the simulation.

$$V = V_0 \tanh\left(\frac{t}{\tau}\right) \tag{9}$$

$$-\mathbf{n} \cdot \mathbf{D} = 0 \tag{10}$$

$$\mathbf{n} \cdot \Gamma_e = 0 \tag{11}$$

$$V = V_0 \tag{12}$$

Equation 10 elaborates that displacement fields cannot penetrate the perimeter by defining boundary conditions, and the entire potential will be discounted across the boundary. Equation 11 defines the normal component of electrons' energy flux as zero. Similarly, Eq. 12 defines the electrode's applied voltage as V_0, which is the ramp function of the applied voltage. The resulting equation for the wall of electronic flux is given.

$$\mathbf{n} \cdot \Gamma_e = \frac{1 - r_e}{1 + r_e}\left(\frac{1}{2}V_{e,th}n_e\right) - \left(\sum \gamma_i(\Gamma_i \cdot \mathbf{n}) + \Gamma_t \cdot \mathbf{n}\right) \tag{13}$$

In the above equation $V_{e,th}$ is the thermal velocity, γ_i Secondary emission coefficient,

3 Results and Discussion

Gas discharges are mainly composed of several particles, mostly electrons, ions, neutral atoms, and molecules. Plasmas are electrical discharges. Since plasmas are chemically reactive, they can degrade insulators chemically. Fast-moving ions found in plasmas have the potential to cause electrode damage. The extent of field homogeneity and strength in the system determines the path to high-voltage breakdown. A well-designed high-voltage system eliminates high-field zones by contouring the electrodes and screening sharp points.

The type of discharge created and the total breakdown voltage are both significantly influenced by the shape of the electrodes. In this simulation model, the impact of different shapes of the electrode on electric field distribution on corona discharge is investigated. The simulation result is evaluated on cut-line 2D after one second so that the results will be accurate and complete, and the simulation will be in a stabilized state.

3.1 Effect on Electric Field Distribution

A bi-dimensional (2D) model was created to investigate the effects of electrode geometries and different applied voltage levels on the electric field distribution and Corona discharge. Figure 1 shows the simulation model results of various shapes of electrodes (sharp, flat, and spherical). ' " The electric field configuration between the high-voltage electrode and the ground was examined using "Electric Current Physics". After one second, the simulation results are evaluated to be in a stabilized state.

The modelling of the distribution of the electric field produced by various electrode types at high voltage is illustrated in Fig. 2. While the bottom plate was grounded, a high voltage was provided to the top electrode. Comparing Figs. 2A, B and C. The sharp electrode tip has the strongest electric field, followed by the flat and spherical electrodes. In comparison to flat and spherical electrodes, the inception field of corona discharge underneath sharp electrodes is the smallest. The maximum charge magnitude is highest under the sharp electrode, followed by the flat and spherical electrodes. Again, this is because of electric field magnitude is the highest at the sharp electrode tip compared to the flat and spherical electrodes. More ionizations can occur when the electric field strength is higher.
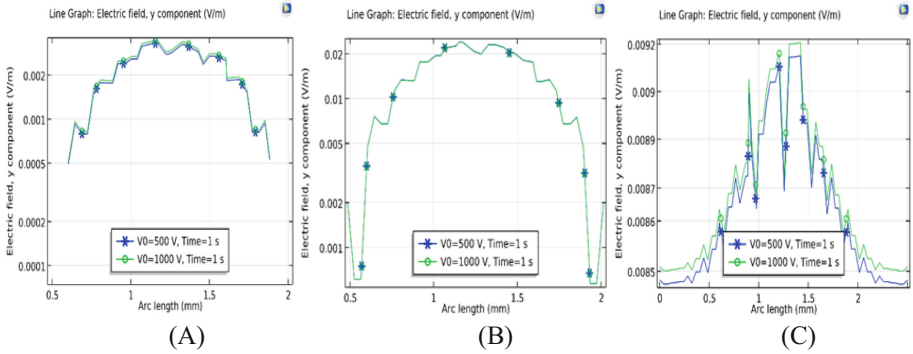
Fig. 2. Electric field distribution for spherical (A), sharp (B), and flat (C) geometries of electrodes.

3.2 Electron Density

The chance of an electron existing in a microscopic portion of space surrounding any particular place is measured by electron density, also known as electronic density. It is a scalar number that depends on three spatial factors and is usually represented as ρ. In this simulation model, I have also investigated the effect of electron density by the various geometry of electrodes and different levels of applied voltages.
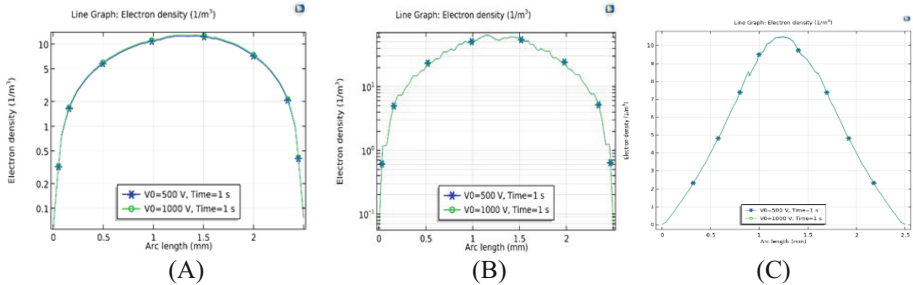
Fig. 3. Effect of the electrode's various shapes (spherical A, sharp B, and flat C) on electron density.

The effect of different shapes of electrode geometries is elaborated graphically in Fig. 3 A, B, and C. It is observed that the effect is more dominant by the sharp electrode's geometry than spherical and flat geometrical shapes on electron density. It strongly influences the corona discharge, keeping the other parameter the same.

3.3 Electron Current Density

The quantity of electric current flowing through a unit cross-sectional area is known as electron current density, which is associated with electromagnetism. It is a vector quantity. When electrons slow down, the particle density rises, maintaining the same

current density. The current density of more particles with lower speeds equals that of fewer particles with higher speeds. In this simulation model, I have investigated the effect of the various geometrical shape of the electrode and the different applied voltage levels on the electron current density.
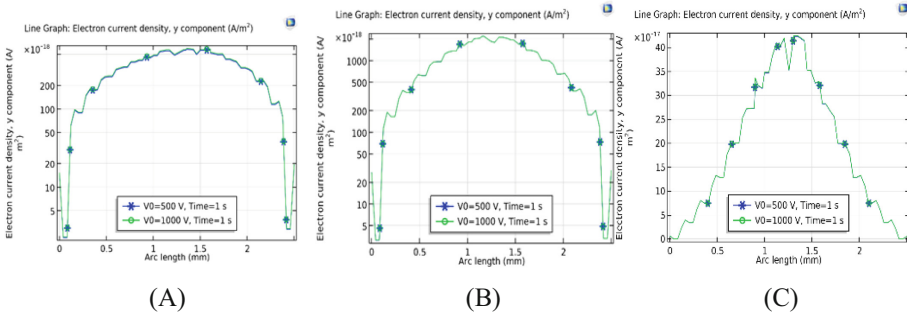
Fig. 4. Effect of electrode geometrical shapes (A-spherical, B sharp, C flat) and different applied voltages on electron current density.

It is clear from the above Fig. 4 A, B, and C that the sharp geometrical shape of the electrode has the highest electron current density compared to the other two geometrical shapes. Electron density and electron current density both have a similar trend of increasing and decreasing regarding the different geometrical shapes of the electrode. We know that electron and current density depend on the creation and destruction of electrons in contained space. By dent of this, the sharp geometrical shape of the electrode has a more penetrating effect than the spherical and flat. That's why it is strongly influenced by corona discharge keeping the other parameter the same and causing earlier discharge.

4   Conclusion

Electric field distributions for all electrodes have been victoriously simulated. By the simulation results and comparing Fig. 2, 3, and 4, the electric field, electron density, and electron current density The sharp electrodes have the greatest possible magnitude at the tip, accompanied by the flat and spherical electrodes. When the electric field magnitude is higher, the maximum charge magnitude becomes higher, and increased ionizations may take place, generating a longer streamer development that causes an earlier discharge. Therefore, the corona inception field is lowest under the sharp electrode in comparison to the flat and spherical electrode. The modelling findings also anticipated that the maximal charge magnitude is at its peak. Beneath the sharp electrode, pursued by the flat and spherical electrodes. That's why electrode geometries strongly influence corona discharge characteristics.

References

1. Morrow, R.: Theory of positive onset corona pulses in SF6. IEEE Trans. Electr. Insul. **26**, 398–404 (1991)
2. Langmuir, I.: Proceedings of the National Academy of Sciences of the United States of America 14
3. Maruvada, P.S.: Corona Performance of High-voltage Transmission Lines. Research Studies Press, Baldock, England (2000)
4. Wadhwa, C.I.: Electrical Power Systems. New Age International Publishers Ltd, India (2009)
5. Van Brunt, R.J.: Physics and chemistry of partial discharge and corona. Recent advances and future challenges. IEEE Trans. Dielectr. Electr. Insul. **1**, 761–784 (1994)
6. Juan, M., Zhou, C., Yuan, J.: Comparison of corona degree between the stranded and the shaped wires of HVDC transmission lines. Int. J. Appl. Electromagnet Mech **55**(2), 271–278 (2017)
7. Ryan, H.M. (ed.): Published by The Institution of Engineering and Technology, London, United Kingdom (2013)
8. Liang J., Jiang L., Li W., et al.: Corona discharge characteristics for conductors of HVDC transmission lines with different heights to ground. In: 2018 China International Conference on Electricity Distribution (CICED). IEEE (2018)
9. Arora, R., Mosch, W.: High Voltage and Electrical Insulation Engineering
10. Yehia, A.: Characteristics of the dielectric barrier corona discharges. AIP Adv. **9**, 045214 (2019). https://doi.org/10.1063/1.5085675
11. Smith, H.B., Charles, C., Boswell, R.W.: Breakdown behavior in radio-frequency argon discharges. Phys. Plasmas **10**(3), 875–881 (2003)
12. Yao, S.L., Suzuki, E., Meng, N., Nakayama, A.: A high-efficiency reactor for the pulsed plasma conversion of methane. Plasma Chem. Plasma Process. **22**, 225–237 (2002)

Effect of Mixed Layout of Parallel Cables on the Core and Sheath Current

Weilin Zou[1], Yong Ruan[1], Hua Bao[1], Jie Yuan[2(✉)], Danhua Cheng[2], and Wentao Yang[2]

[1] Anhui Electric Power Design Institute Co., Ltd., China Energy Engineering Group, Hefei 230601, China
[2] College of Electrical and Information Engineering, Hunan University, Changsha 410082, China
`yuanjie@hnu.edu.cn`

Abstract. With the development of urbanization, overhead lines in urban areas are commonly transformed into the underground power cables. Since the single-circuit cables' load, which is limited by the cross-sectional area of the cable, cannot be matched with the original overhead line, it has become one of the trends to use the parallel cables in phase. The sheath circulating current during normal cables' operation can lead to the rise of temperature and influence the cable capacity and insulation life. In addition, the core current's distribution for parallel cables is a key factor affecting the capacity. In order to investigate the effect of mixed arrangement and inconsistent length on the circulating current and current distribution of parallel cables, a model for calculating each circuit current of cross-connected grounding single-core cable is established, and the circulating current and core current under different arrangements or lengths of cross-connect section are calculated in this paper. The results show that the sheath circulating current can reach up to 30% of the core current when the mix of triangular and vertical arrangement are used for the cables; when the combinations of the length of cross-connected sections are 450 m-500 m-550 m and 450 m-525 m-525 m, both of sheath circulating current are less than 10% of the core current. It is demonstrated that parallel cables core current distribution mainly depends on the layout of each section of cable and after the layout is determined the length of each section has little effect. Thus, the mixed arrangement of parallel cables should be avoided as much as possible, and the length of each section can vary to some extent.

Keywords: Parallel cables · Cross connection · Sheath circulating current · Mixed arrangement · Inconsistent length

1 Introduction

With the urbanization process accelerating, some urban high-voltage overhead lines are constantly transformed into the power cable in order to beautify the city and save urban land resources. Underground cables are widely used in urban transmission lines

of 110 kV and above due to their advantages of stable and reliable power supply, space saving, and low environmental impact. In order to adapt to the rising urban load and match with the overhead line transmission capacity, the double-circuit parallel are used to solve the shortcomings of the single cables with low transmission capacity. Because no fault cable circuit can continue to run in the emergency, the operational stability of the line [1, 2] is improved greatly.

When the core of single-core cable flowing across the load current, the alternating magnetic field which produces an induced voltage in metal sheath are generated. To ensure the safety of the worker, the high-voltage cable sheath must be grounded. If both ends of the sheath are directly or cross-connected grounded, the sheath and the earth will form a circulating current, and in the condition of both ends grounded directly, sheath circulating current will be the same order of magnitude as the core current [3, 4].The standard (Q/GDW 11316-2014) requires that the absolute value of the grounding current is less than 100 A, the ratio of the grounding current to the load current is less than 20%, and the ratio of the maximum value of the single-phase grounding current to the minimum value is less than 3 [5]. The large circulating current not only causes huge losses, its heat also directly affects the cable load capacity and insulation life. Lots of research has been carried out worldwide on cable sheath circulating current in cross-connected grounding methods. Roberto C. studied the effect of different types of sheath connection on circulating current [6]. Liu, Y. compared the circulating current in double-circuit cable with that in single-circuit cable, and suggested that the compact arrangement and larger grounding resistance can effectively reduce the circulating current [7]. Zhu, G. analyzed the impact of cable phase spacing and loop spacing on circulating current in double-circuit cables [8]. Wang, R. analyzed the different circulating current suppression methods and proposed a new combination to achieve better suppression effect [9]. Wang, B. calculated the sheath circulating flow for single and double-circuit cables with different arrangements and section lengths [10, 11]. Zou, H. [12] investigated the effect of three and four-circuit factors on circulating current and proposed the phase sequence with minimum circulating current under different arrangements.

Significantly different from that in the traditional multi-loop cables, the current of each phase of sub-cables in parallel cables may be unevenly distributed, and the system transmission capacity is not fully utilized [13, 14]. Although some scholars have calculated the current distribution and optimized the cables' arrangement based on Carson's theory [15–17], the impact of inconsistent arrangement and section length on parallel cables has been little involved. This paper establishes a model for calculating each circuit current of the cross-connected grounded parallel cables, calculates the circulating current and core current of parallel cables through the simulation software ATP-EMTP, and analyses the current distribution and sheath circulating current of the parallel cables.

2   Parallel Cable Modelling

The cables' core and sheath are equivalent to a hollow transformer. When the cable is in operation and the core through the load current will produce a sinusoidal steady-state magnetic field in space, which lead to an induced voltage in sheath. If the sheath and the earth form a circuit, sheath circulating current will be generated. When the length of

cable is longer than 1000 m, it is usually divided into several sections, and each section of cable sheath is cross-bounded. This paper mainly analyses the core and sheath current of parallel cable in cross-connected grounded situation.

2.1 Cables Impedance

Taking the cross-connected grounded double-circuit parallel cables as an example, it has a total of 12 conductor-earth circuits (Fig. 1).
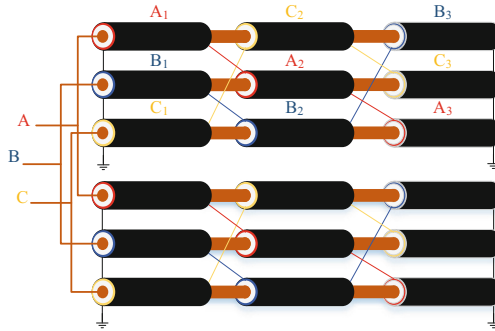
Fig. 1. Illustration of double-circuit parallel cables

The elements in the impedance matrix Z of double-circuit parallel cables can be divided into the four categories, and the impedances are calculated as follows.

$$\begin{cases} Z_{cc} = r_c + r_e + j0.1445\log\frac{D_e}{d_{GMRc}} \\ Z_{ss} = r_s + r_e + j0.1445\log\frac{D_e}{d_{GMRs}} \\ Z_{sc1} = r_s + r_e + j0.1445\log\frac{D_e}{d_{GMRs}} \\ Z_{sc2} = r_e + j0.1445\log\frac{D_e}{D} \end{cases} \qquad (1)$$

where Z_{cc}, Z_{ss}, Z_{sc1}, and Z_{sc2} represent the self-impedance per unit length of the core-earth circuit, the self-impedance per unit length of the sheath-earth circuit, the mutual impedance per unit length of the core-earth and sheath-earth circuits of the same cable, and the mutual impedance between other circuits, respectively; r_c, r_s, and r_e denote AC resistance per unit length of cable core, AC resistance per unit length of cable sheath, and the earth equivalent resistance, respectively; D_e is the equivalent depth with the earth as the equivalent circuit; d_{GMRc} is the geometric average radius of the core; d_{GMRs} is the geometric average radius of the sheath; D is spacing of each circuit.

The 12-order impedance matrix of double-parallel cables can be calculated by Eq. (1). Because the cross connection has changed the relative positions of the sheath and core, the impedance matrix of each section is not the same. If each section is in the same arrangement, only the impedance matrix of the first segment should be computed, and

the impedance matrix of the remaining sections can be transformed from the above-mentioned one. If not, the impedance matrix for each section needs to be calculated separately. The global impedance matrix of the parallel cable is obtained by weighting the impedance matrix of each section by length, and the voltage equation can be written as follows:

$$U = Z \begin{vmatrix} I_{ca1} \\ I_{cb1} \\ I_{cc1} \\ \vdots \\ I_{sa2} \\ I_{sb2} \\ I_{sc2} \end{vmatrix} \tag{2}$$

where the current phasors are the core current of the first circuit ($I_{ca1}, I_{cb1}, I_{cc1}$), the core current of the second circuit ($I_{ca2}, I_{cb2}, I_{cc2}$), the sheath current of the first circuit ($I_{sa1}, I_{sb1}, I_{sc1}$), and the sheath current of the second circuit ($I_{sa2}, I_{sb2}, I_{sc2}$) in sequence, and the voltage phasor is the voltage drop across each conductor.

$$Z = \begin{vmatrix} Z_{cc11} & Z_{cc12} & Z_{cs11} & Z_{cs12} \\ Z_{cc21} & Z_{cc22} & Z_{cs21} & Z_{cs22} \\ Z_{cs11} & Z_{cs12} & Z_{ss11} & Z_{ss12} \\ Z_{cs21} & Z_{cs22} & Z_{ss21} & Z_{ss22} \end{vmatrix} \tag{3}$$

The impedance matrix Z can be reduced to a block matrix, as shown in (3), and the diagonal from top to bottom are the first-circuit core impedance matrix Z_{cc11}, the second-circuit core impedance matrix Z_{cc11}, the first-circuit sheath impedance matrix Z_{ss11}, and the second-circuit sheath impedance matrix Z_{ss22}, respectively.

2.2 Current Calculation

The current in each phase of the parallel cables is shared by sub-cables, and it can be seen from the Kirchhoff current law that the n-circuit parallel cables have the following current equation.

$$\begin{cases} I_{ca} = \sum_{i=1}^{n} I_{cai} \\ I_{cb} = \sum_{i=1}^{n} I_{cbi} \\ I_{cc} = \sum_{i=1}^{n} I_{cci} \end{cases} \tag{4}$$

In (4), I_{ca}, I_{cb}, I_{cc} are the total load current of each phase, and $I_{cai}, I_{cbi}, I_{cci}$ are the load current carried by the number i in each phase of the sub-cables.

The cores of the sub-cables in phase in parallel cables have electrical connections at both ends. It is easy to know that the voltage drop of the sub-cables are equal, and for n-circuit parallel cables, it can be written as,

$$
\begin{cases}
\Delta U_{ca1} = \Delta U_{ca2} = \cdots \Delta U_{can} \\
\Delta U_{cb1} = \Delta U_{cb2} = \cdots \Delta U_{cbn} \\
\Delta U_{cc1} = \Delta U_{cc2} = \cdots \Delta U_{ccn}
\end{cases}
\tag{5}
$$

where ΔU_{can} denote the core voltage drop of A-phase No. *Nth* sub-cables, and ΔU_{san} are the sub-cables sheath voltage drop in the same named regularity. According to the Kirchhoff voltage law, when the cable sheath is grounded, its voltage drop complies with the following equation.

$$
\Delta U_{sa1} = \Delta U_{sb1} = \Delta U_{sc1} = (I_{sa1} + I_{sb1} + I_{sc1})R_G
\tag{6}
$$

where R_G is the sum of the grounding resistances of each sheath.

The cross-connected grounded double-circuit cables need to calculate 12 current phase, the formula (4) can determine three equations, and substituting Eq. (5) & (6) into voltage Eq. (2) can determine the remaining nine equations. Finally, all the current phase quantities can be obtained, and the matrix of joint cubic equation system is drawn as follows.

$$
\begin{vmatrix}
Z_{cc11} - Z_{cc12} & Z_{cc12} - Z_{cc22} & Z_{cs11} - Z_{cs21} & Z_{cs12} - Z_{cs22} \\
Z_{cs11} & Z_{cs21} & Z_{ss11} - R_G & Z_{ss12} - R_G \\
Z_{cs12} & Z_{cs22} & Z_{ss12} & Z_{ss22} \\
E & E & 0 & 0
\end{vmatrix}
\begin{vmatrix}
I_{ca1} \\
I_{cb1} \\
I_{cc1} \\
\vdots \\
I_{sa2} \\
I_{sb2} \\
I_{sc2}
\end{vmatrix}
=
\begin{vmatrix}
0 \\
0 \\
0 \\
\vdots \\
I_{ca} \\
I_{cb} \\
I_{cc}
\end{vmatrix}
\tag{7}
$$

where $R_G = \begin{vmatrix} R_G & R_G & R_G \\ R_G & R_G & R_G \\ R_G & R_G & R_G \end{vmatrix}, E = \begin{vmatrix} 1 & 0 & 0 \\ 0 & 1 & 0 \\ 0 & 0 & 1 \end{vmatrix}$, 0 is the third-order zero matrix.

Select the upper left part of the impedance matrix Z as the core impedance matrix Z′,

$$
Z' = \begin{vmatrix} Z_{cc11} & Z_{cc12} \\ Z_{cc21} & Z_{cc22} \end{vmatrix}
\tag{8}
$$

If the cable sheath is single-ended grounding, as shown in Eq. (8), the global impedance matrix Z will not contain sheath-related impedance elements, and the voltage equation can be written as follow.

$$
\begin{vmatrix} U_1 \\ U_2 \end{vmatrix} = Z' \begin{vmatrix} I_1 \\ I_2 \end{vmatrix}
\tag{9}
$$

where U_1, U_2 are the voltage drops of two circuits of cable cores, and I_1, I_2 are the core currents of each circuit. The sub-cables in parallel of each circuit of core voltage drops are equal. if the core line current distribution is uniform, then the matrix meets the following equation.

$$Z_{cc11} + Z_{cc12} = Z_{cc21} + Z_{cc22} \qquad (10)$$

In order to satisfy (10), the parallel cables' layout must be symmetrical. Double-circuit cables in tunnel can choose a variety of arrangements, and some arrangement has multiple phase sequence combinations, which can make the cable layout symmetrical and have the uniform core current distribution. Under the condition of a unsymmetrical phase sequence resulting in the uneven current distribution, the nonuniformity coefficient ε is defined in order to measure the degree of imbalance of the core current distribution,

$$\varepsilon = I_{max}/I_{min} \qquad (11)$$

In (11), I_{max} and I_{min} are the maximum and minimum absolute value of core current in each sub-cables of each phase in the parallel cables, respectively.

3   Simulation of Parallel Cables

3.1   Triangular and Vertical Arrangements

There are two main types of layouts when the cables are laid in tunnel: triangular layout and vertical layout. The two layouts are illustrated as Fig. 2.
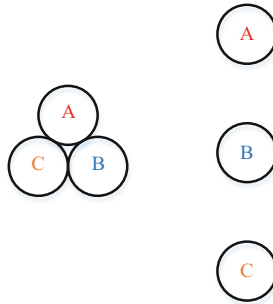
Fig. 2. Illustration of triangular and vertical layout

The voltage phasor diagrams of single-circuit cables in triangular and vertical layouts which only take the core currents into consideration is shown as follows.

As can be seen from Fig. 3, when the cable is triangular layout, the phase volume of induced voltage of each section forms a closed triangle. Due to the cable not meeting the three-phase symmetry in a vertical layout, its phase diagram cannot form a closed graph, however, it can form a zero sequence voltage, which will lead to a large grounding current on the sheath.
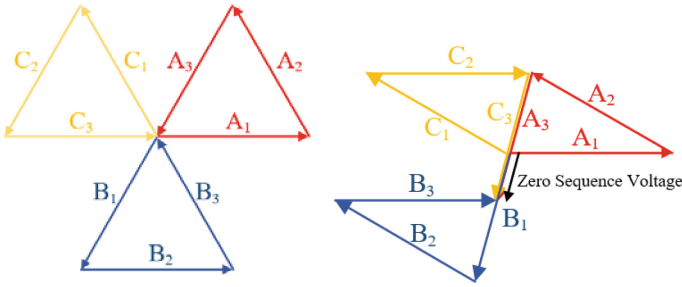
Fig. 3. Phasor diagram for the induced voltage of single-circuit cable sheath

If the core current distribution is not taken into account, the parallel cables can be treated as the multi-loop cables. It is assumed that the core current is evenly distributed in the double-circuit parallel cable, whose layout is triangular. Unlike the single-circuit cables, the double-circuit cable sheath induced voltages are generated by other circuit core and sheath currents in addition to core current induction. The phasor diagram of induced voltage in a double-circuit parallel cables is shown as follows.
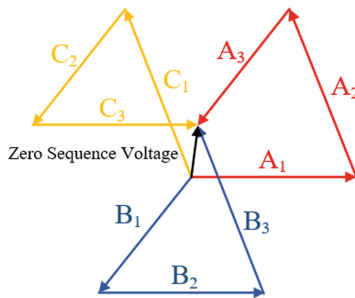
Fig. 4. Phasor diagram for the induced voltage of double-circuit cable sheath

It can be seen that when the number of cable circuit exceeds 1, even if a triangular layout is used, the voltage phase of sheath cannot form a closed graph, and this situation is similar to single-circuit cable in vertical layout. Figure 4 can be decomposed as a superposition of the single circuit voltage phase quantities and one zero sequence voltage phase quantity. With the increase of the number of cable circuit in the tunnel, the essence is that there are multiple zero sequence voltages superimposed on the single circuit voltage phase quantity.

Actually, the currents of three phases in each sub-cables do not necessarily meet the equal amplitude and phase difference of 120°, making the sheath voltage phase diagram deformed.

3.2   Mixed Arrangement

Taking YJLW03 1 × 2000 mm^2 127/220 kV double-circuit cable as an example, its outer diameter of conductor is 54.4 mm and outer diameter of metal sheath is 136.7 mm, the thickness of the sheath is 2.8 mm, the outer longitude of cable is 146.7 mm, the total length of the cable is 1.5 km, the length of each cross-connected section is 500 m, the grounding resistance is 1 Ω, and the load current is 2 × 1000 A.

In order to study the effect of the mixed arrangement on the sheath circulating current and core current distribution, for the basic arrangements, 2 phase sequences are selected and the diagram of four layouts is shown in Fig. 5.
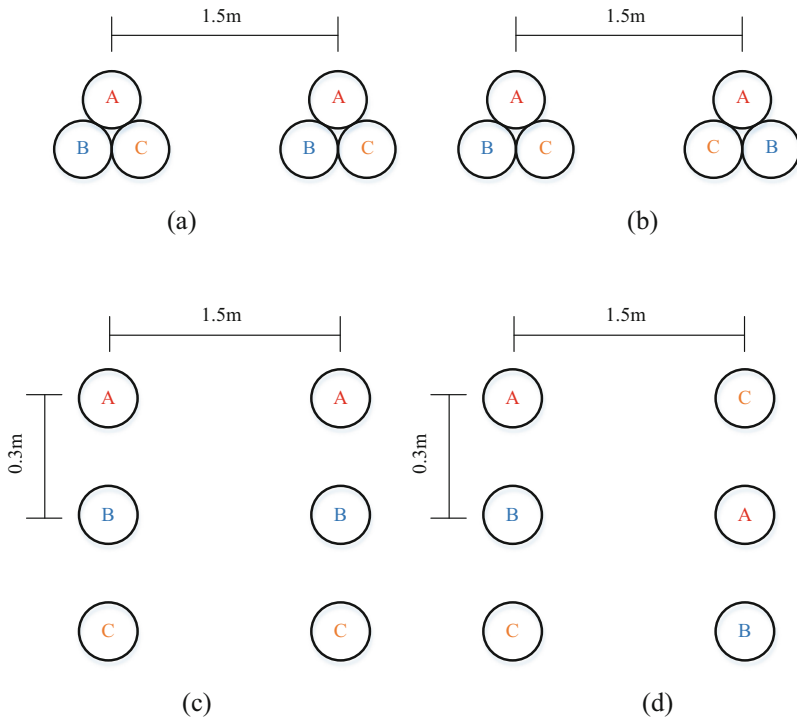
Fig. 5.   Four layouts of parallel cables

The double-circuits cables are symmetrical layout in Fig. 5(b) and (c). The length of each section of cable is 500 m, and the cables' layout of each section is selected from the above four types which form a total of 12 combinations. The sheath circulating current and nonuniformity coefficient are listed in Table 1.

Table 1. Sheath circulating current for mixed arrangements

Arrangement	Maximum and minimum values of circulating current (A)	ε
a-a-a	0.19/0.17	1.0167
b-b-b	1.03/1.01	1
c-c-c	3.08/3.04	1
d-d-d	1.77/1.74	1.2030
a-a-c	314/144	1.0126
b-b-c	312/142	1
a-a-d	288/145	1.0495
b-b-d	285/144	1.0559
a-c-c	307/93	1.0080
b-c-c	350/105	1
a-d-d	274/99.1	1.1250
b-d-d	270/99.3	1.1339

From the results in Table 1, it can be seen that the nonuniformity coefficient of asymmetrical combinations a-a-a and d-d-d under the same layout of each section are larger than 1, and the d-d-d combination has the largest nonuniformity coefficient. The nonuniformity coefficients of b-b-b and c-c-c combinations which are the symmetrical combinations are 1, and their core currents are evenly distributed. The nonuniformity coefficient of single layout can be acted as the nonuniformity coefficient of the layouts. When the layouts of each section are not the same, the global nonuniformity coefficient will be between the nonuniformity coefficient of each section layouts. For instance, the nonuniformity coefficients of a-a-c and a-c-c combinations are between the nonuniformity coefficients of a-a-a and c-c-c combinations. If the layout of each section is symmetrical, the nonuniformity coefficient after the combination is still equal to 1, such as b-c-c and b-b-c combinations. If the nonuniformity coefficient of each section meets the requirements, the overall nonuniformity coefficient will also meets the requirements.

When the each section of parallel cable's layout is the same, the maximum values of sheath circulating current of each phase are close, and they are less than 1% of the core current. If not, the maximum values of the sheath circulating current can reach up to 30% of the core current, which greatly exceeds the standard, i.e. 10%. Due to the cross-bounding sheath, one sheath-earth circuit consists of three different sections of cables sheath. The sheath with a large current will generates a lot of heat and the current will directly affects the load capacity and insulation life of all cables. When the parallel cables are of mixed arrangement, each phase sheath current varies widely, and the sequence component decomposition of the sheath current is shown in the Table 2.

Table 2. Sequence decomposition of sheath current

Arrangement	Positive, negative and zero sequence components (A)
a-a-c	245/101/0.85
b-b-c	242/101/0.57
a-a-d	231/86/0.66
b-b-d	229/85/0.48
a-c-c	220/126/1.91
b-c-c	239/140/1.93
a-d-d	210/102/0.95
b-d-d	199/100/0.73

When the arrangement is triangular-triangular-vertical (a-a-c or b-b-c), the induced voltage generated by the triangular layouts is positive sequence components, and the induced voltage generated by the last section of vertical layouts contains both positive and negative sequence components. The superposition of the two makes the synthetic induced voltage contain a large positive sequence component, whereas the negative sequence component in the synthetic induced voltage is only generated by the section of vertical arrangement. The zero-sequence currents of sheath in Table 2 are at a small level, so the grounding currents do not change significantly compared to the arrangement with single layout. Increasing the grounding resistance can merely suppress the zero-sequence current, and adding a small resistance in the sheath cross interconnection can effectively suppress the positive and negative sequence circulating currents.

3.3 Inconsistent Section Length

Actually, it is difficult to achieve the equal length for each section of sheath. Assuming that the length of the third section of single-circuit cable sheath is slightly less than the other two sections, the induced voltage phasor can be acquired, as shown in Fig. 6.
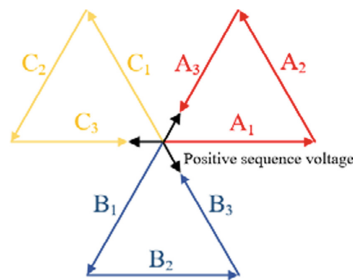
Fig. 6. Voltage phasor under the difference section length.

From Fig. 6, it is easy to know that when the section lengths are not the same, the sheath synthetic induced voltage is positive sequence. Since the vertical layout is not three-phase symmetrical, its sheath synthetic induced voltage also contains part of the negative sequence component in addition to the positive sequence component.

This section still selects YJLW03 1 × 2000 mm² 127/220 kV type double-circuits parallel cables, and other parameters are the same as the previous section except for the section length. The length combinations of three cross-bounding section are 500 m-500 m-500 m, 450 m-500 m-550 m and 450 m-525 m-525 m, respectively. There are four combinations with single layout aiming to the arrangements of parallel cables, and the results in the case of 500 m-500 m-500 m combination are listed in Table 1. Only the last two combinations need to be calculated and the results are shown in Table 3.

Table 3. Calculation results for inconsistent section length

Length combinations (m)	Arrangement	extreme value of sheath circulating current (A)	ε
450-500-550	a-a-a	47.7/47.1	1.0166
	b-b-b	48.5/46.8	1
	c-c-c	72.5/46	1
	d-d-d	60.2/45.6	1.2025
450-525-525	a-a-a	41.3/40.8	1.0166
	b-b-b	41.6/40.2	1
	c-c-c	55.2/31.9	1
	d-d-d	52.6/37.3	1.2030

Compared with the results in Table 1, the sheath circulating current increases significantly when the section lengths are not equal. The result of circulating currents in Table 3 are always less than 10% of the core current, and the difference in the amplitude of the circulating current of each phase is small. The sequence component decomposition of the sheath circulating current shows that the positive sequence component is very high, and the zero sequence component is the same when the section length is equal. Comparing the nonuniformity coefficients in Table 1 with those in Table 3, the results show that the inconsistent section length has little effect on the current distribution of parallel cables.

3.4   Mixed Arrangement and Inconsistent Section Length

When the cables are not arranged in the same layout, the lengths of each section are often not equal. The superposition of two factors may further increase the circulating current and nonuniformity coefficient of parallel cables. In this section, the circulating current and nonuniformity coefficient under the four arrangements are calculated, and the length combination are to select 450 m-500 m-550 m and 450 m-525 m-525 m in

order to investigate the influence of the two factors on parallel cables. The results are depicted in Table 4.

Table 4. Sheath circulating current and nonuniformity coefficient for mixed arrangements and inconsistent section length

Length combination (m)	Arrangement	Extreme value of sheath circulating current (A)	ε
450-500-550	b-b-c	359/193	1
	b-c-c	399/146	1
	a-a-d	335/198	1.0466
	a-d-d	304/128	1.1318
450-525-525	b-b-c	335/172	1
	b-c-c	398/114	1
	a-a-d	314/117	1.0448
	a-d-d	309/127	1.127

The maximum values of circulating currents in Table 4 are larger than those in Table 1, and the circulating currents of each phase in Table 4 has a large difference. As mentioned in Sect. 3.2, the induced voltage of vertical layout contains positive and negative sequence components. The positive sequence induced voltage of vertical layout is several times higher than that of triangular layout. In Table 4, the layout with the longest section is the vertical layout. Now replace the vertical layout with the triangular layout, the recalculated results are indicated in Table 5.

Table 5. Sheath circulating current after replacement

Length combinations (m)	Arrangement	Extreme value of sheath circulating current (A)
450-500-550	c-b-b	262/98
	c-c-b	277/72
	d-a-a	242/101
	d-d-a	240/73
450-525-525	c-b-b	257/93
	c-c-b	303/93
	d-a-a	235/95
	d-d-a	264/93

After the cable arrangement is changed, the maximum value of circulating current is reduced by almost 100 A and the nonuniformity coefficient is altered slightly.

4 Conclusion

When the parallel cables are in the same layout for each section, the circulating current is small and mainly zero sequence current. When the layout of each section are different, the circulating current of three phases differs greatly from each other, and the maximum value of circulating current reaches up to 30% of the core current.

The current distribution of parallel cables depends on the cables layout of each section, the overall nonuniformity coefficient is within the nonuniformity coefficient of each section. If the arrangement of each section is selected properly, the overall nonuniformity coefficient can also meet the engineering standard.

The inconsistent section length leads to a rise in the sheath circulating current but are still within the reasonable range. In the case of mixed arrangement, the inconsistent section length will change the proportion of four layouts in the cable. This will produce moderate impact on the current distribution of parallel cables. Considering its length difference relatively smaller than the full length of cable, the impact can be ignored.

References

1. Wang, H.: Design of transmission scheme for two 220 kV parallel cables in phase. Shenzhen Univ. 30–33 (2018)
2. Cheng, J., et al.: Same-phase and double-circuit transmission mode of high-voltage single-core cables and its operation and maintenance. Guangdong Electr. Power **30**(3), 116–121 (2017)
3. Li, P., Guo, P.: Characteristic analysis of the outer sheath circulating current in a single-core AC submarine cable system. Symmetry **14**, 1088 (2022)
4. Wang, X.: The research on optimal layout and relay protection of same-phase parallel cables. Huazhong Univ. Sci. Technol. 11–16 (2016)
5. Test code for power cables-Q/GDW 11316 (2014)
6. Candela, R., Gattuso, A., Mitolo, M.: A model for the study of sheath currents in medium voltage cables for industrial application. IEEE (2020)
7. Liu, Y.: Calculation of Circulating Current in Sheaths of Two circuit Arranged Cables and Analyses of Influencing Factors. Xi'an Jiaotong University (2007)
8. Zhu, G.: The influence of phase spacing and loop spacing on circulating current of power cable metal sheath. J. Northeast Electr. Power Univ. **42**(2) (2021)
9. Wang, R.: Analysis of suppression method for grounding circular current in metal sheath of high-voltage cable. Proc. CSU-EPSA **11**(31), 108–114 (2019)
10. Wang, B.: Analysis of circulating current in sheaths of 220 kV XLPE single-core cables. High Volt. Appar. **45**(5), 141–145 (2009)
11. Chen, K.: Effect of mixed arrangement on current in sheaths of two-circuit arranged XLPE cables. High Volt. Eng. **44**(11), 37–42 (2018)
12. Zou, H.: Effects of different multi-loop laying ways on circulating current of power cable. High Volt. Eng. **42**(8), 24–33 (2016)
13. Shang, L.: Study on 'temperature field and ampacity of multi-circuit cable lines considering current distribution and circulating current in sheaths. Chongqing Univ. 20–24 (2014)
14. Chen, F., et al.: Influence of parameter difference between parallel cables on current-carrying distribution. High Volt. Appar. **55**(2), 227–233 (2019)

15. Lin, G., et al.: Analysis of electrical parameters and unbalance factors of 220 kV multi-circuit transmission cable based on Carson theory and EMTP simulation. Power Syst. Prot. Control. **47**(20), 142–148 (2019)
16. Fan, Y., et al.: Analysis and optimation for operation of the single-core power cables in parallel. High Volt. Eng. **36**(10), 2607–2612 (2018)
17. Zhang, P., Zhang, H., Li, W., Li, B., Li, L.: Study on optimization of laying mode of two parallel high voltage cables in the same phase of two circuits. Energy Rep. **8**, 1839–1846 (2022)

Effect of Solid Surface on Breakdown Properties of SF$_6$-Epoxy Gas Solid Interface

Liu Lin[1(✉)], Hao Yanpeng[1], Licheng Li[1], Yao Zheng[2], Jiaming Xiong[2], Ruodong Huang[2], Chao Gao[2], Fusheng Zhou[2], Yun Yang[2], and Guoli Wang[2]

[1] School of Electric Power Engineering, South China University of Technology, Guangzhou 510641, China
`hvliulin@scut.edu.cn`
[2] Electric Power Research Institute, China Southern Power Grid, Guangzhou 510080, China

Abstract. The discharge caused by metal particles is one of the key reasons for the fault of SF$_6$ gas insulation system, and the threat of metal particles to gas-solid interface insulation is greater than that of gas gap only. In this paper, cylinder and conical epoxy resin insulator samples as well as a parallel plate electrode fixed by a metal protrusion are employed to simulate the discharge in SF$_6$-epoxy resin interface. The arc channel of samples immersed in 0.06MPa SF$_6$ under negative standard lightning impulse voltage is observed by a photoelectric joint diagnostic platform based on ICCDs. The results show that the breakdown voltage of cylinder insulator is the highest both in the clean and protrusion case, for the protrusion is the farthest from the insulator surface and its electric field is the least distorted. The arc pictures show that compared with the cylindrical insulator, it is easier for the conical insulator to attract the discharge channel to its surface, for the higher normal component of electric field strength along the surface. In conclusion, the attractive effect from the insulator surface is the weakest in the cylinder insulator, and the probability of participating in the discharge process along the surface is the lowest. Therefore, in engineering design, two methods can be used to restrain the harm of metal particles to surface discharge: keep free metal particles away from the solid surface, and avoid the wedge-shaped triple junction structure.

Keywords: Gas Insulation · SF$_6$ · Interface Discharge · Breakdown Voltage · Arc Channel

1 Introduction

SF$_6$ gas insulated equipment is widely used in modern power system for its excellent insulation performance, arc extinguishing performance and chemical stability. Operating experience shows that the conducting metal particle is the most serious threat to the dielectric performance of SF$_6$ gas insulated equipments, especially to the gas-solid interface which may eventually result in surface flashover [1–3].

In order to improve the insulation strength along the surface, the inclined arc surface is generally used to increase the creepage distance along the surface. It is generally believed that the solid dielectric plays a positive role in the gas discharge process, the surface structure will distort the electrostatic field distribution and the photoemission

process on its surface could also provide more charged particles for the discharge process. Verhaart et al. [4] found that in SF_6, photoemission becomes the prevalent contributor to the avalanche below a critical value of field. Jorgenson et al. [5] investigated the effect of dielectric photoemission on surface breakdown process, and they proposed that photoemission plays a role at low field values near the breakdown threshold by Monte Carlo simulations.

In some studies, streamer channels were observed to be attracted to propagate along the dielectric surface rather than through the bulk gas only. Trienekens et al. [6] found that surface streamers along the dielectric surface can be up to twice as fast as streamers through bulk air by recording the discharge process with an ICCD camera. Sobota et al. [7] found that the streamer discharge has a tendency to propagate in all directions along the dielectric surface, not only toward the grounded electrode in argon. Li et al. [8, 9] found that the attraction of streamers to the dielectric is mostly electrostatic which relative with the distance between the discharge channel and dielectric surface in air by numerical simulation model.

In conclusion, scholars believe that the existence of the gas-solid interface could promote the gas discharge channel, but the attractive effect of the gas-solid interface on the discharge channel is doubtful. To clarify the attractive effect from the epoxy resin surface to the gas discharge in SF_6 gas, the photoelectric joint diagnostic platform was built in this paper, and the breakdown voltage, arc channel and electrostatic field distribution of six insulator samples were combined to analysis the attractive effect, and finally the method of restraining the harm of particles to surface discharge is proposed.

2 Experimental Setup

2.1 Photoelectric Joint Diagnostic Experimental Platform

As Fig. 1a shows, the optical observation platform is based on a photomultiplier tube (PMT) a high-speed framing camera (HSFC). For PMT, its wavelength range is 185–900 ns and the response time is 2.2 ns. HSFC is capable to shoot four times successively with a 3 ns shutter time and a 1 ns inter-frame time, and its triggering time sequence is shown in the Fig. 1b. The resolution of the HSFC is 1280 * 1024 pixels, and the observable spectral range is 160–1300 nm, which meets the requirements of optical observation of discharge process in SF_6 [10]. The discharge circuit consists a Marx generator supplying the negative standard lightning impulse (-LI, 1.1/50 µs), a tapered voltage sensor monitoring the impulse waveform and a test vessel providing SF_6 gas at ambient temperature for test samples. The insulator samples are set in the coaxial cylindrical structure in test vessel by threaded connector. Since the time lags and amplitude of the breakdown voltage were both affected by the time interval between successive voltage applications, a pause time about 5 min between the impulse voltage applications was set. All the optical images are all captured at 0.06 MPa SF_6.

2.2 Insulator Samples

Six samples composed of epoxy resin insulator and aluminum parallel plates electrode with a metal protrusion. As shown in Fig. 1a, the insulator samples are set in the coaxial cylindrical structure in test vessel by threaded connector. The height of insulator samples
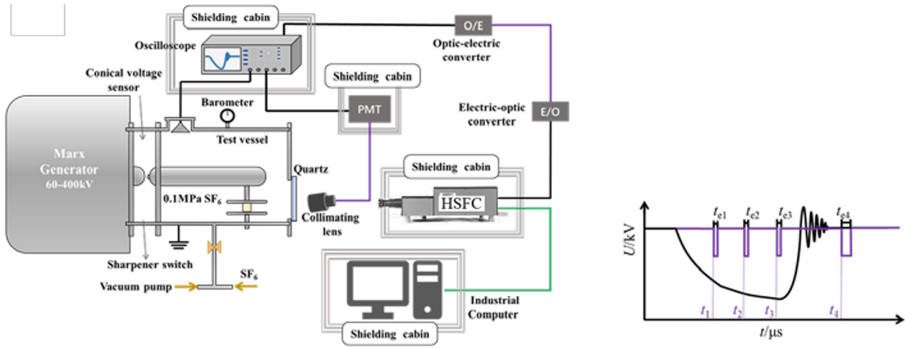
(a) Photoelectric joint diagnostic platform based on PMT and ICCDs   (b) The triggering time sequence of HSFC

Fig. 1. Experimental platform (a) and the triggering time sequence of the HSFC (b).

is 20mm, and top diameter is 20 mm, while the bottom inclination is 90°, 60° and 45°, respectively. The curvature radius of the protrusion tip is 0.5 mm. As shown in Fig. 2b and 2c, the length of protrusion I is 2 mm and it is 3.5 mm away from insulator surface (A, C, E), while the other one is 4 mm in height and 7mm away from insulator surface (B, D, F).
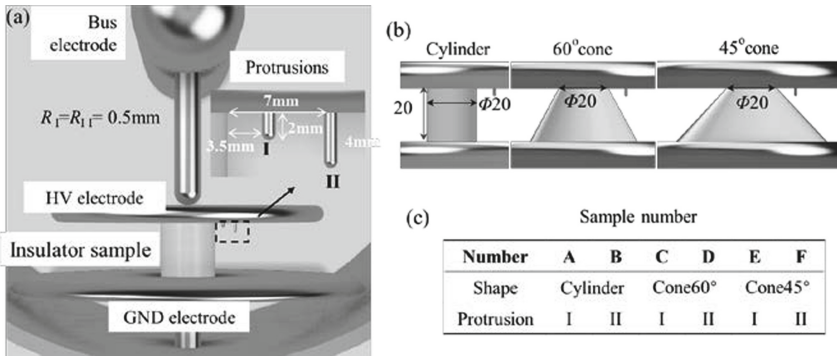
Fig. 2. The mounting structure of sample in the test chamber (a), sample structure (b) and the number rule (c).

3   Results and Discussion

3.1   Breakdown Voltage

The breakdown voltage (U_b) of insulator samples is shown in Fig. 3. Under clean condition, U_b of cylinder insulator is the highest, and U_b of the 60° cone and 45° cone insulator are much lower, which are almost only 60% and 50% of the cylinder one, respectively. When the protrusion I is attached to the high voltage electrode, U_b of three samples
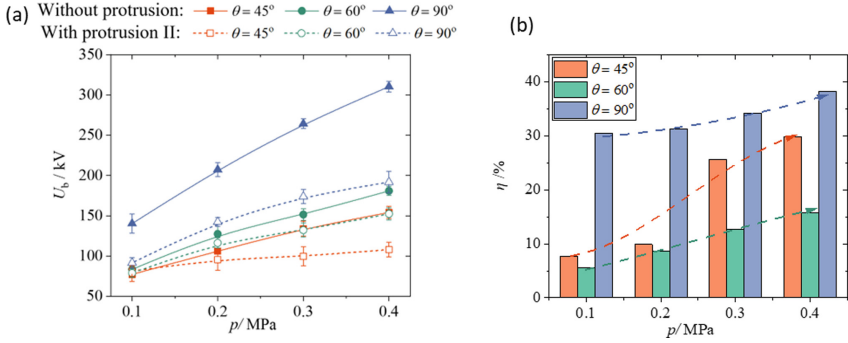
Fig. 3. Breakdown voltage of insulator samples with and without metal particle (a) and the decrease ratio of breakdown voltage caused by metal particle (b).

significantly decreases. In this case, U_b of the cylinder insulator is still the highest, 60° cone and 45° cone insulator is next to it, respectively.

Define the decrease rate of U_b as η according to Eq. (1), and η of three sample shows in Fig. 3b. It is clear that U_b of the cylinder insulator decreases the most, then comes 45° cone, and 60° cone decreases the least. The decreasing rate of U_b increases fastest in 45° cone with the gas pressure increasing. Obviously, when there is a metal particle attached, the increasing rate of U_b decreases with the increasing of gas pressure.

$$\eta = \frac{U_b - U_{bp}}{U_b} \times 100\% \tag{1}$$

where U_b—the breakdown voltage without metal particle, U_{bp}—the breakdown voltage with metal particle, η—the decreasing rate of breakdown voltage caused by meatal particle.

3.2   Breakdown Arc Channel

As shown in Fig. 4a, the arc channel of sample A differs from each other. The arc channel in A1 directly penetrates the gas gap, that in A2 slightly deflects to the insulator surface in the first half but deflects away and penetrates the gas gap in the second half, that in A3 deflects to the insulator surface and arrives at the insulator surface in the second half, that in A4 deflects and arrives at the insulator surface in the first half. The arc channel of sample B, both in B1 and B2, directly penetrates the gas gap and the insulator surface has no attractive effect on it. As the protrusion is too close to the insulator surface, the arc channels of sample C and sample E all develop along the insulator surface. There is obvious attraction effect on the arc channels in sample D and sample F. Although the arc paths are not identical, they all deflect to the insulator surface from the beginning.

The 3D electrostatic field distribution (E-distribution) of six insulator samples is calculated by the finite element analysis method. The relatively permittivity of epoxy resin, SF_6 is set as 5.0 and 1.002, and the electric potential is set as 1 kV and 0 kV in the calculation model. The E-distribution is normalized by the average electric field strength of the gas gap (0.05 kV/mm). The normalized E-distribution of observation section is

shown in Fig. 4b. The maximum value of E (E_{max}) is at the protrusion tip. It is clear that the smaller the inclination, the closer the protrusion to the insulator surface, and the higher value of the E_{max}. The normalized E_{max} of sample F is the highest in these six samples, in other words, its electric field non-uniformity is the highest, and that is why η of sample F increases sharply with the gas pressure increases [11].
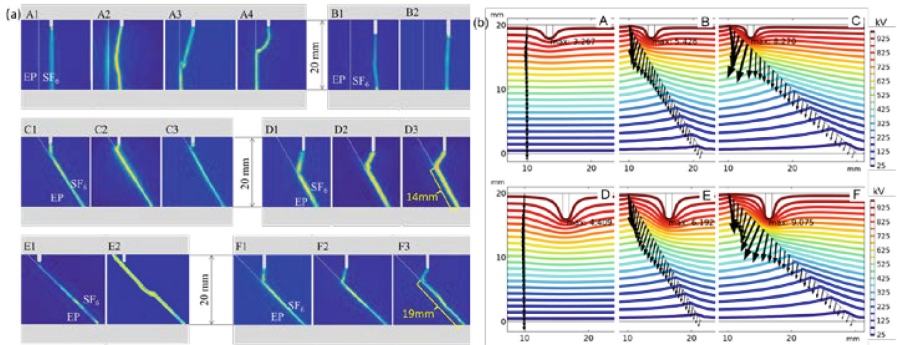
Fig. 4. Arc channel pictures (a) and the electric potential line and normalized electric field strength distribution along insulator surface (b).

The normal component of electric field along the insulator surface is much higher in the cone samples, which means the electrostatic force could help to attract the discharge channel to develop along gas-solid interface. In other words, the attractive effect from the surface is the weakest in cylinder insulator, and the probability of participating in the discharge process along the surface is the lowest. Compare the arc channels of sample D and sample F in Fig. 4a with U_b in Fig. 3a, it is clear that the more the insulator surface participating in the discharge, the lower the breakdown voltage.

Therefore, the cylinder is the best structure of insulator, of which the insulator performance is the best both in case of clean and protrusion condition. The 45° cone is the worst structure, which has the lowest U_b under clean condition and the highest decreasing rate of U_b when attached with metal particle.

4 Conclusions

In this paper, breakdown voltage and arc channel pictures of six epoxy resin insulator samples immersed in 0.06MPa SF_6 were measured and recorded by the photoelectric joint diagnostic experimental platform under negative lightning impulse. Conclusions are drawn as follows:

1) Breakdown voltage of insulator with cylinder surface is the highest both in the clean case and protrusion case, because the protrusion is the farthest from the insulator surface and the electric field is the least distorted.
2) Compared with the cylindrical insulator, it is easier for the conical insulator to attract the discharge channel to its surface, for the electrostatic force promoting attractive

effect caused by normal component of electric field strength is higher. The attractive effect from the insulator surface is the weakest in the cylinder insulator, and the probability of participating in the discharge process along the surface is the lowest.

3) In engineering design, two methods can be used to restrain the harm of metal particles to surface dis-charge: keep free metal particles away from the solid surface, and avoid the wedge-shaped triple junction structure.

References

1. Cookson, A.H.: Review of high-voltage gas breakdown and insulators in compressed gas. IEE Proc.: Phys. Sci. Meas. Instrum. Manag. Educ. Rev. **128**(4), 303–312 (1981)
2. Laghari, J.R., Qureshi, A.H.: A review of particle-contaminated gas breakdown. IEEE Trans. Electr. Insul. **EI-16**(5), 388–398 (1981)
3. Seeger, M., Niemeyer, L., Bujotzek, M.: Partial discharges and breakdown at protrusions in uniform background fields in SF6. J. Phys. D Appl. Phys. **41**(18), 185204 (2008)
4. Verhaart, H.F.A., Tom, J., Verhage, A.J.L., et al.: Avalanches near solid insulators. In: Proceeding of the 5th International Symposium on HV Engineering, paper no. 13.01, Braunschweig (1987)
5. Jorgenson, R.E., Warne, L.K., Neuber, A.A., et al.: Effect of dielectric photoemission on surface breakdown: an LDRD Report. Technical Report SAND2003-1731, 811483 US Department of Energy (2003). https://doi.org/10.2172/811483
6. Trienekens, D.J.M., Nijdam, S., Ebert, U.: Stroboscopic images of streamers through air and over dielectric surfaces. IEEE Trans. Plasma Sci. **42**(10), 2400–2401 (2014)
7. Soloviev, V.R., Krivtsov, V.M., Shcherbanev, S.A., et al.: Evolution of nanosecond surface dielectric barrier discharge for negative polarity of voltage pulse. Plasma Sources Sci. Technol. **26**(1), 014001 (2017)
8. Li, X., Sun, A., Zhang, G., et al.: A computational study of positive streamers interacting with dielectrics. Plasma Sources Sci. Technol. **29**, 065004 (2020)
9. Li, X., Sun, A., Teunissen, J.: A computational study of negative surface discharges: characteristics of surface streamers and surface charges. IEEE Trans. Dielectr. Electr. Insul. **27**(4), 1178–1186 (2020)
10. Yoshida, S., Kojima, H., Hayakawa, N., et al.: Light emission spectrum depending on propagation of partial discharge in SF6. In: Conference Record of the 2008 IEEE International Symposium on Electrical Insulation, pp. 365–368, Vancouver (2008)
11. Wiegart, N., Niemeyer, L., Pinnekamp, F., et al.: Inhomogeneous field breakdown in GIS-the prediction of breakdown probabilities and voltages. IEEE Trans. Power Deliv. **3**(3), 923–930 (1988)

Partial Discharge Characteristics of Oil-Pressboard Insulation Under the Effect of Cellulose Impurities

Ping Yan, Yifei Zhou, and Qiang Shi[(✉)]

Marketing Service Center of State Grid Sichuan Electric Power Company,
Chengdu 610065, China
gnosis666@163.com

Abstract. To investigate the effect of cellulose impurities on partial discharge (PD) of oil-pressboard insulation, a DC voltage experimental platform with needle-plate electrode model and was established. Processes including the generation and bridging of cellulose impurities within the insulation were observed, where the dynamic basis of the latter being analyzed. PD characteristics including the repetition rate, the average discharge intensity and the maximum discharge intensity were recorded on samples with and without cellulose impurities, respectively. Afterwards, plate-plate electrode model was adopted to measure the leakage current of oil-pressboard samples with/without cellulose impurities and moisture, and to further explain the mechanism of PDs' differences due to the influence of the impurities. The results indicated that the cellulose impurities were affected by electric field force, gravity, buoyancy and oil viscous resistance. When the electric field strength was higher than 2.12×10^5 V/m, the impurities began moving and bridging along the direction of maximum voltage gradient. The bridged impurities distorted the electric field, resulting in an increased PD repetition rate, and a decreased discharge intensity. Further experiments showed the cellulose bridge increased the leakage current of oil gap, which led to the local overheating and gasification of water impurities into tiny bubbles. Bubbles with lower conductivity compared to oil with-stand higher DC voltage and stronger electric field considering their minimal size, resulting in breakdown in bubbles, and therefore more concentrated but less severe PDs macroscopically.

Keywords: Oil-pressboard Insulation · DC Voltage · Cellulose Impurity · Partial Discharge

1 Introduction

Oil-pressboard insulation is a typical composite insulating material. The insulating oil has good electrical strength and thermal conductivity. The insulating pressboard has excellent insulating performance, oil absorption performance, and outstanding mechanical strength. The combination can significantly enhance the overall performance as insulations [1, 2]. However, in practical applications, due to the influence of manufacturing process, oil treatment environment, operating conditions and other factors,

oil-pressboard insulation is often mixed with impurities such as cellulose, moisture and metal particles. Their existence affects the insulating performance of oil-pressboard, and even causes discharge, resulting in power system accidents [3–5].

Based on above issues, researches at home and abroad have carried out a series of studies on impurities in oil-pressboard insulation, most of which focus on moisture and metal particle impurities [6–8]. E.g., Chen Qingguo studied the influence of moisture on the discharge characteristics of oil-paper insulation of converter transformer, and considered that the moisture in oil may dissolve low molecular organic acid, and thus has a high conductivity. Meanwhile, the moisture in pressboard increased the carrier concentration, which reduced the partial discharge initial voltage of the oil-paper insulation [9]. R. Tobazeon studied the discharge phenomenon caused by conductive particles in oil under DC voltage, and concluded that the local electric field distortion caused by conductive particles was the main cause of discharges [10]. In summary, scholars have made a variety of explanations on the discharge mechanism of oil-pressboard insulation caused by impurities, including the electric field distortion theory, and the thermal effect theory. However, the rationality and applicability of these explanations have not been verified.

In fact, the most effective way to remove impurities in oil-pressboard insulation is to filter, or to prevent impurities from being mixed into the material from the beginning. However, in addition to moisture and metal particles, self-generated impurities produced by the insulation material itself, such as cellulose impurities in oil-pressboard insulation, also exist in the insulation system in large quantities. Such impurities cannot be removed simply by filtration alone, because cellulose impurities are produced by the surface of pressboard. As long as there is an electric field and the field strength exceeds a certain value, the cellulose impurities will always appear after a period of time. Therefore, self-generated impurities, such as cellulose impurities, have a greater impact on the insulating performance of the materials than other filterable impurities.

This paper is mainly focused on partial discharge characteristics of oil-pressboard insulation under the effect of cellulose impurities. Processes including the generation and bridging of cellulose impurities within the insulation were observed first. PD characteristics including repetition rate, average discharge intensity and maximum discharge intensity were recorded based on samples with and without cellulose impurities afterwards. Leakage current measurement was then carried out to explain the mechanism of PDs' differences due to the impurities.

2 Experimental Platform and Method

The oil adopted in the experiment was KI25X transformer oil produced by Kunlun Company. Before the experiment, the oil was filtered, degassed, and dehydrated under a vacuum heating environment, so to meet the IEC296-82 standard. The pressboard used was produced by Taizhou Weidmann Company, the thickness of which was 0.5 mm. Before the experiment, the pressboard was cut into 100 mm × 100 mm square samples, and vacuum dried at 60 °C for 48 h. Afterwards, the pressboard was placed in the vacuum experimental chamber for oil immersion at the temperature of 60 °C for 24 h.

In order to study the partial discharge characteristics of oil-pressboard insulation under the effect of cellulose impurities, the experimental platform shown in Fig. 1 was

built in a shielded room. A needle-plate electrode oil-pressboard insulation model was used to produce cellulose impurities and to initiate discharges. Diameters of the needle and the plate were 1 mm and 10 mm, respectively. The thickness of the plate, and the distance of the oil gap were both 10 mm. To start the experiment, DC voltage generated by a voltage doubling circuit was applied to the model. High-frequency coupled current sensor with a minimum measuring value of 1 pC was adopted to measure the partial discharges during the voltage applying. The measured signal was transmitted to an oscilloscope for further statistical analysis on the computer.
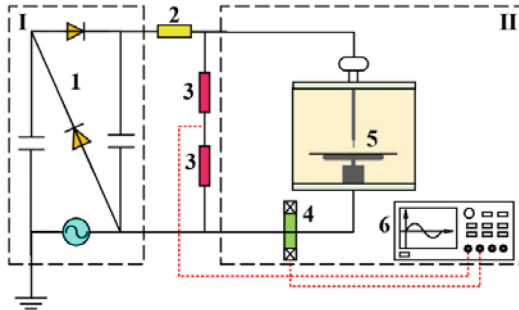
1-voltage doubling circuit; 2-protection resistor; 3-resistance voltage divider; 4-High-frequency coupled current sensor (HFCT); 5-experiment samples; 6-Oscilloscope

Fig. 1. Schematic diagram of the experimental setup

On the other hand, in order to measure the leakage current of oil-pressboard samples with and without cellulose impurities, a plate-plate electrode model was adopted. The diameter and the thickness of the plate electrode was 50 mm and 10 mm, respectively. The oil gap distance was set to 5 mm. Cellulose impurities in the model are extracted from the previous experiment and artificially added. The Keithley 6517a electrometer was selected as the high resistance meter to measure the leakage current within the model, where its measurement range can reach 1×10^{-17} A–2×10^{-2} A, with an error rate of 1%. At the same time, the built-in 1 kV DC power supply of the electrometer facilitated the measurement of insulation dielectric leakage current. The experimental data generated by Keithley was recorded in real time on the computer at a sampling rate of 1 time/min. The data transmission between the high resistance meter and the computer was realized by GPIB IEEE-488 bus.

According to IEC-61620 and IEC-60247, when DC voltage is applied to a solid insulation sample, the current within the sample will gradually decrease to a stable value due to the polarization process. In this experiment, we measured the current within oil-pressboard sample as shown in Fig. 2. The results show that the current of the model becomes stable after 10 min. Therefore, in this experiment, the current value after 10 min is read as the leakage current flowing through the sample.
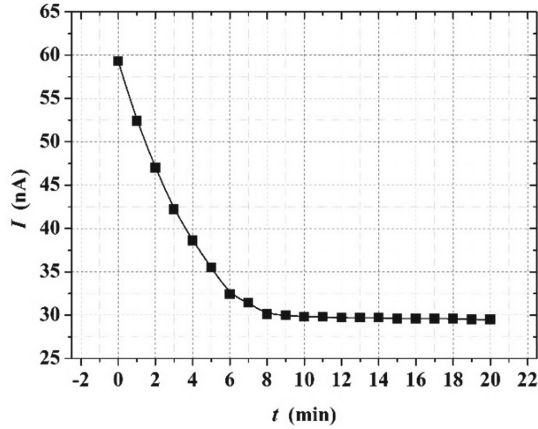
Fig. 2. Relationship between the leakage current and the voltage duration time (Electric field strength 1 kV/mm, oil gap distance 5 mm, Temperature 25 °C)

3   Experimental Results and Analysis

3.1   Generation of Cellulose Impurities and Their Effects on Partial Discharge

To generate cellulose impurities within oil-pressboard insulation, 15 kV positive DC voltage was applied to the model. When the voltage duration time reached 108 min, cellulose impurities were observed at the surface of the pressboard. With the duration time increasing to 189 min, a cellulose bridge formed in the oil gap, as shown in Fig. 3.
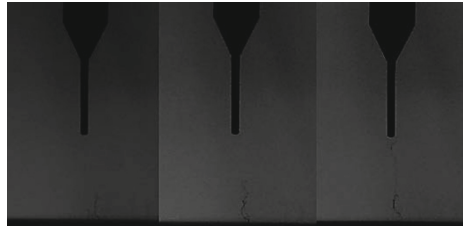
Fig. 3. The generation and bridging of cellulose impurities

After the cellulose bridge was generated, the voltage was stepped up 1 kV within 30 s, and maintained for 10 min each time. During this time, any possible partial discharges were recorded by the high-frequency coupled current sensor. The results shown that when the applied voltage reached 27 kV, partial discharge occurred. The number of partial discharges was approximately 8 in 10 min. Considering that partial discharges emerged at such a high voltage amplitude, where cellulose impurities had already generated far below this, the generation of the cellulose impurities was not caused by partial discharges.

In order to explore the condition for the generation of cellulose impurities, voltage withstand experiments were further carried out on needle-plate electrode oil-paper insulation models, under 5 kV, 10 kV, 20 kV, 25 kV and 30 kV, respectively. The duration time

under each voltage was set to 4 h. Figure 4 shows the cellulose impurity generation time at various voltages. According to the results, the higher the applied voltage amplitude (the greater the electric field strength), the shorter the generation time of cellulose impurities. Therefore, it can be inferred that the generation of cellulose impurities is related to the electric field strength on the surface of the pressboard. The greater the electric field strength on the surface of the pressboard, the faster the generation of cellulose impurities.
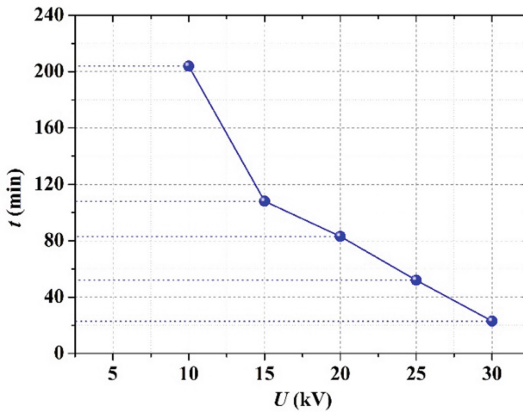
Fig. 4. The generation time of cellulose impurities under each voltage

On the other hand, according to our pre-experiment, partial discharges can always emerge at 30 kV whether there are cellulose impurities in the oil. The generation of cellulose impurities under this voltage, however, takes 23 min. Therefore, we can set up two groups of samples to investigate the influence of cellulose impurities on partial discharge characteristics. One group is artificially added with cellulose impurities, and the other group is not treated. After the sample preparation, 30 kV DC voltage was applied to two groups of the samples, and the partial discharges emerged within the 10th minute to the 20th minute were recorded. Since the cellulose impurities will not generate during this period, the difference in partial discharge characteristics between the two groups of samples was only due to the cellulose impurities. Based on the above method, results in Table 1 were derived, that when there were cellulose impurities in the oil gap, the repetition rate of partial discharge increased, while the discharge intensity decreased obviously.

3.2 Analysis of the Mechanism of Cellulose Impurities Effect on the Partial Discharges

Under AC voltage, when there are cellulose impurities with high dielectric constant in the oil gap, the electric field in the part of the oil channel in series with the impurities will be strengthened, and the discharge in the oil will be induced. If the cellulose impurities are connected to form a small bridge, the oil gap breakdown along the small bridge will

Table 1. PD characteristics of the experimental model with and without cellulose impurites

Group	Cellulose impurities	Repetition rate (Times per minute)	Average discharge intensity (pC)	Maximum discharge intensity (pC)
①	None	11	107	154
②	None	14	124	169
③	None	9	102	161
Average	None	11	111	161
①	Have	23	105	147
②	Have	29	100	132
③	Have	34	87	123
Average	Have	29	97	134

also occur. Similar to AC cases, the influencing mechanism of cellulose impurities on the discharge process under DC voltage can also be analyzed from two aspects: local electric field distortion, and leakage current local overheating.
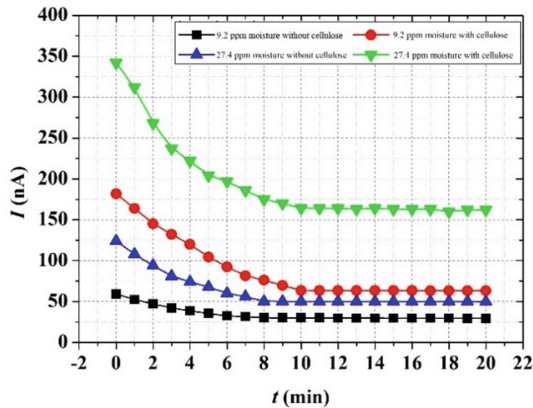
Fig. 5. Leakage current of the experimental samples under different moisture with and without cellulose impurities (Electric field strength 1 kV/mm, oil gap distance 5 mm, Temperature 25 °C)

Figure 5 shows the variation of leakage current with measurement time for the plate-plate electrode oil gap model with and without cellulose. The moisture in the oil samples are 9.2 ppm and 27.4 ppm respectively. The cellulose impurity artificially added was about 4 μg, and the measuring voltage was 1 kV. It can be seen from the results, that under low moisture, the leakage current of the sample increases from 29.8 nA to 63.5 nA when there was cellulose impurity in the oil gap. That is, the cellulose impurity has a higher conductivity than the transformer oil. From the perspective of material structure, the conductivity of the cellulose impurities should be between the transformer oil and the compact pressboard. However, because the density of the cellulose impurities is far less

than that of the pressboard, the structure of the impurities is sparse and porous, so the hydrogen bond between the cellulose molecular monomers is extremely unstable, and the association reaction between the original glucose monomers will occur reversely, as shown in formula (1). A large number of intrinsic carriers appear in the cellulose impurities. As a result, the original impurity carriers plus the newly generated intrinsic carriers increase the carrier concentration along the cellulose, thereby increasing its conductivity.

$$2R\text{-}OH \longleftrightarrow R\text{-}OH_2^+ + R\text{-}O^- \tag{1}$$
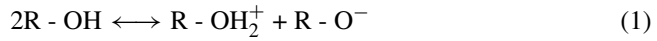
On the other hand, the porous structure of the cellulose will absorb more water from the oil. When no cellulose impurity existed, the moisture in transformer oil increased from 9.2 ppm to 27.4 ppm, the leakage current of the sample increased from 29.8 nA to 50.2 nA, with an increase of 68.46%. In the presence of cellulose impurities, the leakage current increased from 63.5 nA to 164 nA, with an increase of 158.3%, when the moisture in the transformer oil changed as above. That is to say, when there are cellulose impurities in the oil gap, the effect of water on the oil conductivity is significantly enhanced. In the extreme case of the oil with cellulose impurities and moisture of 27. 4 ppm, the leakage current of the sample was 164 nA, which was much higher than the sum of the leakage current of 27.4 ppm without cellulose and 9.2 ppm with cellulose. It proved that cellulose impurities and moisture have a positive synergistic effect on increasing the conductivity of transformer oil.
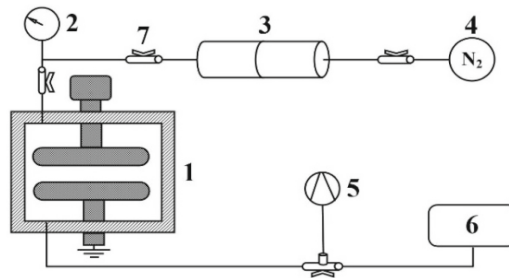
1-experimental cavity; 2-barometer; 3-cylinder; 4-N2gas cylinder; 5-vacuum pump; 6-oil tank; 7-air valve;

Fig. 6. Schematic diagram of the gas platform of the oil pressure experiments

In order to explore the influencing mechanism of cellulose impurity on the discharge process, the partial discharge characteristics of the plate-plate electrode oil-pressboard model was studied under different hydrostatic pressure and cellulose impurity mass. The platform is shown in Fig. 6. In the figure, the left side of the oil cylinder is filled with transformer oil, the right side is filled with nitrogen, and there is a piston block between the oil and gas. By adopting this structure, the oil pressure can be accurately adjusted while preventing external gas from being mixed into the oil. During the experiment, the oil pressure was set to 0.1 MPa, 0.2 MPa, 0.3 MPa and 0.4 MPa; the cellulose impurity

mass was set to 2 µg, 4 µg, 6 µg, 8 µg and 10 µg, and oil gap model with cellulose impurities was measured. Figure 7 shows the partial discharge inception voltage of the model under each condition.
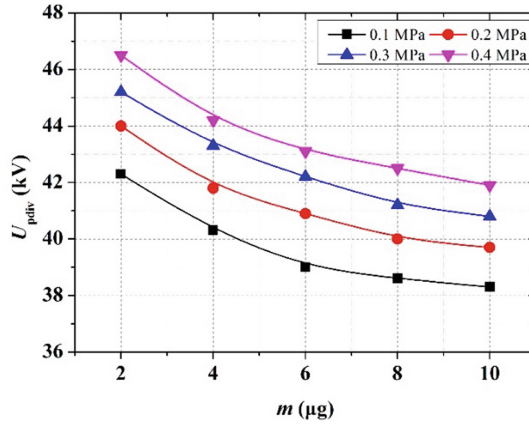
Fig. 7. Relationship of PD inception voltage and cellulose impurity mass under different oil pressure

According to Fig. 7, when the oil pressure changed within the range of 0.1 MPa to 0.4 MPa, the partial discharge inception voltage increased accordingly. It is worth noting that under the above oil pressure, when there was no cellulose impurity, the oil gap does not appear partial discharge phenomenon, and once the voltage reached a sufficient amplitude, the oil gap breaks down directly. Because the oil pressure directly affects the volume and thus inner pressure of microbubbles in the oil, and then affects the breakdown voltage of microbubbles. It can be deduced that for the sample without cellulose impurities, there are no microbubbles in the oil gap that can cause partial discharge. Under this circumstance, no matter how the oil pressure changes, partial discharge will not occur. For the sample with cellulose impurities, there are microbubbles in the oil gap, so the partial discharge occurred, and the inception voltage is different under different oil pressure. To sum up, the existence of cellulose impurities in the oil gap causes the generation of microbubbles in the oil gap.

The leakage current in the oil gap will be greatly increased under DC voltage because of the high conductivity of the cellulose impurities. The higher the applied voltage, the more obvious the increase of leakage current. A significant problem caused by this is the local overheating caused by the leakage current. As a result, the mechanism of the effect of cellulose impurities on the discharge process under DC voltage can be explained as follows: when the transformer oil contains cellulose impurities, water accumulates around the impurities. Under the heating effect of leakage current, the local gasification rate of water increases and is greater than the dissolution rate of water in oil, which produce a large number of microbubbles around the cellulose impurities. Under DC voltage, the bubbles bear a stronger electric field, while the field for breakdown of the bubbles is lower, a large number of bubbles discharge within the oil, leading to

the increasement of the discharge repetition rate. On the other hand, as the temperature increases, the breakdown voltage of the bubble decreases. Therefore, in the experimental results PD characteristics, both the average and maximum partial discharge intensity decreased.

4 Conclusion

In this paper, the generation and bridging of cellulose impurities in oil-pressboard insulation under DC voltage is observed. The influence of cellulose impurities on the partial discharge process of the insulation is studied, and explained based on local electric field distortion and leakage current local overheating theories. The conclusions are draw below:

Cellulose impurities and moisture have a positive synergistic effect on increasing the conductivity of transformer oil. The intrinsic carriers generated by the reverse association reaction of sparse cellulose molecules can also dissolve in the water film on the surface or inside of the cellulose impurities, which further increases the conductivity of the oil. Cellulose impurities increase the leakage current of the oil, leading to local overheating, which caused the gasification of water. This results in a large number of microbubbles. Under DC voltage, the gaseous bubble bears a stronger electric field and discharges before the transformer oil, which is shown macroscopically as the change of the partial discharge characteristics of the oil-pressboard insulation.

Future researches on cellulose impurity within oil-pressboard insulation may focus on its generation mechanism and dynamic basis.

References

1. Zhou, Y.X., Sha, Y.C., Nie, D.X., Wu, Z.R., Deng, J.G., Lu, L.C.: Partial discharge initiating process of transformer oil under combined AC and DC voltage. High. Volt. Eng. **38**, 1163–1171 (2012)
2. Liu, K., Wang, P., Wang, W.: Electric filed distribution in transformer oil under DC electric field. Power Syst. Tech. **39**, 1714–1718 (2015)
3. Li, Y., Zhang, Q.G., Li, J.Z., Wang, T.L., Dong, W.L., Ni, H.L.: Study on micro bridge impurities in oil-paper insulation at DC voltage: their generation, growth and interaction with partial discharge. IEEE Trans. Dielectr. Electr. Insul. **23**(4), 2213–2222 (2016)
4. Peesapati, V., Zachariades, C., Callender, G., Gao, S., Cwikowski, O., Gardner, R.: Investigation of incipient faults in 66 kV oil-filled cable sealing ends. High Volt. **7**(4), 666–675 (2022)
5. Du, Y., Zahn, M., Lesieutre, B.C., Mamishev, A.V., Lindgren, S.R.: Moisture equilibrium in transformer paper-oil systems. IEEE Elect. Insul. Mag. **15**(1), 11–20 (1999)
6. Li, Y., Zhang, Q.G., Zhao, Y., Wen, T., Liu, G.Q., Wang, K.: DC withstand test with partial discharge measurement of convertor transformers: problems and suggestions for improvement. IEEE Trans. Dielectr. Electr. Insul. **24**(2), 1105–1109 (2017)
7. Kebbabi, L., Beroual, A.: Optical and electrical characterization of creeping discharges over solid/liquid interfaces under lightning impulse voltage. IEEE Trans. Dielectr. Electr. Insul. **13**(3), 565–571 (2006)

8. Li, Y., Zhang, Q.G., Wang, T.L., Li, J.Z., Guo, C., Ni, H.L.: Degradation characteristics of oil-immersed pressboard samples induced by partial discharges under DC voltage. IEEE Trans. Dielectr. Electr. Insul. **24**(2), 1110–1117 (2017)
9. Chen, Q.G., Wang, J.L., Lin, L., Chi, M.H., Wei, X.L.: Influence of operation conditions on flow electrification characteristics of oil-paper insulation in converter transformer. High Volt. Eng. **44**(12), 3880–3887 (2018)
10. Tobazeon, R., Filippini, J.C., Marteau, C.: On the measurement of the conductivity of highly insulating liquids. IEEE Trans. Dielectr. Electr. Insul. **1**(6), 1000–1004 (1994)

Study on Influence of Pollution Factors on Corona Initiation Voltage of Overhead Transmission Line Conductor

Xuyang Yang[1], Hongwei Mei[2] , and Xiaobo Meng[1](✉)

[1] Guangzhou University, Guangzhou 51006, China
mengxb@gzhu.edu.cn

[2] Tsinghua University Shenzhen International Graduate School, Shenzhen 518055, China

Abstract. The corona discharge phenomenon of transmission lines is a problem that needs to be paid attention to and solved during line design and operation. Since long-distance transmission lines are affected by dust, sand, and other environmental contamination, it is of great academic significance and engineering value to study the effect of contamination on the corona voltage of transmission lines under negative voltage. The electric field strength of the surface of the fouled conductor under a high-voltage electrostatic field is calculated by simulating the charge method, and then the corona voltage calculation model is designed by combining the photoionization model and gas discharge theory. The model is used to systematically analyze the influence of the form, size, and relative dielectric constant of the fouling on the corona initiation voltage of transmission lines under negative voltage. It is shown that the presence of fouling distorts the electric field on the transmission line surface, which increases the electric field strength and reduces the corona voltage. At the same time, the reduction of the radius of curvature of dirt particles will also significantly reduce the corona voltage. An increase in the relative permittivity of the dirt will also significantly reduce the corona voltage of the attached transmission line, but the effect on the corona voltage decreases when the relative permittivity of the dirt is greater than 8.

Keywords: Conductors · Corona Discharge · Dirt · Dielectric Constant

1 Introduction

China has a wide geographical range, uneven distribution of power resources, and large demand for electricity in some areas, so long-distance DC transmission is an important part of the national power system. With the continuous development of the country, the demand for electricity and voltage level is increasing, and the corona discharge phenomenon of the line is becoming more and more serious. Based on the topographic characteristics of China's low east and high west, long-distance DC transmission will face great changes in environmental factors. And China plans to build several ultra-high voltage DC transmission lines that need to cross high-altitude areas. The existence of dust, sand, and other harsh environments in some areas will make the surface of DC

transmission lines adhere to dirt particles. And for AC transmission lines, DC transmission lines are more likely to produce attached dirt [1]. The attached dirt will make the corona voltage of the wire reduced, and the relative dielectric constant of different materials of dirt is also different. At the same time, the corona voltage is also affected by different shapes and sizes of dirt particles, so the study of the corona characteristics of DC transmission lines affected by the law of dirt has strong theoretical and practical significance.

The current research on the calculation of corona voltage is roughly divided into three methods: the formula empirical method, theoretical simulation method and experimental method. Peek, a foreign scholar summarized the empirical formula for the relationship between the corona voltage and air density. Later, Whitehead, Stochmeyer, Lowke, and others introduced similar formulas one after another, but their studies did not consider that electrons would be attached to air molecules to form negative ions, which would produce relative errors. Although new simulation models have been proposed by many scholars on this basis, the accuracy of the calculation results is insufficient because the parameters of these models are mostly empirical and too idealized [2]. Therefore, this paper adopts the theoretical simulation method in the study, using Matlab software for simulation, and uses the corresponding physical model for simulation. At the same time, for the different relative permittivity of the fouling simulation calculation, in consideration of the AC field simulation can not be achieved, the use of a high-voltage electrostatic field for the replacement, and then studying the fouling on the negative DC wire surface corona voltage effect law.

2 Calculation Model of Corona Onset Voltage with Dirty Negative DC Conductor

2.1 Calculation Model of Negative DC Corona Onset Voltage

The essence of corona generation is a self-sustaining discharge phenomenon formed by the uneven electric field near the uneven conductor, which is a form of gas discharge [3]. In the vicinity of the electric field with uneven distribution of field strength, when the voltage on the curvature of the electrode rises to a certain value, the free electrons in the air are subjected to the action of the electric field force to collide with the gas molecules to ionize the gas molecules, and then the initial electron avalanche is formed. In the process of the initial electron avalanche, the air molecules are ionized, and the ionized molecules continue to collide with photons to form a secondary electron avalanche, and the electron avalanche develops continuously and eventually produces a corona. At this point, the voltage at the time of corona generation is defined as the corona starting voltage.

The corona onset voltage is influenced by many internal and external factors. Among them, whether a free electron can be generated on the cathode surface to trigger the formation of a secondary electron avalanche when the initial electron avalanche occurs is the key to the self-sustainability of the pulse discharge [4]. While the mechanism of secondary electron emission from the cathode surface is still in disagreement among different researchers, here we consider a combination of two mechanisms: surface photoelectron emission and positive ion collision emission [5–9]. These two mechanisms

are collectively referred to as the photoionization model. The corona voltage is calculated based on the photoionization model and the gas discharge theory, which is a more mature and widely accepted method.

A plane right-angle coordinate system is used, and the origin of the coordinates is set at the point of the wire nearest to the earth, with the p-coordinate direction vertically downward and the q-coordinate direction parallels to the earth. Assume that there exists a free electron on the cathode surface, which will develop downward to form an initial electron avalanche. When the initial electron collapse develops to p, the number of electrons $N_e(p)$ contained in the electron collapse is

$$N_e(p) = \exp(\int_0^p (\alpha(p') - \eta(p'))dp')$$ (1)

where $\alpha(p')$ is the ionization coefficient and $\eta(p')$ is the attachment coefficient. The electrons generated at coordinate p cause collisional ionization at Δp distance, and the number of photons generated while collisional ionization is

$$\Delta n_{ph}(p) = \alpha^*(p)N_e(p)\Delta p$$ (2)

where $\alpha^*(p)$ is the photon production rate, proportional to the ionization coefficient, with a scale factor of k.

Because some of the photons formed from the initial electron avalanche will be directed towards the cathode surface, and while emitting towards the cathode surface, the photons will be irradiated evenly in different directions, and at the same time, some of the photons will be attracted by the surrounding air molecules during the process of irradiation towards the cathode surface, which affects the number of photons reaching the cathode surface, so the number of photons reaching the cathode surface is

$$\Delta n_{ph}^s = k\alpha(p)N_e(p)\Delta p g(p)e^{-\mu p}$$ (3)

where $g(p)e^{-\mu p}$ is the ratio of photons reaching the cathode surface to the total number of photons generated at p. It is a function of the distance p from the electrode structure $g(p)$ to the cathode surface and the air photon absorption coefficient μ. The formula for $g(p)$ can be found in the literature [10].

When the effective ionization coefficient $\alpha(p) - \eta(p) < 0$, the number of electrons in the electron avalanche stops increasing and gradually attaches to the molecules thus forming negative ions. The number of photons produced is very small and the vast majority is absorbed by the air molecules and can be neglected.

The ionization region has a radius of p_i. Photons reaching the cathode surface produce at least one photoelectron at the surface, a new secondary electron avalanche can be formed, and the negative DC corona can be self-sustaining. As in Eq. (4).

$$N_{eph} = \gamma_{ph} \int_0^{p_i} \alpha(p)g(p)\exp(-\mu p + \int_0^p (\alpha(p') - \eta(p'))dp')dp \geq 1$$ (4)

N_{eph} is the number of photoelectrons on the cathode surface, γ_{ph} is the surface photoelectron emission coefficient, and the scaling factor k is included in γ_{ph} because it is considered a constant.

To calculate the negative DC wire corona onset voltage U, the voltage is continuously increased in steps of ΔU, and the spatial electric field distribution is calculated using the simulated charge method to calculate the ionization coefficient, attachment coefficient, electrode structure, and the number of photoelectrons on the cathode surface for different electric field strengths in space. The voltage corresponding to Eq. (4) when the equal sign holds is the negative DC corona onset voltage U. The formulas and values of the parameters used in the calculation can be found in the reference [11].

2.2 Modeling of the Voltage Solution at the Corona Point of the Attached Fouling Conductor

Before calculating the onset voltage of the corona of the wire, the spatial electrostatic field distribution of the wire is required. Here, the simulated charge method is used for the calculation [12]. Compared with the finite difference method, the simulated charge method can avoid the numerical differentiation of the potential and directly calculate the field strength at any point in the field, and is not limited by the size of the area [11, 13–15].

The shape of the attached dirty wire is simulated by setting a number of linear charges of infinite length in an infinitely large region. The electrostatic field in the space of the attached wire is then calculated by superposition. In order to facilitate the analysis of the complex situation of the attached dirt in the actual environment, this paper classifies the dirt into three shapes, as shown in Fig. 1, which are conical, spherical, and hemispherical.
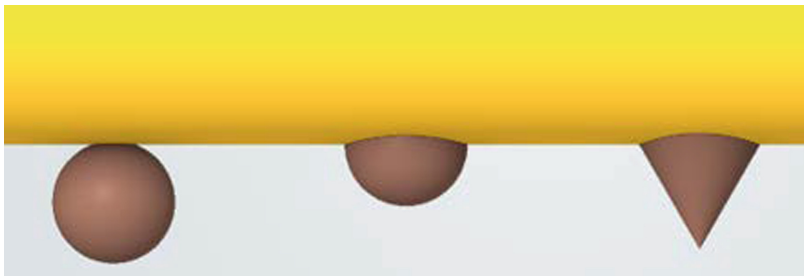
Fig. 1. Sketch map of dirt shape.

Accordingly, the design of the corresponding electric field of the corona of the attached wire corona voltage calculation process is shown in Fig. 2, considering the high-voltage transmission line for the ideal state, is a smooth surface cylindrical shape. The radius of the wire is r, and the height of the wire to the ground is h.

Simulate the charge distribution in the interface section of the attached wire, set the corresponding matching points on the surface of the wire, set the radius of the wire r as 0.005 m, and the height of the wire to the ground h as 0.4 m. Set a distance of 0.1 m, in the vertical direction of the wire and the ground down to 10,000 calculation points.
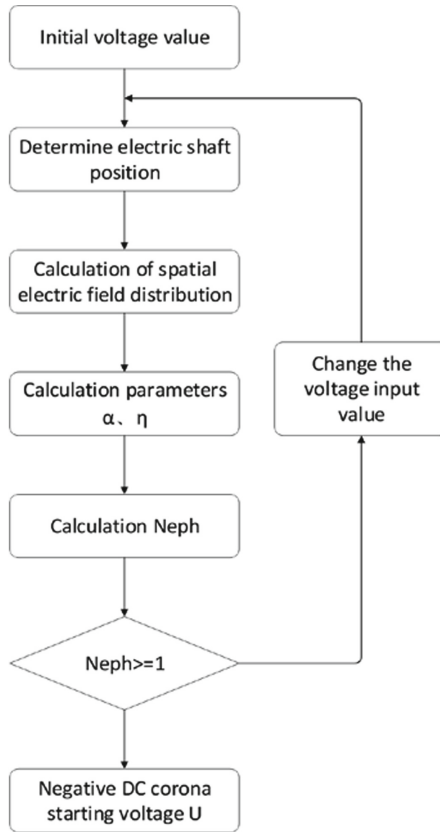
Fig. 2. Calculation process of corona onset voltage of attached dirty conductor.

3   Calculation Results

3.1   Data Comparison

The calculated results of the starting corona voltage when spherical dirt is attached to the smooth conductor are compared with the experimental data done by Zhou at North China Electric University [16]. The radius of the smooth wire is 20.5 mm, and the radius of the dirty particles is 150, 250, and 550 μm. It can be seen from Table 1 that as the dirty particles grow, the degree of reduction of the corona voltage of the wire in the experiments done by Zhou and the calculated results are basically the same.

It shows that the designed simulation experiment can reflect the effect law of dirt on the corona onset voltage of the wire.

3.2   Effect of Conical Dirty Particles on Corona Voltage

The physical characteristics of cone contamination are analyzed, and the factors affecting cone contamination include bottom radius, height, and relative dielectric constant. Based

Table 1. Degree of influence of the growth of the radius of dirty particles on the starting voltage of the corona.

Dirty particles increase radius (μm)	100	300
Dirty particle radius increase ratio	66.67%	120%
Experimental corona voltage reduction ratio	8.85%	6.95%
Simulation of corona voltage reduction ratio	10.26%	8.52%

on this, experiments were designed to calculate the corona onset voltage of the attached cone-contaminated conductor.

The radius length of the bottom of the cone-contaminated conductor was set to 300, 400, and 500 μm respectively. Its height was varied and the corresponding corona onset voltage was calculated. The simulation results are shown in Fig. 3. As the height of the cone increases, the corona onset voltage of the conductor with different bottom radius cone contamination increases.
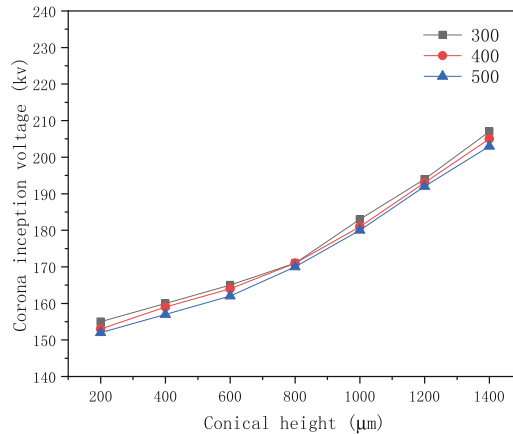
Fig. 3. Variation of corona inception voltage of conical dirt with height.

The height of the cone contamination is set to 400, 500, and 600 μm, the bottom radius is varied and the corresponding corona onset voltage is calculated. The simulation results are shown in Fig. 3. Unlike varying the height, the corona onset voltage of the conductor decreases and then increases as the radius of the bottom of the cone increases, but all are much lower than the corona onset voltage of the smooth conductor (Fig. 4).

Finally, varying the relative permittivity of the cone contamination, the simulation results are shown in Fig. 5. With the increase of relative permittivity, the corona initiation voltage of the conductor gradually decreases.
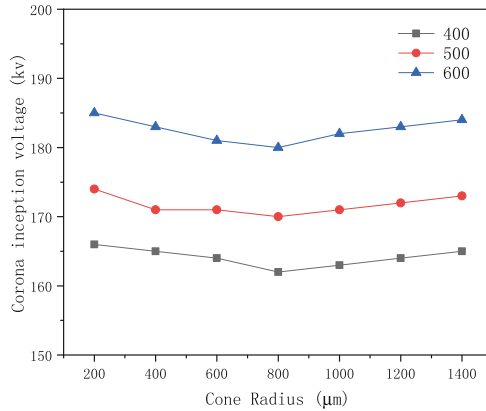
Fig. 4. Variation of corona inception voltage of conical dirt with radius.
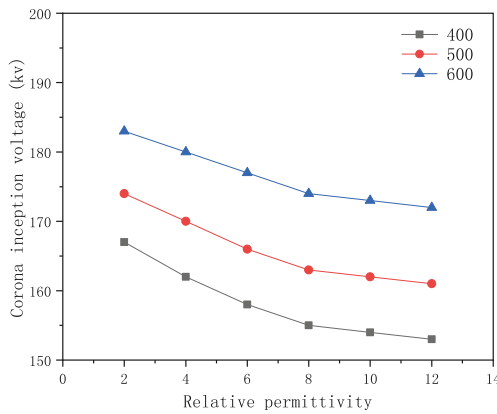
Fig. 5. Variation of corona initiation voltage of conical dirt with relative dielectric constant.

3.3   Effect of Spherical Dirty Particles on the Starting Corona Voltage

The physical properties of the spherical contamination are analyzed, respectively, the radius of the spherical contamination and the relative permittivity. Accordingly, experiments were designed to calculate the corona onset voltage of additional spherical contaminated conductors.

The relative permittivity of the spherical contamination was set to 4, 6, and 8. The radius was varied and the corresponding corona onset voltage was calculated. The simulation results are shown in Fig. 6. As the radius of the spherical contamination increases, the corona onset voltage of the conductor decreases continuously.

The radii of the spherical contamination were set to 1000, 800, and 600 μm. The relative permittivity is changed and the corresponding corona onset voltage is calculated. The simulation results are shown in Fig. 7. As the relative permittivity increases, the corona onset voltage of the conductor gradually decreases.
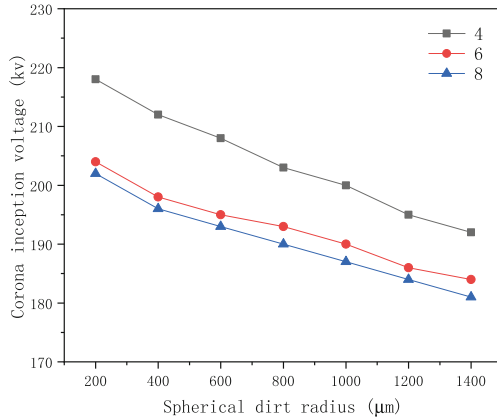
Fig. 6. Variation of corona inception voltage of spherical dirt with radius.
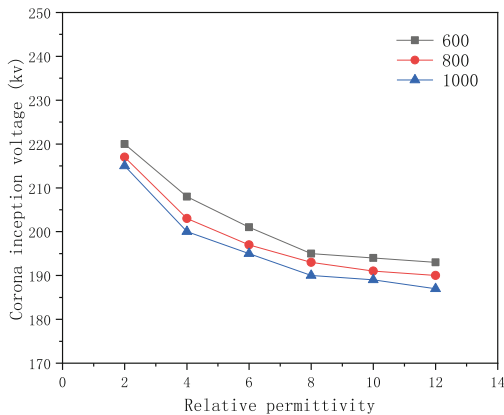
Fig. 7. Variation of corona initiation voltage of hemispherical dirt with relative dielectric constant.

3.4 Effect of Hemispherical Dirty Particles on Corona Voltage

Analysis of the physical properties of hemispherical contamination shows that its properties are similar to those of spherical contamination. It is also influenced by the radius and its relative permittivity.

Accordingly, experiments were designed to calculate the corona onset voltage of the attached hemispherical contaminated conductor by varying its radius to calculate the corresponding corona onset voltage. The simulation results are shown in Fig. 8. As the radius of hemispherical contamination increases, the corona onset voltage of the conductor continues to decrease.

Likewise, the corona onset voltage of the conductor gradually decreases as the relative permittivity of the hemisphere increases. The results are shown in Fig. 9.
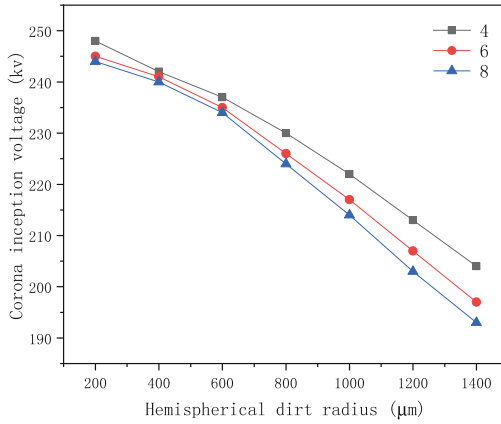
Fig. 8. Variation of corona inception voltage of spherical dirt with radius.
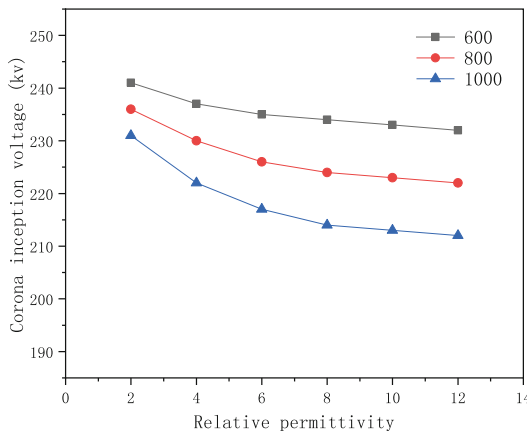
Fig. 9. Variation of corona initiation voltage of hemispherical dirt with relative dielectric constant.

4 The Relationship Between the Attached Fouling and the Corona Starting Voltage of the Wire

4.1 The Effect of Dirt on the Electric Field Strength of the Wire Surface

When three kinds of dirt are attached to the wire, the presence of dirt will make the wire surface electric field intensity increase significantly. The calculated results are shown in Table 2. Compared with the surface electric field strength of the smooth wire, it can be seen that the presence of dirt will make the wire surface electric field distortion, which will affect the corona onset voltage of the wire.

Among them, the impact caused by conical dirt is the most obvious, so the presence of conical dirt caused by the corona onset voltage reduction is also the most dramatic.

Table 2. The electric field strength on the surface of the wire in different cases.

Wire attachment dirt condition	Maximum electric field strength on the surface of the conductor (kV · cm^{-1})
Smooth wire	11826.84
Hemispherical dirt	15041.75
Spherical dirt	19478.99
Conical dirt	35373.07

4.2 Effect of Relative Dielectric Constant of Dirt on Corona Voltage

By comparing the three shapes of soiling in Fig. 10, it is easy to see the effect of changing their relative permittivity on the corona starting voltage. Regardless of which type of soiling, the larger the relative permittivity, the larger the relative permittivity, which makes the corona starting voltage of the attached soiled wire appear to drop significantly. When the relative permittivity is in the range of 2 to 8, the decline is faster. When the relative permittivity is greater than 8, the decrease of corona voltage caused by the increase of relative permittivity slows down significantly.
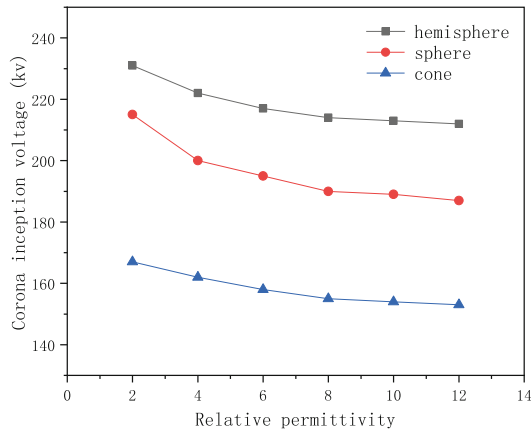
Fig. 10. The corona inception voltage of three shapes of dirt varies with the relative dielectric constant.

5   Conclusion

(a) The presence of contamination distorts the electric field on the surface of the conductor, increasing the electric field strength and thus reducing the corona onset voltage of the conductor.
(b) By comparing the degree of reduction in the corona onset voltage caused by the three types of contamination, it is known that the smaller the radius of curvature of the contamination, the more likely the conductor is to corona.
(c) The relative permittivity of the contamination has a significant effect on the corona starting voltage. As the relative dielectric constant of contamination increases, the corona voltage of the wire will gradually decrease, when the dielectric constant increases from 2 to 8, the corona voltage decreases more obviously. When the dielectric constant is greater than 8, its increase on the corona onset voltage effect gradually weakened.

References

1. Sun, C., Sima, W., Shu, L.: Atmospheric Environment and Electrical External Insulation. China Power Press, Beijing (2002)
2. Liu, Y., Zeng, W.-F., You, S.-H., Lü, F.-C.: Analsysis of corona onest voltage of AC split conductors using small corona cage. High Volt. Eng. **37**(9), 2302–2307 (2011)
3. Meng, X., Bian, X., Zhao, X.-S., Cao, J.: Iufluence of environmental factors on positive DC corona inception voltage of overhead transmission lines. High Volt. Eng. **36**(8), 1916–1922 (2010)
4. Meng, X., Bian, X., Chen, F.: Analysis on negative DC corona inception voltage of stranded conductors. High Volt. Eng. **37**(1), 77-84 (2011)
5. El-Bahy, M.M., El-Ata, M.A.A.: Onset voltage of negative corona on dielectric in air. J. Phys. D: Appl. Phys. **38**(18), 3403–3411 (2005)
6. Gupta, D.K., Mahajan, S., John, P.I.: Theory of step on leading edge of negative corona current pulse. J. Phys. D: Appl. Phys. **33**(66), 681–691 (2000)
7. Napartovich, A.P., Akishev, Y.S., Deryugin, A.A., Kochetov, I.V., Pan'kin, M.V., Trushkin, N.I.: Numerical simulation of Trichel-pulse formation in a negative corona. J. Phys. D: Appl. Phys. **30**(19), 2726–2736 (1997)
8. Paillol, J., Espel, P., Reess, T., Gibert, A., Domens, P.: Negative corona in air at atmospheric pressure due to a voltage impulse. J. Appl. Phys. **91**(9), 5614–5621 (2002)
9. Bessières, D., Paillol, J., Soulem, N.: Negative corona triggering in air. J. Appl. Phys. **95**(8), 3943–3951 (2004)
10. Abdel-Salam M.: Calculation of corona onset voltage for duct type precipitators. IEEE Trans. Ind. Appl. **29**(2), L149–L154 (1976)
11. Bian, X., Hui, J., Huang, K.: Research on negative DC corona characteristics related to air pressure and humidity. Proc. CSEE **30**(4), 118–124 (2010)
12. Ma, X., Gu, W.: Charge simulation method analysis of static field based on MATLAB language. Insul. Surge Arresters (3), 41–46 (2005)

13. Bian, X., Hui, J., Huang, K.: Variation of the characteristics of negative DC corona streamer pulse with air pressure and humidity. Proc. CSEE **30**(10), 134–142 (2010)
14. Hui, J., Guan, Z., Wang, L.: Research on variation of positive DC corona characteristics with air pressure and humidity. Proc. CSEE **27**(33), 53–58 (2007)
15. Fan, J., LI, Z., Shen, G.: Calculation method for DC onset corona voltage. Trans. China Electrotech. Soc. **23**(10), 100–105 (2008)
16. Zhou, G.: Research on the Influence of the Surface Contamination of the Power Transmission Lines. North China Electric Power University, Beijing (2013)

Electric Field Distortion and Corona Inception Characteristics on the Surface of Insulating Material Under High Humidity and High Pollution Conditions

Zhaoxuan Zhan, Shengwen Shu[✉], Junwei Xu, and Wenhua Huang

College of Electrical Engineering and Automation, Fuzhou University, Fuzhou, China
shushengwen@fzu.edu.cn

Abstract. Surface discharge of insulating materials is the main form of insulation failure of electrical equipment under special operating environment such as high humidity, high pollution and easy condensation. Therefore, it is of great significance to study the discharge initiation characteristics of wet insulated material surface to improve the operation reliability of electrical equipment. In this paper, the discharge initiation characteristics of insulating materials under the action of condensation and pollution were studied. Firstly, COMSOL software was used to construct a single droplet model under the action of a flat electrode, and FEM was used to calculate the electric field distribution on and around the surface. Secondly, a method for predicting the initial voltage of surface discharge of wet insulation materials based on photoionization criterion is proposed. Finally, the corona test was carried out on the surface of the wet epoxy resin plate, and the corresponding corona voltage was calculated by the leakage current method. The results show that the error between the experimental value and the simulation value is small, which verifies the validity of the method for predicting the negative polarity DC corona initial voltage.

Keywords: Condensation · Contaminant · Electric field calculation · Photoionization model · Negative DC corona

1 Introduction

With the proposal of the strategic goal of "double carbon", the electric power system in our country will transform to new energy distributed access, multi-state energy interconnection and multi-voltage level AC-DC interconnection [1]. Vigorously developing offshore wind power is an optimal option for achieving carbon peak and carbon neutralization in southeast coastal area of our country [2]. However, the southeast coast of our country is a typical hot and humid climate. The special operating environment of high humidity, high salt fog and high pollution makes the condensation and pollution flash of switch equipment prominent. Condensation will gradually reduce the insulation performance of the insulation parts, and the insulation defects will be constantly

exposed, which will gradually develop from initial discharge to surface flashover and even insulation breakdown, and eventually lead to serious accidents, which brings great challenges to the reliability of the operation of electrical equipment. Therefore, it is of great significance to study the surface discharge of internal insulating parts of switchgear under wet and dirty conditions to accelerate the transformation and upgrading of power system under the background of "carbon peaking and carbon neutrality" strategy.

Surface discharge of wet insulation materials is a complex process involving multistage coupling effects of condensation phase transition [3, 4] and local arc development [5–7], which belongs to the intersection field of engineering thermal physics and discharge plasma. The condensation phase transition involves gas-liquid-solid multiphase flow, and the discharge process is a complex physical process with the synergistic effect of electricity, heat, light and so on. In recent years, many scholars at home and abroad have carried out some exploratory studies on the evolution of condensation and the preparation of anti-condensation materials, but there is still a lack of research on surface discharge under the combined action of condensation and pollution on the surface of insulating materials. Therefore, this paper will study the initial characteristics of surface discharge of wet insulation materials. The main research contents are as follows: First, COMSOL simulation software is used to calculate the electric field distribution when condensate droplets are distributed on the surface of contaminated epoxy resin plate, and the influence of different droplet radius, droplet contact Angle, droplet spacing and plate spacing on the electric field distortion is analyzed. Secondly, based on the existing photoionization model, a negative DC corona voltage prediction model considering temperature and humidity was proposed to predict the corona voltage on the surface of wet insulation materials. In addition, the influences of the effective ionization coefficient and the light absorption coefficient on the corona voltage in the process of discharging electricity in different ambient temperature and humidity are analyzed. Finally, the corona test was carried out on the surface of the wet epoxy resin plate, and the corresponding corona voltage was calculated by the leakage current method. The results show that the error between the experimental value and the simulation value is small, which verifies the validity of the prediction method of negative polarity DC corona initial voltage. The study in this paper will initially reveal the influence mechanism of condensation and pollution on the surface electric field of insulating materials, improve the accuracy of the initial discharge voltage prediction, help to improve the surface discharge mechanism of insulating materials under wet and dirty conditions, and provide the corresponding theoretical reference for the improvement of the reliability of new energy power system and the modification and enhancement of the structure of insulating materials.

2 Single Droplet Electric Field Simulation

2.1 Electric Field Simulation Model Construction

In order to explore the influence of condensation droplets on the surface electric field distribution of contaminated insulating materials, this paper uses COMSOL finite element software to construct a single droplet electric field calculation model on the surface of contaminated epoxy resin plate. The effects of plate spacing d, droplet radius r, water contact angle θ and droplet spacing h on the distribution of surface electric field around

the droplet were investigated by using this model. The simulation model is shown in Fig. 1. A pair of cylindrical stainless steel flat electrodes with a diameter of 50 mm and a length of 40 mm are placed on an epoxy resin plate with a size of 150 mm × 150 mm × 3 mm. In order to simulate the contamination on the surface of the insulation parts under actual conditions, a pollution layer of 150 mm × 150 mm × 0.5 mm is attached to the surface of the epoxy resin plate. A drop of water with a radius of 2 mm and a contact angle of 90° is placed in the center of the board. The air domain size is 200 mm × 200 mm × 200 mm.
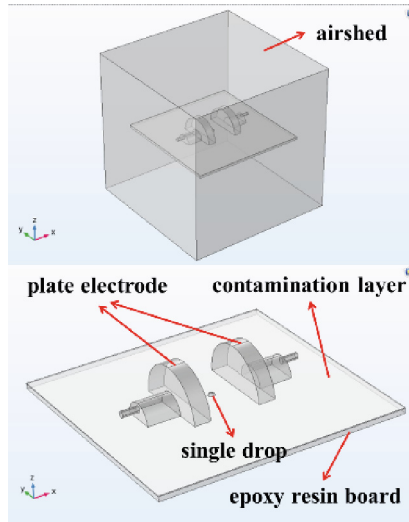
Fig. 1. Simulation model of single droplet electric field on the surface of stained epoxy resin plate.

2.2 Analysis of Electric Field Simulation Results

The simulation results show that the electric field distortion at the junction of "gas-liquid-solid" three-phase is the largest due to the great difference between the relative dielectric constant values of air ($\varepsilon = 1$), water ($\varepsilon = 78.5$) and dirty layer ($\varepsilon = 10$), as shown in Fig. 2. When the applied electric field is low, the air near the surface of the droplets and the dirty layer is prone to corona discharge. In this paper, the distribution of electric field around water drops under -1 kV DC high voltage was studied by the distance between electrode plates, the radius of droplets, the contact Angle of droplets and the distance between droplets, and the influence of the above factors on the corona discharge of wet epoxy resin surface under DC high voltage was analyzed.

Change Plate Spacing. In order to study the effect of applied electric field intensity on the distribution of electric field around water drops, the single droplet electric field distribution on the surface of stained epoxy resin plate was simulated and analyzed
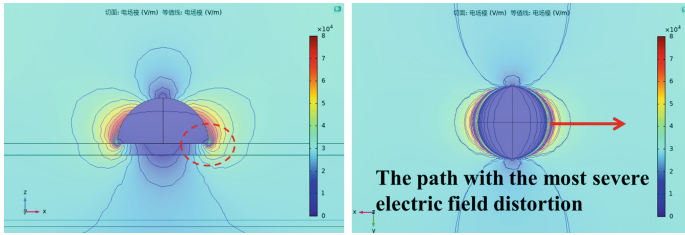
Fig. 2. Simulation of single droplet electric field.

when the plate spacing d was 20 mm, 25 mm, 30 mm, 35 mm, 40 mm and 45 mm, respectively. The electric field simulation results are shown in Fig. 3(a). The results show that the degree of electric field distortion at the three-phase junction decreases with the increase of plate spacing. Since the inter-polar voltage is always fixed at -1 kV, and the equivalent electric field between the plates decreases with the increasing of the distance between the plates, the degree of electric field distortion caused by water drops will also decrease. The electric field simulation results calculated along the selected path are shown in Fig. 3(b). The electric field intensity near the "gas-liquid-solid" three-phase junction on the surface of the water bead presents a "cliff" rise, and with the increase of the distance between the plates, the electric field distribution curve along this path continues to move down. It can be seen that the electric field intensity at the edge of the water bead decreases as a whole with the increase of the distance between the plates. It can be clearly seen from Fig. 3(c). that the maximum electric field mode value at the edge of water drops also increases with the decrease of plate spacing.

(a) Electric field distribution at different plate clearances (c) Maximum electric field distribution under different plate clearances
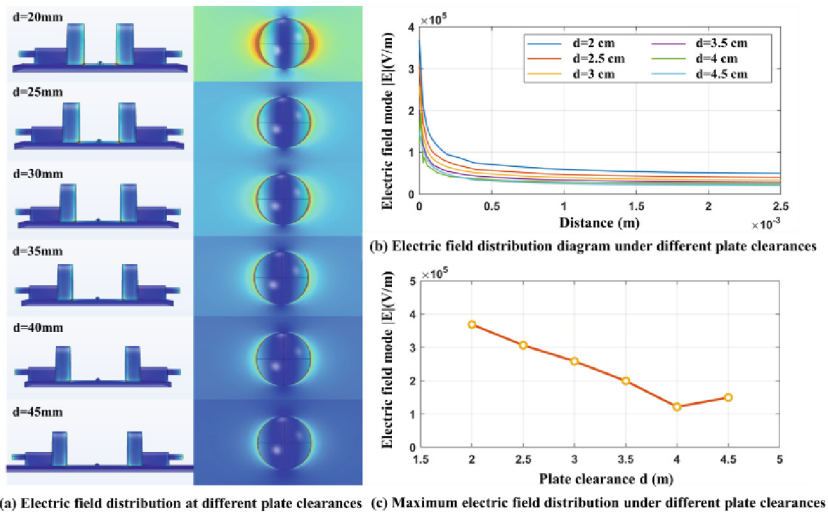
Fig. 3. Simulation results of surface electric field under different plate spacing.

Changing the Radius of the Drop. In order to study the influence rule of droplet radius on the electric field distribution around water drops, the single droplet electric field distribution on the surface of the stained epoxy resin plate was simulated and analyzed when the droplet radius r was 1.0 mm, 1.5 mm, 2.0 mm, 3.5 mm, 4.5 mm and 5.0 mm, respectively, and the static contact Angle of the droplet was 90°. The electric field simulation results are shown in Fig. 4(a). The results show that the radius of the water bead has only a slight influence on the electric field distribution around the water bead. With the increase of the radius of the water bead, the maximum value of the electric field along the surface of the stained epoxy resin plate only increases slightly. The electric field simulation results are shown in Fig. 4. The area where the electric field intensity increases significantly expands with the increase of the droplet radius. With the increase of the droplet radius, the surface electric field distribution between the droplet and the two plates becomes more uniform and the electric field modulus increases. The electric field simulation results calculated along the selected path are shown in Fig. 4(b). The electric field near the edge of the droplet on both sides of the electrode increases sharply, while the electric field inside the droplet is very small and lower than the average electric field intensity outside the droplet. Combined with Fig. 4(b) and Fig. 4(c), it can be seen that the change of drop radius has no obvious influence on the surface electric field distribution of the contaminated epoxy resin.

(a) Electric field distribution at different drops radius

(b) Electric field distribution diagram under different drops radius

(c) Maximum electric field distribution under different drops radius
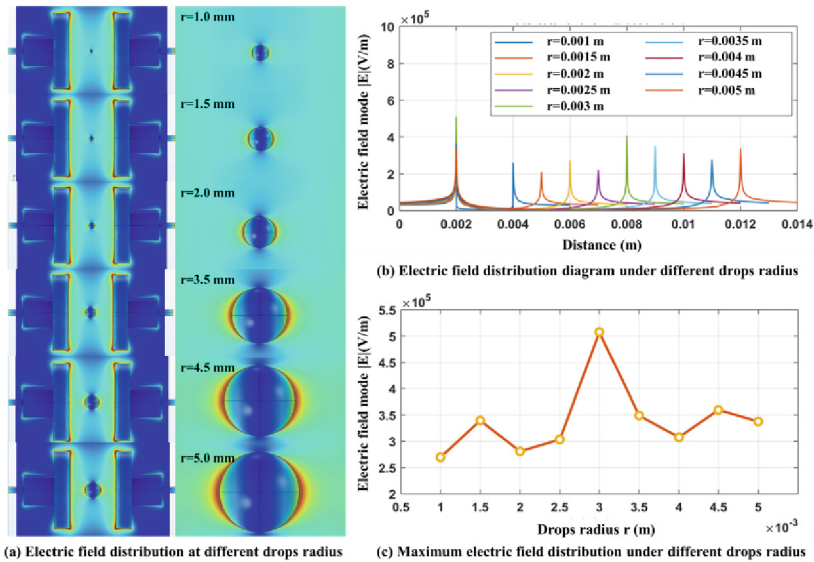
Fig. 4. Simulation results of surface electric field under different droplet radius.

Change the Droplet Contact Angle. In order to study the influence of droplet contact angle on the electric field distribution around water drops, the electric field distribution of single droplet on the surface of epoxy resin plate was simulated when the droplet

contact angle was 30°, 60°, 90°, 120° and 150°, and the volume of droplet was 16.8 μL. The simulation results show that the distortion degree of electric field decreases with the increase of droplet contact angle. The electric field simulation results are shown in Fig. 5(a). The electric field distortion degree at the three-phase junction of droplet edge on the surface of insulating materials with different wettability is significantly different, and the electric field distortion degree decreases with the increase of droplet contact Angle. The electric field simulation results calculated along the selected path are shown in Fig. 5(b) and Fig. 5(c). There is little difference in the internal electric field intensity of droplets with different wettability surfaces, which are all lower than the surface field intensity outside the water droplets, and the modulus is about 1×10^5 V/m. The external field intensity of water droplets on different wettability surfaces also tends to 3×10^5 V/m, and there is no significant difference. However, the maximum field intensity of water bead edge on different surfaces decreased gradually with the increase of contact Angle.
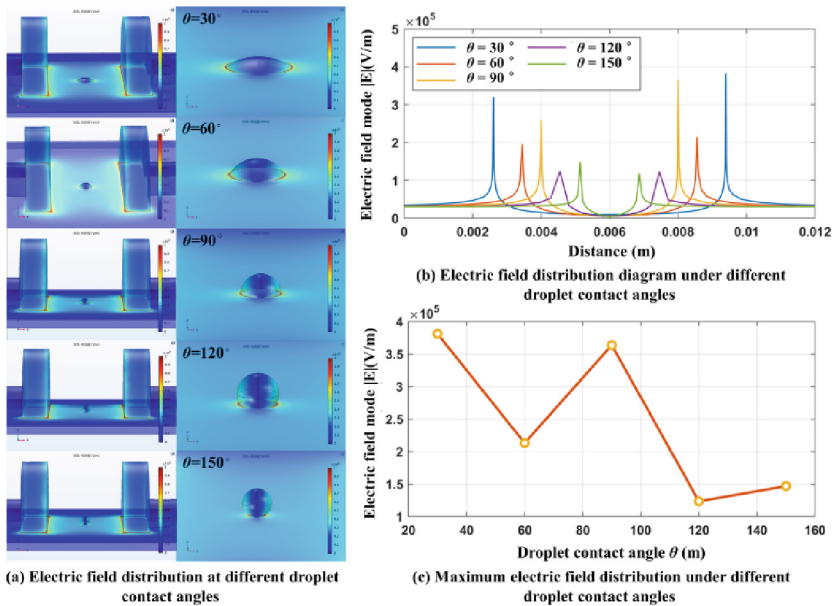
Fig. 5. Simulation results of surface electric field under different droplet contact angles.

Change the Distance Between the Two Drops. In order to study the influence law of droplet spacing on the electric field distribution around water drops, the electric field distribution of single droplet on the surface of the stained epoxy resin plate was simulated when droplet spacing h was 2 mm, 4 mm and 6 mm respectively. The droplet radius was all 2 mm and the contact Angle was all 90°. The simulation results show that with the increase of droplet spacing, the average value of the electric field intensity in the surface region between two droplet drops gradually, and the degree of distortion

decreases significantly. The electric field simulation results are shown in Fig. 6(a). With the widening of the droplet spacing, the field distortion areas along the surface of the two droplets are basically separated from each other, and a low electric field area similar to that on the surface of the droplet appears in the middle. The electric field simulation results calculated along the selected path are shown in Fig. 6(b), and the maximum electric field intensity values under different paths are given in Table 1. According to the analysis of Fig. 6(b) and Table 1, when the droplet spacing is small, the electric field distortion is the most serious and occurs at the inner edge of the droplet near the high voltage electrode. With the increasing of the droplet spacing, the degree of electric field distortion between the droplet decreases.

(a) Electric field distribution at different distances between the two drops

(b) Electric field distribution diagram under different distances between the two drops
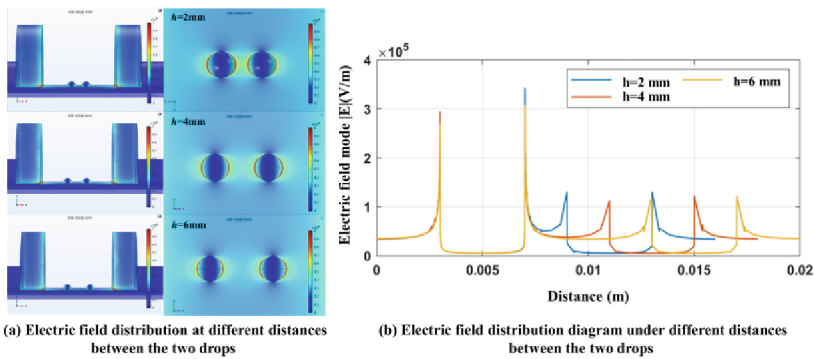
Fig. 6. Simulation results of surface electric field under different distance of two droplets.

Table 1. Maximum electric field intensity along surface path at different distance of two droplets.

The distance between two droplets (mm)	Maximum electric field intensity (V/m)
2	342475.5948
4	303950.8153
6	307554.7245

3   Prediction Model of Initial Discharge Voltage

3.1   Construction of Negative Polarity Photoionization Model Considering Temperature and Humidity

In order to explore the influence of different ambient temperature and humidity on the surface discharge initiation process of wet insulation material, a model of discharge initiation voltage was established considering temperature and humidity. When negative discharge occurs, there are usually three reasons for the emission of electrons from the

negative plate: photoelectric effect, positive ion collision on the cathode surface, and field ionization. Although the intensity of positive ion collision ionization is greater than the photoelectric effect, it rarely occurs. In contrast, the initial free electrons of negative discharge are mainly generated by photoionization. Therefore, wet insulation surface generally belongs to glow discharge. In this paper, based on the negative polarity photoionization criterion [8], and considering the influence of temperature and humidity on ionization coefficient α, adhesion coefficient η, photon absorption coefficient μ and other factors, a prediction model of surface discharge initial voltage and field intensity of wet insulation materials was established. The model can predict the initial discharge voltage and field intensity of insulating material surface under different ambient temperature and humidity and condensation radius, and can be used as a theoretical reference to control the surface discharge of insulating parts.

Physical Model. When the negative DC high voltage is applied on the flat electrode, when the field intensity around the electrode exceeds a certain critical value, the free electron collision ionization coefficient α in the air will be greater than the adhesion coefficient η, the number of electrons and positive ions produced by the collision ionization of free electrons is greater than the number of negative ions produced by the adhesion process of free electrons, the number of electrons increases exponentially, causing the initial electron collapse. The electron collapse head keeps developing away from the negative plate, and the collision ionization of free electrons will radiate photons to the surrounding areas. Photons are photoionized with molecules or atoms of gases in the air to produce photoelectrons, which further collide and ionize, thus triggering a secondary electron avalanche. When at least one photoelectron is generated by the number of photons hitting the cathode surface in the corona layer, the condition of secondary electron collapse is satisfied, and the corona discharge can be self-sustaining. The process diagram of negative DC corona is shown in Fig. 7.
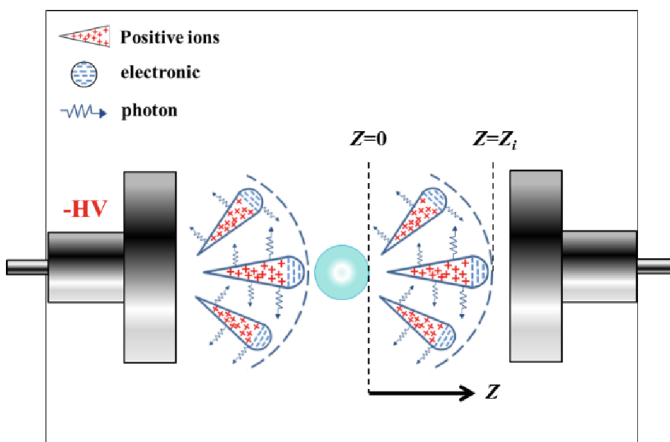
Fig. 7. Schematic diagram of negative DC corona process on wet epoxy resin plate surface

When the initial electron avalanche moves forward to coordinate z, the number of free electrons contained in the electron avalanche head $N_e(z)$ is:

$$N_e(z) = \exp(\int_0^z (\alpha(z') - \eta(z'))dz') \tag{1}$$

Within the initial electron collapse movement Δz, the number of photons radiated during the collision ionization process $\Delta n_{ph}(z)$ is:

$$\Delta n_{ph}(z) = \alpha^*(z)N_e(z)\Delta z \tag{2}$$

where, $\alpha^*(z)$ is the photon generation rate [9, 10], and the relationship between $\alpha(z)$ and the collision ionization coefficient is as follows:

$$\alpha^*(z) = k\alpha(z) \tag{3}$$

In the gap between the water bead and the flat electrode, photons generated by collision ionization will not reach the cathode surface completely, but some photons will be absorbed by air. Affected by the absorption coefficient of air photon μ and geometric factor $g(z)$, the number of photons reaching the cathode surface Δn_{ph}^s is:

$$\Delta n_{ph}^s = k\alpha(z)N_e(z)\Delta z g(z)e^{-\mu z} \tag{4}$$

In the ionization region from $z = 0$ to $z = z_i$, if the photon generated by collision ionization reaches the cathode surface and produces at least one photoelectron, the self-sustaining condition of corona discharge is satisfied. The photoelectric ionization criterion of negative DC corona to self-sustaining discharge is as follows:

$$N_{eph} = \gamma_{ph} \int_0^{z_i} \alpha(z)g(z) \exp(-\mu z + \int_0^z (\alpha(z') - \eta(z'))dz')dz \geq 1 \tag{5}$$

Parameter Choice. In order to construct the prediction model of discharge initial voltage under different ambient temperature and humidity conditions, the calculation methods of ionization coefficient α, adsorption coefficient η and photon absorption coefficient μ in wet air proposed by Abdel-Salam [11] were adopted in this paper, and α, η and μ were expressed as functions of the ratio of field intensity to air pressure. The calculation method of parameters used in this model is as follows:

The ionization coefficient α, adsorption coefficient η and photon absorption coefficient μ are decomposed into water vapor component and dry air component. The relationship is given by (6):

$$\lambda = \frac{P_d}{P}\lambda_d + \frac{P_w}{P}\lambda_w \tag{6}$$

where, λ is the ionization coefficient α, adsorption coefficient η, photon absorption coefficient μ; P is the total pressure; P_d is partial pressure of dry air; P_w is water vapor partial pressure.

Ionization coefficient α.

$$\alpha_d = \begin{cases} 2.0 \times 10^{-20} N \exp\left(-7.248 \times 10^{-19} N/|E|\right), & |E|/N > 1.5 \times 10^{-19} \\ 6.619 \times 10^{-21} N \exp\left(-5.593 \times 10^{-19} N/|E|\right), & |E|/N \leq 1.5 \times 10^{-19} \end{cases}$$

$$\alpha_w = N\left[3.536 \times 10^{17}(|E|/N)^2 - 6.0 \times 10^{-2}(|E|/N) + 2.828 \times 10^{-21}\right] \quad (7)$$

where, E is the electric field intensity, V/m; N is the total number of molecules in the air at pressure P, m³; N = 2.6876 × 1025/m³ under standard atmospheric conditions.

Adhesion coefficient η.

$$\eta_d = \begin{cases} N\left(\dfrac{8.889 \times 10^{-5}|E|/N + 2.567 \times 10^{-23} +}{N \times 3.7986 \times 10^{-74}(|E|/N)^{-1.2749}}\right), & |E|/N > 1.05 \times 10^{-19} \\[2ex] N\left(\dfrac{8.889 \times 10^{-5}|E|/N + 2.567 \times 10^{-23} +}{N \times 3.7986 \times 10^{-74}(|E|/N)^{-1.2749}}\right), & 1.2 \times 10^{-21} \leq |E|/N \\[1ex] & \qquad\qquad \leq 1.05 \times 10^{-19} \\ 1.0681 \times 10^{4}, & |E|/N < 1.2 \times 10^{-21} \end{cases} \quad (8)$$

$$\eta_w = \begin{cases} N\left(\dfrac{-8.841 \times 10^{13}(|E|/N)^2 -}{2.50 \times 10^{-6}|E|/N + 6.645 \times 10^{-24}}\right), & |E|/N \geq 1.09 \times 10^{-19} \\[2ex] N\left(\dfrac{-1.298 \times 10^{15}(|E|/N)^2 -}{2.60 \times 10^{-4}|E|/N - 7.726 \times 10^{-24}}\right), & |E|/N < 1.09 \times 10^{-19} \end{cases}$$

Photon absorption coefficient μ.

$$\mu_d = 500/m$$
$$\mu_w = 3 \times 10^4/m \quad (9)$$

Surface photon emission coefficient γph.

$$\gamma_{ph} = 3 \times 10^{-3} \quad (10)$$

Flow Chart. The calculation process of the negative discharge initial voltage prediction model constructed in this paper is shown in Fig. 8. Firstly, the surface path electric field data calculated in COMSOL software is imported, and the voltage is increased continuously with ΔU as the step. The ionization coefficient α, adhesion coefficient η and photon absorption coefficient μ are calculated by using the corresponding voltage level along the path electric field distribution. Finally, the trapezoidal integral formula and the complex Simpson quadrulation formula are used to judge whether the photoelectric ionization criterion (5) is valid. When the equal sign is true, the corresponding voltage is the corona initiation voltage U_c.

3.2   Discharge Starting Voltage Prediction

Selection of Electric Field Simulation Path. According to the finite element electric field simulation analysis, the electric field distortion degree at the junction of "gas-liquid-solid" three-phase is the largest, which makes the air near the surface of the droplet and

Fig. 8. Flow chart of prediction model of negative polarity corona voltage

the dirty layer prone to corona discharge when the applied electric field is low. Therefore, a line segment close to the surface of the epoxy resin, running through the center of the droplet and connected with two high-voltage electrodes was selected as the calculated electric field path, with a length of 3 cm. The electric field simulation results calculated along this path are shown in Fig. 9. The red dashed line segment in the figure is the path.
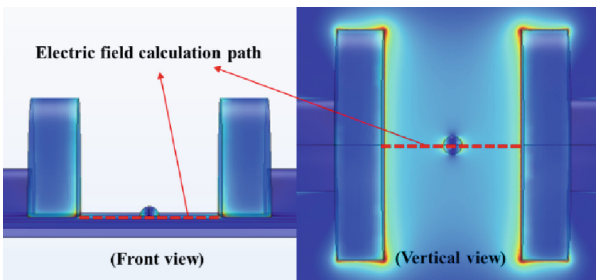
Fig. 9. Schematic diagram of electric field calculation path

Analysis of the Prediction Results of the Initial Discharge Voltage. The electric field simulation results of different plate spacing, droplet radius, droplet contact angle and droplet spacing were respectively used to predict the initial discharge voltage, and the

results were shown in Fig. 10. According to the predicted results, the initial discharge voltage increases with the increase of plate distance, droplet contact angle and droplet distance, but decreases with the increase of droplet radius. From the angle of electric field distortion affecting discharge process, the above conclusions are analyzed: when changing the distance between the plates, the electric field intensity at the edge of the bead decreases as a whole with the increase of the distance between the plates, resulting in a small ionization coefficient. Therefore, it is necessary to continuously increase the voltage to deepen the degree of electric field distortion to meet the conditions of corona self-holding. When the droplet radius is changed, the degree of electric field distortion is deepened with the increase of droplet radius, and the effective ionization coefficient is increased accordingly, and the corona self-sustaining condition becomes easier to meet. Therefore, with the increase of droplet radius, the corona voltage will decrease somewhat. When the droplet contact angle is changed, the degree of electric field distortion decreases with the increase of droplet contact angle. Therefore, the corona initial voltage on the surface of insulating materials with larger contact angle is higher. When the droplet spacing is changed, the distortion degree of the electric field between droplet drops with the increasing of droplet spacing, but the difference is not obvious. Therefore, the corona initiation voltage only increases slightly with the increase of droplet spacing, indicating that droplet spacing has little effect on corona initiation.
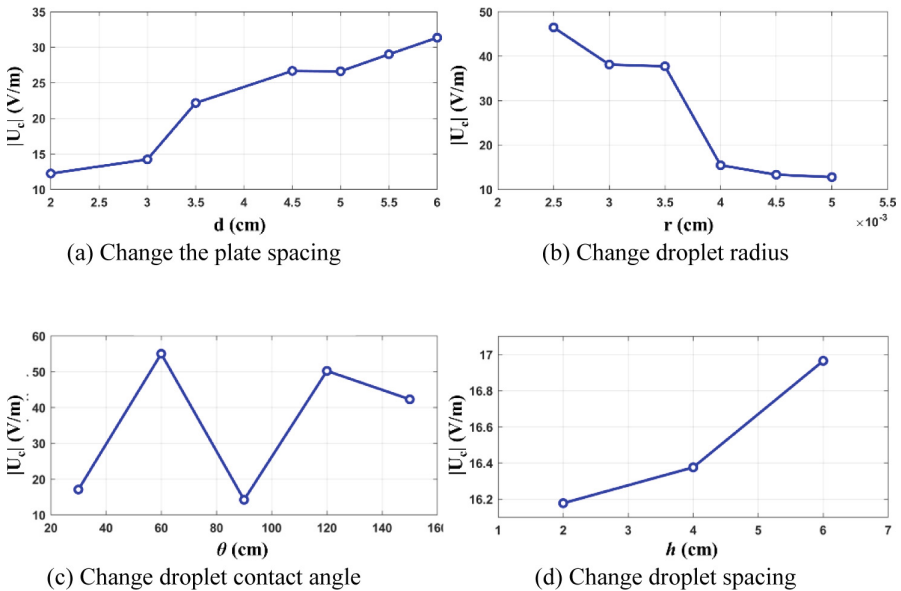
Fig. 10. Prediction of corona initial voltage under different geometric factors at $T = 25\ °C$ and $RH = 90\%$

Influence of Ambient Temperature and Humidity on Corona Voltage. In order to quantitatively analyze the influence rule of ambient temperature and humidity on corona

initiation voltage, the negative polarity photoionization model was adopted in this paper to predict the corona initiation voltage U_c of the stained epoxy resin plate under different temperature and humidity conditions when plate spacing $d = 3$ cm, drop radius $r = 2$ mm, and drop contact angle $\theta = 90°$. The predicted results are shown in Fig. 11. Firstly, the corona voltage is calculated under the conditions of ambient temperature $T = 25$ °C and relative humidity RH of 10%, 20%, 30%, 40%, 50%, 60%, 70%, 80% and 90%, respectively. It can be seen that when the relative humidity in the environment increases, the corona voltage slightly decreases. In addition, when the relative humidity RH is 80% and the ambient temperature T is 20 °C, 25 °C, 30 °C, 35 °C and 40 °C, the corona voltage is calculated, and the result shows that the corona voltage also decreases slightly with the increase of temperature.

(a) Change humidity   (b) Change the temperature
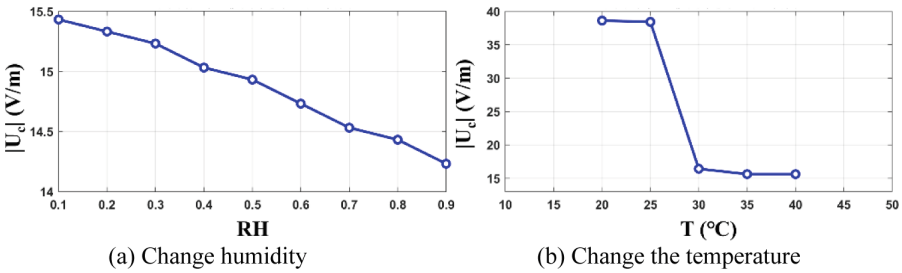
Fig. 11. Prediction of corona initial voltage under different geometric factors when $d = 3$ cm and $r = 2$ mm

The changes of ionization coefficient α, adhesion coefficient η, effective ionization coefficient α-η and photon absorption coefficient μ with the increase of ambient temperature and humidity were compared, as shown in Figs. 12, 13, 14 and 15. With the increase of relative humidity or temperature, the ionization coefficient α curve will shift upward by a small distance, while the adhesion coefficient η curve will decrease downward by a small distance, thus increasing the effective ionization coefficient. It can be seen from the analysis of (1) that the increase of ionization coefficient α and effective ionization coefficient α-η will increase the integrand value of negative polarity photoionization criterion, and it is easier to meet the condition of corona self-holding under the same electric field path. The light absorption coefficient μ also increases with the increase of relative humidity or temperature. As a result, the number of photons absorbed by the ionization region increases, the number of photoelectrons reaching the cathode surface decreases, and the negative corona initial voltage may increase. The influence of temperature and humidity on the corona voltage depends on the game between the effective ionization coefficient α-η and the light absorption coefficient μ. The results show that the corona voltage decreases slightly with the increase of relative humidity or temperature, indicating that the effect of light absorption is not important compared with the ionization intensity per unit length of the ionization zone, but the effective ionization coefficient α-η has a more significant effect on the corona voltage.
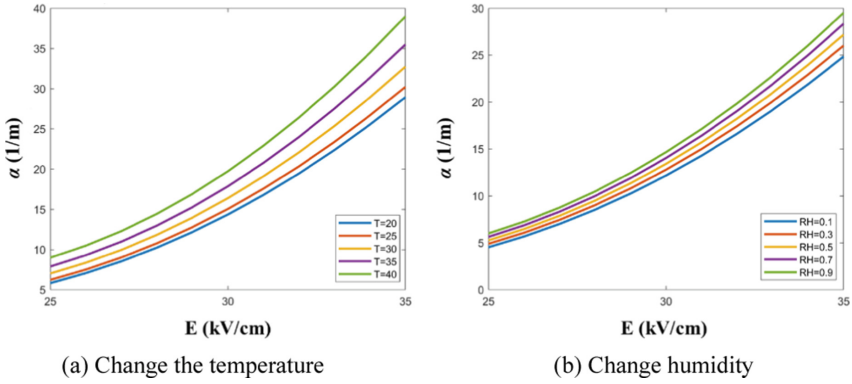
(a) Change the temperature

(b) Change humidity

Fig. 12. Trend diagram of α with T and RH

(a) Change the temperature

(b) Change humidity

Fig. 13. Trend diagram of η with T and RH

(a) Change the temperature

(b) Change humidity

Fig. 14. Trend diagram of α-η with T and RH

(a) Change the temperature   (b) Change humidity
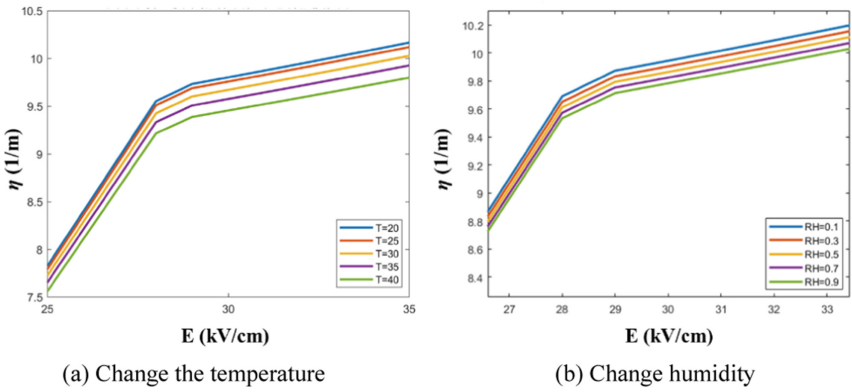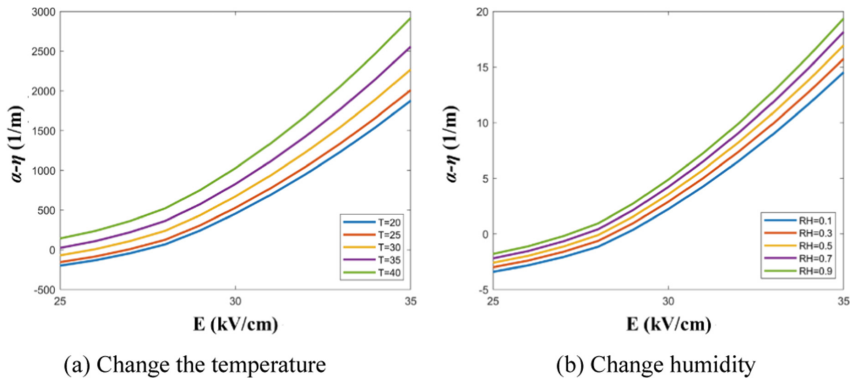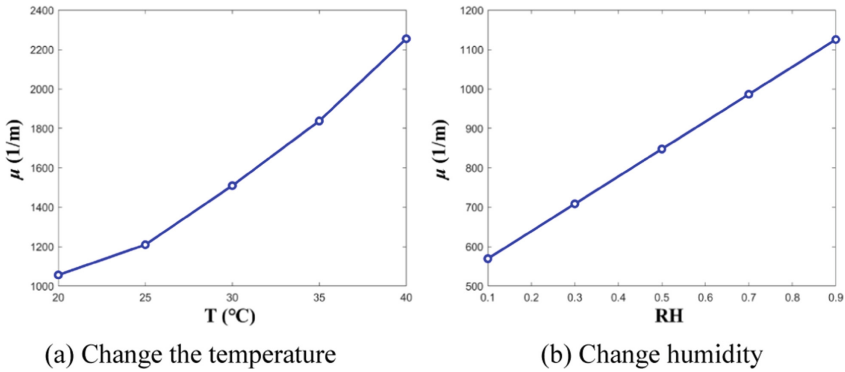
Fig. 15. Trend diagram of μ with T and RH

4 Surface Halo Test of Wet Epoxy Resin Plate

4.1 Test Layout

Figure 16 shows the schematic diagram of the test platform for epoxy resin surface halo and breakdown. The output voltage of the negative DC high voltage generator used in the test ranges from 0 to −200 kV. The high voltage connection line of the DC voltage source is connected with one of the flat electrodes, and the other electrode is grounded through the 1 kΩ resistance. The stainless steel plate electrode was placed on the epoxy resin plate with a thickness of 3 mm. In order to reduce the influence of the burr on the electrode surface on the corona test, the edge of the electrode was chamfered. The PTFE board is used as an insulating partition and placed under the epoxy board. To prevent the high voltage electrode from discharging to the ground, place the teflon plate
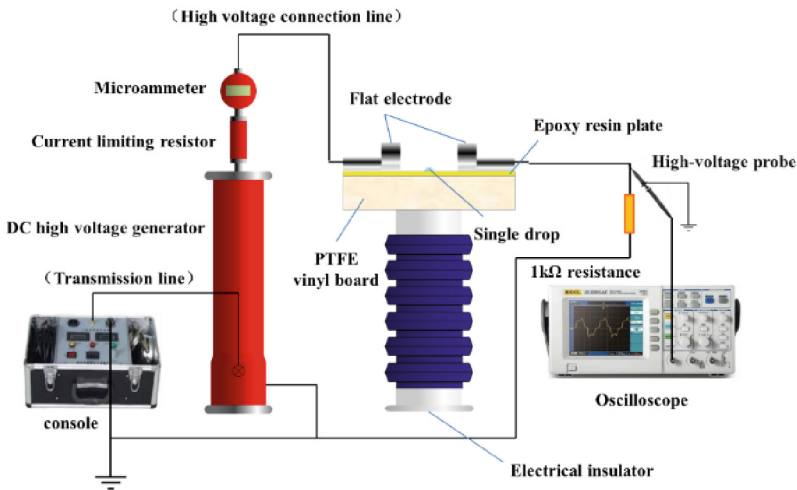
Fig. 16. Schematic diagram of test platform construction

above the insulator. Connect the high voltage probe of the oscilloscope to one side of the 1 kΩ resistance connected electrode, and calculate the leakage current by measuring the voltage at both ends of the resistance.

In this paper, corona and breakdown tests were carried out on the epoxy resin plate with plate spacing $d = 3$ cm and droplet radius $r = 5$ mm. The test was carried out in atmospheric pressure environment, the ambient temperature was about 20 °C and the relative humidity was about 90%. The uniform voltage boost was adopted, and the voltage boost gradient was 1 kV/s. The start of corona was determined by observing the voltage pulse waveform measured by oscilloscope, and the breakdown was determined by the arc between the plates. Due to the randomness of discharge phenomenon, it is necessary to conduct multiple experiments to reduce the influence of error. In addition, the influence of surface space charge on the corona formation process should be excluded, and a new epoxy resin plate should be replaced before each discharge test.

4.2   Interpretation of Result

In the negative corona test, the sampling function of oscilloscope was used to record the voltage waveform corresponding to each voltage level, and the voltage waveform was divided by the 1 kΩ resistance to obtain the leakage current waveform, which was then integrated against the time. The voltage waveform at both ends of the 1 kΩ resistance collected during the voltage boost process of epoxy resin plate with or without water drops was shown in Fig. 17 and Fig. 18. The corona voltage can be roughly judged by the time of negative initial pulse.
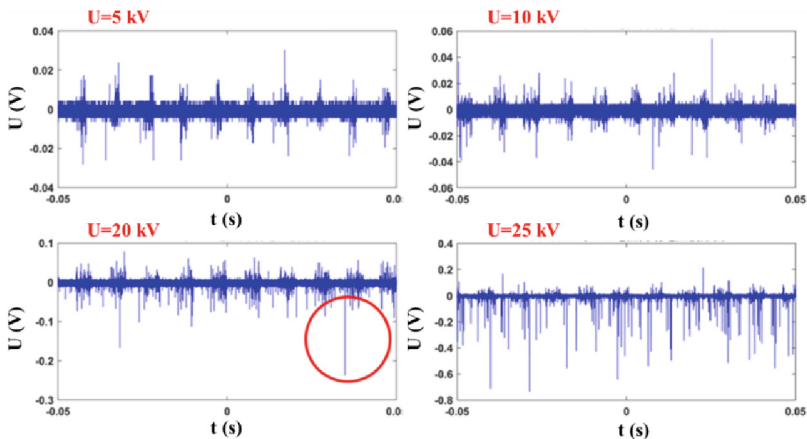
Fig. 17. Voltage waveform changes at both ends of 1 kΩ resistance when there is no water bead on the surface of epoxy resin during voltage boost

According to the analysis of Fig. 17 and Fig. 18, when there is no water drop on the surface of the epoxy resin plate, the leakage current pulse occurs when the voltage rises to −20 kV. When there are water droplets on the surface of the epoxy resin plate, the leakage current pulse occurs when the voltage rises to −15 kV. It indicates that the corona
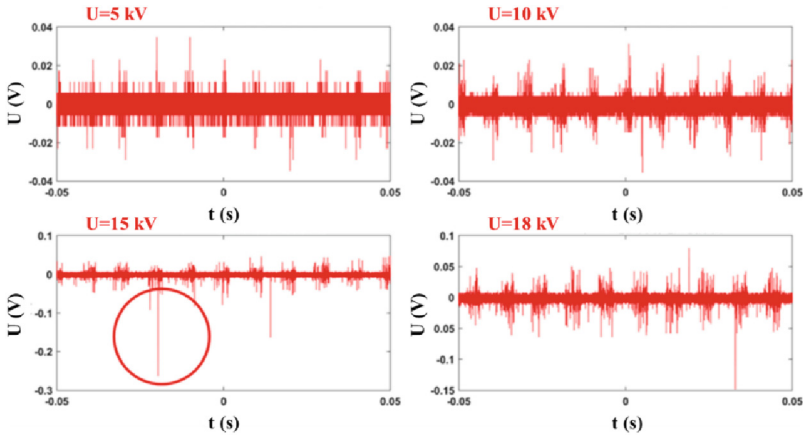
Fig. 18. Voltage waveforms at both ends of 1 kΩ resistors with water droplets on the surface of epoxy resin during voltage boost

voltage is about −15 kV and −20 kV respectively when there is no water droplets. In this paper, the leakage integral value of the voltage waveform obtained from the test is fitted after processing and integration, and the fitting curve is shown in Fig. 19. It can be seen that the integral curve of leakage current corresponding to dew on the surface of the epoxy resin plate changes abruptly when the plate voltage is about 15 kV, and the increase slope reaches the maximum, indicating the beginning of corona at this time. However, the integral curve of leakage current corresponding to the absence of dew on the surface of the epoxy resin plate changes abruptly when the plate voltage is about 24 kV, so it is preliminarily determined that the corona voltage is about 24 kV.
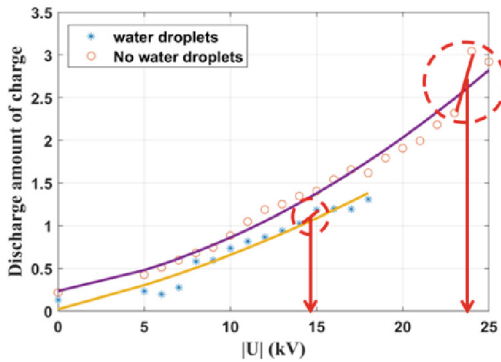
Fig. 19. Leakage current integral change trend diagram

The test results of corona initiation voltage are compared with the predicted value of negative DC corona initiation voltage in Sect. 4, as shown in Table 2. It can be seen that the simulation results are in good agreement with the experimental values, which

verifies the effectiveness of the negative polarity photoionization model in predicting the corona voltage.

Table 2. Comparison of test and simulation values of corona voltage on epoxy resin surface

The presence of water droplets on the surface	Test value of corona initiation voltage (kV)	Predicted value of corona voltage (kV)
Existent	−15	−14.2323
Nonexistent	−24	−21.5663

5   Conclusion

In recent years, scholars at home and abroad have carried out a lot of research work on the mechanism of droplet condensation phase transition and negative DC corona process respectively. However, there is a certain separation between the study of corona discharge and the study of condensation process. In order to solve the above problems, electric field simulation and corona test were carried out considering the influence of condensation on the surface discharge process of wet and dirty insulating materials. Combined with simulation and test, the conclusions are as follows:

1) **A simulation model of single droplet electric field under the action of flat electrode was constructed**. The influences of plate spacing, droplet radius, droplet contact angle and droplet spacing on electric field distortion were compared and analyzed. The simulation results showed that the electric field distortion at the junction of gas-liquid-solid phase was the largest.
2) **A negative corona initial voltage prediction method considering temperature and humidity is proposed.** It is concluded that the discharge initial voltage will increase with the increase of plate distance, droplet contact angle and droplet distance, but will decrease with the increase of droplet radius. It is found that the corona initial voltage decreases slightly with the increase of relative humidity or temperature. The influence of temperature and humidity on corona initiation voltage depends on the game between the effective ionization coefficient α-η and the light absorption coefficient μ.
3) **The effectiveness of the electric field simulation model and the negative polarity corona voltage prediction method was verified by the surface corona test of the wet epoxy resin plate.**

References

1. Jiang, X.C., Xu, Y.P., Li, Y.C., et al.: Digitalization transformation of power transmission and transformation under the background of new power system. High Volt. Eng. **2022**(48), 1–10 (2022)
2. Fu, Y., Zhou, Q., Jia, F., et al.: Fault prediction of offshore wind turbines based on graphical processing of SCADA data. Proc. CSEE **42**(20), 7465–7474 (2022)
3. Rose, J.W.: Further aspects of dropwise condensation theory. Int. J. Heat Mass Transf. **19**, 1363–1370 (1976)
4. Sikarwar, B.S., Khandekar, S., Muralidhar, K.: Mathematical modelling of dropwise condensation on textured surfaces. Sadhana **38**(6), 1135–1171 (2013). https://doi.org/10.1007/s12046-013-0190-9
5. Wang, L.M., Li, X., Cao, B., et al.: Influence of partial arc on leakage current and surface conductivity of insulators. High Volt. Eng. **2019**(45), 1624–1629 (2019)
6. He, C., Zhang, X.R., Yuan, W.Z., et al.: Surface partial discharge measurement and numerical calculation under AC and lightning impulse superimposed voltage in SF6 gas. Proc. CSEE **2021**(41), 200–210 (2021)
7. Liu, L., Li, X.A., Zhang, Q.G., et al.: Effect of electric field along the surface on the flashover voltage of GIS insulators. High Volt. Eng. **2020**(46), 2906–2913 (2020)
8. Bian, X.M., Hui, J.F., Huang, H.K., et al.: Variation of the characteristics of negative DC corona streamer pulse with air pressure and humidity. Proc. CSEE **2010**(30), 134–142 (2010)
9. Loeb, L.B.: Electrical Coronas: Their Basic Physical Mechanisms. University of California Press, Berkeley (1965)
10. Abdel-Salam, M.: Calculation of corona onset voltage for duct-type precipitators. IEEE Trans. Ind. Appl. **29**, 274–280 (1993)
11. Abdel-Salam, M.: High Voltage Engineering: Theory and Practice. Marcel Dekker Inc., New York (2000)

The Influence of Environmental Factors on Corona Voltage with Raindrops on the Surface of Positive DC Conductors

Zhenhong Cao[1], Hongwei Mei[2] (ID), and Xiaobo Meng[1(✉)] (ID)

[1] Guangzhou University, Guangzhou 510006, Guangdong, China
mengxb@gzhu.edu.cn

[2] Tsinghua Shenzhen International Graduate School, Shenzheng 518055, Guangdong, China

Abstract. Corona discharge can cause energy loss in high-voltage transmission lines, and can also seriously threaten the stable operation of the line. The distortion of the surrounding electric field by water droplets on the surface of the conductor in the rain environment becomes an important factor affecting the corona, and the environmental factors in different areas will also have an impact on the conductor corona, so the study of environmental factors on the impact of the corona voltage of positive DC conductors with raindrops has high practical engineering significance. According to the gas discharge theory, a simulation model is established for a comprehensive study, and whether the number of secondary electron avalanche positive ions is greater than the number of initial electron avalanche positive ions is used as a criterion for corona initiation. The results show that the corona voltage is influenced by both environmental factors and raindrop morphology. Under the same environmental factors, the larger the raindrop, the smaller the corona voltage, because the electric field strength near the large raindrop is large, the effective ionization coefficient is large; the pressure drops, the temperature rises, the ionization area increases simultaneously with the effective ionization coefficient, so that the corona voltage decreases; the humidity rises, the effective ionization coefficient rises, the collisional ionization ability in space increases, so that the corona voltage decreases, but the decrease is small.

Keywords: Corona · positive direct current · raindrops · environmental factors

1 First Section

Corona is an important factor that must be considered in the construction of ultra-high voltage transmission lines. At present, the scale of China's ultra-high voltage transmission lines is growing, based on the large geographical cross-service and uneven energy distribution, China has built a number of high-voltage transmission lines such as Jinbei-Jiangsu, Ningdong-Zhejiang, etc., to realize the redistribution of energy. Since the DC transmission method has the advantages of large capacity and low loss during transmission, most of the current UHV transmission lines adopt the DC transmission method.

With the increasing voltage level of transmission lines, the electric intensity on the line surface may exceed the free strength of air molecules, leading to the occurrence of corona phenomenon. Corona can interfere with some radio equipment, causing loss of energy, and can be accompanied by a series of chemical reactions that can easily corrode metal electrodes. In normal weather conditions, the wire generally does not occur corona, but when the raindrops attached to the wire, equivalent to an increase in the wire surface with the ability to conduct a bump, making the wire around the space around the electric field uniformity decreases, corona phenomenon is more likely to occur [1–4]. And because of the transmission lines across a wide area, different areas of the air pressure, temperature and humidity and other environmental factors there are obvious differences, the corona has a different degree of impact [5, 6]. In addition, although positive DC is more difficult to corona than negative DC transmission, the degree of corona is more intense and produces more harmful effects. Therefore, it is of high practical engineering significance to study the effect of environmental factors on the corona voltage of positive DC with raindrop conductors.

Many scholars at home and abroad are currently engaged in the study of corona characteristics of conductors, but few have combined environmental factors with rain-drops to study their effects on the corona voltage of conductors [7–9]. Xiaobo Meng and Xingming Bian of Tsinghua University studied the relationship between smooth wire corona and environmental factors, but did not explore the working conditions of the wire with raindrops [10]; Fan Jianbin of the Chinese Academy of Electrical Sciences studied the effect of raindrops on wire corona, but it did not combine environmental factors [11]. And most of the current research on conductive wire corona is conducted through experiments in the corona cage, which requires high equipment and equipment, complex experiments, and there are certain safety risks [12–14].

In this paper, the MATLB simulation model will be built according to the air discharge theory using numerical calculation method, firstly, the corona voltage of the wire attached to different forms of raindrops is calculated, and then the corona law of the wire attached to raindrops under different environmental factors is studied, in which the electric field is calculated by the simulated charge method.

2   Computational Model

2.1   Calculation of Electric Field

The essence of the influence of raindrop shape on the corona onset voltage is that it changes the spatial electric field distribution around the conductor. The calculation of the spatial electric field mainly includes the finite element method, the finite difference method, and the charge simulation method. In this paper, the simulated charge method is used to replace a continuous charge distribution in space with a finite number of discrete charges. Compared with other methods, it can solve the electric field distribution in the infinite field, and the solution is simple. The Electric field calculation model is shown in Fig. 1.

Let the radius of the conductive wire is 10 mm, the distance between the wire and the ground h is 4 m. When the radius of 1 mm semi-circular raindrop attached to the wire, when the 350 kV voltage is applied, the field strength at the end of the raindrop
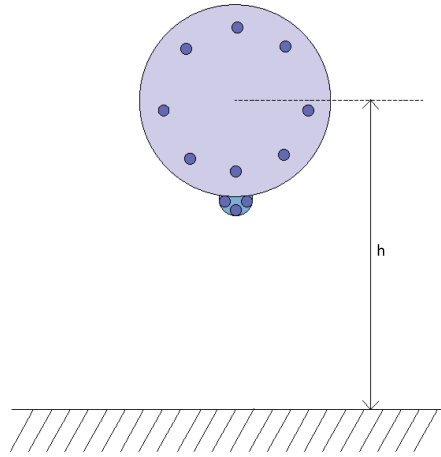
Fig. 1. Electric field calculation model

in the vertical ground direction is shown in Fig. 2. It can be seen that the high field strength area near the wire is mainly concentrated at the end of the raindrop, and then drops sharply to near zero. Therefore, the corona area of the wire should occur in a very small area at the end of the raindrop.
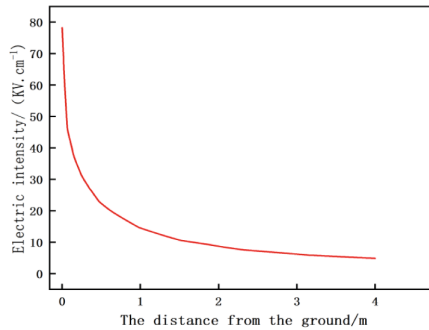
Fig. 2. Electric intensity as a function of the distance from the ground

2.2 Calculation of the Initial Corona Voltage

For overhead positive DC transmission conductors, when the applied voltage rises gradually, the electric field in the space near the conductor will also increase, and when the electric intensity rises to a certain level, the collision ionization coefficient α of electrons will be greater than the attachment coefficient η. The region where $\alpha > \eta$ is called the ionization region, the region due to the role of external ionization factors, free electrons will move in the direction of the anode that is the wire.

In the process of movement electrons collide with air molecules, collisional ionization occurs, and electrons will increase exponentially and continuously, and this avalanche growth of electron flow is called the initial electron avalanche. The charge density in the initial electron avalanche is large, and the compounding process is frequent, which causes the air molecules to excite and emit photons outward. In the region of strong electric field at the head or tail of the avalanche, the air molecules absorb the photons and then cause photoionization to produce new photons. The photon moves in the direction of the positive conductor under the action of the applied electric field, and collides with the air molecules during the movement to produce a secondary electron avalanche. When the voltage rises to a certain value the number of electrons in the secondary electron avalanche will be greater than or equal to the initial electron avalanche, corona discharge will occur. DC transmission conductor corona discharge can be self-sustaining condition is the number of positive ions in the secondary electron avalanche N2 is not less than the number of positive ions in the initial electron avalanche N1, when the two are exactly equal, the corresponding voltage Ui that is the corona voltage [15–17].

The ionization and attachment coefficients are influenced by air pressure and air humidity and are calculated as Eqs. (1) and (2) [18, 19].

$$\alpha = \frac{P_d}{P}\alpha_d + \frac{P_w}{P}\alpha_w \tag{1}$$

$$\eta = \frac{P_d}{P}\eta_d + \frac{P_w}{P}\eta_w \tag{2}$$

α_d and α_w are the ionization coefficients in dry air and wet air, respectively; η_d and η_w are the attachment coefficients in dry air and wet air, respectively; P_d and P_w are the dry air partial pressure and water vapor partial pressure, respectively [20, 21].

The steps for calculating the positive DC starting corona voltage are shown in Fig. 3, and the calculation parameters are selected according to Reference 6.
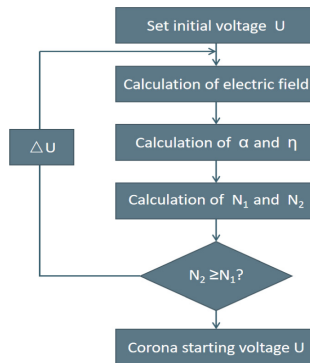
Fig. 3. Calculation steps of the initial voltage

A right-angle coordinate system with the parallel ground direction as the X-axis, the vertically downward direction as the Y-axis, and the closest point of the wire to the

ground as the coordinate origin is established. And let the vertical coordinate of the ionization zone boundary be y_i, then the initial electron avalanche produces the number of positive ions as shown in Eq. (3) [22].

$$N_1 = \exp\left(\int_0^{y_i} (\alpha(y) - \eta(y))dy\right) \tag{3}$$

Let the electron diffusion coefficient be De; the electron drift velocity be Ve, then the radius of the electron avalanche is [22]:

$$r_1 = \sqrt{6\int_0^{y_i} \frac{De}{ve}dy} \tag{4}$$

Let the number of photons emitted for one collisional ionization be f_1, and the probability of photoionization after absorption of photons by air molecules be f_2. The location of the initial electron avalanche to the boundary of the ionization region is divided into of layers thickness dy, and the coordinates of a layer are y and its distance from the head of the electron avalanche $y - r1$. The number of photons generated by the absorption of photons by the air in this layer is $f_1 f_1 N_1 m e^{-m(y-r_1)}g(y)$, where μ is the photon absorption coefficient and g(y) is the geometric coefficient considering partially vanishing photons. Then the total number of positive ions in the secondary electron avalanche N_2 is [22]:

$$N_2 = \int_{r_1}^{y_i} f_1 f_2 N_1 \mu e^{-\mu(y-r_1)}g(y) \exp\left(\int_{r_1}^{y_i} (\alpha(y') - \eta(y'))dy'\right)dy \tag{5}$$

2.3 Validation of the Calculation Procedure

The calculation was programmed using Matlab software as described above, and the results of the smooth wire were compared with the classical experimental results of Abdel-Salam in Table 1 [22].

Table 1. Comparison table of simulation results and experimental results

Radius of conductor/mm	5	10	15	20
Calculation results/KV	218	360	488	602
Experimental results/KV	138 – 220	282 – 373	395 – 491	472 – 605

It can be seen that the calculation results of this program are within the range of experimental results, so it can be verified that this program can meet the requirements of positive DC initial corona voltage calculation conditions and has the reasonableness.

3   Calculated Results

3.1   Effect of Raindrops on Corona

In this paper, three different forms of raindrops, namely, hemispherical raindrops with a radius of 1 mm; semi-ellipsoidal raindrops 1 with a short axis of 1 mm and an axis ratio of 3; and semi-ellipsoidal raindrops 2 with a short axis of 1 mm and an axis ratio of 5, are selected to simulate the process of raindrops continuously converging and being stretched at the end under the dual action of electric and gravitational fields. A smooth wire surface is considered to have zero volume of raindrops attached, and the raindrops are classified into 1, 2, 3, and 4 categories according to the order of their volume from small to large (Fig. 4).
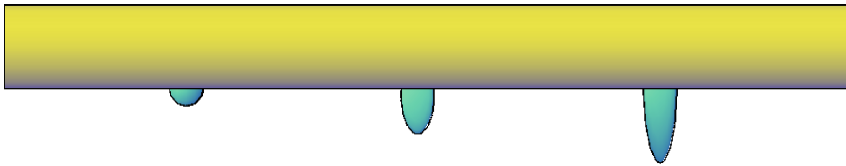
Fig. 4. Raindrop shape

At standard atmospheric pressure, a temperature of 293 K, and a humidity of 15 g.m^{-3}, the effect of different sizes of raindrops on the corona of the wire is calculated in Fig. 5.
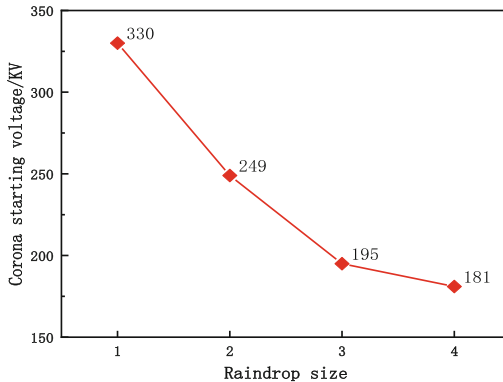
Fig. 5. Initial corona voltage as a function of raindrop size

With the increase of raindrop level, the corona voltage is decreasing, from the smooth wire to the process of attached hemispherical raindrop, the corona voltage decreased by 24.5%; from the attached hemispherical raindrop to the process of the attached semi-ellipsoidal raindrop 1, the corona voltage decreased by 21.7%; from the attached semi-ellipsoidal raindrop 1 to the process of attached semi-ellipsoidal raindrop 2, the corona

voltage decreased by 7.2%. It can be seen that the corona voltage will drop rapidly after the wire is attached to the raindrop, but the drop will gradually become slower as the raindrop increases.

Corona occurs mainly within a very small area at the end of the raindrop, and the maximum electric field strength in this area is calculated in relation to the raindrop in Fig. 6. After the hemispherical raindrops were attached to the wire, the maximum electric field intensity increased by 73.3%; the maximum electric field intensity increased by 23.6% in the process of changing the shape of raindrops from hemispherical to semi-ellipsoidal 1; then the maximum electric field intensity increased by 3.7% in the process of changing from semi-ellipsoidal 1 to semi-ellipsoidal 2. It can be seen that the maximum electric field intensity increases rapidly after the wire is attached to the raindrops, but the increase of the maximum electric field intensity slows down with the increase of the raindrops, which is consistent with the trend of the corona voltage.
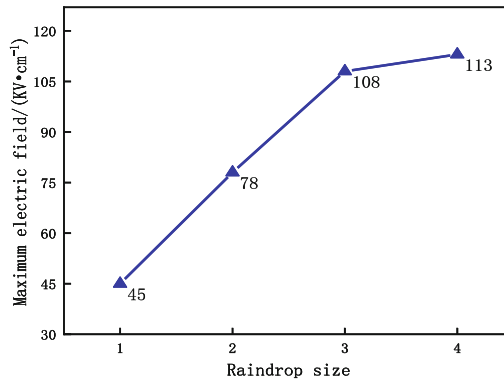
Fig. 6. Maximum electric field as a function of raindrop size at the same voltage

The effective ionization coefficient is calculated as a function of the maximum field strength in Fig. 7. It can be seen that the electric field strength directly affects the effective ionization coefficient, which rises with the electric field strength when the environmental factors are the same.

3.2   The Effect of Environmental Factors on Corona

The Effect of Air Pressure on Corona. The relationship between the initial corona voltage and air pressure was calculated for three types of raindrops, hemispherical and semi-ellipsoidal 1 and 2, when attached to a 10 mm wire, setting the temperature at 293 K and the humidity at 15 g.cm^{-3}, and the results are in Fig. 8.

It can be seen from Fig. 8 that the initial corona voltage of the three types of wires attached with raindrops increases linearly with the air pressure. For every 0.01 MPa increase in air pressure, the corona starting voltage of the wire attached with semi-spherical raindrops increases by about 21 kV; The corona starting voltage of the conductor with semi ellipsoidal raindrop 1 increases by about 18 kV; The corona starting
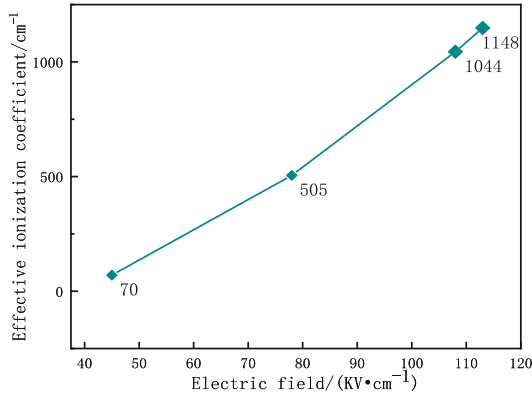
Fig. 7. Effective ionization coefficient as a function of electric field
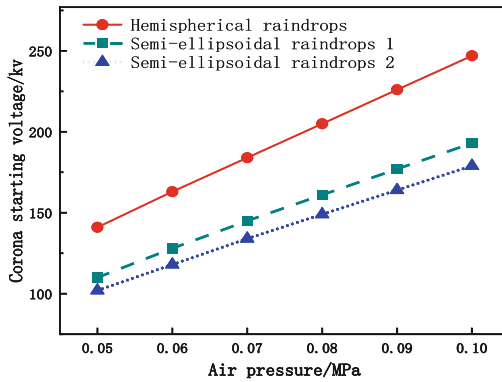
Fig. 8. Variation of corona onset voltage associated with raindrops at different air pressures

voltage of the conductor with semi ellipsoidal raindrop 2 increases by about 16 kV. It can be seen that the larger the raindrop is, the smaller its corona onset voltage is affected by the air pressure. This is because the corona onset voltage is also affected by the electric field strength. Under the same environmental conditions, the electric field strength is higher near large raindrops, and the influence of air pressure is relatively weak [23].

The calculation of the effective ionization coefficient on the air pressure is shown in Fig. 9.

At the same electric field strength, the effective ionization coefficient decreases with the increase in air pressure. At 0.05 MPa, the increments of the effective ionization coefficient were 670 and 131 when the electric field strength increased from 78 KV.cm^{-1} to 108 KV.cm^{-1} and then to 113 KV.cm^{-1}, respectively; at 0.1 MPa, the increments of the effective ionization coefficient with the change of electric field were 443 and 86. The increase in air pressure also effectively weakened the effect of electric field strength.

When the initial corona occurs on three kinds of wires with raindrops attached to the surface, the ionization zone length versus air pressure is calculated as shown in Fig. 10.
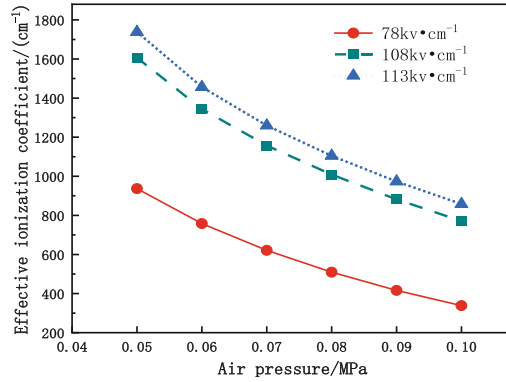
Fig. 9. Variation of corona onset voltage with respect to electric field at different air pressures.

It can be seen from the above figure that the ionization zone length at the initial corona decreases for all three wires with attached raindrops as the air pressure increases. This is due to the fact that the effective ionization coefficient decreases with increasing air pressure at the same field strength, and the ionization zone decreases with the decrease of the effective ionization coefficient. However, the relationship between the length of the initial ionization region and the raindrop size is not reflected in the figure. The reason for this is that the initial voltage decreases with an increasing raindrops, and the electric field strength of large raindrops at low voltage may be lower than that of small raindrops at high voltage, which in turn affects the length of the ionization zone.
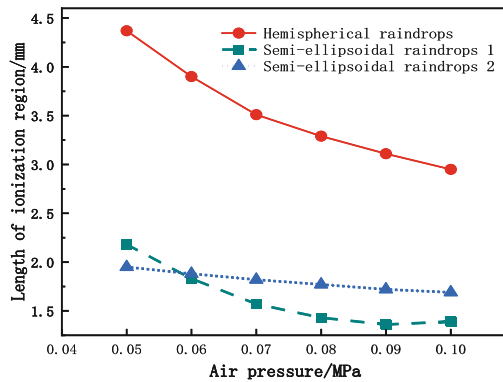
Fig. 10. Variation of the length of the ionization region associated with raindrops at different air pressures

Effect of Temperature on Corona. Corona voltage versus temperature was calculated for a temperature range of 273 K to 523 K with a temperature gradient of 50 at standard atmospheric pressure and a humidity of 15 g.cm^{-3}.

As can be seen from Fig. 11, regardless of the size of the raindrops attached to the wire surface, the corona voltage decreases with the rise of temperature, and its
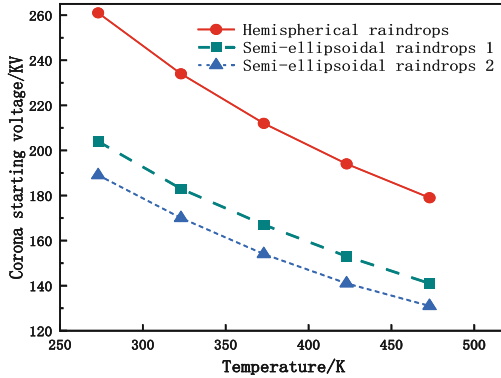
Fig. 11. Variation of corona onset voltage associated with raindrops at different temperatures

decreasing trend is approximately linear overall. In the interval from 273 K to 523 K, the change of corona voltage is about 20 kV for hemispherical raindrops, 16 kV for semi-ellipsoidal raindrops 1, and 15 kV for semi-ellipsoidal raindrops 2 for every 50 K change in temperature. It can be seen that the larger the raindrop, the smaller the influence of temperature on the corona voltage, and the electric field strength can also weaken the influence of temperature on the corona voltage.
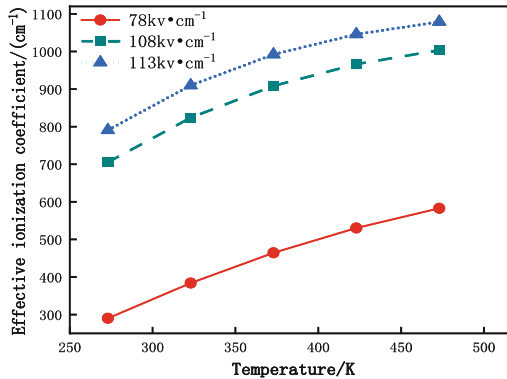
Fig. 12. Variation of effective ionization coefficient related to electric field at different temperature

The relationship between the effective ionization coefficient and the temperature was calculated and the results are shown in Fig. 12. The effective ionization coefficient of the wire with attached raindrops is positively correlated with the electric field strength at the same electric field strength and is independent of the electric field strength. At 273 K, the increment of electric field strength from 78 kV-cm^{-1} to 108 kV-cm^{-1} to 113 kV-cm^{-1} corresponds to the increment of effective ionization coefficient of 421 and 85, respectively; at 473 K, the effective ionization coefficient increases with an electric field strength of 415 and 75, respectively. The results show that the variation of the effective ionization coefficient with field strength becomes smaller as the temperature
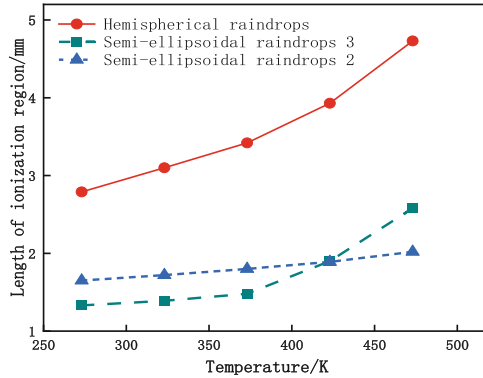
Fig. 13. Variation of the length of the ionization region associated with raindrops at different temperatures

increases, and the temperature also weakened the effect of the electric field on effective ionization.

As shown in Fig. 13, the length of the ionization zone of the three wires with raindrops on the surface increases with the increase in temperature at the initial corona. This is due to the increase of the effective ionization coefficient with temperature, and the length of the ionization zone varies with the effective ionization coefficient. In addition, the electric field strength at the initial corona is not proportional to the size of the raindrops because of the different initial voltages of the raindrop wires at the corona, so this graph does not reflect the relationship between the size of the raindrops at the initial corona and the length of the ionization zone.

Effect of Humidity on Corona. The humidity in the air varies greatly in rainy weather, and the relationship between humidity and initial corona voltage is studied in the interval from 0 to 15 g.m^{-3} as shown in Fig. 14.
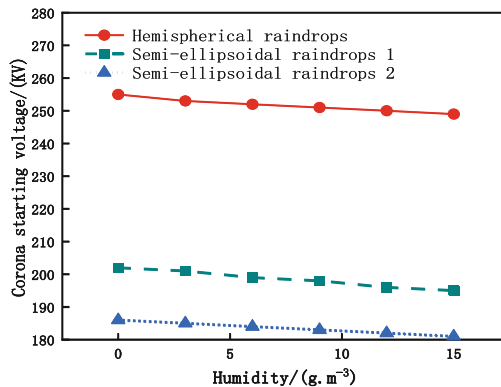
Fig. 14. Variation of corona onset voltage associated with raindrops at different humidity levels

As can be seen from Fig. 14, when water droplets exist on the wire surface, the corona voltage decreases with the increase in humidity, and the decreasing trend is approximately linear. Absolute humidity per 1 g.cm^{-3} rise, the corona voltage of the three raindrop wires are decreased by 1 kV, the decline is not affected by raindrops, which is due to the comparison with air pressure and temperature, humidity on the corona voltage of the wire is weak.

From Fig. 15, it can be seen that the effective ionization coefficient increases with the increase of humidity at the same electric field strength, and the increase is approximately linear. For each 1 g.cm^{-3} increase in absolute humidity, the effective ionization coefficient increases by 0.1 at 78 kV.cm^{-1} electric field strength, by 0.3 at 108 kV.cm^{-1} electric field strength, and by 0.4 at 113 kV.cm^{-1} electric field strength. It can be seen that the effect of humidity on the effective ionization coefficient at high electric fields is greater than that at low electric fields, but the increase in the effective ionization coefficient with The increase of the effective ionization coefficient with humidity is small for both high and low electric fields, thus confirming the weak effect of humidity on the corona of the wire.
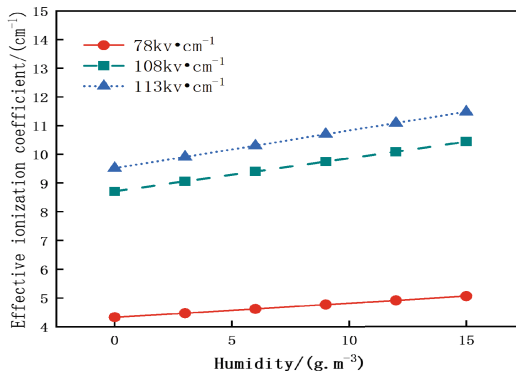
Fig. 15. Variation of effective ionization coefficients associated with electric fields at different humidity

As can be seen from Fig. 16, if the voltage on the wire with attached raindrops is equal to the initial corona voltage, the ionization region length decreases with the rise of the initial corona voltage, and the opposite trend of the effective ionization coefficient, the reason for this is that the change in effective ionization coefficient is very small when the air pressure changes and the length range of the ionization region is mainly influenced by the electric field strength. The electric field of the same type of attached raindrop wire decreases synchronously with the corona voltage, and when the initial corona occurs under low humidity, the corona voltage is high, which leads to a large electric field strength near the raindrop and therefore a large length of the ionization region.
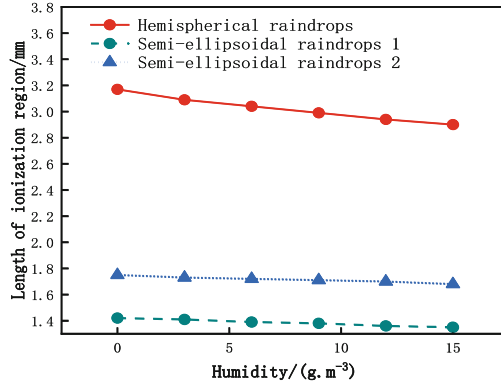
Fig. 16. Variation in the length of the ionized region associated with raindrops at different humidity levels

4   Analysis of Results

4.1   Analysis of the Effect of Raindrop Morphology

Under the same environmental factors, when raindrops attach to the smooth conductor, the initial corona voltage decreases rapidly, but the decrease will gradually slow down with the increase of raindrops. This is because the raindrop attached to the wire surface is a conductor, which is equivalent to adding a bulge with a certain radius of curvature on the wire. The charge converges at the end of the raindrop, distorting the surrounding electric field strength. The larger the raindrop, the greater the electric field distortion, but the amplitude of distortion increase will gradually slow down. The effective ionization coefficient increases when the electric field intensity increases with the raindrop. The criterion of positive DC conductor corona can be expressed as Eq. (6) [22].

$$f_1 f_2 g \mu \int_{r_1}^{y_i} (\exp(-\mu(y - r_1) + \int_{r_1}^{y} (\alpha - \eta) dy') dy \geq 1 \tag{6}$$

Therefore, the greater the field strength is, the greater the effective ionization coefficient is, the more likely the conductor is to corona, and the lower the initial corona voltage is.

4.2   Analysis of the Influence of Environmental Factors

Air pressure, temperature, humidity, and other environmental factors will affect the corona inception voltage of the conductor attached with raindrops. Taking the conductor with hemispherical raindrops as an example, for every 0.01 MPa increase in air pressure, the corona onset voltage increases by 21 kV, which is 8.5% at 0.1 MPa; When the temperature rises by 50 K, the corona starting voltage decreases by 20 kV, which is 7.7% of 273 K; When the humidity rises by 1 g.cm^{-1}, the corona onset voltage decreases by 1 kV to 0 g 0.4% at cm^{-3}, it can be seen that the air pressure has the greatest influence on the initial corona voltage of the conductor, and the humidity has little influence on it.

Corona is affected by the rain droplet form, environmental factors, when the larger the droplet, its end has a larger electric field strength can weaken the impact of environmental factors on it. When the air pressure rises and the temperature falls, the ionization area length decreases simultaneously with the effective ionization coefficient, at this time when the voltage remains unchanged, the left side of Eq. (6) becomes smaller, and it is difficult to reach the corona conditions, so the corona voltage will rise; when the humidity changes, the ionization area length and the effective ionization coefficient change in the opposite trend, the two interact with each other, and the corona voltage is mainly affected by the effective ionization coefficient, the reason is that the effective ionization coefficient increases with the When the humidity rises, the collisional ionization capacity in space is enhanced.

5   Conclusion

1) The corona onset voltage decreases significantly after raindrops are attached to the conductor; as the size of attached raindrops increases, the corona onset voltage decreases, but the trend slows down.
2) The corona voltage of the conductor with raindrops attached rises with increasing air pressure, and the effect of air pressure on corona voltage decreases with increasing size of raindrops attached to the wire.
3) When the temperature increases, the corona onset voltage decreases accordingly; an increase in raindrop size also attenuates the effect of temperature on the corona onset voltage.
4) With the increase of humidity, the corona onset voltage will decrease, but the change amplitude is far less than the impact of air pressure and temperature on the corona onset voltage. The impact can be ignored when the humidity changes little.
5) The corona onset voltage of a conductor is influenced by a combination of raindrops and environmental factors. Under the same environmental conditions, the electric field near the conductor with large raindrops attached to the surface is stronger, and the influence of environmental factors on the corona onset voltage is relatively small.

References

1. Ma, A.: Effect of raindrops under DC power transmission lines on corona vibration considering of environmental factors. Proc. CSEE **36**(23), 6579–6585 (2016)
2. Zhu, J.: Influence of surface water drop on corona characteristics of AC transmission lines. High Voltage Apparatus **51**(01), 13–17 (2015)
3. Chen, L.: Influence of rain drops on corona discharge in AC transmission lines under high rainy condition. High Voltage Eng. **38**(11), 2863–2868 (2012)
4. Lu, J.: Current status of study on the effects of airborne particles on DC corona discharge: space-charge effect of particles. Proc. CSEE **35**(23), 6222–6234 (2015)

5. Wu, D.: Research on influences of temperature on positive streamer corona discharge characteristic of rod-plane gap. High Voltage Apparatus **58**(2), 50–59 (2022)
6. Bian, X.: Influence of air pressure and humidity on positive DC corona streamer pulse characteristics. High Voltage Eng. **35**(10), 2371–2382 (2009)
7. Yin, F.: Influence of AC electric field on conductor icing. IEEE Trans. Dielectr. Electr. Insul. **23**(4), 2134–2144 (2016)
8. He, G., et al.: Impact of icing severity on corona performance of glaze ice-covered conductor. IEEE Trans. Dielectr. Electr. Insul. **24**(5), 2952–2959 (2017). https://doi.org/10.1109/TDEI.2017.006536
9. He, G.: Influence of rain drops on corona discharge in AC transmission lines under high rainy condition. Proc. CSEE **41**(24), 8610–8619 (2021)
10. Meng, X.: Influence of environmental factors on positive DC corona inception voltage of overhead transmission lines. High Voltage Eng. **36**(8), 1916–1922 (2010)
11. Fang, J.-B.: Effect of water dropon UHV DC transmission corona performance in corona cage. High Voltage Eng. **35**(10), 2340–2343 (2009)
12. Jinhe, U.: Analysis of characteristic quantities of space charges in AC corona discharge. Proc. CSEE **41**(24), 619–8630 (2021)
13. Yin, F.: Influences of electric field of conductors surface on conductor icing. High Voltage Eng. **44**(3), 1023–1033 (2018)
14. Du, L., et al.: Measurement of AC corona onset voltage conductor by space charge. Anal. Proc. CSEE **40**(15), 5061–5070 (2020)
15. Abdel-Salam, M., Allen, N.L.: Onset voltage of positive glow corona in rod-plane gaps as influenced by temperature. IEE Proc. Sci. Meas. Technol. **152**(5), 227–232 (2005). https://doi.org/10.1049/ip-smt:20045024
16. Meng, X.: Analysis on negative DC corona inception voltage of stranded conductors. High Voltage Eng. **37**(1), 77–84 (2011)
17. Meng, X.: Variation of AC corona discharge pulse characteristics with air pressure and humidity. Proc. CSEE **31**(28), 128–135 (2011)
18. Abdel-Salam, M.: Positive wire-to-plane coronas as influenced by atmospheric humidity. IEEE Trans. Ind. Appl. **21**(1), 35–40 (1985). https://doi.org/10.1109/TIA.1985.349640
19. Abdel-Salam, M., Abdellah, M.: Dielectric strength of compressed insulating gases and their mixtures. IEEE Trans. Ind. Appl. **14**(6), 516–522 (1978). https://doi.org/10.1109/TIA.1978.4503584
20. Fouad, L., Elhazek, S.: Effect of humidity on positive corona discharge in a three electrode system. J. Electrostat. **35**(1), 21–30 (1995)
21. Morrow, R.: Streamer propagation in air. J. Phys. **30**(4), 614–627 (1997)
22. Abdel-Salam, M.: The onset voltage of coronas on bare and coated conductors. Appl. Phys. Europhys. J. **31**(19), 2550–2556 (1998)
23. Zhang, H.: Influence of DC electric field intensity on conductor glaze icing and its corona loss. High Voltage Apparatus **58**(8), 0275–0279 (2022)

Partial Discharge Characteristics of Damp Oil-Immersed Paper Under Combined AC and DC Voltage

Binhao Chen[1], Chunjia Gao[1(✉)], Juzhen Wu[2], Yanming Cao[2], and Bo Qi[1]

[1] State Key Laboratory of Alternate Electrical Power System with Renewable Energy Sources, North China Electric Power University, Beijing 102206, People's Republic of China
kiddgcj@163.com

[2] State Grid Economic Technology Research Institute Co., Ltd., Beijing 102209, China

Abstract. Moisture is one of the main factors affecting the insulation performance of transformer oil paper in operation, and it is of great engineering value to carry out diagnostic analysis of the moisture state of the paper. In order to study the partial discharge characteristics of oil-impregnated paper after dampness, this paper selects the turn-to-turn discharge models as normal model and damp model according to the actual situation of valve-side winding of the converter. The experimental platform of AC-DC composite voltage partial discharge test is built. Through the experimental study, it is found that the partial discharge characteristics of the two models are different under the action of AC-DC compound voltage. The partial discharge onset voltage of the damped model is 7.69% lower than that of the normal model, and the discharge volume and pulse repetition rate of different discharge stages are higher than those of the normal model as the discharge develops. The types of gas production in the two models were also not the same, and the methane content was higher in the damped model. The electrical strength of the oil-impregnated paper after dampness is lower than normal, and the results of this paper can provide some reference for the operation and maintenance of the converter transformer.

Keywords: Oil-impregnated Damp Paper · Partial Discharge · Oil-paper Insulation · Discharge Gas Production

1 Introduction

In recent years, with the construction of high-voltage DC transmission projects, the reliability of the DC transmission system has also attracted much attention. The reliable operation of the converter station and converter transformer is an important guarantee for the safe operation of the DC transmission system. Among them, the insulation level of the converter transformer directly affects the operation status of the converter station. Due to the complex operating conditions of the converter transformer, it is difficult to design and operate and maintain the insulation due to the joint action of AC, DC and AC/DC compound voltage for a long time. According to the research, nearly half of the accidents

of converter transformers are caused by the deterioration of insulation performance. Among them, moisture in oil-paper insulation is the most important cause of transformer insulation failure. The moisture in the air is easily invaded into the transformer tank during the process of installation or operation. When the moisture is invaded, it will be dissolved in the insulation oil, and then the moisture will spread to the oil-impregnated insulation paper in the insulation oil, which will lead to the damp paper seriously affecting the electrical strength of the oil-paper insulation, gradually triggering the discharge, expanding the insulation defects, and finally the insulation failure.

Researchers at home and abroad have long been concerned with the problem of moisture in oil-paper insulation structures, and have conducted numerous studies on moisture exposure in operating conditions. For the moisture exposure of the oil paper structure, Quanmin Dai et al. concluded that the moisture content in the longitudinal upper part of the multi-layer oil paper structure is higher than that in the lower and middle parts of the transformer oil tank [1]. Ming Dong et al. studied the polarization and conductivity processes of the oil paper structure under the influence of moisture. And moisture has a significant effect on the surface discharge activity of oil-paper insulation [2]. It was shown that the discharge onset voltage and flashover voltage decreased with the increase of water content [3, 4].

The current research focuses on the dielectric properties of damped paper, but the quantitative analysis of the discharge characteristics of insulating paper after dampness is less, so it is necessary to study the partial discharge characteristics of damped oil-impregnated paper. Therefore, a partial discharge detection platform under the action of AC-DC compound voltage is established, and the results such as discharge volume and gas production characteristics of the damped model of oil-impregnated paper at different stages are obtained, and the partial discharge characteristics of the processed damped model are compared with those of the normal model. The results show that the partial discharge characteristics of different models are different, and the partial discharge accident of the internal insulation of the converter transformer cannot be detected according to the uniform fault monitoring standard, and the results of this paper provide some reference for transformer fault monitoring.

2 Test Model and Test Method

2.1 Test Platform

Since the operating conditions of the converter transformer are very complex, this paper takes into account the requirements of experimental temperature, oil flow, electric field conditions and online oil extraction in the test conditions in order to simulate the actual operating conditions. In order to realize the above requirements, the test platform has circulating oil circuit, magnetic oil pump, heating system, flow rate detection and online oil extraction port and other parts in addition to the test chamber, and the experimental chamber is shown in Fig. 1(a).

The entire experimental circuit is heated using an external oil bath, and the oil circulation function is performed by a magnetic pump and a flow meter. The circulation pump is responsible for driving the flow of transformer oil within the test chamber, and

the flow meter is used to monitor the transformer oil flow in real time and control the real time flow rate through a valve [5].

When the test platform is used, first connect the AC voltage and DC power supply to the test chamber respectively, put the model to be tested and test products in the test chamber, close the test chamber, open the oil filter, circulation pump and oil bath heating box to fill the transformer oil, wait for the oil bath heating box to heat the transformer oil to the specified temperature, adjust the valve at the flow meter to control the oil flow rate of the whole circulating oil circuit, wait for the whole test platform environment to reach the required When the entire test platform environment reached the required, connect the detection and acquisition equipment. The experimental circuit diagram is shown in Fig. 1(b).

(a) Experimental chamber   (b) Test circuit
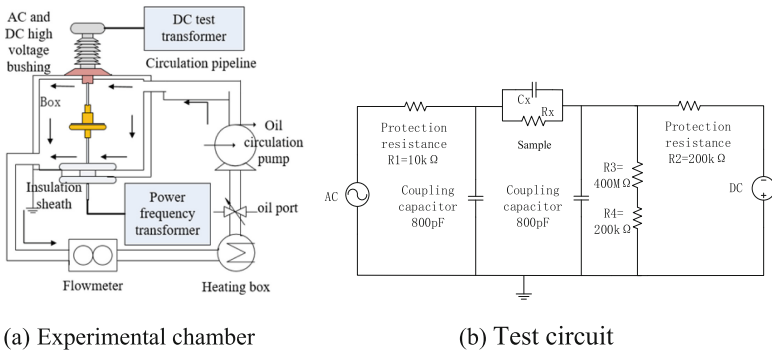
Fig. 1. Experimental chamber and test circuit

2.2   Test Model

In this paper, two test models were designed, a normal model and a damped model. Both models have the same dimensions and are installed in the same way inside the cavity. The purpose of the damped model is to control the moisture in the insulating paper to simulate the operating condition after moisture intrusion in the converter transformer. The insulating paper was treated by first drying it through a blast drying oven for 24 h. Then the vacuum drying oven was set at 85 °C with a vacuum of 100 Pa and the insulating paper was dipped in oil for 24 h. After setting the vacuum drying oven at room temperature and continuing the oil dipping cooling treatment for 24 h, the water content in the normal model insulating paper was 0.5%, which met the actual operating requirements of the transformer. After putting the dried insulating paper into a constant temperature and humidity box under certain conditions, a specimen with 2% water content in the paper is obtained as a model with moisture defects.

The paper used for the test is the actual transformer insulation paper and the transformer oil is Kunlun Kramer 25# transformer oil, and the specific effects of the two models are shown in Fig. 2.
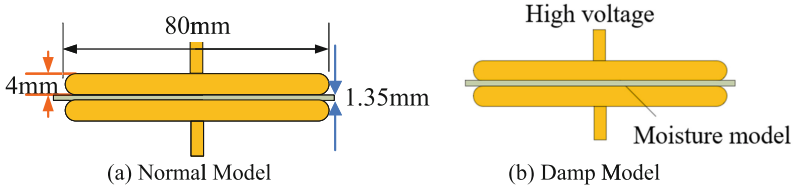
Fig. 2. Test model

3   Analysis of Test Results

In this paper, the ratio of AC-DC compound voltage is set to 1:3, and the partial discharge tests are conducted on the normal model and the damped model under the action of AC-DC compound voltage. The partial discharge characteristics of the two oil-paper insulation models are obtained from the test, and the whole partial discharge process is divided into three stages of initiation, development and danger, and the change of discharge law is summarized.

3.1   Experimental Model Discharge Gas Production Law

Figure 3 shows the gas production characteristics of the two models during partial discharge under the action of AC-DC compound voltage. The test circuit realized the online oil extraction function, and the dissolved gas in the oil was taken every 20 min and analyzed by gas chromatograph. The changes of gas in the oil were mainly recorded from the beginning of pressurization to 120 min. The changes of dissolved hydrogen and acetylene in the oil were more obvious with the development of partial discharge after the occurrence of normal model. However, the content of hydrogen did not increase significantly after the partial discharge of the damped model, and the change of methane was very obvious, reaching about 3 ppm after 120 min, and acetylene was still not detectable in the oil after the partial discharge of the damped model, and the content of ethane was also very small.
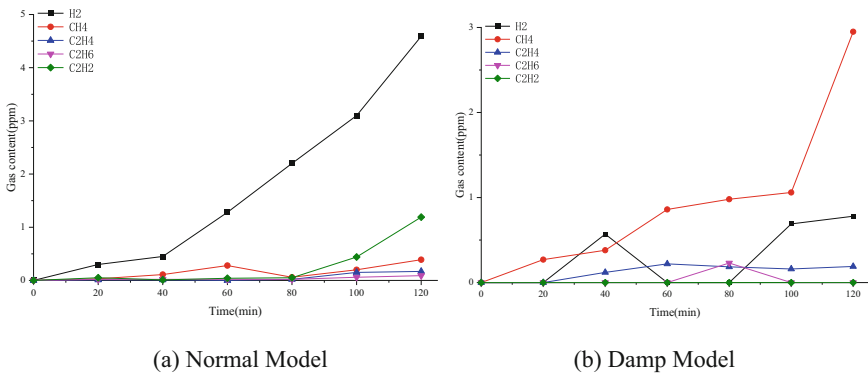
Fig. 3. Model partial discharge gas production characteristics

3.2   Variation Law of Partial Discharge Onset Voltage of the Test Model

The test uses the step-up method to test the partial discharge onset voltage, and the experimental result statistics are shown in Fig. 4(a). Since this paper uses AC-DC composite voltage, the partial discharge onset voltage is defined as the sum of AC voltage RMS and DC voltage average as the total onset voltage U_i. By comparing the test results in the figure, the partial discharge onset voltage of the damped model is 12 kV, which is smaller than the partial discharge onset voltage of the normal model. Compared with the normal model, the partial discharge onset voltage of the damped model decreased by 7.69%. In addition, the phenomena recorded by the video show that there are no obvious bubbles or sparks during the whole process of inter-turn discharge of oil-paper insulation under the action of compound voltage.

(a) Partial discharge starting voltage   (b) Pulse repetition rate
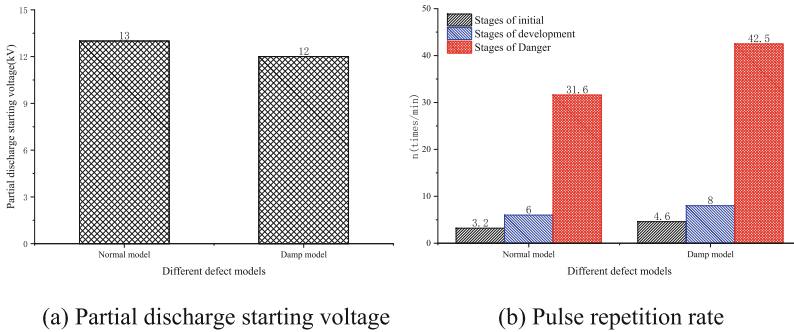
Fig. 4.   Starting voltage and pulse repetition rate

3.3   Variation Pattern of Local Discharge Pulse Repetition Rate and Discharge Volume

In this paper, the pulse repetition rate is defined as the number of discharges per unit time [8]. The AC-DC compound voltage is applied to the test model and the partial discharge test is performed on the oil-paper insulation model, and the results are statistically presented in Fig. 4(b). The figure mainly shows the trend of the repetition rate of discharge pulses for the normal model and the damped model in the discharge initiation phase, development phase and danger phase. During the development of partial discharge, the repetition rate of discharge pulses of the damped model is always higher than that of the normal model. The pulse repetition rate of both models was not high in the initial stage of discharge, and was 3.2 for the normal model and 4.6 for the damp model per unit time. The measured pulse repetition rate increased for both the normal and damp models during the development of partial discharge, and the number of partial discharges increased significantly and the development speed was faster for the damp model. When the partial discharge develops to the dangerous stage, the pulse repetition rate of the damp model has reached 42.5, which is 3486% higher than the initial stage. This is due to the fact that the electric field inside the insulating paper is assumed by the presence of

water molecules in the damp model compared to the normal model, resulting in many electric field distortion points and a higher probability of partial discharge, which leads to a higher repetition rate of discharge pulses.

Figure 5(a) shows the trend of the maximum discharge volume of the oil-paper insulation partial discharge starting stage, development stage and dangerous stage under the action of AC-DC compound voltage for both models. The maximum discharge q_{max} refers to the maximum value of all discharges at that stage. Figure 5(b) indicates the trend of the average discharge (the ratio of the total discharge to the number of discharges in this phase) for both models. Figure 5(c) represents the trend of the total discharge for both models. The results in the figure show that the metal impurity model has a higher maximum discharge than the normal model throughout the development of partial discharge, which is due to the presence of the metal impurity model that produces a large distortion in the electric field of the oil-paper insulation, and the probability of partial discharge at the location where the electric field is distorted is more than that of the normal model.

(a) Maximum discharge capacity (b) Average discharge capacity (c) Total discharge capacity
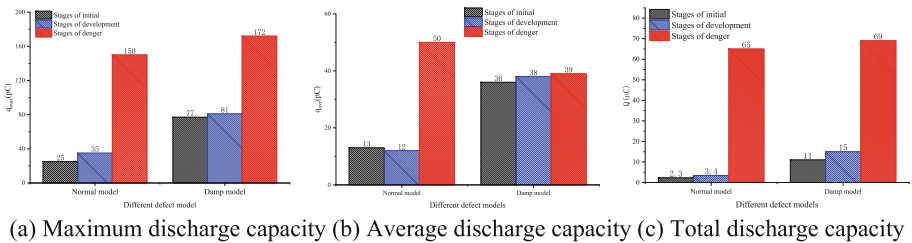
Fig. 5. Variation of discharge amount in different stages

3.4 The Variation Law of the Discharge Phase of the Test Model

The figure shows the phase distribution of partial discharges of the two models. From the results of the figure, it can be seen that the discharge points are less in the beginning and development stages of the normal model, and the phases in the later stages of the discharge are mainly concentrated in $120° - 180°$, $220° - 260°$, $330° - 360°$. With the development of partial discharge, the discharge defects are expanded resulting in a large number of discharge points in several phases. Under the influence of moisture, the damp model has a large number of discharge points in the positive half of the discharge when it first appears, and the discharge in the negative half is mainly concentrated in $240°$ and $300°$. With the development of the discharge, the discharge phases of the developing and dangerous phases of the damped model are basically the same as the initial phase, but the number of discharge points increases significantly (Table 1).

Table 1. Phase change of two model discharges
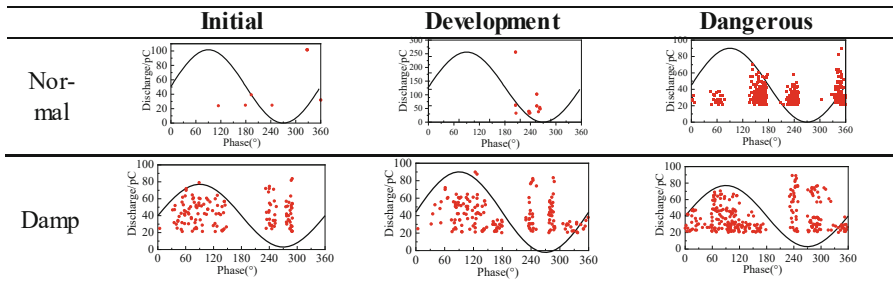
4   Conclusion

(1) According to the installation and operation specifications of converter transformers, moisture intrusion into the transformer interior can result in elevated moisture content in transformer oil and insulating paper. In this paper, partial discharge tests were conducted on the damp model and the normal model of insulating paper under the action of AC/DC compound voltage. It is found that the electrical strength of the damp model is significantly lower than that of the normal model, and the partial discharge characteristics of the two models are different.

(2) This paper mainly compares the partial discharge characteristics of the two models. The discharge onset voltage of the damp model is lower and more likely to have partial discharge accidents. And the number of discharges in the damp model is 34.49% higher than that of the normal model in unit time. Comparing the partial discharge characteristics, the discharge volume and discharge phase of the two models are very different, and the gas production characteristics of the discharge are also different.

(3) It is suggested that the subsequent study can set up the insulating paper discharge model with moisture gradient and explore the relationship between moisture content and the discharge characteristics of oil-paper insulation. Alternatively, the creepage characteristics and breakdown strength variation of insulating paper with high moisture content under the action of different voltage types could be investigated.

References

1. Ran, Z., Ye, T., et al.: Study on moisture distribution of multi-surround oil-paper insulation under moist environment. In: International Conference on Condition Monitoring & Diagnosis, vol. 12, pp. 365–367. IEEE, Guangzhou, China (2018)

2. Li, X., Cui, Y., et al.: Effect of oil-paper damped state on characteristics of surface discharge process under AC-DC combined voltage. In: 12th IEEE International Conference on the Properties and Applications of Dielectric Materials, vol. 8, pp. 1070–1073. Xi'an, China (2018)
3. Hu, Y., et al.: Parameters extraction and mechanism analysis of the moisture in oil-paper based on the spectral decomposition of dielectric response. IEEE Trans. Dielectr. Electr. Insul. **29**(4), 1441–1449 (2022)
4. Sha, Y., Zhou, Y., Zhang, L., Huang, M., Jin, F.: Measurement and simulation of partial discharge in oil-paper insulation under the combined AC–DC voltage. J. Electrostat. **71**(3), 540–546 (2013). https://doi.org/10.1016/j.elstat.2012.11.013
5. Chang, W., et al.: Study on partial discharge characteristics of oil-immersed paper in wrinkled state under alternating current and direct current compound voltage. J. Phys. Conf. Ser. **2030**(1), 012020 (2021). https://doi.org/10.1088/1742-6596/2030/1/012020

Simulation Study on Influencing Factors of Electric and Mechanical Energy Hybrid Harvester for Power Transmission Lines

Liu Cao[1], Yulong Liu[1], Fei Sheng[1], Zufen Wu[2(✉)], Dongyang Hu[2], Xiaolong Huang[2], and She Chen[2]

[1] State Grid Wulumuqi Electric Power Supply Company, Wulumuqi 830054, China
[2] College of Electrical and Information Engineering, Hunan University, Changsha 410082, China
{wuzufen,chenshe}@hnu.edu.cn

Abstract. The stable power supply of monitoring devices on the transmission lines has been a practical problem for a long time. In this work, we propose an electric filed and mechanical energy hybrid harvester (EFMEH). With a coaxial rotatory freestanding triboelectric nanogenerator combined with a high-potential electric filed energy harvester as the basic structure, the EFMEH can capture the electric filed energy from the grid transmission line and the mechanical energy such as wind and raindrop energy from the external environment simultaneously. Compared with mechanical energy harvester (MEH), it can significantly improve the power supply reliability of the monitoring devices on the transmission lines. In order to study the output characteristics of the EFMEH and clarify the influence of key parameters on the output, a finite element model has been built. The simulation results show that both the operating voltage and the triboelectric effect cause periodic changes in the potential of the stator electrode. It has been demonstrated show that the output voltage amplitude can reach 810.81 V when the radius of the transmission line is 1 cm, and the total coupling capacitance is 38.79 pF when the number of stator electrodes is 16.

Keywords: Condition monitoring device · electric filed energy harvesting · triboelectric nanogenerators

1 Introduction

With the economic growth, human society's demand for electricity is increasing, and sustainable energy sources has also been developing in order to achieve national carbon peak and carbon neutral goals [1]. In the power system, it is particularly important to monitor working conditions of the equipment or real-time monitoring of power lines status, such as lightning, ice cover, fouling, vibration, etc. [2] Most of the high-voltage lines are in remote areas and it will consume a lot of manpower for daily operation and maintenance. The deployment of monitoring devices can achieve remote monitoring and solve the problem. However, the monitoring device needs to work on or around the high-voltage power lines, how to supply stable power to them is a difficult problem [3].

In the practical engineering, solar, wind, electric field and other energy harvesting methods are typically used, and other energy are converted into electrical energy through the energy harvester. The obtained electrical energy is stored in the battery and discharge when the monitoring device needs electricity [4]. However, solar energy harvester efficiency is low, and it is vulnerable to weather and time. In rainy weather or night, it cannot be used, resulting in unstable power supply. Although wind energy harvester technology is mature, it still has some disadvantages and is difficult to put into an encapsulated structure. Therefore, its service life is limited and it requires frequent maintenance. Electric filed energy harvester is stable and the structure is simple, but the output is AC small current. The circuit presents high capacitive impedance, and there is a dead zone of power supply [5–7]. In order to overcome this drawback, a composite power supply system combining electric filed energy on the high-voltage side and artificial light source on the low-voltage side have been proposed [8], using artificial light source as a backup power source. This system can solve the problem of dead zone of electric field induction. However, the low-voltage side artificial light source requires external power supply, which is more inconvenient to use, and the energy is not highly efficient to utilize after secondary conversion.

In this work, we take advantage of the fact that the triboelectric nanogenerator can effectively convert the mechanical energy into electrical energy and combine the electric field energy harvester and the triboelectric nanogenerator. Then, we propose a dual-capture energy harvester combining electric field energy and vibration energy. In order to study the output characteristics of the hybrid harvester and clarify the effects of different design parameters on the output, a finite element model of the hybrid harvester was established. The hybrid harvester mode can effectively capture both electric field energy and mechanical energy.

2 Principle of Dual Capture Energy Technology

2.1 Principle of Electric Field Energy Harvester Technology

The basic principle of Electric filed energy harvesting (EFEH) is the basic principle is to charge the capacitor through the displacement current between the high-voltage line and the electrode. After the capacitor acquires enough energy, it then supplies the load through the management circuit [8, 9]. There are stray capacitance C_{ce} between transmission line and metal plate, and coupling capacitance C_{ed} between metal electrode and ground. The equivalent capacitance C_{eq} between transmission line and ground is:

$$C_{eq} = \frac{C_{ce}C_{ed}}{C_{ce} + C_{ed}} \tag{1}$$

The voltage of the transmission line is U_{ac}, then the current I_{ac} between the transmission line and ground is:

$$\dot{I}_{ac} = \frac{\dot{U}_{ac}}{jwC_{eq}} \tag{2}$$

The transmission line voltage U_{ac} is a stable value and the capacitance C_{eq} between the transmission line and ground is a fixed value. So the current I_{ac} is a stable value from Eq. (2). The electric field energy harvester technology is to use this stable current to convert electric field energy into electrical energy and store it with capacitor or directly power the load. In the high potential energy harvester mode, the load is connected in parallel at the capacitor C_{ce}, which can directly power the load. The main influence of the current is the coupling capacitor C_{ed}, and the stray capacitor C_{ce} has little influence on the current (Fig. 1).
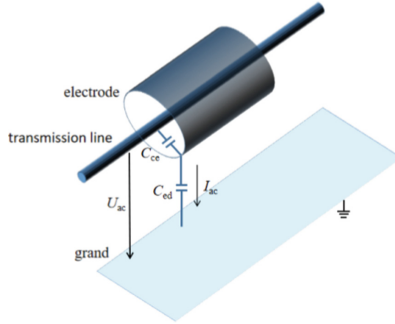
Fig. 1. Schematic diagram of electric field harvester

2.2 Principle of Triboelectric Nanogenerator Energy Harvester Technology

Triboelectric nanogenerator (TENG) is an energy harvester technology that converts mechanical energy into electrical energy, working on the combination of both frictional and electrostatic induction effects. This technology converts mechanical energy into electrical energy by using mechanical movements derived from body movements, wind energy, and environmental vibrations. According to the operating principle, TENG is divided into four main categories: vertical contact separation, lateral sliding, single electrode, and independent frictional electric layer modes [10–12]. In this work, the transverse sliding mode is selected, and the specific process is shown in Fig. 2.

The outer metal electrode rubs against the friction material under the action of external mechanical energy. Due to the different electronegativity of the metal and the friction material, electrons move from the outer metal electrode to the friction material, so the metal electrode is positively charged and the friction material is negatively charged. Because the surface area of the outer metal electrode is the general surface area of the friction material, the charge density of the outer metal electrode is twice the charge density of the friction material. Step 1: The inner left metal electrode is induced as positive potential, and the right electrode is induced as negative potential, so the current direction is from left to right. Step 2: The outer metal electrode gradually moves to the right under the action of external vibration, reaching the middle of the two inner metal electrodes. There is no potential difference between the two pole plates, and the load has no current. Step 3: When the outer metal electrode moves to the top of the right inner electrode, the

right electrode induces a positive potential, the left electrode induces a negative potential, and the current direction is from right to left. Change the structure in the figure to a ring shape, then the load can be powered continuously.
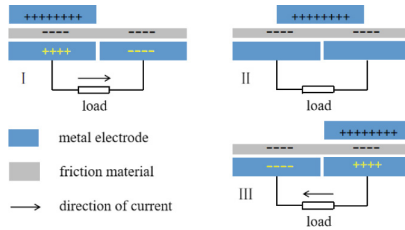
Fig. 2. Principle of energy harvester of triboelectric nanogenerator

3   Hybrid Harvester Model Design and Simulation

A dual-capture simulation model was built using COMSOL Multiphysics as shown in Fig. 3, in which the triboelectric nanogenerator structure is composed of rotor electrode, PTFE and stator electrode together, and the field energy harvester structure is composed of transmission line, insulation layer and stator electrode.
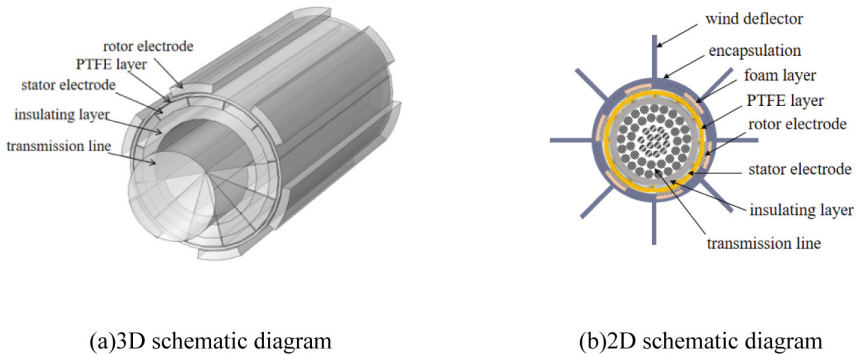
(a)3D schematic diagram   (b)2D schematic diagram

Fig. 3. Schematic diagram of hybrid harvester

3.1   Electric Field Energy Harvester Model Simulation

To investigate the factors affecting the output voltage amplitude of the electric field induction, three main aspects are analyzed: the transmission line radius r_1, the insulation layer thickness d_i, and the dielectric constant ε_i of the insulation layer.

1)   The effect of transmission line route radius r_1

The thickness of the insulation layer is 1cm and the relative dielectric constant of the insulation layer is 10. The effect of r_1 on the output voltage amplitude is investigated by changing the wire radius of the transmission line, which is shown in the Fig. 4. The output voltage waveform at $r_1 = 2$ cm is shown in the Fig. 5. As the line radius increases, the output voltage amplitude decreases gradually from 810.81 V to 413.37 V. However, the magnitude of the decrease gradually decreases. When the transmission line radius is 1.03 cm, the voltage amplitude is reduced by about 127.75 V because of an increase of 0.3 cm line radius. When the transmission line radius is 2.37 cm, the voltage amplitude is reduced by about 38.6 V because of an increase of 0.3 cm line radius.
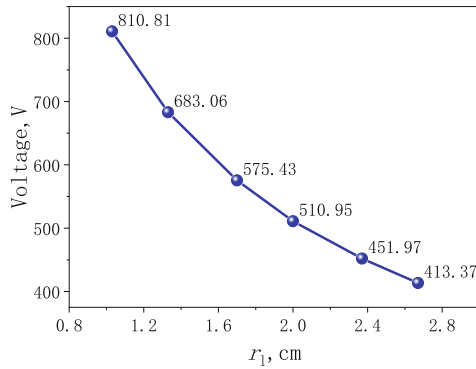
Fig. 4. Effect of r_1 on output voltage amplitude
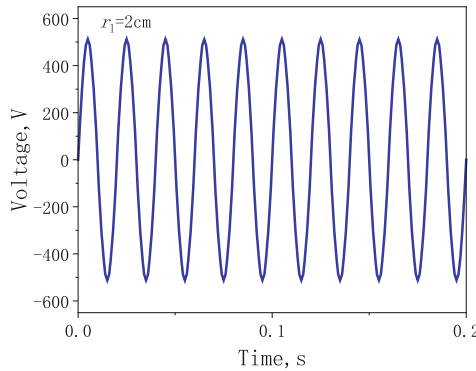
Fig. 5. Output voltage waveform when $r_1 = 2$ cm

2) The effect of insulation layer thickness

The radius of the transmission line is 2 cm and the relative dielectric constant of the insulation layer is 10. The thickness of the insulation layer is varied and the results is shown in Fig. 6. It can be seen that as the thickness of the insulation layer increases,

the output voltage amplitude increases accordingly, but the magnitude of the increase decreases. The transmission line is cylindrical, and the electric field in close proximity can be approximated as a uniform electric field with constant voltage. So the increase in insulation thickness makes the potential difference larger, which means the output voltage increases. But the further away from the transmission line, the smaller the field strength, so the amplitude increase is reduced.
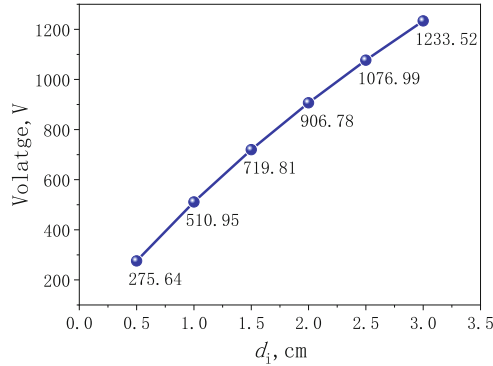
Fig. 6. Effect of insulation thickness on output voltage amplitude

3) The effect of the relative dielectric constant of the insulation layer

The radius of the transmission line is 2 cm and the thickness of the insulation layer is 1 cm. The relative dielectric constant of the insulation layer is changed and the results is obtained in Fig. 7. It can be seen that the output voltage amplitude decreases with the relative dielectric constant of the insulation layer. When the relative dielectric constant of the insulation layer increases from 5 to 10, the voltage amplitude decreases from 1019.01 V to 511.15 V. When the relative dielectric constant increases from 30 to 35, the voltage amplitude decreases from 171.27 V to 146.84 V.
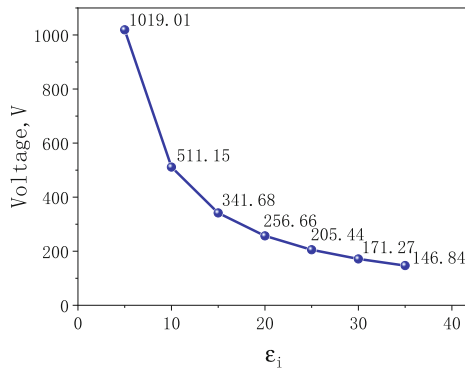
Fig. 7. Effect of relative dielectric constant of the insulation layer on the output voltage amplitude

From the previous analysis, it can be demonstrated that the device can be installed on the transmission line of small radius. If we want to increase the output voltage of the electric field energy harvester, the thickness of the insulation layer can be increased and the relative dielectric constant of the insulation layer can be reduced. However, it is necessary to consider the line insulation and the actual local environment to avoid the impact on the line. In addition, the larger device is more likely to cause damage, so the insulation thickness should not be too large.

3.2 Triboelectric Nanogenerator Model Simulation

To investigate the factors affecting the output voltage amplitude of the triboelectric nanogenerator, two main aspects are analyzed: the PTFE surface charge density σ and the PTFE thickness d_p.

1) The effect of PTFE surface charge density σ

The PTFE thickness is 2 mm, Fig. 8 and Fig. 9 show the effect of PTFE surface charge density on the output voltage amplitude of TENG. With the increase of σ, the output voltage amplitude gradually increases, and the voltage amplitude is linearly related to σ. When σ increases by 2×10^{-6} C/m^2, the output voltage amplitude increased by about 305.69 V.
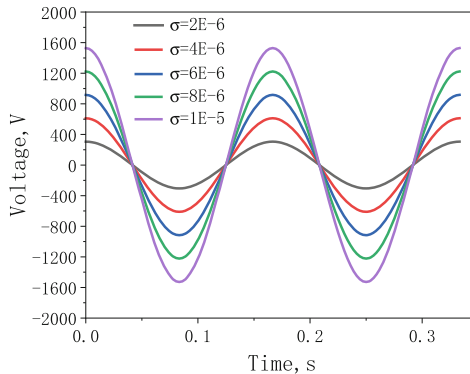
Fig. 8. Output curves of triboelectric nanogenerator

2) Effect of PTFE thickness d_p

The σ is kept at 2×10^{-6} C/m^2, and Fig. 10 shows the effect of PTFE thickness on the output voltage amplitude of TENG. With the increase of PTFE thickness, the output voltage amplitude gradually decreases, and the magnitude of the decrease gradually decreases. When the d_p is 1 mm, the output voltage amplitude can reach 1294.1 V, and when the d_p is 5 mm, the output voltage amplitude is 483.97 V, which is only 37.40% of that at 1 mm.
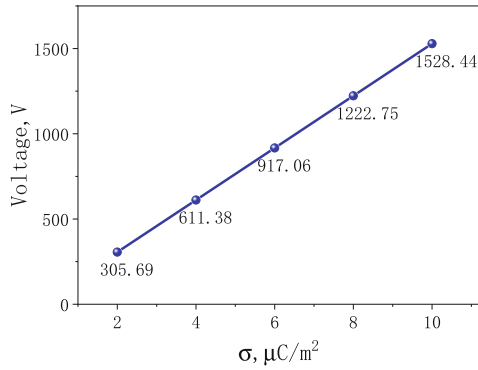
Fig. 9. Effect of σ on output voltage amplitude
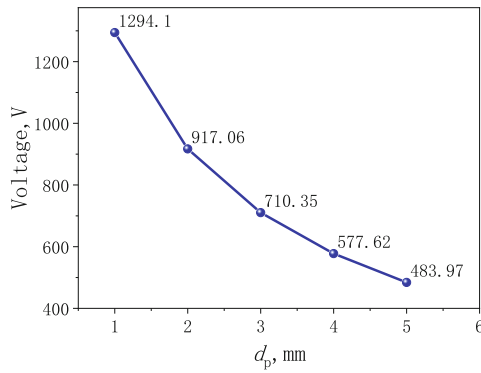
Fig. 10. Effect of d_p on output voltage amplitude

From the above analysis, it can be found that the output voltage amplitude of the triboelectric nanogenerator is positively related to σ and negatively related to d_p. Therefore in order to increase the output voltage, the friction material is suitable for the use of materials that are easy to gain and lose electrons, and the material thickness should be thin.

4   Discussion on Coupling Capacitance

From the working principle of energy harvester by electric field, it is known that when the capacitance of the energy harvester electrode plate to ground is larger, the capacitance impedance is smaller and the current flowing through the load is larger. Due to the small size of the stator electrode, the single electrode capacitance is small, so the coupling capacitance value can be improved by connecting the stator electrodes in parallel. In order to study the influencing factors of coupling capacitance, a simulation model has been established.

The simulation results show that the single capacitance decreases and the coupling capacitance increases as the number of stator electrodes increases. When the number

of stator electrodes is 4, the individual capacitance value is 3.54 pF and the coupling capacitance is 14.15 pF. When the number of stator electrodes is 16, the individual capacitance value is 2.42 pF and the coupling capacitance is 38.79 pF. As the number of stator electrodes increases, the width of electrodes decreases, so the size of single capacitance decreases. Due to the small size of the electrodes, the single capacitance decreases, but the reduction is not significant. The magnitude of the coupling capacitance is approximately linearly related to the number of stator electrodes, and the results obtained from the theoretical analysis and simulation are the same (Fig. 11).

Therefore, to make the total coupling capacitance larger, the number of stator electrodes can be increased. But if the number of stator electrodes become greater, it means that the width of the electrodes is thinner and the strength is smaller, which is more likely to cause damage to the stator electrodes. Therefore, it is necessary to choose a suitable number of stator electrodes in the device, which can increase the total coupling capacitance and have a certain strength at the same time.
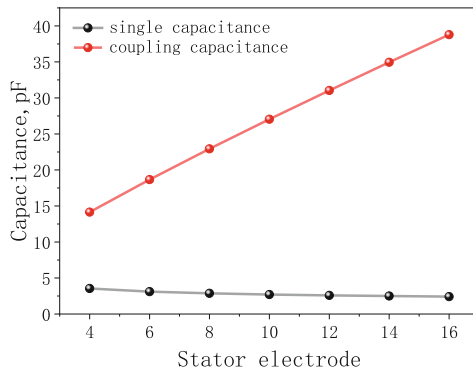
Fig. 11. Effect of the number of stator electrodes on capacitance

5 Conclusions

In this work, a power supply technology has been proposed for condition monitoring devices based on the dual capture method of electric field and vibration energy. A hybrid harvester structure has been established, in which electric field induction and triboelectric nanogenerator are used to capture energy through the same structure. The electric field energy comes from the internal grid and the mechanical vibration energy comes from the external environment, and the energy harvester sources are complementary, which can improve the reliability of power supply.

We have analyzed the influencing factors of the electric field energy harvester module and the triboelectric nanogenerator energy harvester. The transmission line radius, insulation layer thickness, insulation layer relative dielectric constant, PTFE surface charge density and PTFE thickness are investigated. It has been demonstrated show that the EFEH output voltage amplitude can reach 1233.52 V and the TENG output voltage

amplitude can reach 1528.44 V. In addition, the single coupling capacitance is 2.42 pF and the total coupling capacitance is 38.79 pF when the number of stator electrodes is 16.

References

1. Xiao, X.Y., Zheng, Z.: New power systems with new energy sources under the "double carbon" target: contributions, key technologies and challenges. Eng. Sci. Technol. **54**(01), 47–59 (2022)
2. Guo, S., Wang, P., Zhang, J., et al.: An overview of electromagnetic energy collection and storage technologies for a high voltage transmission system. Energy Storage Sci. Technol. **8**(01), 32–46 (2019)
3. Zhi, R., Liu, Z., Zhang, L., Lu, W.: Research and application of online monitoring power supply for high-voltage transmission lines. Power Technol. **39**(02), 413–415 (2015)
4. Guo, D., Wang, P., Zhang, J., et al.: A review of electromagnetic energy harvesting and storage technologies for high-voltage transmission systems. Energy Storage Sci. Technol. **8**(01), 32–46 (2019)
5. Kang, R., Lin, H., Yang, M.: Review on power supply technology for on-line monitoring device of middle and high voltage electrical equipment. Electr. Energy Manage. Technol. **06**, 1–7 (2016)
6. Lei, J.: Analysis of key technologies in wind power and photovoltaic power generation. Integr. Circuit Appl. **39**(11), 324–325 (2022). https://doi.org/10.19339/j.issn.1674-2583.2022.11.146
7. Wang, L., Li, Z., Meng, X., et al.: Power supply technology for low power online monitoring sensors based on electric field induction. High Voltage Technol. **46**(02), 538–545 (2020)
8. Luo, Y.P., Zeng, X.J., Lei, Y.P., et al.: High-voltage electric field induction energy harvester technology based on discharge method. Power Syst. Autom. **39**(08), 113–119 (2015)
9. Wang, L., Li, Z., Meng, X., et al.: Optimal design of a wireless energy harvester power supply for AC electric field. High Voltage Electron. **56**(05), 121–127 (2020)
10. Menendez, O., Cheein, F.A.A., Rodriguez, J.: Displacement current-based energy harvesters in power grids: topologies and performance evaluation. IEEE Ind. Electron. Mag. **16**(3), 52–66 (2021)
11. Zeng, Q.X., Wu, Y., Tang, Q., et al.: A high-efficient breeze energy harvester utilizing a full-packaged triboelectric nanogenerator based on flow-induced vibration. Nano Energy **70**, 104524 (2020)
12. Yang, Y., Zhang, H.L., Chen, J., et al.: Single-electrode-based sliding triboelectric nanogenerator for self-powered displacement vector sensor system. ACS Nano **7**(8), 7342–7351 (2013)

Analysis of DC Inductive Arc Restriking Characteristics of HVDC Relays

Xin Huang, Wanqing Chen, and Jingxuan Lin[(✉)]

State Grid Fujian Economic Research Institute, Fuzhou, China
172276781@qq.com

Abstract. Arc restriking will prolong the arc extinguishing time and increase the erosion of the contacts, seriously reduces the electrical life and reliability of the relays. In particular, arc restriking is more likely to happen in DC circuit with inductive load. Therefore, based on MHD theory, this paper uses COMSOL Multiphysics to establish a two-dimensional mathematical model of arc plasma of HVDC relays. By applying different sizes of magnetic field, the arc voltage, current and images are obtained to analyze the arc restriking characteristics in a circuit with a load of 100 V/100 A. The results show that increasing the external magnetic field in a certain range is beneficial to accelerate the arc extinguishing. However, as the external magnetic field increases further, the arc restriking is more easily and earlier to happen.

Keywords: HVDC relay · DC arc · restriking · magnetohydrodynamics

1 Introduction

In the process of DC arc movement, there are only high-temperature gases and a small amount of metal vapor exist in the arc gap [1]. When the electric field strength of the arc gap reaches the critical restriking field strength, arc restriking happens. At the same time, the arc will temporarily stay between the arc gap or the arc root will move on the surface of the contact, which is called arc stagnation [2]. The arc restriking phenomenon of relays with a arc extinguishing chamber has been the focus of scholars [3, 4]. Literature [2] showed the influence of different current on arc stagnation and restriking, and obtained the critical restriking field strength through the combination of experiment and simulation. Multiple arc column restriking phenomenon are showed in literature [5] under the condition of 450 V/10 A DC, and relationship between the restriking frequency of silver contacts and the strength of the magnetic field and electric field. Literature [6] showed the restriking phenomenon at DC V. The probability of arc restriking phenomenon under different voltages is studied in literature [7], and a simplified simulation model of analyzing the mechanism of restriking is established. The above studies on arc restriking did not consider the effect of metal vapor and was all carried out under high voltage direct current.

In this paper, the arc restriking characteristics of 100 V/100 A DC are studied. The result shows that the arc restriking increases increases the arcing time and the erosion of

the contacts, which will reduce the electrical life and reliability of the relays. Therefore, a mathematical model of DC arc is established based on MHD and the influence of external magnetic field on arc restriking characteristics is studied.

2 Experiment

2.1 Structure of the Arc Test System

In this paper, a DC arc test system is used to collect arc images and parameters of the HVDC relay. The test system includes main circuit, controlling circuit, high-speed camera, and data acquisition part, as shown in Fig. 1. The main loop current is 100 A and the switching voltage is 100 V. A high-speed camera is used to capture images of the arc during the breaking process, and the data acquisition part collects the arc current and voltage. A permanent magnet is added to the back of the two pairs of contacts to provide transverse magnetic field with different magnetic field strength.
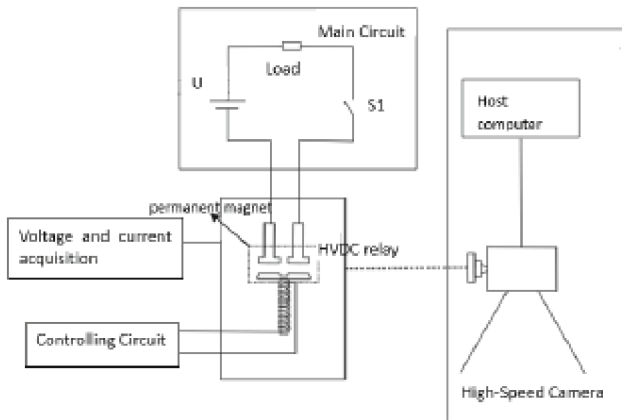
Fig. 1. Structure of the arc test system

2.2 Experiment

Figure 2 shows the images of DC inductive arc restriking during the breaking process when the magnetic flux density is 40 mT and the arc voltage and current is 100 V and 100 A respectively. As shown in the picture, at t = 1.18 ms, a prebreakdown channel is formed at point A, which is white spot, namely luminescent plasma. At t = 1.24 ms, the luminescent plasma is transformed into arc, and the arc reignites between the contact and the arc column.

   The free gas remains due to the temperature of arc area, and needs a certain amount of time to spread, decreasing the strength of the insulation of the arc gap. The arc root moves to the edge of the contact. Then the arc is elongated, the arc voltage increases rapidly, which leads to the arc restriking. The new arc column and the original arc column

form a parallel channel, which makes the arc resistance drop rapidly. Figure 3 is the arc voltage waveform. It can be seen from the figure that the arc voltage drops at point 1 marked in the figure, corresponding to point A in Fig. 2. The drop of voltage is precisely because the arc restriking, two arcs are connected in parallel, and the resistance drops, and the voltage also drops.

Arc restrikig will be affected by voltage, current, magnetic field and arc extinguishing medium. In this paper, the experiment of breaking 100 V/100 A inductive load was carried out for 40 times for HVDC relay. The obtained arc restriking times in air medium are shown in Fig. 4. It can be seen from the figure that with the increase of the applied magnetic field, the frequency of arc restriking also increases. When the applied magnetic field is greater than 40 mT, the probability of arc restriking is more than 50%, and when it is 60 mT, the probability of arc restrking is 95%.
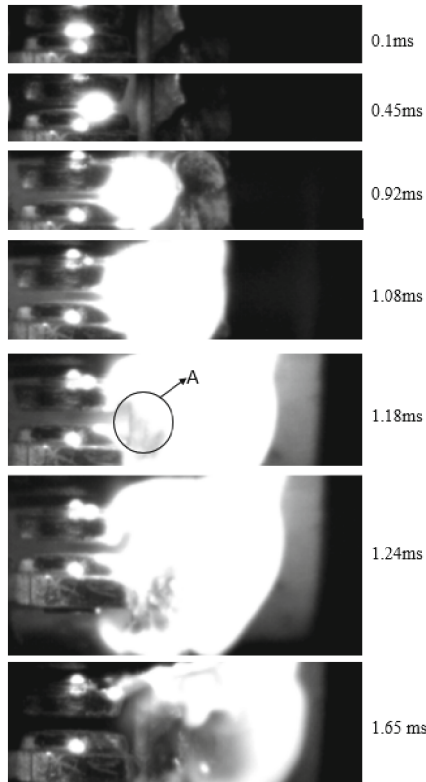
Fig. 2. Arc restriking images during the breaking process
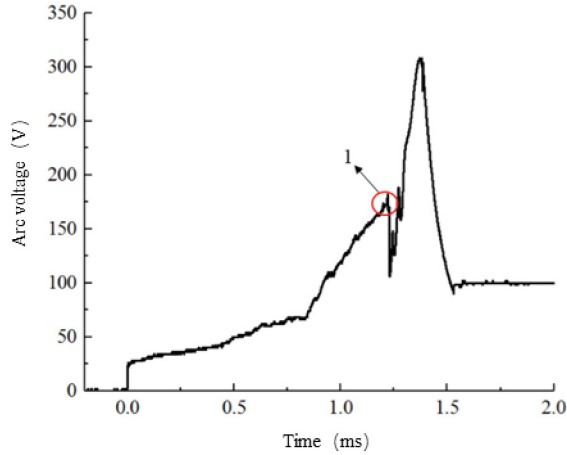
Fig. 3. Arc restriking voltage during the breaking process
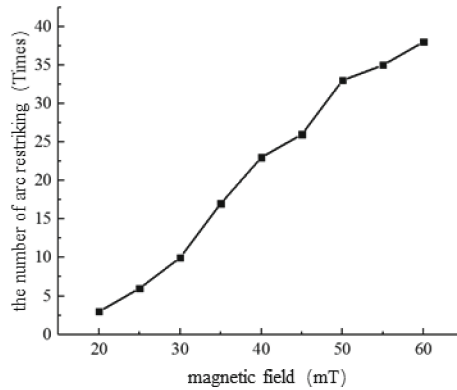
Fig. 4. The number of arc restriking times under different magnetic field sizes

3   Numerical Model

3.1   Geometric Model

In this paper, a high voltage DC relay with bridge double break point structure is studied. The rated voltage of the relay is 150 V, the current is 100 A, the diameter of the moving contact and the fixed contact is 8 mm, and the material is silver tin oxide. Its structure is shown in Fig. 5. In the simulation of arc plasma, the improved model makes the calculation easier and reduces the simulation time. Because the contact system is symmetrical, only half of the arc extinguishing chamber needs to be simulated. The structure of the improved model is shown in Fig. 6. In the figure, the upper part is fixed contact and the lower part is moving contact, which moves in the negative direction of the y-axis. Through the relationship between moving contact time and displacement, the change of arc re-ignition during contact movement can be obtained.
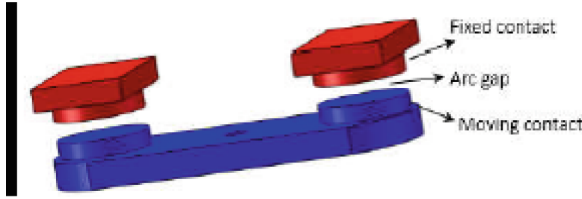
Fig. 5. Contact structure
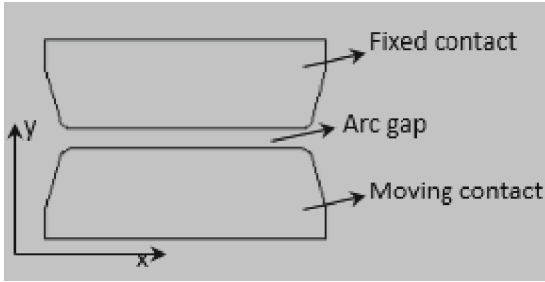
Fig. 6. Simplified model of the contacts

3.2 Government Equations

Through the above simulation, the change law of arc in the arc extinguishing chamber can be obtained. The flow field can be expressed by N-S equation and energy conservation equation, and the electromagnetic field can be expressed by Maxwell equation group [10].

The mass conservation equation as shown by (1):

$$\frac{\partial \rho}{\partial t} + div(\rho \vec{v}) = 0 \tag{1}$$

where ρ is the plasma density, which is related to the local temperature, t is the simulation time, and $\vec{v}$ is the velocity vector. B is obtained by solving the N-S equation, as shown in (2).

$$\frac{\partial \rho v_i}{\partial t} + div(\rho v_i \vec{v}) = -\frac{\partial P}{\partial x_i} + div(\eta grad v_i) + (\vec{J} \times (\vec{B}_{arc} + \vec{B}_{PM})) \tag{2}$$

where v_i is the ith component of the velocity vector. In 2-D MHD method, it stands for x and y components of the velocity p is the pressure which is also dependent on the temperature and η is the dynamic viscosity of plasma. The body force exerted on the arc plasma is the Lorentz's force which is generated by the self-generated magnetic field provided by the arc itself as well as the external magnetic field provided by the permanent magnets. The Lorentz's force exerted on each cell is calculated by $\vec{J} \times \vec{B}$, here, $\vec{J}$ is the current density and, $\vec{B}$ is the total magnetic flux density that consists of the magnetic flux densities generated by the arc itself $\vec{B}_{arc}$ and that generated by the permanent magnets $\vec{B}_{PM}$.

Where v_i is the ith component of $\overrightarrow{v}$. In two-dimensional space, it represents the component of velocity on the x and y axes. P is the pressure, indicating the dynamic viscosity of the plasma, and its value is related to the temperature. The arc plasma is affected by Lorentz force, which is generated by the arc itself and the permanent magnet. Lorentz force on each battery is represented by $\overrightarrow{J} \times \overrightarrow{B}$, and $\overrightarrow{J}$ is the current density and $\overrightarrow{B}$ is the total magnetic flux density.

Moreover, the physical property of the ambient atmosphere is closely related to the temperature. In MHD model, the solution of temperature is shown in formula (3).

$$\frac{\partial(\rho h)}{\partial t} + div\left(\rho h \overrightarrow{v}\right) = -div\left(\frac{\lambda}{c_p} gradh\right) + \sigma E^2 \tag{3}$$

where h is the enthalpy, λ is the thermal conductivity, c_p is the specific heat under constant pressure, σ is the electrical conductivity, and E is the magnitude of the electric field strength, σE^2 is the heat source for the arc which is the Joule's heat generated by the huge current density inside the arc column.

Where h is enthalpy, λ is thermal conductivity, c_p is specific heat, σ is conductivity, E is electric field strength, and σE^2 is heat generated by large current in the arc column.

It can be seen from the above equation that each physical quantity generated by the arc itself can be obtained from (4) – (6), as follows:

$$div(\sigma grad\varphi) = 0 \tag{4}$$

$$\overrightarrow{J} = \sigma \overrightarrow{E} = -\sigma \, grad\varphi \tag{5}$$

$$div(gradA_i) = -\mu_0 J_i \tag{6}$$

$$\overrightarrow{B}_{arc} = rot(\overrightarrow{A}) \tag{7}$$

where φ is the potential and $\overrightarrow{A}$ is the vector of magnetic potential.

3.3   Assumptions and Boundary Conditions

The arc motion is generated by the interaction of multiple physical quantities. The simulation assumptions are as follows [11, 12]:

(1) The arc environment is assumed to be LTE constant.
(2) Ignore the time of arc starting, and assume that the arc starts to burn steadily from 0.4 mm. Set the starting value of transient simulation as the temperature obtained by static simulation.
(3) Ignore the function of arc sheath.

The boundary conditions are determined by the theoretical basis of hydrodynamics, electromagnetism and plasma. In the electric field, as shown in Fig. 5, the movable contact is represented as anode, and the fixed contact is represented as cathode. The

current flows in from the anode, flows out from the cathode, and flows back to the anode through the external circuit current. Assuming that there is no current flow at the boundary of the simulation area, the calculation formula is $\vec{n} \cdot \vec{J} = 0$. In the air flow, the boundary of the simulation area is open, and the fluid can flow out of the boundary. The temperature involved in the calculation is the steady-state temperature value.

4　Simulation and Analysis

In this paper, uniform and constant transverse magnetic field is adopted, and its magnetic flux density of 40 mT, 50 mT and 60 mT is applied in simulation. The temperature change of the arc when the magnetic flux is 40 mT is shown in Fig. 7. The arc moves to the edge of the contact under Lorentz force at t = 0.86 ms, and the pre-breakdown channel appears at the root of the arc at t = 1.06 ms. At t = 1.15 ms, the luminescent plasma is transformed into arc, and the arc restriking between the contact and the arc column. Two arcs are connected in parallel way, and the resistance decreases.
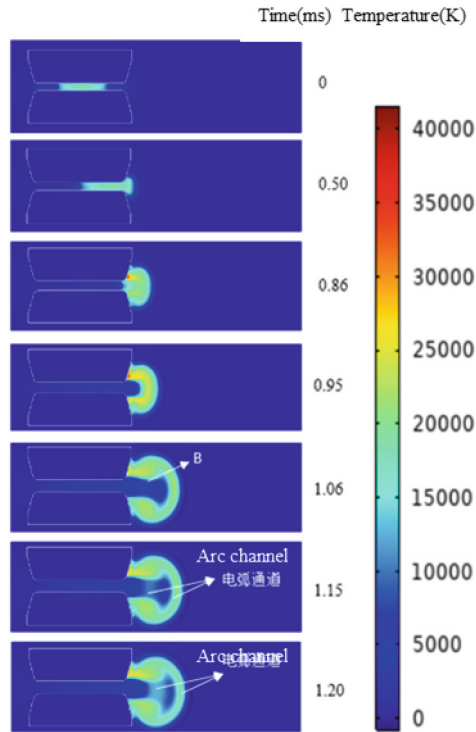
Fig. 7. Variation of arc temperature with time under 40 mT magnetic field

The simulated and measured arc voltage when the magnetic flux is 40 mT are shown in Fig. 8. The time 0 point corresponds to the time 0 of the experimental test, and the

simulation starts from when the distance of contact is 0.2 mm, corresponding to t = 0.22 ms in the actual measurement. The arc voltage rises rapidly after 0.86 ms seen from the figure when the arc moves to the edge of the contact. At point 2 in the figure, at t = 1.15 ms, the voltage drops suddenly, which corresponds to point B in Fig. 7. This is mainly because the arc restriking decrease the resistance, which leads to the decline of the arc voltage and the prolongation of arcing time. The simulation calculation is consistent with the variation trend of the measured voltage curve, but there is a slight difference in the numerical value. During the movement of arc root, the measured arc voltage increase, but the trend is not obvious in the simulation, and the arc movement time in the contact is shorter. It is because the sheath is simplified in simulation and the concentration of metal vapor is different. In addition, the displacement current is ignored in the simulation model, and the arc plasma is assumed to be laminar incompressible, and only one side contact is simulated. And the starting point of the arc in the experiment is random, and the unbalanced combustion of the arc may be caused in the bridge double-breakpoint structure.
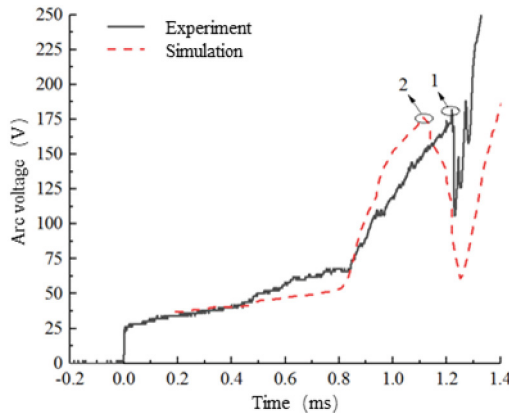
Fig. 8. Arc voltage under 40 mT magnetic field

Based on the accuracy of simulation model, the influence of magnetic field on arc restriking is discussed. The arc voltage are simulated when the magnetic flux are 40 mT, 50 mT and 60 mT. As shown in Fig. 9, as the magnetic flux increases the arc movement time decreases and moment of rapid rise of arc voltage is advanced. It can be seen that when the magnetic flux is 40 mT, 50 mT and 60 mT, the time of the arc restriking is 1.16 ms, 1.01 ms, and 0.85 ms, respectively.

The critical breakdown field strength of arc gap which is affected by the temperature of the arc gap and distance between the contacts, is the main factor affecting arc restriking. The smaller the critical breakdown field strength is, the easier the arc gap is to be broken down. On one side, As the moving speed of the arc root increases, the critical breakdown field strength decreases. On the other side, the critical breakdown field strength increases with the increase of dielectric thickness, which is the distance between the contacts in this paper. Under different sizes of magnetic field, the arc restriking time is different, so is the

distance between the contacts. The distance between contacts during arc restriking can be calculated according to the displacement-time curve of moving contacts. When the magnetic field is 40 mT, 50 mT and 60 mT, the distance between contacts is 1.010 mm, 0.852 mm and 0.768 mm, respectively. Therefore, with the increase of magnetic field, the dielectric thickness decreases, the critical breakdown field strength decreases, and the the probability of arc restriking increases.

The increase of the magnetic field has a dual effect on the movement characteristics of the breaking arc. On the one hand, the increase of the magnetic field increases the movement speed of the arc root, reduces the arc stagnation time and the metal vapor, which is beneficial to the arc movement. On the other hand, the larger the magnetic field is, the faster the arc moves, so the high temperature gas can not be emitted immediately, and the arc gap insulation strength decreases. Because the arc column moves out of the arc gap quickly and the contact gap is small, it is easy to cause dielectric breakdown and arc restriking.
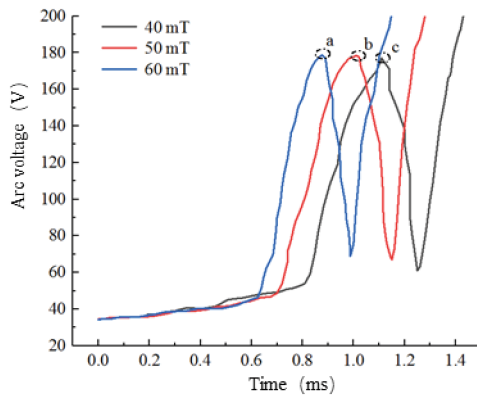
Fig. 9. Arc voltage under different magnetic field

5   Conclusion

Based on the magnetohydrodynamics (MHD) model, under the conditions of different magnetic flux density plate, this paper carries out simulation and analysis on the arc restriking characteristics. The conclusions are as follows:

(1)   As the magnetic flux density increases, the probability of arc restriking and erosion of the contacts increase. The simulation model in this paper can be used in finding the best magnetic flux density to shorten the arcing time and reduce the erosion of the contacts.

(2)   When the temperature of the arc zoneis high, there will be a large amount of silver vapor, which will hinder the arc movement and increase the probability of arc restrikin. Therefore cooling the arc can reduce the probability of arc restriking to a certain extent.

References

1. Zhou, X.: Simulation and Experimental Research on Breaking Arc of Aerospace Relay and its Suppression Measures. Harbin Institute of Technology (2011)
2. Bo, K., Zhou, X., Zhai, G.: Investigation on arc dwell and restriking characteristics in DC high-power relay. IEEE Trans. Plasma Sci. **45**(6), 1032–1042 (2017)
3. Ma, R., Rong, M., Yang, F., et al.: Investigation on arc behavior during arc motion in air DC circuit breaker. IEEE Trans. Plasma Sci. **41**(9), 2551–2558 (2013)
4. Fievet, C., Petit, P., Perrin, M.Y., et al.: Residual conduction in low voltage circuit breaker. In: The 11th International Conference on Gas Discharges and Their Applications. Tokyo (1995)
5. Ono, H., Sekikawa, J.: Arc length of break arcs magnetically blown-out at arc extinction in a DC 450 V/10 A resistive circuit. IEICE Trans. Electron. **96**(9), 1132–1137 (2013)
6. Zhou, X., Cui, X., Chen, M., et al.: Experimental study on arc behaviors of a bridge-type contact when opening a resistive load in the range of from 280 V DC to 730 V DC. In: IEEE 60th Holm Conference on Electrical Contacts, pp. 1–7. New Orleans, LA (2014)
7. Zhai, G., Bo, K., Zhou, X., et al.: Investigation on breaking arc in DC high-power relays: a review. Trans. China Electrotechnical Soc. **32**(22), 251–263 (2017)
8. Volm, D., Winkler, F.: Development of a compact relay for high voltage switching of up to 1000 V and 40 A. In: ICEC 2014 The 27th International Conference on Electrical Contacts, pp. 1–5. Dresden, Germany (2014)
9. Liu, Z.: Simulation and Experimental Study on Arc Movement and Arc Burning Time of Contact Breaking Process of High-power DC Relay. Huazhong University of Science and Technology (2018)
10. Hasegawa, M., Tokumitsu, S.: Influences of external magnetic field application and increased contact opening speeds on break arc duration characteristics of AgSnO2 contacts in DC inductive load conditions. In: 2017 IEEE Holm Conference on Electrical Contacts, pp. 200–204. Denver, CO (2017)
11. Hasegawa, M., Tokumitsu, S.: Break arc duration characteristics of AgSnO2 contacts under magnetic field application with contact opening speeds in the range up to 200 mm/s in DC load conditions. In: 2016 IEEE 62nd Holm Conference on Electrical Contacts (Holm), pp. 119–224. Clearwater Beach, FL (2016)
12. Cao, Q., Liu, X.: Simulation analysis and experimental study on arc motion of HVDC relay. J. Electr. Technol. **34**(22), 4699–4707 (2019)

Electric Field and Influencing Factors Analysis of Converter Transformer Bushing and Grading Ball

Shuoyang Zhao[✉], Tianhao Peng, and Daochun Huang

School of Electrical Engineering and Automation, Wuhan University, Wuhan 430072, China
2020302192019@whu.edu.cn

Abstract. The excessive electric field intensity on the surface of the grading ball of the converter transformer bushing will lead to corona discharge, which may damage the secondary control system of the thyristor. Therefore, it is necessary to calculate the electric field intensity on the surface of the converter transformer bushing and the grading ball. In this paper, a three-dimensional finite element model of bushing and grading ball of converter transformer is established, the electric field distributions on the surface of bushing and grading ball are obtained, and the maximum electric field intensity is extracted. The results show that the maximum electric field intensity is at the end of the grading ball in the upper bushing, which is 9.02 kV/cm. The influence of the maximum diameter of grading ball, the distance to the wall, the distance to the ground and the capacitor core on the electric field is analyzed. The results show that the maximum electric field intensity of the upper grading ball can be reduced to 8.46 kV by reducing the distance to the ground. The results can provide reference for the optimization design of the bushing and grading ball structure of the converter transformer, and ensure the safe and stable operation of the converter transformer.

Keywords: converter transformer · valve-side bushing · grading ball · electric field · finite element method

1 The Introduction

High voltage direct current (HVDC) transmission has become an important development direction of power system due to its advantages such as large transmission capacity, long transmission distance and strong economy [1]. Converter transformer plays an important role in HVDC transmission system. The electric charge generated by the corona of DC hardware fittings will seriously distort the electric field on the insulating material of converter station equipment or the surface of hardware fittings. Therefore, corona must be strictly prevented to avoid the generation of corona charge. The calculation of the electric field intensity on the surface of the hardware fittings inside the valve hall can provide guidance for the design of the hardware fittings and is of great significance for the safe operation of the valve hall [2–4].

At present, some researches have been carried out on the calculation of electric field on the surface of fittings in the valve hall in China. Literature [5–8] has carried out simulation analysis on surface electric field of local fittings. The literature [9–12] focuses on the numerical simulation inside some equipment such as converter transformer bushing in valve hall, or the analysis of insulation coordination in converter station. Literature [13–17] conducted full model numerical calculation for ±500 kV, ±600 kV and ±800 kV valve halls.

In this paper, three-dimensional finite element models of converter valve-side bushing and grading ball of converter transformer are established by finite element method. The electric field distributions on the surface of transformer bushing and grading ball were obtained and the maximum electric field intensity was extracted. The influence of the maximum diameter of the grading ball, the distance to the wall, the distance to the ground and the capacitor core on the electric field was analyzed.

2 Original Model and Calculation Results of Bushing and Grading Ball of the Converter Transformer

2.1 Calculation Model and Parameters

The relevant dimensions of the converter valve-side bushing are shown in Fig. 1. The maximum diameter of the grading ball is 2300 mm. The distance from the end of the grading ball of the bushing located on the top to the wall is 7932 mm, and the distance from the ground is 6472 mm.

In this paper, a three-dimensional finite element model for electrostatic field analysis of bushing and its grading ball is established. Since the electric field distributions around bushing and grading ball are focused on, only bushing, grading ball and air enclosure are established. The overall model is shown in Fig. 2. The outer air enclosure is a 40 m long cube.

The tetrahedron element is used to divide the model, and the total element quantity is 5412066. The bushing and grading ball grids are shown in Fig. 3. The loading potential of the grading ball and capacitor core at the top position is 800 kV, and the loading potential of the grading ball and capacitor core at the bottom position is 715 kV. The shell is loaded with zero potential, and the metal part at the bottom of the bushing is also loaded with zero potential.
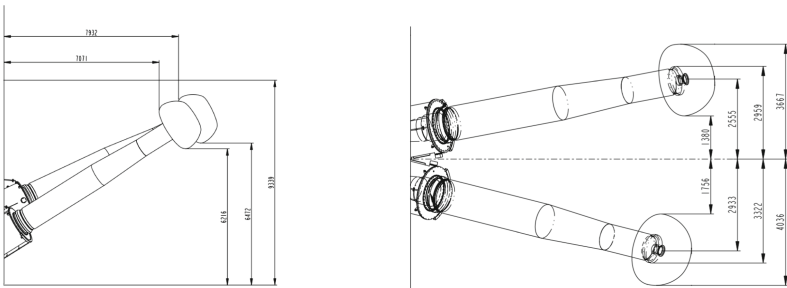
Fig. 1. Schematic diagram of structural parameters of bushing (mm)
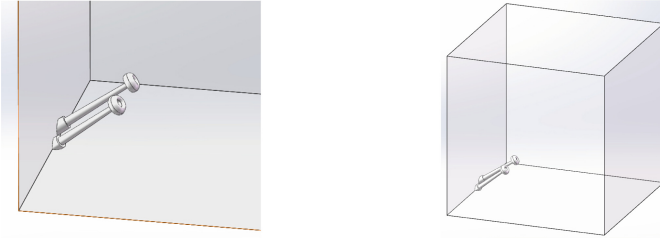
Fig. 2. 3D computing model
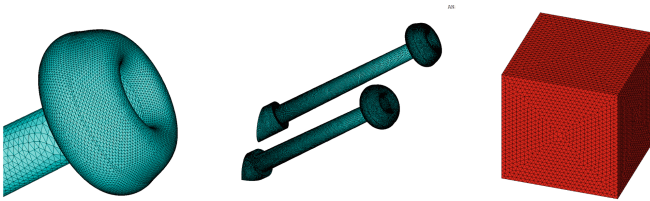
Fig. 3. Schematic diagram of grid

2.2   Calculation Results of the Original Model

The electric field on the surface of the grading ball of the original model is shown in Fig. 4. The electric field distributions of bushing overall surface are shown in Fig. 5. The electric field intensity distributions of the middle section of the bushing are shown in Fig. 6.

a) The upper grading ball   b) The lower grading ball
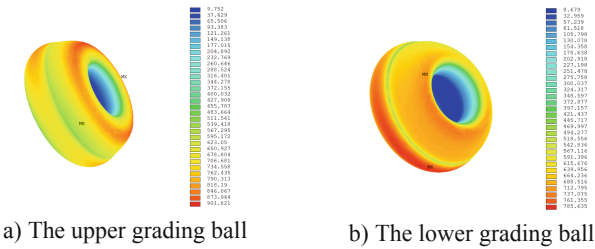
Fig. 4. The original model grading ball surface electric field (kV/m)

It can be seen from Fig. 4 that the maximum electric field on the surface of the grading ball of the high voltage end bushing is at the end of the grading ball of the upper bushing, and the maximum electric field intensity is 9.02 kV/cm, while the maximum electric field on the lower bushing grading ball surface is 7.86 kV/cm.
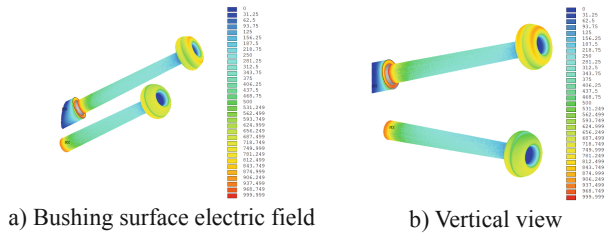
a) Bushing surface electric field   b) Vertical view

Fig. 5. Overall surface electric field distributions of bushing (kV/m)

a) The upper bushing   b) The lower bushing
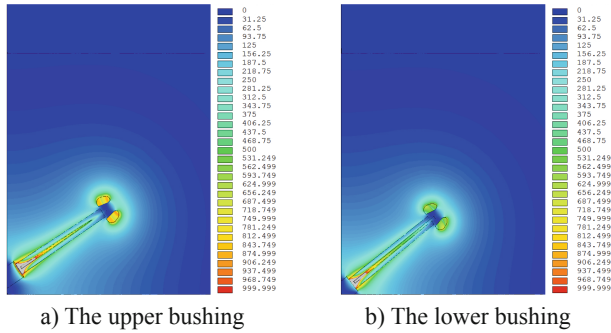
Fig. 6. Electric field distributions of bushing section (kV/m)

3 Electric Field Influence Analysis of Different Factors

The influence of the maximum diameter of grading ball, the distance to the wall, the distance to the ground and the capacitor core on the electric field is analyzed.

3.1 Influence of the Maximum Diameter of the Grading Ball

In the original model, the maximum diameter of the grading ball was 2300 mm, keep other parameters unchanged and change the maximum diameter of the grading ball to 1500 mm. The calculation results are shown in Figs. 7, 8 and 9.

It can be seen from the analysis that when the maximum diameter of the grading ball is reduced to 1500 mm, the maximum electric field intensity of the upper grading ball is 12.86 kV/cm, which is 42.57% higher than the original model, and the maximum electric field intensity of the lower grading ball surface is 10.13 kV/cm, which is 28.88% higher than the original model.

a) The upper grading ball   b) The lower grading ball

Fig. 7. The original model grading ball surface electric field (kV/m)

a) Bushing surface electric field   b) vertical view
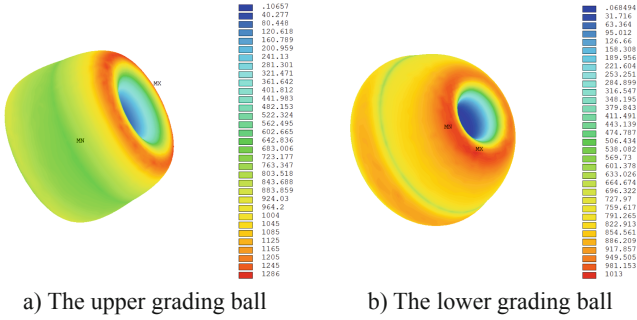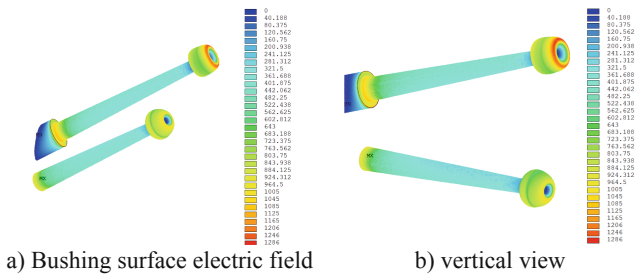
Fig. 8. Overall surface electric field distributions of the bushing (kV/m)

a) The upper bushing   b) The lower bushing
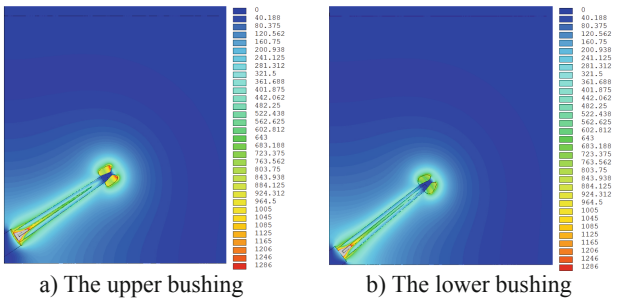
Fig. 9. Electric field distributions of bushing section (kV/m)

3.2   Influence of the Wall Distance and the Ground Distance

The electric field distributions are calculated and analyzed respectively when the distance to the wall is reduced by 1 m, the distance to the ground is reduced by 1 m, the distance to both the wall and the ground is reduced by 1 m, and the distance to the ground is symmetrical to the wall. The distance from the upper bushing to the strong and the ground is 7776 mm when the distance to the wall is symmetrical to the ground.

It can be seen from Table 1 that with the change of the distance between the bushing and the wall and the ground, the change trend of the electric field of the grading ball on

the two bushings is basically the same. When only the distance to the wall is reduced, the electric field intensity on the surface of the grading ball increases, and the amplitude of increase is within 3%. When only the distance to the ground is reduced, the electric field on the surface of the grading ball decreases. Compared with the reduction of the distance to the wall, the reduction of the distance to the ground has a greater impact on the electric field on the surface of the grading ball. When the distance to the wall and the ground is reduced at the same time, the maximum electric field intensity on the surface of the grading ball increases. When the distance to the wall and the ground is symmetrical, it is equivalent to reducing the distance to the wall, increasing the distance to the ground, and the maximum electric field intensity on the surface of the grading ball decreases. The electric field distributions are shown in Fig. 10. Electric field distributions when the distance to both wall and ground is reduced by 1 m and Fig. 11.
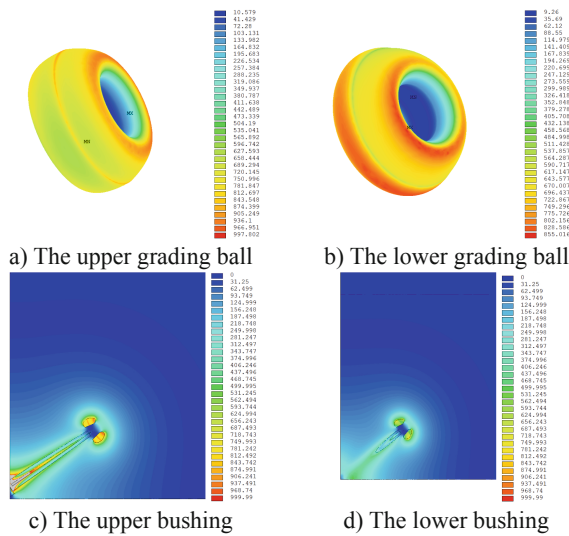
a) The upper grading ball   b) The lower grading ball

c) The upper bushing   d) The lower bushing

Fig. 10. Electric field distributions when the distance to both wall and ground is reduced by 1 m (kV/m)

a) The upper grading ball   b) The lower grading ball

c) The upper bushing   d) The lower bushing
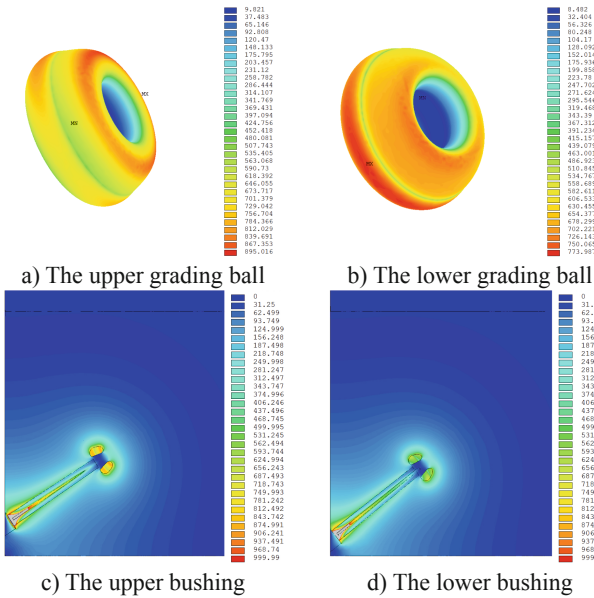
Fig. 11. Electric field distributions under symmetrical condition (kV/m)

3.3 Influence of the Capacitor Core

On the basis of the original model, remove the capacitor core and load the potential. The calculation results are shown in Figs. 12, 13 and 14.

a) The upper grading ball   b) The lower grading ball
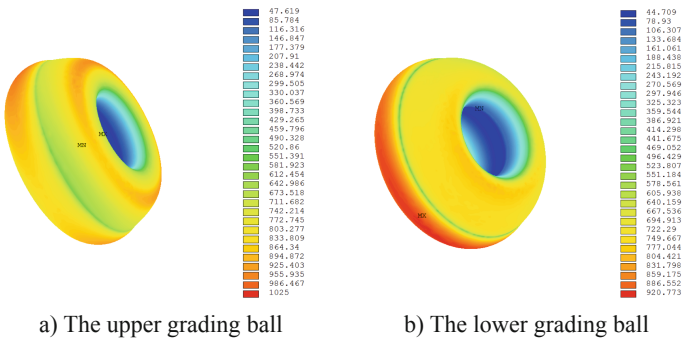
Fig. 12. Electric field on the surface of the grading ball (kV/m)

It can be seen from the analysis that the maximum electric field intensity of the upper grading ball is 10.25 kV/cm without a capacitor core, which is 13.64% higher than the original model, and the surface electric field of the lower grading ball is 9.21 kV/cm, which is 17.18% higher than the original model. It can be seen that the maximum electric field intensity of the surface of the grading ball increases without a capacitor
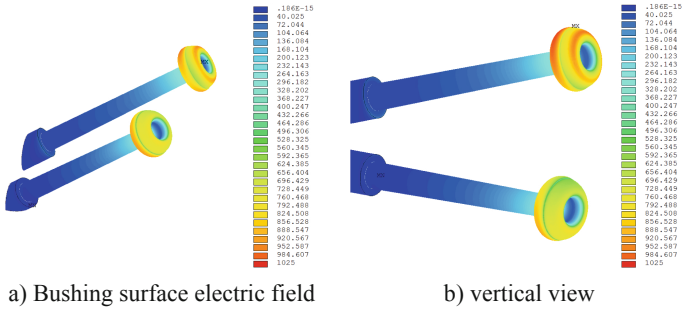
a) Bushing surface electric field   b) vertical view

Fig. 13. Overall surface electric field distributions of bushing (kV/m)

a) The upper bushing   b) The lower bushing
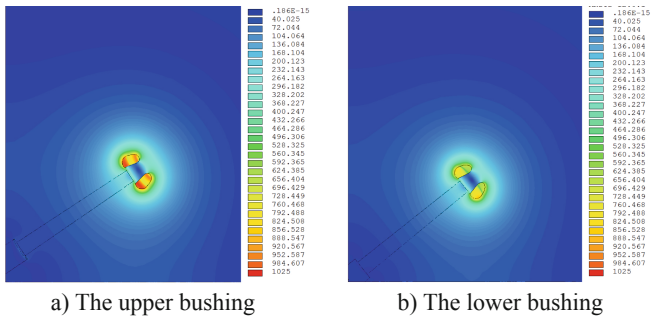
Fig. 14. Electric field distributions of bushing section (kV/m)

core. Because there is no capacitor core, the electric field intensity of the low-voltage end of the bushing is significantly reduced.

Table 1. Calculation results of the maximum electric field intensity

Model	The upper grading ball (kV/cm)	Percentage difference/%	The lower grading ball (kV/cm)	Percentage difference/%
original model	9.02	/	7.86	/
The maximum diameter of grading ball is 1.5 m	12.86	42.57	10.13	28.88
The distance to wall is reduced by 1 m	9.11	1.00	8.02	2.04

(*continued*)

Table 1. (*continued*)

Model	The upper grading ball (kV/cm)	Percentage difference/%	The lower grading ball (kV/cm)	Percentage difference/%
The distance to ground is reduced by 1 m	8.46	−6.21	7.06	−10.18
The distance to both wall and ground is reduced by 1 m	9.98	10.64	8.85	12.60
symmetric	8.95	−0.78	7.74	−1.57
Removing capacitor core	10.25	13.64	9.21	17.18

4 Conclusion

In this paper, a three-dimensional finite element model of the converter valve-side bushing and the grading ball is established, and the electric field distributions on the surface of the bushing and the grading ball are calculated and the maximum electric field intensity is extracted. Conclusions can be drawn that:

1. The maximum electric field on the surface of the grading ball of the high voltage end of the bushing is at the end of the bushing ball of the upper bushing, with a maximum electric field intensity of 9.02 kV/cm, and the maximum electric field on the surface of the grading ball of the lower bushing is 7.86 kV/cm.
2. The effects of the maximum diameter of the grading ball, distance to the wall and to the ground and the capacitor core on the electric field intensity were analyzed. It is found that the optimization effect of reducing the distance to the ground is the best. The maximum electric field on the surface of the upper grading ball can be reduced to 8.46 kV/m by reducing the distance to the ground by 1 m, which is 6.21% lower than the original model.

References

1. Huang, D., Xie, X., Huang, Z., et al.: Grading ring parameter design and corona characteristic test arrangement of 1000 kV AC compact transmission line. High Voltage Eng. **39**(12), 2933–2942 (2013)

2. Nie, D., Zhang, H., Chen, Z., et al.: Optimization design of grading ring and electrical field analysis of 800 kV UHVDC Wall wall bushing. IEEE Trans. Dielectr. Electr. Insul. **20**(4), 1361–1368 (2013)

3. Zhang, S., Peng, Z., Liu, P., et al.: Design and dielectric characteristics of the ±1100 kV UHVDC wall bushing in china. IEEE Trans. Dielectr. Electr. Insul. **22**(1), 409–419 (2015)

4. Yue, B., Chen, D., Ying, F., et al.: A static field equivalence method for simulation of fitting surface electric field in ±1100 kV DC yards of converter stations. Power Syst. Technol. **41**(11), 3427–3434 (2017)

5. Qi, L., Wang, X., Li, C., et al.: Electric field simulation and optimization of ±1100 kV HVDC converter valve in insulation type test. High Voltage Eng. **41**(4), 1262–1271 (2015)

6. Liu, S., Wei, X., Cao, J., et al.: UHVDC converter valve shielding case surface electric field calculation using hybrid-weight-function boundary element method. Proc. CSEE **33**(25), 180–186 (2013)

7. Jia, W., Niu, W., Wang, B., et al.: Electric field simulation for ±1100 kV DC valve hall fittings. Electr. Technol. **17**(7), 13–19 (2016)

8. Zhang, S., Peng, R., Ning, X., et al.: Insulation structure design of ±400 kV converter transformer valve side bushing. Electr. Power Autom. Equipment **41**(06), 199–208 (2021)

9. Li, W., Zhang, Z., Li, X., et al.: Field analysis of 800 kV converter transformer for DC transmission. Transformer **46**(6), 1–5 (2009)

10. Zhang, X., Wang, J., Wu, Z., et al.: Numerical analysis of electric field in valve side lead-out wire for UHVDC converter transformer. Transformer **46**(7), 1–4 (2009)

11. Li, J., Luo, L., Xu, J., et al.: Study on electric field characteristics at ends of valve-side winding in converter transformer. High Voltage Eng. **32**(9), 121–124 (2006)

12. Chen, Q., Zhang, J., Gao, Y., et al.: Analysis of complex electrical field on valve side winding of converter transformer. High Voltage Eng. **34**(3), 484–488 (2008)

13. Wang, D., Ruan, J., Du, Z., et al.: Numerical solution of the surface electric field of electric power fittings in ±500 kV DC converter station valve hall. High Voltage Eng. **37**(2), 404–410 (2011)

14. Wang, D., Ruan, J., Du, Z., et al.: Numerical solution of electric power fittings about surface electric field in ±660 kV DC converter station valve hall. High Voltage Eng. **37**(10), 2594–2600 (2011)

15. Wang, D., Ruan, J., Du, Z., et al.: Numerical solution of potential and electric field intensity in field domain of valve hall of DC converter station by sub-model method. Power Syst. Technol. **35**(9), 158–163 (2011)

16. Ruan, J., Zhan, T., Du, Z., et al.: Numerical solution of electric power fittings about surface electric field in ±800 kV UHVDC converter station valve hall. High Voltage Eng. **39**(12), 2916–2923 (2013)

17. Ji, D., Liu, Z., Deng, T., et al.: Analysis of overall electric field in high-voltage valve hall end on steady state of UHVDC system. High Voltage Eng. **39**(12), 3000–3008 (2013)

Study on Thermal Characteristics and Movement Law of Water Droplets Discharges on Insulator Surface

Yashuang Zheng[1(✉)], Jikai Bi[1], Yanpeng Hao[1], Haofeng Zhang[2], Bing Luo[2], Tingting Wang[2], and Wei Xiao[2]

[1] School of Electric Power Engineering, South China University of Technology, Guangzhou 510006, China
zysscut@scut.edu.cn

[2] Electric Power Research Institute, China Southern Power Grid, Guangzhou, China

Abstract. Temperature changes usually accompany the deformation and discharge of conductive water droplets on the insulator surface. This work aims to reveal the internal temperature evolution characteristics during the deformation and discharge of the conductive water droplets on the silicone rubber surface. Three fiber Bragg gratings are implanted at the interface between the silicone rubber plate and the epoxy resin plate to measure the interface temperature. Results show that the elongation of water droplets can characterize the deformation state of water droplets under an electric field. The significantly different interfacial temperature rise rates can be used to distinguish between the water droplets' deformation and the water droplets' flashover discharge on the silicon rubber surface, with a temperature rise rate of 1.68×10^{-3} °C/s for water droplet deformation and 4.46×10^{-2} °C/s for flashover. This work is of great significance in realizing the surface condition detection of composite insulators.

Keywords: Interface Temperature · Surface Temperature · Droplet Deformation

1 Introduction

Due to the high humidity and high salt content of fog in coastal areas, it is easy to form discrete water droplets with high salt and conductivity on the surface of hydrophobic composite insulators [1]. The discharge and flashover of water droplets on the surface of composite insulators are not only electrical processes but also closely related to thermal processes. Xie *et al.* studied the temperature change of water droplets at the initial discharge stage using infrared thermography. They find that the discharge develops from droplets with high potential to droplets with low potential, and the temperature rise of low-potential droplets is more pronounced [2]. Hao *et al.* implanted fiber Bragg gratings (FBG) at the interface between the composite sheath and the mandrel to measure the internal temperature. They observed that the interface temperature drops sharply and then increases rapidly in the presence of surface arc discharge [3, 4].

To date, the relationship between the temperature and the surface discharge on the hydrophilic insulator surface has been well studied, but the temperature characteristics of water droplets' deformation and discharge on hydrophobic surfaces have seldom been studied. In this paper, we made a specimen by implanting FBGs at the interface between a hydrophobic silicone rubber plate and an epoxy resin plate. We then conducted discharge tests on the sample with water droplets arranged in a straight line on the silicon rubber surface. The temperature at the interface between the silicon rubber plate and the epoxy resin plate (T_i) is measured during the deformation and discharge of water droplets. The relationship between T_i and the discharge state on the hydrophobic surface was explored.

2   Experimental Setup

Figure 1 shows the experimental measurement system, including the power supply, grating demodulator, infrared thermal imager, ultraviolet imager, camera, and silicone rubber-epoxy resin flat specimen. The thickness of the sample is 4 mm, and the spacing between the two electrodes is 100 mm. 8 drops of water droplets with a size of about 50 µL and a conductivity of 20 mS/cm are arranged on the surface of the specimen, numbered as droplet #1 to droplet #8. Three FBGs, marked FBG1, FBG2, and FBG3, are arranged at the silicon rubber-epoxy resin interface. The temperature measurement principle by FBGs is referred to reference [3]. After the voltage is applied to the specimen, if no partial discharge occurs, the voltage resistance time is not less than 60 s, and then continuing to boost the voltage amplitude. The UV imager and the camera are used to observe the discharge processes. The interface FBGs are used to measure T_i.
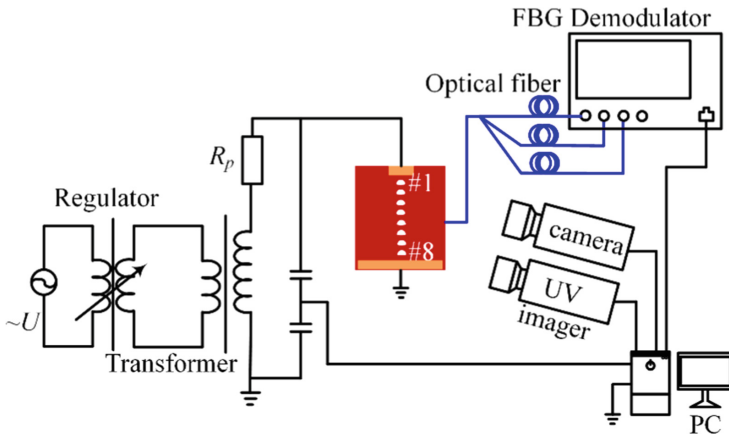
Fig. 1. Experimental measurement system for the water droplets discharge on the silicone rubber surface.

3   Results and Discussion

After applying voltage, the water droplets of the silicon rubber surface elongate along the electric field direction due to the electric field force and the surface tension, as shown in Fig. 2. The water droplet #1 begins to elongate rapidly at 600 s, and the maximum elongation is 0.19. At around 628 s, water droplet #2 elongates quickly with a maximum elongation of 0.32. Water droplet #3 shows a significant extension from 1020 s to 1200 s and begins to move at 1200 s. The combined action of gravity, surface tension and electric field force might cause the movement of droplet #3. The shape of water droplet #2 changes from ellipsoid to triangle, with the semi-major axis decreasing significantly.
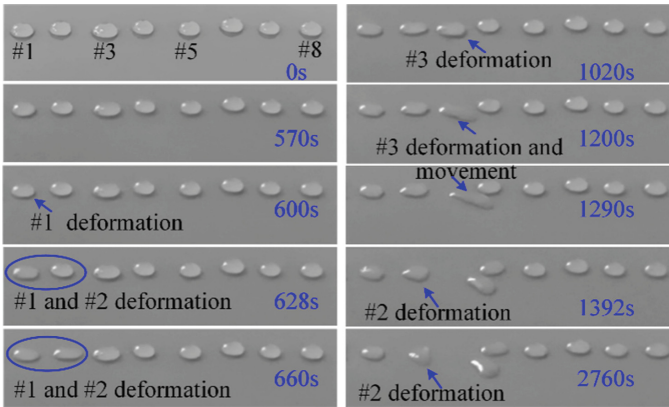
Fig. 2. Dynamic deformation of water droplets on the silicon rubber surface.

The interface temperature between the silicon rubber plate and the epoxy resin plate (T_i) shows two significant rises during the deformation and flashover of water droplets, but the characteristics of the two temperature rises are significantly different, as shown in Fig. 3. The temperature rise caused by the water droplets deformation occurs from 1020 s to 1740 s. The temperature measured by FBG1, FBG2, and FBG3 increases by 1.2 °C, 0.85 °C and 0.86 °C, respectively, with rise rates of 1.68×10^{-3} °C/s, 1.19×10^{-3} °C/s and 1.20×10^{-3} °C/s, respectively. On the other hand, the temperature rise produced by the water droplets flashover occurs from 4930 s to 4943 s. During this time, the temperature measured by FBG1, FBG2, and FBG3 increase by 0.64 °C, 0.75 °C and 0.58 °C with the increase rate of 4.92×10^{-2} °C/s, 5.77×10^{-2} °C/s, and 4.46×10^{-2} °C/s, respectively.

The temperature rise of the flashover process is smaller than that of the deformation process. Since the duration of the flashover discharge is short in our experiments, the heat release is less. The temperature rise rate generated by the water droplets' flashover is more than 10 times that produced by the water droplets' deformation. The primary heat source during the flashover of water droplets is arc discharge, while Joule heat is the main source of temperature rise in the deformation of water droplets.
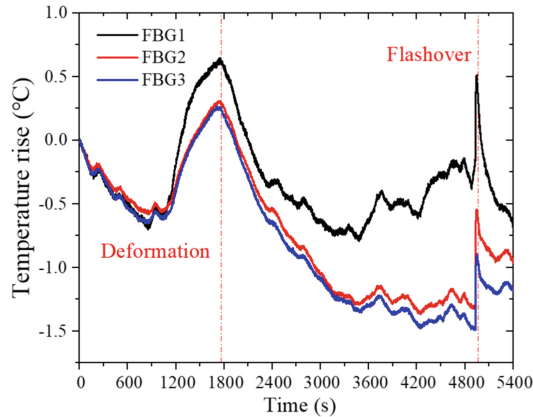
Fig. 3. Temperature rise at the interface between the silicon rubber plate and the epoxy resin plate during the water droplets' deformation and discharge processes.

4   Conclusion

This paper explores the relationship between the temperature at the interface between the silicon rubber plate and the epoxy resin plate and the deformation and discharge of water droplets on the silicon rubber surface based on the principle of FBG temperature measurement. Results show that the significantly different interfacial temperature rise rates can be used to distinguish surface water droplets deformation and flashover discharge. The temperature rise rate generated by the water droplets' deformation is 1.68 $\times$ 10^{-3} °C/s, and that produced by water droplets flashover is 4.46 $\times$ 10^{-2} °C/s.

References

1. Liu, Y., Wu, Y., Du, B.: Dynamic formation mechanism of water droplet and induced surface discharges on silicone rubber composites. High Voltage **4**(1), 59–64 (2019)
2. Xie, G., Luo, J., Yang, Y., Guo, D., Si, L.: Water droplets on a hydrophobic insulator surface under high voltages: a thermal perspective. Appl. Phys. Lett. **101**(13), 131602 (2012)
3. Hao, Y., Bi, J., Wang, Q., Yang, L.: Interface temperature evolution exposed to arc discharges occurred on the uniform moist pollution layer of composite insulators based on interface fibre Bragg gratings. High Voltage **7**(3), 763–770 (2022)
4. Hao, Y., Bi, J., Wang, Q., Wei, J., Chen, Y., Yang, L.: Method of quasi-distributed interface fiber Bragg gratings monitoring dry band arc on the moist pollution layer of composite insulators. Electr. Power Syst. Res. **209**, 107956 (2022)

Basic Process, Diagnosis and Simulation in Plasmas

Diagnosis of Spatial Distribution and Low Energy Level Density of Argon Plasma Jet Active Particles

Dawei Zhang[✉], Xiaoying Chen, and Sha Hao

Shenyang Ligong University, Shenyang 110159, Liaoning, China
springdavid@163.com

Abstract. With the deepening of the application of atmospheric pressure low-temperature plasma in the field of biomedicine, the accurate regulation of active particle components and doses also needs to be broken, and all aspects of plasma still need to be studied in depth. Based on this, Ben In this paper, a needle-ring electrode was used to build a plasma discharge device to study the characteristics of 0.1 MPa argon plasma jet number, plasma irradiation at 4 mm, 8 mm, 12 mm, 16 mm, 20 mm away from the nozzle was collected degree, analyze the change law of the type and number of active particles in argon plasma. The results showed that argon plasma. The active particles are mainly oxygen atoms and hydroxyl groups; When argon plasma acts on the copper foil, the surface of the copper foil is low in argon. The relationship between the density of energy levels is $ns_4 > ns_5 > ns_2 > ns_3$; Metastable ($1s_3$ and $1s_5$) number density versus resonant state ($1s_2$ Similar to $1s_4$), the number density changes the linear type, and the change trend increases first and then decreases with the increase of axial distance. This paper provides methods and ideas for the generation and optimization of argon plasma jet and the optimization of diagnostic methods, and establishes plasmacy. The control model of the descendant provides a reference and basis.

Keywords: active particles · metastability · resonance state · Number density

1 Introduction

Atmospheric pressure cold plasma has a wide range of applications in the biomedical field, among which the most concerned include: biomutagenesis breeding, disinfection and sterilization, wound treatment, cosmetic and dermatological treatment, tooth whitening and root canal disinfection, cancer treatment, etc. [1]. Plasma jets greatly broaden the scope of application of plasma medicine because they can generate plasma in an open space, so that the treated sample is not limited by the size of the discharge gap [4].

With the rapid development of plasma biomedicine in the past 20 years, some new key problems need to be broken, and the accurate regulation of active particle components and dosage [2] is one of them. A large number of studies have found that the biomedical effects of plasma are mainly achieved through active particles, including charged particles, oxygen-containing active particles, nitrogenous active particles, etc. Therefore,

in plasma biomedical applications, it is ultimately necessary to control the composition and dose of these active particles [2], and Lu Xinpei et al. of Huazhong University of Science and Technology proposed the equivalent total oxidation potential as the plasma dose for the leading role of reactive oxygen species in plasma biological effects, which is a major breakthrough for the application of plasma in medicine. Yue Yuanfu [5], a student of Lu Xinpei, applied laser-induced fluorescence spectroscopy to diagnose and optimize hydroxyl and oxygen atoms in atmospheric pressure low-temperature plasma jets. Senior brother Yang Chen [3, 6] used PLS-800 equipment and argon plasma jet spray gun to confirm the composition in the argon plasma jet. At present, the regulation of active particle components and dosage still faces the problem that the microscopic mechanism of plasma chemistry is not clear enough, and it is difficult to comprehensively consider various factors to achieve fine control. In view of this, it is necessary to take a variety of measures to break down complex plasma chemistry [7], classify and study the biomedical effects of active particles at a quantitative level; It is necessary to precisely control the plasma generation conditions, especially to fully consider the influence of surrounding environmental factors, so that the active particle components and doses generated during the discharge process remain unchanged under different environmental conditions and in the long-term operation of the plasma source.

Based on this, this paper builds a plasma generation device under the needle-ring electrode structure, generates argon plasma jet in an open environment of 0.1 MPa, uses emission spectroscopy to obtain spectral data of different axial distances in the plasma jet process, analyzes the changes of active particles in argon plasma, calculates the number density of argon metastable state and resonance state, and analyzes and discusses its change law.

2   Argon Plasma Jet Experimental Platform Established

The experimental platform can be divided into three parts, namely the drive power supply [8], needle-ring discharge electrode, and spectral acquisition diagnostic system. Among them, the drive power supply is composed of 0–220 V adjustable DC power supply, PWM drive unit, half-bridge circuit and resonant high-voltage transformer. The output frequency is adjustable from 15–40 kHz, and the voltage amplitude is adjustable from 0–15 kV; The high-voltage electrode of the needle-ring discharge electrode is a copper rod with a length of 30 mm and a diameter of 1mm, the ground electrode is a copper ring with a width of 6 mm, and the length of the high-voltage electrode from the ground electrode is 6 mm. The insulating medium is a uniform texture quartz glass tube with a length of 50 mm, an inner diameter of 6 mm and an outer diameter of 8 mm. The plasma generation and measurement device is shown in Fig. 1, wherein the working gas is argon with a volume fraction of 99.99%, and the spectrometer model used for the experimental acquisition of plasma emission spectroscopy is ULS2048-USB2. In order to exclude the influence of external light sources on the experimental results, this experiment was carried out with the lights turned off at night.
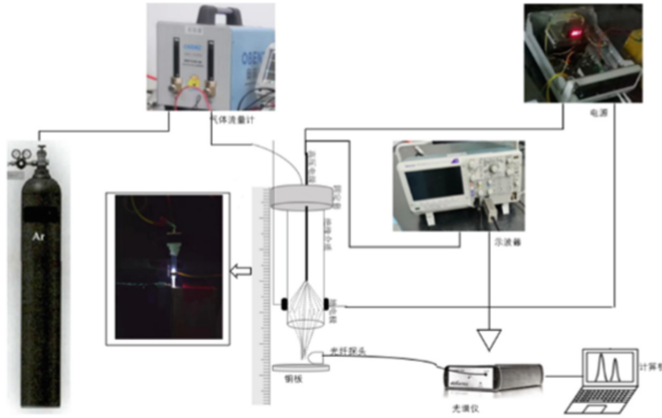
Fig. 1. Plasma generation and measurement device

2.1 Pin-to-Ring Discharge Electrode

Compared with other dielectric blocking discharge electrode structures, the biggest difference is that the ground electrode is above the high-voltage electrode, so that the electrons generated by the discharge at the tip of the needle are more likely to migrate to the ground electrode driven by the air flow, thus forming a plasma jet. In addition, the electric field strength at the tip of the needle is large, and it is easy to discharge to generate plasma. As a result, the plasma jet source can break down the gas at lower voltages, creating a discharge-stable plasma jet.

2.2 Plasma Spectral Acquisition System

In the experiment, the working gas is first introduced into the discharge device, the power supply is turned on, the voltage value is adjusted, the plasma is observed to observe whether the discharge nozzle is generated, and the spectrum is acquired when the nozzle produces a relatively stable plasma jet. Treat the glass tube spout as the starting point as 0 cm. It is observed that the length of the plasma natural jet produced by this experimental device under different input voltages is different, and the maximum jet length is 20 mm. Taking the distance from copper foil to glass tube nozzle as the independent variable, considering the experimental operability, 4 mm intervals were selected, that is, the distances between copper foil and glass tube nozzle were 4 mm, 8 mm, 12 mm, 16 mm, and 20 mm, respectively, and plasma spectral data were collected.

During the experiment, it is always ensured that the fiber optic probe and the glass tube mouth of the needle-loop discharge device are on the same horizontal line, and the distance between the optical fiber probe and the copper foil is always consistent at 2 mm. The experiment was repeated at least ten times, and three sets of spectral data were saved under the same experimental conditions at each distance to ensure the accuracy of the experimental results and reduce the influence of accidental factors on the experimental results.

2.3 Plasma Spectroscopy Analysis System

When the plasma system is affected by external factors such as electric field, the particle number density of the excited state increases. But excited particles are inherently extremely unstable and short-lived, and they transition to lower energy levels and release photons through spontaneous and stimulated radiation, a process that forms the emission spectrum. Different kinds of particles correspond to different wavelengths of emission spectral lines, so the emission spectrum can diagnose the specific particle species in the plasma discharge system.

In addition, the parameters of other plasmas can also be obtained by the analysis of emission spectroscopy, and the emission spectroscopy method is used to acquire the spectra in the plasma jet process. Through Avasoft software, the irradiance changes of each particle spectral line in the plasma can be intuitively observed, and the generated Excel table contains the accurate value of the irradiance of each particle wavelength of the plasma, and important parameters such as electron temperature and electron density can be obtained through the analysis of irradiance.

3 Spatial Distribution of Argon Plasma Jets

In the experiment, the spectrum is acquired by spectrometer (effective range of 200–1000 nm), where the abscissa is the wavelength, and the particle type can be determined; The ordinate is irradiance, which refers to the radiation flux that falls on the surface area of the unit detector.

3.1 Particle Species and Spatial Distribution

After analysis, it is found that the length of argon plasma jet produced by the needle-ring discharge device starting from the nozzle is 20 mm, and a total of 22 argon atomic lines at 690–1000 nm, 21 nitrogen molecular lines at 300–500 nm, 1 hydroxyl radical line at
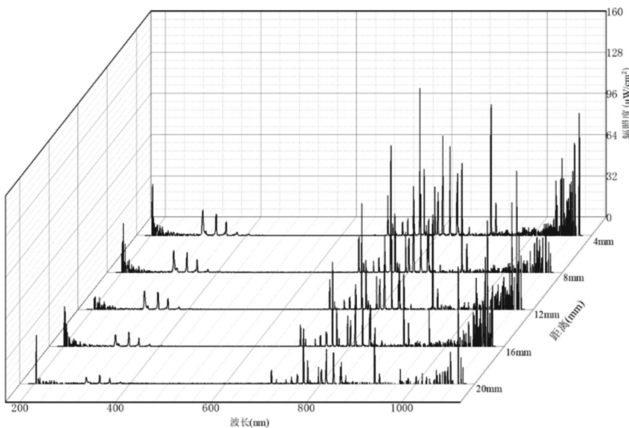
Fig. 2. Spectral line variation plot of each particle increasing with distance

306–318 nm, and 2 oxygen atom lines at 750–850 nm were collected. The spectral lines of each particle increase with axial distance are shown in Fig. 2.

With the increase of the distance between the copper plate and the nozzle, the irradiance of each particle gradually decreases. The highest irradiance at 4 mm, which may be due to the fact that at 4 mm, the plasma acts on the copper plate closestly, and the copper plate has an adsorption effect on the plasma, so that more particles move along the glass tube nozzle to the copper plate, accumulating near the copper plate to increase the irradiance.

This device adopts sinusoidal AC power supply, and the gas flow rate is adjusted by the gas flow meter, and the length of the jet is related to the gas flow rate. According to the theory of gas dynamics, it is divided into laminar flow, transition state and turbulent flow by Reynolds number [8]. Re $= \rho v d / \mu$ where: the working gas is argon, ρ take 1.6228 kg/m^3; v is the gas flow rate, m/s; d is the diameter of the glass tube, d $= 6 \times 10^{-3}$ m, μ is the kinematic viscosity coefficient, take $2.23 \times 10 - 5$ kg/(m · s) [9]. When Re < 2300, the gas flow is in a laminar flow state; When $2300 <$ Re < 8000, the gas flow is in a transitional state; When Re > 8000, the gas flow is in turbulent state [10]. According to the formula: when Re $= 2300$, v $= 5.27$ m/s; When Re $= 8000$, v $= 18.32$ m/s. According to a large number of studies in fluid dynamics, the length of the jet produced when the gas flow is in a transitional state is the maximum [11], that is, the maximum length of the jet should theoretically occur between 5.27 m/s and 18.32 m/s in argon flow velocity. The gas flow rate in this experiment is about 12 m/s, which belongs to the transition state, and the maximum length of the plasma jet is 20 mm, and the place with the largest number of plasma particles is 4 mm.

3.2 Spatial Distribution Analysis of Active Particles

The active particles in the argon plasma jet are oxygen atoms and OH radicals, and the irradiance changes of the three active particles are shown in Table 1 below.

Table 1. Irradiance of active particles at different distances

Active particles	wavelength λ(nm)	4 mm $I(\mu W/cm^2)$	8 mm $I(\mu W/cm^2)$	12 mm $I(\mu W/cm^2)$	16 mm $I(\mu W/cm^2)$	20 mm $I(\mu W/cm^2)$
Oxygen atoms	777.5	1.16	1.39	1.63	0.89	0.76
Oxygen atoms	844.6	1.01	1.18	1.32	1.04	0.95
OH	308	9.48	7.77	7.08	3.35	2.77

It can be seen from the table that the irradiance of oxygen atoms increases first and then decreases with the increase of the distance from the copper foil to the surface of the material, and the irradiance of OH radicals gradually decreases with the increase of the distance from the copper foil to the surface of the material and the analysis of the gradual decrease in the irradiance of oxygen atoms suggests that the oxygen atoms in the

atmospheric pressure low-temperature plasmonic jet are mainly the following reactions [14]:

$$e + O_2 \rightarrow O^* + O + e$$
$$O^* + Ar \rightarrow O + Ar$$
$$e + O_2 \rightarrow O + O^* + e$$
$$e + O_2 \rightarrow 2O + e$$
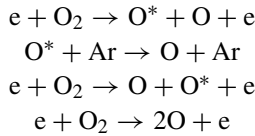
Oxygen atoms are mainly produced by the reaction of electrons and metastable oxygen atoms with gas molecules or atoms. During the experiment, the plasma jet came into contact with the air, and it is obviously unrealistic to assume that oxygen atoms do not react with other particles since they are generated. The reaction of oxygen atoms and other particles is bound to cause the attenuation of oxygen atoms, coupled with the impact of the life of oxygen atoms themselves, which will inevitably cause the irradiance to show a downward trend or even disappear.

According to the analysis of the gradual decrease of OH irradiance, the mechanism of free radicals in atmospheric pressure low-temperature plasmonic jets [12] mainly comes from electron collision, metastable particle decomposition, ion-electron and ion-ion recombination, etc. [13]. These processes are mainly concentrated during or in a very short time after discharge, and the subsequent processes are mainly the disappearance and attenuation of free radicals [15]. In argon plasma, the first excited state OH(A2Σ+) is produced by the collision of high-energy electrons e* in the plasma and argon atom Ar* in the excited state with water vapor doped in the air, respectively [15, 16].

$$e^* + H_2O \rightarrow OH\left(A^2\Sigma+\right) + H + e$$
$$Ar^* + H_2O \rightarrow OH\left(A^2\Sigma+\right) + Ar + H$$
$$OH(A2\Sigma+) \rightarrow OH\left(X^2\Pi\right) + hv$$
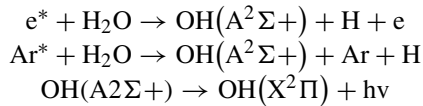
The disappearance and attenuation of free radicals is mainly affected by chemical reactions, free diffusion, surface adsorption, and gas flow [15]. In the atmospheric pressure low-temperature plasma jet, because the jet is in direct contact with the air, OH radicals may also react with some other particles such as O, O2, etc., and some of the reaction formulas are as follows [11],

$$OH + O \rightarrow O_2 + H$$
$$OH + H \rightarrow H_2O$$
$$OH + O_2 \rightarrow HO_2 + O$$
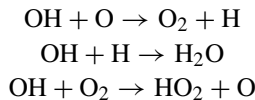
These reactions are another important attenuation mechanism for free radicals in atmospheric pressure low-temperature plasma jets. In addition, OH free radicals themselves have a certain lifespan, assuming that OH does not react with other particles since it is generated, as long as the collection time during the experiment exceeds the life of the OH free radical itself, then OH free radicals will disappear. Therefore, these factors may cause OH irradiance to decrease or even disappear.

Therefore, in this experiment, when the distance between the copper plate and the glass tube nozzle increases, the irradiance of OH radicals decreases, partly due to the life

of OH radicals themselves, and partly due to the chemical reaction between OH radicals and other particles in the air.

According to the irradiance change of each particle, in order to further study the argon plasma discharge mechanism, the argon metastable state and resonance state density in the argon plasma jet process are calculated and analyzed.

4 Argon Metastable and Resonant State Density Calculation

In plasma, an optical transition from energy level i to energy level j occurs at the r position, and photons with a frequency of v_0 (or wavelength λ_0) are emitted during this optical transition. In general, only a portion of photons can leave the plasma volume, while other photons are reabsorbed by J-class atoms as they are transported through the plasma. In spatially resolved OES measurements, only photons emitted along the line of sight are considered, in which case a one-way escape factor (r_{ij}) can be used to describe the self-absorption effect [13]. Assuming that the atomic density of class i is n_i and the Einstein coefficient of i to j is A_{ij}, the emission intensity can be expressed as [19]

$$I_{ij}(r) = r_{ij}A_{ij}n_i \tag{1}$$

We consider a transition from a common high energy level i to different lower levels j and k, and the emission intensity ratio can be expressed as:

$$\frac{I_{ij}(r)}{I_{ik}(r)} = \frac{r_{ij}A_{ij}}{r_{ik}A_{ik}} \tag{2}$$

As can be seen from the above equation, the spectral line emission intensity ratio depends on the escape factor and Einstein coefficient, and is independent of the n_i of the upper energy level density. By using a global approximation of the escape factor, the analysis can be greatly simplified. In the work of this article, we use Mewe's expression [20]:

$$r_{ij} \approx \frac{2 - \exp\left(-10^{-3}k_{ij}(\Delta v = 0)L\right)}{1 + k_{ij}(\Delta v = 0)L} \tag{3}$$

where L is the plasma volume depth accessible to the photon detector, and k_{ij} ($\Delta v = 0$) is the absorption coefficient [19], defined as:

$$k_{ij}(\Delta v) = \frac{\lambda_{ij}^2}{8\pi}P_{ij}(\Delta v)\frac{g_i}{g_j}\bar{n}_jA_{ij} \tag{4}$$

where λ_{ij} is the wavelength, g_i and g_j are statistical weights, n_j is the low-level density, and P_{ij} is the spectral line frequency distribution.

This experiment is carried out in an atmospheric pressure environment, the spectral line is affected by these four mechanisms, combined with the literature that has been consulted, this paper only calculates the logarithmic density from the Doppler broadening angle to analyze the change trend of the number density. When the Doppler effect is the

main broadening mechanism, the spectral line frequency distribution P_{ij} [21] is defined as:

$$P_{ij} = \lambda_{ij}\sqrt{\frac{m}{2\pi k_B T}} \tag{5}$$

where m is the mass of the atom, k_B is the Boltzmann constant, and T is the gas temperature.

In summary, the emission intensity ratio can be expressed as [22] for the transition from a common high energy level i to different lower energy levels j and k

$$\frac{I_{pi-sj}}{I_{pi-sk}} = \frac{\dfrac{2-\exp\left(-10^{-3}C_{pi-sj}n_{sj}l/\sqrt{T_g}\right)}{1+C_{pi-sj}n_{sj}l/\sqrt{T_g}}}{\dfrac{2-\exp\left(-10^{-3}C_{pi-sk}n_{sk}l/\sqrt{T_g}\right)}{1+C_{pi-sk}n_{sk}l/\sqrt{T_g}}}\frac{A_{pi-sj}}{A_{pi-sk}} \tag{6}$$

where C_{pi-sj} is

$$C_{pi-sj} = \frac{\lambda_{pi-sj}^3}{8\pi}\frac{g_{pi}}{g_{sj}}\sqrt{\frac{m}{2\pi k_B T}}A_{pi-sj} \tag{7}$$

The spectral lines and associated parameters selected for calculating metastable ($1s_3$ and $1s_5$ levels) and resonant density ($1s_2$ and $1s_4$ levels) are shown in Table 2.

Most of these lines have strong emission intensity in the visible range. The experiment selected the ratio of the cooperation intensity of two sets of spectral lines with the same upper energy level. The specific combination arrangement is as follows: $2p_2 \rightarrow 1s_5$, $2p_2 \rightarrow 1s_2$; $2p_2 \rightarrow 1s_4$, $2p_2 \rightarrow 1s_2$; $2p_3 \rightarrow 1s_5$, $2p_3 \rightarrow 1s_2$; $2p_3 \rightarrow 1s_4$, $2p_3 \rightarrow 1s_2$; $2p_4 \rightarrow 1s_3$, $2p_4 \rightarrow 1s_2$. A total of five combinations were selected to establish a system of equations, and the density of metastable states ($1s_3$ and $1s_5$ energy levels) and resonant state densities ($1s_2$ and $1s_4$ energy levels) was fitted by the least squares method. Make

Table 2. Argon emission lines used to calculate metastable and resonant state densities [23]

number	$\lambda(nm)$	$A_{ki} \times 10^6$ (s^{-1})	Paschen	g_i	g_j
1	826.45	1.53	$2_{P2} \rightarrow 1_{S2}$	3	3
2	727.29	1.83	$2_{P2} \rightarrow 1_{S4}$	3	3
3	696.54	6.39	$2_{P2} \rightarrow 1_{S5}$	3	5
4	840.82	22.3	$2_{P3} \rightarrow 1_{S2}$	5	3
5	738.4	8.47	$2_{P3} \rightarrow 1_{S4}$	5	3
6	706.72	3.8	$2_{P3} \rightarrow 1_{S5}$	5	5
7	852.14	13.9	$2_{P4} \rightarrow 1_{S2}$	3	3
8	794.84	18.6	$2_{P4} \rightarrow 1_{S3}$	3	1

D minimal during fitting [24]:

$$D = \sum_i \sum_j \sum_k \left(\frac{I_{i \to j}}{I_{i \to k}} - \frac{r_{ij} A_{ij}}{r_{ik} A_{ik}} \right)^2 \tag{8}$$

The trend of number density changes in metastable states ($1s_3$ and $1s_5$ energy levels) and resonant state densities ($1s_2$ and $1s_4$ energy levels) at different distances is plotted as shown in Fig. 3.
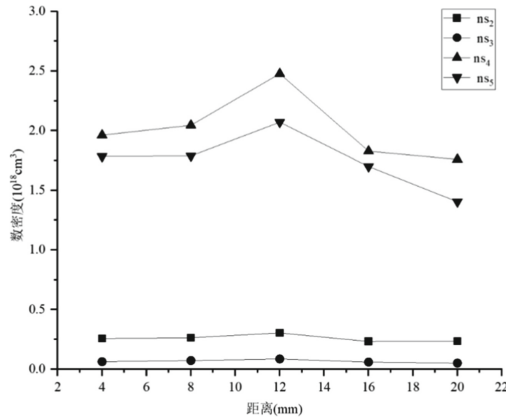
Fig. 3. Trend chart of number density change

It can be seen from Fig. 3 that with the increase of the distance between the copper plate and the glass nozzle, the metastable and resonance state number density of argon shows a trend of first increasing and then decreasing, which is different from the trend of particle irradiance gradually decreasing with the increase of distance. When the distance from the copper plate to the glass nozzle is 4 mm, 8 mm, 12 mm, 16 mm, and 20 mm, the number density relationship is $ns_4 > ns_5 > ns_2 > ns_3$, and when the distance is 4 mm, 8 mm, 12 mm, 16 mm, 20 mm, the number density of the $1s_5$ energy level is similar to the density of the $1s_4$ energy level, and the number density of the $1s_2$ energy level is similar to the number density of the $1s_3$ energy level.

It is believed that the ionization energy of argon metastable atoms and the excitation energy to higher excited states are smaller than those of ground state atoms, and the vast majority of low-energy electrons in the plasma can directly ionize or excite argon metastable atoms to higher energy levels, making them the most important source of electrons, ions and highly excited particles in addition to ground state argon atoms [25]. For the obtained number density relationship $ns_4 > ns_5 > ns_2 > ns_3$, the analysis believes that argon plasma is produced in atmospheric pressure air in the experiment, and when the plasma acts on the copper foil, the particle irradiance increases, the particle reacts more violently, and a large number of low-energy electrons will excite the metastable argon atom to a higher energy level. In addition, due to the energy it carries, argon metastable atoms can decompose gas molecules to produce active particles in the mixed discharge

of argon gas and other molecular gases [26], so the resulting metastable number density will be lower than that of the resonance state.

5   Conclusion

In this paper, a needle-ring medium is used to block the plasma discharge device to generate a stable argon plasma jet under atmospheric pressure conditions, and its spectral data are collected and diagnosed, and the metastable and resonant state number density changes of the active particles and argon acting on the surface of copper foil by argon plasma jet are studied, and the results show that:

The active particles in the argon plasma jet produced by the needle-ring type medium that blocks the plasma discharge device in atmospheric pressure air are mainly oxygen atoms and hydroxyl radicals; When argon plasma acts on the copper plate, the oxygen atom increases first and then decreases with the increase of the distance from the copper plate to the nozzle, and the hydroxyl radical gradually decreases.

When argon plasma is applied to the copper plate, the relationship between the metastable ($1s_3$ and $1s_5$) number density of argon and the number density of the resonant state ($1s_2$ and $1s_4$) is $ns_4 > ns_5 > ns_2 > ns_3$, and the number density of metastable ($1s_3$ and $1s_5$) is similar to that of the resonant state ($1s_2$ and $1s_4$), and the trend of first increasing and then decreasing with the increase of axial distance.

References

1. Zhang, X., Zhang, X.F., Li, H.P., et al.: Atmospheric and room temperature plasma (ARTP) as a new powerful mutagenesis tool (mini review). Appl. Microbiol. Biotechnol. **98**(12), 5387–5396 (2014)
2. Kong, M.G., Kroesen, G., Morfill, G., et al.: Plasma medicine: an introductory review. New J. Phys. **11**(11), 115012 (2009)
3. Lloyd, G., Friedman, G., Jafri, S., et al.: Gas plasma: medical uses and developments in wound care. Plasma Process. Polym. **7**(3–4), 194–211 (2010)
4. Lu, X.: High Voltage Eng. **37**(06), 1416–1425 (2011)
5. Yue, Y.: Diagnosis and optimization of hydroxyl and oxygen atoms in atmospheric pressure plasma jet. Huazhong University of Science and Technology (2017)
6. Yang, C.: Spatial distribution analysis of argon plasma jet spectroscopy. China Equip. Eng. **2022**(03), 16–18 (2022)
7. Wang, F.: Computational Fluid Dynamics Analysis - Principles and Applications of CFD Software. Tsinghua University Press, Beijing (2004)
8. Li, Z.: Research on cold plasma jet technology for wound suture. Shenyang University of Science and Technology (2016)
9. Miles, R.B., Lempert, W.R., Forkey, J.N.: Laser Rayleigh scattering. Meas. Sci. Technol. **12**(5), R33 (2001)
10. Dilecce, G., Ambrico, P.F., Simek, M., De Benedictis, S.: LIF diagnostics of hydroxyl radical in atmospheric pressure He-H2O dielectric barrier discharges. Chem. Phys. **398**, 142–147 (2012)
11. Irons, F.E.: J. Quant. Spectrosc. Radiat. Transfer **22**, 1 (1979)
12. Li, J., et al.: J. Phys. D: Appl. Phys. **44**, 292001 (2011)
13. Breton, C., Schwob, J.L.: C. R. Acad. Sci. Paris **260**, 461 (1965)

14. Pei, X.: Research on atmospheric pressure low-temperature plasma jet source and diagnosis of its key active particles. Huazhong University of Science and Technology (2014)
15. Schulze, M., Yanguas-Gil, A., von Keudell, A., Awakowicz, P.: A robust method to measure metastable and resonant state densities from emission spectra in argon and argon-diluted low pressure plasmas. J. Phys. D: Appl. Phys. **41**(6), 065206 (2008)
16. Mewe, R.: Z. Naturf. a **25**, 1798 (1970)
17. Lymberopoulos, D.P., Economou, D.J.: Fluid simulations of glow discharges: effect of metastable atoms in argon. J. Appl. Phys. **73**, 3668–3679 (1993)
18. Ali, A.W., Griem, H.R.: Theory of resonance broadening of spectral lines by atom-atom impacts. Phys. Rev. **140**(4A), A1044 (1965)
19. Measurement of Ar resonance and metastable level number densities in argon containing plasmas. J. Phys. D: Appl. Phys. **43**, 345202 (2010)
20. National Institute of Standards and Technology [DB]
21. Zhu, X.M., Pu, Y.K.: A simple collisional-radiative model for low-temperature argon discharges with pressure ranging from 1 Pa to atmospheric pressure: kinetics of Paschen 1s and 2p levels. J. Phys. D: Appl. Phys. **43**, 015204 (2010)
22. Li, J., Zhu, X.M., Pu, Y.K.: The population distribution of argon atoms in Paschen 1s levels in an inductively coupled plasma. J. Phys. D: Appl. Phys. **43**, 345202 (2010)
23. Kiehlbauch, M.W., Graves, D.B.: Modeling argon inductively coupled plasmas: the electron energy distribution function and metastable kinetics. J. Appl. Phys. **91**, 3539–3546 (2002)
24. Rauf, S., Kushner, M.J.: Argon metastable densities in radio frequency Ar, Ar/O$_2$ and Ar/CF4 electrical discharges. J. Appl. Phys. **82**, 2805–2813 (1997)
25. Balamuta, J., Golde, M.F.: Quenching of metastable Ar, Kr, and Xe atoms by oxygen-containing compounds: a resonance fluorescence study of reaction products. J. Chem. Phys. **76**, 2430–2440 (1982)
26. Sadeghi, N., Cheaib, M., Setser, D.W.: Comparison of the Ar(3P$_2$) and Ar(3P$_0$) reactions with chlorine and fluorine containing molecules: propensity for ion-core conservation. J. Chem. Phys. **90**, 219–231 (1989)
27. Worsley, M.A., Bent, S.F., Fuller, N.C.M., et al.: Characterization of neutral species densities in dual frequency capacitively coupled photoresist ash plasmas by optical emission actinometry. J. Appl. Phys. **100**, 083301 (2006)

Optimization Control of Power Supply for Ion Propulsion System in Multi-operating Points Mode

Yuan Jiang[1], Liying Zhu[2(✉)], Zhan Lei[1], Hong Du[2], and Dong Yang[2]

[1] School of Automation and Electrical Engineering, University of Science and Technology Beijing, Beijing 100083, China

[2] Beijing Institute of Spacecraft System Engineering, Beijing 100194, China

350909269@qq.com

Abstract. Space probe is one of the important areas for commercial space industry. In order to make the ion propulsion system have good control performance under the regulation of wide voltage and wide power, a nonlinear controller with adjustable multi-operating points is designed based on the synergetic approach to control (SAC) theory. The duty cycle of DC/DC converter can be calculated by combining the state space equation of DC/DC converter and the evolution law of manifold. In order to ensure that the overshoot of inductor current is small and the response speed is fast when the operating point is switched, according to the convergence characteristics of manifold, the adaptive control parameter is designed based on capacitor voltage error. According to the simulation results, the steady-state error of bus voltage under SAC control is 3.3%, which is less than 6% of PI control. For the transient process of switching, the overshoot of capacitor voltage and inductor current under PI control are close to 30%, much larger than that under SAC control, and the duty cycle under PI control also shows a large oscillation. SAC control has advantages over PI control in terms of steady-state performance, dynamic performance and duty cycle control.

Keywords: Space probe · ion propulsion system · power electronics · Nonlinear control

Commercial spaceflight is now the main battleground in the competition among space powers. Deep space exploration technology is an important field of commercial space industry. In the future, it can be relied on to realize space travel, space mining, space base construction and so on. Ion electric propulsion has the advantages of high efficiency and high specific impulse, so it has become the first choice for deep space exploration spacecraft [1, 2]. For example, The America's "Deep Space One" probe launched in October 1998 is the first deep space probe with electric propulsion as its main propulsion, the ion electric propulsion system completed the main propulsion task in the cruise stage. Launched in May 2003, Japan's Hayabusa probe, the ion electric propulsion system undertook the main task of cruise phase propulsion. The Dawn probe, launched in September 2007, used the ion electric propulsion system to complete the exploration mission in a real sense. It used the solar ion electric propulsion system to realize the rendezvous and orbit exploration of Vesta and Ceres [3–8].

Ion electric propulsion system uses discharge chamber, discharge cathode, neutralizer and other facilities to achieve ion production, ion acceleration and ion neutralization, and uses ion optical components (grid power supply, acceleration gate power supply) to complete the separation, focus and acceleration of the ions in the discharge chamber, so as to generate thrust. The Power Processing Unit (PPU) is used to convert the spacecraft bus voltage into the electrical power required by each part of the ion electric propeller. Typical power supply structure of ion thruster is shown in Fig. 1. As electrical equipment, ion electric thrusters generally have the characteristics of large power consumption and multiple working modes (wide voltage and wide power range). For example, the PPU of Hayabusa's electric propulsion system has a bus voltage range of 70–120 V. The PPU of Dawn's electric propulsion system bus has a voltage range of 80–120 V and a power range of 600–3000 W [9, 10]. The adjustable multiple operating points put forward higher requirements for the control of spacecraft power system.
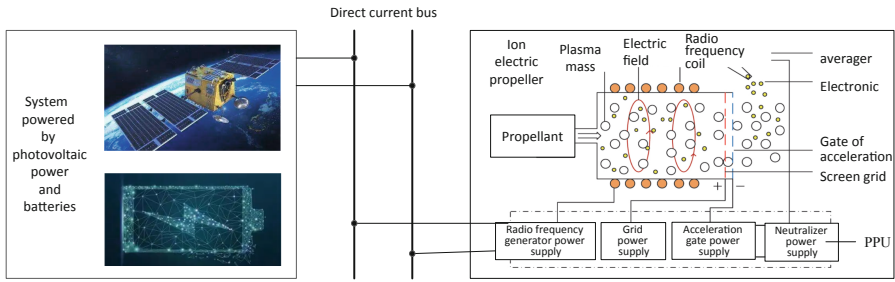
Fig. 1. Power supply structure of ion electric propulsion

According to the requirements of wide range adjustment of ion electric propulsion, the power electronic converter of the spacecraft power supply and distribution unit will show the nonlinear characteristics of discrete and variable structure. Meanwhile, the converter needs to meet the load changes in a wide range and the adjustment process is affected by various disturbances. The above problems make the converter control process and controller design more complicated. Therefore, the linear control method based on the state space average model and the classical cybernetics PI/PID controller are difficult to achieve the expected effect [11, 12]. At present, there are few researches on the control method of spacecraft power supply system with wide voltage and wide power range in China. But in other power systems, some nonlinear control methods, such as theory of differential geometry, robust control, sliding mode variable structure control, adaptive control, cooperative control, etc., are applied to PWM control of power electronic converter. In reference [13], a nonlinear control method based on differential geometry theory and sliding mode was proposed to solve the problems of low accuracy and poor dynamic performance of the compensated current control strategy of active power filter, which realized fast tracking of the command current and accurate control of the output current. In reference [14], aiming at the robustness of grid-connected resonant inverters caused by non-ideal conditions such as weak grid, distortion and imbalance, direct control strategies through feedback robust current with additional unit delay and robust current with suppression of harmonic current were proposed. In reference [15],

when the modular multilevel converter is disturbed, PI control and passivity control cannot guarantee the reliability and dynamic performance of the system, so passive sliding mode control which could improve the anti-interference ability and response speed was proposed. In reference [16], an adaptive control strategy that takes into account multiple parameters such as power, frequency and virtual moment of inertia of the virtual synchronous generator was proposed, so that the off-grid switching process has excellent transient characteristics. In reference [17] a method applied the collaborative control theory to DC/DC converter control was proposed, so that the converter output can have a better inhibition effect on the disturbance such as bus voltage and load change.

To sum up, when switching over multiple operating points of ion electric thruster, the power supply is essentially a wide range of output adjustment, so it requires variable structure control of the power converter. In the application of sliding mode variable structure control, chattering and changeful switching frequency are easy to occur [18], which increases the difficulty of design. Therefore, in this paper, the synergetic approach to control (SAC) theory will be used, a variable structure nonlinear control method which can control the spacecraft power system better. The method can directly model and derive the nonlinear control law by using the equation of state, which is especially suitable for the operation mode of wide voltage and wide power regulation.

1   Control Object Mathematical Model

1.1   Deep Space Probe Power Supply Model

The power supply system of the deep space probe generally adopts the mode of combined power supply of photovoltaic cells and batteries, and the DC bus is drawn through the DC/DC converter to supply power to the rear stage load. The control of the power supply system is essentially the control of the DC/DC converter. Therefore, this section only discusses the modeling of the converter. The topology selected is full-bridge DC/DC, and its structure is shown in Fig. 2. In this paper, the following assumptions about the converter will be made. The on-resistance of bridge arm S_1–S_4 and rectifier diode D_1–D_4 is r. The circuit operates in inductance current continuous mode, and the inductance L is linear and unsaturated. Ignoring line impedance.
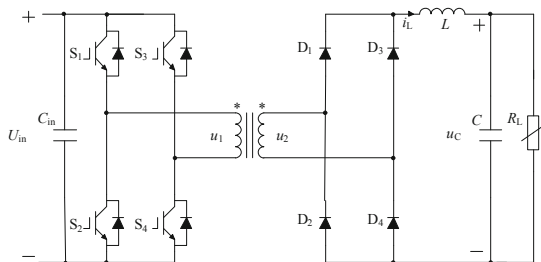
Fig. 2. Model of deep space detector power converter

According to the state of inductance current, the full-bridge converter can be divided into two modes within a full switching cycle. Mode one is that the inductor is in the

charged state. At this time, the transformer secondary voltage u_2 is approximately equal to U_{in} (or $-U_{in}$). After the diodes D_1 and D_4 (or D_2 and D_3) are rectified, the inductor L and capacitor C are charged, and the energy of load comes from the transformer primary side. Mode 2 is that the inductor is in a state of follow current, and the transformer secondary voltage u_2 is approximately equal to 0. Diodes D_1 and D_2, D_3 and D_4 are in series and connected into two continuous flow channels. The energy of load comes from inductor L and capacitor C. According to the above physical process, the state space equation with $x_1 = i_L(t)$ and $x_2 = u_C(t)$ as state variables can be constructed as follows:

$$\dot{x}(t) = Ax(t) + BU_{in} \tag{1}$$

Among them, $x(t) = [i_L(t)\ u_C(t)]^T$ is the state vector, A is the system matrix, B is the control matrix, and U_{in} is the input voltage of converter. According to the average model theory, when the duty cycle of $S_1 - S_4$ in a switching period is $d(0 < d < 50\%)$, the following relation can be expressed:

$$\begin{cases} A = A_1 \cdot 2d + A_2 \cdot (1 - 2d) \\ B = B_1 \cdot 2d + B_2 \cdot (1 - 2d) \end{cases} \tag{2}$$

Among them, A_1 and B_1 are the system matrix and control matrix of mode 1, and A_2 and B_2 are the system matrix and control matrix of mode 2. According to the circuit equation, the matrix A and B can be written as:

$$A = \begin{bmatrix} -\frac{[k^2 + (2k^2+4)d]r}{Lk^2} & -\frac{1}{L} \\ \frac{1}{C} & -\frac{1}{R_L C} \end{bmatrix}, B = \begin{bmatrix} \frac{2d}{kL} \\ 0 \end{bmatrix}, k \text{ is the primary secondary side ratio}$$

of the transformer. Thus, the mathematical model of full bridge DC/DC can be written as follows:

$$\begin{cases} \dot{x}_1 = -\frac{[k^2 + (2k^2+4)d]r}{Lk^2} x_1 - \frac{1}{L} x_2 + \frac{2d}{kL} U_{in} \\ \dot{x}_2 = \frac{1}{C} x_1 - \frac{1}{R_L C} x_2 \end{cases} \tag{3}$$

1.2 PPU Equivalent Model of Ion Electric Thruster

In the mission of far-reaching detection, due to the limited energy supply, the ion electric thruster mostly adopts the mode of multi-operating point adjustment, that is, the supply voltage and power of the PPU (including the screen grid power supply, acceleration grid power supply, etc.) can be adjusted. From the power side, a PPU with adjustable voltage and power is equivalent to a variable resistance, so in this paper, the PPU is equivalent to a variable load RL.

2 Design of Controller

2.1 Synergetic Approach to Control Theory

Synergetic approach to control (SAC) is a state-space method for designing nonlinear controllers. The control law can be obtained according to the selected macro variables

and the defined manifold functions. The basic process is shown in Fig. 3. After establishing the state space of the controlled object, macro variables are selected in the space and manifold functions are constructed to realize the indexes of steady-state and dynamic control. In addition, the higher order system can be reduced by increasing the number of manifolds. If the mathematical model of the system is obtained, the calculation process of deducing the control law based on the synergetic control theory is simple, with the characteristics of strong nonlinear adaptability and strong control followability. Results show that the nonlinear synergetic controller has strong robustness to the system parameters and can obtain better performances of steady-state and dynamic.

```
                    ┌──────────┐
                    │  Start   │
                    └──────────┘
                         │
                         ▼
          ┌──────────────────────────────┐
          │   Select macro variables      │
          │                               │
          │   ψ_i = Σ a_ij x_j + β_i      │
          │        j=1                    │
          └──────────────────────────────┘
                         │
                         ▼
          ┌──────────────────────────────┐
          │   Construct manifold          │
          │                               │
          │   ψ_i = Σ a_ij x_j + β_i = 0  │
          │        j=1                    │
          └──────────────────────────────┘
                         │
                         ▼
          ┌──────────────────────────────┐
          │ obtain control law according  │
          │  to the law of evolution      │
          │                               │
          │   T ψ̇_i + ψ_i = 0             │
          └──────────────────────────────┘
                         │
                         ▼
                    ┌──────────┐
                    │   end    │
                    └──────────┘
```

Select macro variables
$$\psi_i = \sum_{j=1}^{n} a_{ij} x_j + \beta_i$$

Construct manifold
$$\psi_i = \sum_{j=1}^{n} a_{ij} x_j + \beta_i = 0$$

obtain control law according to the law of evolution
$$T\dot{\psi}_i + \psi_i = 0$$
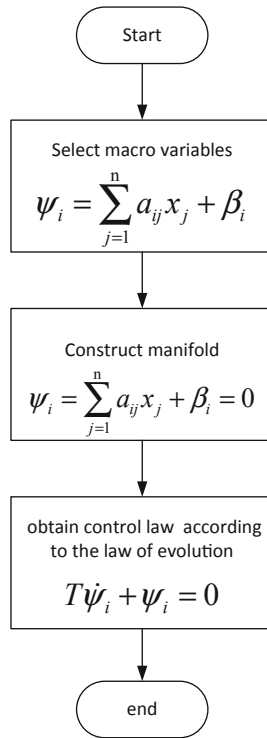
Fig. 3. Design flow of synergetic approach to control

Selecting macro variables is the first but key step in the design of synergetic controller, which requires the macro variables to contain the steady-state characteristics of the system. Macro variables are usually defined as linear combinations of state variables $x(t)$:

$$\psi = \psi(x, t) = \alpha x(t) + \beta \qquad (4)$$

Among them, $\psi = [\psi_1 \ \psi_2 \ \dots \ \psi_m]^T$, $x(t) = [x_1(t) \ x_2(t) \ \dots \ x_n(t)]^T$, α is coefficient matrix $[\alpha_{ij}]_{m \times n}$, β is vector of intercept $[\beta_1 \ \beta_2 \ \dots \ \beta_m]^T$. In the synergetic approach to control theory, the essence of the control process is to make the system go from any

initial state to the manifold $\boldsymbol{\psi} = 0$ and finally to the steady state. For a system whose state-space equation is $\dot{x} = f(\boldsymbol{x}, \boldsymbol{u}, t)$, the dynamic evolution law of its manifold is:

$$T\dot{\boldsymbol{\psi}} + \boldsymbol{\psi} = T\frac{\partial \boldsymbol{\psi}}{\partial \boldsymbol{x}}\dot{x} + \boldsymbol{\psi} = 0, \quad T > 0 \tag{5}$$

T is the time constant of the differential equation, which can characterize the convergence rate of the system tending to the manifold $\boldsymbol{\psi} = 0$. The control law can be derived by using the Eq. (5). Since manifold $\boldsymbol{\psi} = 0$ contains all the control information of the system, when the system runs on manifold $\boldsymbol{\psi} = 0$, if control variables are added to stabilize the system, the system will converge to the steady-state equilibrium point along the manifold. According to Lyapunov and the sliding mode stability theorem, the sufficient and necessary condition for the manifold $\boldsymbol{\psi} = 0$ to be stable is that there is a continuously differentiable function $V(t, \boldsymbol{x}, \boldsymbol{\psi})$ in the subspace of x where (1) $V(t, \boldsymbol{x}, \boldsymbol{\psi})$ is positive definite about $\boldsymbol{\psi}$; (2) The full derivative of $V(t, \boldsymbol{x}, \boldsymbol{\psi})$ against t is negative by dividing by $\boldsymbol{\psi} = 0$ [19].

We can construct a function $V(t, \boldsymbol{x}, \boldsymbol{\psi}) = \boldsymbol{\psi}^T\boldsymbol{\psi}$. Obviously, $V(t, \boldsymbol{x}, \boldsymbol{\psi})$ is positive definite about $\boldsymbol{\psi}$. Then, find the full derivative of $V(t, \boldsymbol{x}, \boldsymbol{\psi})$ with respect to t:

$$\dot{V} = \frac{\partial \boldsymbol{x}}{\partial t}\sum_{i=1}^{m}2\psi_i\frac{\partial \psi_i}{\partial \boldsymbol{x}} = 2\sum_{i=1}^{j}\psi_i\dot{\psi}_i \tag{6}$$

According to the variable definition in formula (4) and (5), it can be obtained:

$$\begin{cases} \dot{\psi}_i = -\dfrac{\psi_i}{T}, & T > 0 \\ \dot{\psi}_i \cdot \psi_i < 0, & T > 0 \end{cases} \tag{7}$$

When the time constant $T > 0$, the full derivative of $V(t, \boldsymbol{x}, \boldsymbol{\psi})$ with respect to t is negative except where $\boldsymbol{\psi} = 0$. In conclusion, it can be proved that the system is stable about manifold $\boldsymbol{\psi} = 0$ and the control law exists.

2.2 Synergetic Controller of Deep Space Detector Power Supply

For the full-bridge DC/DC mathematical model defined by the formula (3), the macro variable selected in this paper is:

$$\psi = (x_2 - x_{2\text{ref}}) + \alpha \cdot (x_1 - x_{1\text{ref}}) \tag{8}$$

Among them, $x_{2\text{ref}}$ is the given value of the output voltage of the converter. $x_{1\text{ref}}$ is the steady-state value of the inductance current, which can be calculated according to the given value of the output power P_{ref} and the given value of the output voltage. α is the synergetic control parameter. Then, the dynamic evolution trajectory expressed in formula (5) can be expressed as:

$$T\dot{\psi} + \psi = T \cdot (\dot{x}_2 + \alpha\dot{x}_1) + (x_2 - x_{2\text{ref}}) + \alpha\left(x_1 - \frac{P_{\text{ref}}}{x_{2\text{ref}}}\right) \tag{9}$$

According to the formula (9), the duty cycle d of S_1–S_4 within a switching cycle can be written as:

$$d = \left[\begin{array}{c} \dfrac{(RLC\alpha + TRL - RCT\alpha r)x_1 - (LT + RCT\alpha - RLC)x_2}{RLC} \\ -x_{2\text{ref}} - \dfrac{\alpha P_{\text{ref}}}{x_{2\text{ref}}} \end{array} \right] \Bigg/ \dfrac{(2k^2 + 4)rT\alpha x_1 - 2kU_{\text{in}}T\alpha}{k^2 L}$$

(10)

The parameter α affects the dynamic performance of manifold convergence: when the value is larger, the overshoot can be reduced, and when the value is smaller, the dynamic response can be accelerated, but it may cause overshoot. The principle of parameter α influencing the convergence process is shown in Fig. 4.
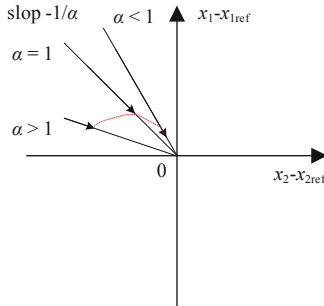
Fig. 4. Geometric representation of the dynamic process of the system by α

As shown in Fig. 4, when the system is in the initial stage of convergence, the capacitor voltage error ($x_2 - x_{2\text{ref}}$) is large. If α is large, -1/α is small, and the slope of the corresponding line is small, which makes the inductive current overshoot ($x_1 - x_{1\text{ref}}$) small and not easy to cause system oscillation. When the system approaches the steady state, the capacitor voltage error ($x_2 - x_{2\text{ref}}$) is small. If the value of α is small, the value of $-1/\alpha$ is large, and the slope of the corresponding straight line is large. As a result, the adjustment speed of the inductor current ($x_1 - x_{1\text{ref}}$) is accelerated, and the time of approaching the equilibrium point is shortened. Therefore, the ideal value of parameter α can be dynamically adjusted according to the capacitor voltage error ($x_2 - x_{2\text{ref}}$): when the capacitor voltage error is large, it can amplify the error. And when the capacitor voltage error is small, it can attenuate the error. Taking advantage of the property of quadratic function, α chosen in this paper is:

$$\alpha = a(x_2 - x_{2\text{ref}})^2 + b$$

(11)

3   Simulation Analysis

3.1   Simulation Parameter Setting

In order to verify the superiority of the proposed synergetic control method in the multi-operating point control of the power supply of ion electric propulsion system, the simulation model is built in the Matlab Simulink, compared with the classical PI controller to analyze the dynamic response of the output voltage and the inductive current overshoot of the full-bridge converter under wide voltage and wide power regulation. The simulation parameters are shown in Table 1.

Table 1. The simulation parameters

Symbol of parameter	Parameter value	Unit	Physical meaning
U_{in}	80	V	DC/DC converter input voltage
U_o (x_{2ref})	60,100,120	V	DC/DC converter output voltage (bus voltage)
P_{ref}	4800, 6600,7200	W	DC/DC converter output power given value
R_L	0.5,1.5,3	Ω	The operating point of simulated ion thruster is adjustable
L	4	mH	DC/DC converter rectifier side inductance
C	200	μF	DC/DC converter output side capacitance
r	0.005	Ω	On - state equivalent resistance of switching tube
k	1:2	1	Ratio of turns of primary secondary side of transformer
f	20	kHz	DC/DC converter switching frequency
T	6	ms	Synergetic controller time constant
a	0.0002	$V^{-1} \cdot A^{-1}$	Synergetic control parameter 1
b	0.03	$V \cdot A^{-1}$	Synergetic control parameter 2

3.2   Simulation Results

In the simulation time of 0.3 s, there are two switching points. At 0 s, the converter is required to work in high voltage mode, the bus voltage is 120 V, the output power is 4800 W. At 0.1 s, the operating point of the converter is required to be switched to the rated operating point, the bus voltage is 100 V, and the output power is 6600 W. At 0.2 s, the converter is again required to switch to the low-voltage working mode, the bus voltage is 60 V, and the output power is 7200 W.

Figure 5 shows the dynamic response process of the bus voltage at the output side when the DC/DC converter is respectively controlled by PI control and synergetic control in multi-operating point switching mode. It can be seen that the steady-state performance of the two controllers is similar, both can make the converter work in the required voltage mode, but in low-voltage mode, the steady-state value of the PI controller is lower than 56 V, and that of the SAC controller is about 58.2 V. In terms of dynamic performance, the overshoot of PI controller at 0 s is 26.7% and that is 27% at 0.1 s. While that of SAC controller is 4.8%. The first two adjustment time of PI control is about 0.01 s and 0.014 s, which are also longer than SAC controller.
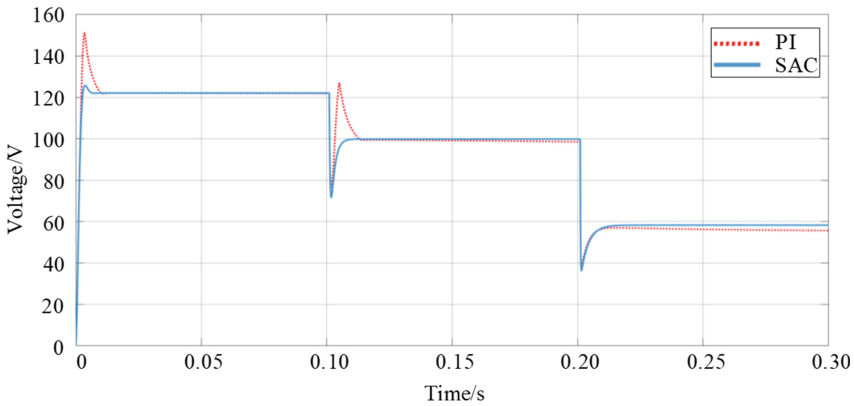
Fig. 5. Dynamic response process of capacitor voltage in multi-operating point mode

Figure 6 shows the overshooting state of inductance current on the rectification side when the DC/DC converter is respectively controlled by PI and coordinated control in multi-operating point switching mode. At 0 s and 0.1 s switching, the inductance current under PI control is overshot, which is 28.7% and 30.6%, respectively. Although there is no overshoot at 0.2 s switching, there is obvious steady-state error. In contrast, due to the adaptive adjustment of parameter α according to capacitor voltage error designed in Sect. 2.2, the overshoot of SAC control is smaller than that of PI control when the operating point is switched, and the adjustment time of 0s initial state is also faster than that of PI control.

In conclusion, compared with traditional PI control, SAC control has certain advantages in steady-state performance and dynamic performance.

Fig. 6. Overshoot state of inductor current in multi-operating point mode

4   Conclusion

In order to make the deep space detector ion electric propulsion system have good control performance under wide voltage and wide power regulation, the state space model of full-bridge DC/DC converter is established by using the idea of state average. And then, a nonlinear controller based on the cooperative control theory is designed and its stability is proved. The control law of the converter can be obtained by combining the state equation of capacitor voltage, inductor current and manifold functio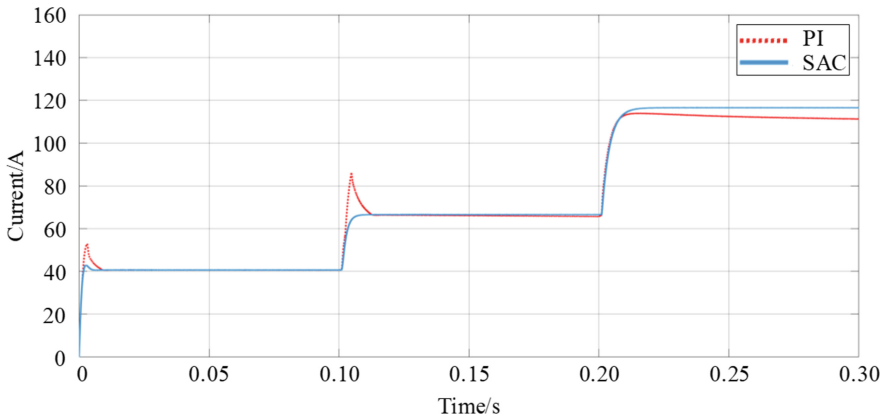n. In order to ensure that the inductor current overshoot is small and the adjustment speed is fast, adaptive collaborative control parameters based on capacitor voltage error feedback are also designed in this paper. It is proved by Matlab simulation that the synergetic control has certain advantages over the traditional PI control in steady-state performance and dynamic performance. The synergetic controller designed in this paper provides an effective method to solve nonlinear control problems such as multi-point switching of power electronic converters in deep space detectors and other scenarios.

References

1. Zhang, T., Geng, H., Zhang, X., et al.: Current status and future development of ion electric propulsion. Aerospace Shanghai **36**(6), 88–96 (2019)
2. Zhang, T., Long, J., Sun, M.: A review of electrical propulsion applications in deep space exploration missions//Chines Society of Astronautics. In: Proceedings of the ninth Annual Conference of Deep Space Exploration Technology Committee, vol. the middle volume, pp. 394–405. Hangzhou, Zhejiang Province (2012)
3. Polk, J.E., Brinza, D., Kakuda, R.Y., et al: Demonstration of the NSTAR ion propulsion system on the deep space one mission. In: 27th International Electric Propulsion Conference. Pasadena (2001)
4. Rawlin, V.K., Sovey, J.S., Hamley, J.A.: An ion propulsion system for NASA's deep space mission. In: 37th Space Technology Conference and Exposition. Albuquerque (1999)

5. Kuninaka, H., Nishiyama, K., Shimizu, Y., et al.: Flight status of cathode-less microwave discharge ion engines onboard Hayabusa asteroid explorer. In: 42nd Joint Propulsion Conference. Fort Lauderdale (2004)

6. Kuninaka, H., Nishiyama, K., Shimizu, Y., et al: Re-ignition of microwave discharge ion engines on Hayabusa for homeward journey. In: 30th International Electric Propulsion Conference. Florence (2007)

7. Brophy, J.R., Etters, M.A., Gates, J., et al: Development and testing of the Dawn ion propulsion system. In: 44th Joint Propulsion Conference. Sacramento (2006)

8. Brophy, J. R., Garner, C. E., Mikes, S.: Dawn ion propulsion system–initial check out after launch. In: 46th Joint Propulsion Conference. Hartford (2008)

9. Chen, C., Wu, R.: Design of wide range input and output beam power supply for ion electric propulsion. J. Deep Space Explor. **7**(4), 407–416 (2020)

10. Zhang, Y., Wang, S., Wu, R., et al.: Research status and development suggestions of radio frequency ion electric propulsion system PPU. Space Eng. **29**(5), 101–106 (2020)

11. Erdogan, A.D., Aydemir, M.T.: Use of input power information for load sharing in parallel connected boost converters. Electr. Eng. **91**(4), 229–250 (2009)

12. Wang, Q.: Research on Synergetic Control Theory of Switching Power Supply and Application Technology of Pulse Width Modulation. South China University of Technology, Guangzhou (2010)

13. Wu, Z.: Research on Nonlinear Control Strategy of Parallel APF Based on Differential Geometry Theory. Hefei University of Technology, Hefei (2017)

14. Wang, Q.: Robustness Analysis and Optimal Control of LCL Grid-Connected Converter Under Complex Network Conditions. Taiyuan University of Technology Taiyuan (2020)

15. Cheng, Q., Li, J., Lai, Y., et al.: Passivity-based sliding-mode control strategy for power electronic transformer based on MMC under non-ideal conditions. High Voltage Engineering, https://doi.org/10.13336/j.1003-6520.hve.20220214. Accessed (2022)

16. Cao, X., Han, J.: Multi-parameter adaptive control strategy for new source virtual synchronous generator. Power Electron. **56**(3), 43–46+50 (2022)

17. Wang, J.: Synergetic control for full bridge converters of switching power supply. J. Railway Sci. Eng. **12**(4), 936–940 (2015)

18. Tan, S.C., Lai, Y.M., Tse, C.K.: General design issues of sliding-mode controllers in DC-DC converters. IEEE Trans. Indust. Electron. **55**(3), 1160–1174 (2008)

19. Cheng, D., Hu, X., Shen, T.: Analysis and Design of Nonlinear Control Systems. Springer, Heidelberg (2010)

Effect of Temperature on PD Characteristics Under Nanosecond Pulses

Jianwei Zhang[1], Zhexi Chang[1], Feng Yan[2], Dekun Cao[3], Zhaohui Liu[1], Ning Tian[1], and Jiawei Zhang[1(✉)]

[1] School of Electrical Engineering, Xi'an University of Technology, Xi'an 710048, China
jwzhang@xaut.edu.cn
[2] School of Humanities and Foreign Languages, Xi'an University of Technology, Xi'an 710048, China
[3] State Grid Jilin Electric Power Company Tonghua City Power Supply Company, Tonghua 134001, Jilin, China

Abstract. Protecting inverter-fed motor insulation system from failure of inverter overvoltage is nowadays of paramount interest in the fields of electric vehicles (EVs), especially when the insulation structure undergoes partial discharge (PD) and electrical-thermal aging. In this work, the effect of temperature on the PD characteristics of insulating paper of inverter-fed motor slot is investigated with bipolar repetitive pulses. The PD spectra with different temperature are plotted. The distribution of surface charges will change with the growth of temperature. As a result, the distribution of electric field and generating probability of initial electrons are affected accordingly. Besides, to verify the experimental results, numerical simulations of PD characteristics are studied. The distribution of electric field and density of electrons are obtained. These results can provide valuable information for the study of PD characteristics of insulation systems in inverter-fed motor.

Keywords: partial discharge · space charge · temperature · modeling

1 Introduction

The booming development of EVs is one of the most effective paths to solve the global energy crisis and mitigate environmental degradation. However, safety remains to be overcome in EVs. For instance, the pulse width modulation (PWM) technology used in EVs leads to drive motors being subjected to overvoltage during the operation. Furthermore, the abrasion on the insulation structure of motor stator wingding during the operation leads to air gaps between the stator core and insulation layer. As a result, the probability of PD occurrence grows. The drive motor suffers from the PD erosion for several years [1], which will destroy the insulation performance and threaten the safety and stability of EVs [2]. The Nomex type 410 insulating paper has high dielectric strength, heatproof and mechanical properties, which is widely used in the slot insulation of motor stator windings [3]. Therefore, the investigation of its insulation durability is essential for assessing the safety level of the entire motor insulation system.

Vast researches have already been conducted on PD erosion to investigate its degradation behavior on the insulation materials. The aging phenomenon and discharging mechanism of the rotating machines under nanosecond pulse were analyzed by Wang. The influence of voltage frequencies, duty cycles and rise times on the PD characteristics were discussed [4, 5]. Wu conducted accelerated thermal aging experiments on Nomex insulating paper, and investigated the characteristics of material surface charges accumulation and dissipation after charges injected into the insulating paper at different aging cycles [6]. Illisa established a physical model of PD activity of the void inside the cable [7]. The PD physical phenomenon of the inhomogeneous electric field inside the void was simulated with finite element method. The distribution of surface charges and electric field were obtained. Nevertheless, few studies have been conducted to report the statistical characteristics of PD of insulating materials and the distribution of electric field energy under temperature promotion.

In this paper, a PD test system under nanosecond pulse voltage is built, and the effect of temperature on PD characteristics of Nomex type 410 insulation paper is analyzed. The PD signals and activities are studied with experimental diagnosis. Besides, the process of PD of Nomex type 410 insulation paper is simulated with the Parallel Streamer Solver with Kinetics (PASSKEy) [8]. The distribution of electric field and density of electrons are obtained.

2   Experimental and Modeling Parameters

There are two sections. In the first section, a PD test system is built. PD experiments are conducted under different temperatures to extract and analyze the PD signals. In the second section, the simulation model and parameters of PD activities at different temperatures with the actual experimental conditions are introduced.

2.1   PD Test System

The PD test system is shown in Fig. 1, which mainly consists of the nanosecond impulse power supply, ultra-high frequency antenna, high voltage probe, oscilloscope, and the
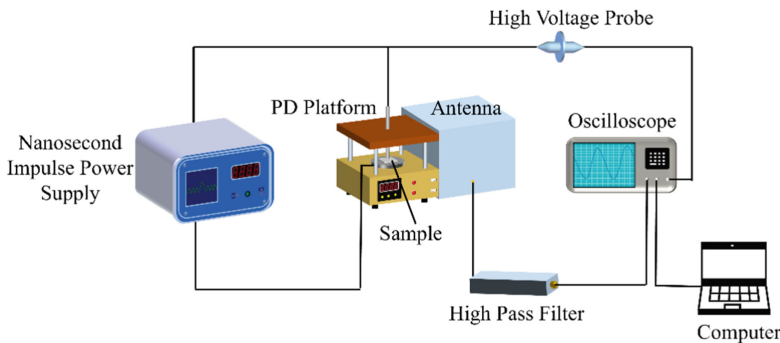

Fig. 1. Schematic of the PD test system.

heating platform. The test sample is selected for the DuPont Nomex type 410 paper, and the dimension of the samples is 20 × 20 × 0.18 mm. Before the experiment, the samples are cleaned with anhydrous ethanol and dried with ionizing air blower. Finally, the samples are divided into four groups and subjected to two hours of discharge treatment at 50 °C, 100 °C, 150 °C and 200 °C, respectively. The applied voltage used in the experiment is the bipolar repetitive pulses with the peak-to-peak value of 2.6 kV.

2.2 Simulation Modeling

A PASSKEy code [9] is used for the PD simulation under nanosecond pulses, which can be designed to calculate the electric field and hydrodynamic space time evolution process in gas discharge plasma containing complex chemical reactions. The Poisson's equation is used to obtain the distribution of electric field. Besides, the chemical kinetic equation is solved to simulate the process of discharge. In our model, 38 reactions and 18 substances are involved. The particles considered in simulation are e, N_2, O_2, O^-, etc. The scheme of simulation model is shown in Fig. 2. The sample size is set to 20 × 20 × 0.18 mm, and the diameter of the driven electrode is 8 mm. The pulse voltage is applied on the driven electrode area, which equals to ± 1.3 kV. Simulation experiments are carried out at one atmospheric pressure, and the gas discharge temperatures are set to 50 °C, 100 °C, 150 °C and 200 °C, respectively.
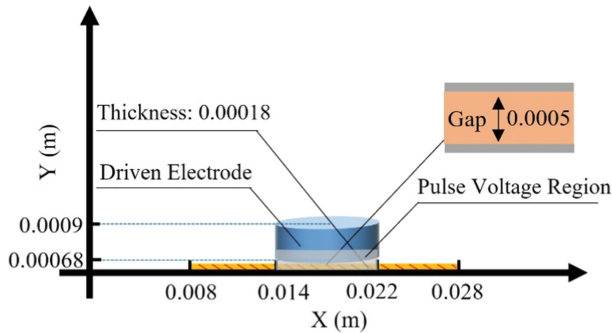
Fig. 2. The scheme of simulation model.

3 Results and Discussion

3.1 Effect of Temperature on PD Features Under Nanosecond Pulse Voltage

The Phase Resolved Partial Discharge (PRPD) patterns for 2 h at different temperatures are shown in Fig. 3. The red points in the Fig. 3 represent the maximum magnitude of PD at a moment. The PD signal is mainly concentrated at the rising edge of the nanosecond pulse voltage, the maximum magnitude increases with increase of temperature. Besides, the phase decreases with increase of temperature. There is no obvious variation in the PD amplitude at 150 °C and 200 °C.

The temperature affects the cumulative effect of the surface charges of the insulation materials [10], and the accumulation of more anisotropic charges is prone to form a strong distortion of electric field at the insulation air gap for PD [11]. According to the Richardson-Schottky law, the increase of temperature makes it more likely to excite the initial electrons generated by PD, resulting in the decrease of Partial Discharge Inception Voltage (PDIV). Thus, the PD is prone to occur, and the phase decreases.
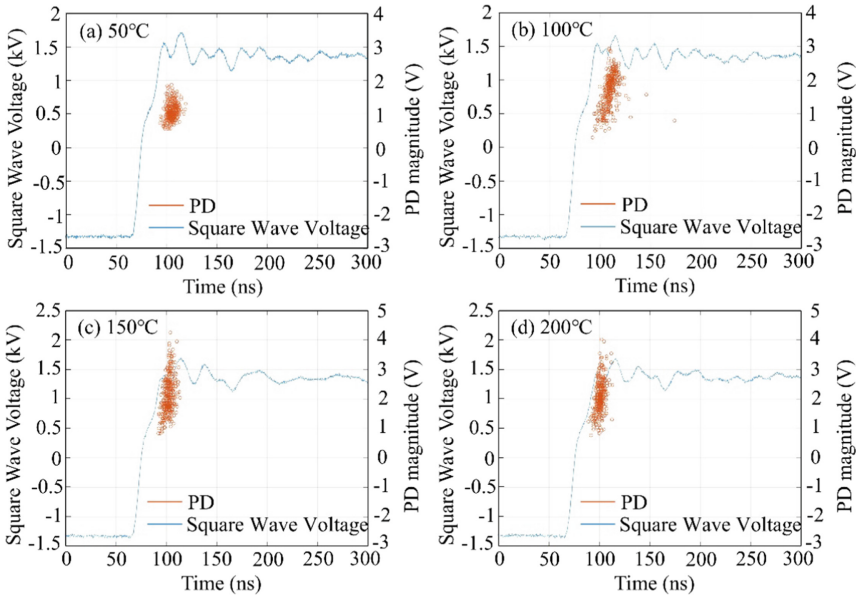
Fig. 3. PRPD patterns under different temperatures.

Moreover, it is clear that increasing temperature means more active PD activity, as shown in Fig. 4. The superposition of multiple PD magnitudes leads to increasing magnitudes of PD. However, the excessive temperature will increase the conductivity of the material surface, which makes the accumulated charges diffusion and inhibits the occurrence of PD. Therefore, the PD magnitude does not increase further at 200 °C.

3.2 Effect of Temperature on Simulated Electric Field Activity

The distribution of electric field at the same moment for different temperatures is calculated by the simulation, as shown in Fig. 5. And the discharge area is shown in Fig. 2. The bipolar repetitive pulses are applied to the drive electrode, and the discharge process occurs in the gap between the drive electrode and the Nomex type 410 insulating paper.

The region with high strength of electric field at low temperature is concentrated near the left and right tips of the electrodes, as illustrated in Fig. 5. However, with the growth of temperature, the region with high strength of electric field is uniformly distributed on the material surface. The density of electrons is shown in Fig. 6. The density of electrons
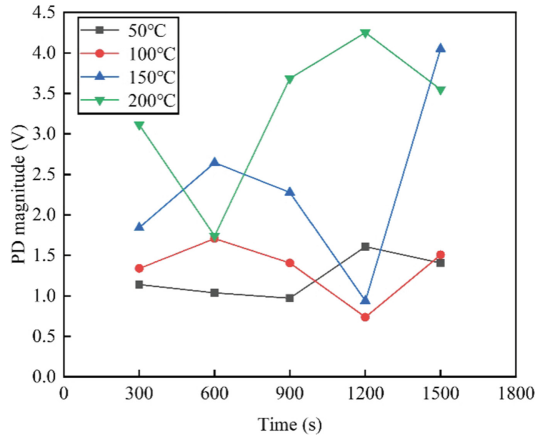
Fig. 4. Changes in the maximum magnitude of PD with aging time.
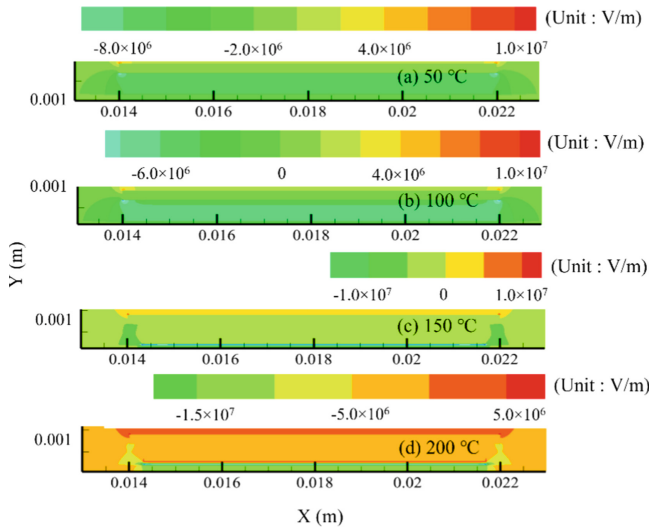
Fig. 5. Distribution of electric field at different temperatures.

multiplies for a shorter time at high temperatures and accumulates around the surface of the sample. When the temperature is 50 °C, the density of electrons accumulates almost near the electrode. Thus, higher temperatures imply more active electrons activities on the material surface [12], and the corresponding Fig. 7 reflects the same trend from the energy of electrons perspective. The high energy region means the region with high density of electrons. The high collision frequency of electrons reduces the PDIV and shortens the PD statistical delay. Eventually, PD at higher temperature is more prone to occur and is repeated with the increase of collision frequency.
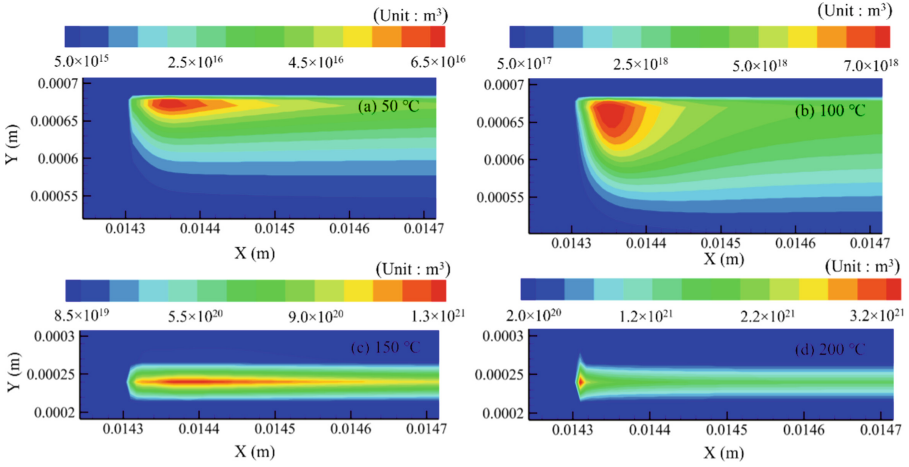
Fig. 6. Distribution of density of electrons at different temperatures.
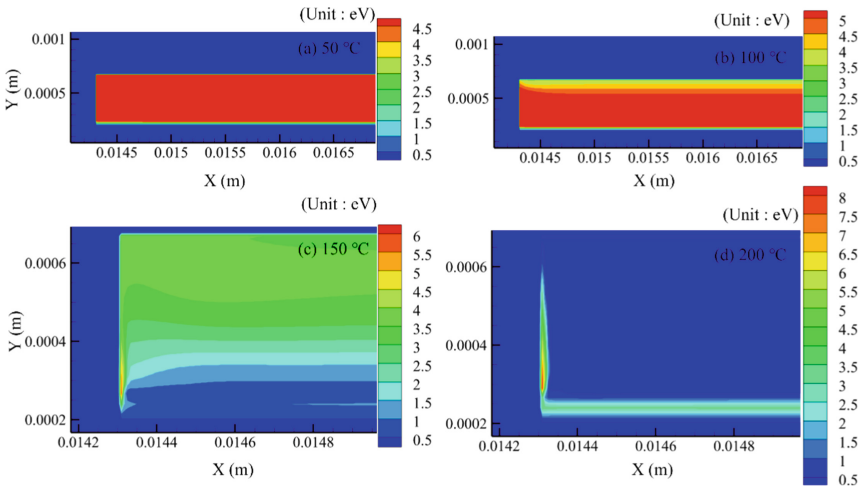
Fig. 7. Distribution of energy of electrons at different temperatures.

4   Conclusion

The effect of temperature on PD characteristics is investigated by Nomex insulating paper for drive motor. With the increase of temperature, the amplitude of PD increases and the phase of PD decreases. The PD behavior is more active at higher tempera-ture. The experimental results are in good agreements with the simulation results. The higher temperature is more conducive to the formation of stable electric field with high strength and the multiplication of higher density of electrons. At the same time, the ratio of electrons with high energy increases, which has a facilitating effect on PD activ-ity. Furthermore, the experimental and simulation results proposed in this paper can

be expected to be applied in the artificial intelligence based on big data analysis, environmental protection, exhaust gas disposal technology, which have social impact and humanity influence.

References

1. Sun, P.T., Sima, W.X., et al.: A review on accumulative failure of winding insulation subjected to repeated impulses. High Voltage **4**(1), 1–11 (2019)
2. Wang, P., Zhao, Z.J., et al.: Electrical insulation problems in power electronics devices. High Voltage Eng. **44**(7), 2309–2322 (2018)
3. Zhang, J.W., Chen, J.H., et al.: Electrical aging characteristics of Aramid paper under nanosecond impulse and AC voltages for the stator slot of electric vehicle motors. Jpn. J. Appl. Phys. **61**(4), 46002 (2022)
4. Wang, P., Cavallini, A., et al.: The influence of repetitive square wave voltage parameters on enameled wire endurance. IEEE Trans. Dielectr. Electr. Insul. **21**(3), 1276–1284 (2014)
5. Wang, P., Montanari, G.C., et al.: Characteristics of PD under square wave voltages and their influence on motor insulation endurance. IEEE Trans. Dielectr. Electr. Insul. **22**(6), 3079–3086 (2016)
6. Li, X.Y., Wu, G.N., et al.: Effect of thermal aging on surface charge accumulation and dissipation of Nomex paper. Proc. CSEE **40**(17), 10 (2020)
7. Illias, H.A., Tunio, M.A., et al.: Partial discharge phenomena within an artificial void in cable insulation geometry: experimental validation and simulation. IEEE Trans. Dielectr. Electr. Insul. **23**(1), 451–459 (2016)
8. Chen, X.C., Zhu, Y.F., et al.: Modeling of streamer-to-spark transitions in the first pulse and the post discharge stage. Plasma Sourc. Sci. Technol. **29**(9), 95006 (2020)
9. Zhu, Y.F., Shcherbanev, S., et al.: Nanosecond surface dielectric barrier discharge (nSDBD) in atmospheric pressure air: I. Measurements and 2D modeling of morphology, propagation and hydrodynamic perturbations. Plasma Sourc. Sci. Technol. **26**(12), 125004 (2017)
10. Pan, C., Tang, J., et al.: Numerical modeling of partial discharges in a solid dielectric-bounded cavity: a review. IEEE Trans. Dielectr. Electr. Insul. **26**(3), 981–1000 (2019)
11. Li, L., Song, J.C., et al.: Investigation on space charge properties of Nomex insulation paper in the mining dry type transformer during hygrothermal aging. IET Sci. Meas. Technol. **14**(12), 576–584 (2020)
12. Kang, A.L., Tian, M.Q., et al.: Contribution of electrical–thermal aging to slot partial discharge properties of HV motor windings. J. Electr. Eng. Technol. **14**, 1287–1297 (2019)

Discharge and Impulse Bit Characteristics of Pulsed Plasma Thruster with PTFE-Based Modified Propellants

Rui Zhang[1](✉) , Wenxiong Xi[2] , and Dongjin He[1]

[1] Airforce Aviation Repair Institute of Technology, Changsha, Hunan, China
nudtzhang@163.com
[2] School of Aeronautics and Astronautics, Central South University, Changsha 410012, China

Abstract. The advantages of simple construction, high specific impulse, and low energy consumption are provided by Ablative Pulsed Plasma Thrusters (APPTs). As a result, APPTs have been used for small satellite station-keeping, drag makeup, and attitude control. The APPT's low propellant utilization, however, significantly limits its performance, particularly the system's efficiency. To achieve a breakthrough in the propellant selection for APPT performance enhancement, in this research, a systematic theoretical and experimental study on the discharge characteristics, propellant ablation characteristics, plasma movement characteristics, and thruster performance of APPT using PTFE-based modified propellants doped with various contents of carbon fiber, aluminum powder, and boron powder was conducted. The results show that the different doping components not only affect the structural and optical properties of the propellant materials but also change the peak discharge current, discharge period, and equivalent resistance of the APPT discharge circuit. All mass shots of doped propellants are more than that of PTFE propellant. When compared to an APPT using pure PTFE as the propellant, the APPT with 10% Al90% PTFE as the propellant has the maximum impulse bit and system efficiency, whereas the APPT with 3% Al97% PTFE as the propellant has the lowest impulse bit. Due to the increased mass of the single pulse ablation propellant, the specific impulse of the APPT with doped propellants was lower than that of the APPT with pure PTFE as the propellant.

Keywords: Pulsed Plasma Thruster · Discharge Characteristic · Impulse Measurement · Inverted Pendulum Thrust Stand

1 Introduction

Pulsed Plasma Thruster (PPT) is a kind of pulsed plasma thruster with solid propellant. Compared with the PPT which uses liquid and gas as propellant, its biggest advantage is that the supply of non-toxic propellant and the thruster body are combined into a module, which saves the complicated propellant storage and supply system. It has the advantages of high specific impulse (generally greater than 1000 s), small impulse (50–200 μN-s), low average power consumption (1–150 W), simple structure, and so on. It is especially

suitable for small satellites and the implementation of propulsion tasks requiring high control accuracy [1].

The properties of propellant will greatly affect the ablative properties of APPT. Therefore, in addition to optimizing the discharge characteristics of PPT, researchers also try to use substances of different materials as APPT propellants, in order to find a breakthrough in the selection of propellants to improve the performance of APPT.

In 1995, Leiweke et al. installed PTFE mixed with high-density polyethylene in the middle of a fork made of PTFE and studied the propellant ablation characteristics and the macro performance of the thruster according to different arrangement modes. The results show that the carbon in the surface area of high-density polyethylene (HDPE) prevents the heat transfer of the arc to the propellant surface, and the ablation of the single pulse propellant is less than that of the pure PTFE propellant under the same initial conditions [2]. The specific impulse and average propellant discharge velocity of the thruster are basically the same when the two propellants are used.

Palumbo et al. conducted an experimental study on the PPT performance of Teflon, Celcon, Halar, Tefzel, Halon, 10%InBr3 90% Teflon and 30%InBr3 70%Teflon propellants respectively [3]. The study showed that the APPT using Teflon as propellant has the best overall performance. Since 2001, Kamhawi et al. from the University of Tokyo in Japan have extensively studied the operating characteristics of APPT using different densities of PTFE, and the propellants used include powdered PTFE, high-density PTFE, low-density porous PTFE, and carbon-doped PTFE. The results show that compared with other propellants, the thruster system with pure PTFE as propellant has the best performance. The thrust power ratio of thrusters can be improved by using powdered and low-density PTFE as propellants, but the specific impulse of thrusters is reduced because the powdered PTFE has more propellant loss. Using 2% carbon-doped PTFE as a propellant thruster, because of the reduction of propellant consumption, the efficiency of the thruster system has been improved, but because of the carbon mixing will make the PPT discharge fluctuations, greatly reduce the stability of the thruster work [4, 5].

Kyushu Institute of Technology in Japan, in cooperation with the National Association of Advanced Industrial Science and Technology, has carried out PPT performance tests using different mass ratios of HTPB/AP composite energetic materials as propellants, and compared with the PPT using PTFE as propellants. Research shows that with the increase of AP content in HTPB/AP, the impulse bit of the thruster system increases. However, the ablation mass of propellant increases with the increase of AP content, so the specific impulse and efficiency of the system decrease with the increase of AP content [6]. Schonherr et al. respectively conducted a comparative analysis of PPT discharge characteristics using PTFE, al-PTFE, and Zn-PTFE as propellants, and measured the motion characteristics of PPT plasma using different propellants by using high-speed photography. Limited by the experimental conditions, the PPT performance of different propellants is not significantly different [7].

Due to the shortcomings of APPT using Teflon as propellants, such as the non-uniformity of propellant ablation and the serious pollution of C and F particles in the ablation products on the performance of space-based optical components, researchers are trying to find the use of gas and liquid as a substitute for Teflon. The PPT using gas and

liquid propellant is better than that using solid propellant, and the system performance will be greatly improved [8, 9].

However, it is undeniable that the propellant storage, supply and heating and insulation devices of GPPT and LPPT greatly increase the complexity of the thruster system, and their structure, size, and weight also further affect the practicability of use on satellites. Therefore, the current research focus of APPT is still on solid propellant APPT. In order to improve the propellant selection of APPT, PTFE-based modified propellants doped with different contents of carbon fiber, aluminum powder, and boron powder were used in this study. The discharge characteristics, ablation characteristics of propellant, plasma motion characteristics, and propeller performance of APPT were systematically studied theoretically and experimentally.

2   Experimental Details

2.1   Thruster and Vacuum Chamber

The experimental setup is shown in Fig. 1. Four 3 uF polyester film capacitors with a rated voltage of 2 kV were used in the experiment. They were charged to 1500 V and the discharge energy was E0 = 13.5 J.
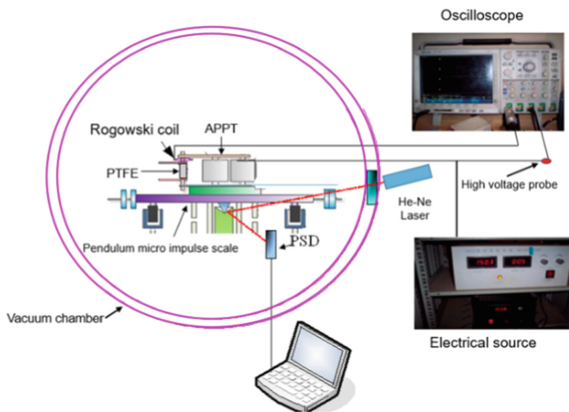
Fig. 1. Schematic of the experimental set-up.

Choose the 3M company PTFE molding powder (Dyneon, size 25 μm), by doping in PTFE micro aluminum powder, boron powder, and carbon fiber material on modification of propellant manufacture. 97%PTFE3%Al, 90%PTFE10%Al, 97%PTFE3%B, 90%PTFE10%B and 97%PTFE3%Cf were fired respectively. In order to eliminate the influence of different PTFE production processes on the experimental results, 100%PTFE was used as pure PTFE propellant in the experiment.

Due to the limitation of APPT configuration, it is required that the material used as propellant should have good insulation characteristics. UT502 insulation resistance tester was used to test the insulation resistance of the doped modified propellant. The

measurement results show that the insulation resistance of the fired propellants is infinite at 2500 V voltage, which can be used as the propellants of APPT.

PTFE-based propellants with different proportions were processed to $35 \times 15 \times 45$ mm^3. The thrust electrode is made of oxygen-free copper material. The electrode configuration is rectangular, the size is $35 \times 15 \times 3$ mm^3, and the distance between the electrodes is 35 mm.

A vacuum chamber 2.5 m in diameter and 3 m in length provides a simulated space environment for the thruster. The vacuum chamber pressure is 3×10^{-3} Pa when the thruster is working.

2.2 Discharge Parameter Measurement and Estimation Method

The Tek P5100 high-voltage probe was used to measure the discharge voltage of APPT and the CWT150 Rogowski coil was used to measure the discharge current. The four-channel Tek DPO4034 oscilloscope is powered by the UPS and used to collect and measure signals.
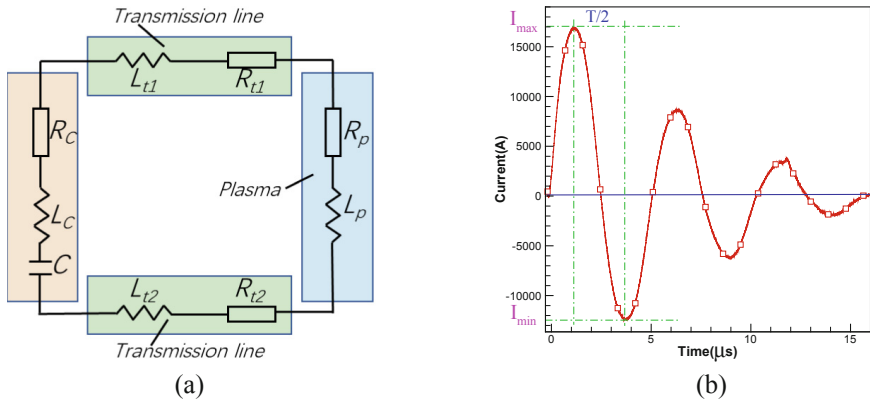
Fig. 2. (a) Equivalent circuit diagram and (b) typical discharge current waveform of APPT.

The discharge circuit of APPT can be equivalent to the inductor-capacitor-resistance (LCR) circuit [10, 11]. Figure 2 shows the typical discharge current waveform of APPT. By fitting the waveform, the equivalent resistance R_{eq} and inductance L_{eq} of the discharge circuit can be obtained as

$$L_{eq} = \left(\frac{T}{2\pi}\right)^2 \frac{1}{C} \tag{1}$$

$$R_{eq} = \frac{4L_{eq}}{T} \ln\left[\frac{|I_{max}|}{|I_{min}|}\right] \tag{2}$$

and thus

$$L_{eq} = L_{ext} + L_p \tag{3}$$

$$R_{eq} = R_{ext} + R_p \tag{4}$$

L_{ext} is the sum of L_C, L_{t1}, and L_{t2}. R_{ext} is the sum of R_C, R_{t1}, and R_{t2}, and T is the discharge cycle. I_{max} is the maximum discharge current value, and I_{min} is the minimum discharge current value. L_{ext}, R_{ext}, and the electrode.

The measured discharge voltage and current can be used to calculate the energy input into the APPT discharge channel E_{tr} and the efficiency of the system energy translated into discharge energy η_{tr}.

$$E_{tr} = \int_0^\infty V(t)i(t)dt \tag{5}$$

$$\eta_{tr} = E_{tr}/E_0 \tag{6}$$

2.3 Performance Parameters
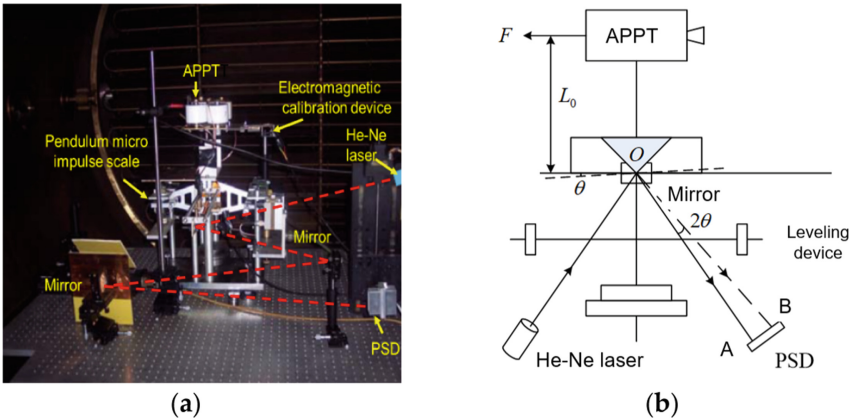
Fig. 3. (a) Pendulum micro impulse scale and (b) schematic diagram of working principle.

As shown in Fig. 3, the impulse bit I_{bit} was measured using a pendulum micro impulse scale [1]. The XS205DU electronic scale will measure the change in mass of the propellant after it is discharged 5400 times. The mass of single-pulse ablative solid propellant m_{bit}, can be calculated by averaging system-specific impulse I_{sp}, efficiency η, and average velocity of the ablated propellant v_e can be obtained as

$$I_{sp} = I_{bit}/m_{bit}g \tag{7}$$

$$\eta = I_{bit}^2/2m_{bit}E_0 \tag{8}$$

$$v_e = I_{bit}/m_{bit} \tag{9}$$

The APPT impulse bit is the sum of the impulses generated by Lorentz force and aerodynamic force [14]

$$I_{bit} = I_{EM} + I_{gas} \tag{10}$$

I_{EM} can be obtained by the Guman estimation formula [14]

$$I_{EM} = \int_0^\infty F_{EM}\,dt = \frac{1}{2}L'\int_0^\infty I^2(t)dt \tag{11}$$

Ψ is the time integral value of the square of the current.

$$\psi = \int_0^\infty I^2(t)dt \tag{12}$$

β is ratio of the impulse which is generated by the Lorentz force to the impulse bit, which can be expressed as

I_{bit} also can be expressed as

$$I_{bit} = m_{bit}(1-\alpha)C_{gas} + m_{bit}\alpha V_p \tag{13}$$

where α is the proportion of the ablated propellant which is accelerated by the Lorentz force, C_{gas} is the movement speed of the ablated propellant accelerated by the aerodynamic force.

Four double Langmuir probes with a bias voltage of 27 V were placed in the thrust shaft APPT plume region 8 cm, 12 cm, 16 cm, and 20 cm away from the propellant exposure surface. Plasma velocity Vp was measured by the time of flight method [15].

3   Experimental Results and Discussion

3.1   Physical Properties of the Modified Propellant

It can be seen from Fig. 4 that the fired propellant has porous morphology, which is mainly caused by the fact that the propellant is fired in the Ar protective gas environment. The existence of pores will lead to the increase of adsorbed gas on the propellant surface. Therefore, before the propellant is applied to APPT for performance tests, degassing treatment for a certain period of time is required to prevent the influence of adsorbed gas on the experimental results. The doped aluminum, boron, and carbon fiber particles are embedded in the PTFE crystal matrix, and defects such as cracks and pores can be observed on the fired propellant matrix. The existence of these defects will have a certain effect on the mechanical properties of the fired propellant matrix.

Figure 5 shows the surface reflection optical characteristics of different propellants measured by UV-4100U UV-visible spectrometer. Compared with pure PTFE, the modified propellant has different reflection characteristics in the range of light spectrum due to the different types and mass percentages of doped particles. In the range of 200–1500 nm, the reflectance of doped modified propellant decreases. In the range of 1500–2500 nm, the reflectance of doped modified propellant increases. The ablative properties of the propellant will be affected by the change in surface optical properties.
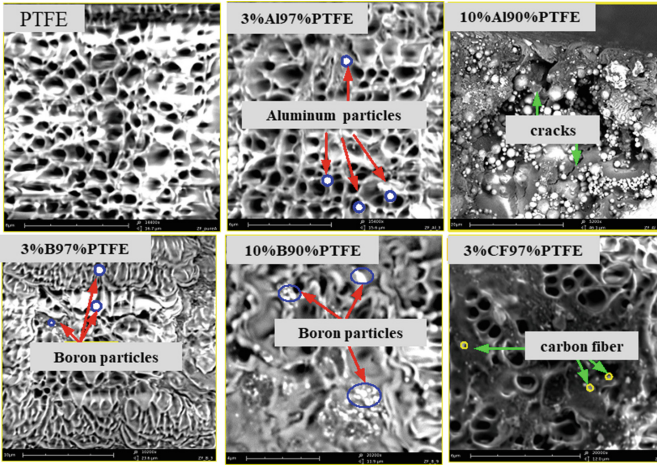
Fig. 4. SEM photomicrographs of different propellants
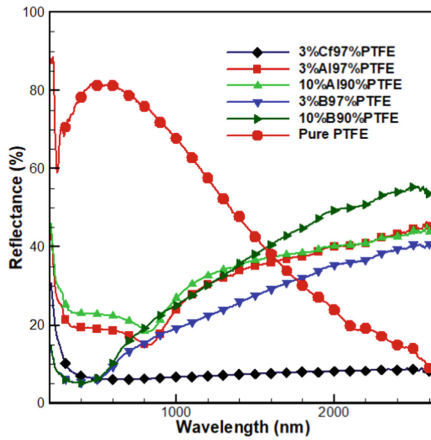
Fig. 5. Surface reflection optical properties of different propellants

3.2 Discharge Characteristics and Discharge Parameters

In the experiment, when the PTFE-based modified material doped with Al and carbon fiber is used as a propellant, the APPT can work stably. But with PTFE propellant doped with B, the APPT discharge has great dispersion, and the thruster is very unstable. As shown in Fig. 6, when PTFE doped with B is used as a propellant, the form of APPT ejection plasma can be seen. The thruster plasma arc only exists near the propellant end face in the discharge channel, and effective ejection cannot be generated.
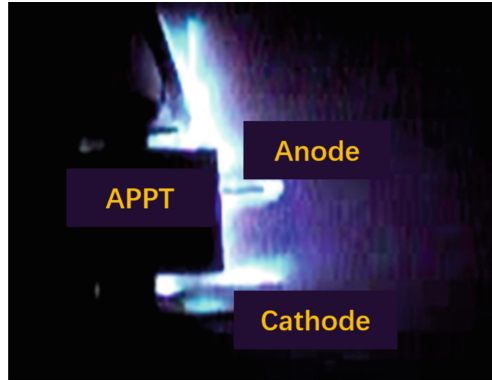
Fig. 6. Discharging photo of APPT discharge using B-doped PTFE as propellant

Figure 7 shows the discharge current and voltage wave patterns with each propellant APPT. It can be seen from the figure that, compared with APPT using pure PTFE as propellant, doping modification of propellant has a certain influence on the discharge characteristics of thruster, and the discharge current peak and discharge period of different doping modified propellant APPT have certain changes.
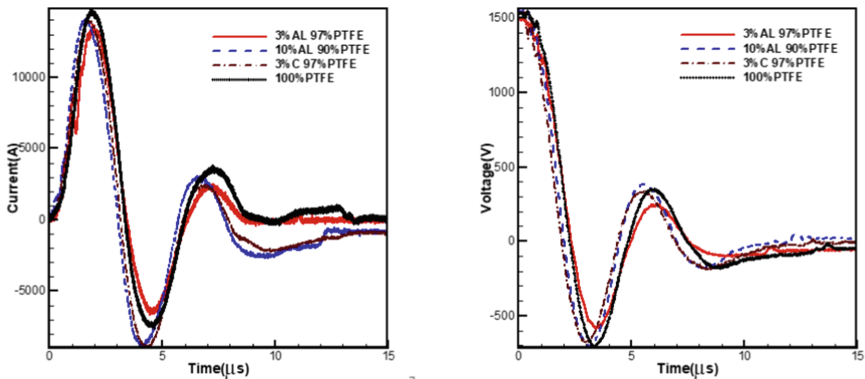
Fig. 7. APPT discharge current and discharge voltage waveforms with different propellants

As shown in Table 1, APPT with pure PTFE propellant has the largest peak forward discharge current; Compared with the APPT using pure PTFE as the propellant, the equivalent resistance of the discharge circuit of the APPT using 10%Al90%PTFE and 3%Cf97%PTFE is obviously reduced, and the square integral of the discharge current is increased to a certain extent. The equivalent resistance of the discharge circuit and the equivalent impedance of the discharge channel of APPT with 3%Al97%PTFE propellant increase, while the discharge current squared integral value decreases.

Table 1. APPT discharge circuit parameters

propellant	Imax [KA]	Leq [nH]	Req [mΩ]	Ie [KA]	Ze [mΩ]	Ψ [A² • s]
100%PTFE	14.56	50.01	25.71	4.62	35.53	365.75
3%Al97%PTFE	13.61	50.14	28.94	4.28	40.32	296.66
10%Al90%PTFE	13.98	48.37	18.22	4.32	34.91	384.81
3% Cf 97%PTFE	13.98	47.90	17.14	4.39	34.22	393.79

3.3   Ablative Mass of Different Propellants

As can be seen from Table 2, pure PTFE propellant has the smallest ablation mass, while doped propellant has a relatively larger ablation mass, in which the propellant doped with 10% Al has the largest ablation mass.

Table 2. Ablative properties of propellant

	100%PTFE	3%Cf 97%PTFE	3%Al97%PTFE	10%Al90%PTFE
mbit [μg]	41.94 ± 0.35	53.21 ± 0.42	55.19 ± 0.21	58.63 ± 0.25

The weak phase interface between the filler and the matrix reduces the mechanical properties of the matrix, and the propellant firing process does not select the appropriate coupling agent, resulting in a poor interface binding force between the PTFE matrix polymer and the filler. As a result, the loss of doped propellant increases.

3.4   Performance of Thruster with Different Propellants

As can be seen from Fig. 8, under a given working condition, APPT plasma velocity with different propellant materials are distributed between 28–33 km/s, with no significant difference.

From Fig. 9, it can be seen that the performance of APPT system with different doping propellants is significantly different. Compared with the pure PTFE propellant, the APPT with 10%Al90%PTFE propellant has the largest APPT element impulse, which reaches 263.7 μN-s. The APPT impulse of 3%Al97%PTFE propellant is 169.6 μN-s, which is the lowest.

It can be seen from Table 3 that, compared with APPT using pure PTFE as propellant, when 10%Al90%PTFE as propellant, the Lorentz force, the aerodynamic impulse bit of APPT and the equivalent ejection velocity of the propellant accelerated by aerodynamic force are all improved to a certain extent. The significant increase in aerodynamic impulse bit may be caused by the increase of the ablation mass of propellant, which leads to the increase of the ejected neutral gas. It may also be caused by the chemical exothermic
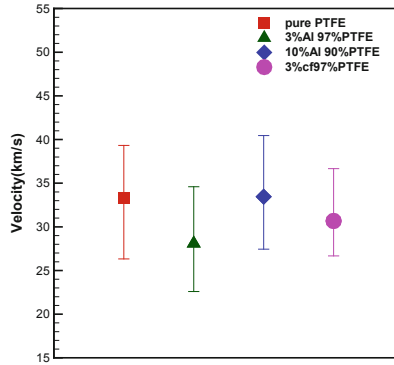
Fig. 8. Plasma velocity of APPT with different propellants

Table 3. Performance parameters of APPT

	I_{EM} [μN-s]	Igas [μN-s]	α [%]	β [%]	Cgas [km/s]	ve [km/s]
100%PTFE	151.19	57.37	11.57	72.49	1.65	5.32
3%Al97%PTFE	125.24	44.43	8.11	73.84	0.87	3.07
10%Al90%PTFE	160.13	103.62	8.16	60.71	1.92	4.50
Cf%Al97%PTFE	158.41	50.79	9.71	75.72	1.06	3.93

reaction between the F produced by the ablation and dissociation of PTFE and the doped Al in the propellant, which increases the aerodynamic impulse of the thruster. The specific reasons are to be further studied in the future.

When 10%Al90%PTFE was used as the propellant, the Lorentz force impulse to the impulse bit proportion, the Lorentz force accelerated propellant proportion and the average ablation propellant discharge velocity v_e were all reduced, and the propellant mass consumed in a single pulse was increased, so that compared with the APPT using pure PTFE as the propellant, When the propellant is used, the specific impulse of APPT system decreases, but the efficiency of APPT system increases at the same time.

Under the same condition, the performance of the APPT system using 3%Al97%PTFE as propellant is different from that using 10%Al90%PTFE as propellant. The impulse bit, specific impulse, and system efficiency of the APPT with 3%Al97%PTFE as propellant are smaller than those with 10%Al90%PTFE as propellant. Compared with the APPT using pure PTFE as propellant, the performance of the APPT using 3%Al97%PTFE as propellant is significantly reduced. It can be seen from the above analysis that the amount of Al doping has a direct impact on the improvement of APPT system performance.

The doping of carbon fiber in PTFE has no significant effect on the impulse of APPT. However, the addition of carbon fiber did not reduce the propellant ablation mass, but

(a) Impulse bit

(b) Specific impulse

(c) System efficiency
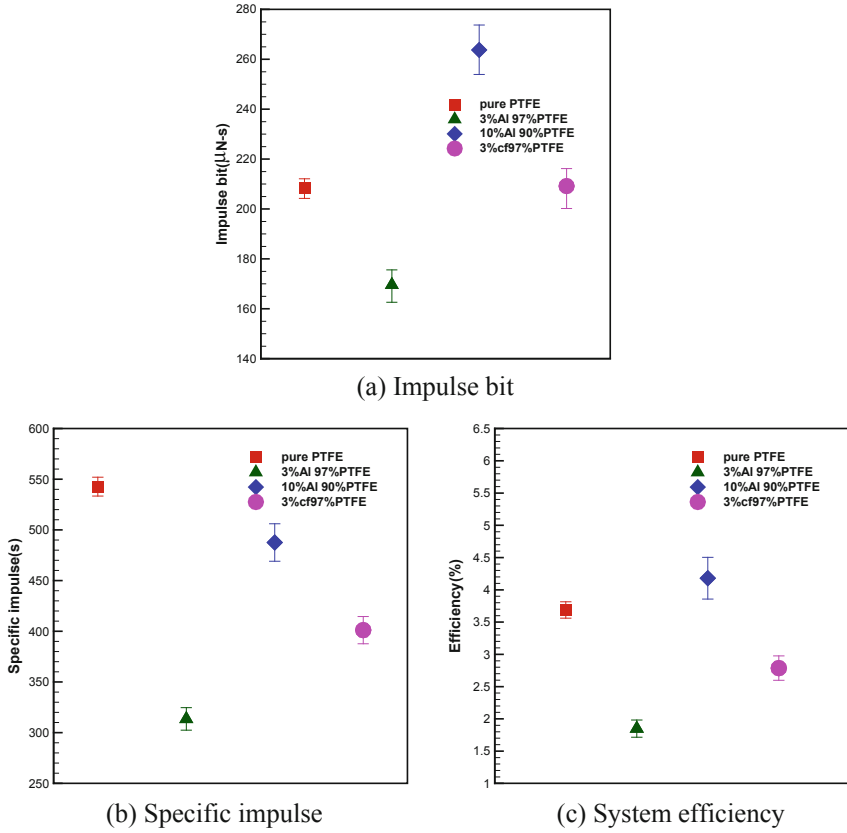
Fig. 9. System performance parameters of APPT with different propellants

increased the propellant mass of single pulse ablation, thus reducing the specific impulse of the thruster and system efficiency.

4   Conclusions

Under the given initial energy, the discharge characteristics, the ablative characteristics, and the system performance of APPT with different PTFE-based modified propellants were studied experimentally and theoretically. Several conclusions were drawn, as follows:

(1) Compared with the APPT using PTFE as propellant, doping modification of the propellant has an effect on the structure and optical properties of the material.
(2) The discharge current peak and discharge period of propellant thrusters modified with different doping have changed to some extent. Compared with the pure PTFE propellant, the mass of the doped propellant is relatively larger.

(3) The performance of the APPT thrust system with different doping propellants has great differences. Compared with the APPT with pure PTFE as propellant, the APPT with 10%Al90%PTFE as propellant has the maximum impulse bit and system efficiency, while the APPT with 3%Al97%PTFE as propellant has the minimum impulse bit.

(4) The amount of Al doping has a certain influence on the performance improvement of APPT system. The specific impulse of APPT with doped propellant is lower than that with pure PTFE because of the increase of propellant mass in single pulse ablation.

References

1. Zhang, Y., Zhang, D., Wu, J., He, Z., Zhang, H.: A novel laser ablation plasma thruster with electromagnetic acceleration. Acta Astronaut. **127**, 438–447 (2016)
2. Spanjers, G.G., Malak, J.B., Leiweke, R.J., Spores, R.A.: Effect of propellant temperature on efficiency in the pulsed plasma thruster. J. Propul. Power **14**(4), 545–553 (1998)
3. Palumbo, D.J., Guman, W.J.: Effects of propellant and electrode geometry on pulsed ablative plasma thruster performance. J. Spacecr. Rockets **13**(3), 163–167 (1976)
4. Pencil, E., Kamhawi, H.: Alternate propellants evaluation for 100-Joule-class pulsed plasma thrusters. In: 39th AIAA/ASME/SAE/ASEE Joint Propulsion Conference and Exhibit, p. 5171 (2003)
5. Pencil, E.J., Kamhawi, H., Arrington, L.A., Warren, W.B.: Evaluation of alternate propellants for pulsed plasma thrusters. In: Proceedings of the 27th International Electric Propulsion Conference on IEPC (2001)
6. Mashidori, H., Kakami, A., Muranaka, T., Tachibana, T.: A coaxial pulsed plasma thruster using chemical propellants. Vacuum **80**(11–12), 1229–1233 (2006)
7. Schönherr, T., Abe, Y., Okamura, K., Koizumi, H., Arakawa, Y., Komurasaki, K.: Influence of propellant in the discharge process of PPT. In: 48th AIAA/ASME/SAE/ASEE Joint Propulsion Conference & Exhibit, Atlanta, Georgia (2012)
8. Böhrk, H., Lau, M., Herdrich, G., Hald, H., Röser, H.P.: A porous flow control element for pulsed plasma thrusters. CEAS Space J. **3**(1), 1–6 (2012)
9. Koizumi, H., Furuta, Y., Watanabe, K., Komurasaki, K., Sasoh, A., Arakawa, Y.: A pulsed plasma thruster using water as the propellant. In: 40th AIAA/ASME/SAE/ASEE Joint Propulsion Conference and Exhibit (2004)
10. Zhang, R., Xi, W., Huang, Q.: Influence of different energy supply methods on performance of ablative pulsed plasma thrusters. Front. Energy Res. **9**, 752017 (2021)
11. Zhang, R., Xi, W., Huang, Q.: Effect of charging voltage of energy storage capacitor on performance of ablative pulsed plasma thruster. In: 2021 IEEE 4th International Electrical and Energy Conference (CIEEC). IEEE. Wuhan, China (2021)
12. Author, F.: Article title. Journal **2**(5), 99–110 (2016)
13. Zhao, Y.Z., Zhang, Y., Wu, J., Ou, Y., Zheng, P.: Characteristics of plasma in a novel laser-assisted pulsed plasma thruster. Rev. Mod. Phys. **3**, 3–5 (2019)

14. Pottinger, S.J., Krejci, D., Scharlemann, C.: Pulsed plasma thruster performance for minia-
turised electrode configurations and low energy operation. Acta Astronaut. **68**(11–12),
1996–2004 (2011)
15. Gatsonis, N., Zwahlen, J., Wheelock, A., Pencil, E., Kamhawi, H.: Characterization of
a pulsed plasma thruster plume using a quadruple Langmuir probe method. In: 38th
AIAA/ASME/SAE/ASEE Joint Propulsion Conference & Exhibit, Indiana (2002)

Co-simulation Model of EM Characteristics of Plasma Sheath Based on CFD and PIC Methods

Yuqing Chen, Tong Wu, Lishan Zhao, Lei Wang, and Juntao He[✉]

The College of Advanced Interdisciplinary Studies, National University of Defense Technology, Changsha 410073, China
m15668741620@163.com

Abstract. A plasma sheath is generated on the surface of a hypersonic vehicle during high-speed flight, significantly changing the vehicle's electromagnetic (EM) characteristics. In this paper, a model of the EM characteristics of a plasma sheath is proposed that combines the flow field and EM wave propagation. A numerical solution for the plasma flow field on the surface of vehicle is obtained using a Computational Fluid Dynamics (CFD) method. Then, the parameters of the field are discretized and input into the open-source Particle-in-Cell (PIC) simulation software EPOCH. This is used to calculate EM wave transmission in the plasma sheath and to analyze the EM properties of the sheath. Most studies that use a PIC method to analyze the EM characteristics need to set the plasma density distribution using the distribution density function. In this paper, the density distribution of the plasma is calculated using a CFD method. This makes the plasma density distribution closer to real plasma sheath, which greatly improves the accuracy and practicality of the simulation model. Moreover, EPOCH is an open-source software, which is easy to obtain and maintain. It modifies code according to requirements, and is highly flexible. This paper provides a convenient and flexible simulation platform for the study of the EM characteristics of a plasma sheath.

Keywords: plasma sheath · co-simulation · Epoch software

1 Introduction

When the vehicle is flying in the atmosphere at a high hypersonic velocity, the air on its surface is compressed, and a shock wave layer is formed. The temperature of the layer is so high that air passing through it is rapidly heated, causing air on the surface of the vehicle to become dissociated and ionized, creating a plasma sheath around the vehicle. The sheath absorbs, reflects, and scatters electromagnetic (EM) waves, greatly changing the EM characteristics of the vehicle. This seriously affects the communication and positioning of the vehicle [1–3].

With the rapid development of hypersonic vehicles, many scholars have started to investigate the EM characteristics of plasma sheaths. In 2016, Bo et al. obtained the plasma sheath distribution for different flight states using flow field simulations; they

studied the transmission and reflection characteristics of microwaves incident on the plasma using a Z-transform finite difference time domain method [4]. In 2019, Wu Wei et al. simulated the radar scattering cross section of a complex composed of a hypersonic vehicle and a plasma sheath [5]. In 2020 Bian et al. investigated the dynamic EM scattering characteristics of a hypersonic vehicle covered by a plasma sheath [6]. In 2021 Wang et al. developed a multi-physics field simulation model of Electromagnetic Field and Fluid Field of a plasma sheath in thermodynamic equilibrium and chemical nonequilibrium [7]. In these studies, numerical simulation plays an essential role due to its many advantages, such as low cost, fast results, and flexibility. Numerical simulation models for plasma are divided into three main categories: fluid models, kinetic models, and Particle-in-Cell (PIC) models. A fluid model, which studies the evolution equations of local average quantities, such as plasma density, temperature, and velocity, posits continuous media and is applicable where the gyration radius of charged particles is much smaller than the characteristic spatial scale of the plasma. A kinetic model is used to directly study the variation in a plasma distribution function in phase space by means of statistical mechanics; The process used to obtain a solution is rigorous and self-consistent, but the numerical solution is difficult. A PIC model is set up with a large number of microscopic particles in the study area, which follow Newton's laws of motion and Maxwell's equations to solve the motion of every particle in the simulation area and the evolution of the EM field. The macroscopic properties of the plasma, such as density, velocity, and temperature, are obtained from the coordinates of each particle, its velocity, and the EM field components in the simulated area. The fluid model is easy to solve but less accurate, and the kinetic model is more accurate but difficult to solve. The PIC model directly simulates the motion of individual particles inside the plasma without need of phenomenological parameters and can be considered a method that lies between the fluid model and the kinetic model.

EPOCH is an open-source plasma simulation computing software that uses a PIC algorithm. The software has the advantages of easy access, low cost, easy maintenance, dynamic allocation of computing resources, convenient parallel computing, and convenient data processing. It is widely used in plasma numerical simulation, in industry [8, 9], and is used mainly for laser plasmas. Most recent studies that use the PIC method to study the EM properties of plasma sheaths use functions to set the distribution of parameters, such as plasma density, temperature, and velocity [10], but the real distributions of parameters in a plasma sheath are strongly non-uniformity [11–13]. Distribution functions do not describe the plasma distribution well, lowering the accuracy of simulation results. However, the use of computational fluid dynamics (CFD) to simulate plasma sheath generation is well established and is significantly accurate [14–16]. To improve the accuracy of the simulation results, a co-simulation model based on CFD and PIC is proposed in this paper. Macroscopic parameter distributions, such as plasma density, temperature, and pressure, in the plasma sheath are solved for using CFD, and these parameters are discretized and entered into EPOCH software as initial conditions. Then, simulation of the EM properties of the plasma sheath is performed using the EPOCH software. We compared the simulation results with other EM simulation software (Vsim) and proved that the simulation results of EPOCH have high accuracy. Moreover, EPOCH is an open-source software, we can obtain it for free, and can add calculation modules

according to requirements. This paper provides a convenient and flexible simulation platform for the study of the EM characteristics of a plasma sheath.

2   Simulation Model

The simulation model consists of two parts: a hypersonic fluid model and an EM wave transmission model, as shown in Fig. 1. The velocity, altitude, angle of attack, and temperature of the hypersonic vehicle are input into the hypersonic fluid model. The CFD method is used to obtain the density, temperature and pressure of the plasma sheath on the surface of the vehicle. These parameters are discretized, after which, they and the EM wave parameters are input into the EM transmission model as initial variables. The EM wave transmission model is constructed using EPOCH software to obtain the EM wave transmission in the plasma sheath. Finally, the EM characteristics of the plasma sheath are obtained by analyzing transmittance, reflectance and absorbance.
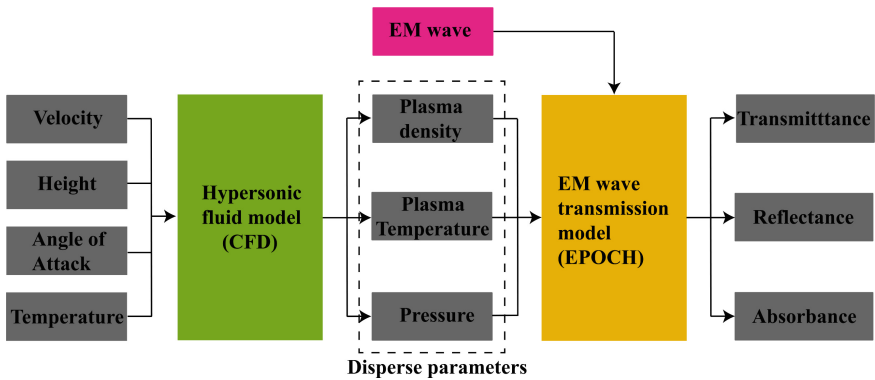
Fig. 1. Simulation model structure.

2.1   Hypersonic Fluid Model

As shown in Fig. 2, the geometry of the vehicle used in the simulation model is the same as that of an RAMC-II vehicle, with a nose cap radius of 15.24 cm, a half-cone angle of 9°, and a length of 1.295 m [17] Outflow boundary is that lets fluid flow out of the domain, but does not let it flow in; Inflow boundary is opposite to outflow boundary; noSlip boundary means all velocity components on the boundary are 0. The flight altitude of the hypersonic vehicle is 40 km, the speed is 3150 m/s, the angle of attack is 0°, and the atmospheric temperature is 265 K. The mass fractions of N_2 and O_2 in the atmosphere are 0.77 and 0.23, respectively. In this paper, seven components (N_2, O_2, N, O, NO, NO^+, and e) and 18 chemical reactions are used in the chemical reaction model [18].
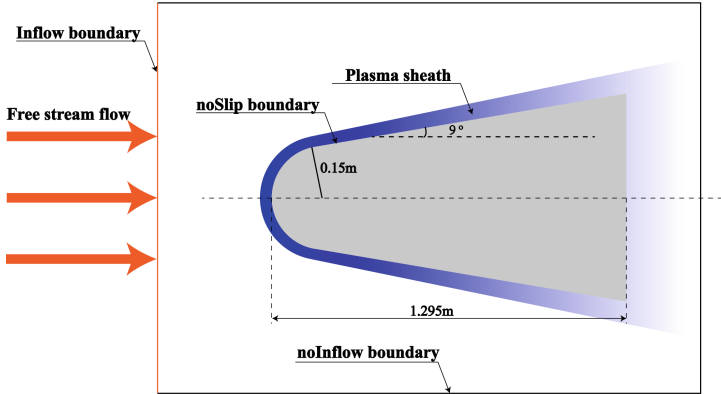
Fig. 2. Schematic of the hypersonic vehicle geometry and boundary conditions.

The hypersonic flow field model is constructed using a multi-component single velocity flow model [19, 20]. The simulation model consists of two parts, the Navier–Stokes equation and the component transport equation. The Navier–Stokes equations [Eqs. (1)–(3)] represent the conservation of mass, momentum, and energy of the fluid, respectively.

$$\frac{\partial \rho}{\partial t} + \nabla \cdot (\rho \boldsymbol{u}) = 0 \tag{1}$$

$$\frac{\partial (\rho \boldsymbol{u})}{\partial t} + \nabla \cdot (\rho \boldsymbol{u}\boldsymbol{u} + p\boldsymbol{I}) = \nabla \cdot \boldsymbol{\tau} \tag{2}$$

$$\frac{\partial e}{\partial t} + \nabla \cdot (\boldsymbol{u}(e + p)) = \nabla \cdot (\boldsymbol{\tau} \cdot \boldsymbol{u}) + \nabla \cdot (k \nabla T) \tag{3}$$

Here, ρ is the mass density, $\boldsymbol{u}$ is the speed, $\boldsymbol{I}$ is the identity matrix, p is the pressure; $\boldsymbol{\tau}$ is the stress tensor; e is the energy density; k is the thermal coefficient; T is the temperature.

The component transport equation is used to calculate the evolution of each component of the plasma sheath with time, as shown in:

$$\frac{\partial n_i}{\partial t} + \nabla \cdot (\boldsymbol{u} n_i) = s_i \tag{4}$$

where n_i is the number density of component i, and s_i is the chemical reaction source term of component i. In hypersonic flow, chemical reactions are divided into three types of flow: chemical freezing flow, in which the chemical reaction rate is 0, and the components of the fluid micro-element leave the flow field before the reaction occurs; chemical nonequilibrium flow, in which the chemical reaction rate is a finite value, and the components of the fluid micro-element react at a finite chemical reaction rate, with unequal forward and reverse reaction rates, and are in a flow state; and chemical equilibrium flow, in which the chemical reaction rate is infinite, and the components in the fluid micro-element fully react and reach equilibrium. Chemical reaction modes are usually differentiated from each other using the Damkohler number [21], as shown in Table 1.

Table 1. Relation between chemical reaction mode and Damkohler number on vehicle surface.

Da	Chemical Reaction Mode
<<1	chemical freezing flow
~1	chemical nonequilibrium flow
>>1	chemical freezing flow

The Damkohler number is $Da = \tau_f/\tau_c$, the characteristic time of the flow is $\tau_f = l/v$, the characteristic length of the flow is l, and the flow velocity is v. τ_c is the characteristic time of the chemical reaction. According to section II.A., the length of the vehicle is 1.295 m and the flow velocity is 3150 m/s; thus, $\tau_f = 4.11 \times 10^{-4}$ s. In the simulation conditions considered here, the vehicle is in a chemically nonequilibrium flow, i.e., *Da* ~ 1. Therefore, the order of magnitude for calculating the characteristic time of the chemical reaction is 10^{-4}. The EM wave transmission time added here is around 10 ns, and the order of magnitude for calculating the electrical characteristic time of the flow field is 10^{-8}. The chemical reaction characteristic time is considerably larger than the electrical characteristic time. Therefore, the chemical reaction of the fluid field is almost static when calculating the electrical characteristics of the flow field; i.e., the effect of a hypersonic fluid model can be disregarded when calculating the EM wave transmission model.

2.2 Parameters Passing

Since the geometry of a hypersonic vehicle is irregular, it is necessary to use an unstructured mesh when constructing the hypersonic fluid model. This makes the mesh fit the surface of the vehicle; therefore, an unstructured quadrilateral mesh is used in this paper, as shown in Fig. 3(a). EPOCH software uses a positive quadrilateral mesh, as shown in Fig. 3(b). As shown in Fig. 3, the grid shape and density used by CFD and EPOCH software are different.

(a)   (b)
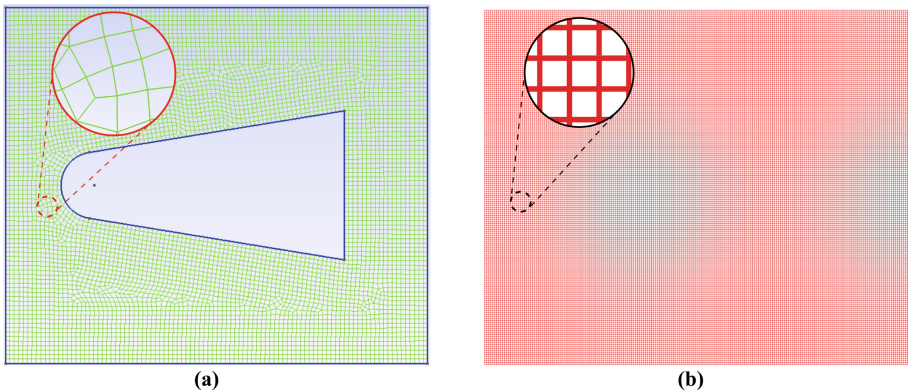
Fig. 3. Grid shape and density distribution: (a) CFD and (b) EPOCH.

In order to make the simulation result calculated in the hypersonic fluid model to pass to the EM wave transmission model, it is necessary to discretize the parameters in each grid to individual data points; and then, with these data points, the parameters are assigned to the corresponding EPOCH grid.
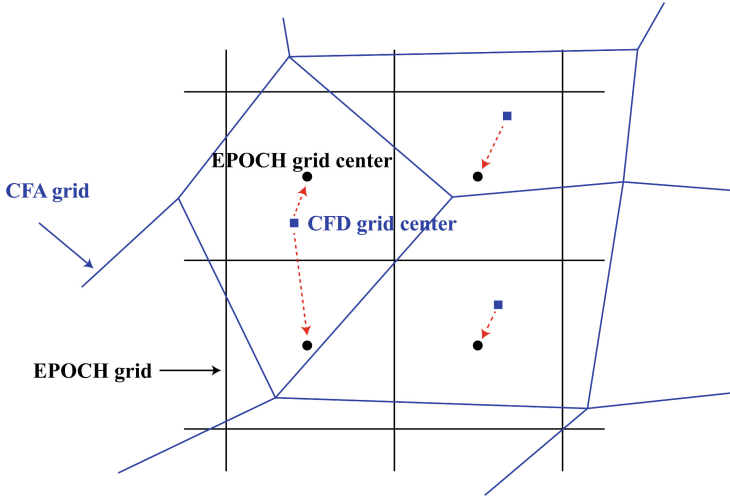
Fig. 4. Parameter passing process.

The parameter passing process is shown in Fig. 4. Calculate the coordinates of each CFD and EPOCH grid center, then, find the CFD grid center closest to the center of each EPOCH grid and assign the parameters of the CFD grid to the EPOCH grid. Since the number of EPOCH grids is much larger than the number of CFD grids, each CFD grid corresponds to multiple EPOCH grids, which reduces the error arising from the different grid shapes.
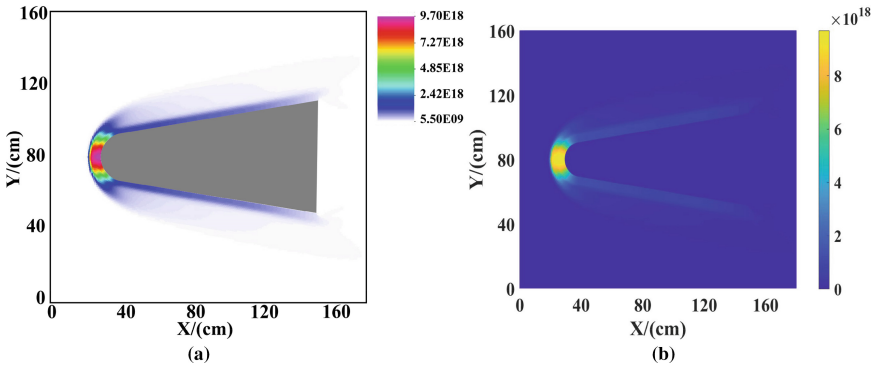
Fig. 5. Parameter passing of electron density.

Figure 5(a) shows the plasma density distribution calculated using the hypersonic fluid model, and Fig. 5(b) shows the plasma density distribution entered into the EPOCH software as the initial condition. These two plasma density distributions have high agreement.

2.3   EM Wave Transmission Model

The boundary conditions of the simulation model are set as shown in Fig. 6. The left boundary is the incident boundary of EM waves, which only allow EM waves to enter the boundary, and the incident EM waves are plane waves. The other boundaries are set as PML (perfectly matched layer), which means the EM wave can be attenuated without reflection. We set up a large number of iron atoms in the simulation area to simulate the shell of the vehicle.
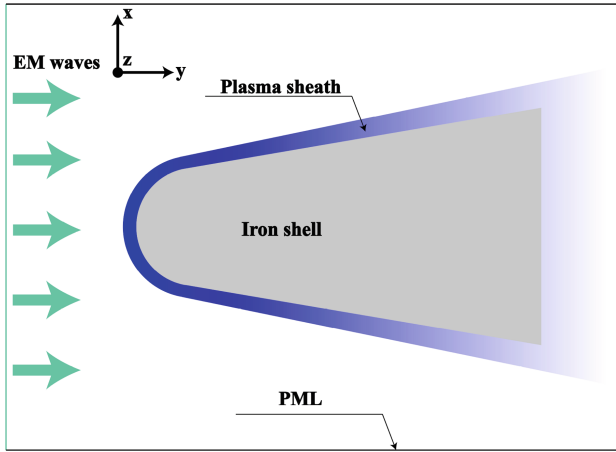
Fig. 6. Boundary conditions of EM wave transmission model.

EPOCH uses Maxwell's curl equations, Lorentz force equation, and Newton's laws of motion, as shown in Eqs. (5)–(7)

$$\nabla \times \boldsymbol{E} = -\frac{\partial \boldsymbol{B}}{\partial t} \tag{5}$$

$$\nabla \times \boldsymbol{B} = \mu_0 \boldsymbol{J} + \mu_0 \varepsilon_0 \frac{\partial \boldsymbol{E}}{\partial t} \tag{6}$$

$$\boldsymbol{F}_i = m_i \frac{d\boldsymbol{v}_i}{dt} = q_i(\boldsymbol{E}_i + \boldsymbol{v}_i \times \boldsymbol{B}_i) \tag{7}$$

where $\boldsymbol{E}$ and $\boldsymbol{B}$ are the self-consistent electric and magnetic fields in the simulation region, respectively; $\boldsymbol{J}$ is the current density vector; m_i is the mass of particle i; q_i is the charge of particle i; F_i is the Lorentz force on particle i; B_i is the magnetic field on particle i; and E_i is the electric field on particle i.

The EPOCH calculation involves the following main steps:

(1) Set the number of real particles, initial coordinates and velocity distribution represented by each macro article according to the physics problem.
(2) The macro particles are assigned to the grid points of the square grid, and the charge density and current density vectors are calculated for each grid point according to the area occupied by the grid.
(3) The value of the EM field component at each grid point is obtained using the discrete form of Maxwell's curl equations combined with the specific boundary conditions and the current density vector found in step (2).
(4) Using the EM field components at the grid points, we obtain the electric and magnetic field for each macro particle.
(5) The motion of each macro particle in one time step is calculated using the Lorentz force equation and Newton's law of motion to obtain the location and velocity of each macro particle at the next moment.
(6) Calculate the collision between particles and update the motion state of the particles.
(7) Repeat steps (2)–(6).

In step (1), the number of macro particles needs to be set according to the particle distribution of the plasma sheath. The particle density distribution function is often used in numerical simulations to simulate the particle density distribution in the plasma sheath:

(1) Bilinear distribution

$$
y(x) = \begin{cases} -\dfrac{b}{a_1}x + b & x_1 \leq x \leq 0 \\ \dfrac{b}{a_2}x + b & 0 \leq x \leq x_2 \end{cases} \tag{8}
$$

(2) Double exponential distribution

$$
y(x) = \begin{cases} be^{\frac{x}{a_1}} & x_1 \leq x \leq 0 \\ be^{-\frac{x}{a_2}} & 0 \leq x \leq x_2 \end{cases} \tag{9}
$$

(3) Skew normal distribution

$$
y(x) = \begin{cases} be^{-(\frac{x}{a_1})^2} & x_1 \leq x \leq 0 \\ be^{-(\frac{x}{a_2})^2} & 0 \leq x \leq x_2 \end{cases} \tag{10}
$$

(4) Segmented Epstein function distribution

$$y(x) = \begin{cases} 2b(1 + e^{-x/a_1})^{-1} & x_1 \le x \le 0 \\ 2b(1 + e^{x/a_2})^{-1} & 0 \le x \le x_2 \end{cases} \tag{11}$$

where y is the particle number density; b is the peak particle number density; a_1 and a_2 are particle number density attenuation constants; and x_1 and x_2 are the coordinates of the nearest and farthest plasma sheaths with respect to the surface of the vehicle, respectively. These distribution functions reach a maximum particle density at $x = 0$. Since the electron density in the plasma sheath can be approximately equal to the plasma density, it directly affects the EM properties of the plasma sheath [22]. Figure 7 shows the electron density distribution obtained using the different distribution functions, setting $a_1 = 0.1$, $a_2 = 0.2$, $x_1 = -0.5$, and $x_2 = 0.5$. Figures 7(a)–7(d) show the bilinear distribution, double exponential distribution, skew normal distribution, and segmented Epstein distribution.
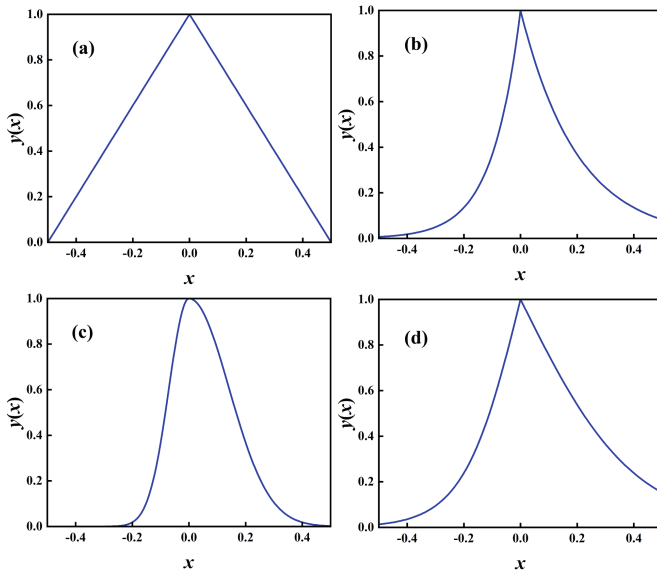
Fig. 7. Commonly used electron density distribution functions: (a) bilinear distribution, (b) double exponential distribution, (c) skew normal distribution, and (d) segmented Epstein function distribution.

Figure 8 shows the electron density distribution of a real plasma sheath. The electron density distribution differs considerably from that in Fig. 7, and the electron density distribution of the plasma sheath varies significantly as a function of position on the vehicle. Therefore, using distribution functions to represent the plasma density distribution would have significant errors. Consequently, using the electron density distribution of a real plasma sheath improves the accuracy of the simulation results.
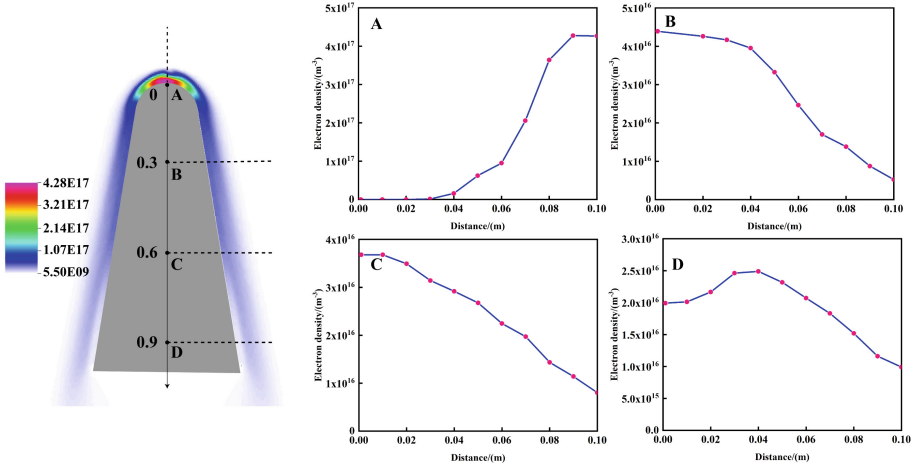
Fig. 8. Electron density at different locations of a realistic plasma sheath.

3 Simulation Results

3.1 Plasma Sheath Simulation Results

The distributions of electron density, N_2 density, N density, O_2 density, O density, NO density, NO^+ density, and temperature of the plasma sheath on the surface of the hypersonic vehicle were obtained by hypersonic fluid model calculations, shown in Figs. 9 (a)–9(h).

The particles are concentrated in the region between the shock wave layer and the surface of the vehicle, and their distribution is strongly inhomogeneous. The particle density is high at the head of the vehicle, and then gradually decreases with increasing axial distance. The particle distributions and temperature distribution on the surface of the vehicle are used as the input of the EM wave transmission model.
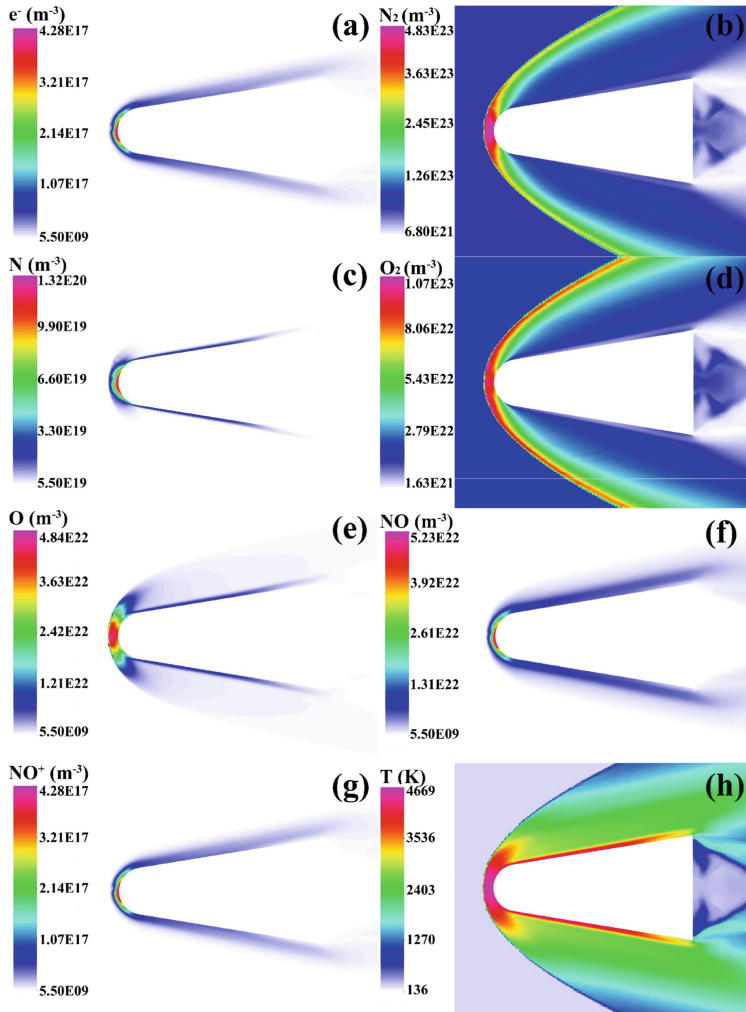
Fig. 9. Particle distribution in the plasma sheath on the surface of the vehicle.

3.2   Microwave Transmission in a Real Plasma Sheath

The commonly used communication bands for hypersonic vehicles are the L and S bands [23]. Considering the dependence of frequency on the grid during the EM wave simulation (each EM wave wavelength contains at least 10 grids), the frequencies of the EM waves in this study are set to 1 GHz, 1.2 GHz, 1.6 GHz, and 2 GHz. Figures 10(a)–10(d) show the transmission of EM waves in the plasma sheath that have an E-field amplitude of 100 V/m and frequencies of 1 GHz, 1.2 GHz, 1.6 GHz, and 2 GHz, respectively. The E-field polarization direction is the same as the z-axis.

Figure 10 shows that EM waves at these frequencies are almost completely reflected by the plasma sheath. The reason for this is that the electron density in the sheath is high,

and EM waves accelerate the electrons there. The electrons transfer energy to neutral particles through collisions, resulting in a loss in EM wave energy.
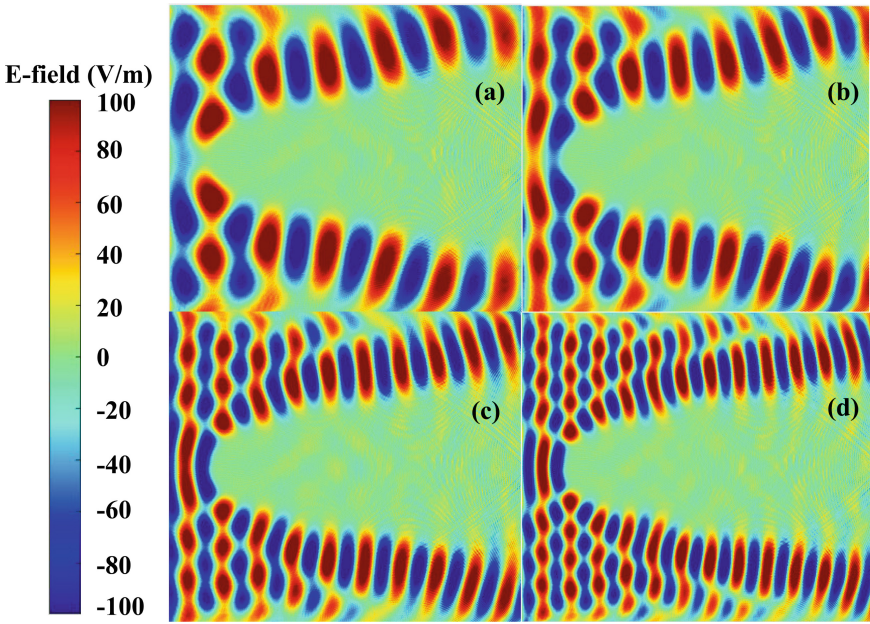
Fig. 10. EM waves transmission in a plasma sheath calculated by EPOCH: (a) 1 GHz, (b) 1.2 GHz, (c) 1.6 GHz, and (d) 2 GHz.

To verify the accuracy of the calculated results, we used the electromagnetic simulation software Vsim to simulate EM waves transmission in the same plasma sheath. Figures 11(a)–11(d) show the transmission of EM waves in the plasma sheath that have an E-field amplitude of 100 V/m and frequencies of 1 GHz, 1.2 GHz, 1.6 GHz, and 2 GHz, respectively. The E-field polarization direction is in the z-axis direction.

The E-field distribution calculated using EPOCH is the same as that calculated using Vsim. This indicates that the transmission of EM waves in a real plasma sheath can be simulated accurately using EPOCH software.

To further verify the accuracy of the simulation results, we investigated the attenuation of the EM waves at different locations on the surface of the vehicle. The attenuation of the signal can be expressed in terms of the E-field ratio of the EM wave:

$$G = 20 \log(\frac{E_0}{E_{free}}) \tag{12}$$

where E_0 is the E-field amplitude at the observation point and E_{free} is the reference E-field amplitude in free space. Figure 12 shows the location distribution of the monitoring points on the surface of the vehicle.
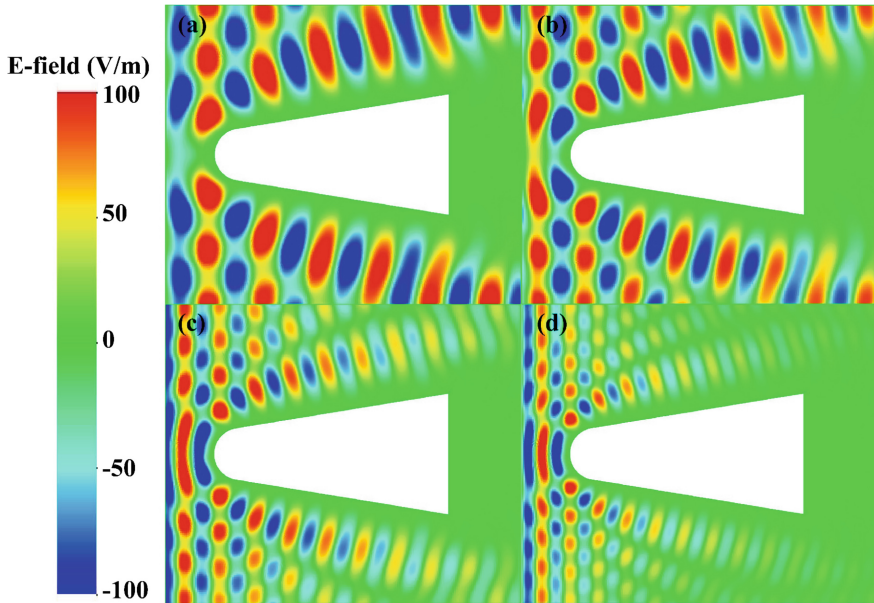
Fig. 11. EM waves transmission in a plasma sheath calculated by Vsim: (a) 1 GHz, (b) 1.2 GHz, (c) 1.6 GHz, and (d) 2GHz.
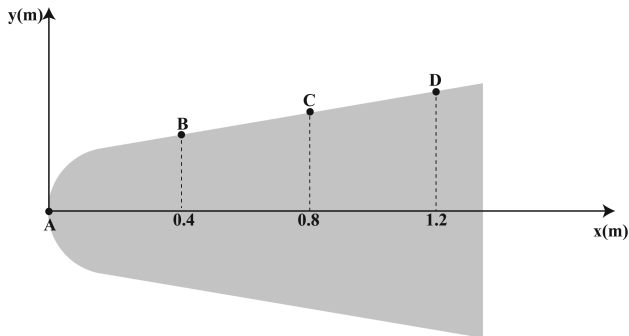
Fig. 12. Location distribution of the monitoring points on the surface of the vehicle: A. 0.0 m, B. 0.4 m, C. 0.8 m, and D. 1.2 m.

Figure 13 shows the attenuation of 1 GHz EM waves at a monitoring point calculated using EPOCH and Vsim.

The simulation results show that the attenuation of EM waves is highest in the head region (near point A in Fig. 12), after which the attenuation decreases with increasing axial distance from the vehicle. The attenuation values calculated using EPOCH software are close to those calculated using other EM simulation software (Vsim), which further verifies the accuracy of the simulation results.
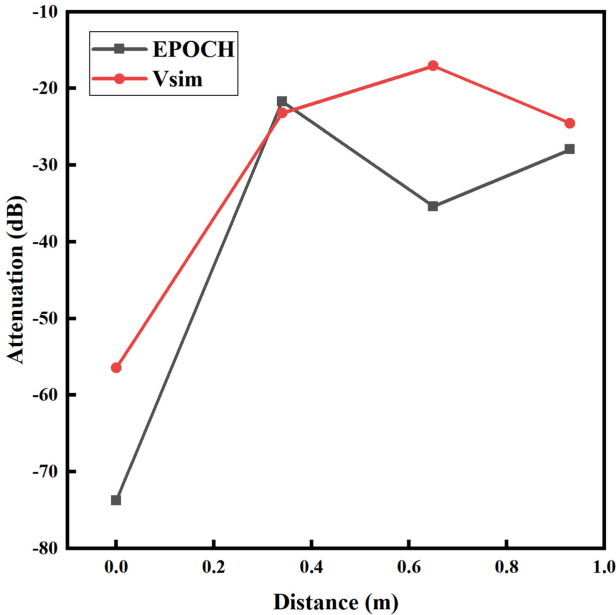
Fig. 13. Attenuation of EM waves at different locations on the vehicle.

4   Conclusion

In order to study the EM characteristics of a surface plasma sheath during the flight of a hypersonic vehicle, a joint CFD and PIC simulation model was proposed to simulate the transmission of EM waves in the sheath. The distribution of each kind of particle and the plasma temperature distribution in the sheath under different flight conditions were simulated using a CFD method. These parameters were then discretized and input into the open-source PIC simulation software EPOCH to calculate the EM wave transmission in the plasma sheath. The EM characteristics of the sheath and the simulation results were compared with those obtained using other EM simulation software, which proved that the model was highly accurate. EPOCH is open-source software and is, therefore, easily accessible, easy to maintain, and highly flexible, providing a convenient and flexible simulation platform for EM wave transmission in plasma sheaths.

References

1. Blazek, J.: Comput. Fluid Dyn. Princ. Appl **55**(2), 1–4 (2001)
2. Li, J., He, M., Li, X., Zhang, C.: IEEE Trans. Antennas Propag. **66**, 3653 (2018)

3. Arshad, K., Lazar, M., Mahmood, S., Rehman, A., Poedts, S.: Phys. Plasmas. **24**, 033701 (2017)
4. Bo, Y., Zhao, Q., Luo, X., Liu, Y., Chen, Y., Liu, J.: Acta. Phys. Sin. **65**, 035201 (2016)
5. Wu, F.W., Liu, F., Zhong, J., et al.: Chinese J. Radio Sci. **34** (5), 610–621 (2019)
6. Bian, Z., Li, J., Guo, L.: Remote sensing **12**(17), 2740 (2020)
7. Wang, K., Li, J.: IEEE Trans. Microw. Theory Techn. **69**(12), 5228–5240 (2021)
8. Arber, T.D., et al.: Plasma Phys. Controlled Fus. **57**(11), 113001 (2015)
9. Allanson, O., Watt, C.E., Allison, H.J., Ratcliffe, H., Ratcliffe, H.: JGR Space Phys. **126**, e2020JA028793 (2021)
10. Krek, J., Jelic, N., Duhovnik, J.: Nuclear Eng. Des. **241**(4), 1261–1266 (2011)
11. Kundrapu, M., Loverich, J., Beckwith, K., Stoltz, P., Shashurin, A., Keidar, M.: J. Spacecr. Rockets **52**, 853 (2015)
12. Ouyang, W., Liu, Y., Deng, W., Zhang, Z., Zhao, C.: Microw. Opt. Technol. Lett. **62**, 660 (2019)
13. Hudson, M., Chokani, N., Candler, G.: AIAA J. **5**, 958 (1997)
14. Farbar, E., Boyd, I.D., Martin, A.: J. Thermophys. Heat Trans. **27**, 593 (2013)
15. Doihara, R., Nishida, M.: Shock Waves **11**, 331 (2002)
16. Holden, M.S., Wadhams, T.P.: AIAA paper **1137** (2003)
17. Grantham, W.L.: NASA TN D–6062, Technical Report, Washington, D.C. (1970)
18. Ouyang, W., Liu, Y.: Phys. Plasm. **27**, 033507 (2020)
19. Loverich, J., Hakim, A., Shumlak, U.: J. Comput. Phys. **9**, 240 (2011)
20. Veitzer, S., Kundrapu, M., Stoltz, P., Beckwith, K.C.: Rev. Sci. Instrum. **87**, 02B142 (2016)
21. Inger, G.R.: J. Spacecr. Rocket. **38**(2), 185–190 (2001)
22. Kolobov, V., Godyak, V.: Phys. Plasmas **26**, 060601 (2019)
23. Belov, I.F., Borovoy, V.Y., Gorelov, V.A., Kireev, A.Y., Korolev, A.S., Stepanov, E.A.: J. Spacecr. Rockets **38**, 249 (2012)

Discharge Characteristics and Dynamic Process of Directional Spraying Binary and Ternary Alloy Coating via Electrical Explosion Method

Chen Li[1], Juan Feng[1], Wei Yuan[1], Yuchen Cao[1], and Ruoyu Han[2(✉)]

[1] School of Physics, Beijing Institute of Technology, Beijing 100081, China
[2] State Key Laboratory of Mechatronics Engineering and Control, Beijing Institute of Technology, Beijing 100081, China
r.han@bit.edu.cn

Abstract. Electrical explosion spraying, due to its high reaction temperature and intense mechanical effect, like strong shock wave and high-speed expanded explosive products, is a kind of satisfactory thermal spraying method. It had used to prepare single- or multi-element wire coating; however, the investigation of middle physical process was lacked, which was not beneficial to deeply understand the coating formation characteristics with the explosive process. In this study, a directional electrical explosion device was designed, which was available for synthesizing dense and homogeneous coating. Experiments were performed with intertwined Cu-Ni wire, and intertwined Cu-Ni-Al wire. Electrical and radiational diagnoses including current/voltage waveforms and self-emission images were used to investigate the explosive characteristics. SEM and XRD characterizations were used to study the morphology and crystallography of the produced coating. For intertwined two-wire (Cu-Ni) explosion, the parameters were measured separately to explore more details according to the corresponding dynamic high-speed images. The results indicated that the multi-wire explosion was non-synchronously with different explosive behaviors of wires; therefore, the discharge product channel showed a mixture of plasma, un-ionized metal vapor, and un-vaporized metal drops. Accordingly, the sprayed coating was composed by μm-scaled chunks or plates with some nanoparticles adhering on them.

Keywords: Electrical explosion · Multi-principal-element alloy · Explosive spraying · Nanoparticles and coating

1 Introduction

Electrical explosion, characterized by ultra-fast atomization and quenching ($dT/dt \sim 10^{10}$–10^{12} K/s) of the sample, is a unique approach for the one-step synthesis of nanomaterials [1, 2]. Different species of metals (wire, rod, or foil) who possess good conductivity can be driven to explode by the pulse current; moreover, electrical explosion can occur in selectable medium ambience, like air, inert gases, and water. As a result, pure metal, metal oxides, nitrides, carbides, etc. [3–6].

Due to the high reaction temperature (>10000 K) and intense mechanical effect of electrical explosion, like strong shock wave (several to dozen of MPa) and high-speed expanded velocity of discharge product channel (approximately km/m), it is a kind of satisfactory thermal spraying method. Wang *et al.* [7] prepared a uniform and dense Ag/C composite coating with the coating area 39.25 mm^2 and thickness 50 µm in a single spray by the electrical explosion spraying of powders. Han *et al.* [8] synthesized refractory Ta10W and non-refractory Ni60A coatings by exploding alloy wire via a self-designed wire electrical explosion spraying (WEES) device, the surface coating morphology showed it is composed of flattened splats and some nanoparticles; furthermore, the coating changed from rough and nonuniform to dense and even with increased energy densities. In our previous work [9], we designed a directional electrical explosion spraying device and prepared the multi-principal-element alloy coating of $Al_{13}Cu_{20}Ti_{13}Mo_{15}W_4Sn_{35}$. The synthesized alloy coating showed graded element distribution and high-entropy effect, and the distribution regularity depended on the different explosive behaviors of wires because of their discrepant electrical and thermal parameters. In multi-wire simultaneous explosion, due to the discrepant electrical and thermal characteristics, the explosive behaviors are always complex and result in specific coating morphology. Pervikov *et al.* [10] investigated the energy characteristics of the electrical explosion of two intertwined wires, the results illustrated that energy deposited into the wire may depend on the relation between the thermophysical parameters and specific electric resistivity of the metals, and wires explosion can be divided into synchronously and non-synchronously with different metal species. It surely indicated that the physical process is complex in multi-wire explosion; however, researches paid more attentions on the single-wire condition. It is necessary to further study the physical mechanism and clarify the corresponding relations between physical patterns and explosive products.

In this paper, a directional electrical explosion device was self-designed to prepare single or multi-principal-element coating. Electrical and radiational diagnoses including current/voltage waveforms, and self-emission images were used to investigate the explosive characteristics from single wire to intertwined multi-wire. Morphology and crystallography of the produced coating are characterized and analyzed by SEM and XRD. A coalition analysis of electrical explosion physical process and explosive products was preliminarily proceeded to reveal more details in multi-wire explosive spraying alloy coating.

2   Experimental Setup

The experiments were conducted using a µs-timescale pulsed current source based on a 6 µF pulse capacitor and a triggered spark gap. The circuit was shown in Fig. 1(a), the DC power supply charged the capacitor up to 9.0 kV (about 250 J stored energy). Once the spark gap was triggered, the pulsed current would pass through the load and drove electrical explosion inside the discharge chamber. The schematic diagram of the chamber was illustrated in Fig. 1(b), and the picture in top right corner gave the detailed load structure, which was designed as the directional spraying device. The device was composed by a couple of copper electrodes, a semi-closed tube, an intertwined wire, and

a silicon substrate. When explosion happened, the high-speed metal jet would spray out and form alloy coating on the silicon substrate.

The discharge voltage u and current i were measured with a PVM-5 probe (bandwidth of 80 MHz) and Pearson 101 coil (bandwidth of 4 MHz), respectively. The resistive load voltage u_R was estimated as

$$u_R(t) = u - L_s \frac{di}{dt} \tag{1}$$

where L_s refers to the inductance of the wire and its holder. The correctness of voltage and current measurement was examined by conducting the pulsed current with a low-inductance (nH level) ceramic resistor [11]. The energy deposition E_d was calculated as

$$E_d = \int u_R(i) \cdot i(t) dt \tag{2}$$

High-speed cameras (Phantom VEO) were used to record time-resolved images of the explosion. Morphology and crystallography characterizations included SEM (Regulus/Zeiss) and XRD (Rigaku, Ultima IV), respectively. XRD pattern of the sample was taken using Cu Kα radiation ($\lambda = 0.15406$ nm) at the working voltage and current of 40 kV and 20 mA, and the recorded range at 2θ was from 5° to 80° with a step size of 0.02°.
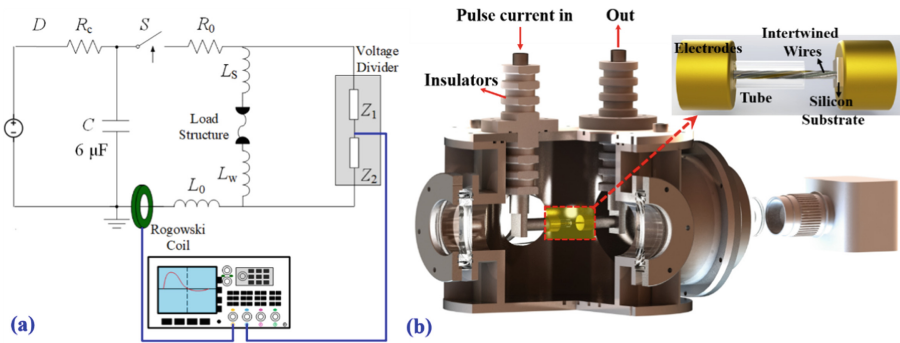
Fig. 1. Schematics of the experimental setup and configurations: (a) circuit diagram and (b) cross-section view of the chamber.

3   Experimental Results

3.1   Typical Coating Morphology for Single-Element Wire Explosive Spraying

Single-element wire electrical explosion used to spray the surface or inner wall of the workpiece is the most common application for explosive coating. A 300 μm-diameter, 4 cm-long Cu wire was used to explode in air under the stored energy 250 J. Figure 2

shows the typical morphology of coating of the Cu wire explosion. A dense and homogeneous coating is formed with extremely low porosity. Some sub-micron or micron particles are observed; however, the nanoparticles are dominant. The large-size particles may come from the un-vaporized metal drops during wire explosion, and the rest nanoparticles may result from the hot metal vapor who undergoes quenching and nucleation processes. It is closely related to the explosive behaviors of wire itself, which has detailed investigated in our last work [2].

Figure 3 shows the crystalline phase characterized by XRD result. Due to high reaction temperature and large specific surface area, the explosive products will be oxidized before and when collide with the substrate; therefore, the formed coating is mainly composed of both pure metal and its oxides, namely pure Cu, CuO, and Cu_2O. The diffraction peaks of corresponding phase also accord with the crystalline plane distance, as shown in Fig. 2(d). The experimental result of single-element wire explosion is in common with general results in electrical explosion, and the detailed researches of multi-element wire explosion will be further discussed in next section.

Fig. 2. Typical morphology characterized by SEM of Cu explosive products in air under 250 J stored energy.

Fig. 3. XRD result of the Cu wire explosive products.

3.2 Typical Physical Process and Coating Characteristics for Cu-Ni Binary Wires Explosive Spraying

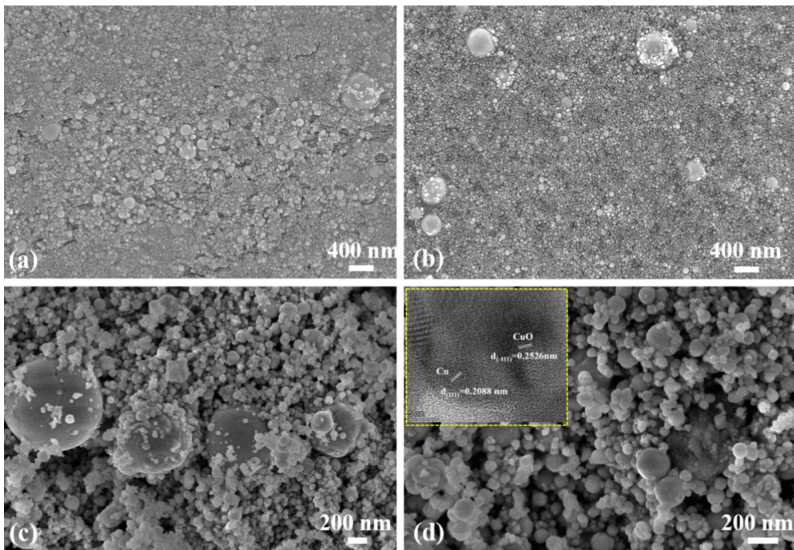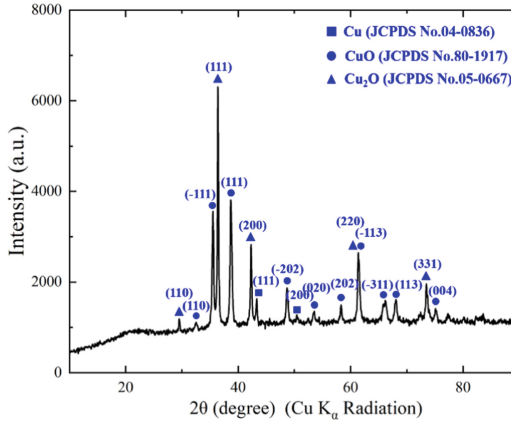High-quality coating is verified to be successfully produced under such directional electrical explosion device in last section. In this section, copper and nickel wires are used to investigate the discrepant physical process and corresponding alloy coating characteristics when explodes multi-wire simultaneously. Cu and Ni wires with 200 μm-diameter, 4 cm-long are made into the intertwined wire as the explosive load to spray coating. The semi-closed tube is with the 5 mm inner diameter and 3 cm long. Under 250 J initial stored energy, the electrical parameters and dynamic high-speed images are shown in Fig. 4.

Figure 4(a) shows the voltage and current waveforms of the Cu-Ni intertwined wire explosion. The discharge belongs to a periodic mode, the peak values of current and voltage are 11.2 kA and 7.4 kV, respectively. The breakdown moment occurs at approximately 3.1 μs, and then followed by formation of the high-conductive plasma channel. The whole discharge process lasts at about 29.5 μs. Figure 4(c) gives the corresponding high-speed images of the intertwined wire explosion in a semi-closed tube. The interval of each frame is 5 μs, and the exposure time is 0.97μs. The feedback signal is shown as the blue line, and the falling edge of each pulse represents the shoot moment of every frame. From the dynamic process, a cylindrical discharge is formed in early 20 μs, and the drastic flash means an intense plasma process. Form frames #6 to #9, due to no extra energy injection, the quenching process begins, and the plasma is going to extinguish. It is worth noticing that the channel is composed of a mix of plasma (high-temperature and low-density) and un-ionized metal vapor or un-vaporized metal drops (low-temperature and high-density). Until approximately 50 μs, the plasma part quenches and experiences later nucleation process. During explosion, part of the wire who confined in the tube brings the local high pressure, before tube fragmentation, it can only be released from the open end of the tube. As a result, a high-speed and directional metal jet will form and spray to the Si substrate, which seems as mushroom-like spraying trajectory, as shown in frames #9 and #10.

In order to investigate more details in this physical process, the intertwined wire is separated into two adjacent wires in parallel, and the current of each wire is detected respectively. The load structure is illustrated in the first picture in Fig. 4(d). In parallel wires explosion, discrepant current waveform is shown in Fig. 4(b). Due to the different load structures (with/without tube, load inductance), the total current has some discrepancies; however, we consider that it can still describe the characteristics of parallel wires explosion. At early time, the currents of Cu and Ni wires are mostly identical, until approximately 0.84 μs, they develop into an opposite trend. The current continually increases for Cu, however, it decreases for Ni, which means Ni wire experiences vaporization early than Cu. Higher resistivity (6.93 μΩ·cm for Ni, and 1.68 μΩ·cm for Cu) will achieve greater deposited energy, therefore, leading to a fast phase process. Then, at approximately 1.9 μs, current of Ni begins to increase, and the Cu current rapidly decrease, which means that breakdown occur in Ni channel and the Cu channel is short-circuited. Combined with the self-emission images in Fig. 4(d), it can be seen the bright Ni plasma channel and the lightless Cu vapor channel. It is well accorded with the characteristics that is shown in current waveform.

To sum up, in binary wires explosion, current between wires will re-distribute which depends on the different electrical and thermal characteristics of wires, typical as resistivity, latent heat, and etc. In Cu-Ni system, Ni can form high-temperature and low-density
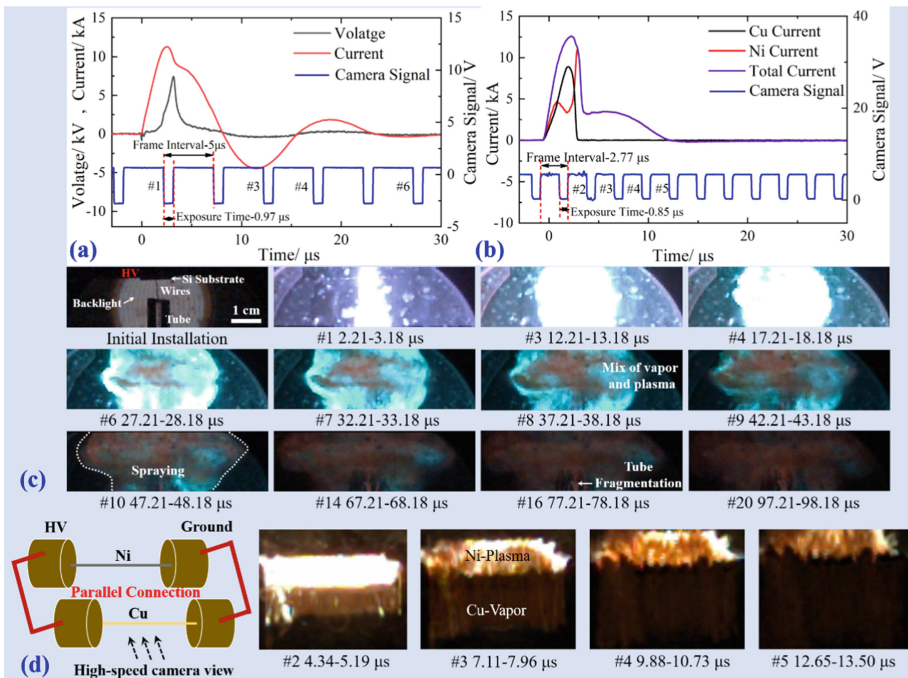
Fig. 4. Electrical parameter waveforms of the Cu-Ni intertwined wire explosion (a) and Cu-Ni parallel wires explosion (b), and the corresponding high-speed images of the intertwined wire explosion (c) and the parallel wires explosion (d).

plasma; however, low-temperature and high-density vapor or un-vaporized drops for Cu. And that is the reason why the discharge channel of the intertwined wire explosion shows a mixture of plasma and metal vapor/drops.

Figure 5 gives the SEM results of the surface morphology of the Cu-Ni alloy coating. Figure 5(a–c) shows the relatively macroscopic morphology at a low-amplifying degree, it can be seen that the coating is composed of μm-scaled chunks, which is very like the single wire explosion condition. Furthermore, from the amplifying images in Fig. 5(d–e), the nanocrystalline adheres on the chunks. The chunks are still considered to result from the un-vaporized metal drops, and Cu element should be dominant here according to the analysis of electrical characteristics and dynamic process. And the nanocrystalline comes from the cooled Ni plasma products, as well as part of the Cu metal vapor, who undergo nucleation and growth into nanoparticles.

Fig. 5. Typical morphology characterized by SEM of Cu-Ni alloy coating formed by the directional electrical explosion device in air under 250 J stored energy.

Figure 6 is the XRD characterization result of Cu-Ni alloy coating, similar to the single-element coating, the phases are mainly corresponding metal oxides and little pure metal. Diffraction peaks at 35.4°, 35.5°, and 38.7° correspond to the CuO crystalline plane (002), (−111), and (111), respectively. And peaks at 36.4° and 42.3° come from the (111) and (200) planes of Cu_2O, in addition, no obvious peak of pure Cu is detected. For Ni element, diffraction peaks appear at 37.2° and 43.2° representing the (111) and (200) planes of NiO. An un-conspicuous peak at 44.6° means a small amount of pure metal Ni in the alloy coating.
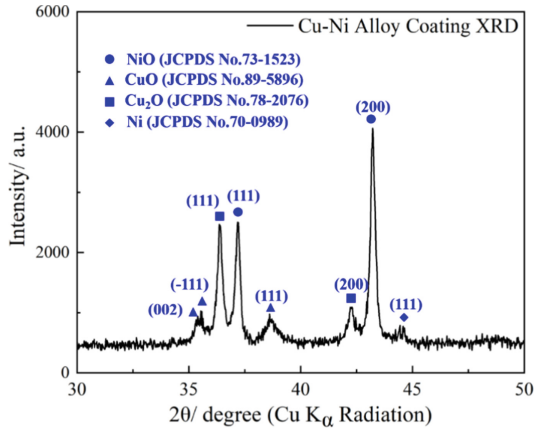
Fig. 6. XRD result of the Cu-Ni coating.

3.3 Typical Physical Process and Coating Characteristics for Cu-Ni-Al Ternary Wires Explosive Spraying

When adding Al wire into the original binary system into a ternary alloy system, the characteristics of the discharge and coating morphology are simply investigated. Figure 7 shows the electrical parameters and the high-speed images. From the waveforms, the discharge is similar to the binary wires explosion. The difference is that the breakdown time delay from approximately 3.1 µs to 4.3 µs, and the duration time of the whole discharge decreases from approximately 29.5 µs to 23.3 µs. These phenomena can be easily explained that explosive process needs more time and energy for phase change with the increased load mass. It can be seen that the discharge still be a mix of plasma and high-density metal vapor or drops. Obviously, the inner part clearly shows the spraying trajectory, leaving the low-density plasma surrounding it.
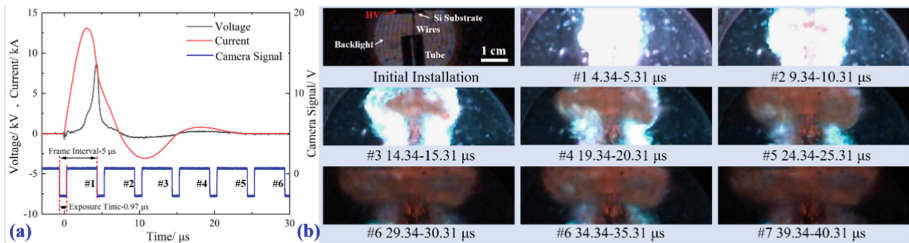
Fig. 7. Electrical parameter waveforms of the Cu-Ni-Al intertwined wire explosion (a), and the corresponding high-speed images (b).

Observing the surface morphology of Cu-Ni-Al alloy coating, the characteristics are also similar to the former results. The chunks become larger than before, and the size can reach a dozen micrometers. This may be due to that energy is so insufficient to vaporize most of the wires that they exist as the large metal drop, forming the main bulk of the

coating. And the vaporized part still undergoes nucleation and growth processes, finally forming the nanoparticles, as shown in Fig. 8(d–f).
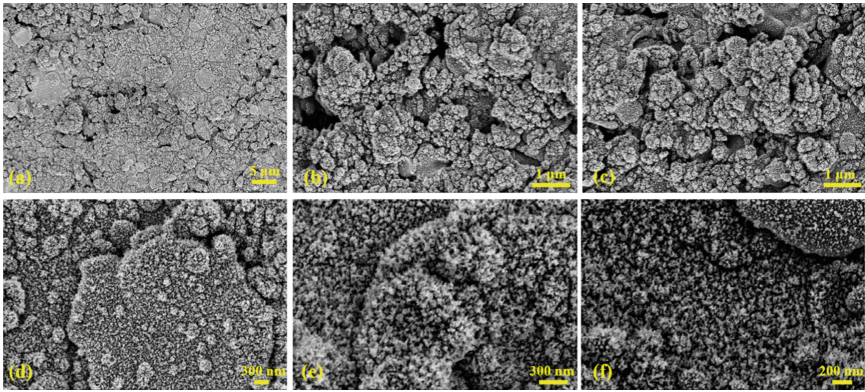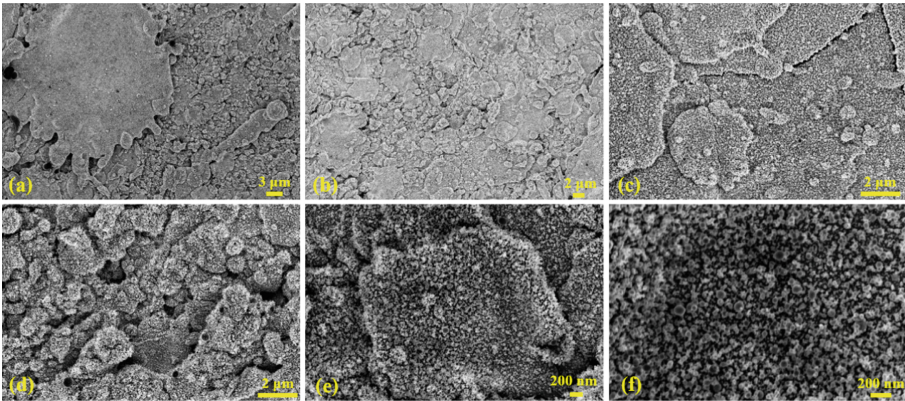

Fig. 8. Typical morphology characterized by SEM of Cu-Ni-Al alloy coating formed by the directional electrical explosion device in air under 250 J stored energy.

For XRD pattern in Fig. 9, it is almost identical to the result of Cu-Ni system. In our opinion, a relatively reasonable interpretation is that due to the low melting point of Al (934 K for Al, 1728 K for Ni, and 1358 K for Cu), when pulse current injection, Al wire will begin phase change firstly, and the current will be short-circuited because of the rapidly increased resistance. As a result, the Al element exists mainly as the metal drop and locates at the front of the metal jet, thus it deposits on the bottom of the coating. Due to the XRD equipment having measurement depth, according to our former research [9], the very bottom element may be difficult to detect in such a μm to several tens μm thick coating.
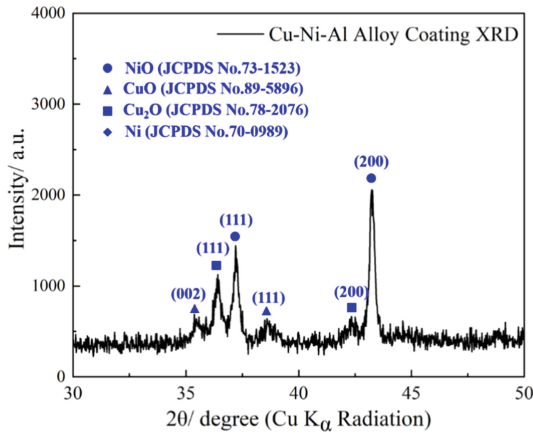
Fig. 9. XRD result of the Cu-Ni-Al coating.

4 Conclusion

To conclude, under the directional electrical explosion spraying device, the surficial homogeneous coating is produced with single- and multi-element. The characteristics of the coating unit is composed of μm-scaled chunks and plates with some nanocrystalline adhering on it. Solidified chunk-material is considered to come from the un-vaporized metal drops, and the rest metal vapor who undergoes quenching, nucleation, and growth process should be responsible for the formation of nanoparticles. In multi-element wire (binary and ternary) explosion, due to the discrepant characteristics of electrical and thermal, the explosive behaviors are different, and the current will re-distribute between wires which will lead to different product states, like plasma, un-ionized metal vapor, or un-vaporized metal drops. As a result, the sprayed explosive products are always a mixture of plasma and metal vapor/drops. This research gives the suggestion to the practical application that should consider the detailed electrical explosion behaviors of wires in multi-element wire explosive spraying.

References

1. Kotov, Y.A.: Electric explosion of wires as a method for preparation of nanopowders. J. Nanopart. Res. **5**(5–6), 539–550 (2003)
2. Li, C., Han, R., Li, J., Deng, C., Yang, B., Ouyang, J.: Exploring the influence of the evolution of discharge plasma channel on the characteristics of electric explosion products. IEEE Trans. Indust. Appl. **59**(1), 456–464 (2023). https://doi.org/10.1109/TIA.2022.3212984
3. Cho, C.H., Park, S.H., Choi, Y.W., Kim, B.G.: Production of nanopowders by wire explosion in liquid media. Surf. Coat. Technol. **201**(9–11), 4847–4849 (2007)
4. Aravinth, S., Sankar, B., Chakravarthi, S.R., Sarathi, R.: Generation and characterization of nano tungsten oxide particles by wire explosion process. Mater. Charact. **62**(2), 248–255 (2011)
5. Debalina, B., Kamaraj, M., Murthy, B.S., Chakravarthi, S.R., Sarathi, R.: Generation and characterization of nano-tungsten carbide particles by wire explosion process. J. Alloys Compd. **496**(1–2), 122–128 (2010)
6. Gao, X., Chen, P., Wang, X., Xu, C., Song, Q., Yin, H.: Production of AlN nanopowders by electrical wire explosion in liquid nitrogen. Mater. Sci. Forum **910**, 46–51 (2018)
7. Wang, X., Zhou, H., Wei, Y., Zhang, A., Zhu, L.: Electrical explosion spray of Ag/C composite coating and its deposition behavior. Ceramics Int. **48**(4), 4497–4504 (2022)
8. Han, F., Zhu, L., Liu, Z., Gong, L.: The study of refractory Ta10W and non-refractory Ni60A coatings deposited by wire electrical explosion spraying. Surf. Coat. Tech. **374**, 44–51 (2019)
9. Han, R., et al.: Compositionally graded multi-principal-element alloy coating with hybrid amorphous-nanocrystalline structure by directional electrical explosion. J. Alloy Compd. **933**, 167780 (2023)
10. Pervikov, A., Glazkova, E., Lerner, M.: Energy characteristics of the electrical explosion of two intertwined wires made of dissimilar metals. Phys. Plasma **25**, 070701 (2018)
11. Sarkisov, G.S.: Temperature of metal wires for nanosecond and microsecond electrical explosions in vacuum. J. Appl. Phys. **128**, 183302 (2020)

Guided Ionization Discharge Characteristics of N$_2$ and O$_2$ Driven by Pulsed DC Power

Jianben Liu[1], Jiangong Zhang[1], Lanlan Nie[2(✉)], Ni Li[1], and Ruizhi Zhang[2]

[1] State Key Laboratory of Power Grid Environmental Protection, China Electric Power Research Institute, Wuhan, Hubei, People's Republic of China
[2] State Key Laboratory of Advanced Electromagnetic Engineering and Technology, Huazhong University of Science and Technology, Wuhan, Hubei 430074, People's Republic of China
nielanlan2017@163.com

Abstract. In recent years, the non-equilibrium plasma show great application in material processing. The nitrogen and oxygen gas driven by Pulsed DC power at lower pressure in a long dielectric tube have been investigated. With fixed voltage parameter, the stable and homogeneous plasma propagates along the tube at pressure ranging from 20 Pa to 1×10^4 Pa like the guided ionization wave. The length of the plasma plume has the maximum value about 100 cm at 100–200 Pa. With the voltage amplitude increasing, the length of N$_2$ plasma plume and O$_2$ plasma plume increase. With the frequency is lower than 8 kHz, the length of N$_2$ plasma plume is larger than that of oxygen, and after that, the length of O$_2$ become larger. When the pulse width is higher than $10\,\mu s$, the length of O$_2$ reduced sharply. N$_2$ and O$_2$ plasma plume contains bright "bullet" from the high spatio-temporal resolution photographs. However, the N$_2$ "bullet" has a long tail differing from O$_2$ at the same E/N. The gas temperature simulated by the second positive system of N$_2$(C$^3\Pi_u$-B$^3\Pi_g$) is 330 K for N$_2$ plasma at 100 Pa and 1×10^3 Pa, while it is 320 K and 330 K for O$_2$ which is suitable for the plasma medicine and other material application.

Keywords: Non-equilibrium plasma · nitrogen and oxygen discharge · pulsed DC power · lower pressure

1 Introduction

In recent decades, atmospheric pressure plasma jets have been extensively studied [1–5]. The researchers have gotten physical insights into its plasma physical properties. Nowadays, noble gases (He, Ar and Neon) [6–9] are usually used as the discharge gas otherwise discharges using molecular gases (such as N$_2$, O$_2$, air et. al) [10–13]. Using molecular gases have two difficulties: one is higher breakdown voltage and the other one is increasing of temperature. With the development of nanosecond pulse power technology, non-equilibrium discharge with molecular gases especially nitrogen, oxygen and air has come true. The jets driven by high pulse voltage have attracted many attentions due to its fast energy transfer effect [14–17].

The main focus of this manuscript is the discharge characteristics of nitrogen and oxygen with pulsed high voltage as the motivation source. There are two reasons for choosing the lower pressure, one is the pressure always lower for the material surface modification and the other one is the pulsed power limitations on the amplitude and frequency. The motivation of this study is to provide theoretical guidance for the pulsed N$_2$ and O$_2$ discharge. In this work, the pressure range for uniform discharge has been studied. Besides, the optical characteristics of N$_2$ and O$_2$ discharge have been investigated. The sustained voltage has been studied as well. The length of the plasma plume versus the gas pressure and the voltage parameters have been studied in details. The propagation processes of the plasma plume have been captured by the ICCD camera and the propagation velocity inside the plasma plume has been calculated by the ICCD photographs as well. Besides, the gas temperature has been measured by the second positive system of N$_2$(C$^3\Pi_u$-B$^3\Pi_g$).

2 Experiment Setup

As shown in Fig. 1, one side of the discharge tube is terminated with stainless steel needle electrode covered by the quartz barrier and the other side is connected with the gas control system. The gas pressure in the tube is monitored by the barometers (Inficon, Model: PCG550) and regulated by the gas control system. The gas control system performs two functions, gas insert and exhaust. The gas insert is controlled by the gas flow controller (MKS Instruments M100B) and the turbo-molecular pump (Agilent, TPS-Bench) is used as exhaust equipment. The inner and outer diameters of the discharge tube are 6 mm and 8 mm, respectively. The minimum degree of vacuum in the tube is 0.05 Pa. The 99.99% N$_2$ and 99.99% O$_2$ is used as the working gas in this manuscript.
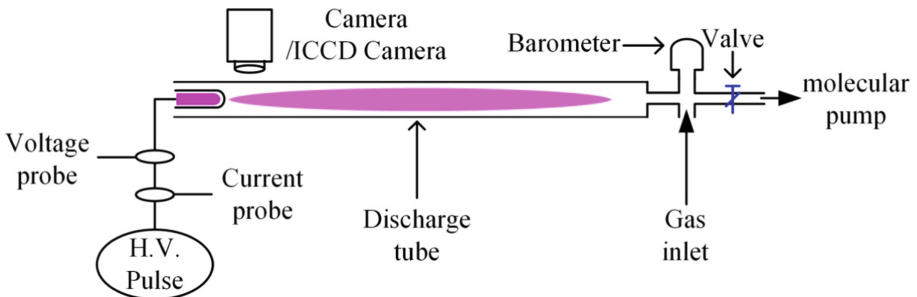
Fig. 1. Schematic of the experimental setup

The discharge is driven by the high-voltage pulses with amplitude up to 10 kV, pulse width variable from 200 ns to dc, rise/fall time of 100 ns, and pulse repeatable frequency up to 10 kHz. The applied voltage is measured by a P6015 Tektronix HV probe and the current by a Tektronix TCP312A current probe. The voltage and current waveforms are recorded by a Tektronix DPO7104 digital oscilloscope.

3 Results and Discussion

3.1 The Plasma Plume of N_2 and O_2 Discharge

Figure 2 is the photograph of N_2 (Fig. 2a) and O_2 (Fig. 2b) discharge at pressure (from 20 Pa to 1×10^4 Pa) with the voltage parameters of 8 kV, 4 kHz, 1.6 μs. It can be shown that two kinds of plasma are stable and homogeneous. And the plasma plume propagates along the tube straightly. The discharge morphology is similar to APPJs. The color of the nitrogen discharge is pink one and the oxygen discharge is much more canary yellow color. It can be shown from Fig. 2 that the discharge has been strengthened and then weakened with the increasing of the pressure at fixed voltage parameters. With the fixed voltage parameters, N_2 and O_2 plasma plume reaches its maximum length at 100 Pa to 200 Pa gas pressure.
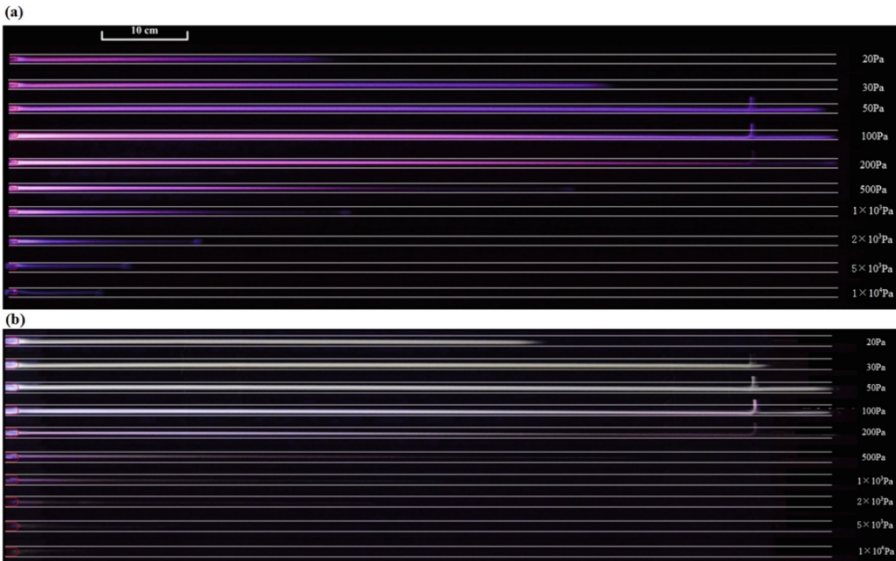
Fig. 2. Photograph of N_2 and O_2 discharge.

As has been shown in Fig. 2, the length of N_2 and O_2 plasma plume achieved the maximum length at 100 pa to 200 Pa with fixed voltage parameters. The physical mechanism of this phenomenon should be investigated. As the applied voltage is fixed, the electrical field inside the tube is almost the same at the same pressures. The reduced field strength E/N decrease with the pressure increasing. It is well known that the electrons acquired more energy from the electrical field with larger E/N. . But why the length of the plasma plume decreases when the pressure is lower than 100 Pa? In order to solve this doubt, the sustained voltage of N_2 and O_2 has been measured as shown in Fig. 3. It can be seen from Fig. 3 that the N_2 and O_2 have the minimum sustained voltage.

It has been mentioned in Ref. [17] that the length of the plasma jet is related to the integrated total charge due to the discharge at the rising edge of voltage as the bullet
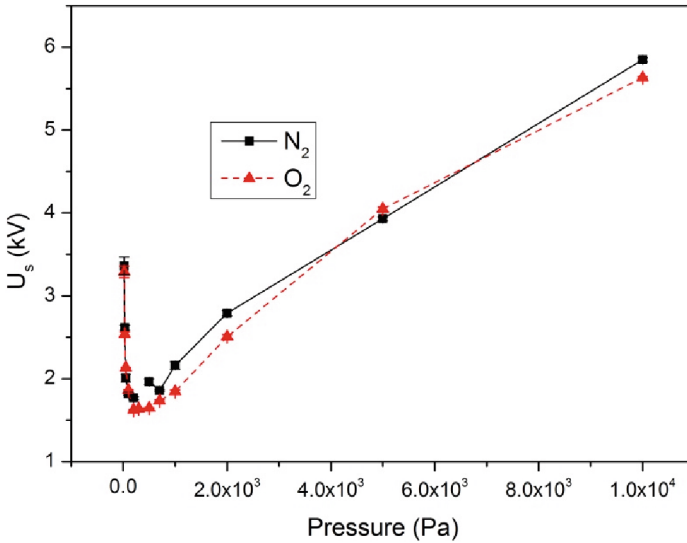
Fig. 3. The sustain maintained voltage of N_2 and O_2.

propagation will be shut down with the arriving of the bullet. As the excited voltage is pulsed DC, the ratio of the overvoltage K is very important which can be calculated as $K = (U_a - U_s)/U_s$. The sustain maintained voltage U_s has been measured as shown in Fig. 4. It has exhibited From Fig. 4 that N_2 and O_2 has the minimum U_s at about 100 Pa. When the voltage parameter is fixed 8 kV, 4 kHz, 1.6 μs, the length of plasma plume depends linearly on the ratio of the overvoltage K.

In order to have an insight of the discharge of nitrogen and oxygen, the length of discharge under different applied voltage parameters such as the voltage amplitude, frequency and the pulse width have been studied in details as shown in Fig. 4. By the comparison analysis, it exhibited that the length of discharge increases with the increasing of the applied voltage amplitude in Fig. 4(a). And when the voltage is smaller than 8 kV, the length of O_2 plasma plume is shorter than N_2. But, the length of O_2 plasma plume increases more than N_2 plasma plume when the voltage is larger than 8.5 kV. With increasing of the applied voltage, reduced field strength E/N has been enhanced and as a result that the ionization coefficient increases.

It can be shown from Fig. 4(b) that with the f increasing from 1kHz to 9 kHz, the length of N_2 plasma plume decreases and that of O_2 decreases firstly and then increases when the f is larger than 6 kHz. As the plasma plume is terminated by the discharge (the second discharge) at falling edge of the voltage, the residual species increase with increasing f which make the second discharge come early and the plasma plume length reduces.

With the pulse width increasing from 200 ns to 200 μs as shown in Fig. 4(c), the plasma length of N_2 increase and then decrease slowly, otherwise that of oxygen increase firstly and decrease sharply at 10 μs, and when t_w is larger than 10 μs, the length of O_2 is much smaller than N_2.
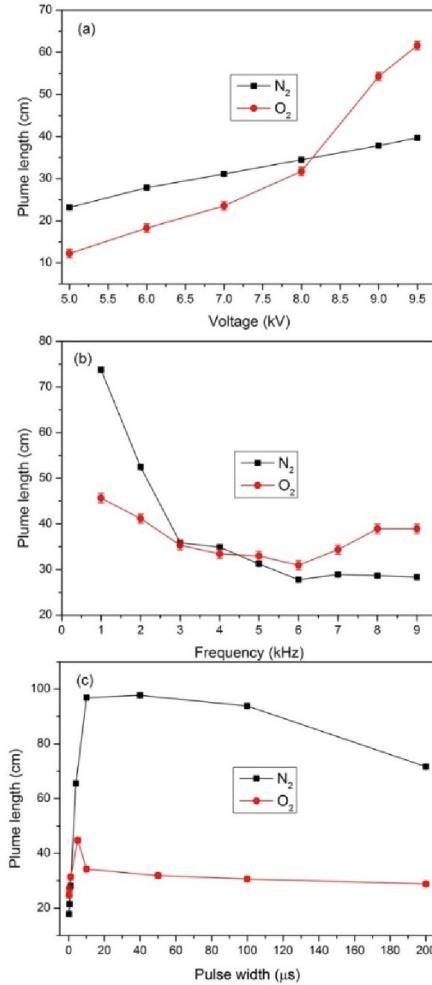
Fig. 4. The length of the nitrogen plasma plume versus (a) voltage amplitude (b) frequency (c) pulse width at 1×10^3 Pa.

Liu et al. has found that the Ar plasma plume terminates right after the falling edge of each voltage pulse when $t_w < 20 \ \mu s$, whereas it terminates before the falling edge. When t_w is larger than 30 μs, the duration of plasma plume starts to decrease, and the termination is found to occur at the current zero moment of the discharge current through the high-voltage electrode, which is much different from that through the ground electrode. In this paper, for N_2 and O_2, the transition t_w is 10 μs.

3.2   The Optical Emission Spectrum

The optical emission spectrum (OES) is another important characteristic. And the OES of N_2 and O_2 ranging from 300 nm to 800 nm is shown in Fig. 5. Firstly, the OES

intensity of oxygen at the same discharge parameters is about 100 times lower than that of N$_2$ discharge. Secondly, it can be seen from Fig. 5 that the discharge spectra of N$_2$ is dominated by molecular nitrogen, while the discharge spectra of O$_2$ discharge is molecular nitrogen and atom oxygen.
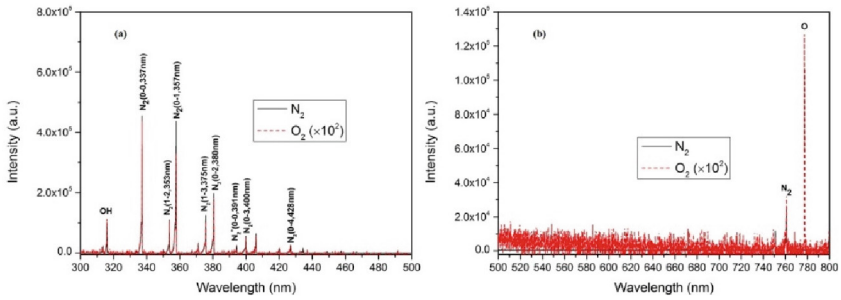
Fig. 5. The optical emission spectrum of N$_2$ and O$_2$ plasma at 1×10^3 Pa ($U_a = 8$ kV, $f = 4$ kHz, $t_w = 1.6\ \mu$s).

Gas temperature is one of the most important parameters for plasma applications. The rotational temperatures of N$_2$(C–B) molecules are often applied to estimate the plasma gas temperature by spectra-fitting the experimental emission bands. In this paper, the second positive system of N$_2$(C$^3\Pi_u$-B$^3\Pi_g$) at rotation-vibrational transitions at (0–2) has been used to simulate the gas temperature. It should be mentioned here that the nitrogen percent of O$_2$ gas is about 10–20 ppm and there is N$_2$ emission spectrum as shown in Fig. 5, so the temperature of O$_2$ plasma plume is simulated by the second positive system of N$_2$(C$^3\Pi_u$-B$^3\Pi_g$) as well. The gas temperature is about 330 K of the N$_2$ discharge at 100 Pa and 1×10^3 Pa as shown in Fig. 6. And that is 320 K for O$_2$ at 100 Pa and 330 K at 1×10^3 Pa as shown in Fig. 7. The temperature in both cases is appropriate for biomedical application.
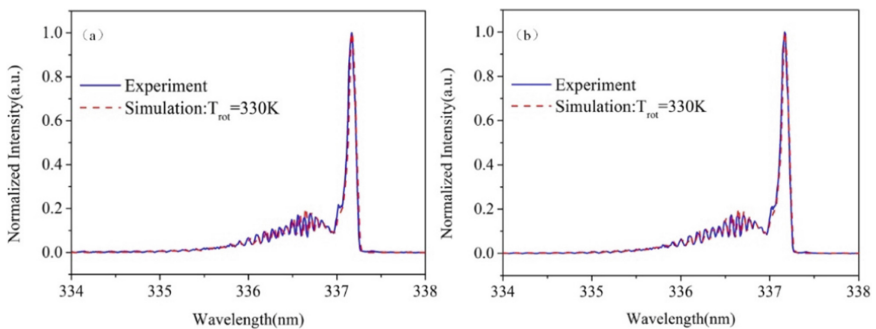
Fig. 6. Experimental and simulated spectra of N$_2$ plasma plume at 100 Pa (a) and 1×10^3 Pa (b) by N$_2$ second positive system 0–0 transition.
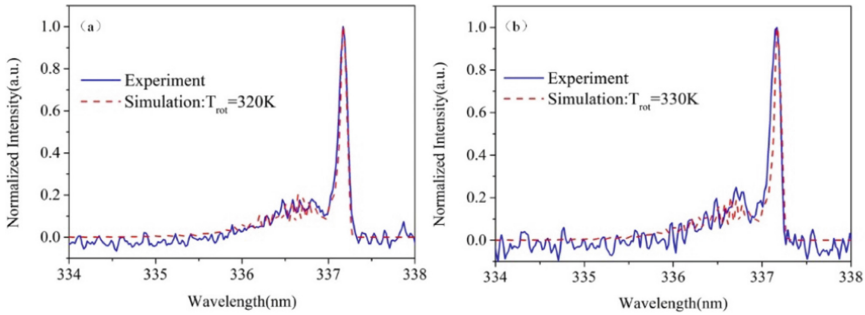
Fig. 7. Experimental and simulated spectra of O_2 plasma plume at 100 Pa (a) and 1×10^3 Pa; (b) by N_2 second positive system 0–0 transition.

3.3 The Dynamic Propagation Process Analysis of the Guided "Bullet"

It's well known that the bright plasma plume of atmospheric pressure plasma jet(APPJs) is driven by "plasma bullet", so the high-speed photograph of N_2 and O_2 plasma plume has been captured by Andor DH340 camera in order to investigate the propagation processes as shown in Fig. 8. The stable homogeneous plasma plumes are driven by the plasma bullets as well as the APPJs. However, the plasma bullet of N_2 has a longer tail while the bullet of O_2 is much shorter. In order to investigate the physical mechanism of the length of the bullet, the discharge parameters have been changed and there are shorter cases in N_2 bullet as well as longer cases in O_2 bullet. When the applied voltage amplitude is lower or the pressure is higher, the N_2 bullet length deduces and when the pressure is lower, the O_2 bullet length increases as shown in Fig. 9. It need be mentioned that the O_2 bullet maybe increase with higher voltage while the longer O_2 bullet with higher voltage haven't gotten due to the limit of the power supply. And in our experiments, the frequency and the pulse width time have less influence on the length of bullet.
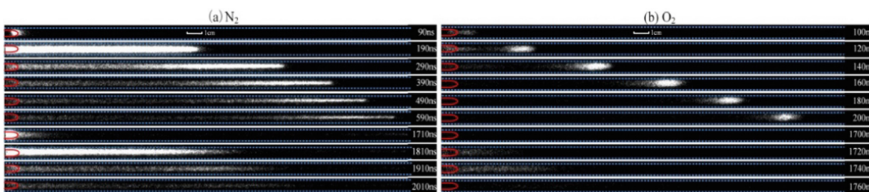
Fig. 8. High-speed photograph of the plasma plume at 1×10^3 Pa pressure (a) N_2; (b) O_2; the voltage parameters is fixed as $U_a = 8$ kV, $f = 4$ kHz, $t_w = 1.6$ μs.

    The physical mechanism of bullet needs to be declared that the bullets seen by eyes are lights emitted by the excited state particles. There are more excited state particles behind the bullet head in N_2 plasma bullet. We think the reason for this phenomenon should be divided into two aspects. Firstly, there are many metastable states in N_2 plasma. The electrons behind the bullet head motivate the N_2 metastable species to higher state easily. The other is that the quantity of electrons behinds the bullet head in N_2 discharge is larger than that of in O_2 discharge due to the attachment of O_2 molecules.
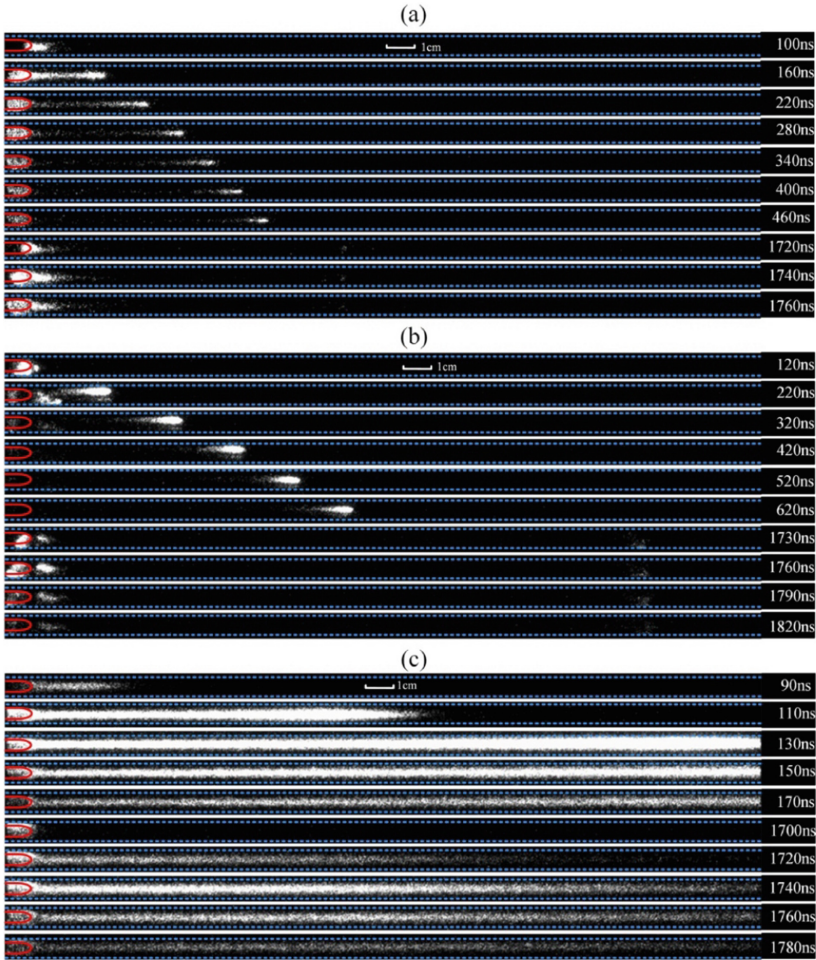
Fig. 9. High-speed photograph of the plasma plume at (a) N_2 (1×10^3 Pa pressure, $U_a = 3$ kV, $f = 4$ kHz, $t_w = 1.6$ μs); (b) N_2 (7×10^3 Pa pressure, $U_a = 8$ kV, $f = 4$ kHz, $t_w = 1.6$ μs); (c) O_2 (1×10^3 Pa pressure, $U_a = 8$ kV, $f = 4$ kHz, $t_w = 1.6$ μs).

In order to have an insight of the bullet propagation process, the averaged velocity of bullet along the discharge tube can be calculated by the high-speed photograph. Figure 10 shows the averaged velocity changes with the gas pressure at different position. It can be seen that the bullet has been accelerated firstly and then reduces when it propagates along the tube. The averaged velocity at the same position reached the maximum value at 100 Pa. The averaged velocity decreases with increasing of the pressure at the range of 100 Pa to 3×10^3 Pa. The major difference is that the O_2 bullet velocity increases greatly after it left the anode electrode while the N_2 bullet increases slightly. There is an interesting phenomenon by comparing Fig. 10(a) and (b) that the averaged velocity at the termination point is almost the same at the fixed pressure.
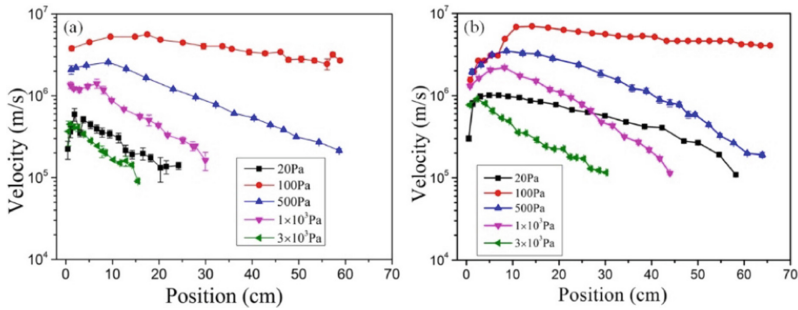
Fig. 10. The averaged velocity of N_2 and O_2 plasma bullets versus position under different pressure.
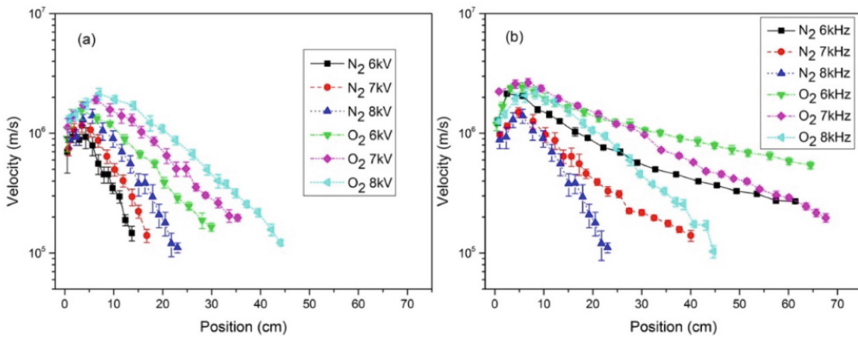
Fig. 11. The averaged velocity of N_2 and O_2 plasma bullets versus position under different voltage amplitude (a) and frequency (b).

The gas pressure of Fig. 11 is fixed at 1×10^3 Pa. In Fig. 11(a), the frequency is fixed at 4 kHz and the pulse width is fixed as 1.6 µs. It exhibits that the averaged velocity increases when voltage amplitude increases from 6 kV to 8 kV. But at the same voltage, the velocity of O_2 is larger than N_2. The oxygen bullet has accelerated in a longer distance. There are amount of positive space charges nearby the anode electrode which reduce the applied electrical field, in return, the N_2 bullet accelerates for a shorter time. However, the amount of positive species is less than that of N_2 so the O_2 bullet gets more electrical energy to accelerate.

Figure 11(b) shows the averaged velocity versus with the frequency. With the increasing of the frequency, the averaged velocity at the same position decreases and the distance of the plasma bullet that can arrive reduces. At the same frequency, the velocity of N_2 is less than that of O_2. It should be mentioned the maximums of the velocity of the bullet with 8 kHz are almost the same with those of the frequency is 7 kHz but velocity decreases sharply after the acceleration phase especially for O_2 discharge. How the O_2 bullet velocity is affected by the frequency after the acceleration phase? This maybe explained as following. The bullet is mostly driven by the space charges electrical field,

so there are more residual species which can react with the space charges with f increasing. For O_2 gas, there are more O_2^- residued in the tube so the positive ions at the head of the bullet recombine with O_2^- quickly resulting in the velocity decreases a lot.

4 Conclusion

When the pulsed power is fixed in almost the highest output parameters, we can get stable and homogeneous nitrogen plasma and oxygen plasma inside the tube at pressure ranging from 20Pa to 1×10^4 Pa. The discharge morphology is similar to atmospheric pressure plasma jets (APPJs). The plasma plume length can reflect the plasma volume and it is important for material modification. There are four variable parameters to investigate the plume length (gas pressure, voltage amplitude, frequency and pulse width). The length of the plasma plume has the maximum value at 100–200 Pa. Besides, the plume length under different voltage parameters has been investigated as well. With the amplitude increasing, N_2 plasma plume and O_2 plasma plume increase almost linearly. However, the length of N_2 and O_2 plasma plume is inversely proportional to the frequency. With the frequency is lower than 8 kHz, the length of N_2 plasma plume is larger than that of oxygen, and after that, the length of O_2 become larger. The pulse width plays important influence on the plasma length. The length increases firstly and then reduces with increasing the pulse width. When the pulse width is higher than 10 μs, the length of O_2 reduced sharply.

N_2 and O_2 plasma plume contains bright "bullet" from the high spatio-temporal resolution photographs. However, the N_2 "bullet" has a long tail differing from O_2 at the same discharge parameter. We explained this by the adsorption electron characteristic of O_2. And in order to prove the suspect, the long tail of O_2 bullet appear with lower pressure at higher voltage parameter.

The gas temperature simulated by the second positive system of $N_2(C^3\Pi_u\text{-}B^3\Pi_g)$ is 330 K for N_2 plasma at 100 Pa and 1×10^3 Pa, while it is 320 K and 330 K for O_2 which is a little higher than the room temperature 300 K. But it is almost suitable for the plasma medicine and other material application.

References

1. Urabe, K., Ito, Y., Tachibana, K., Ganguly, B.N.: Behavior of N2 ions in He microplasma jet at atmospheric pressure measured by laser induced fluorescence spectroscopy. Appl. Phys. Express **1**, 066004 (2008)
2. Lu, X., Laroussi, M.: Dynamics of an atmospheric pressure plasma plume generated by submicrosecond voltage pulses. J. Appl. Phys. **100**, 063302 (2006)
3. Goossens, O., Dekempeneer, E., Vangeneugden, D., Van de Leest, R., Leys, C.: Application of atmospheric pressure dielectric barrier discharges in deposition, cleaning and activation. Surf. Coat. Technol. **142**, 474–481 (2001)

4. Ishaq, M., Evans, M.M., Ostrikov, K.: Effect of atmospheric gas plasmas on cancer cell signaling. Int. J. Cancer **134**, 1517–1528 (2014)

5. Shashurin, A., Keidar, M., Bronnikov, S., Jurjus, R., Stepp, M.A.: Living tissue under treatment of cold plasma atmospheric jet. Appl. Phys. Lett. **93**, 44–47 (2008)

6. Uhm, H.S., Byeon, Y.S., Song, K.B., Choi, E.H., Ryu, H.-Y., Lee, J.: Analytical investigation of electrical breakdown properties in a nitrogen-SF6 mixture gas. Phys. Plasmas **17**, 113510 (2010)

7. Walsh, J.L., Kong, M.G.: Room-temperature atmospheric argon plasma jet sustained with submicrosecond high-voltage pulses. Appl. Phys. Lett. **91**, 221502 (2007)

8. Laroussi, M.: Low temperature plasmas for medicine? IEEE Trans. Plasma Sci. **37**, 714 (2009)

9. Breden, D., Miki, K., Raja, L.: Computational study of cold atmospheric nanosecond pulsed He plasma jet in air. Appl. Phys. Lett. **99**, 111501 (2011)

10. Jánský, J., Delliou, P.L., Tholin, F., Tardiveau, P., Bourdon1, A., Pasquiers, S.: Experimental and numerical study of the propagation of a discharge in a capillary tube in air at atmospheric pressure, J. Phys. D Appl. Phys. **44**, 335201 (2011)

11. Jánský, J., Bourdon, A.: Surface charge deposition inside a capillary glass tube by an atmospheric pressure discharge in air. Eur. Phys. J. Appl. Phys. **55**, 13810 (2011)

12. Liu, D., Gu, J., Feng, Z., Li, D., Niu, J.: Plasma deposition of fluorocarbon thin films using pulsed/continuous and downstream radio frequency plasmas. Thin Solid Films **517**, 3011 (2009)

13. Es-sebbar, E., Benilan, Y., Jolly, A., Gazeau, M.-C.: Characterization of an N2 flowing microwave post-discharge by OES spectroscopy and determination of absolute ground-state nitrogen atom densities by TALIF. J. Phys. D: Appl. Phys. **42**, 135206 (2009)

14. Wu, S., Xu, H., Lu, X., Pan, Y.: Effect of pulse rising time of pulse dc voltage on atmospheric pressure non-equilibrium plasma. Plasma Process. Polym. **10**, 136–140 (2013)

15. Iza, F., Walsh, J.L., Kong, M.G.: From submicrosecond to nanosecond-pulsed atmospheric-pressure plasmas. IEEE Trans. Plasma Sci. **37**, 1289–1296 (2009)

16. Lu, X., Laroussi, M., Puech, V.: On atmospheric-pressure nonequilibrium plasma jets and plasma bullets. Plasma Sources Sci. Technol. **21**, 034005 (2012)

17. Rong, M., Xia, W., Wang, X., et al.: The mechanism of plasma plume termination for pulse-excited plasmas in a quartz tube. Appl. Phys. Lett. **111**, 074104 (2017)

Optimization of Insulator and Shield Geometry of 225 kV Electron Gun

Silin Wang[1,2] , Junbiao Liu[1,2(✉)] , Pengfei Wang[1] , Zengya Dong[1] , and Geng Niu[1]

[1] Institute of Electrical Engineering, Chinese Academy of Sciences, Beijing 100190, China
`liujb@mail.iee.ac.cn`
[2] University of Chinese Academy of Sciences, Beijing 100049, China

Abstract. In this paper, the electrical performance of 225 kV electron gun is optimized based on the avalanche theory of secondary electron emission. Due to the electron gun shield, the Angle between the electric field direction of the electron gun insulator and the insulator surface changes in positive and negative directions. Different discussions should be made on the insulators in the acting area of the shield and other areas. Bessel curve and spline curve were selected to parameterize the model of insulator and shield. The ratio of normal electric field and tangential electric field of insulator outer contour, integral value of tangential electric field of insulator outer contour along the outer contour and maximum field intensity of shield surface were taken as the optimization objective function, and the Nelder-Mead approximate gradient algorithm method was used to solve the problem. After optimization, the maximum electric field strength on the shield surface is reduced by 37.3%, the field strength at the cathode triple junction (CTJ) is reduced by 76.7%, and the maximum electric field strength on the insulator surface is reduced by 25.5%. The tangential electric field distribution on the insulator surface is also optimized.

Keywords: X-ray · Electron gun · High Voltage Engineering · surface flashover · Shape optimal design

1   Introduction

Electron gun is electron beam sources for X-ray nondestructive testing instruments, electron beam lithography (EBL), high-power microwave tubes, accelerators, electron beam welding (EBW) and electron microscopy (EM), and it is an important part of these devices [1, 2]. The electron gun works in a vacuum environment, and the electrons need a high voltage to get enough speed for processing and testing. Therefore, the electrical performance of insulators working under vacuum plays a crucial role in the performance of equipment. Because the electron gun works at a high voltage, the gas breakdown discharge [3, 4], surface flashover breakdown discharge [5] and partial discharge [6] will affect the reliability and stability of the electron gun, and the insulator flashover discharge along the surface is one of the main reasons to reduce the reliability and stability of the electron gun. At present, although there is no definite explanation for the mechanism of

surface flashover, the Secondary Electron Emission avalanche SEEA) model has been widely accepted. [7, 8] and the Theory of electronically triggered polarization relaxation (ETPR) [9–11]. Based on the secondary electron emission avalanche (SEEA) model, this paper optimized the electric field distribution on the insulator surface to reduce the secondary electron yield on the insulator surface, so as to improve the surface flashover voltage.

Based on SEEA model analysis, we have designed the electron gun structure of 90 kV microlocal X-ray source [12]. At present, the 225 kV electron gun is being developed. With the increase of voltage, the shape of the electron gun insulator and the related parts of the electron gun need to be optimized. Aiming at the application of electron gun at 225 kV DC voltage, this study improves the electrical performance of electron gun by optimizing the geometry of insulator and shield. Bessel curve [13] is used to draw the outer contour of insulator, and spline curve is used to draw the shield contour for parametric modeling. Finally, The Nelder-Mead approximate gradient algorithm [14] was used to solve the minimum value of the selected objective function, in order to obtain the best electrical performance of the geometric shape.

2   Analysis of Surface Flashover Phenomenon

2.1   Electron Gun Structure
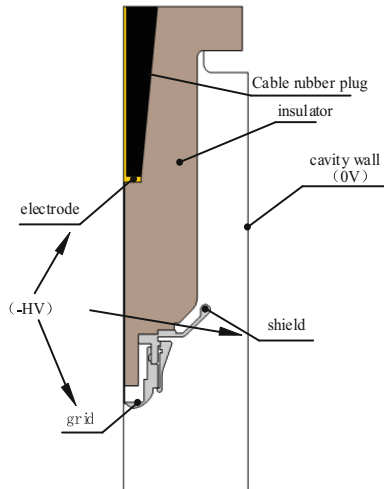

Fig. 1. Triode electron gun structure.

In the previous study, a shield was added to reduce the electric field intensity at the cathode triple junction and the emission phenomenon of initial electrons at the cathode triple junction, but the influence of field emission electrons from the shield and the shield on the electric field intensity distribution on the insulator surface were not

considered. The electron gun is mainly composed of a gate assembly, an insulator and a shield. As shown in Fig. 1, the head of the electron gun and the power supply are connected by a high-voltage cable. The high-voltage cable head is made of standard rubber material, which is used to discharge air and ensure the stability of electrical properties. The high voltage cable head is connected to the filament, gate and shield through electrodes. Insulators separate the cathode from the grounded part and serve to connect and support the cathode. During the operation of the equipment, we observed the discharge phenomenon between the shield and the insulator, and also found obvious carbon marks on the surface of the insulator, as shown in Fig. 2. This study mainly focuses on reducing the cathode triple junction field intensity and optimizing the shape of the shield and insulator.

Fig. 2. The trail of destruction

2.2 Model of Flashover Discharge Introduction

The secondary electron emission Avalanche (SEEA) model [7, 8] believes that when a high voltage is applied, the initial electron is usually emitted from the three junction points of the cathode, and the initial electron hits the surface of the insulator, leading to the secondary electron emission and doubling process. In the process of electron movement, the current increase of various factors can be triggered. The process of desorption of the gas on the insulator surface and generating the Townsend Townsend discharge, resulting in flashover. The secondary electron emission Avalanche (SEEA) model [7, 8] believes that when a high voltage is applied, the initial electron is usually emitted from the three junction points of the cathode, and the initial electron hits the surface of the insulator, leading to the secondary electron emission and doubling process. In the process of electron movement, the current increase of various factors can be triggered. The process of desorption of the gas on the insulator surface and generating a townlike discharge, resulting in flashover.

As shown in Fig. 3, in this study, the electrode of the electron gun runs through the insulator, which will have an impact on the direction of the electric field on the insulator surface. However, for the part where the shield works, the shield is closer to the insulator surface than the electrode, so the electric field intensity generated by the shield is larger.

Therefore, the direction of the normal electric field strength in the part of the shield acting is directed towards the shield. In this study, the point where the normal field strength is 0 is the boundary, and the part where the normal electric field strength on the insulator surface points to the shield is called the shielding shield acting section. Take the Angle $\theta < 0$ between the electric field intensity and the insulator surface. The part of the normal field strength pointing to the axis is called the non-shield acting section. Take the Angle $\theta > 0$ between the electric field strength and the insulator surface. For the shield acting section with $\theta < 0$, the average energy injected into electrons when the initial electrons reach the insulator surface again through the electric field action [15] is

$$\overline{A} = \overline{A_0}\left[1 + 2\left(\frac{E_t}{E_n}\right)^2\right] = \overline{A_0}\left[1 + 2(tan|\theta|)^{-2}\right](\theta < 0) \tag{1}$$

$\overline{A_0}$ is the average emission energy of the initial electron; E_n is the normal electric field intensity on insulator surface. E_t is the tangential electric field intensity on insulator surface; θ is the Angle between the electric field intensity and the insulator surface. According to formula (1), when $\theta < 0$, increasing the value of θ in the acting part of the shield can effectively reduce the energy of the initial electrons to reach the insulator surface again, so as to reduce the secondary electron production. However, in practice, for $\theta < 0$, the larger the value of θ does not necessarily mean the larger the flashover voltage. According to the study of Yu Kaikun et al. [16] and Xun T et al. [17], when θ is $-45°$, the flashover voltage along the surface is the highest. For the part $\theta > 0$, increasing the Angle θ between the electric field intensity inside the non-shielding shielding section and the insulator surface can reduce the probability of electron collision on the insulator surface.
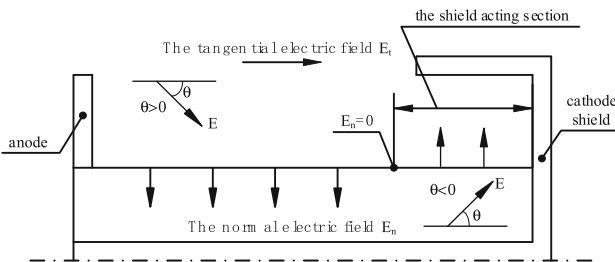

Fig. 3. Schematic diagram of electric field distribution of electron gun with shield
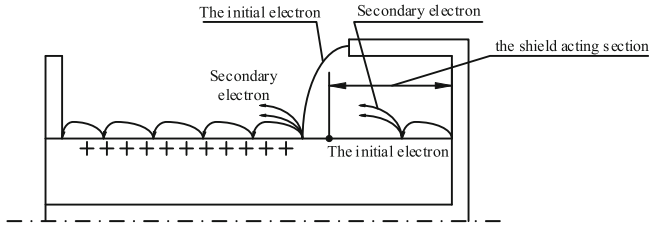
Fig. 4. Schematic diagram of flashover of electron gun with shield

As shown in Fig. 4, in the process of flashover discharge initial electronic sources can be divided into two parts, one is the cathode three point (CTJ) produced by the initial electron in $\theta < 0$ of the electric field under the action of once again return to the surface of the insulator, secondary electron hitting the insulator surface, and then under the action of electric field, the secondary electron is once again return to the surface of the insulator, The electron avalanche spreads to the vicinity of the insulator surface with $\theta = 0$, and as the initial electron strikes the non-shield acting section of the insulator surface with $\theta > 0$, causing flashover along the surface. Second, from the microscopic point of view, the surface of the shield has many tiny bumps, and the electric field intensity at the bumps is very large, which may lead to the emission of initial electrons from the tip of the shield, and the initial electrons fall near the surface of the insulator with $\theta = 0$, causing flashover along the surface.

According to the Secondary electron emission Avalanche (SEEA) model and the electric field distribution model of electron gun in this study, the optimal design principles of insulator and shield of HV electron gun in vacuum are as follows:

1) Reduce initial electron emission;
2) Inhibition of secondary electron generation;
3) Make the electric field distribution along the insulator surface uniform;
4) Reduce the difficulty of mechanical processing appropriately and consider the economy and rationality of mechanical structure.

2.3   Analysis of Electric Field of Electron Gun

In this study, the high-voltage electron gun works in a high-voltage DC environment and can be analyzed by electrostatic field finite element method. When building the model, the thread at the connection is ignored, the filament electrode is simplified as a cylindrical copper pole, and the simplified shape of the cable junction is replaced by a flat cylinder. The boundary conditions set the cavity wall as a ground potential, and the electrode, gate and shield as a potential of -225 kV. In the electrostatic field simulation calculation, the relative permittivity of each component material is 1.0 for vacuum material, 2.5 for PEEK material, and 3.0 for rubber material. In order to calculate the permittivity of metal conductor, it is usually set to 1.0. COMSOL Multiphysics finite element simulation software was used to simulate the electrostatic field. The electric field distribution of electrostatic field finite element calculation results is shown in Fig. 5 and Fig. 6, and the maximum field intensity is 2.8e7 V/m at the outermost edge of the shield. As shown
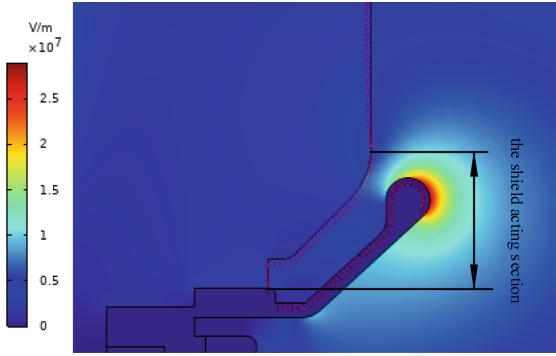
Fig. 5. Electrostatic field simulation electric field distribution diagram
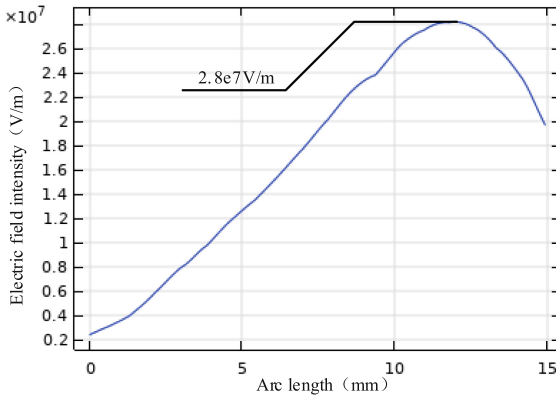
Fig. 6. Electric field curve of shield surface
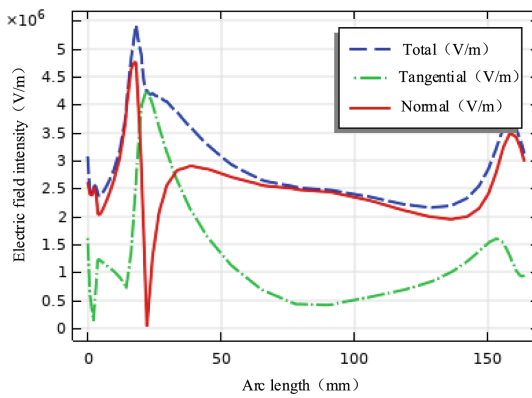
Fig. 7. Electric field distribution curve on insulator surface
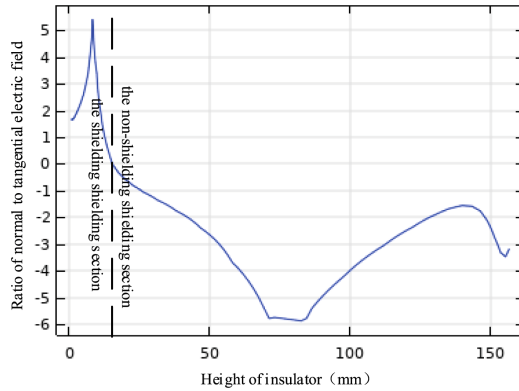
Fig. 8. The ratio of the normal electric field to the tangential electric field on the insulator surface

in Fig. 7, the electric field intensity at the three junction points of the cathode is 3.0e6 V/m, and the maximum electric field intensity on the insulator surface is 5.5e6 V/m. The minimum tangential electric field intensity of the insulator surface on the upper part of the shield is 0.49e6 V/m, and the maximum is 1.7e6 V/m. In this study, the vertical height between the cathode triple junction point (CTJ) and the insulator surface where the normal electric field is 0 V/m is called the shielding shield acting section. As shown in Fig. 8, the ratio of normal electric field to tangential electric field has a maximum value of 5.5.

According to the simulation results, in order to obtain better electrical performance of the high-voltage electron gun, we can reduce the field strength of the cathode triple junction point and the shielding cover, reduce the ratio of the normal electric field to the tangential electric field of the shielded section of the insulator surface, reduce the tangential electric field of the non-shielded section of the insulator surface, and increase the Angle θ between the electric field strength and the insulator surface. Increases the difficulty for electrons to fall to the insulator surface again.

3   Parametric Modeling

3.1   Insulator Shape Design

In order to ensure the smooth and continuous geometry of insulator outer contour and make the field intensity evenly distributed, Bessel curve is selected as insulator outer contour. Bessel curve is a basic tool of computer graphics image modeling and one of the most widely used basic lines [12]. It can control the geometry of insulators with the least number of variables on the premise of meeting the shape requirements. As shown in Fig. 9, four points P_1 (starting point), P_2, P_3 (middle point) and P_4 (cut-off point) control the shape of the curve, and the curve expression is shown in Eq. (2).

$$B(t) = P_1(1-t)^3 + 3P_2t(1-t)^2 + 3P_3t^2(1-t) + P_4t^3, t \in [0, 1] \tag{2}$$
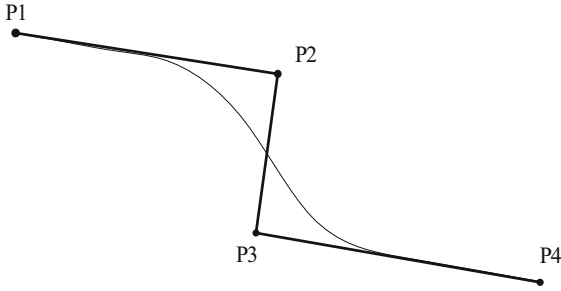
Fig. 9. Bessel curve
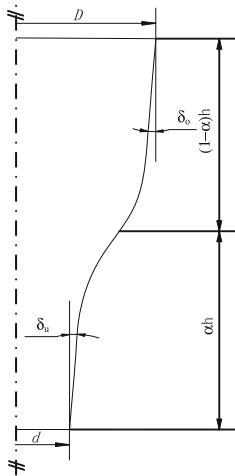
Fig. 10. Parametric modeling of insulator

As shown in Fig. 10, d is the diameter of the end of the insulator near the cathode; D is the diameter of the end of the insulator near the ground; h is insulator height; α is the insulator shape parameter; δ_u is the initial Angle of the end of the insulating surface near the cathode; On δ_o is the initial Angle of the end of the insulating surface near the ground. According to the parameterized model in Fig. 8, the positions of the four points in the r-z coordinate system are determined as

$P_1(0.5d, 0)$
$P_2(0.5d + \alpha h tan(\delta_u), \alpha h)$
$P_3(0.5D - (1 - \alpha)h tan(\delta_o), (1 - \alpha)h)$
$P_4(0.5D, h)$

3.2 Shield Design

(See Fig. 11).
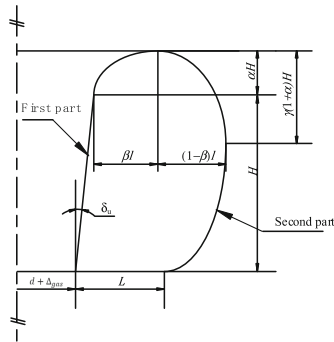
Fig. 11. Parametric modeling of shield

Where α, β, γ are the shape parameters of the shield. Under δ_u is the Angle of the end of the insulator surface near the cathode; d is the diameter of the end of the insulator near the cathode; Δ_{gas} is the air gap between the shield and the insulator surface; L is the horizontal distance between the starting point and the ending point of the spline curve of the shield; l is the distance between the furthest point of the shield and the starting point of the spline curve. H is the height of the straight-line part of the shield.

The parameter modeling of the shield part is divided into two parts. The first part is a straight line, which is controlled by parameters H and δ_u. . The second part is the spline curve, which controls the shape by the position of the four points, the tangential direction of the starting point of the spline and the curvature of the end point (Fig. 12).
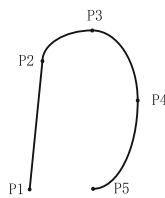
Fig. 12. Spline curve control point

The position of the first part in the r-z coordinate system is

$$P1\big(0.5d + \Delta_{gas}, 0\big)$$
$$P2\big(0.5d + \Delta_{gas} + H\tan(\delta_u), H\big)$$

The position of the second part in the r-z coordinate system is

$$P2\big(0.5d + \Delta_{gas} + H\tan(\delta_u), H\big)$$

$$P3\big(0.5d + \Delta_{gas} + H tan(\delta_u) + \beta l, (1 + \alpha)l\big)$$
$$P4\big(0.5d + \Delta_{gas} + H tan(\delta_u) + l, \gamma(1 + \alpha)l\big)$$
$$P5\big(0.5d + \Delta_{gas} + L, 0\big)$$

The tangent value of the starting point of the spline curve is $tan(\delta_u)$. The curvature of the end point of the spline curve is zero.

4 The Selection and Solution of Objective Function

4.1 The Selection of the Target Function

In this study, the electrical performance of the electron gun is improved mainly by reducing the field-induced electron emission from the shield and suppressing the generation of secondary electron emission from the insulator surface.

According to the above description, in order to increase the flashover voltage, it is necessary to inhibit the generation of secondary electrons so that no "electron avalanche" can occur on the insulator surface. For the case of $\theta < 0$, the value of θ should be close to $-45°$ to reduce the energy of electrons hitting the insulator surface and inhibit the generation of secondary electrons. For the case that $\theta > 0$, the tangential electric field value of the non-shield acting section on the insulator surface can be reduced to increase the value of θ, which makes it more difficult for electrons to fall on the insulator surface again.

In conclusion, the shield acting section of θ value will affect the effect of shield, by optimizing the insulator outer contour line on the tangential electric field arc long integral value to control the tangential electric field distribution, on the premise of ensure uniform electric field, increase the unshielded shield acting section of θ value, increase the flashover voltage.

$$f = q \int_L E_t(r, z)dl + w\left(\left|\max\left(\frac{E_n(r, z)}{E_t(r, z)}\right) - \tan\big(45°\big)\right|\right) + \max(E_s(r, z)) \quad (3)$$

According to the above views, the objective function is summarized as shown in Eq. (3), $\int_L E_t(r, z)dl$ is the integral of the tangential electric field along the outer contour of the insulator; $\max\left(\frac{E_n(r,z)}{E_t(r,z)}\right)$ is the maximum value of the ratio of the tangential electric field to the normal electric field in the shield acting section; $\max(E_s(r, z))$ is the maximum electric field intensity on the shield surface; L is the outer contour line of insulator surface; q and w are the weighting coefficients of the objective function, In this study, in order to make the smaller components of the objective function not be masked by the larger components, q is 50 and w is 1.0e8. $E_n(r, z)$ is the normal electric field on the insulator surface; $E_t(r, z)$ is the tangential electric field on the insulator surface; $E_s(r, z)$ is the electric field on the surface of the shield. At the same time, the maximum electric field intensity of all parts shall not exceed 1.0e9 V/m; The maximum diameter of insulator is not more than 96 mm; The maximum curvature of the outer contour of the shield shall

not be greater than 0.5 mm^{-1}. Therefore, the optimization model is shown in Eq. (4).

$$minf = \min\left(q\int_L E_t(r,z)dl + w\left(\left|\max\left(\frac{E_n(r,z)}{E_t(r,z)}\right) - 1\right|\right) + max(E_s(r,z))\right)$$
$$s.t. \quad E_{all} \leq 1.0 \times 10^9 \text{ V} \cdot \text{m}^{-1}$$
$$max(r_L) \leq 48 \text{ mm}$$
$$\rho_s \leq 0.5 \text{ mm}^{-1}$$

$$(4)$$

4.2 Nelder-Mead Approximate Gradient Algorithm and Procedure

After the model is established, it is difficult to find the gradient relationship between geometric parameters and the objective function. Nelder-Mead approximate gradient algorithm can solve this problem well. Nelder-Mead approximate gradient algorithm is a heuristic algorithm, although the efficiency is lower than the gradient algorithm, but does not need the strict gradient relationship between variables and the objective function. The solution process of Nelder-Mead approximate gradient algorithm [14] is shown in Fig. 13.
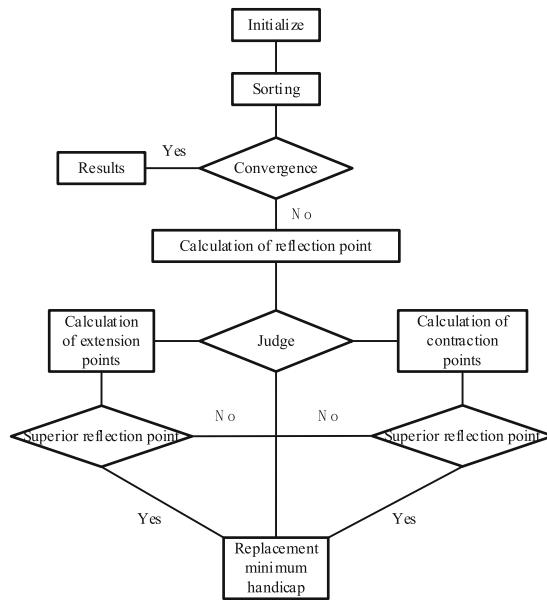
Fig. 13. The Nelder-Mead Simplex Procedure for Function Minimization

5 Optimization Results and Discussion

5.1 Optimized Insulator and Shield Electrical Performance

After calculation and analysis, the optimization results are shown in Tables 1 and 2. The optimized electric field distribution is shown in Figs. 14 and 17. The maximum

field strength is 1.8e7 V/m at the outermost edge of the shield, which is reduced by 37.3% compared with that before optimization. As shown in Fig. 15, the field strength of the cathode triple junction is 0.7e6 V/m, which is 76.7% lower than that before optimization, and the maximum field strength of the insulator surface is 4.1e6 V/m, which is 25.5% lower than that before optimization. The minimum tangential electric field on the insulator surface of the non-shield acting section is 0.3e6 V/m, and the maximum tangential electric field on the insulator surface is 1.6e6 V/m, which decreases slightly compared with that before optimization. As shown in Fig. 16, the maximum ratio of normal electric field to tangential electric field after optimization is 1.1, and the proportion of the length of θ between $-40°$ and $-50°$ in the shield acting section increases from 4.6% before optimization to 38.8%, closer to $\theta = -45°$. The electrical performance of the optimized electron gun has been greatly improved, which indicates the feasibility of the optimization method. After obtaining the preliminary results of optimization, the difficulty of machining is also considered, so the calculated geometric structure is changed, and the optimal solution is obtained under the premise of taking into account the economic and electrical performance (Table 3).

Table 1. Optimization results of insulator geometry structure

Parameter	Calculation results	Unit
d	68	*mm*
D	90	*mm*
h	160	*mm*
α	0.5	1
δ_u	0.068642	*rad*
δ_o	0.068642	*rad*

Table 2. Optimization results of shield geometry structure

Parameter	Calculation results	Unit
α	0.3	1
β	0.3	1
γ	0.62	1
Δ_{gas}	6	*mm*
L	9	*mm*
l	12	*mm*
H	15	*mm*

Table 3. Comparison of electrical performance before and after optimization

Optimizing index	Before optimization	After Optimization	Unit
Maximum electric field strength of shield	2.8e7	1.8e7	V/m
Electric field strength of CTJ	3.0e6	0.7e6	V/m
Maximum electric field intensity on insulator surface	5.5e6	4.1e6	V/m
Minimum tangential electric field intensity on insulator surface	0.49e6	0.3e6	V/m
The *tanθ* value of the acting section of the shield	5.5	1.1	1
The proportion of the length of θ from −40° to −50° in the action section of the shield	4.6%	38.8%	1
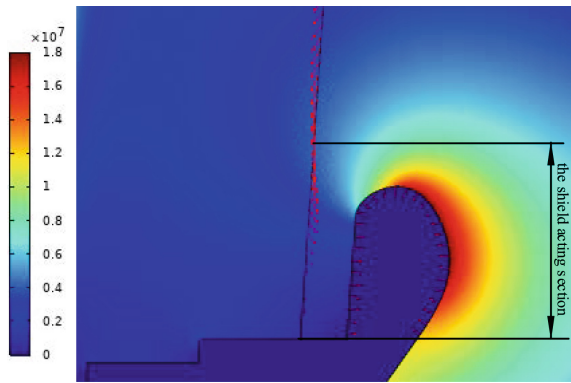
Fig. 14. Electric field distribution diagram of electrostatic field simulation after optimization
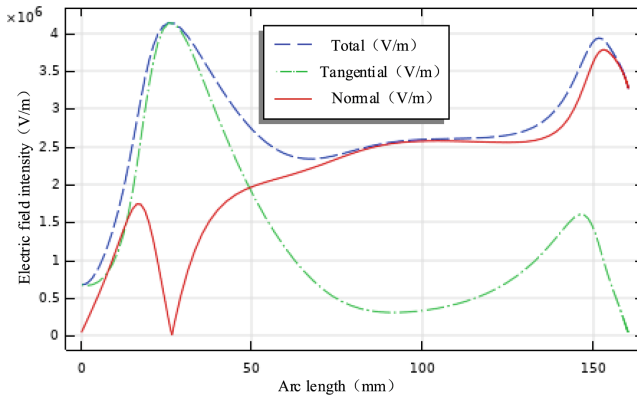
Fig. 15. Electric field distribution curve on insulator surface after optimization
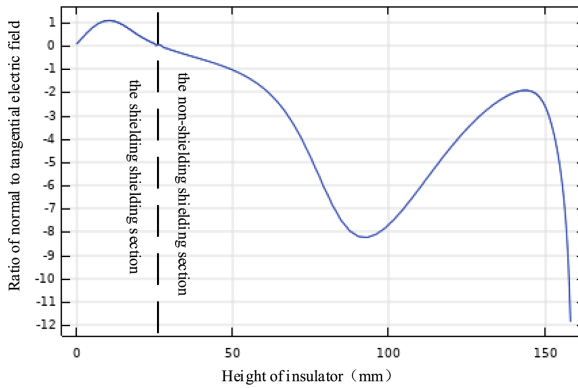
Fig. 16. Ratio of normal electric field to tangential electric field on insulator surface after optimization
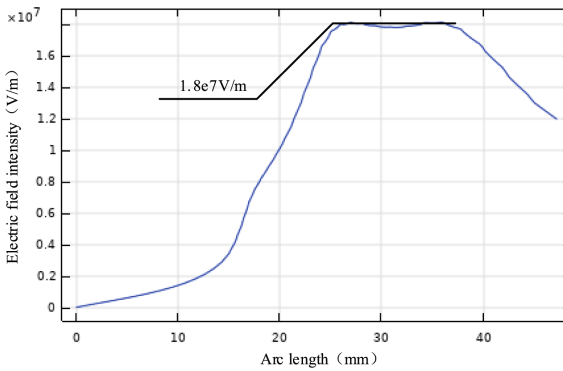
Fig. 17. Electric field curve of shield surface after optimization

5.2   Influence of Different Parameters on the Electrical Properties of Insulators and Shields

As shown in Fig. 18, the ratio of normal electric field to tangential electric field on insulator surface decreases with the increase of parameters Δ_{gas} and l, mainly because the normal electric field between air gaps is reduced. As δ_u increases, the vertical distance between the air gaps decreases so that the ratio of the normal electric field to the tangential electric field increases. The maximum electric field intensity at the shield increases with the increase of Δ_{gas}, which is mainly caused by the shortening of the distance between the outermost edge of the shield and the cavity wall. The maximum electric field intensity of the shield decreases with the increase of δ_u and H, mainly because the contour of the shield is changed, which leads to the decrease of the curvature of the shield surface. Increasing l reduces the distance between the shield and the cavity wall, so the electric field intensity of the shield increases, but increasing l also reduces the curvature of the shield, so the field intensity of the shield decreases. According to the calculation results, increasing l will lead to the decrease of the electric field strength of the shield. For this
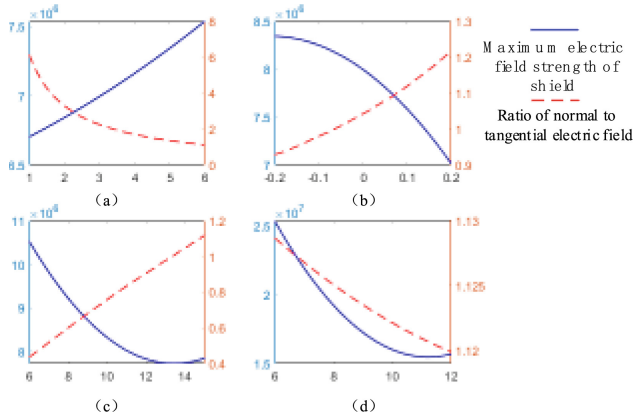
Fig. 18. Effect of parameter variation on electrical properties of insulators and shields (a) Δ_{gas} Impact on Electrical Performance (b) δ_u Impact on Electrical Performance (c) H Impact on Electrical Performance (d) l Impact on Electrical Performance

shield, the change of the curvature of the shield has a greater impact on the electric field strength than the change of the distance.

6   Conclusion

(1) This paper analyzes the electric field distribution of the electron gun with a shield. The optimization problem is divided into $\theta < 0$, which is called shield acting section, and $\theta > 0$, which is called non-shield acting section. Different methods should be used to optimize different insulator parts. The optimization is mainly carried out from the following three parts: 1) *tanθ* value of the insulator surface in the acting section of the shield. 2) Integral value of tangential electric field along the outer contour of insulator. 3) The maximum electric field intensity of the shield. The objective function is obtained and the constraints are determined.

(2) A parametric model is established for the high voltage electron gun under 225 kV DC high voltage environment. Bessel curve and spline curve are used to control the geometry of insulator and shield with the least number of variables on the premise of meeting the parameter requirements. At the same time, Bessel curves and splines make the geometry smooth and continuous. The Nelder-Mead approximate gradient algorithm is used to solve the objective function, which can be calculated without the first order gradient or second order gradient. The algorithm does not require the objective function to be smooth.

(3) In this study, the optimization method mainly considers improving the gas breakdown voltage of insulator-shield and reducing the occurrence of flashover on insulator surface. After optimization, the maximum field strength of the shield is reduced by 37.3%, The field strength at the cathode triple junction point is reduced by 76.7%, The maximum electric field intensity on the insulator surface decreases by 25.5%, The tangential electric field on the insulator surface of the non-shield acting

section decreased slightly, and the maximum ratio of the normal electric field to the tangential electric field in the shield acting section was optimized to 1.1.

References

1. Kato, H., Suzuki, R., Wang, J., Ooi, T., Nakajima, H., et al.: Development of an X-ray tube for irradiation experiments using a field emission electron gun. Nucl. Instrum. Methods Phys. Res. **807**, 41–46 (2016)
2. Węglowski, M.S., Błacha, S., Phillips, A., et al.: Electron beam welding – techniques and trends – review. Vacuum **130**, 72–92 (2016)
3. Townsend, J.S.: The theory of ionization of gases by collision by John S. Townsend (1910)
4. Shen, Q.: High Voltage Technology, 4th edn, pp. 24–27. China Electric Power Press, Beijing (2012)
5. Li, S., Nie, Y., Min, D., Pan, S., et al.: Research progress on vacuum surface flashover of solid dielectric. Trans. Electrotech. Soc. **32**(08), 1–9 (2017)
6. Zhang, Q., Li, C., et al.: Research progress of partial discharge under X-ray excitation. Trans. Electrotech. Soc. **32**(08), 22–32 (2017)
7. Anderson, R.A.: Role of the secondary electron emission avalanche in surface flashover or insulators in vacuum. In: Conference on Electrical Insulation & Dielectric Phenomena - Annual Report, pp. 435–441 (1974)
8. Miller, H.C.: Estimation of flashover voltage along cylindrical insulator in vacuum. IEEE Trans. Electr. Insul. **24**(5), 765–786 (1989)
9. Blaise, G., Gressus, C.L.: Charging and flashover induced by surface polarization relaxation process. J. Appl. Phys. **69**(9), 6334–6339 (1991)
10. Li, C., Ding, L., Lv, J., Liang, Y.: Trap mechanism of alumina ceramic insulator during surface flashover in vacuum. In: Proceedings of the CSEE, no. 09, pp. 1–5 (2007)
11. Gao, W., Sun, G., Yan, P., Shao, T.: Vacuum insulation flashover of electronic trigger polarization relaxation theory. High Voltage Technol. **2004**(08), 3–5+8 (2004)
12. Wang, P., Dong, Q., Wu, G., Liu, J., Li, W.: Practical design of triple junction for a 90 kV electron gun. IEEE Trans. Dielectr. Electr. Insul. **26**(4), 1043–1047 (2019)
13. Forrest, A.R.: Interactive interpolation and approximation by Bezier polynomials. Comput.-Aided Des. **4**(5), 286 (1972). Forrest, A.R.: Comput. J. **15**(1), 71–79
14. Olsson, D.M., Nelson, L.S.: The Nelder-Mead simplex procedure for function minimization. Technometrics **17**(1), 45–51 (1975)
15. Anderson, R.A.: Role of the secondary electron emission avalanche in surface flashover or insulators in vacuum. In: Conference on Electrical Insulation & Dielectric Phenomena Report (2016)
16. Yv, K., Zhang, G., Zhen, N., Zhao, W., Qiu, S.: Simulation study on surface electrification of insulator before flashover in vacuum. Proc. CSEE **29**(04), 104–109 (2009)
17. Xun, T., Yang, H.W., Zhang, J.D.: A high-vacuum high-electric-field pulsed power interface based on a ceramic insulator. IEEE Trans. Plasma Sci. **43**(12), 1 (2015)

Numerical Simulation of Gliding Arc Plasma Motion Characteristics

Mengfei Yang[1], Zongyu Wang[2,3(✉)], Wei Zhang[1], Jifeng Zhang[1,2], Hai Zhang[3], and Yulong Ji[1]

[1] College of Marine Engineering, Dalian Maritime University, Dalian 116206, China
jiyulong@dlmu.edu.cn
[2] Yangtze Delta Region Institute of Tsinghua University Zhejiang, Jiaxing 314006, China
wangzongyu09@163.com
[3] College of Energy and Power Engineering, Tsinghua University, Beijing 100084, China

Abstract. In this paper, a mathematical model of DC gliding arc plasma was established based on magneto-hydrodynamic theory (MHD), and the finite element software COMSOL was used to solve the coupling process of electromagnetic field, temperature field and velocity field. The effects of flow rate, electrode throat and voltage on the gliding arc velocity, temperature and current density distribution were studied. The results show that the gliding arc discharge presents a cyclic process of arc breakdown, elongation, disappearance, and re-breakdown. The flow rate has a significant effect on the arc characteristic distribution, and the gas blowing makes the arc discharge appear "arc shape". When arc breakdown, the arc temperature and current density have the maximum value at the electrode. As the arc gradually stabilizes to form an arc column, the maximum moves to the center of the arc column and gradually decreases along the radial direction. As the flow rate increases, the maximum velocity increases, while the temperature and current density decreases. With the electrode throat gap narrowing, the temperature and current density reach the maximum quickly. It only needs 0.4 ms to reach the maximum when gap is 2 mm. And the smaller the gap, the easier it is for the arc to re-breakdown. The temperature and current density increase with the voltage. This work reveals the motion characteristics of the gliding arc between the electrodes. The influence of characteristic parameters on gliding arc plasma is clarified. It provides a certain basis for optimizing the structure of the gliding arc reactor.

Keywords: Gliding arc discharge · Plasma · MHD · Multiphysics · Movement characteristics

1 Introduction

Plasma, a system composed of a large number of charged and neutral particles, has received much attention in recent years and plays an important role in biomedicine [1], materials processing [2, 3], energy conversion [4, 5], pollutant degradation [6, 7], and environmental protection [8]. At present, the more mature low-temperature plasma jet

and jet array technologies have good treatment effects in the above-mentioned fields. However, they have the disadvantages of small treatment area and uneven treatment area. The gliding arc discharge (GAD), as a way to generate plasma at atmospheric pressure [9], has a simple generation device, long electrode life, and a wide operating range (i.e., pressure range is Torr-atm and above, and the arc current is mA–A). It can generate a wide plasma in open space, thus increasing the plasma treatment area and improving the treatment efficiency. It has been successfully applied to plasma-assisted gas treatment in chemical and environmental protection fields [10, 11].

Many researchers have done a great deal of research on gliding arc plasma because of its broad range of applications and exceptional benefits. In terms of experiment, He et al. [12] investigated the effects of electrode expansion angle and air flow rate on the gliding arc discharge characteristics, and examined the influence of power supply voltage magnitude on the development of the accompanying breakdown gliding discharge mode to the stable gliding discharge mode. Sun et al. [13] explored the effect of air gas flow rate on the percentage of the two modes. Chen et al. [9] studied the effect of different gas composition addition on the nitrogen gliding arc discharge. Sun et al. [14] analyzed the arc motion mode of gliding arc. In terms of numerical simulation, Wang et al. [15] studied the discharge characteristics of the gliding arc. The results show that the arc axis temperature could reach 5700–6700 K. Zhao et al. [16] used magneto-hydrodynamic theory to establish the mathematical model of DC arc plasma and simulated the characteristics of the multi-physics field distribution of the arc plasma. Liu et al. [17] compared the characteristics of AC and DC vacuum arc plasma and found that the AC arc and DC arc plasma parameters distribute similarly under the same current excitation. And the AC arc is easier to be opened and broken because its energy decreases faster. Chen et al. [18] studied the numerical simulation of DC arc plasma torch and found that the highest value of the plasma temperature appeared near the cathode and decreased with the axial distance. The working gas flow rate has little effect on the temperature distribution inside the torch.

At present, most of the numerical simulations are carried out only for the arc plasma torch. It has fewer simulations for the physical characteristics of the two-dimensional gliding arc, transient motion processes, etc. Therefore, in order to better understand the motion characteristics of the gliding arc, this paper constructed a two-dimensional model of the gliding arc discharge plasma by the magneto-hydrodynamic equation. The motion characteristics of the sliding arc between the electrodes was simulated. The influence of the characteristic parameters on the gliding arc plasma was clarified. It provides a certain basis for optimizing the structure of the sliding arc reactor.

2 Arc Modeling and Simulation

2.1 Geometry Model

The simulation geometry model used in this paper is shown in Fig. 1. A knife-shaped copper electrode model is used, setting AF as the cathode, BC as the anode, AB as the fluid inlet and DE as the fluid outlet. The electrode throat is set as 2–6 mm.
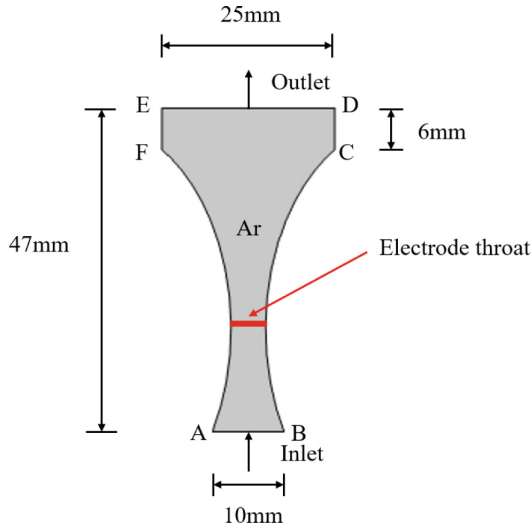
Fig. 1. Gliding arc simulation geometry model

2.2 Model Assumptions

The arc can usually be divided into three parts, namely cathode area, arc column area and anode area [19]. The generation of the arc plasma is an extremely complex process. In order to simplify the computational process and reduce the complexity of the simulation analysis, the following assumptions are made [20–23]:

1) The arc plasma is in local thermodynamic equilibrium state.
2) The gas density, viscosity, specific heat capacity, thermal conductivity, electrical conductivity and other physical parameters are only a function of temperature.
3) The arc plasma is a constant flow and two-dimensional distribution.
4) The plasma arc is in a laminar flow state and incompressible.
5) The influence of the sheath layer in the electrode region is ignored.

2.3 Boundary Conditions

The simulation boundary conditions are set as follows.

1) Fluid heat transfer conditions: The electrode is set as solid. The fluid is set as argon. The inlet and outlet temperatures of the fluid domain are set as 293.15 K. And the rest of the surface is thermally insulated.
2) Pressure boundary conditions: The upper boundary is set as the fluid outlet with a pressure value of 1 atm. The lower boundary is the fluid inlet with different inflow velocities. The electrode boundary is set as a non-slip boundary condition.
3) Voltage boundary conditions: The left electrode boundary is set as cathode. The right electrode boundary is set as anode. A DC voltage is applied to the cathode, and the ballast resistance Rb is set as 1000 Ω. Current conservation is observed in all areas. And the whole outer boundaries are electrically insulated.

2.4 Simulation Scheme

The following simulation calculation scheme was used to examine the impacts of inlet gas flow rate, electrode throat, and excitation voltage on the features of the arc parameters (Table 1).

Table 1. Simulation scheme

number	Inlet gas flow rate (m/s)	Electrode throat (mm)	Excitation voltage (V)
1	3, 5, 7, 9	5	3700
2	5	2, 3, 4, 5, 6	3700
3	5	5	3500, 3600, 3700, 3800, 3900, 4000

3 Results and Discussions

3.1 Simulation Model Validation

Figure 2 shows the shape of the gliding arc discharge and the change of its motion process when the electrode throat is 2 mm and the inlet gas flow rate is 5 m/s. Arc breakdown, elongation, disappearance, and re-breakdown are all observed. Firstly, a short conductive path is formed in the electrode throat, that is, the arc breakdown. And then the arc slides upward along the electrode and arc is gradually elongated. This process is called arc elongation. Finally, the arc breaks and disappears. And a conductive path appears at the electrode throat. This process is essentially identical with the arc discharge shape captured by high-speed photography in the literatures [24, 25], demonstrating the accuracy of the model presented in this research.
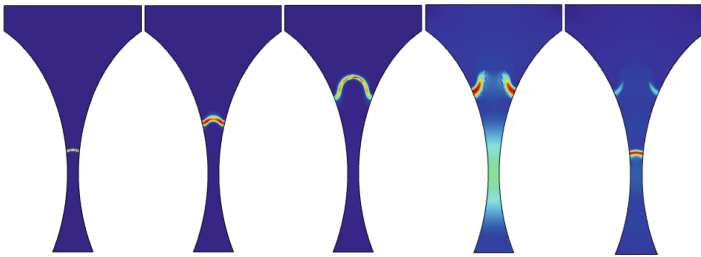
Fig. 2. Gliding arc discharge process

3.2 Velocity Field

Figure 3 shows the maximum inter-electrode velocity versus time curves for different inlet gas rates, different electrode throats and different excitation voltages for the blade type electrodes. The variation of inter-electrode maximum velocity with time for different inlet gas flow rates at 5 mm electrode throat and 3700 V excitation voltage is shown in Fig. 3a. The results show that the larger the inlet flow rate, the bigger the maximum velocity between electrodes. The maximum velocity between electrodes can reach 21 m/s when the inlet flow rate is 9 m/s. When the excitation voltage is 3700 V and the inlet flow rate is 5 m/s, the maximum velocity between electrodes under different electrode throats varies with time as shown in Fig. 3b. The maximum velocity between electrodes increases with the electrode throat spacing. This is because the shortening of the electrode throat increases the degree of gas flow compression, which leads to the increase of velocity. When the spacing is 2 mm, the maximum velocity shows a periodic change, which is mainly due to the arc re-breakdown and it will be analyzed in detail later. When the inlet air flow rate is 5 m/s and the electrode throat is 5 mm, the maximum velocity between electrodes with different excitation voltages varies with time as shown in Fig. 3c, and it is found that the voltage has almost no obvious effect on the maximum velocity, which may be caused by the small excitation voltage range selected. In order to further investigate whether the excitation voltage influences the velocity, this paper also selected a voltage
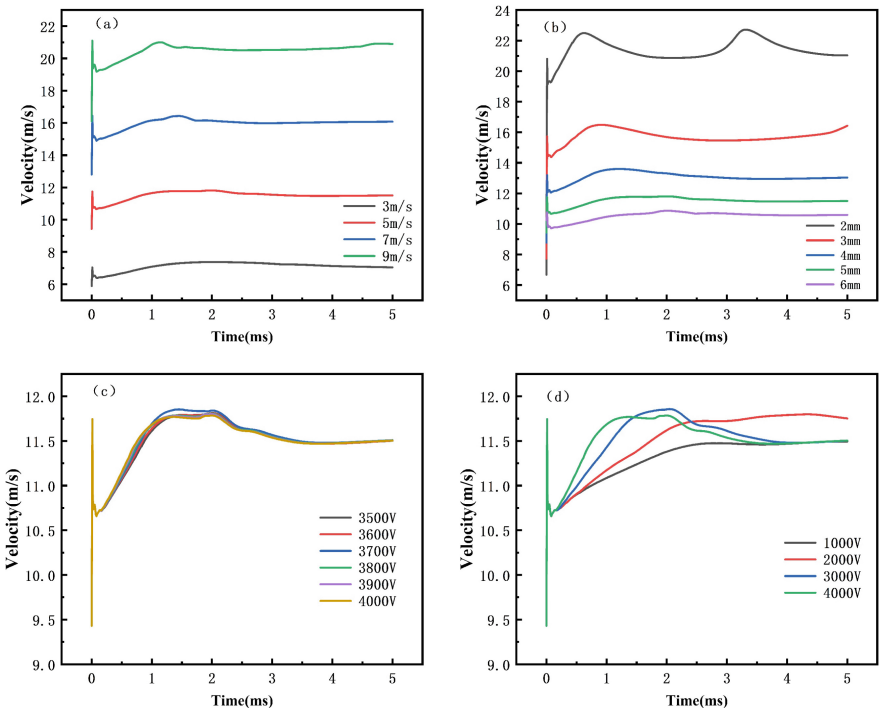
Fig. 3. Plot of the maximum velocity versus time. (a) different inlet gas rates; (b) different electrode throats; (c–d) different voltages

of 1000–4000 V for simulation calculation, as shown in Fig. 3d, the results show that the larger the voltage, the faster the maximum velocity is reached.

In order to observe the maximum velocity change between the electrodes more intuitively, the velocity streamline distribution cloud diagram is given when the inlet flow velocity is 9 m/s, the electrode throat spacing is 5 mm, and the excitation voltage is 3700 V, shown as Fig. 4a. The fluid velocity in the throat presents the maximum, about 21 m/s. With the increase of time, the velocity distribution is similar to the jet. And the velocity gradually decreases along the radial direction at the tail of the flow. The flow process of fluid between electrodes can be regarded as in the Laval nozzle. Due to fluid inertia, the fluid mass does not immediately adhere to the wall, but leaves the wall at the sudden expansion of the pipe. Therefore, a vortex flow appears [26]. Figure 4b shows the isobaric distribution cloud. It shows that there is a pressure difference at the throat. And under the action of the pressure difference, the fluid accelerates along the direction of the pressure gradient. So the velocity is maximum at the throat.
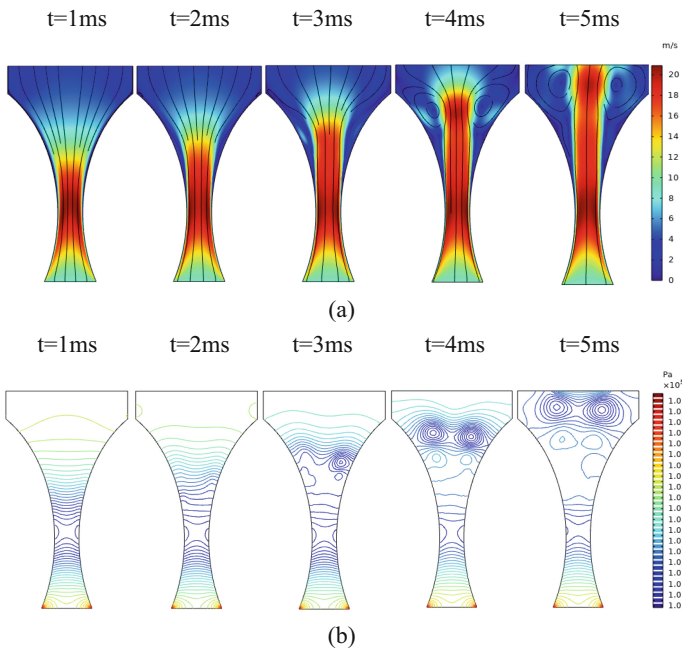
Fig. 4. (a) Velocity flow line distribution cloud (b) Isobaric distribution cloud

3.3 Temperature Field

The arc temperature generally in the range of 3000–20000 K [16, 18, 27–29], is one of the important parameters of the arc. The maximum arc temperature calculated by the model in this paper is about 7500 K, which verifies the correctness of the model. Figure 5 depicts the graphs of the maximum temperature between the blade electrodes with time

for different inlet flow rates, different electrode throats, and different excitation voltages. It can be seen that the arc temperature basically reaches the maximum value within 1 ms and then is keeps in a relatively stable state. This is because after the voltage is applied to the electrodes, the argon between the electrodes is ionized by strongly heated. And under the action of electric field, the cation moves toward the cathode, and the anion and free electron move toward the anode. A large number of strong particle collisions occur, resulting in a high temperature arc between the electrodes. Subsequently, the arc is in a stable burning state under the maintenance of voltage.
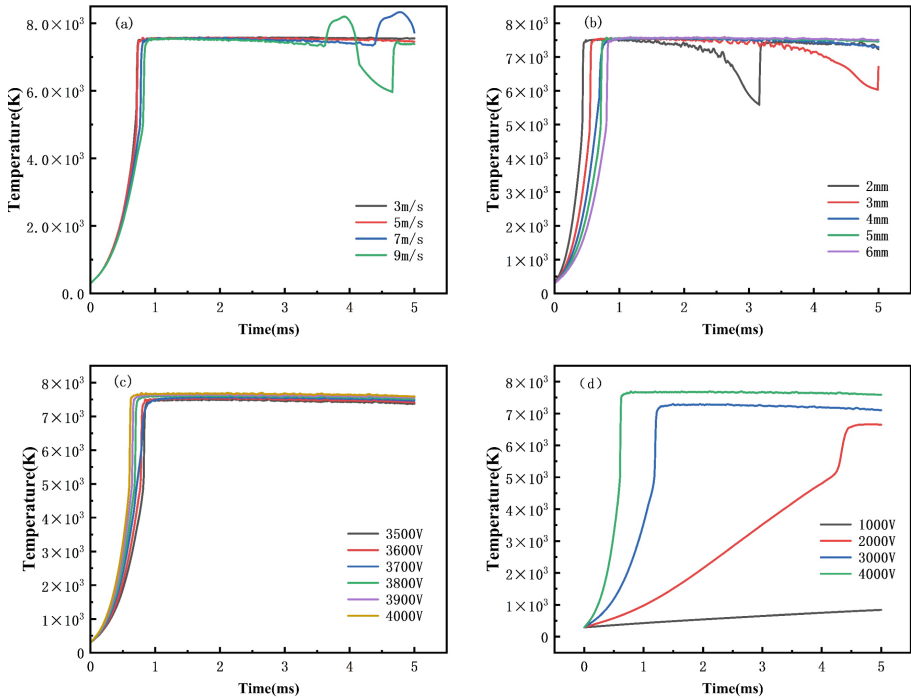
Fig. 5. Plot of maximum temperature versus time (a) different inlet flow rates (b) different electrode throats (c–d) different voltages

When the electrode throat is 5 mm and excitation voltage is 3700 V, different inlet gas flow rate between the electrode maximum temperature change with time is shown in Fig. 5a. When the inlet gas flow rate is 9 m/s, the arc temperature will appear large fluctuation, in 3.7 ms–4.7 ms.It is caused by the arc re-breakdown. When the flow rate is 7 m/s, it also begins to appear this phenomenon at 4.5 ms. And the larger the inlet gas flow rate, the shorter the arc re-breakdown time. When the excitation voltage is 3700 V and inlet gas flow rate is 5 m/s, different electrode throat between the electrode maximum temperature change with time is shown in Fig. 5b. When the electrode throat is 2 mm, the temperature will appear to fall and then rise at 2.5 ms. It is caused by the arc re-breakdown. When the electrode throat is 3 mm, it will also appear this phenomenon at 4 ms.It indicates that the smaller the electrode throat, the earlier the arc re-breakdown

occurs. When the electrode throat is 5 mm and inlet gas flow rate is 5 m/s, different excitation voltage between the electrode maximum temperature variation with time is shown in Fig. 5c. The arc temperature is basically not affected by voltage in the range of 3500–4000 V. In order to show the relationship between voltage and arc temperature more clearly, arc temperature changes with the voltage of 1000–4000 V is shown in Fig. 5d. When the voltage is 1000 V, the gas is not breakdown. The temperature of the electrode boundary is also small, indicating that no arc generation at small voltage. When the voltage reaches a certain value, an arc will be generated. And the higher the voltage, the faster the arc temperature reaches a stable value. However, when the voltage exceeds 3500 V, the arc temperature is little affected by the voltage.

The arc re-breakdown phenomenon is shown in Fig. 6. Figure 6a shows the arc temperature distribution cloud when the electrode throat is 5 mm, the excitation voltage is 3700 V, and the inlet gas flow rate is 9 m/s. The temperature of arc plasma presents "arc" distribution. The arc plasma maximum temperature is at the cathode during the arc breakdown stage. And as the arc gradually stabilizes to form an arc column, the maximum value moves to the center of the arc column, and the temperature gradually decreases along the radial direction. A new arc can be seen at 4.7 ms. This is because the fluid has the effect of blowing arc. On the one hand, it can accelerate the heat diffusion and reduce the arc temperature. The original arc temperature drops rapidly before the generation of the new arc channel. On the other hand, it can accelerate the arc elongation process. The arc voltage rapidly increases, causing the arc to re-breakdown. Therefore, in order to obtain a stable arc plasma, the inlet gas flow rate should not be too large, and the electrode throat should not be too small. When the electrode throat is 2 mm, the excitation voltage is 3700 V and the inlet gas flow rate is 5 m/s, arc temperature distribution cloud is shown as Fig. 6b. It can be seen that in the process of arc elongated, the arc burns steadily and the arc column temperature remains basically unchanged. While at the periphery of the arc, the temperature decreases along the radial direction according to a certain gradient under the effect of heat transfer.
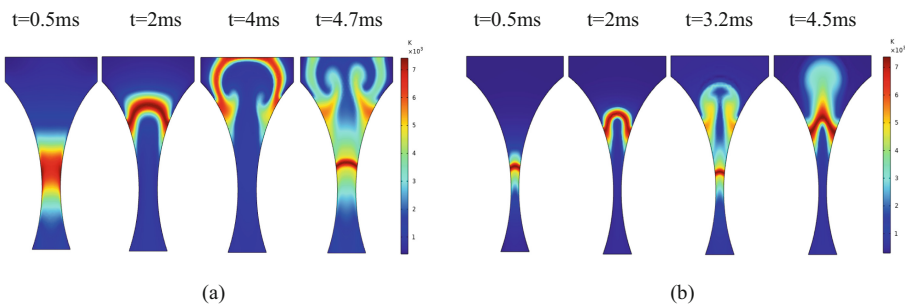
Fig. 6. arc temperature distribution cloud (a) u = 9m/s, U = 3700V, d = 5 mm (b) d = 2 mm, U = 3700V, u = 5 m/s

In addition, this paper investigates the difference of arc starting time under different conditions, seeing Fig. 7. When the excitation voltage is 3700 V and inlet gas flow rate is 5 m/s, different electrode throat corresponding to the arc starting time is shown in Fig. 7a.

The results show that the arc starting time is proportional to the electrode throat spacing when both the excitation voltage and the inlet gas flow rate are fixed. Figure 7b shows the arc starting time corresponding to different excitation voltages when the electrode throat spacing is 5 mm and the inlet gas flow rate is 5 m/s. The results show that the arc starting time is inversely proportional to the excitation voltage when both the electrode throat spacing and the inlet gas flow rate are fixed. From the principle of arc generation, a large number of electrons will be gathered on the cathode plate after applying a certain voltage. Then the electrons fly to the anode at high speed under the action of electric field and strike the argon atoms, thus producing ions and free electrons. Among them, the cations move towards the cathode, and the anions and free electrons move towards the anode. And an arc starts to be generated between the electrodes under the effect of strong collision. Therefore, when the excitation voltage is certain, the shorter the electrode throat, the faster the ions and electrons collide with the cathode, the earlier the arc appears. When the electrode throat is fixed, the higher the voltage, the more electrons the cathode emits under the action of the electric field, the faster the electrons move to the anode direction, thus accelerating the formation of the arc.
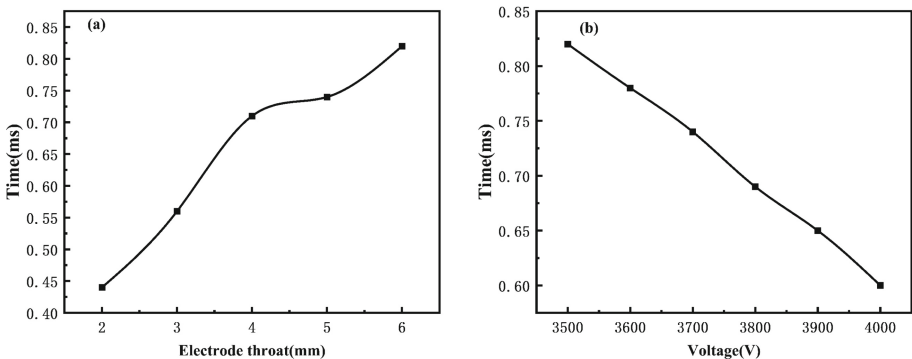
Fig. 7. Arc starting time under different conditions (a) different electrode throats; (b) different excitation voltages

3.4 Electric Field

From $J = \sigma E$, it is known that the current density is approximately proportional to the electric field. And the current density provides energy for the formation of the arc. and it has a large effect on the distribution of arc characteristics [16]. Figure 8 shows the maximum current density between the blade electrodes with time for different inlet gas flow rates, different electrode throats, and different excitation voltages. It can be seen that under different conditions, the current density sharply increases first and then decrease, stabilized at last. The trend can be explained by the arc voltage-current graph. Figure 9 is the arc voltage-current diagram when the inlet gas flow rate is 5 m/s, the electrode throat is 5 mm and the electrode voltage is 3700 V. The arc voltage decreases rapidly at 0.73 ms, the current rises rapidly. The gas is broken down to form an arc. Due to current

density refers to the current per unit area, the arc current density increases rapidly with current. After 0.73 ms, the current density starts to decrease because of the arc current starts to reduce. The arc voltage-current diagram obtained in this paper is consistent with the literature [30], which again verifies the correctness of the model.
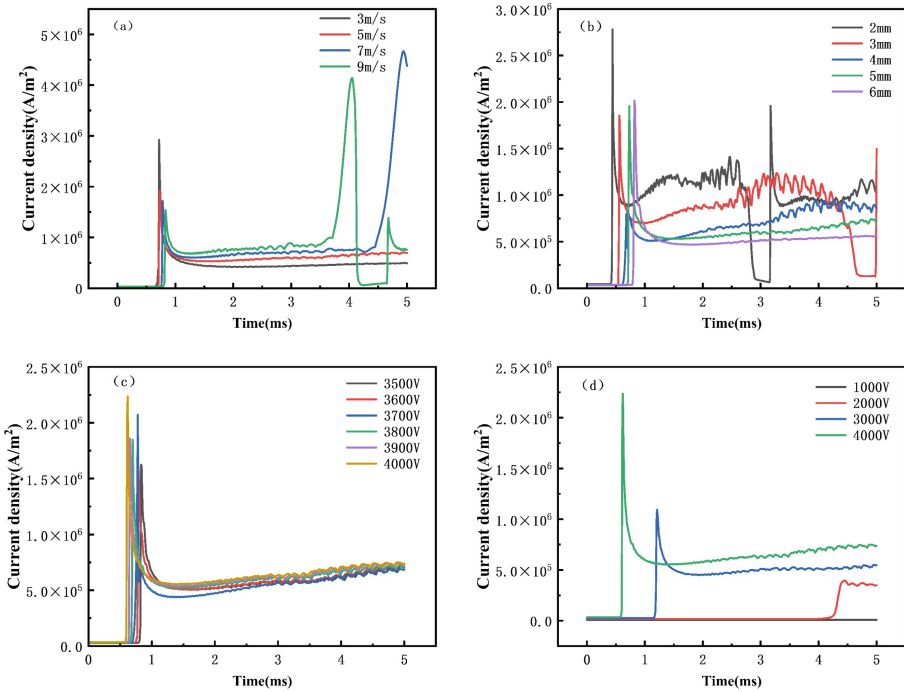
Fig. 8. Plot of maximum current density versus time (a) different inlet gas flow rates (b) different electrode throats (c-d) different voltages
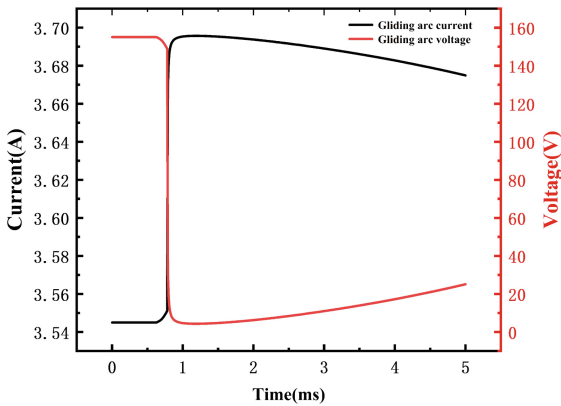
Fig. 9. arc voltage - current diagram, U = 3700 V, d = 5 mm, u = 5 m/s

When the electrode throat is 5 mm and excitation voltage is 3700 V, different inlet flow rate between the electrode maximum current density with time is shown in Fig. 8a. After the current density tends to stabilize, the greater the inlet flow rate, the bigger the current density. The current density of 9 m/s and 7 m/s appears peak at 3.8 ms and 4.8 ms, respectively. This is due to the limitations of the model space structure. Before the arc being blown off, the top of the arc will gather at the exit cross-section. At this time the charge accumulates rapidly. The current density rises rapidly and appears peak. Thereafter, the arc disappearance and re-breakdown at about 4.7 ms. The current density distribution is consistent with the distribution of the first arc start. And this phenomenon also occurs at 7 m/s. When the excitation voltage is 3700 V and inlet gas flow rate is 5 m/s, different electrode throat under the electrode maximum current density changes with time is shown in Fig. 8b. When the electrode throat is 2 mm, the current density trend is the same as the first arc. So as the electrode throat is 3 mm. This is because the arc re-breakdown occurs during this time. When the electrode throat is 5 mm and the inlet gas flow rate is 5 m/s, different excitation voltage between the electrode maximum current density with time is shown in Fig. 8c. The voltage and current density have no obvious relationship. In order to show the relationship between the two more clearly, the voltage range was expanded to 1000–4000 V shown in Fig. 8d. The results shows that the higher the excitation voltage, the higher the current density. The current density is 0 A/m^2 at the excitation voltage of 1000 V. And the gas is not penetrated. There is no conductive path formed in the throat. That is, no arc generation.

In addition, this paper also compares the arc cycle under different inlet gas flow rate and electrode throat spacing at 3700 V, shown as Fig. 10. When the electrode throat spacing is 2 mm and inlet gas flow rate is 5 m/s, the arc cycle is about 2.8 ms. As the inlet gas flow rate increases to 7 m/s, the cycle is correspondingly shortened to about 1.6 ms. Under the condition of fixed voltage and electrode throat spacing, the larger the inlet gas flow rate, the shorter the arc cycle. When the inlet gas flow rate is 7 m/s, the arc cycles of 2 mm and 5 mm electrode throat spacing are 1.6 ms and 5 ms respectively, which shows that the arc cycle shortens as the electrode throat spacing decreases. Therefore, in order to get a stable combustion of the gliding arc, the inlet gas flow rate should not be too large, and the electrode throat spacing should not be too small.
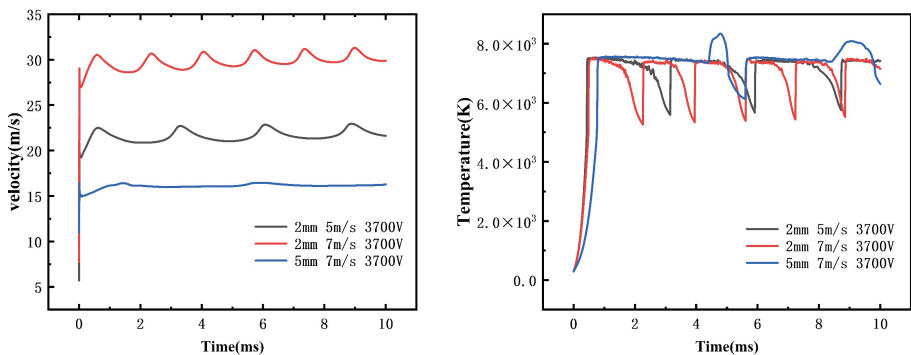
Fig. 10. Different conditions of the arc velocity, temperature and time variation graph

4 Conclusion

In this paper, the argon arc discharge is simulated based on a simplified geometric model with a magneto-hydrodynamic theory, coupled with the electric field equations and considering the gas heat transfer conditions. The conclusions are as follows:

1) The gliding arc discharge presents a cyclic process of arc breakdown, elongation, disappearance and re-breakdown. The arc cycle is correspondingly shortened as the inlet gas flow rate increases and the electrode throat spacing decreases.
2) The inlet air velocity has obvious influence on the arc characteristic distribution. The air velocity drives the arc to glide upward along the electrode, which makes the arc plasma temperature and current density show "arc shape" distribution. The arc plasma temperature and current density are maximum at the cathode during the arc breakdown stage. And as the arc gradually stabilizes to form an arc column, the maximum value moves to the center of the arc column. The temperature and current density gradually decrease along the radial direction.
3) As the flow rate increases, the maximum velocity increases, the temperature and current density decreases. With the narrowing of the electrode throat gap, the temperature and current density reaches the maximum faster. And the smaller the gap, the easier the arc to re-breakdown. The temperature and current density gradually increase with voltage. When the voltage is higher than 3000 V, the change is not obvious.
4) In order to get a stable burning arc, the inlet gas flow rate should not be too large, the electrode throat spacing should not be too small.

References

1. Lu, X.: Plasma jets and their medical applications. High Voltage Technol **37**(06), 1416–1425 (2011)
2. Ma, Y., Zhang, C., Kong, F., et al.: Effect of plasma jet array-assisted thin film deposition on the electrical properties of epoxy resin surface. High Voltage Technol. **44**(09), 3089–3096 (2018)
3. Zhang, R., Xia, Y., Zhou, X., et al.: Effect of He plasma jet treatment on improving the water repellent migration of heavily fouled stained silicone rubber. High Voltage Technol. **43**(12), 3988–3993 (2017)
4. Mei, D.H., Fang, C., Shao, T.: Current status of research on the characteristics and applications of low-temperature plasma at atmospheric pressure. Chinese J. Electric. Eng. **40**(04), 1339–58+425 (2020)
5. Zhang, H., Zhu, F.S., Li, X.D., et al.: Analysis of key technologies for methane reforming by gliding arc discharge plasma. High Voltage Technol. **41**(09), 2930–2942 (2015)
6. Lu, N., Zhang, C.K., Xia, Y., et al.: Research progress of plasma conversion of CO_2. High Voltage Technol. **46**(01), 351–361 (2020)
7. Yao, S.L., Zhang, X.M., Lu, H.: Key technology of low temperature plasma purification of VOCs. High Voltage Technol. **46**(01), 342–350 (2020)
8. Zhang, J.: Research progress of plasma application in the field of energy and environment Safety. Health Environ **21**(10), 1–7 (2021)

9. Chen, J., Shi, Y., Mei, D., et al.: Influence of different gas composition additions on the mode and characteristics of nitrogen gliding arc discharge. High Voltage Technol. 1–10

10. Czernichowski Pure, A.J., Chemistry, A.: Gliding arc: applications to engineering and environment control **66**(6), 1301–1310 (1994)

11. Fridman, A.J.P.C.: Plasma Chemistry (2008)

12. He, L.M., Chen, I., Liu, X.J., et al.: Discharge characteristics of an AC gliding arc at high pressure. High Voltage Technol. **42**(06), 1921–1928 (2016)

13. Lu, N., Sun, D., Wang, B., et al.: Discharge characteristics of AC rotating gliding arc. High Voltage Technol. **44**(06), 1930–1937 (2018)

14. Mei, D., Zeng, Y., Tu, X.: Spectral diagnosis of atmospheric pressure argon gliding arc (in English). High Voltage Technol. **39**(09), 2180–2186 (2013)

15. Wang, Y., Li, X., Yu, Q., et al.: Numerical simulation study of gliding arc low-temperature plasma discharge characteristics. Phys. Lett. **60**(03), 404–410 (2011)

16. Zhao, M., Wang, Y., Yang, S., et al.: Characteristics of multiphysics field distribution in arc plasma. J. Mech. Eng. **58**(08), 153–159 (2022)

17. Liu, X., Liu, C.Y., Zou, J.Y.: Comparative analysis of AC and DC vacuum arc plasma characteristics. J. Vacuum Sci. Technol. **35**(10), 1203–1208 (2015)

18. Chen, W., Chen, L., Liu, C., et al.: Numerical simulation study of DC arc plasma torch Vacuum **56**(01), 56–58 (2019)

19. Bao, J., Yang, Z., Liu, T., et al.: Numerical simulation study of the temperature field of vacuum free-burning helium arc **43**(4), 4 (2006)

20. Hui, L.S., Trelles, J.P., Murphy, A.B., et al.: Numerical simulation of the flow characteristics inside a novel plasma spray torch (2019)

21. Trelles, J.P., Pfender, E., Heberlein, J.J.P.C., et al.: Multiscale Finite Element Modeling of Arc Dynamics in a DC Plasma Torch **26**(6), 557–575 (2006)

22. Jian, X.,Wu, C.S.: Numerical analysis of the coupled arc-weld pool-keyhole behaviors in stationary plasma arc welding - ScienceDirect **84**, 839–847 (2015)

23. Chen, H.: Research on plasma flow characteristics of arc heating. Nanjing University of Technology (2014)

24. Tu, X., Gallon, H.J., Whitehead, J.C.: Dynamic Behavior of an Atmospheric Argon Gliding Arc Plasma. **39**(11), 2900–2901 (2011)

25. Zhang, R., Luo, G., Huang, H., et al.: The law of influence of electrode structure on the size of gliding arc discharge plasma **45**(10), 8 (2019)

26. Feng, L.-W.: Simulation of flow in expansion tubes and its local loss control. Technol. Market **26**(11), 57–58 (2019)

27. Guo, J., Liu, J., Yan, X., et al.: Two-dimensional numerical simulation of plasma discharge characteristics of DC arc plasma jet method based on FLUENT software. J. Vacuum Sci. Technol. **36**(03), 312–318 (2016)

28. Liu, Y., Wu, G., Guo, Y., et al.: Analysis of DC arc motion characteristics of the inviting arc angle electrode. J. Southwest Jiaotong Univ. 1–8

29. Zhong, Y.M.: MHD model simulation of small-current DC air arc and its experimental study. Chongqing University (2020)

30. Cheng, W.: Study of high voltage DC air discharge model. Nanjing University of Aeronautics and Astronautics (2018)

On the Distribution of N_2^+ and N_2 Bands in Ionization Region of Positive DC Corona Discharge

Wanxia Zhang[1], Lingzhi Xia[2], Hao Sun[3], Yang Cheng[2], Yushun Liu[2], Hengxin He[1(✉)], and Shen Chen[1]

[1] State Key Laboratory of Advanced Electromagnetic Engineering and Technology, Huazhong University of Science and Technology, Wuhan 430074, China
`hengxin_he@hust.edu.cn`

[2] State Grid Anhui Electric Power Company, Electric Power Research Institute Anhui Province, Hefei 230022, China

[3] Institute of Electrical Engineering of the Chinese Academy of Sciences, International S&T Cooperation Base for Plasma Science and Energy Conversion, Beijing 100190, China

Abstract. The value of electric field in the ionization region of positive DC corona discharge is a key parameter that affects the accurate calculation of ground electric field of UHVDC transmission line. In order to research on the measurement of the electric field in positive DC corona ionization zone, we established an experimental observation system of emission spectrum of positive corona discharge in the rod to plate air gap under atmospheric pressure. The gas temperature and the spatial distribution of excited particles of N_2^+(FNS,0–0), N_2(SPS,0–0) and N_2(SPS,2–5) in the ionization zone under different DC voltages were obtained, where the electrode radius is 3 mm. From the measurement results, it is noted that with voltage increase the corona ionization layer thickness tends to be constant and the spectral line ratio of N_2^+ and N_2 decreases. To obtain quantitative relationship between the electric field and the spectrum line ratio, a fluid model with 29 species and 135 chemical reactions was established. Through simulation, we discussed the influence of the chemical reaction rate related to the number density of excited state particles in the ionization zone on the ratio of spectral lines. Based on the inversion of the experimental spectral ratio, the distribution of the electric field in the ionization zone of positive glow corona discharge was further obtained. The above work provides a theoretically feasible solution for measuring the electric field of UHVDC transmission lines in the future.

Keywords: Glow Corona Discharge · Electric Field · Optical Emission Spectroscopy · Nitrogen Spectral Bands · Numerical Model

1 Introduction

1.1 A Subsection Sample

With the outstanding advantages of large transmission capacity, long transmission distance and low transmission loss, the UHV DC transmission technology plays an important role in the development of renewable energy bases in northwest and southwest China

and the external transmission of electric energy [1]. The corona discharge of UHV DC lines can generate ion flow and cause hazards such as rising ground electric field, radio interference and audible noise [2, 3]. The corona discharge characteristics and electromagnetic environmental effects are the key issues in the design and operation of UHV DC transmission projects. Especially, the control of total electric field at sensitive points in the environment has become an important factor to determine the structure of DC transmission lines and affect the project cost. At present, in order to predict the total electric field distribution on the ground accurately, the Kaptzov assumption is generally used as the boundary condition for calculation in engineering. By assuming that the electric field on the surface is maintained at the critical corona onset electric field, the current continuity equation is solved to determine the positive ion density on the conductor[2, 3]. It has been found that the value of the electric field on surface of the conductor is a dominated parameter affects the accuracy of the calculation of the total electric field on the ground and ion flow distribution [3–5].

In order to obtain the corona onset electric field of the conductor, the corona cages and test line sections are usually used to measure the corona onset voltage, so as to invert and calculate the corona critical electric field. However, the roughness of the surface of the conductors is difficult to simulate accurately, which directly affects the accuracy of the calculation. Therefore, it is of great significance to carry out direct measurement of the DC corona onset electric field to improve the accurate calculation of the total electric field on the ground.

The DC electric field measurement methods include rotating-vane electric field meter, electro-optic sensor based on Pockels effect, electric field induced second harmonic generation (EFISH) and bispectral ratio of optical emission spectrum. Due to the geometric dimensions electro-optic sensor and Pockels cannot meet the requirements of electric field measurement in the corona ionization region. EFISH has the advantages of high spatial resolution and non-intervention, but the measurement system composition is complex and the equipment cost is expensive. The emission spectral ratio method uses the ratio of the spectral band intensities of the second positive and the first negative spectral systems of molecular nitrogen is a well recognized method for indirectly estimate the reduced electric field (E/N) [6–10]. This method not only has the advantage of non-interventional measurements, but also can achieve spatial and temporal resolution of the electric field, therefore it is widely used in plasma diagnostics and electric field estimation of the transient luminous events [11–13].

Paris et al. 2005, obtained a quantitative relationship between the spectral intensity ratio and the average reduced electric field based on the emission spectral ratio method, used the integrated intensities of the 337.1 nm and 394.3 nm spectral bands intensities in the second positive band system of molecular nitrogen and the 391.4 nm spectral band in the first negative band system of nitrogen ions [14]. In 2016, Hoder et al. analyzed the electric field and electron multiplication phenomena of a DC negative corona discharge near the cathode using the emission spectral ratio method [15]. Combined with the research results of Paris, the reduced electric field measured by the emission spectral ratio method has a high accuracy in the range of 200–1000 Td. Subsequently, scholars also carried out a lot of research work using the emission spectroscopy ratio method. In [16] they investigated an experimental study on the average reduced electric field of

negative DC corona discharge in the needle-plate air gaps and analyzed the distortion of the electric field caused by the spatial behavior of positive ions. However, the maintained electrical field of the positive DC corona ionization region at atmospheric pressure may be lower than 150 Td (36.75 kV/cm at standard atmosphere). At present, there are fewer studies on the distribution characteristics of the emission spectra of the positive DC corona ionization region at low reduced field and the quantitative relationship between the spectral characteristics with the electric field.

To solve these problems, an experimental observation system of the emission spectrum of positive glow corona discharge under atmospheric pressure conditions is established. From the observation under different voltages, the emission spectra characteristics of N_2 and N_2^+ and the gas temperature in ionization zone under different voltages are obtained. The spatial distribution of the first negative band system N_2^+(FNS, 0–0) of nitrogen molecular ions and the second positive band system N_2 (SPS, 0–0) and N_2 (SPS, 2–5) of molecular nitrogen in the ionization region are also acquired. At the same time, a zero-dimensional hydrodynamic model is established to simulate the variation of excited state particles in the ionization zone of positive glow corona discharge in dry air at atmospheric pressure, and to study the relationship between the density of excited states and electric field. Finally, combined with simulation, the spatial distribution characteristics of the electric field in the ionization zone under the low reduced electric field conditions are discussed. The above work will provide theoretical support for the measurement of the electric field in the ionization zone of positive corona discharge based on the emission spectrum ratio.

2 Method

2.1 Experiment Setup

The experimental measurement system is shown in Fig. 1. The system includes an air spaced ultraviolet achromatic focusing lens, two-dimensional electric moving stage, a spectral acquisition system consists of an ICCD camera and Andor spectrometer, the high-potential current measurement device, high voltage probe and an oscilloscope, and other signal acquisition and reception devices.

A high voltage DC source generates the constant voltage through a protective resistor and is applied to the rod-plate electrode with a 2 cm air gap distance. The entire discharge gap is placed in a sealed pot and filled with the dry air. The sealed pot is placed on a displacement that can adjust both horizontally and vertically to achieve two-dimensional movement. The real-time measurement of the discharge current is carried out by the transient current measurement module with a bandwidth of 200 MHz and a sampling rate of 500 Ms/s. The light source radiated from the discharge region in the experiment is imaged by the focusing lens onto the entrance slit of the spectrometer, and is divided by a diffraction grating and then converged to the exit slit through the focusing mirror to enter the ICCD sensing imaging. The experimental spectrometer grating is 2400 I/mm, spectral resolution is 0.03 nm, the slit width is 250 μm and ambient temperature is 26.75 ± 2°C.
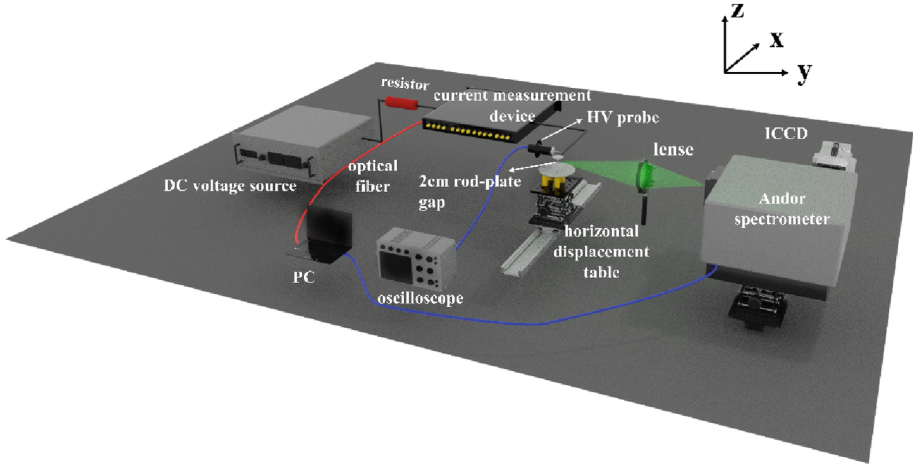
Fig. 1. Schematic diagram of experimental layout.

2.2 0-dimensional Hydrodynamic Model in the Ionization Region

To further understand the intrinsic connection between electric field and optical emission of positive glow corona, a zero-dimensional hydrodynamic model is established, where a comprehensive kinetic scheme in the N$_2$/O$_2$ mixtures consisting of 29 chemical species and 135 chemical reactions is proposed. The number density of excited states of N$_2$$^+$(B$^2\sum_u^+$,v = 0) and N$_2$(C$^3\prod_u$,v = 0) is acquired through simulation, hereinafter referred to as N$_2$$^+$ (B) and N$_2$ (C). The luminescence mechanism of the emission spectrum is that, under the excitation of electric field, the excited particles jump up from the energy level q to a higher energy level p by electron impact excitation and decay into level k by spontaneous emission. The intensity of emission is correlated with the particle density in the excited state p, so that the characteristic wavelength of 391 nm is related to the number density of N$_2$$^+$(B) and the 337nm is related to number density of N$_2$ (C). Therefore, the reaction system includes the mechanism of generation and the loss of electrons.The generation of electrons includes ionization, detachment, associative ionization and the loss of electrons includes attachment, electron-ion recombination and generation and quenching mechanism of excited state particles.

The detail of the mechanism of generation and loss of electrons is interpretated in [17], and the typical species considered in the numerical model are shown in Table 1. The simplified symbols N$_2$(A), N$_2$(a$^'$), O$_2$(a), N$_2$(C), N$_2$(B), O$_2$(b), N$_2$$^+$(B), N$_2$(X^1), N$_2$$^+$(X^2) represent the excited state N$_2$(A$^3\sum_u^+$), N$_2$(a$^{'1}\sum_u^-$), O$_2$(a$^1\Delta_g$), N$_2$(C$^3\prod_u$), N$_2$(B$^3\prod_g$), O$_2$(b$^1\sum_g^+$), N$_2$$^+$(B$^2\sum_u^+$), N$_2$(X$^1\sum_g^+$) and N$_2$$^+$(X$^2\sum_g^+$).

The chemical reactions about excited species N$_2$$^+$ (B) and N$_2$ (C) are shown in Table 1. For the simplified reactions of typical excited state species that are related to the emission line ratio and reflect the electric field are proposed in [8]. The deviation of the reduced electric field R(E/N) estimated by the excited state particle number density from simplified reactions system is less than 1% compared with the complete 617 reactions system in the established N$_2$/O$_2$ mixture.

Table. 1. The most important process for the excited state species.

i	Reaction	Rate, k_i
1	$e + N_2(X^1) \rightarrow N_2 + e + e$	$f(E/N)$
2	$N_2{}^+(B^2) \rightarrow N_2(X^2) + hv$	$(1.11\text{–}2.43) \times 10^7 (s^{-1})$
3	$N_2{}^+(B^2) + N_2(X^1) \rightarrow N_2{}^+(X^2) + N_2(X^1)$	$9.8 \times 10^{-10} (cm^3 s^{-1})$
4	$e + N_2(X^1) \rightarrow N_2(C^3) + e$	$k_i F(T_v, E/N)$
5	$N_2(C^3) \rightarrow N_2(B^3) + hv$	$(1.78\text{–}3.57) \times 10^7 (s^{-1})$
6	$N_2(C^3) + N_2(X^1) \rightarrow N_2(a^{'}) + N_2(X^1)$	$1.0 \times 10^{-11} (cm^3 s^{-1})$
7	$e + N_2(X^1) \rightarrow N_2{}^+(X^2) + e + e$	$k_i F(T_v, E/N)$
8	$N_2{}^+(B^2) + O_2 \rightarrow N_2{}^+(X^2) + O + O(^1S)$	$1.0 \times 10^{-9} (cm^3 s^{-1})$
9	$N_2(C^3) + O_2 \rightarrow N_2(X^1) + O + O(^1S)$	$2.9 \times 10^{-10} (cm^3 s^{-1})$
10	$N_2{}^+(B^2) + N_2(X^1) + N_2 \rightarrow N_4{}^+ + N_2$	$6.2 \times 10^{-29} (300/T_{eff}N_2)^{1.7}$
11	$N_2{}^+(B^2) + O_2 \rightarrow O_2{}^+ + N_2$	$6.0 \times 10^{-11} (300/T_{eff}N_2)^{0.5}$
12	$e + N_2{}^+(X^2) \rightarrow e + N_2{}^+(B^2)$	$f(E/N)$
13	$N_4{}^+ + e \rightarrow N_2 + N_2(C^3)$	$2 \times 10^{-6} (300/T_e)^{0.5}$
14	$N_2(A) + N_2(A) \rightarrow N_2(C^3) + N_2$	$1.6 \times 10^{-10} (cm^3 s^{-1})$
15	$N_2(C^3) + O_2 \rightarrow N_2 + O + O(^1D)$	$2.5 \times 10^{-10} (cm^3 s^{-1})$
16	$N_2(C^3) + N_2 \rightarrow N_2(B) + N_2$	$1.0 \times 10^{-11} (cm^3 s^{-1})$

The transport of the electrons, positive and negative ions in ionization region is given by:

$$\frac{\partial n_n}{\partial t} = (v_{att2} + v_{att3})n_e - \beta_{ep} n_n n_p \tag{1}$$

$$\frac{\partial n_p}{\partial t} = v_i n_e - \beta_{ep} n_e n_p - \beta_{np} n_n n_p \tag{2}$$

$$\frac{\partial n_e}{\partial t} = (v_i - v_{att2} - v_{att3})n_e + v_{det} n_n - \beta_{ep} n_e n_p \tag{3}$$

Within this reaction system, the 29 ordinary differential equations are formed, taking $N_2{}^+(B)$ and N_2 (C) as examples:

$$\frac{\partial n(N_2^+(B^2))}{\partial t} = n_e\left(k_1 n(N_2) + k_{12} n(N_2^+)\right) - k_2 n(N_2^+(B^2))$$
$$- n(N_2^+(B^2))n(N_2)(k_3 + k_{10}n(N_2)) - n(N_2^+(B^2))n(O_2)(k_8 + k_{11}) \tag{4}$$

$$\frac{\partial n(N_2(C^3))}{\partial t} = \left(n(N_2)k_4 + n(N_4^+)k_{13}\right)n_e + k_{14}n(N_2(A))n(N_2(A))$$
$$- k_5 n(N_2(C^3)) - n(N_2(C^3))n(N_2)(k_6 + k_{16}) - n(N_2(C^3))n(O_2)(k_9 + k_{15}) \tag{5}$$

where n(i) denotes species i number density, k(j) is the rate coefficient for process j as listed in Table 2.

The band emission intensity and the number density of upper excited state p is given as:

$$I = n(p)A_P \frac{hc}{4\pi\lambda_0} \qquad (6)$$

where $n(p)$ (cm^{-3}) denotes the number density of excited state p, A_p (s^{-1}) is the Einstein coefficient, $\lambda_0(nm)$ is the central wavelength of line emission, h is planck constant, c(m/s) is the speed of light and 4π represents the solid angle $d\Omega$ (isotropic radiation), measured in steradian (sr).

Table 2. Species considered in the numerical model.

Elelctronics	Neutral molecules	Excited state particles	Positive ions	Negative ion
e	O_2 N_2 NO O N N_2O O_3 NO_2	$N_2(A)$ $N_2(a^{'})$ $O_2(a)$ $N_2(C^3)$ $N_2(B)$ $O_2(b)$ $O(^1S)$ $N_2^+(B^2)$ $N(^2D)$ $O(^1D)$	O_2^+ N_2^+ NO^+ O^+ N_4^+ O_4^+ $O_2^+N_2$	O^- O_2^- O_3^-

Since the densities depend on the reduced electric field through the electron-impact processes, the relation between steady state FNS(N2 + (B))/SPS(N2(C)) intensity ratio and the reduced electric field is given:

$$\frac{I_{391}}{I_{337}} = \frac{I_{FNS}}{I_{SPS}} = \frac{T_1 A_{k1} n(N_2^+(B))}{T_2 A_{k2} n(N_2(C))} = R(\frac{E}{N}) \qquad (7)$$

T_k is a transmission coefficient, which depends on the characteristics of the optical system and the sensitivity of the detector. In this work, the deuterium lamp is used as the radiation light source to calibrate the intensity of the spectral system, the result shows that $T_1/T_2 = 0.8934$.

3 Characteristics of Positive Glow Corona Discharge

3.1 Electrical Properties

The Voltage-Current characteristic curve obtained in the experiment and the corresponding luminous images are shown in Fig. 2, where U_i is the glow corona onset voltage. According to the current waveform, as the voltage increases continuously the discharge

enters a stable glow corona stage when the applied voltage is greater than 15 kV. Figure 3 shows the discharge current waveforms when the applied voltages is 22 kV, 24 kV, and 26 kV. The results show that the discharge current of the glow corona at atmosphere pressure is continuous and stable, presenting DC superimposed ripple state, and the discharge current is only in the order of μA. The average corona discharge current corresponding to the applied voltage of 26 kV is 67 μA, which is about twice of the average corona current when the voltage is 22 kV. As the applied voltage increases, the average corona current increases significantly and the current oscillation period decreases.
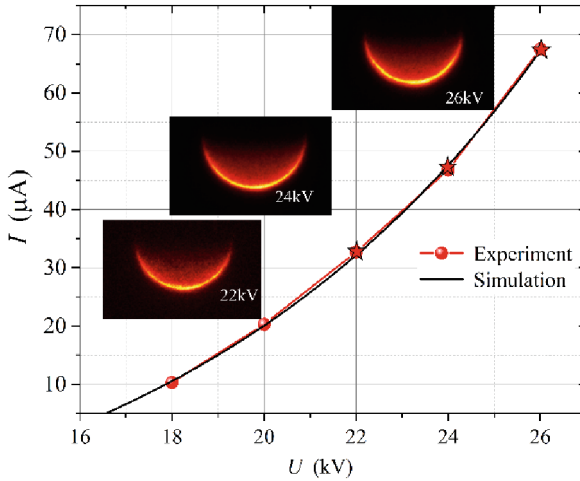

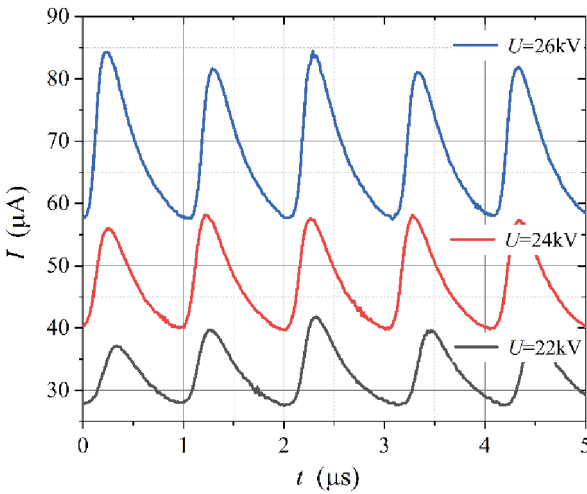**Fig. 2.** *U-I* characteristic curve of corona discharge.

Fig. 3. Variation of corona discharge current with time under different voltages.

3.2 Luminous and Temperature Characteristics

The emission spectra of the rod to plate glow corona discharge under atmospheric pressure in the wavelength range of 300 nm–400 nm is given in Fig. 4. The distribution of spectral lines in this range does not change when the voltage increases. The discharge voltage applied in this experiment is 20 kV. The parameters of the spectral system are set as follows: the exposure time is 0.7 s, the accumulation times is 50, and the gain is 1000. It can be seen from the Fig. 4 that the emission spectrum of glow corona discharge at atmospheric pressure is mainly composed of the second positive band system of nitrogen molecules N_2 (SPS) and contains a weak luminescence of the first negative band system of nitrogen molecule ions N_2^+(FNS). Meanwhile, the spectral intensity of N_2(SPS,0–2) and N_2(SPS,4–7) is highly susceptible to the influence of gas chemical reactions, which may cause 30% fluctuations, while N_2(SPS,3–6) is unstable and has a low signal-to-noise ratio. Therefore, N_2(SPS,0–0), N_2(SPS,2–5) and N_2^+(FNS,0–0) are generally used for the spectral line ratio method to measure the reduced electric field.
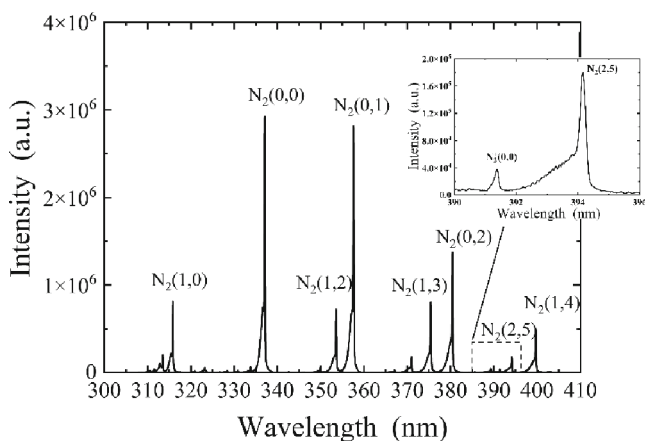
Fig. 4. Emission spectrum of positive DC corona discharge (300–400 nm).

The gas temperature can be acquired from the analysis of rotational lines of a vibrational band of a diatomic molecule. Since the energy distance between rotational levels in one vibrational state is very small, about a tenth of an electronvolt in general, the rotational population can be characterized by a rotational temperature Trot. Trot is obtained from a comparison of measured vibrational bands with the spectral simulation based on molecular constants using Specair. The intensity of the first negative band N_2^+ (FNS,0–0,391.4 nm) of nitrogen molecular ions in the glow corona discharge of the atmospheric pressure is very weak. While the spectral intensity of N_2(SPS,0–0,337 nm) is very strong, it is difficult to distinguish its rotation band and cannot be used to fit the rotation and vibration temperatures of the glow corona discharge. Therefore, we use the spectra of N_2(SPS,2–4,371.0 nm), N_2(SPS,1–3,375.5 nm), and N_2(SPS,0–2,380.5 nm) with good rotational spectral bands resolution to fit the gas temperature.
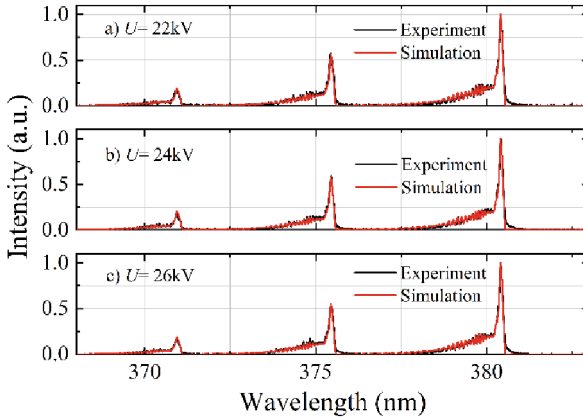
Fig. 5. Variation Rotation temperature and vibration temperature obtained by N2 (SPS) simulation.

As shown in Fig. 5, the fitted spectra of N_2(SPS,2–4,371.0 nm), N_2(SPS,1–3,375.5 nm), and N_2(SPS,0–2,380.5 nm) are compared with the experimental spectral lines when the applied voltage is 22 kV, 24 kV, and 26 kV, respectively. The results show that when the applied voltage changes, the temperature did not change significantly: the rotation temperature Tr is 450 ± 10 K and the vibration temperature Tv is 3250 ± 100 K. Due to the fact that the energy distance between rotational levels in one vibrational state is very small, so the translational and rotational energies can be easily balanced by the high-frequency collisions between particles, and the rotational temperature can be approximated to the gas temperature. Therefore, the corona discharge is a discharge dominated by collisional ionization, which is suitable for the emission spectroscopy ratio method.

3.3 Spatial Distribution Characteristics Corona Discharge Emission Spectrum

The spatial distributions of the spectral intensities of the vibrational bands N_2(SPS,0–0,337 nm), N_2(SPS,2–5,394 nm), and N_2^+(FNS,0–0,391 nm) are shown in Fig. 6, when different voltages are applied. The electrode area is within the white dashed line, and the electrode tip position is determined by the focal process of the optical path at the beginning of the experiment. It shows that the morphology of the corona ionization region is a crescent shape covering the tip of the rod electrode. At the same voltage, the intensity of the 337 nm spectral line is the strongest and 391 nm is the weakest. With the increase of voltage, the intensity of the spectral lines in the same vibrational band is obviously enhanced. In order to accurately characterize the changes of the corona ionization layer at different voltages, the distance from the electrode head along the axis z direction where the spectral line intensity decreases to 5% of its maximum value is defined as the ionization layer thickness L of the corona discharge.

As can be seen from Table 3, the ionization layer of glow corona discharge at atmospheric pressure is on the order of mm. The excited state with the central wavelength of 337 nm has the thickest ionization layer, and 391 nm has the thinnest ionization layer.
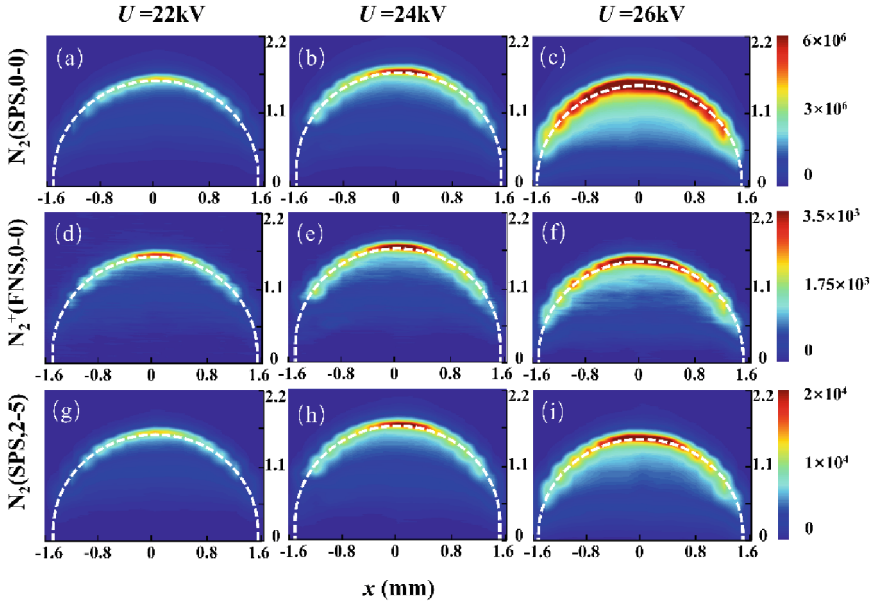
Fig. 6. Spatial distribution of spectral intensity of N$_2$ and N$_2^+$ vibrational bands at different voltage, (a)–(c) is the distribution of N$_2$(SPS,0–0,337 nm), (d)–(e) belong to the luminescence of N$_2^+$(FNS,2–5,391 nm) and (g)–(i) is the distribution of N$_2$(SPS,2–5,394 nm).

With the increase of voltage, although the luminescence of the same excited species is enhanced, the thickness of the corona ionization region almost unchanged. One possibility is that the lifetime of the excited state species is short, so that its generation and de-excitation almost in the same spatial location.

Table. 3. Corona ionospheric thickness at different voltage.

Applied voltage/kV	L(337)/mm	L(391)/mm	L(394)/mm
22	0.269	0.194	0.239
24	0.253	0.179	0.239
26	0.270	0.195	0.240

Figure 7 shows the distribution of the intensity ratio of the emission spectrum of excited state particles with characteristic wavelengths 391 nm and 337 nm along the electrode axis under different voltage conditions. The results show that the intensity ratio in the ionization region decreases away from the electrode at the same voltage. With the increase of applied voltage, the intensity ratio at the same position decreases, indicating that the electric field in the ionization zone decreases. Due to the low mobility of positive ions, they are approximately unable to move. The number density of positive

ions generated by ionization increases with the applied voltage increases, thus enhancing the inhibition of the electric field in the ionization zone.
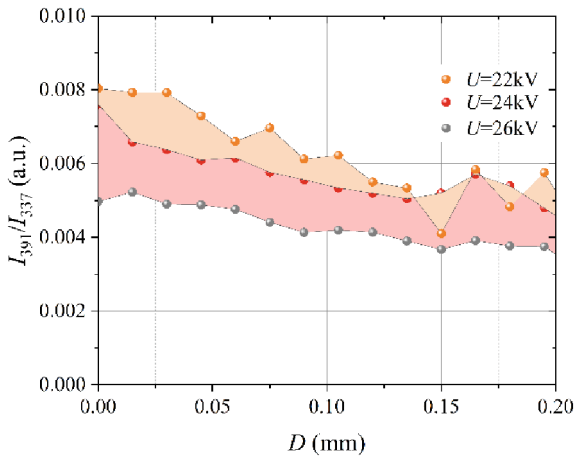
Fig. 7. The distribution of the intensity ratio along the electrode axis.

4   Simulation Results of Corona Discharge Numerical Model

The electrical field and measured rotation temperature Tr, vibration temperature Tv are used as input parameters, and the variation law of different particle number density is obtained by simulation. Through Eq. (7) the intensity ratio can be further calculated. By Changing different input electric field, the quantitative relationship between the intensity ratio and electric field can be acquired. Since the reactions R2 and R5 reflect the process of the excited state species decay to the ground state and generate spontaneous emission, it is important for the intensity ratio. The uncertainty of the I391/I337 ratio can be calculated by changing the radiation de-excitation rate within the reference range, as shown in the yellow banded area in Fig. 8. As can be seen from the Fig. 8, the average intensity ratio calculated by the model in this paper is in good agreement with the experimental results of Paris. It can further indicate that the simplified model for the excited state species is appropriate and reflect the characteristics of the electric field in the ionization region of the corona discharge.

The distribution of R391/337 ratio obtained by experimental measurement, combined with the quantitative relationship between intensity ratio and electric field obtained by simulation, can further inverse the distribution of electric field in the ionization zone. Take the electrode axis as an example, the electric field distributions at the axis when the applied voltage is 22, 24 and 26 kV are shown in Fig. 9. The uncertainty of the inverse electric field is caused by the wide range of the simulation parameters, especially the reaction rate of excited state luminescence. The results show that the axial electric field decreased exponentially with the increase of distance. As the applied voltage increases,
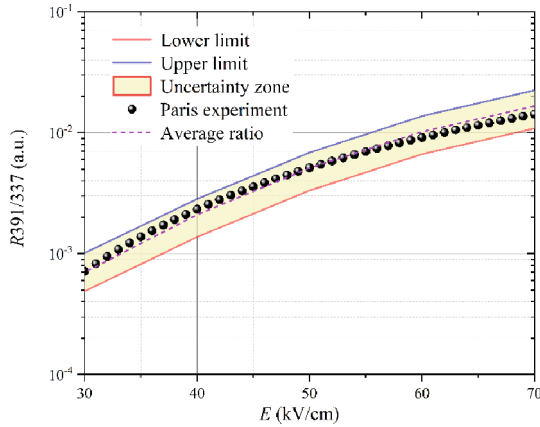
Fig. 8. The relation between the ratio of intensities of the two band systems and the electric field.

the electric field decreases slightly. This is because more positive ions are generated in the ionization region to inhibit the increase of the electric field, and thus the electric field in the ionization region is lower than that calculated by the Peek criterion.
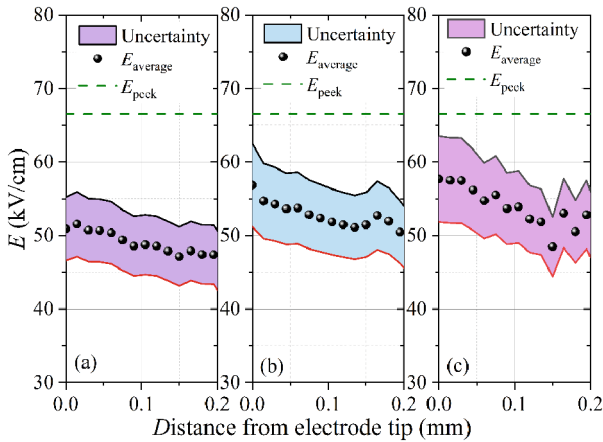
Fig. 9. Distribution of axial electric field under different voltages (a) $U = 26$kV, (b) $U = 22$kV, (c) $U = 22$kV.

5   Conclusion

In this paper, the emission spectral characteristics of the N$_2^+$ first negative system and the N$_2$ second positive system in the ionization zone of positive glow corona discharge are obtained by carrying out the emission spectrum experiments of the ionization zone in positive glow corona. The electric field in the ionization region is acquired through simulation inversion, and the conclusions are as following:

1) The experimental observation system for the emission spectra of positive corona discharge under atmospheric pressure is constructed, and the emission spectra of the first negative band system N_2^+ (FNS) and the second positive band system N_2 (SPS) of nitrogen molecular ions in the ionization region are obtained in the wavelength range of 300 nm–400 nm. Meanwhile, the average current of corona discharge is 32 μA–67 μA when the applied voltage is 22 kV–26 kV. By comparing the measured N_2 vibrational bands with the spectral simulation based on molecular constants, the glow corona discharge has a rotational temperature of 340 ± 10 K.

2) The spatial distribution of the intensity of the first negative band system N_2^+(FNS,0–0) and the second positive band system N_2(SPS,0–0) and N_2(SPS,2–5) of nitrogen molecular ions at different voltages is obtained. The results show that the thickness of corona ionization layer tends to be constant with the voltage increase, and the three excited state particles produced by electron collisions are concentrated on the electrode surface.

3) The variation law of excited state particles in the ionization zone of positive corona discharge in dry air under different electric fields at atmospheric pressure is simulated by 0-dimensional hydrodynamic simulation, reflects the characteristics of the electric field in the ionization zone. According to the measured intensity ratio distribution in the ionization zone, the electric field is inversely calculated. It is noted that the axial electric field decreased exponentially with the increase of distance. As the applied voltage increases, the electric field decreases and is lower than that calculated by the Peek criterion. Due to the uncertainty of the simulation, it is necessary to further study the factors affecting the excited state reaction rate, such as the electron energy distribution function and the collision cross section, to further improve the accuracy of the inversion results.

References

1. Linie, L.: Technical characteristics and engineering application of UHVDC transmission. Automation of Electric Power Syst. **29**(24), 5–6 (2005)
2. Xiang, C., Xiangxian, Z., Tiebing, L.: Recent progress in the calculation methods of ion flow field of HVDC transmission lines. Proceedings of the CSEE **32**(36), 130–141 (2012)
3. Xiuli, L., Xinhua, X., Dahui, W.: Calculation and influential factors analysis of ionized electric field generated by bipolar HVDC transmission line. High Voltage Eng. **10**, 54–58 (2017)
4. Lanjun, Y., Wei, W., Cen, L., et al.: Experimental and theoretical research progress in ionic wind produced by corona discharge and its application. High Voltage Eng. **042**(004), 1100–1108 (2016)
5. Jianfeng, H., Zhicheng, G., Liming, W., et al.: Research on variation of positive DC corona characteristics with air pressure and humidity. Proceedings of the CSEE **33**, 53–58 (2007)
6. Stepanyan, S.A., Soloviev, V.R., Starikovskaia, S.M.: An electric field in nanosecond surface dielectric barrier discharge at different polarities of the high voltage pulse: spectroscopy measurements and numerical modeling. J. Physics D: Applied Physics **47**(48), 485201(2014)

7. Paris, P., Aints, M., Laan, M., et al.: Measurement of intensity ratio of nitrogen bands as a function of field strength. J. Phys. D Appl. Phys. **37**(8), 1179 (2004)
8. Obrusník, A., Bílek, P., Hoder, T., et al. Electric field determination in air plasmas from intensity ratio of nitrogen spectral bands: I. Sensitivity analysis and uncertainty quantification of dominant processes. Plasma Sources Science and Technol. **27**(8), 085013 (2018)
9. Bílek, P., Obrusník, A., Hoder, T., et al.: Electric field determination in air plasmas from intensity ratio of nitrogen spectral bands: II. Reduction of the uncertainty and state-of-the-art model. Plasma Sources Science and Technol. **27**(8), 085012 (2018)
10. Kozlov, K.V., Wagner, H.E., Brandenburg, R., et al.: Spatio-temporally resolved spectroscopic diagnostics of the barrier discharge in air at atmospheric pressure. J. Phys. D Appl. Phys. **34**(21), 3164–3176 (2001)
11. Matsumoto, T., Inada, Y., Shimizu, D., et al.: Qualitative gas temperature distribution in positive DC glow corona using spectral image processing in atmospheric air. Japanese J. Applied Physics **54**(1S), 01AB07 (2014)
12. Wu, S., Cheng, W., Huang, G., et al.: Positive streamer corona, single filament, transient glow, dc glow, spark, and their transitions in atmospheric air. Physics of Plasmas **25**(12) (2018)
13. Le, X.: Research on Diagnostics of Gas Temperature Field of Atmospheric Pressure DC Microplasmas. Chongqing University (2018)
14. Paris, P., Aints, M., Valk, F., et al.: Intensity ratio of spectral bands of nitrogen as a measure of electric field strength in plasmas. J. Physics D:Applied Physics **38**(21), 3894 (2005)
15. Yu, Z.: Characteristics of DC Corona Discharge and its Spatial Ions. Institute of Technology, Beijing (2016)
16. Bílek, P., Šimek, M., Bonaventura, Z.: Electric field determination from intensity ratio of and N2 bands: nonequilibrium transient discharges in pure nitrogen. Plasma Sources Sci. Technol. **28**(11), 115011 (2019)
17. Liu, L., Becerra, M.: Gas heating dynamics during leader inception in long air gaps at atmospheric pressure. J. Physics D Applied Phys. **50**(34), 345202 (2017). Accessed 21 Nov 2016

Discharge of Inductively Coupled Plasma at Different Thicknesses

Wenyuan Zhang[✉], Haojun Xu, Xiaolong Wei, and Binbin Pei

Science and Technology on Plasma Dynamics Laboratory, Air Force Engineering University, Xi'an 710038, China

751746892@qq.com

Abstract. Plasma stealth technology has the characteristics of an adjustable wave absorption band, which is a new stealth technology with wider application prospects. The geometry of the cavity is an important external condition that affects the plasma discharge characteristics, while the thickness of the cavity directly determines the transmission distance of radar waves in the plasma, and a decrease in thickness will reduce the attenuation effect of the plasma on electromagnetic waves. In this paper, the effect of cavity thickness on the discharge characteristics of inductively coupled plasma (ICP) is studied, and the fluid model of inductively coupled plasma is established by the multi-physics field coupling method to obtain the distribution laws of n_e and T_e in ICP discharge. The heating electric field of n_e is influenced by the coil structure, the peak region of n_e is concentrated in the geometric center of the cavity for larger thickness, and the electron density increases with the increase of the discharge power. The results have important reference significance for the application of plasma technology in the local stealth of aircraft.

Keywords: Inductively Coupled Plasma · Plasma Discharge · Fluid Model

1 Introduction

The planar type inductively coupled plasma source has a wide operating air pressure, high electron density, large discharge area, and simple device structure, and has outstanding potential advantages in the direction of plasma stealth. When wave-transparent cavity plasma is applied to absorb radar waves, the thinner the cavity, the better it is for installation and use in special areas such as aircraft fuselage surfaces, so the effect of cavity thickness on the discharge characteristics of ICP is investigated in this paper.

The study of plasma stealth technology dates back to 1957 when scientists in the former Soviet Union observed that the electromagnetic scattering properties of artificial satellites under the influence of a plasma layer were different from those of ordinary metal spheres. During the Cold War in the last century, both the United States and the former Soviet Union observed the "black barrier" effect on radar waves by the formation of hundreds of kilometers of plasma regions during low-altitude nuclear explosion tests [1]. In 1962, Swarner published the first research article on the application of plasma

to target RCS reduction [2]. After the 1980s and 1990s, with the rapid development of plasma sources, plasma for attenuation of electromagnetic waves entered a breakthrough stage of development, the most famous experiment was observed in Hughes Lab in 1992 in the 4 ~ 14 GHz band, the RCS attenuation of 13 cm long microwave reflector by plasma generated in a ceramic cover reached 2025 dB [3]. Since then, research related to plasma stealth technology has entered an explosive phase of development.In July 2010, the T-50 fighter jet completed flight tests on the outskirts of Moscow, and related reports claimed that the fighter jet used electron beam plasma stealth technology with electron beam vents installed at the inlet of the air intakes [4]. For the diagnosis of the plasma parameters, several related studies have been carried out [5, 6]. Jingfeng [7] has proposed an effective method to measure the plasma parameters without the interference of the fluctuating electric field and studied the characteristics of the hollow alternating current helium glow discharge. Rui [8] has studied the characteristics of DBD micro-discharge at a different pressure. Tabaie [9] has studied a dielectric barrier discharge device producing atmospheric argon plasma needle and used spectroscopy to calculate the plasma parameters.

In this paper, the simulation study of inductively coupled plasma discharge at different thicknesses is carried out for the stealth requirements of thin wave-transparent cavities applied to local parts of aircraft, and it is found that the plasma distribution generated within the cavities at different thicknesses is different, and the results of the study can provide a reference basis for the stealth application of plasma in local parts of aircraft.

2 Plasma Discharge Simulation Model

Fluid dynamics modeling is one of the common methods used in current numerical simulations of low-temperature plasmas. The fluid model includes the particle continuity equation, the momentum conservation equation, the electron energy equation, and the Poisson equation. Among them, the continuity equations for the density of various types of particles in a plasma discharge are as follows.

$$\frac{\partial n_{e,i,neu}}{\partial t} + \nabla \cdot \Gamma_{e,i,neu} = R_{e,i,neu} \tag{1}$$

where the subscripts e, i, and neu represent electrons, ions, and neutral particles, respectively; n denotes the particle number density; R denotes the corresponding source term for each reactant particle; and Γ is the flux density of each type of particle, derived from the law of conservation of momentum. Under the drift-diffusion approximation, this is given by the following equation.

$$\Gamma_{e,i} = \mp n_{e,i}\mu_{e,i}E - D_{e,i}\nabla n_{e,i} \tag{2}$$

$$\Gamma_{neu} = -D_{neu}\nabla n_{neu} \tag{3}$$

where μ and D are the mobility and diffusion coefficients of the particles, respectively, and the negative and positive signs in the first term on the right side of Eq. (2) apply to electrons and ions, respectively.

The electron energy can be obtained by solving the Electron Energy Equation.

$$\frac{\partial n_\varepsilon}{\partial t} + \nabla \cdot \Gamma_\varepsilon = R_\varepsilon - \Gamma_e \cdot E \tag{4}$$

$$\Gamma_\varepsilon = -(\mu_\varepsilon \cdot E)n_\varepsilon - D_\varepsilon \cdot \nabla n_\varepsilon \tag{5}$$

where n_ε is the electron energy density; R_ε is the electron energy change due to inelastic collisions; $\Gamma_e \cdot E$ is the electron energy obtained by electric field acceleration (Joule heating); Γ_ε is the electron energy flux, μ_ε and D_ε are the mobility and diffusion coefficient of electron energy in space, respectively.

For the spatial electric field strength E, it can be described by Poisson's equation.

$$\nabla \cdot E = -\frac{e(n_i - n_e)}{\varepsilon_0} \tag{6}$$

where ε_0 is the dielectric constant of the working gas.

(a) Plasma model in COMSOL   (b) Plasma profiling grid
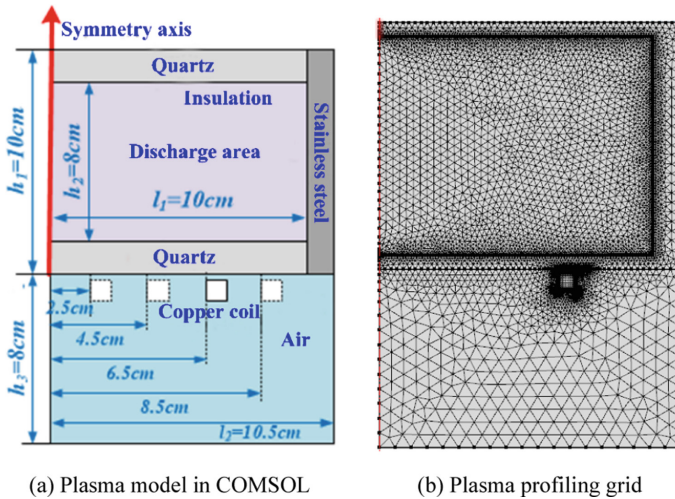
Fig. 1. Geometry and mesh section of the fluid model of the wave-transparent cavity ICP

In this paper, the fluid model is built using the plasma fluid module of the COMSOL Multiphysics platform, and the geometry of the transmissive cavity ICP is referenced in the experimental setup, as shown in Fig. 1 (a). The coil antenna is set up as a solid copper tube with a diameter of 6 mm, the thickness of the dielectric window is 1 cm and the material is quartz, the thickness of the cavity wall is 0.5 cm and the material is stainless steel.

The grid profile is shown in Fig. 1(b). The initial electron number density n_{e0} and the initial average electron energy ε_0 need to be set in the model, and reasonable initial conditions are helpful to improve the iteration speed of the model. n_{e0} and ε_0 were set to 10^9 cm^{-3} and 5 eV, respectively, and the temperature was set to 297 K. The coil antenna was used in power excitation mode with power values consistent with the forward power of the experimental power source.

3   Discharge Simulation and Experimental Results
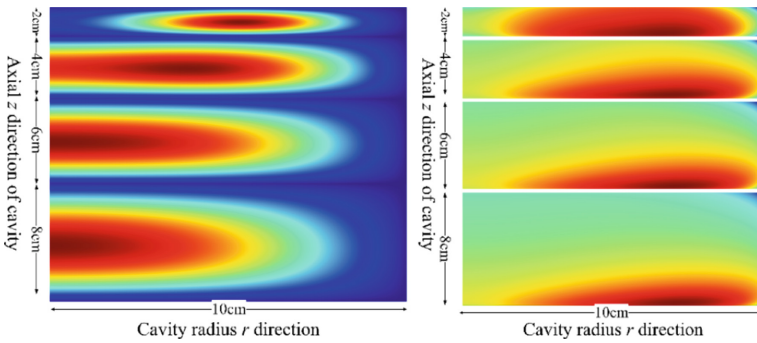
Fig. 2. Variation of ne and Te distribution with cavity thickness at 10 Pa, z-r cross section

The effect of different cavity thicknesses on the distribution of characteristic parameters was studied by using the established hydrodynamic model. 2 cm, 4 cm, 6 cm and 8 cm cavity thicknesses were selected, the discharge gas was Ar, the discharge pressure was 10 Pa, the discharge power was 300–600 W, and other discharge conditions were kept constant. The effect of thickness change on ne and Te distribution at 10 Pa is given in Fig. 2. When the ICP thickness decreases from 8 cm to 2 cm, the peak region of ne starts to deviate from the center of the cavity, and the deviation distance increases as the thickness decrease. When the thickness is reduced to 2 cm, the peak area of ne moves to the area directly above the coil antenna. At the same power, ne increases with decreasing thickness, while the distribution of Te is similar for different thicknesses, and the effect of thickness on the electron temperature is not significant.

The analysis suggests that at a pressure of 10 Pa, the plasma has moved out of the Langmuir state and random heating dominates in the power absorption mode. Due to the electromagnetic shielding effect, the RF electric field intensity is small in the area above the skinning layer. In contrast, the RF electric field at the cavity axis (r = 0 m) increases with decreasing thickness, so the peak region of the bipolar potential moves toward the region above the skinning layer, and the central region of ne continues to deviate from the cavity center with decreasing thickness, while electrons are heated within the skinning layer and are bounced back to the main plasma region so that ne is lower in the skinning layer.

In order to compare the effect of thickness variation on n_e distribution more visually, Ar-ICP discharge tests were carried out in a transmissive cavity with a quartz cavity thickness of 4 cm and 2 cm, and microwave interference transmission was used to diagnose ne. It is observed that the ICP discharge morphology changes significantly as the cavity thickness decreases, which mainly shows that the thinner the cavity and the higher the air pressure, the more obvious the annular characteristics of the plasma, and the radial width of the annular plasma widens with the increase of power, which is consistent with the trend of plasma morphology changes predicted by the fluid model.
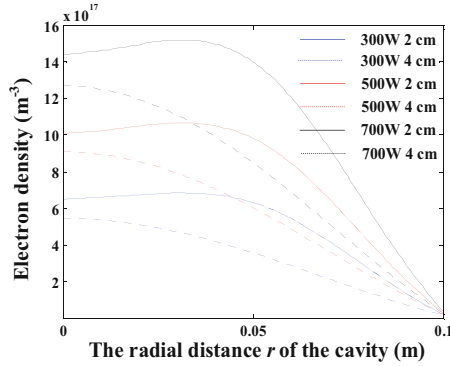
Fig. 3. Comparison of radial results at different thicknesses in 10 Pa
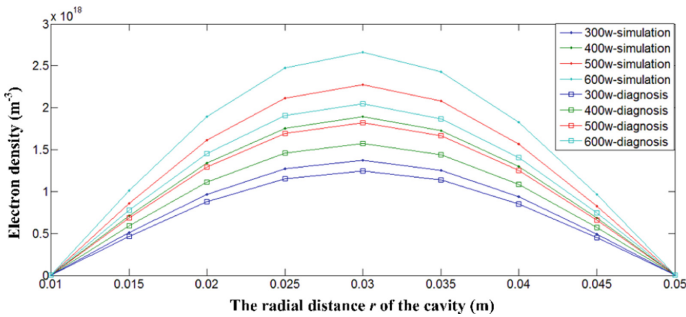
Fig. 4. Variation of electron density with power for a cavity of 4 cm

Figure 3 gives the results of the radial ne comparison under different thickness conditions at 10 Pa. The effective improvement of ne with the reduction of thickness is due to the reduction of cavity volume resulting in more power energy obtained per unit volume of ICP at the same discharge power, and its peak value increases from 9.56×10^{17} m^{-3} to 1.47×10^{18} m^{-3}.

Figure 4 shows the radial comparison results for different power conditions at 4 cm thickness. Overall the electron density increases as the discharge power increases, with the peak electron density about doubling as the power increases from 300 W to 600 W. The analysis suggests that as the power increases, the energy coupled into the cavity by the discharge coil also increases, leading to an increase in the density of the plasma produced by the excitation. Comparing the simulation results with the experimental results for the same power case, it is found that the peak electron density of the experimental results is lower than that of the numerical simulation results. It is analyzed that the reason for this phenomenon is that during the numerical simulation, the power loss and other phenomena existing in the experimental process are not taken into account, resulting in low experimental results, but the overall trend remains consistent and the results of both are in good agreement.

4   Conclusion

For localized plasma cloaking of aircraft, especially on the surface of the airframe or inside the air intakes, the thin-layer wave-transparent cavity ICP discharge technology has a greater potential for engineering applications. In this paper, the discharge of inductively coupled plasma at different thicknesses is studied, and the results of experiments and numerical simulations describe the trend of n_e space variation in agreement. The experimental measurements of n_e are lower than the fluid model results, and the established fluid model can reflect the spatial distribution of n_e more accurately. When the thickness is large, the n_e of ICP is distributed axially. The electrons first gain energy in the heated electric field near the coil, and as the low-energy electrons are expelled from the skinning layer, the peak region of ne moves directly above the heated field region, and the potential distribution in space also changes simultaneously with the diffusion migration of electrons, and after reaching the steady state, n_e reaches its maximum in the geometric center of the cavity. Since the external power provides the energy for plasma excitation, the electron density increases with the increase of the discharge power.

References

1. Sollfrey, W., et al.: Effets of propagation on high-frequency electromagnetic radiation from low-altitude nuclear explosions. Proc. IEEE. **53**, 2035 (1965)
2. Swarner, W.G., Peters, L.: Radar cross sections of dielectric or plasma coated conducting spheres and circular cylinders. IEEE. T. Antenn. Propag. **11**(5), 558–569 (1963)
3. Gregoire, D.J., Santoru, J., Schumacher, R.W.: Electromagnetic-Wave Propagation in Unmagnetized Plasma. AD-A 250710. (1992)
4. Pinglan, W., Liping, H.: Development of plasma technology for stealth. Missiles and Space Vehicles **5**, 008 (2009)
5. Adams, S.F., Bogdanov, E.A., Demidov, V.I., Koepke, M.E., Kudryavtsev, A.A., Williamson, J.M.: Metastable atom and electron density diagnostic in the initial stage of a pulsed discharge in Ar and other rare gases by emission spectroscopy. Physics of Plasmas **19**(2) (2012)
6. Engeln, R., Klarenaar, B., Guaitella, O.: Foundations of optical diagnostics in low-temperature plasmas. Plasma Sources Sci. Technol. **29**(6) (2020)
7. Yao, J., Yuan, C., Yu, Z., Zhou, Z., Kudryavtsev, A.: Measurements of plasma parameters in a hollow electrode AC glow discharge in helium. Plasma Science and Technol. **22**(3) (2020)
8. Liu, R., Yu, Z., Cao, H., Liu, P., Zhang, Z.: Characteristics of DBD micro-discharge at different pressure and its effect on the performance of oxygen plasma reactor. Plasma Science and Technol. **21**(5) (2019)
9. Tabaie, S.S., Iraji, D., Amrollahi, R.: Measurement of electron temperature and density of atmospheric plasma needle. Vacuum **182**, 109761 (2020)

Optical and X-ray Radiation from Pulsed Discharge at Low-Pressure Air

Bangdou Huang[1] , Victor Tarasenko[2] , Cheng Zhang[1](✉) , Evgeny Baksht[2] ,
Tao Shao[1] , and Dmitry Sorokin[2]

[1] Beijing International S&T Cooperation Base for Plasma Science and Energy Conversion,
Institute of Electrical Engineering, Chinese Academy of Sciences, Beijing 100190, China
zhangcheng@mail.iee.ac.cn

[2] Institute of High Current Electronics, Siberian Branch of the Russian Academy of Sciences,
Tomsk 634055, Russia
VFT@loi.hcei.tsc.ru

Abstract. The plasma radiation from a pulsed streamer discharge at 0.2–2 Torr
in the air has been studied. Pulsed discharges at these pressures at a distance
from the electrodes consist of diffuse ionization waves and, therefore, are widely
studied, including within the framework of modeling high-altitude atmospheric
discharges, in particular, columnar sprites. Two setups with different excitation
parameters were used to excite air at low pressures. When plasma was formed using
a capacitive single-barrier discharge feeding by voltage pulses with an amplitude of
up to 7 kV, diffuse red-colored ionization waves up to 120 cm long were formed.
Due to the formation of an ionization wave by a discharge forming by voltage
pulses with an amplitude of up to 33 kV between two electrodes, X-ray and
runaway electron beam were recorded.

Keywords: pulsed discharge · streamer · ionization wave · low-pressure air ·
optical and X-ray radiation

1 Introduction

Over the past three decades, much attention has been paid to the study and modeling of
red sprites and other transient light phenomena associated with large-scale discharges in
the upper atmosphere of the Earth [1]. The red spirit usually appears at an altitude of about
7080 km. It consists of several ejectors, which eject towards the surface of the earth and
in the opposite direction. They are usually observed over areas of thunderstorm activity.
Advances in the study of sprites are mainly due to research carried out using instruments
installed on aircraft or on the International Space Station. The red color of sprites resulted
from the emission of the first positive nitrogen system (FPS; N_2). Sprite propagation
velocities are 2–10 mm/ns. A sprite radiation pulse duration reaches ~ 100 ms. It is well
known that the propagation and velocity of streamers (ionization waves) depend on the
direction and magnitude of the electric field. Recently, the following has been widely
discussed. Is the formation of red sprites, including column ones, accompanied by the
generation of runaway electrons (RAEs) and X-rays.

The purpose of this work is to create setups on which it is possible to form and study red ionization waves at air pressures of 0.2–2 Torr characteristic of the area where red sprites are observed, as well as to register X-rays during a streamer discharge at these pressures.

2 Experimental Equipment and Methods

Two experimental setups were used to investigate the optical and X-ray radiation properties of the streamer discharge plasma in air at low pressures. In setup #1, compared with papers [2, 3], new systems for the initiation of a streamer discharge (a diffuse ionization wave – DIW) were used. Its block diagram is shown in Fig. 1. Diffuse ionization waves, in this case, were initiated by a discharge with one dielectric barrier.
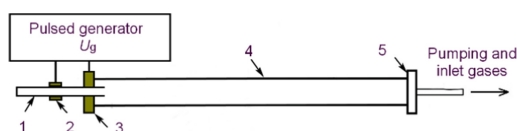

Fig. 1. Scheme of the experimental setup #1– quartz tube with an outer diameter of 21 mm with a closed left (relative to the reader) end; 2 – annular high-voltage electrode; 3 – grounded aluminum flange electrode; 4 – quartz tube; 5 – dielectric flange.

The main part of the setup is a chamber connected to the pump. The chamber consisted of two quartz tubes with electrodes connected to a voltage generator Ug. A glass-shaped tube 1 had a wall thickness of 1.5 mm and an outer diameter of 21 mm. A 1-cm-width high-voltage (HV) annular electrode 2 was mounted on the outside of tube 1. The latter was inserted into a metal flange 3, which was the second electrode and was grounded. The second tube 4 had an outer diameter of 55 mm, a wall thickness of 2.5 mm, and a length of 120 cm. On the right side, it was closed with a dielectric flange 5, which had a fitting with a 5-mm-diameter hole for the gas inlet and outlet. This tube was made of GE 214 quartz with high transparency in the spectral region 210–1500 nm. Flanges 3 and 5 were vacuum-tightly connected to quartz tubes. To initiate a DIW, the voltage from Ug was applied across electrodes 2 and 3. The generator Ug formed voltage pulses of positive or negative polarity with rise and fall times of ~ 350 ns, an amplitude up to 7 kV, and a duration at half a maximum of $\approx$ 2 μs. The pulse repetition rate in these experiments was 21 kHz. The discharge current between the electrodes flowed inside the chamber and was limited by a dielectric barrier – the wall of quartz tube 1. Ambient air with a humidity of 23% was used in the experiments, which was pumped into the chamber after its preliminary evacuation to the residual pressure of 0.01 Torr. The discharge current between the ring electrodes was measured using a shunt, and the voltage at the HV electrode was measured with an AKTAKOM ACA-6039 divider. All the signals from were recorded with an oscilloscope (MDO 3104,1 GHz, 5 GS/s). Optical radiation of the discharge plasma was registered with a spectrometer (HR2000 + ES OceanOptics Inc.), which has a known spectral sensitivity in the range 200–1000 nm
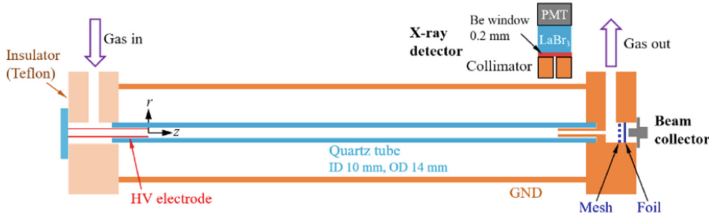
Fig. 2. Scheme of the experimental setup #2.

(optical resolution ~ 0.9 nm). Integral images of the streamer discharge were taken with a digital camera (SONY A100).

The second setup for the formation of a fast ionization wave (FIW) with RAEs and X-rays is shown in Fig. 2, see [4, 5] as well. The discharge was implemented in a quartz tube with an inner diameter of 10 mm and the outer one of 14 mm. High voltage and ground electrodes were cylindrical tubes. The distance between them was ~ 20 cm. There were grounded shield plates serving as a current loop. The discharge was driven by a negative HV generator producing 30-kV-amplitude pulses at the pulse repetition rate of 10 Hz. The discharge environment was air at the pressure of ~ 2 Torr. RAEs in a FIW discharge was detected with a beam collector having a good impedance matching to 50 Ω. Signals from the collector were recorded with a digital oscilloscope (LeCroy, 808Zi-A with a bandwidth of 8 GHz and a sample rate 40 GS s^{-1}). A copper mesh provided shielding against the discharge displacement current and an 18-μm-thickness aluminum foil (electron energy cutoff is ~ 45 keV) was used as an energy filter. X-rays from the FIW discharge arising near the ground electrode were recorded by a LaBr$_3$ scintillator combined with a photomultiplier. To limit the collecting solid angle a collimator with a slit width of ~ 1 cm was used.

3   Results and Discussion

Figure 3 demonstrates photographs of the discharge plasma glow at various pressures The photos were captured in the dark with a camera exposure time of 0.2 s and an aperture of 5.6.
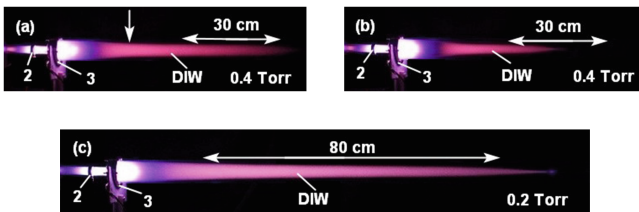

Fig. 3. Photographs of the discharge plasma glow at air pressures of 0.4 (a,b) and 0.2 Torr (c). The polarity of the HV electrode 2 (see also Fig. 1) is positive (a) and negative (b, c), the generator voltage is 7 kV, and the pulse repetition rate is 21 kHz. Setup #1. Ambient temperature and humidity are 28 °C and 23%, respectively.

During this exposure time, 4.2 thousand discharges occur in the tube, which made it possible to register the integral plasma glow consisting of radiation pulses with weak intensity. It was found that the breakdown of air at pressures of 0.2–2 Torr occurs at the voltage pulse front if its amplitude is 7 kV. The highest electric field strength in this setup was achieved near the ring electrodes and in the space between them. With a decrease in pressure (below 6 Torr) and (or) an increase in the generator voltage, the capacitive discharge plasma initiated the propagation of diffuse ionization waves (streamers). The DIW length increased with decreasing pressure and reached 115 cm at the pressure of 0.2 Torr, see Fig. 3c. At air pressures of 0.2–1 Torr, the ionization waves had a red color, which corresponded to the color of red sprites at altitudes of more than 50 km. The DIW was also affected by the polarity of the voltage applied to electrode 2. With the positive polarity of this electrode, the DIW length increased, see Fig. 3a and Fig. 3b.

Figure 4 presents plasma emission spectra at a distance of 21 cm from the right electrode taking into account the sensitivity of the spectrometer.
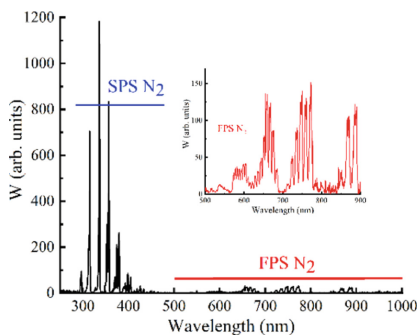
Fig. 4. Emission spectra of the air discharge plasma at the pressure of 0.4 Torr recorded at the distance of 21 cm from the electrode 3 (see arrow in Fig. 3a). Bands in the ranges of 300–400 and 500–1000 nm are the second (SPS) and the first (FPS) positive systems of a nitrogen molecule (see inserted spectrum). Setup #1.
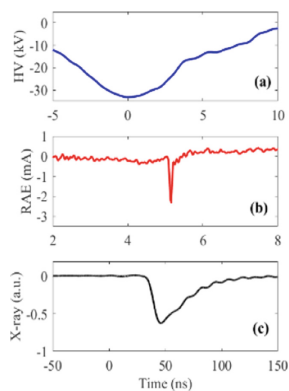
Fig. 5. HV, RAE beam current, and X-ray radiation pulse obtained with the setup #2 at the air pressure of ~ 2 Torr. The incident voltage amplitude is ~ − 33 kV and the pulse repetition rate is 10 Hz.

The bands of the second positive nitrogen system (N_2; SPS; UV range) contain the highest spectral radiation energy density W in the region of 200–1000 nm for the discharge regions with a DIW at air pressures of 0.2–2 Torr. The maximum energy was emitted at the second positive system (SPS N_2) and first positive system (FPS N_2), Fig. 4. With a decrease in pressure to 0.2 Torr, this trend persists, but the ratio between the radiation energy density of the SPS and FPS (SPS/FPS) changes. The red color of the discharge plasma, which is observed visually and captured in photographs (Fig. 3), is associated with a relatively high spectral energy density of the FPS N_2 radiation at low pressures. However, in this case, the spectral energy density of the radiation of the most intense SPS bands was significantly higher than that of the FPS ones. SPS/FPS was

~ 50 at the air pressure of 0.4 Torr. Under these conditions, the observed color of the discharge was red. When the air pressure decreased to 0.2 Torr, the color of the discharge changed somewhat, Fig. 3c. This is due to the appearance of the FNS lines (UV and visible region) in the spectrum.

Figure 5 shows the HV waveform, RAE beam current, and X-ray radiation pulse obtained with Setup #2. The HV pulse rise time was ~ 5 ns and the amplitude was ~ -33 kV. The breakdown occurred around the peak voltage and a FIW started to propagate as HV decaying. RAE beam with an energy higher than ~ 45 keV was detected when the FIW front approached the ground electrode. The rise time of the RAE beam current pulse is ~ 50 ps. This means that RAE with an energy higher than the voltage amplitude appears during the FIW propagation process. Meanwhile, the X-ray radiation pulse was detected around the ground electrode, which is due to the bremsstrahlung caused by RAEs. Note that the X-ray pulse rise time was ~ 3 ns, which was much longer than that of the RAE beam current pulse and limited by the transition time of the PMT used in the X-ray detector.

4   Conclusion

It was found that the color of diffuse ionization waves and emission spectra can be similar to those recorded in column sprites. RAE beam with energies up to 45 keV and X-ray pulse, which is due to the bremsstrahlung of RAEs was detected around the ground electrode at air pressure 2 Torr. In future studies, it is planned to obtain the same radiation characteristics as the first setup.

References

1. Füllekrug, M., Mareev, E., Rycroft, M.: Sprites, Elves and Intense Lightning Discharges. Springer Science & Business Media. **225** (2006). https://doi.org/10.1007/1-4020-4629-4
2. Tarasenko, V., Panarin, V., Skakun, V., Sosnin, E.: Laboratory demonstration in the air red and blue mini-jets. J. of Physics: Conf. Series **927**(1), 012062 (2017)
3. Tarasenko, V., Vinogradov, N., Baksht, E., Sorokin, D.: Experimental simulation of red sprites in a laboratory. J. Atmos. Science Res. **05**(04), 26–36 (2022)
4. Huang, B., Carbone, E., Takashima, K., Zhu, X., Czarnetzki, U., Pu, Y.: The effect of the pulse repetition rate on the fast ionization wave discharge. J. Phys. D: Appl. Phys. **51**, 225202 (2018)
5. Huang, B., Zhang, C., Qiu, J., Zhang, X., Ding, Y., Shao, T.: The dynamics of discharge propagation and x-ray generation in nanosecond pulsed fast ionisation wave in 5 mbar nitrogen. Plasma Sourc. Sci. and Technnol. **28**(9), 095001 (2019)

Study on the Plasma Parameters of RF Negative Ion Source for Associated Particle Neutron Generator

Zhiping Zou, Zhen Yang[✉], Yubo Xing, Zeyang Zhang, Shengda Tang, Xiang Cao, Wei Ma, Liping Zou, and Liang Lu

Sino-French Institute of Nuclear Engineering and Technology, Sun Yat-Sen University, Zhuhai 519082, China
`yangzh97@mail.sysu.edu.cn`

Abstract. A two-dimensional (2-D) fluid model is developed to investigate a radio frequency (RF) negative ion source with the magnetic filter and the electromagnetic coupling, for associated particle neutron generator (APNG). The influences of the discharge pressure, RF power and magnetic filter field intensity on the electron density, electron temperature, electric potential, high vibrational hydrogen molecular density and negative hydrogen ion (H^-) density in discharge region, diffusion region and magnetic filtration region were investigated, respectively.

Simulation results show that the electron temperature in the magnetic filtration region is lower than that in the discharge region, forming a good electron temperature gradient. The electron density, electric potential, H^- density in the discharge region, and vibrationally excited hydrogen molecules (VEHM) density all increase with the discharge pressure, but the electron temperature decreases; With an increase in RF power, the electron density, electron temperature in the discharge region, electric potential, H^- density and VEHM density all increase; However, the electron temperature in the diffusion region decreases and those in the magnetic filtration region increases slightly; As the intensity of the magnetic filter field increases, the electron density, H^- density and VEHM density gradually increase, while the electron temperature and electric potential gradually decrease.

Considering the magnetic field shielding is not set in the simulation, the magnetic filter field will affect the discharge region and the diffusion region.

Keywords: Associated particle neutron generator (APNG) · Fluid model · Radio frequency (RF) negative ion source · Magnetic filter

1 Introduction

Associated particle imaging (API) technology and the corresponding detection equipment have the advantages of high-cost performance, strong processing capacities, compact structures and ease of maintenance. Apart from nuclear material detection, it also has broad applications in aerospace [1], astral detection, nuclear reaction [2], carbon

neutralization [3–5], soil element determination, and other fields. API is one of the most popular techniques [6, 7] for active neutron activation analysis in the field of nuclear material identification [8, 9]. As one of the core devices, the associated particle neutron generator (APNG) [10, 11] still suffers from big beam spot and low yield, which limits the spatial resolution and signal-to-noise ratio of API technique [12, 13]. Recent studies have reported the development of neutron generators based on negative ion sources both at home and abroad. Q. Ji et al. [14] of LBNL have carried out a study of the APNG based on RF ion source and ECR ion source, analyzing the induced current density and the ratio of single-atom deuterium ions (D^-), as well as a comparative study of target-side high voltage and target-side grounding designs to investigate the relationship between α-detector high-voltage breakdown probability and beam spot size. A. J. Antolak [15] of SNL, has used RF ion source to generate D^- in the APNG studies. Several advantages of negative ions have been demonstrated, such as high concentrations of single atom ions in beam, small beam spot size and high neutron yield, etc.

In this paper, a two-dimensional (2-D) fluid model is developed within COMSOL MULTIPHYSICS to investigate the plasma variation inside the RF negative hydrogen ion source under different discharge parameters. Based on the numerical results of this study, it is possible to better understand the distribution of H^- density under different discharge conditions, so as to improve the performance of negative hydrogen ion source, optimize the design of negative ion sources, and further develop the technology of API.

2 Theory

Magnetic potential [16–18] is used to describe and solve magnetostatic problems in which no current exists, the following equation:

$$-\nabla \cdot (\mu_0 \nabla V_m - \mu_0 \boldsymbol{M}) = 0, \tag{1}$$

are used to simulate the magnetostatics of magnetic filter fields, where μ_0 is the permeability of vacuum, $\boldsymbol{M}$ is the magnetization vector, V_m is the magnetic scalar potential.

To simulate the electromagnetic field of an RF coil, combine the Maxwell- Ampère's law [19, 20]:

$$\nabla \times \boldsymbol{H} = \boldsymbol{J} + \frac{\partial \boldsymbol{D}}{\partial t} = \sigma \boldsymbol{E} + \sigma \boldsymbol{v} \times \boldsymbol{B} + \boldsymbol{J}_e + \frac{\partial \boldsymbol{D}}{\partial t}, \tag{2}$$

with the constitutive relationships $B = \mu_0(H + M)$ and $D = \varepsilon_0 E$ to rewrite Ampère's law as

$$\left(j\omega\sigma - \omega^2\varepsilon_0\right)A + \nabla \times \left(\mu_0^{-1}\nabla \times A - M\right) - \sigma v \times (\nabla \times A) = J_e, \tag{3}$$

where $\boldsymbol{J}_e$ is an externally generated current density, $\boldsymbol{v}$ is the velocity of the conductor, j is the imaginary unit, ω is the angular frequency of the RF source, σ is the conductivity, ε_0 is the vacuum dielectric constant, μ_0 is the vacuum magnetic permeability, $\boldsymbol{A}$ is the magnetic vector potential.

Electron transport is described by the Boltzmann equation, which is a nonlocal continuity equation in phase space ($\textbf{r}$, $\textbf{u}$). The Boltzmann equation can be approximated by fluid equations by multiplying by a weighting function and then integrating over velocity space. The fluid equations describe the electron number density, the mean electron momentum and the mean electron energy as a function of configuration space and time. The rate of change of the electron density is described by:

$$\frac{\partial}{\partial t}(n_e) + \nabla \bullet \Gamma_e = R_e, \tag{4}$$

where n_e is the electron density, Γ_e is the electron flux vector and R_e is either a source or a sink of electrons. The rate of change of the electron momentum is described by:

$$\frac{\partial}{\partial t}(n_e m_e \textbf{u}_e) + \nabla \bullet n_e m_e \textbf{u}_e \textbf{u}_e^T = -(\nabla \bullet \textbf{P}_e) + q n_e \textbf{E} - n_e m_e \textbf{u}_e v_m, \tag{5}$$

where m_e is the electron mass, u_e is the drift velocity of the electrons, $\textbf{P}_e$ is the electron pressure tensor, q is the electron change, $\textbf{E}$ is the electric field and v_m is the momentum transfer frequency. The rate of change of the electron energy density is described by:

$$\frac{\partial}{\partial t}(n_\varepsilon) + \nabla \bullet \Gamma_e + E \bullet \Gamma_e = S_{en}, \tag{6}$$

where n_ε is the electron energy density and S_{en} is the energy loss or gain due to inelastic collisions.

For ions and neutral species [21–23], the transport processes can be calculated with the multi-component equations. Suppose a reacting flow consists of $k = 1, …, Q$ species and $j = 1, …, N$ reactions. The equation for the first $Q − 1$ species is given by.

$$\rho \frac{\partial}{\partial t}(w_k) + \rho(\textbf{u} \bullet \nabla)w_k = \nabla \bullet \textbf{j}_k + \textbf{R}_k, \tag{7}$$

where $\textbf{j}_k$ is the diffusive flux vector, $\textbf{R}_k$ is the rate expression for species k, $\textbf{u}$ is the mass averaged fluid velocity vector, ρ denotes the density of the mixture, and w_k is the mass fraction of the kth species.

The diffusive flux vector is defined as:

$$\textbf{j}_k = \rho w_k V_k \tag{8}$$

where V_k is the multicomponent diffusion velocity for species k. The definition of V_k depends on the option chosen for the Diffusion Model property.

3   Setup of the Ion Source Model

To simplify the calculation and improve the convergence of the model, a 2-D geometric model was constructed, as shown in Fig. 1. The plasma module and the electromagnetic field module were coupled within COMSOL MULTIPHYSICS, which facilitated the study of the influence of the filtered magnetic field on the plasma parameters. A 13.56 MHz RF coil is located on top of the model and maintains the discharge process

of the ion source. The negative hydrogen ion source chamber is within the range of z = 0 to z = 80 mm in the axial direction, which is divided into three regions from top to bottom: the discharge region, diffusion region and magnetic filtration region. At the lower left and right corners of the 2-D model, two permanent magnets provide parallel magnetic filter fields for the extraction area. The red line at r = 0 represents the position of radial measurement, and the axial detection positions of diffusion region and magnetic filtration region are set at z = 35 mm and z = 2.5 mm, respectively, due to difficulty in distinguishing the axial changes between diffusion region and magnetic filtration region.

A simplified model of the negative hydrogen reaction is shown in Table 1, which includes electron collision reactions, heavy particle reactions, and wall surface reactions.
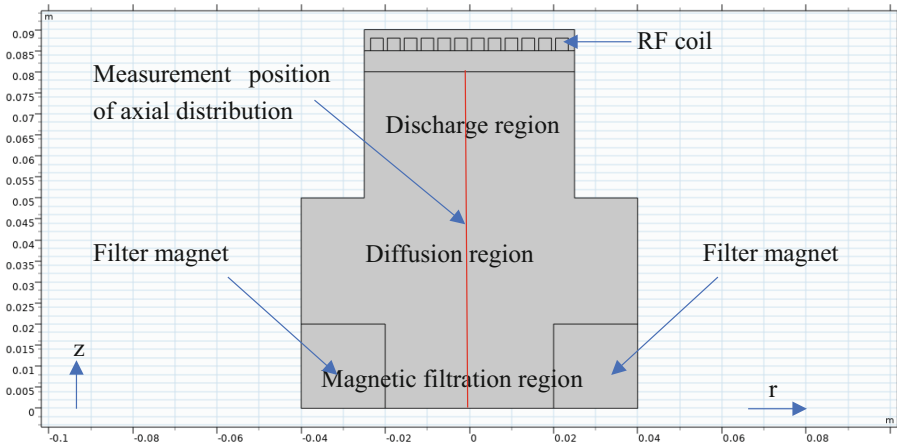
Fig. 1. 2-D profile of geometric model

Table 1. Reactions considered in the model

Reactions	Description	Reference
1. $e + H_2 \rightarrow e + H_2$	Elastic scattering	[24]
2. $e + H_2 \rightarrow e + H_2(s)$	Electronic Excitation	[25]
3. $e + H_2(s) \rightarrow e + H_2$	Electronic Excitation	[25]
4. $e + H_2 \rightarrow e + H_2(v)$	Vibrational Excitation	[25]
5. $e + H^- \rightarrow 2e + H$	Electron detachment	[25]
6. $e + H \rightarrow 2e + H^+$	ionization	[26]
7. $e + H_2^+ \rightarrow e + H + H^+$	Dissociative excitation	[27]
8. $e + H_2 \rightarrow 2e + H_2^+$	ionization	[25]
9. $e + H_2(v) \rightarrow H + H^-$	Dissociative Electron Attachment	[25]

Reactions	Description	Reference
10. $e + H_3^+ \rightarrow e + H_2 + H^+$	Dissociative recombination	[25]
11. $e + H^+ \rightarrow H$	Electron detachment	[25]
12. $H^+ + H^- \rightarrow 2H$	Mutual Ion-Ion Neutralization	[28]
13. $H^+ + H^- \rightarrow e + H_2^+$	Associative Detachment	[28]
14. $H + H^- \rightarrow e + H_2$	Associative Detachment	[25]
15. $H + H^- \rightarrow e + 2H$	Electron Detachment	[28]
16. $H_2 + H_2^+ \rightarrow H + H_3^+$	Heavy Particle Exchange	[28]
17. $H + H_2^+ \rightarrow H_2 + H^+$	Single Charge Exchange	[29]
18. $H + H_2 \rightarrow 3H$	Dissociative Excitation	[28]
19. $H_2(s) \rightarrow H_2$	H(s) wall recombination	[30]
20. $H_2(\upsilon) \rightarrow H_2$	Vibrational de-excitation	[30]
21. $H^+ \rightarrow H$	Ion wall recombination	[31]
22. $H_2^+ \rightarrow H_2$	Ion wall recombination	[31]
23. $H_3^+ \rightarrow H + H_2$	Ion wall recombination	[31]

4   Result and Discussion

In this paper, we mainly study the influence of discharge pressure, RF power and magnetic filter field intensity on the plasma parameters in the discharge region, diffusion region and magnetic filtration region. There are several key parameters to investigate, including electron density, electron temperature, positive and negative hydrogen ion densities, VEHM density, and so on. The effects of discharge pressure, RF power and magnetic filter field intensity on the discharge of negative hydrogen ion source are discussed below in detail.

4.1   Effects of Discharge Pressure

For the investigation of the effect of discharge pressure, other physical parameters were left unchanged, including the RF power of 1500 W and the intensity of the magnetic filter field of 0.3 T.

As illustrated in Fig. 2(a), the 2-D electron density distribution is shown when the discharge pressure is 25 Pa. The electron density has a higher value in the discharge region due to the feed-in energy of the RF power, and decreases gradually as the distance away from the discharge region. The axial electron density distribution for different discharge pressure is shown in Fig. 2(b). Under different discharge pressures, the electron density distribution has a large value in the discharge region and gradually decreases away from it. Moreover, as the discharge pressure increases, the electron density in each axial region increases.
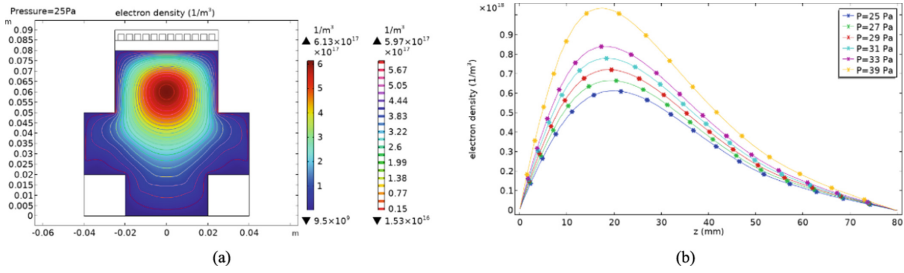
(a)   (b)

Fig. 2. 2-D profile of the electron density with the discharge pressure of 25 Pa (a); the electron density in the axial direction for different discharge pressure (b). The RF power is set to 1500 W, the magnetic filter field intensity is 0.3 T.

(a)   (b)
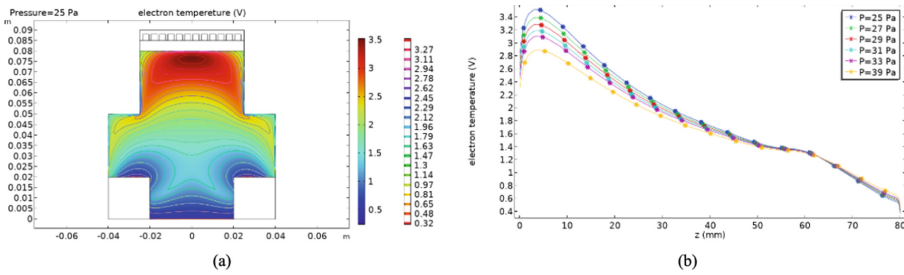
Fig. 3. 2-D profile of the electron temperature with the discharge pressure of 25 Pa (a); the electron temperature in the axial direction for different discharge pressure (b). The RF power is set to 1500W, the magnetic filter field intensity is 0.3 T.

Figure 3(a) shows the 2-D electron temperature distribution when the discharge pressure is 25 Pa. The electron temperature presents a good temperature gradient among the discharge region, diffusion region and magnetic filtration region, with 3.5 eV in the discharge region and only 0.24 eV in the magnetic filtration region. Obviously, the collision reaction between low energy electrons and VEHM in the magnetic filtration region is conducive to the generation of negative hydrogen ions. However, the electron temperature range in the discharge region is not the most suitable for the generation of high VEHM, which is also the point that the model needs to be optimized in the future.

Axial electron temperature changes under different discharge pressures are shown in Fig. 3(b). With the change in the discharge pressure, the electron temperature in the discharge region changes greatly, but that in the diffusion region and the magnetic filtration region changes little. Furthermore, as the discharge pressure increases, the collisions between particles intensify, and the electron temperature in the discharge region decreases gradually.
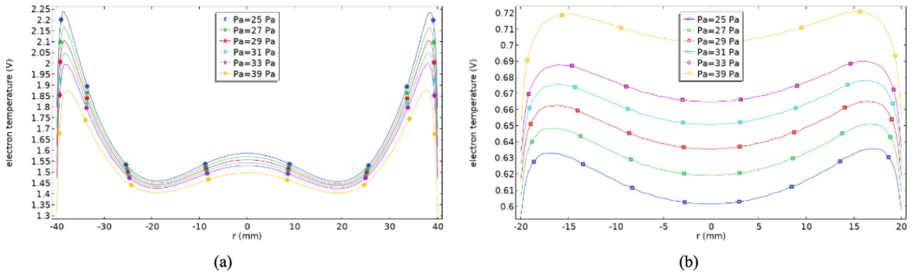
Fig. 4. Radial electron temperature distribution in the diffusion region (a); radial electron temperature distribution in the magnetic filtration region (b).

Radial electron temperature distribution in the diffusion region under different discharge pressures are shown in Fig. 4(a). The temperature of the electrons in the diffusion region drops slowly as the discharge pressure increases. However, in the magnetic filtration region, the electron temperature increases slightly, as shown in Fig. 4(b). By increasing collisions between particles, more energy is transferred into the magnetic filtration region, causing the temperature of the electrons to rise slightly, when the incoming energy exceeds the energy consumed by the collision. Therefore, a higher discharge pressure is not the better for keeping the electron temperature in the magnetic filtration region low.
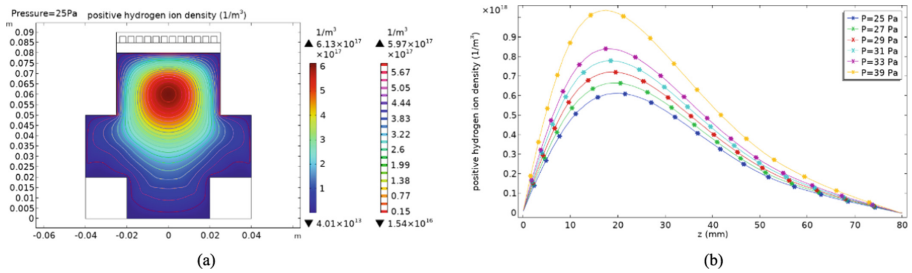
Fig. 5. 2-D profile of the H^+ density, with the discharge pressure of 25 Pa (a); the H^+ density in the axial direction for different discharge pressure (b). The RF power is set to 1500 W, the magnetic filter field intensity is 0.3 T.

The distribution of H^+ density is similar to that of electron density, with a large value in the discharge region, as shown in Fig. 5(a). Figure 5(b) shows the variation trend of H^+ density in the axial direction under different chamber pressures. It is similar to the electron density that the axial H^+ density increases significantly in all regions as the discharge pressure increases.

The 2-D distribution, axial and radial changes of VEHM in different regions are shown in Fig. 6. Due to the higher electron density and electron temperature in the discharge region, the VEHM density is higher as well. In the discharge region, the density of VEHM increases as the discharge pressure increases, while it decreases in the diffusion region. The electron temperature in the discharge region decreases and the electron
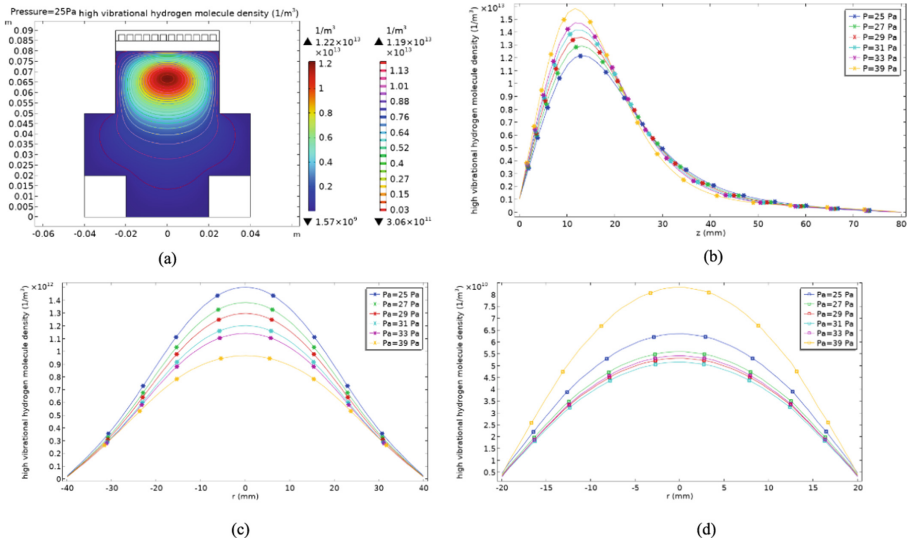
Fig. 6. 2-D profile of the $H_2(v)$ density with the discharge pressure of 25 Pa (a); The axial $H_2(v)$ density for different discharge pressures (b); Radial variation of $H_2(v)$ density in the diffusion region (c); Radial variation of $H_2(v)$ density in the magnetic filtration region (d). The RF power is set to 1500W, the magnetic filter field intensity is 0.3 T.

density increases as the discharge pressure gradually rises. VEHM is generated by collisions between high-energy electrons and hydrogen molecules, so an increase in electron density is conducive to the formation of VEHM. Even though the electron temperature decreases, they still remains at a high level. However, the electron temperature in diffusion region is at a low level, the slightly increased electron density cannot compensate for the negative effects of electron temperature. For the magnetic filtration region, the gradually increased electron temperature with the increase of discharge pressure is conducive to the formation of VEHM.

According to Fig. 7, the correlation of H^- density is basically consistent with the VEHM density since the VEHM density has a great influence on the H^- density, but the increasing electron temperature of magnetic filtration region inhibits the formation of negative hydrogen ions. The H^- density in the discharge region is relatively high. As the discharge pressure increases, the H^- density in the discharge region gradually increases, while the H^- density in the diffusion region and the magnetic filtration region gradually decreases.

4.2   Effects of RF Power

For the investigation into the law of influence of RF power, the discharge pressure is set to 25 Pa and the magnetic filter field intensity is 0.3 T.

The electron density is higher in the discharge region, and increases in each axial region with the increase of RF power, as shown in Fig. 8. The axial and radial distributions of electron temperature under different RF power are shown in Fig. 9. As the RF power
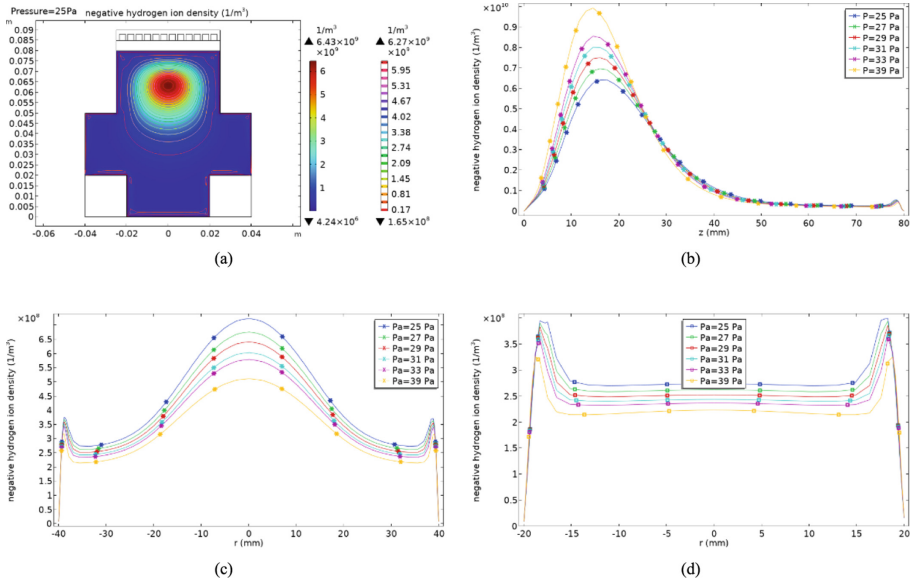
Fig. 7. 2-D profile of the H^- density, with the discharge pressure of 25 Pa (a); The axial H^- density for different chamber pressure (b); Radial variation of H^- density in the diffusion region (c); Radial variation of H^- density in the magnetic filtration region (d). The RF power is set to 1500 W, the magnetic filter field intensity is 0.3T.

Fig. 8. 2-D profile of the electron density with the RF power of 1500 kW (a); The electron density in the axial direction for different RF power (b); The discharge pressure is set to 25 Pa, the magnetic filter field intensity is 0.3 T.

increases, the electron temperature increases gradually in the discharge region, decreases gradually in the diffusion region and increases slightly in the magnetic filtration region. The discharge region is most affected by the RF coil due to the input of RF coil energy, where the energy feeding of the coil will intensify the interparticle motion. Compared to the energy transferred from the discharge region, particle collisions in the diffusion region consume more energy. However, for the magnetic filtration region, the electron density is relatively low, and the energy consumption caused by particle collisions is gradually less than the energy transferred from the diffusion region. Therefore, high RF

power may cause the electron temperature in the magnetic filtration region to rise, which is not conducive to generate H^-.
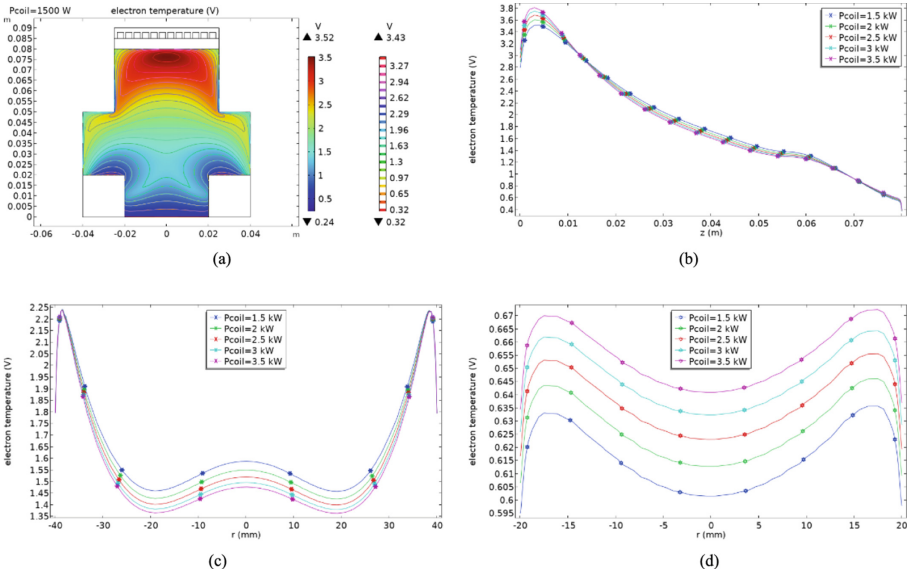
Fig. 9. 2-D profile of the electron temperature, with the RF power of 1500 W (a); The axial electron temperature for different RF power (b); Radial variation of electron temperature in the diffusion region (c); Radial variation of electron temperature in the magnetic filtration region(d). The chamber pressure is set to 25 Pa, the magnetic filter field intensity is 0.3 T.

Fig. 10. 2-D profile of the H^+ density with the RF power of 1500 kW (a); The H^+ density in the axial direction for different RF power (b). The discharge pressure is set to 25 Pa, the magnetic filter field intensity is 0.3T.

The H^+ density in the discharge region is higher, and with the increase of RF power, the H^+ density in all axial regions will increase, as shown in Fig. 10.

As shown in Fig. 11, the density of VEHM increased gradually in the discharge region and diffusion region with increasing the RF power, while the VEHM density remained nearly unchanged in the magnetic filtration region.
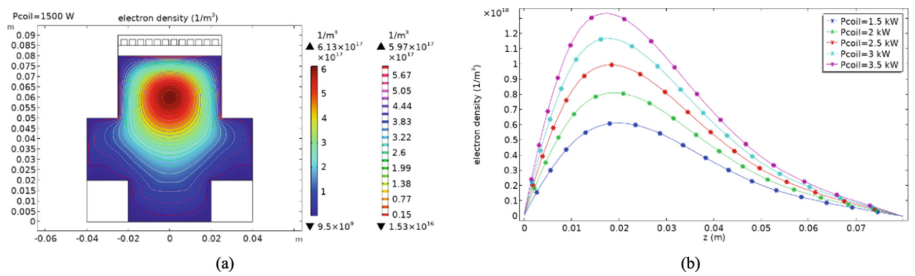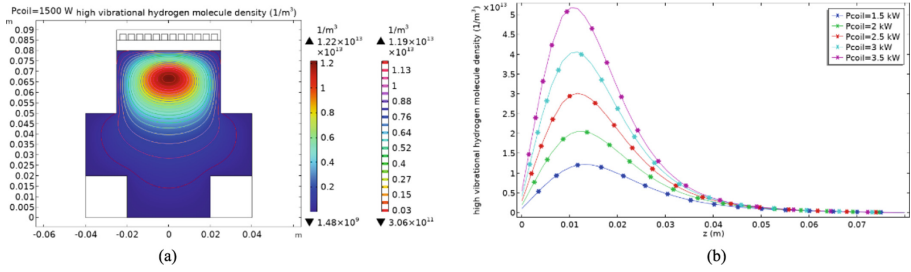
Fig. 11. 2-D profile of the $H_2(\nu)$ density with the RF power of 1500 W (a); The $H_2(\nu)$ density in the axial direction for different RF power (b). The discharge pressure is set to 25 Pa, the magnetic filter field intensity is 0.3T.
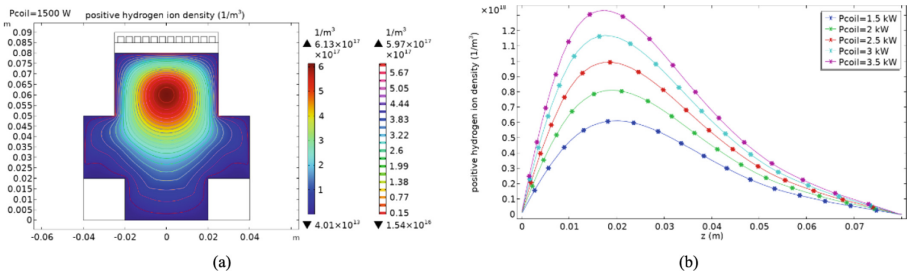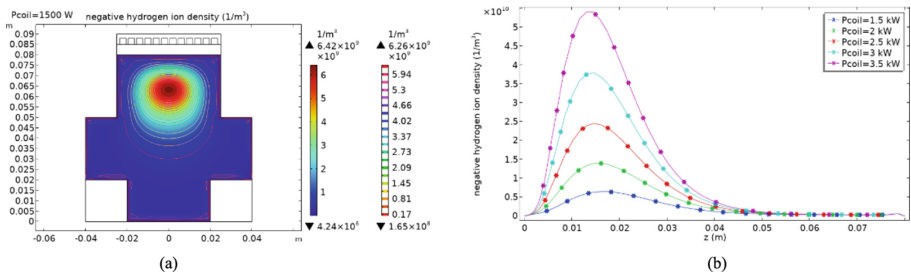

Fig. 12. 2-D profile of the H^- density with the RF power of 1500 W (a); The H^- density in the axial direction for different RF power (b). The discharge pressure is set to 25 Pa, the magnetic filter field intensity is 0.3T.

As shown in Fig. 12, the distribution and variation trend of H^- density are consistent with the density of VEHM.

4.3   Effects of Magnetic Filter Field Intensity

In order to investigate the law of influence of magnetic filter field intensity, the discharge pressure is set to 25 Pa and the RF power is set to 1500 W.

As shown in Fig. 13, the electron density increased in each axial region with an increasing magnetic filter field intensity, but the increase rate in the diffusion region and the magnetic filtration region gradually slowed down.

According to Fig. 14, the electron temperature at different magnetic filter field intensity has a good gradient. As the magnetic filter field intensity increases, the electron temperature decreases in each region of the axial direction.

The filter magnet is designed to increase particle collisions in the magnetic filtration region which is the H^- extraction area, thereby lowering the electron temperature. Since the 2-D model lacks any magnetic field shielding structure, the filter magnet has an inevitably effect on the discharge region and the diffusion region. The intensity distribution of the magnetic filtered field in different regions are shown in Fig. 15 and the variation of H^+ density is shown in Fig. 16.

Fig. 13. 2-D profile of the electron density with the magnetic filter field intensity of 0.3T (a); The axial electron density for different magnetic filter field intensity (b); Radial variation of electron density in the diffusion region (c); Radial variation of electron density in the magnetic filtration region (d). The discharge pressure is set to 25 Pa, the RF power is 1500 W.
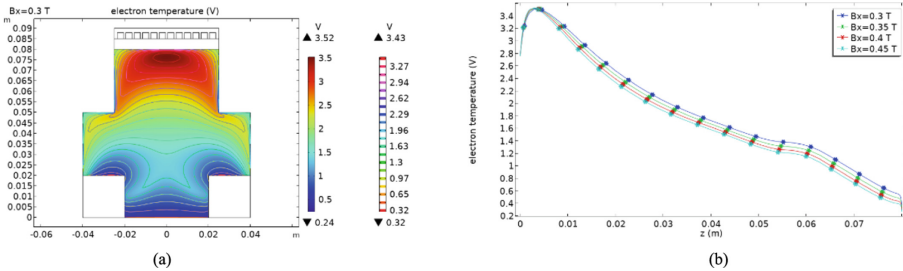
Fig. 14. 2-D profile of the electron temperature with the magnetic filter field intensity of 0.3 T (a); The electron temperature in the axial direction for different magnetic filter field intensity (b). The discharge pressure is set to 25 Pa, the RF power is 1500 W.

According to Fig. 17, the density of VEHM increases gradually in the discharge region, but decreases gradually in the diffusion region and magnetic filtration region as the magnetic field intensity increases. The magnetic filter field will increase the level of collisions between particles. Due to the high electron temperature in the discharge region, it is conducive to the formation of VEHM. As shown in Fig. 14, the electron temperature in the diffusion region and magnetic filtration region decreases continuously, which will reduce the density of VEHM.

The density of VEHM and electron temperature have great influence on the H^- generation. The electron temperature and the density of VEHM with the intensity of the

(a)

(b)

(c)

(d)
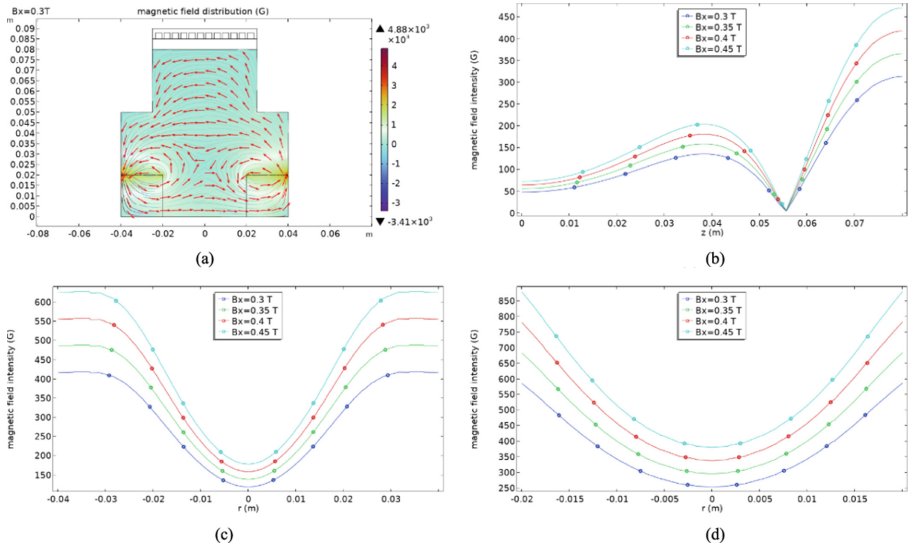
Fig. 15. 2-D profile of the magnetic filter field intensity with the magnetic filter field intensity of 0.3 T (a); The axial magnetic filter field intensity for different magnetic filter field intensity (b); Radial variation of filter magnetic field intensity in the diffusion region (c); Radial variation of magnetic filter field intensity in the magnetic filtration region(d). The discharge pressure is set to 25 Pa, the RF power is 1500 W.

(a)

(b)
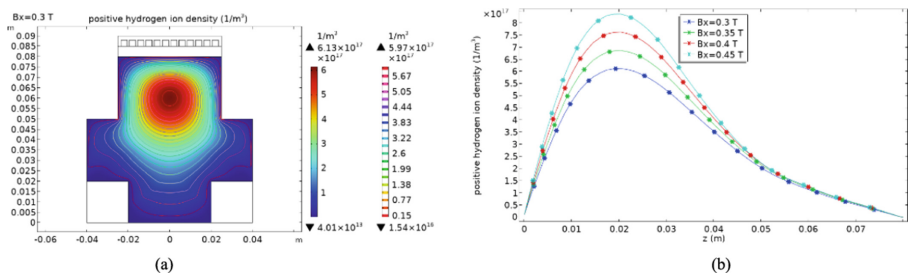
Fig. 16. 2-D profile of the H^+ density with the magnetic filter field intensity of 0.3 T (a); The H^+ density in the axial direction for different magnetic filter field intensity (b). The discharge pressure is set to 25 Pa, the RF power is 1500 W.

magnetic filter field have been discussed above. The final change of H^- density which is shown in Fig. 18 is determined by the change of electron temperature and VEHM density in each region.

4.4 Summary

With the increase of discharge pressure, the electron density and H^+ density both increase in the axial region, the electron temperature decreases in the discharge region and the diffusion region, but slightly increases in the magnetic filtration region; The $H_2(v)$
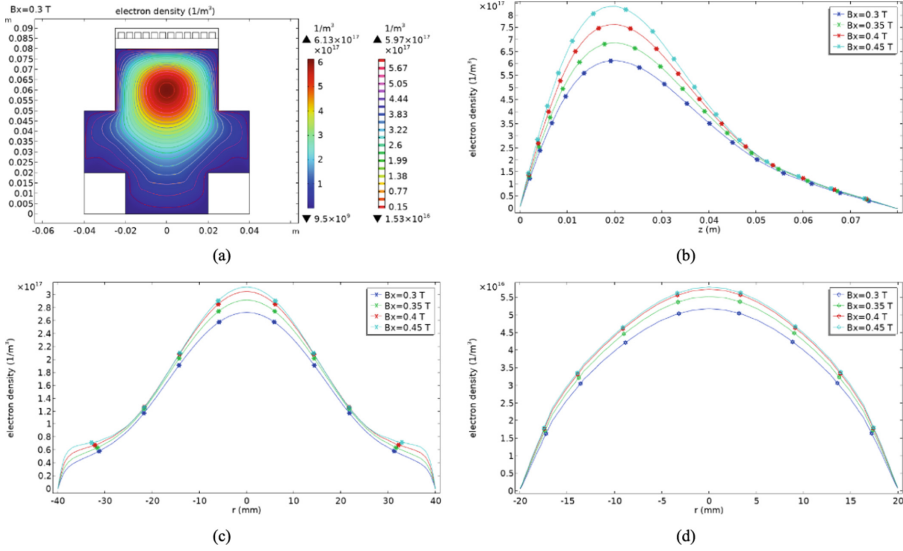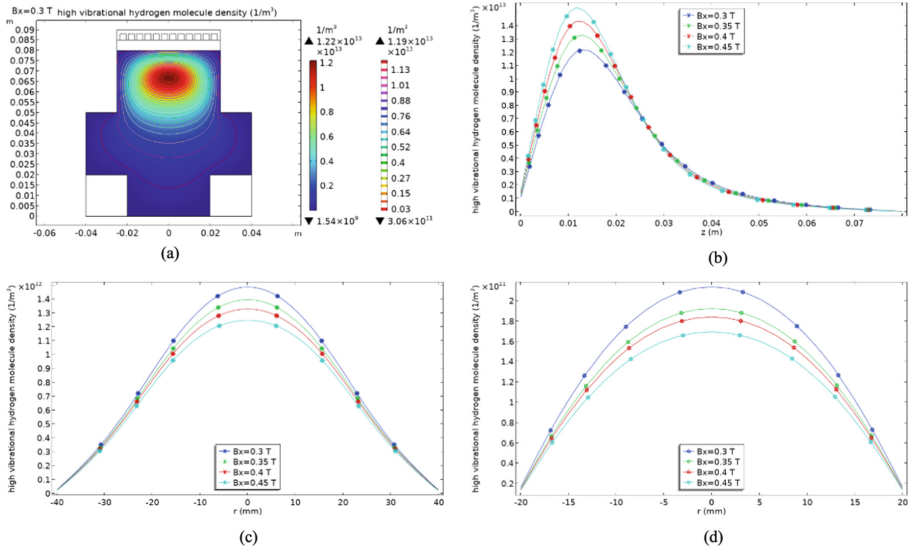
Fig. 17. 2-D profile of the $H_2(v)$ density with the magnetic filter field intensity of 0.3 T (a); The axial $H_2(v)$ density for different magnetic filter field intensity (b); Radial variation of $H_2(v)$ density in the diffusion region (c); Radial variation of $H_2(v)$ density in the magnetic filtration region(d). The discharge pressure is set to 25 Pa, the RF power is 1500 W.

density, H^- density both rise in the discharge region and decrease in the diffusion and magnetic filtration region. Obviously, the high discharge pressure is not conducive to maintaining the low electron temperature in the magnetic filtration region, resulting in the reduction of the H^- density in the extraction area.

With the increase of RF power, the electron density and H^+ density both increase in the axial direction, the electron temperature increases in the discharge region and the magnetic filtration region, but decreases in the diffusion region. The $H_2(v)$ density and H^- density both rise in the discharge region and the diffusion region, while remaining almost unchanged in the magnetic filtration region. The results show that the high RF power does not increase the H^- density in the magnetic filtration region, but will cause the increase of electron temperature in the magnetic filtration region.

With the increase of the magnetic filter field intensity, the electron density and H^+ density both increase in the axial direction, while the electron temperature decreases along the axial direction. The $H_2(v)$ density increases in the discharge region and decreases in the diffusion region and magnetic filtration region. The H^- density increases in the discharge region, rises first in the diffusion region and then falls, and remains almost unchanged in the magnetic filtration region. From the perspective of diffusion region, there is a suitable magnetic filter field intensity which makes the H^- density reach the maximum.
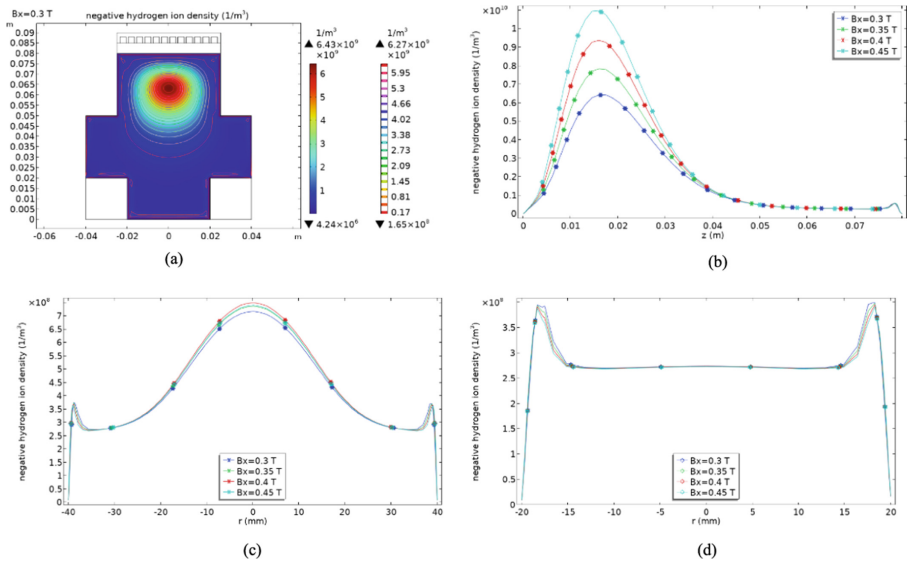
Fig. 18. 2-D profile of the H^- density with the magnetic filter field intensity of 0.3 T (a); The axial H^- density for different magnetic filter field intensity (b); Radial variation of H^- density in the diffusion region (c); Radial variation of H^- density in the magnetic filtration region(d). The discharge pressure is set to 25 Pa, the RF power is 1500 W.

5   Conclusion and Future Study

Based on fluid model simulation, the discharge pressure, RF power and magnetic filter field intensity were parameterized, as well as the changes in electron density, electron temperature, H^+ density, $H_2(\nu)$ density and H^- density were discussed. As described in chapter 4.4, the study of plasma parameter variation rules under different physical conditions is of great significance to optimize the performance of neutron generator and promote the development of API technology.

For the future study, other physical parameters, including chamber size, coil turns and position, will be parameterized. The experiments with RF negative hydrogen source will be carried out to compare the results of the simulation. In addition, the transport of negative hydrogen ion beam will be simulated in order to study the influencing factors of beam spot size.

References

1. Litvak, M.L., Barmakov, Y.N., Belichenko, S.G., et al.: Associated particle imaging instrumentation for future planetary surface missions. Nucl. Inst. Methods Phys. Res. A **922**, 19–27 (2019)

2. Ruskov, I., Kopach, Y., Bystritsky, V., et al.: TANGRA multidetector systems for investigation of neutron-nuclear reactions at the JINR frank laboratory of neutron physics. EPJ Web of Conf. **256**, 00014 (2021)

3. Yakubova, G., Kavetskiy, A., Prior, S.A., et al.: Tagged neutron method for carbon analysis of large soil samples. Appl. Radiat. Isot. **150**, 127–134 (2019)

4. Unzueta, M.A., Ludewigt, B., Tak, T., et al.: Achieving high resolution with an all-digital associated particle imaging system for the 3D determination of isotopic distributions. Rev. Sci. Instrum. **92**, 063305 (2021)

5. Kavetskiy, A., Yakubova, G., Sargsyan, N., et al.: Neutron-stimulated gamma ray measurements for chlorine detection. IEEE Trans. Nucl. Sci. **68**, 1495–1504 (2021)

6. Petrović, J., Göök, A., Cederwall, B.: Rapid imaging of special nuclear materials for nuclear nonproliferation and terrorism prevention. Sci. Adv. **7**, 3032 (2021)

7. Mangiagalli, G., Morichi, M., Pepperosa, A., et al.: Special nuclear material identification through one-minute measurement with a new backpack radiation device in real scenario conditions. Int. J. Safety Security Eng. **11**, 427–433 (2021)

8. Pino, F., Fontana, C.L., Nebbia, G., et al.: Detection module of the C-BORD rapidly relocatable tagged neutron inspection system (RRTNIS). Nucl. Inst. Methods Phys. Res. A **986**, 164743 (2021)

9. Delarue, M., Simon, E., Pérot, B., et al.: Localization of nuclear materials in large concrete radioactive waste packages using photofission delayed gamma rays. EPJ Web of Conf. **253**, 08003 (2021)

10. Hausladen, P.A., Blackston, M.A., Gilbert, A.J., et. al.: Progress on Associate-Particle Imaging Algorithms. ORNL/SPR-2020/1766 (2020)

11. Beyerle, A., Hurley, J.P., Tunnell, L.: Design of an associated particle imaging system. Nucl. Inst. Methods Phys. Res. A **299**, 458–462 (1990)

12. Huang, M., Zhu, J.Y.. Zhu, J.: Study of spatial resolution of the associated alpha particle imaging time-of-flight method. Nuclear Science and Techniques 30:64 (2019)

13. Abel, M.R., Nie, L.H.: Monte Carlo simulations of elemental imaging using the neutron-associated particle technique. Med. Phys. **45**, 1631–1644 (2018)

14. Ji, Q., Ludewigt, B., Wallig, J., et al.: Development of a time-tagged neutron source for SNM detection. Phys. Procedia **66**, 105–110 (2015)

15. Antolak, A.J., Leung, K.N., Morse, D.H., et al.: Negative ion-driven associated particle neutron generator. Nucl. Inst. Methods Phys. Res. A **806**, 30–35 (2016)

16. Kovetz, A.: The Principles of Electromagnetic Theory, Cambridge University Press (1990)

17. Jin, J.: The Finite Element Method in Electromagnetics, 2nd ed., Wiley-IEEE Press (2002)

18. Wangsness, R.K.: Electromagnetic Fields, 2nd ed., John Wiley & Sons (1986)

19. Hagelaar, G.J.M., Pitchford, L.C.: Solving the Boltzmann equation to obtain electron transport coefficients and rate coefficients for fluid models. Plasma Sources Sci. Technol. **14**, 722–733 (2005)

20. Gogolides, E., Sawin, H.H.: Continuum modeling of radio-frequency glow discharges. I. theory and results for electropositive and electronegative gases. J. Appl. Phys. **72**, 3971 (1992)

21. Smirnov, B.M.: Theory of Gas Discharge Plasma. Springer (2015). https://doi.org/10.1007/978-3-319-11065-3

22. McDaniel, E.W.: Collision Phenomena in Ionazed Gases. John Wiley and Sons (1964)

23. Ellis, H.W., Pai, R.Y., McDaniel, E.W., Mason, E.A., Viehland, L.A.: Transport properties of gaseous ions over a wide energy range. At. Data Nucl. Data Tables **17**, 177–210 (1976)

24. Petrov, G.M., Giuliani, J.L.: J. Appl. Phys. **90**, 619 (2001)

25. Janev, R.K., Lan, W.D.: H-HE-PLASMA (1987)

26. Janev, R.K., Smi, J.J.: IAEA-APID-4 (1993)

27. Zammit, M.C., Phys, D.V.: Rev. A **90**, 022711 (2014)

28. Barnett, C.F.: 1990 ORNL-6086 (1990)
29. Krstic, P.S.: 2005 Nuclear Instruments and Methods B, 241 (2005)
30. Booth, J.P., Sadeghi, N.: J. Appl. Phys. **70**, 611 (1991)
31. Lee, C., Lieberman, M.A.: J. Vac. Sci. Technol. A **13**, 368 (1995)

High Voltage Insulation

The Detection of SF_6 Decomposition Components Based on Infrared Laser Spectroscopy

Yufeng Lu[1(✉)], Yi Su[1], Xiajin Rao[1], Xiaoxing Zhang[2], Yijie Cai[2], Zhengyi Zhu[2], and Yin Zhang[2]

[1] Electric Power Research Institute of Guangxi Power Grid Co., Ltd, Nanning 530012, China
`116122474@qq.com`

[2] School of Electrical and Electronic Engineering, Hubei University of Technology, Wuhan 430068, China

Abstract. When SF_6 gas insulated electrical equipment has latent defects, SF_6 insulation gas in the equipment is subject to high temperature or electric arc, which will decompose and generate decomposition products, these products lead to the degradation of insulation and arc extinguishing performance of electrical equipment. It is of great significance to detect the decomposition products of SF_6, which can reflect the internal conditions of the equipment. The main decomposition product of SF_6 is SO_2. In order to detect SO_2 in the electrical equipment, in this paper, an experimental platform for gas detection is built, which is based on infrared spectrum analysis and wavelength modulation technology. Through analyzing the second harmonic waveform of SO_2 with different concentrations, it is concluded that the SO_2 concentration and the average value of the second harmonic peak have a good linearity, and the error analysis of different concentrations of SO_2 is further carried out. The experimental results show that there is a good linear relationship between SO_2 concentration and the average peak value of the second harmonic wave, and the R^2 is 0.992. The inversion error of SO_2 with different concentrations are all within 5%. The experimental results prove that the detection method in this paper can effectively detect trace SO_2.

Keywords: Decomposition products of SF_6 · Infrared spectrum analysis · Wavelength modulation technology · SO_2 detection

1 Introduction

In modern power systems, gas insulated switchgear (GIS) are widely used as important electrical equipment [1]. SF_6 gas has a large number of uses in GIS because of its excellent insulation and arc extinguishing properties [2]. When a partial discharge fault is released inside a gas-insulated combination appliance, it may lead to the decomposition of SF_6 in the equipment [3, 4]. In the process of SF_6 decomposition, a series of unstable low-fluorine sulfides(SF_X, x = 1–5) are generated inside the GIS, and a series of complex chemical reactions occur with other components in the equipment, and decomposition

components such as $CS_2,SO_2,H_2S,SOF_2,SO_2F_2$ are generated [5–8]. The generation of SF_6 decomposition components affects the insulation and arc extinguishing performance of SF_6, and increases the operational risk of GIS. Therefore, the effective detection of SF_6 decomposition components in GIS is of great significance in the safe operation of equipment. As one of the main decomposition components of SF6, the content of SO_2 corresponds to the amount of discharge inside the equipment. Effective detection of SO_2 helps to judge the discharge situation inside the equipment, which is important for the evaluation of the insulation status of GIS [9, 10].

At present, the detection of SF_6 decomposition components mainly includes gas chromatography, mass spectrometry, infrared spectroscopy, electrochemical sensor method, gas detection tube method, ion mobility spectrometry, carbon nanotube sensor [11–14]. Tunable diode laser absorption spectroscopy (TDLAS) is a technique for monitoring trace gases in the atmosphere. The technology uses a tunable semiconductor laser to measure a single or several absorption lines. [15]. The method has the advantages of fast response time, high sensitivity and strong anti-interference ability. Molecules in the mid-infrared region have a stronger vibrational transition frequency than in the near-infrared region, and the sensitivity of gas detection using the mid-infrared band is higher than the near-infrared band, SO_2 has absorption peaks in mid-infrared and near-infrared. Therefore, mid-infrared TDLAS can accurately detect changes in SO_2.

In this paper, the infrared spectrum of SO_2 gas is analyzed in depth, and a SO_2 gas detection method based on mid-infrared laser spectroscopy is proposed. The mid-infrared TDLAS is selected to build a SO_2 detection experimental platform based on mid-infrared tunable laser spectroscopy. In the mid-infrared band, by analyzing the detection signals of different concentrations of SO_2, the linear relationship between the second harmonic signal and the gas concentration value is obtained, and the quantitative detection of SO_2 is realized.

2 Principle of Detection

2.1 Detection Band Selection

For the selection of the SO_2 detection band, the absorption spectrum of SO_2 is simulated using the HITRAN database. The absorption peaks of SO_2 in the mid-infrared and near-infrared regions are obtained.

The absorption of SO_2 gas is shown in Fig. 1 and Fig. 2. In the near-infrared region, SO_2 has infrared absorption peaks in the range of 4000–4093 cm^{-1}, but the absorption spectral intensity of SO_2 is low compared to the spectral intensity of SO_2 gas in the mid-infrared region. Therefore, the detection band of SO_2 is selected in the mid-infrared region to enhance its spectral absorption.
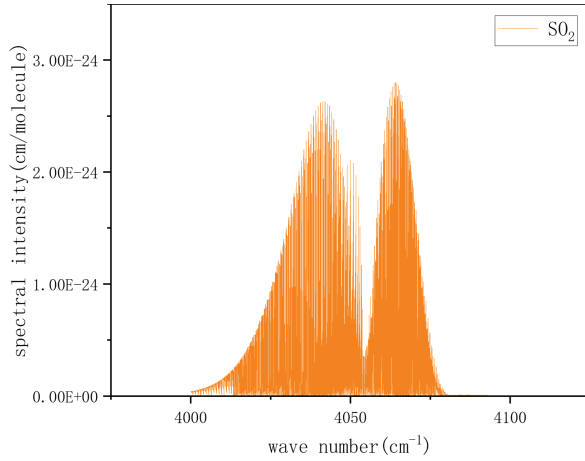
Fig. 1. Spectral line intensity of SO$_2$ gas in near infrared region
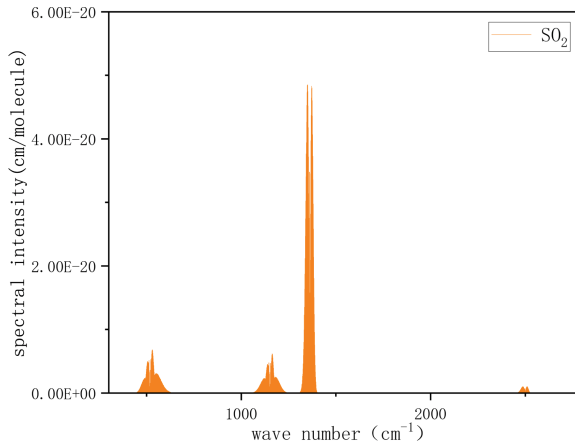
Fig. 2. Spectral line intensity of SO$_2$ gas in mid-infrared region

2.2 Wavelength Modulation

This study is based on the wavelength modulation technique. The concentration of the measured gas is inferred by measuring the harmonic peak. The measurement principle is shown in Fig. 3.

Harmonic modulation uses a high-frequency sine wave as the wavelength modulation signal and a sawtooth wave as the wavelength scanning signal to scan the gas in wavelength range. The output light intensity I (v,t) is obtained by the Beer-Lambert law.

↓

The output light intensity is Fourier expanded to obtain the first harmonic I_f and the second harmonic I_{2f}.

↓

Improve the sensitivity of gas volume fraction detection by calculating I_{2f}/I_f and eliminating the effect of output light intensity on detection results

↓

Since the I_{2f}/I_f peak corresponds to the absorption peak of the absorption spectrum of the measured gas, the concentration of the measured gas can be inverted by measuring the peak of I_{2f}/I_f

Fig. 3. Wavelength modulation principle

3 Experimental Platform

The experimental platform of SO_2 detection based on mid-infrared TDLAS built in this paper is shown in Fig. 4.
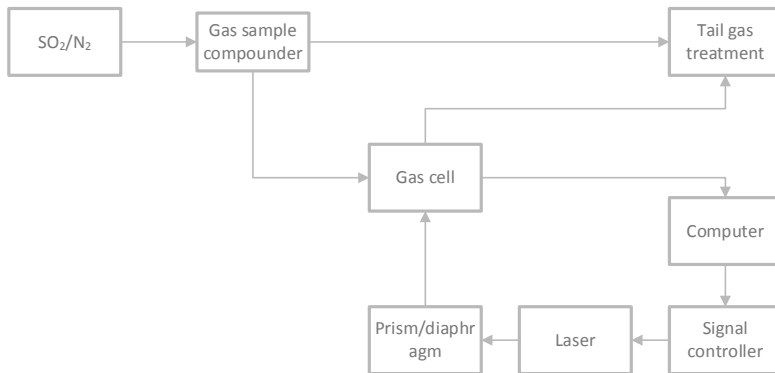
Fig. 4. SO_2 detection experiment platform

The experimental platform is mainly composed of laser, gas absorption cell, photoelectric detector, signal controller, gas sample compounder, upper computer terminal and so on. Quantum cascade laser is selected as the laser, and the output band is

1353 cm^{-1}–1356 cm^{-1}. The laser output band can be adjusted by temperature and driving current.

The gas absorption cell adopts the Herriot type structure with a light range of 15 m. Reflectors are set on both sides of the gas absorption cell to reflect the incoming laser light several times and improve the absorption of infrared laser light by the detection gas in the cell. The inner wall of the cell is coated with corrosion-resistant material to prevent SO$_2$ adsorption and corrosion.

The optical path of the device adopts the spatial optical path, and there is a collimator mirror to adjust the incident laser at the laser outlet and the incidence of the absorption cell. Gas sample compounder can be configured µL/L level of the experimental gas, the maximum dilution ratio of 300:1.

4 Experimental Result Analysis

4.1 SO$_2$ Concentration Detection

In the experiment, 52.2 µL/L gas is used as the standard gas to prepare the experimental gas, and the SO$_2$ experimental gas with the concentration of 50.01 µL/L, 34.75 µL/L, 24.92 µL/L, 10.02 µL/L and 1.08 µL/L is prepared. During the experiment, the temperature is constant at 25 °C. The gas absorption cell is first cleaned by high-purity helium at a constant flow rate of 500 mL/min for several minutes to remove the interference of impurities in the gas absorption cell. After cleaning the gas absorber cell, different concentrations of SO$_2$ experimental gas are passed into the gas absorber cell at a constant flow rate of 500 mL/min, and the optical signal is detected by a photoelectric sensor, and the optical signal is processed and displayed in the upper computer. The second harmonic waveform is shown in Fig. 5. This range of second harmonic peaks can be used for SO$_2$ concentration detection.
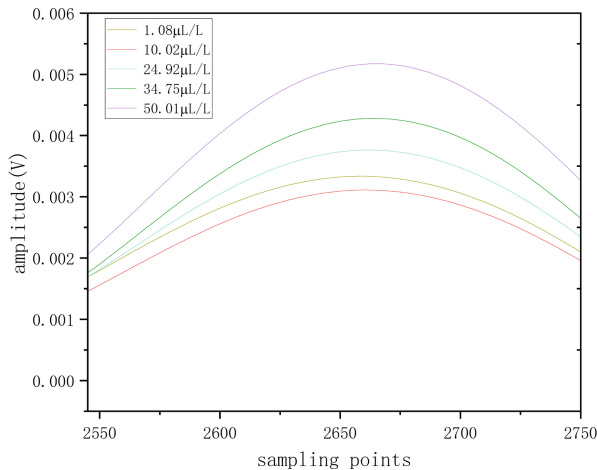
Fig. 5. The second harmonic waveform of different concentration of SO$_2$

For the selected second harmonic peaks, different concentrations of SO_2 experimental gas are used for testing, and SO_2 experimental gases with concentrations of 50.01 μL/L, 34.75 μL/L, 24.92 μL/L, 10.02 μL/L, and 1.08 μL/L are prepared by using a dynamic gas distributor and passed into the gas absorption cell, and different concentrations of SO_2 are passed into the gas absorption cell at a constant flow rate of 500 mL/min during testing. 500 s harmonic peaks are taken for each concentration separately and averaged to reduce the effect of random errors, and the average values of the second harmonic peaks at each concentration are shown in Table 1.

Table 1. Different concentration of SO_2 corresponds to the average value of the second harmonic peak value

SO_2 concentration (μL/L)	Average value of the second harmonic peak
50.01	0.004 926
34.75	0.004 415
24.92	0.003 952
10.02	0.003 309
1.08	0.003 127
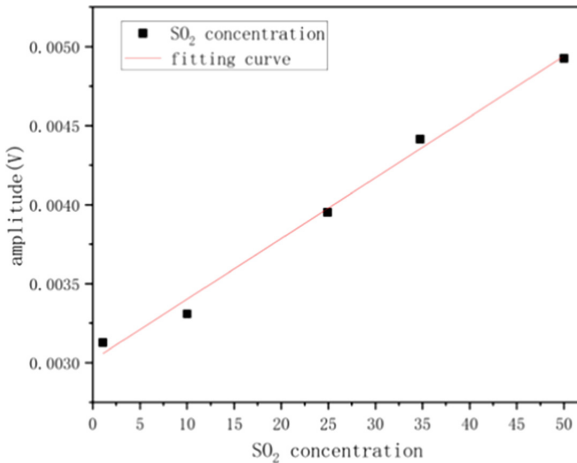
Fig. 6. Correspondence between different concentrations of SO_2 corresponding to the average value of the second harmonic peak value

The linear relationship between SO_2 gas concentration and the average value of the second harmonic peak is fitted from the data in Table 1, and the fitting curve is shown in Fig. 6.

From the results of the analysis of the second harmonic data of different concentrations of SO_2, it can be obtained that there is a good correlation between the concentrations. The linear relationship between SO_2 gas concentration and the average value of the

second harmonic peak can be obtained by the fitting calculation as y = 0.0000384641x + 0.00302, and its linear fit goodness R^2 is 0.992, which has a good linearity.

4.2 Different Concentrations of SO$_2$ Gas Verification

Validation analysis is performed for the fitted curves obtained from the above experiments. SO$_2$ experimental gases with concentrations of 4.99 µL/L, 15.02 µL/L, 30.04 µL/L and 39.88 µL/L are prepared using 52.2 µL/L of SO$_2$ gas as the standard gas for SO$_2$ experimental gas testing. For each concentration, 500 s harmonic peaks are taken and averaged, and the average values of the second harmonic peaks at each concentration are shown in Table 2.

Table 2. Different concentration of SO$_2$ corresponds to the average value of the second harmonic peak value

SO$_2$ concentration (µL/L)	Average value of the second harmonic peak
39.88	0.004 605
30.04	0.004 220
15.02	0.003 444
4.99	0.003 206

Table 3. Error analysis of different concentrations of SO$_2$

SO$_2$ Concentration (µL/L)	Average Value of the Second Harmonic Peak	Second harmonic peak fitting value	Error (%)
39.88	0.004 605	0.004 554	1.11
30.04	0.004 220	0.004 175	1.06
15.02	0.003 444	0.003 598	4.46
4.99	0.003 206	0.003 191	0.19

The measured SO$_2$ concentration value is substituted into the fitting curve obtained above, the fitting value of the second harmonic peak is calculated, and the error between the fitting peak and the actual peak is analyzed. The error is shown in Table 3. The errors between the actual and fitted second harmonic peak values of SO$_2$ experimental gases with concentrations of 4.99 µL/L, 15.02 µL/L, 30.04 µL/L and 39.88 µL/L are no more than 5%, and most of the errors between the actual and fitted values are within 2%, and the average values of SO$_2$ concentration and second harmonic peak had a good linear relationship.

4.3 Response Speed and Recovery Time

The response speed and recovery time is a measure of the detection sensitivity of the platform during continuous detection. Since different concentrations of SO$_2$ gas pass

through the detection device at a constant flow rate during the detection process, the sensitivity of the detection device to different concentrations of SO_2 gas has an impact on the detection time and gas consumption. Therefore, the response speed and recovery time of the detection platform need to be analyzed.

A dynamic gas distributor is used to prepare 20 µL/L and 0 µL/L of SO_2 experimental gas for response rate and recovery time testing, and the flow rate of both gases is controlled to 500 mL/min during the testing period.

The experiments are conducted at ambient temperature and pressure with a total measurement time of 2500 s. The experiments are conducted by passing high purity nitrogen gas to be stabilized and then passing SO_2 experimental gas with a concentration of 20 µL/L, and then continuing to pass high purity nitrogen gas after stabilization. From the experimental results, the response time of the experimental gas from low concentration to high concentration is slower than the recovery time from high concentration to low concentration. The two times are 202.2 s and 49.4 s respectively. Response time and recovery time include gas line switching time and gas distribution time.

5   Conclusion

In this paper, we firstly briefly discuss the necessity of SO_2 detection, introduce the principle of TDLAS detection, and build a test platform for SO_2 detection based on mid-infrared TDLAS to detect different concentrations of SO_2 gas.

1) HITRAN is used to simulate the near-infrared and mid-infrared absorption bands of SO_2. In the near infrared band, the absorption line intensity of SO_2 is weak. In the mid-infrared band, the spectral absorption capacity of SO_2 is strong, so the mid-infrared band can be used as an effective detection band.
2) The linear relationship between the second harmonic peak and the concentration of SO_2 is established by detecting different concentrations of SO_2 experimental gas and extracting the second harmonic peak, and the linearity of the goodness of fit R^2 is 0.992. Four different concentrations of SO_2 experimental gases are used to verify the obtained SO_2 fitting curve. The verification results showed that the fitting curve is effective for different concentrations of SO_2, and the detection of low concentration SO_2 is realized within the allowable range of error.
3) The response speed and recovery time of the device are studied by using different concentrations of SO_2 experimental gas, and the response speed and recovery time of the device are 202.2 s and 49.4 s.

References

1. Cai, T., Wang, X., Zhu, Y.: Quantitative analysis for SF$_6$ and its compositions in GIS. High Voltage Eng. **36**(10), 2478-2482 (2010)
2. Zhou, W., Zheng, Y., Yang, S., et al.: Research progress and trend of SF$_6$ alternative with environment friendly insulation gas. High Voltage Apparatus **52**(12), 8–14 (2016)
3. Cui, Z., Meng, F., Cheng, Z., et al.: Quantitative detection of the CS$_2$ produced by sf$_6$ decomposition based on ultraviolet differential optical absorption spectrometry. Trans. China Electrotechnical Society **33**(18), 4389–4396 (2018)
4. Zhang, X., Ren, J., Xiao, P., et al.: Multi-wall carbon nanotube films sensor applied to SF$_6$ PD detection. Proceedings of the CSEE **29**(16), 114–118 (2009)
5. Huang, J., Liu, C., Liu, Y., et al.: Characteristics of partial discharges at metal protrusion under oscillating impulse V oltages in SF$_6$ gas. High Voltage Eng. **41**(11), 3872–3880 (2015)
6. Zhang, X., Wu, F., Tie, J., et al.: TiO$_2$ nanotube array sensor for detecting SF$_6$ decomposition component SO$_2$F$_2$. High Voltage Eng. **40**(11), 3396–3402 (2014)
7. Zhang, X., Wu, F., Tie, J., et al.: Simulation on the b-doped single-walled carbon nanotubes detecting the partial discharge of SF$_6$. High Voltage Eng. **37**(07), 1689–1694 (2011)
8. Ren, M., Dong, M., Ren, Z., et al.: Transient earth Voltage measurement in PD detection of artificial defect models in SF$_6$. IEEE Trans. Plasma Sci. **40**(8), 2002–2008 (2012)
9. Zhang, X., Zhou, H., Cui, Z., et al.: Quantitative detection of SO$_2$, a characteristic decomposition product of SF$_6$ using ultraviolet fluorescence method. Electric Power Automation Equipment **38**(06), 177–182 (2018)
10. Wang, H., Li, X., Li, Z.: Research progress of SO$_2$and H$_2$S gas sensors for insulation fault detection of SF$_6$ electrical equipment. High Voltage Apparatus **55**(08), 1-9 (2019)
11. Dou, X., Ye, R., Fu, J., et al.: Research status of SF$_6$ gas decomposition products detection methods and their application. Power Syst. Clean Energy **35**(07), 24-31 (2019)
12. Yang, Y., Xu, H., Wu, J., et al.: Research status and development of SF$_6$ decomposition products detection technology. Zhejiang Electric Power **35**(10), 15–21+39 (2016)
13. Zhang, X., Fang, J., Cui, H., et al.: Review: adsorption principle and application of carbon nanotubes to SF$_6$ decomposition components. Proceedings of the CSEE **38**(16), 4926–4941+4997 (2018)
14. Zhai, X., Shi, H., Liu, X., et al.: Review of SF$_6$ decomposition detecting methodology for SF$_6$ electrical devices based on optical technology. Industrial Safety Environ. Protection **44**(01): 61-64 (2018)
15. Kan, L., Ye, L., Wang, X., et al.: Methane gas concentration recognition system based on TDLAS. Control and Instruments in Chemical Industry **48**(02), 122–127+133 (2021)

500 kV GIS Branch Bus Bar Grounding Scheme Optimization and Heat Verification

Huang Wentao[1], Zhang Yaqi[2], and Han Yongxia[1(✉)]

[1] School of Electric Power Engineering, South China University of Technology, Guangzhou 510006, China
`epyxhan@scut.edu.cn`
[2] College of Automation, Guangdong Polytechnic Normal University, Guangzhou 510665, China

Abstract. The Gas Insulated Switchgear (GIS) with voltage levels of 500 kV and above adopts three-phase sub-box structure, so the electromagnetic induction effect generated by wire current may generate a large induction current on the shell, as well as its connection and support components, which will further cause local heating and affect the insulation performance of the equipment. However, the accuracy of GIS circulation calculation in existing studies is insufficient. As for the grounding scheme, there are only regular optimization measures, no heating check of full current-carrying components, and no measured data for verification. Therefore, it is essential to establish an electromagnetic transient model to calculate GIS branch bus circulation accurately, design a grounding scheme and perform heat verification. In this paper, a GIS coupling model considering the phase difference of three-phase current is built to calculate the circulation. Besides, the influence of the terminal collector strip, the scheme of grounding wire and shorting strip on circulation is analyzed. Furthermore, a two-dimensional flow-temperature field coupling model is established using finite element simulation method to calculate the heating of each current-carrying component and ensure that the temperature result in the optimized scheme does not exceed the limiting value. Finally, the optimization measures of grounding scheme are put forward to reduce the circulation.

Keywords: GIS · Circulation · Grounding Scheme · Finite Element · Heat Verification

1 Introduction

Gas Insulated Switchgear (GIS) with voltage level of 500kV and above adopts a structure of independent cabinets in three phases. Thus, there is a strong electromagnetic coupling between the conductor and the enclosure [1], which causes the growth of the potential on the enclosure and generates a large circulation current and ground current between the enclosure and the grounding device. This current will further aroused heating of the enclosure and grounding equipment, accelerate the aging of the equipment and even threaten the safe operation of the system [2–4].

For the calculation methods of circulation current and ground current, the main problems are insufficient accuracy of calculation of equivalent circuit parameters of GIS branch bus and insufficient accuracy of electromagnetic transient simulation modeling method.

Firstly, the establishment of the 500 kV GIS branch bus model should not only considers the electromagnetic induction of the phase wire to the enclosure, but also considers the induction of the other two-phase wires to the phase enclosure. Considering the small capacitive coupling at power frequency, the influence of coupling capacitance between enclosures has been ignored in existing studies. The mutual inductance calculation methods of conductors and enclosures are mostly based on theoretical calculations, which means the magnetic flux and inductance are calculated based on the law of electromagnetic induction [2, 5], dividing the conductor into different inductor units according to the Partial Element Equivalent Circuit (PEEC) algorithm [6] or estimating based on empirical formulas [7]. However, the theoretical results of inductance based on actual engineering parameters are quite different from the simulation results of the finite element model.

Secondly, for the calculation of the induced current of enclosure and the current of the ground strips, the literatures [1, 3, 8] use the electromagnetic transient program EMPT, finite element or MATLAB-SIMULINK to build the model respectively. Most of the existing literature has regarded the coupling effect of GIS conductor and enclosure as the T-type equivalent of space transformer. However, for the modeling of the three-phase independent structure, the phase difference of current is not considered, so the rationality of the model under different conditions is controversial.

Besides, the optimization of grounding scheme in domestic and foreign literature only considers reducing the circulating current of GIS enclosure or grounding current alone. For example, the literature [6] proposes a method to reduce the enclosure circulation by adjusting the GIS structural parameters and adding grounding points, but does not verify whether the ground circulation exceeds the limit after the improvement. Literatures [7, 8] offer an approach to reduce ground circulation by adding shorting strips, but does not take into account that the optimized enclosure circulation may reached the upper limit. At present, there is no research on the optimization method of grounding scheme that comprehensively considers the simultaneous reduction of enclosure circulation and ground current.

Furthermore, it is obvious that the calculation results will affect the temperature rise calculation results of each device [4]. Aiming at the calculation of equipment temperature rise caused by circulating current and grounding current, the existing research mainly establishes a finite element model of electromagnetic-flow-temperature coupling field for single-phase busbars. The literatures [9–15] were studied on the rationality of heat exchange process simplification, parameter dynamic characteristics, accuracy of simulation results, and temperature calculation fitting formula. The accuracy of the model has been widely recognized, but the thermal calculation of non-current-carrying equipment does not take into account, and only the heat verification is performed for GIS conductor and enclosure [16].

In order to solve the above problems, this paper first uses the finite element method to calculate the accurate coupling parameter equivalent circuit of each component. Then

uses PSCAD to build a 550 kV GIS branch bus electromagnetic transient model considering the phase difference of the three-phase current to calculate the circulation current. Besides, this thesis compares and analyzes the influence of different laying schemes of shorting strips on the current calculation results. Moreover, the COMSOL is used to build a magnetic-flow-temperature field finite element model to verify the temperature rise of key components. Finally, the suggestions for the optimization of GIS branch bus grounding scheme are summarized.

2   Calculation Model of 500 kV GIS Enclosure Circulation

2.1   GIS Structure and Coupling Parameter Calculation

The material of 550 kV GIS conductor and enclosure is aluminum alloy and the insulating gas is SF_6. The specific structural parameters are shown in Table 1 and the electrical parameters are shown in Table 2.

Table 1.   Structure Parameters of GIS Branch Bus

Parameter	Value	Unit
Rated Voltage	500	kV
Rated Current	4000	A
Rated Frequency	50	Hz
Outer Diameter of Enclosure	2.54E−01	m
Enclosure Thickness	8.00E−03	m
Outer Diameter of Conductor	8.00E−02	m
Conductor Thickness	1.00E−02	m
Rated Density of Insulated Gas	39.6	kg/m^3
Rated Pressure of Insulated Gas	0.4	MPa
Phase Spacing	1/1.5	m
Height	5.175/6.97	m

Table 2.   Electrical Parameters of GIS Branch Bus

Component	Self-induction (H/m)	Resistance (Ω/m)	Capacitance (F/m)
Enclosure	2.29E−07	6.90E−06	4.40E−11
Conductor	2.29E−07	8.00E−06	4.40E−11

    The two-dimensional static magnetic field model is established using finite element simulation software to calculate the mutual inductance parameters. The magnetic flux density distribution diagram of GIS branch bus finite element simulation is shown in Fig. 1 and Table 3 shows the mutual inductance calculations between the shell and the three-phase conductor.
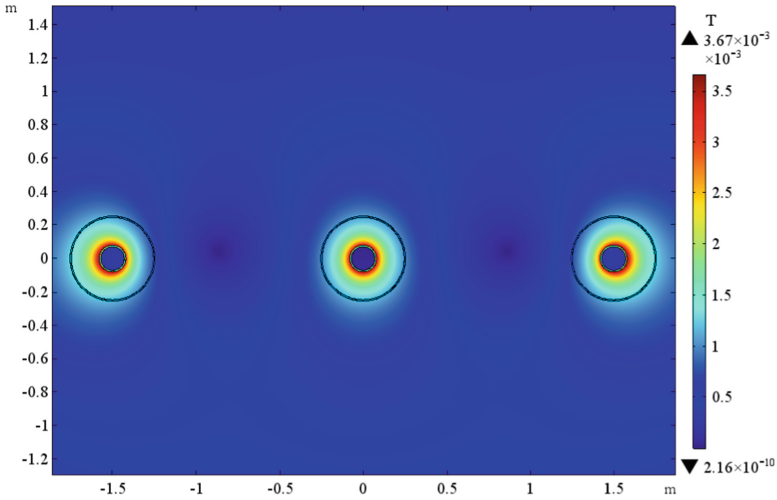
Fig. 1. GIS Branch Bus Finite Element Simulation Magnetic Flux Density Distribution

Table 3. Finite Element Calculation Results of Mutual Inductance Parameters

Mutual Inductance Between Enclosure and Conductor	Finite Element Calculation Results (H/m)
M_{AA}	2.19E−07
M_{AB}	2.39E−08
M_{AC}	1.14E−08
M_{BB}	2.19E−07
M_{BA}	2.42E−08
M_{BC}	2.42E−08
M_{CC}	2.19E−07
M_{CA}	1.14E−08
M_{CB}	2.39E−08

The specifications of the shorting strip and the grounding wire should compliance with standards of grounding current, fault duration and melting temperature of grounding wire material. The specific parameters are shown in Table 4, where the copper resistivity is 1.75×10^{-8} ($\Omega \cdot$m).

The circuits equivalent of the shorting strip and grounding wire are inductor and resistance series circuits. The resistor and inductance are calculated as follows [4, 17].

$$R = \rho \frac{l}{\omega t} \tag{1}$$

Table 4. Specifications of Shoring Strip and Grounding Strip

Shoring Strip	Indoor (mm × mm)	Cu 2 × 100 × 10
	Outdoor (mm × mm)	Cu 2 × 100 × 10
Grounding Strip	Indoor (mm × mm)	Cu 50 × 6
	Outdoor (mm × mm)	Cu 40 × 5

$$L = \frac{\mu_0 l}{2\pi}\left(ln\frac{2l}{\omega + t} + 0.5\right) \tag{2}$$

where ρ is the copper resistivity (1.74×10^{-8}(Ω/m)); μ_0 is the vacuum permeability ($4\pi \times 10^{-7}$(H/m)); l is unit length (m); ω is the cross-sectional length (m); t is the cross-sectional width (m). The calculation results are shown in Table 5.

Table 5. Equivalent Circuit Parameter of Shoring Strip and Grounding Strip

Component	Type	Resistance (Ω/m)	Inductance (H/m)
Shoring Strip	Indoor	5.80E−05	8.15E−07
	Outdoor	8.70E−05	8.59E−07
Grounding Strip	H Grounding	8.70E−06	6.63E−07
	H shorting	8.70E−06	6.63E−07
	E Indoor Grounding	5.80E−05	8.15E−07
	E Outdoor Grounding	8.70E−05	8.59E−07
	W Grounding	8.70E−05	8.59E−07
	ES/FES Grounding	5.80E−05	8.15E−07

The resistivity of steel is 9.78×10^{-8} (Ω/m), and the grounding resistance is 0.5 (Ω). Similarly, the equivalent circuit parameters of the bracket can be obtained as shown in Table 6.

Table 6. Equivalent Circuit Parameter of Holder

Holder	Impedance (Ω)
Single Phase Holder	0.534∠19.80°
Bushing Holder	0.505∠8.28°
VT Holder	0.510∠10.62°

2.2 Coupled Model Considering the Phase Difference

In this paper, a coupling model considering the phase difference of the three-phase current is used to construct a 500 kV GIS whole line electromagnetic simulation model. A schematic of the three coupling models is shown in Fig. 2. M_{XY} represents the mutual inductance between the X-phase conductor and the Y-phase shell (X = A,B,C; Y = A,B,C), I_{Xcon} represents the X-phase conductor current (X = A,B,C), I_{Xout} represents the X-phase conductor current (X = A,B,C), I_{Xd} represents the grounding current (X = A,B,C), and R_j and L_j represent equivalent resistance and inductance of grounding wire separately (j = 1,2,3…).
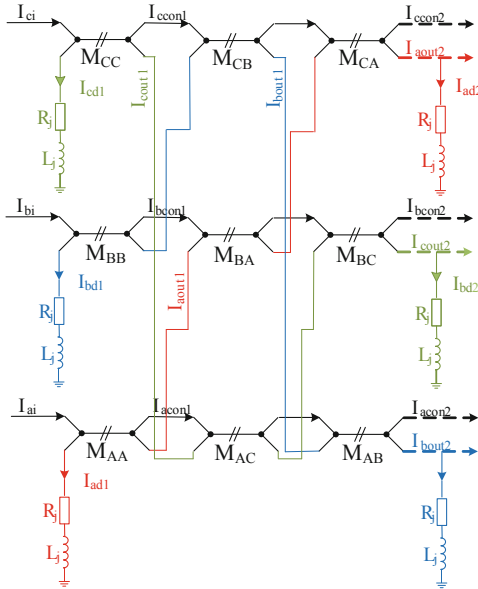
Fig. 2. Coupling Model Considering the Three-phase Difference

The actual GIS line routing diagram is shown in Fig. 3: the line is divided into twenty sections with A phase as the reference. The head of the line is connected to a HVDC transformer with the grounding strips led down from the shell and then connected between phase, while the end is connected to the circuit breaker. Meanwhile, there are six three-phase shorting strip set in the middle of the line, which the single grounding strip is set in the middle of the B and C phases. Moreover, there are two single-phase grounding in the middle. The connection represented by the letters in the figure is as follows: H represents that the enclosure is led down by the copper bar and then shorted in three phases; E indicates that the enclosure is single-phase grounded; W means that the three-phase enclosure is shorted and then grounded; ES/EFS stands for single-phase holder surface-mounted copper bar grounding.
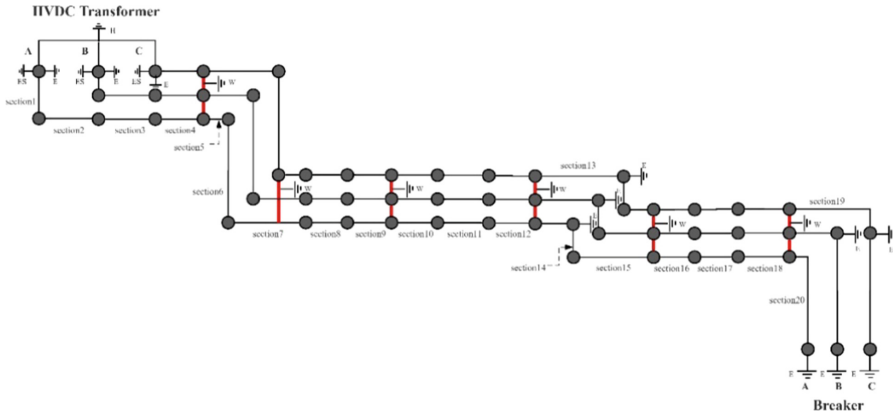
Fig. 3. Schematic Diagram of GIS (Original Scheme)

The RMS values of enclosure circulation, induced voltage, shorting strip current, and ground current are shown in Fig. 4. Firstly, the overall circulating of the enclosure showed a trend of high in the middle and low at both ends. The maximum value appeared in the A and C phases between the 13rd and the15th section, reaching 3.42 kA. This is because the enclosure current is looped through the shorting strips especially the strips close to the end of the line. That is also the reason why the current of the end shorting strip is as high as 3.09 kA. Secondly, the induced voltage and ground current show the opposite U-shaped trend of high at the middle and low at end. The maximum induced voltage appears at the head of the line and the maximum ground current occurs at the head of the line, reaching 4.82 V and 9.62 A separately. This is due to the distribution of the induced voltage generated in each section of the enclosure along the line. The enclosure circulation forms a loop through the ground flowing from one grounding point to another and the direction of the induced voltage of each section is consistent, resulting in the higher the induced voltage value closer to the two ends, as well as the greater the grounding current, which can be seen from the principle of circuit superposition.

3 Simulation Comparison of Shorting Strip Laying Scheme

3.1 The Ground Form of the Shorting Strip at the Head of the Line

The GIS branch bus is connected to a HVDC transformer at the head of line and a circuit breaker at the end. The span is much larger than in the middle of the line. There are two schemes for using copper strip to shorting between phases in the first section: the existing scheme is to use copper row to lead down initially and connect three-phase on the ground subsequently and then access to the ground network; The comparison scheme is to connect a single copper bar to the ground grid after connecting three-phase shorting strips at the enclosure, as shown in Fig. 5.

a) Enclosure Circulation (RMS)

b) Induction Voltage on the Enclosure (RMS)

c) Current of Shorting Strip (RMS)

d) Grounding Current (RMS)

Fig. 4. Current and Voltage Calculation Results of GIS

a) Original Scheme

b) Comparison Scheme
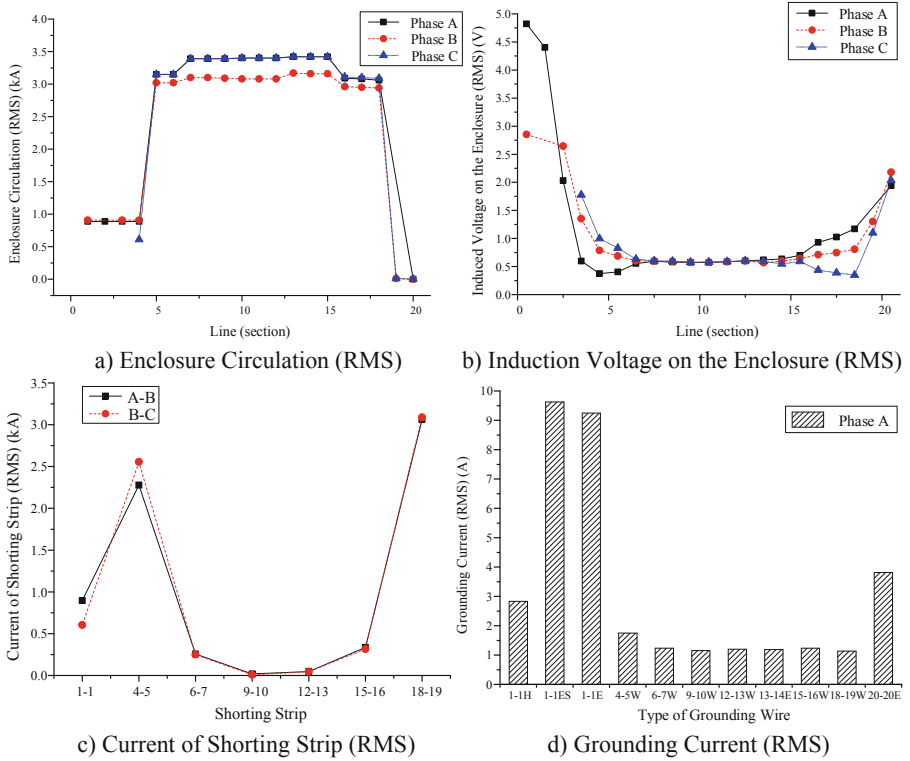
Fig. 5. Two Grounding Schemes of the First Shorting Strip

The current calculation results for both schemes are shown in Fig. 6. The calculation results illustrate that the first-end shorting strip only has a slight effect on the current and voltage calculation results at the head of the line and has almost no effect on the middle and end of lines. Compared with the original scheme, the growth is slight in the

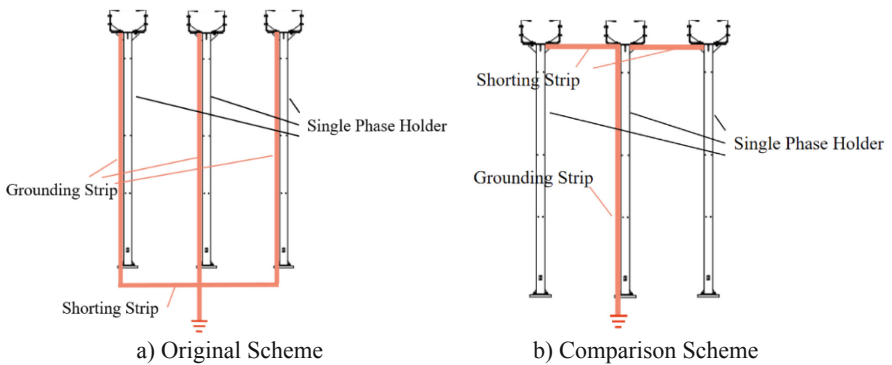circulating current of the first section of enclosure about 0.37 kA (+41.57%), as well as the current of first shorting strip about 0.36 kA (+40.00%) and the ground current of the first shorting strip about 1.35 A (+47.70%). On the contrary, there is a modest decrease of 0.55 V (−11.39%) in the induced voltage and 1.11 A (−11.54%) in the ground current of the first section. The enclosure circulation and the first end of the shorting strip current have increased, but do not affect the heating verification and component specification selection with the maximum value of the whole line as the input. Although the grounding current of the first shorting strip will increase (<1.5 A), it has little impact on the heating check and specification of the grounding bar. However, it is recommended that the first-end shorting strip adopt the scheme of leading down and then connecting considering the large distance in phases, in order to improve the mechanical properties of wind and earthquake resistance.

a) Enclosure Circulation (RMS)   b) Induction Voltage on the Enclosure (RMS)

c) Current of Shorting Strip (RMS)   d) Grounding Current (RMS)
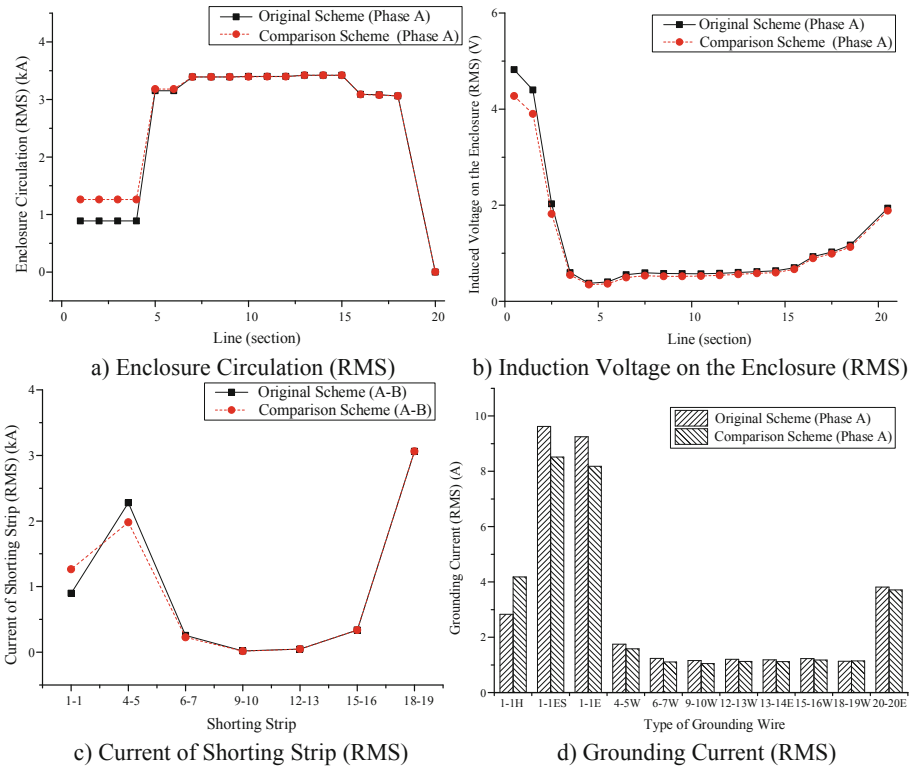
Fig. 6. Calculation Results Under 2 Schemes of First Shorting Strip

3.2 The Ground Form of the Shorting Strip in the Middle of the Line

The phase spacing in the middle of the GIS line does not exceed 1.5 m and the the layout scheme is to short-circuit and then lead down to ground. In order to analyze

the influence of the different grounding scheme of shorting strips on the calculation results, the following two schemes are designed: the original scheme is to access a single ground bar between the B and C phases; the comparison scheme is that the three phases are grounded separately, as shown in Fig. 7.
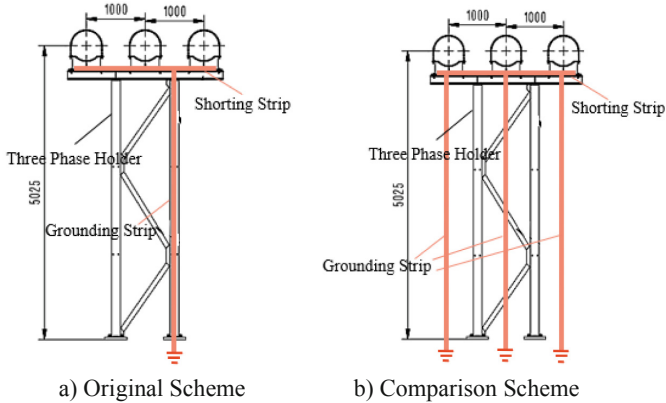

a) Original Scheme   b) Comparison Scheme

Fig. 7. Two Grounding Schemes of Middle Shorting Strip

The current calculation results for both schemes are shown in Fig. 8. It can be seen from the results that the grounding form of the shorting strip has basically no effect on the circulation of the enclosure and shorting strips. However, considering the actual economic point of view, it is suggested that the shorting strip in the project should adopt the form of accessing a single ground strip between two phases (A/B or B/C).

3.3   Shorting Strip Laying Scheme in the Middle of the Line

Three typical layout schemes of shorting strips are designed to analyze the influence of the mid-line short strip laying on the current calculation results, as shown in Fig. 9. Figure 9 a) is the first scheme, that is, no shorting strip is laid in the middle of the line; b) for option two, to add shorting strip between Sect. 4 and 5, 18 and 19 (close to the side); c) for option three, to add shorting strips between Sect. 6 and 7, 15 and 16 (near the inside).

The calculation results under the four schemes, including the original scheme, are shown in Fig. 10. In scheme 1, the circulating current of the enclosure in the middle of the line does not increase significantly and the current of the whole line is less than 1.5 kA, but the induced voltage and grounding current increase remarkably in the middle and back sections of the line reaching the maximum at the end of the line (induced voltage: 16.73 V, grounding current: 32.70 A). The key reason is that the circulation only forms a loop through the steel holder and the grounding bar, which could be equivalent to the impedance of the two paths in parallel. While the steel impedance is greater than the copper shorting strip and greater than the copper grounding strip, so that the circulation is mainly carried by the grounding wire. Meanwhile, the three-phase spacing between
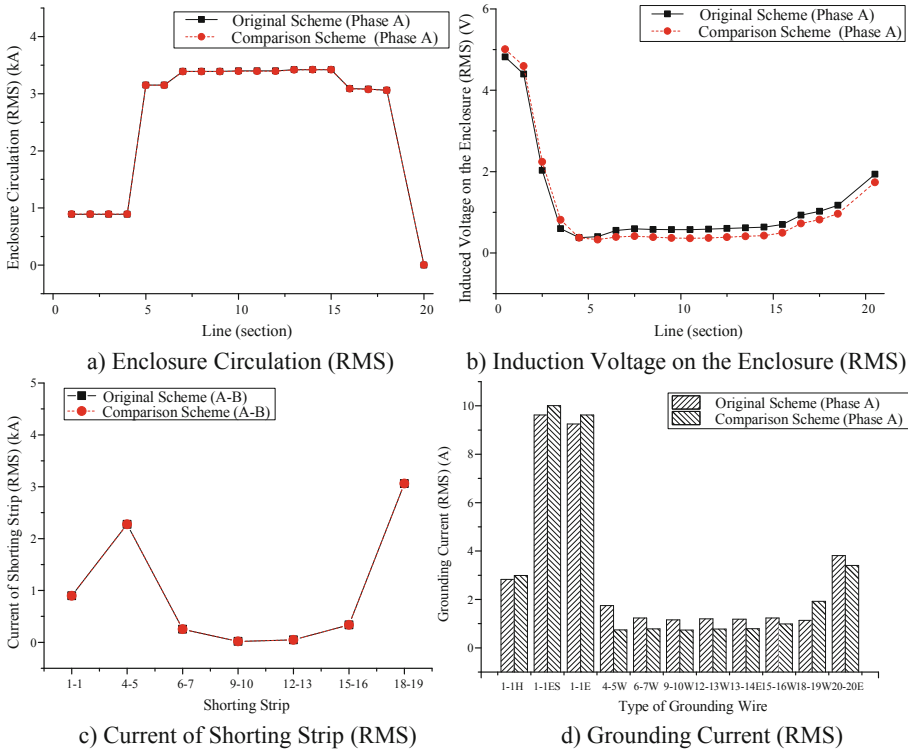
a) Enclosure Circulation (RMS)

b) Induction Voltage on the Enclosure (RMS)

c) Current of Shorting Strip (RMS)

d) Grounding Current (RMS)

**Fig. 8.** Calculation Results Under 2 Grounding Schemes of Shorting Strip

GIS in the middle of the line is only 1m, while the distance between the two ends of the line can reach 7 m. Thus, the induced magnetic flux generated by the three-phase current could mostly cancel each other out in the middle of the line, but this offset is very small at the first end. In short, the addition of a shorting strips can change the main path of the circulation, reducing the induced voltage and ground current greatly. On the other hand, it will also increase the enclosure circulation in the middle of the line. Therefore, the optimization of the shorting strips laying scheme needs to be considered comprehensively.

The calculation results of the original scheme and the second scheme were compared to analyze the influence of the number of shorting strips on the calculation results. The difference between the enclosure circulation, induced voltage, maximum load current of shorting strip, and grounding current is minimal. After the shorting strips are added in the middle of the line, the circulation is mainly carried by the outer end of the shorting strips and the middle have no significant effect on reducing the middle circulation, the terminal induced voltage and ground current in the middle of the line. Hence the actual project can only add shorting strip on both sides near the line and the middle part has no need to add it to improve economy.
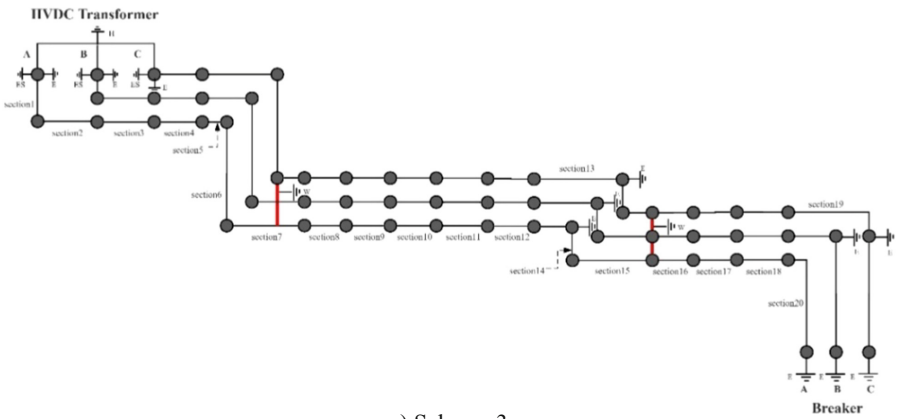
The influence of the laying position of the shorting strips on the calculation result can be seen by analyzing the calculation results of scheme 2 and scheme 3. The circulation
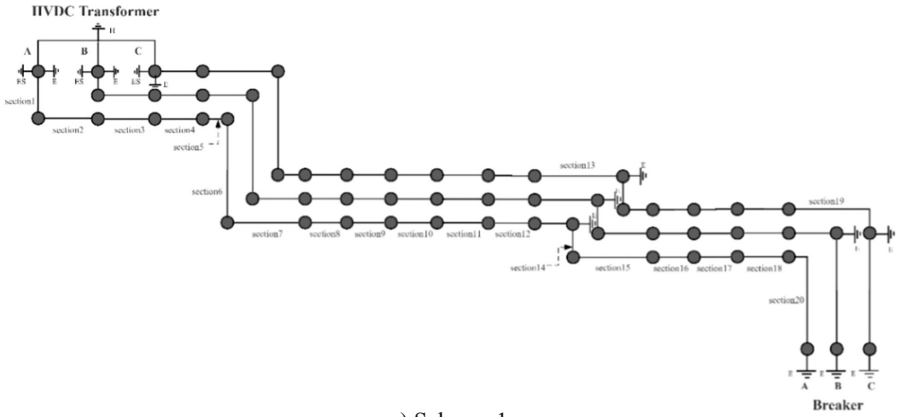
a) Scheme 1
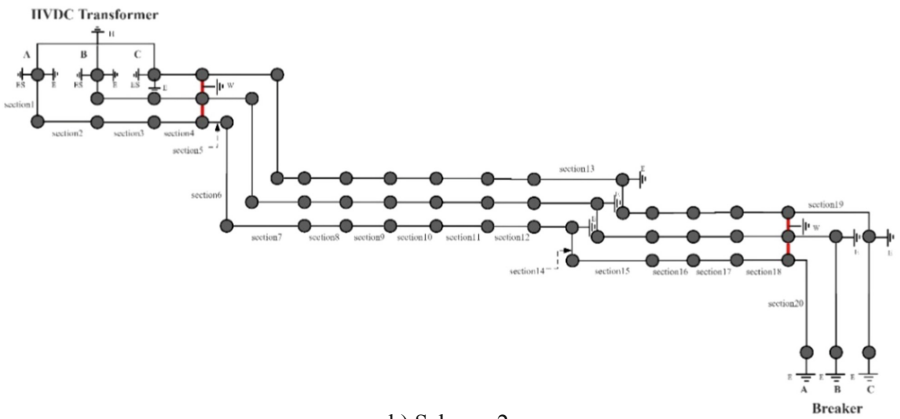
b) Scheme 2

c) Scheme 3

Fig. 9. Four Schemes of Middle Shorting Strip

between the shorting strips surge under the two schemes, but the maximum difference between the two schemes is small (3.3 kA and 3.26 kA, respectively). The shorting stirp of scheme 3 is close to the middle compared with scheme 2. There is a slight decline of the maximum current of shorting strip by 0.27 kA (-8.28%), while the induced voltage and ground current at both ends of the line increase (forward deviation of terminal induced voltage 4.62 V, positive deviation of ground current 9.05 V). Therefore, it is proposed to add shorting strips which is close to both ends of the line to reduce the induced voltage and ground current.

a) Enclosure Circulation (RMS)

b) Induction Voltage on the Enclosure (RMS)

c) Current of Shorting Strip (RMS)

d) Grounding Current (RMS)
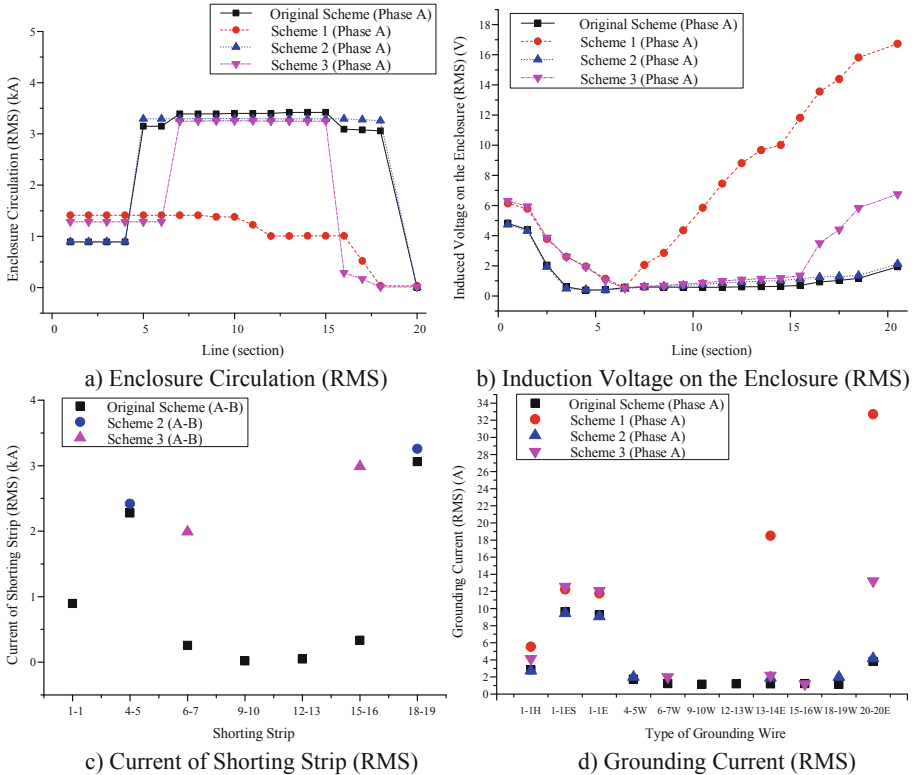
Fig. 10. Calculation Results Under 4 Schemes of Middle Shorting Strip

4   GIS Branch Bus Heat Verification

4.1   Temperature Calculation Modeling Methods

The coupling model of flow field and temperature field is established based on the calculation results of electromagnetic field loss to simulate the temperature and gas flow in single-phase GIS busbar. First, the electromagnetic loss at the wire current of 4000 A (RMS) and the enclosure current of 3500 A (RMS) are calculated. The calculation

results explain that the electromagnetic loss density of the conductor is 20330 W/m^3 and the electromagnetic loss density of the enclosure is 2162.6 W/m^3. Furthermore, the electromagnetic loss per unit length of single-phase conductor is 97.502 W/m and the enclosure are 27.175 W/m. Eventually, the above-mentioned steady-state periodic loss is used as the heat source in the GIS flow field and temperature field model built by COMSOL for calculation.

The finite element model of GIS busbar pipe is shown in Fig. 11. The 550 kV GIS branch bus conductor and enclosure are made of aluminum and the insulated gas is SF$_6$. The model considers the influence of fluid density, dynamic viscosity, thermal conductivity on fluid velocity. The pressure of SF$_6$ gas is set to 0.4 MPa, the molar mass of the gas is 146.05 g/mol, and the gas constant is 0.008314 MPa· L/(K·mol). Set the ambient temperature to 40 °C and the wind speed to 2 m/s. In this model, the heat loss when the conductor and the enclosure are energized is used as the heat source. Besides, the radiation heat dissipation of the conductor to the shell, the contact between the conductor and SF$_6$ gas and convection heat dissipation, the convection and radiation heat dissipation of the enclosure to the surrounding air, and the solar radiation are considered. It is necessary to solve the problem of skin effect by adopting subdivision grid and boundary layer mesh partitioning to calculate the SF$_6$ fluid distribution in the cavity [18–20]. The meshing method uses multi-level meshing, as shown in Fig. 12.
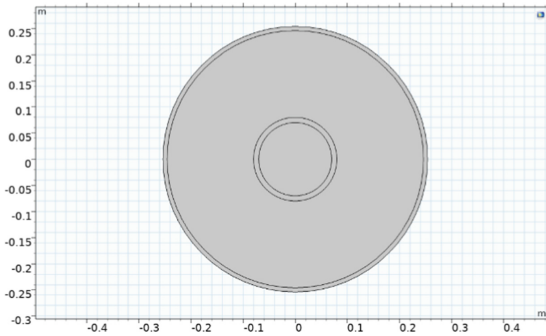
Fig. 11. Two-dimensional Finite element Model for GIS   **Fig. 12.** Grid Division Diagram
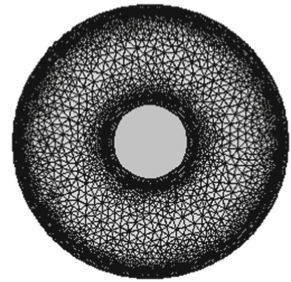
4.2 Temperature Calculation Results of GIS Branch Bus

The temperature calculation results of the GIS branch bus tube are shown in Fig. 13. When the ambient temperature is 40 °C, the maximum temperature of the conductor in the steady state is 60.67 °C (temperature rise 20.67 °C)and the maximum temperature of the enclosure is 48.27 °C (temperature rise 8.27 °C). The temperature of two components is lower than the limit value (60 °C for the personnel accessible part, 70 °C for the inaccessible part) and the temperature rise is also below the limit value (60 K for the conductor, 30 K for the enclosure).

The simulated GIS busbar tube temperature field temperature distribution cloud is shown in Fig. 14. The temperature of GIS conductor and enclosure roughly shows a

Fig. 13. Temperature Curve of Conductor and Enclosure Surface With Time

geometric distribution trend of symmetrical left and right and the upper part is higher than the lower. The flow velocity cloud of SF_6 in the annular cavity is shown in Fig. 15. Since the GIS busbar tube is a cylindrical geometry, the gas flow path also shows a left-right symmetrical trend when there is no fo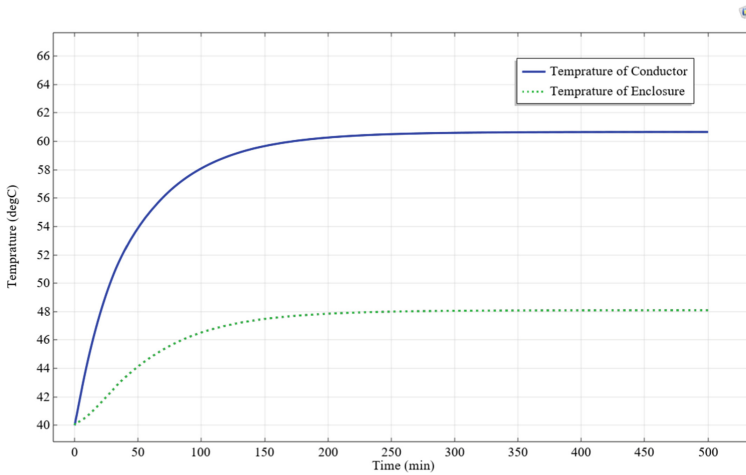rced convection in the outside surroundings. At the same time, the gas molecules are affected by the acceleration of gravity and the gas density changes with the temperature, so the gas return movement at the top of the cavity is strong, resulting in an S-shaped distribution of the inner surface temperature of the shell near the top, that is, the isotherm reversal phenomenon occurs in the annular cavity along the radius of the busbar tube, the farther away from the hot surface and the greater the temperature [9, 21]. The simulation results of temperature and gas flow rate are consistent with the existing simulation results under the same environmental conditions [22–24].

4.3 Temperature Calculation Results of Shorting Strip, Grounding Strip and Holders

For components such as shorting strips, grounding strips and holders, the finite element model does not have a laminar flow module. In this paper, a three-dimensional finite element model is built to calculate the temperature rise for these components. The ambient temperature is set to 35 °C and the wind speed is 2 m/s. Firstly, the short row applies a current of 3.1 kA in the model of shorting strips, the emissivity of the copper surface is 0.65, and the convective heat transfer coefficient is 25. Secondly, 11 A current is applied and the convective heat transfer coefficient is 7.3 in the model of grounding wire. Thirdly, the state of the steel in the model of holder is polished and unoxidized, the surface emissivity of the steel is 0.2 and the convective heat transfer coefficient is 7.3, with current of 300 A.

The temperature distribution cloud of the shorting strips, grounding strips, and holder is shown in Fig. 16. The temperature of the shorting strips showed a trend of high
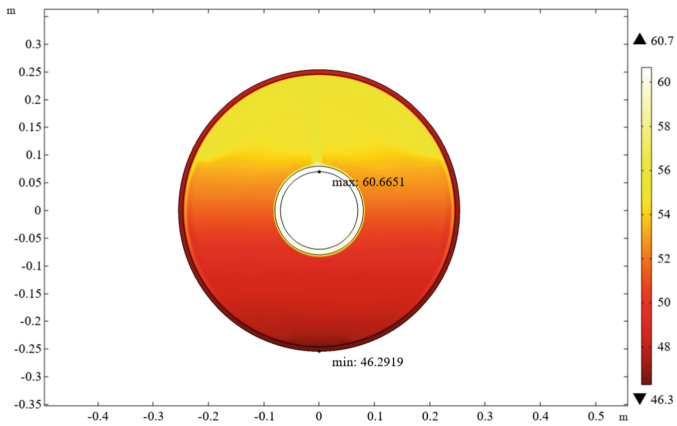
Fig. 14. Steady-state Temperature Distribution Cloud Image of GIS (degC)
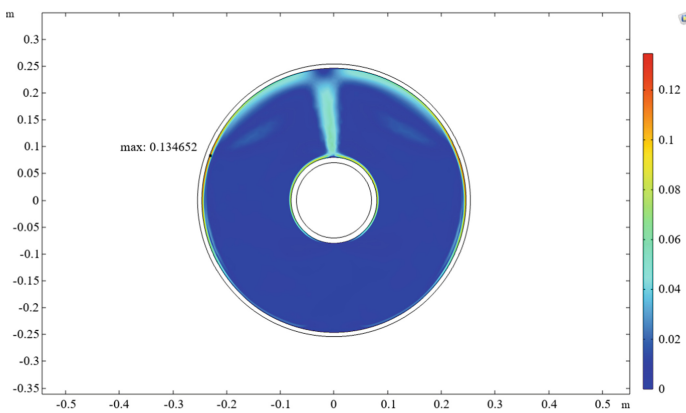
Fig. 15. Steady-state Gas Flow Diagram of GIS (m/s)

and low in the middle and the maximum temperature reached 61.27 °C (temperature rise 26.27 °C). The temperature rise was lower than the limit value (30 K). The local difference in the temperature rise of the grounding strips is very small, with the maximum temperature at 35.01 °C. The maximum temperature rise is less than 1 °C, which is lower than the temperature rise limit of the copper bar. The temperature distribution of the bracket shows a slightly lower side and a high middle part. The maximum temperature in the middle is 35.61 °C, which is lower than the temperature limit of Q235 steel (the normal use temperature of Q235A steel does not exceed 350 °C; the normal use temperature of aluminum alloy shell with pressure requirements does not exceed 160 °C).

a) Shorting Strip (Cu 100mm×10mm)

b) Grounding Strip (Cu 40mm×5mmm)

c) Holder (H-shaped)
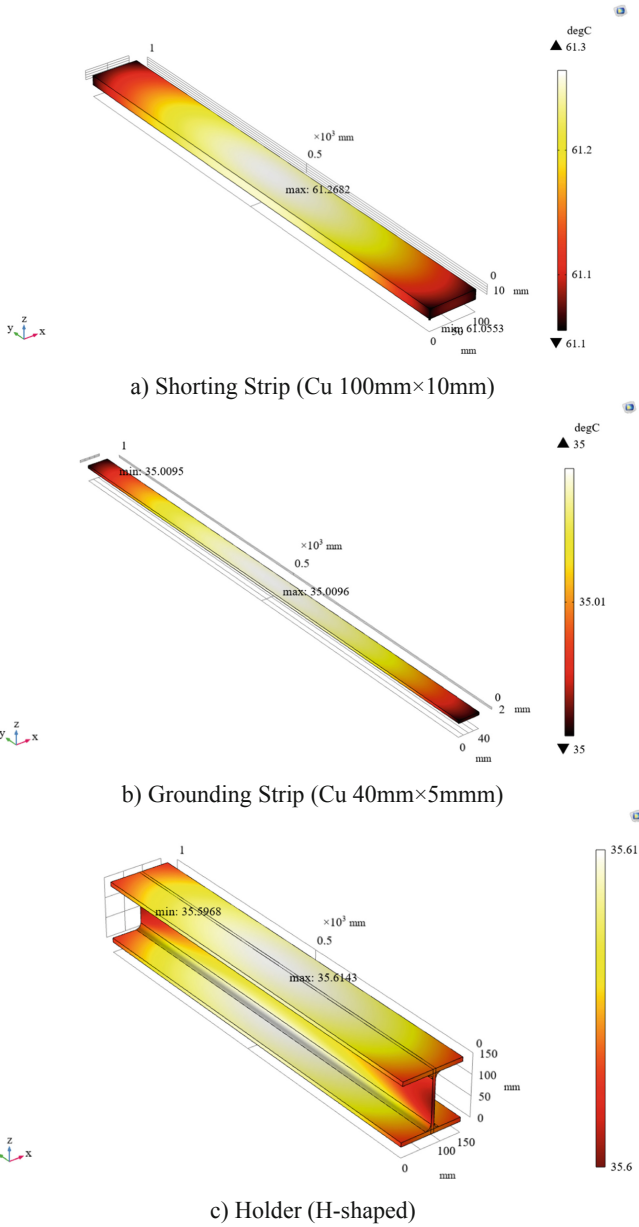
Fig. 16. Temperature Distribution Cloud Image of Components (degC)

5   Conclusion

By establishing a three-phase coupling electromagnetic transient model of GIS branch bus of 500 kV HVDC back-to-back converter station, this paper calculates the enclosure

circulating current, induced voltage, current of shorting strips and grounding strips. The following conclusions can be obtained by comparing and analyzing different wiring schemes and loading the current calculation results as input to verify the temperature of each component in the finite element coupling model.

1) The circulation of GIS branch busbar enclosure showed a distribution trend of high in the middle and low at the end of line, while the induced voltage and grounding current show a distribution trend of low middle and high at both ends. Among them, the enclosure circulation is mainly formed through the shorting strips and the maximum carrying current of the shorting strip reaches about approximately 77% of the rated current of the conductor.

2) In the actual project, the head of the GIS line has a large phase spacing. In order to improve the windproof and seismic mechanical properties of the components, it is recommended that the first-end shorting strip should adopt the grounding form that the enclosure is first led down by the copper bar and then connected in third phase.

3) Under the premise of economic consideration, it is proposed that the shorting strips in the middle of the line should adopt the grounding form that a single copper grounding wire is led down in the middle of the A/B phase or B/C phase.

4) Adding a shorting strip can effectively reduce the induced voltage and ground current at both ends of the line, but will greatly improve the circulation of the shell in the middle of the line at the same time. In actual engineering, if the temperature of the grounding wire at both ends of the line does not exceed the limit, there is no need to laying shorting strips; Otherwise, adding short strips which are only close to both ends is the most efficient and economical way to reduce the ground current.

5) Only by selecting the cross-sectional specifications of the shorting strips in strict accordance with the carrying current of shorting strips, the thermal and temperature rise of GIS branch bus and each component can ensure that the limit value is not exceeded.

References

1. Guo, L., Fan, M., Yao, Y.-A.: Simulation analysis on the circulating current in bus enclosure of the 550kV GIS. J. Hubei Univ. Technol. **27**(1), 74–78 (2012)
2. Zhao, Y.-S., Wang, F.-M., Lang, F.-C., et al.: Circulation and loss calculation model of high voltage GIS shell. Electric Power Eng. Technol. **40**(1), 201–207 (2021)
3. Zhang, H., Liu, Y.-P., Xu, K.-H., et al.: Characteristic analysis and finite element calculation method for shell circulating current of 252 kV GIS substation. High Volt. Apparatus **56**(12), 51–58 (2020)
4. Liu, Y.-P., Zhang, H., Liu, S.-H., et al.: Analysis of induced voltage and circulating current in 800 kV three-phase sub-box GIS substation. Insulators Surge Arresters **05**, 38–46 (2020)
5. S.-w. W, F.: Study on Large Capacity Power Transmission Method and Influencing Factors of Transmission Capacity. Harbin University of Science and Technology (2019)
6. Chen, T.-Y.: Research on Shell Circulating and Transient Ground Potential Rise of GIS in Hybrid Reactive Power Compensation Substation. Shandong University (2019)
7. Zhang, Y.-T., Bo, B., Jia, L., et al.: Characteristics of the circulating current on 800 kV insulated phase bus enclosure. Insulators Surge Arresters **06**, 31–35+40 (2008)

8. Tang, L.-l., Cai, W., Zhao, C., et al.: Circulation characteristics and influencing factors of GIL grounding system. High Volt. Eng. **46**(06), 2098–2105 (2020)

9. Yin, J.-M., Ou, Y., Zhen, Z.-N.: Electromagnetic-fluid-temperature field calculation on the loss and heat of GIS bus bar and the analysis on relevant factors. Water Power **38**(04), 28–31 (2012)

10. Liu, K., Peng, Z.-X., Wang, S., et al.: Research on GIS internal overheating engineering simulation technology. High Volt. Apparatus **56**(06), 13–18 (2020)

11. Wang, Z.-Q., Ding, Z.-S., Wang, N.: Thermal analysis of GIS busbar based on coupled magnetic-fluid-temperature fields. Zhejiang Electric Power **40**(01), 44–49 (2021)

12. Jin, H., Peng, Z.-X., Wang, S., et al.: Research on temperature field distribution characteristics of 252 kV three-phase enclosed GIS bus bar shell. High Volt. Apparatus **53**(12), 20–25 (2017)

13. Liu, Y.-N., Shu, N.-Q., Li, Y.-Z., et al.: Temperature-rise calculation of GIS disconnecting switch based on equivalent thermal-circuit model. Electr. Measure. Instrum. **54**(19), 7–12 (2017)

14. Luo, C.-l., Yang, J.-l., Li, S.-l., et al.: Study on temperature rise of GIS based on equivalent thermal circuit and finite element analysis. High Volt. Apparatus **57**(05), 67–76 (2021)

15. Chen, Q., Li, Q.-M., Hao, H.-X., et al.: Numerical calculation and correlative factors analysis on temperature distribution of GIS bus bar based on coupled multi-physics methodology combined with multiple boundary conditions. Trans. China Electro. Soc. **31**(17), 187–195 (2016)

16. Wang, F., Kang, T.-H., Rao, X.-J., et al.: Analysis and calculation of magnetic-thermal coupled field for high-voltage coaxial GIS busbar. J. Hunan Univ. **41**(08), 73–77 (2014)

17. Lin, X., Li, S., Xu, J.-Y., et al.: Simulation of transient enclosure voltage in EHV GIS. High Volt. Apparatus **47**(03), 12–17 (2011)

18. Wu, X.-X., Cheng, S.-M., Zhou, F., et al.: Influence of temperature rise due to rated current flowing through busbar on the internal insulation characteristics of GIS: a simulation study. High Volt. Apparatus **56**(02), 7–14 (2020)

19. Li, Y.-M., Bai, Z.-M., Wang, E.-l., et al.: 3D multi-field coupling analysis of three-phase GIS bus bar. In: IOP Conference Series: Materials Science and Engineering, ICAMMT, vol. 423, pp. 25–27. Nanchang, China (2018)

20. Kang, T.-H.: Analysis of Coupling Field for Voltage GIS and Development of the Temperature Monitoring System. Hunan University (2014)

21. Fan, Z.-N., Zhang, D.-W., Chen, X.-P., et al.: Electromagnetic field and fluid field calculation and analysis about the loss and heat of GIS bus bar. Proc. CSEE **29**(S1), 241–244 (2009)

22. Kaufmann, B., Kudoke, M., Grossmann, S.: Experimental verification of convective heat transfer computations for gas insulated switchgear. In: 4th International Youth Conference on Energy 2013, IYCE, pp. 1–6. Siófok, Hungary (2013)

23. Hou, G.-B., Deng, X.-F., Li, X.-W., et al.: Multi-physics coupling simulation and experiment of temperature rise in GIS and heat flux distribution characteristic. High Volt. Eng. **45**(07), 2322–2328 (2019)

24. Guo, Y.-J., Zhang, B., Wang, Z.-J., et al.: Simulation technique on temperature rise of GIS bay and typical current-carrying structure optimization. Proc. CSEE **38**(S1), 257–265 (2018)

Multi-physical Field Coupling Analysis
of a Small Switchgear Based on COMSOL

Wei Huang, Xiaoxing Zhang[(✉)], Xiajin Rao, Lei Zhang, Liangyuan Chen, and Rui Li

Electric Power Research Institute of Guangxi Power Grid Co., Ltd., Nanning 530023, China
`xiaoxing.zhang@outlook.com`

Abstract. The switchgear is an essential part of the power distribution system, widely used in substations, Marine ships, and ore mining. With the increasing concern for environmental protection, the substitution of SF_6 gas has become a trend in the power industry, and new environmentally friendly switchgear has emerged. To adapt the insulation performance of the alternative gas to the cabinet's structure, the electric and temperature field distribution within the cabinet is studied, and a suitable structural optimization method is explored in this paper. The Solid-Works software is used to simplify the modeling of the cabinet body and import it into the finite element analysis software. An electrical-magnetic-thermal coupling analysis model of the switchgear cabinet is established to obtain the electromagnetic field distribution and temperature distribution inside the switchgear cabinet and explore optimizing the structure. The results show that there are significant eddy current losses in the switchgear cabinet, which can be reduced by spatial distance; the field strengths at bus bar joints and corners are enormous, which can be reduced by chamfering; the error between the simulated cabinet temperature rise and the actual temperature rise is within 2.3k, and the simulation is reliable.

Keywords: Environmentally friendly switchgear · Temperature rise · Electromagnetic field · Structure optimization

1 Introduction

Gas-insulated switchgear has been widely used in various fields, such as power grid substations and marine vessels, from the 1960s to the present day [1], and SF_6 gas accounts for more than 80% of its total production in the power industry [2–4], however, SF_6 is a gas with the global warming potential (GWP) 23500 times that of CO_2. SF_6 was listed as one of the six major greenhouse gases by the Kyoto Protocol in 1997 [5–8]. With increased concern for environmental protection, the trend has been to reduce or eliminate the use of SF_6 gas in the power industry. Therefore, a new type of environmentally friendly gas-insulated switchgear has emerged [9].

Due to fluctuations in distribution line loads and frequent circuit breaker operations, faults may occur inside the switchgear. To ensure the stable operation of the switchgear and improve the electrical performance, The finite element method to simulate the internal physical field of the electrical equipment has become a common means, and the

problems of a long cycle and extensive investment in the field test have been solved. P. Zhang et al. [10] simulated a gas-insulated busbar's temperature and airflow fields under three-dimensional modeling by simplifying the components and minor features of a 126 kV gas-insulated busbar and using the finite element method with only heat conduction and heat convection in mind. J. Qu et al. [11] used ANSYS finite element software to simulate the temperature field of a low-voltage switchgear chamber and predicted the temperature rise of a low-voltage switchgear chamber by considering contact resistance, eddy current, heat flow, and electromagnetic heat flow coupling models, and carried out relevant temperature rise tests under 500 A current flow conditions. Hong et al. [12] carried out solid modeling of a 12 kV air-insulated switchgear using SolidWorks software. They simulated the effects of eddy currents and contact resistance on the temperature rise of the switchgear, considering heat conduction, convection and radiation, and reasonable boundary conditions. Pawar et al. [13] analyzed the temperature rise of a circuit breaker with SF_6 as the filling medium through simulation. Liao et al. [14] studied the temperature rise of a transformer with insulating oil as the filling medium. The advantages and disadvantages of the coupled AnsysApdl-Cfx and Maxwell-Fluent methods were analyzed in a subsequent work by Wang [15] based on an electromagnetic fluid temperature field model for medium voltage air-insulated switchgear [16]. The above research explored the switchgear structure with SF_6 and insulating oil as the filling medium. However, at present, the insulation performance of the new environmentally friendly alternative gas is still far from the traditional insulation medium. Adapting the alternative gas to the switchgear structure to enhance the insulation performance and improve the heat dissipation rate in the cabinet is still a problem that needs to be explored.

In this paper, the SolidWorks software was used to simplify the modeling of the cabinet, and the finite element analysis software COMSOL Multiphysics was introduced to establish the electric-magnetic-thermal coupling analysis model of the switch cabinet, obtain the electromagnetic field distribution and temperature distribution inside the switch cabinet, and verify the rationality of the simulation model. Finally, according to the simulation results, the structure optimization method of the switchgear is proposed.

2 Simulation Principles

2.1 Fundamentals of Electromagnetic Field Theory

Maxwell's equations are at the heart of electromagnetic field analysis and contain four laws: Ampere's law of loops, Faraday's law of electromagnetic induction, Gauss's law, and Gauss's law of magnetism. Maxwell equations expressed in differential form are shown in Eq. (1).

When the electromagnetic field solved is close to the steady state because the electric flux density solved by Maxwell's equations is minimal, it can be wholly ignored compared with the conduction current density, and the magnetic field generated by the changing electric field can be ignored. The eddy current field can also be expressed as a near-steady electromagnetic field with conducting material in the solution domain, for

which Maxwell's system of equations can be ignored in terms of Gauss' law.

$$\begin{cases} \nabla \times \vec{H} = \vec{J} + \frac{\partial \vec{D}}{\partial t} = \vec{J}_S + \vec{J}_e + \frac{\partial \vec{D}}{\partial t} \\ \nabla \times \vec{E} = -\frac{\partial \vec{B}}{\partial t} \\ \nabla \times \vec{D} = \rho \\ \nabla \times \vec{B} = 0 \end{cases} \tag{1}$$

2.2 Theoretical Foundations of Heat Transfer

Heat transfer is the study of the laws of heat transfer between different parts of an object or the same at different temperatures [17, 18]. Heat can be conducted in three ways - conduction, convection, and radiation and all three have commonalities and differences in the three-dimensional heat transfer equation for equipment in the steady state thermal case expressed as:

$$\lambda \left(\frac{\partial^2 T}{\partial x^2} + \frac{\partial^2 T}{\partial y^2} + \frac{\partial^2 T}{\partial z^2} \right) = -Q \tag{2}$$

In Eq. (2): T is the temperature; λ is the thermal conductivity; Q is the heat source.

3 Switchgear Simulation Modeling

3.1 Switchgear Model Establishment

According to the switchgear entity, Solidworks's three-dimensional drawing software is used to establish the calculated switchgear model. In the cabinet, the dimensions of the mounting holes for the insulators and the sleeves for wrapping the conductors belong to the millimeter level. The impact on the calculation results is small and such structures are ignored. The overall model is shown in Fig. 1.
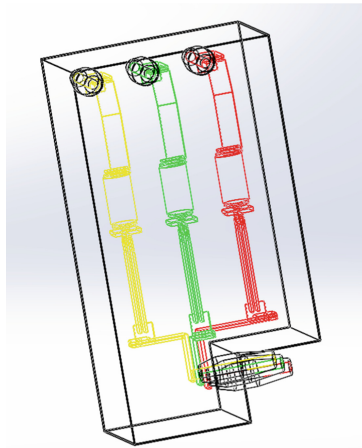

Fig. 1. The overall model of the switchgear

3.2   Mesh Dissection

In the simulation model of this paper, the thickness of the bus bar and the size of the insulator are relatively small compared with the size of the whole model [1]. In order to make the simulation meet the requirements of accuracy and convergence, multi-level mesh dissection and boundary layer mesh dissection methods are adopted. The mesh dissection of the busbar and insulator parts is shown in Fig. 2.

Fig. 2. Busbar and insulator grid sections

4   Analysis of Results and Improvement Options

4.1   Analysis of Switchgear Electric Field Calculations and Suggestions for Improvement

Analysis of Calculation Results
Eddy Current Loss
The simulation results of eddy current loss are shown in Fig. 3. The results show that the eddy current losses in the cabinet are mainly concentrated in the inlet and outlet, where the maximum surface density loss reaches 310 W/m^2. Because the busbar passes through the cabinet, the spatial distance is only a few millimeters, the magnetic flux density is higher, and the induced current is more significant, so the eddy current here is much greater than in the rest of the cabinet.

Electric Field Strength
The electric field strength distribution inside the switchgear is shown in Fig. 4. After the simulation analysis, the electric field strength of phase B in the switchgear is greater than that of phases A and C. In addition, the electric field strength of the busbar joints, busbar corners, and busbar connection insulators is also greater, reaching an order of magnitude of 10^5 V/m, with the maximum field strength getting 4.54*10^5 V/m. Through the above analysis, it is not difficult to conclude that the areas prone to partial discharge within the switchgear cabinet are the contact between the load switch and the bus bar, the connection between the bus bar and the cabinet, the corner of the bus bar, etc. Optimizing
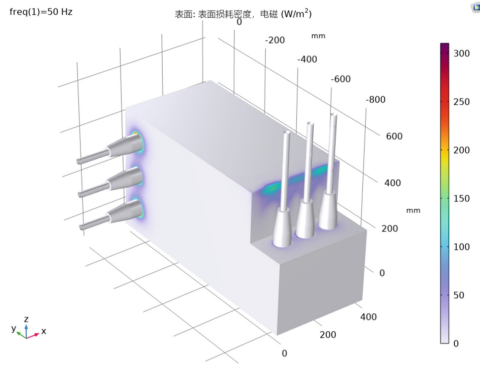
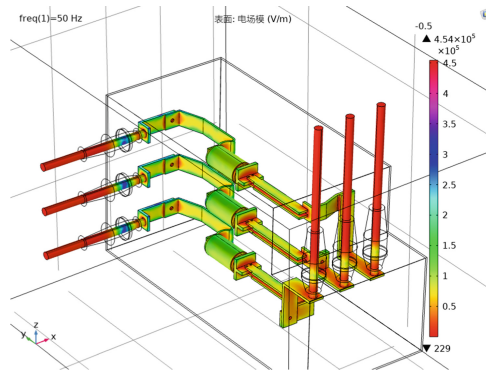**Fig. 3.** Overall eddy current loss of switchgear

Fig. 4. Overall electric field intensity distribution in the switchgear

the busbar structure and reducing the electric field intensity in such areas can improve electrical performance and prevent faults.

Structural Optimization Improvements

Increase the Distance. Increase the Distance between the busbar outlet and the bottom of the cabinet. Other conditions remain unchanged. The vortex field distribution shown in Fig. 5 is obtained.

Induction heating is the leading cause of cabinet temperature rise, and eddy currents also exist at the bottom of this type of switchgear. Comparing Fig. 5 with Fig. 3, it is found that the eddy current loss present on the cabinet is significantly reduced after increasing the distance between the outlet and the bottom of the cabinet, which is due to the increase in spatial distance and the reduction in magnetic induction strength.

Suitable Chamfering. The corner of the bus bar is chamfered, and all other conditions remain the same. the electric field distribution is obtained as shown in Fig. 6.

A comparison with Fig. 4 shows that the electric field strength is significantly reduced when the busbar is chamfered. Therefore, in practical design, the busbars can be chamfered to reduce the probability of failure. In addition, for the problem of excessive field
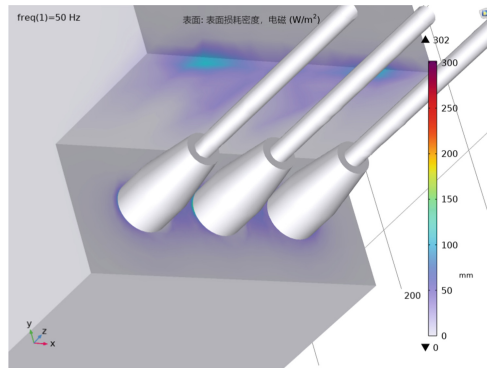
Fig. 5. Eddy current losses in the cabinet at the outlet (after increasing the distance from the bottom of the cabinet)
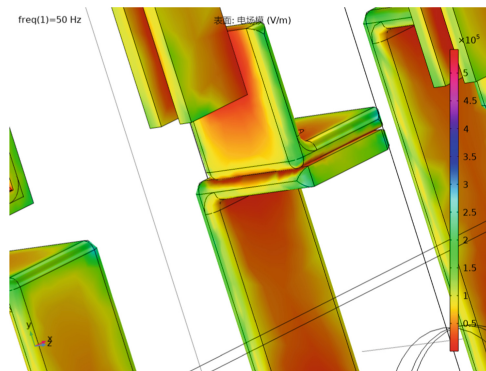
Fig. 6. Local enlargement of the field strength at the corner of the exit line (after chamfering)

strength at the connection between the busbar and the cabinet, insulators can be added to the connection. The insulators need to be wrapped entirely around the busbar, and complete wrapping cannot be reflected in the modeling. Contact crossing errors will occur, so they are not simulated.

Other Optimization Methods. The parts of the switchgear cabinet with busbars passing through them generate significant eddy current losses, leading to higher temperatures. To reduce the above adverse effects, consider using low magnetic permeability materials for the top frame, providing copper plates with lower resistance on the inside of the cabinet, and increasing the area of the stainless-steel sealing plate at the busbar inlet.

4.2 Analysis of Switchgear Temperature Calculations and Suggestions for Improvement

Analysis of Experimental and Simulation Results
As shown in Fig. 7, five temperature detection points are selected for the temperature

rise experiment of the switchgear. The test current is set to 1.1 times the rated current according to the standard DL593-2006, and the corresponding temperature rise data are measured with thermocouples after stabilization. The results are compared with the simulation results, as shown in Fig. 8. The maximum temperature difference is only 2.3 °C. The errors are all within 5%, which verifies the reasonableness of the simulation model.

The results of the busbar temperature distribution in the simulation model are shown in Fig. 9. The highest temperature inside the switchgear cabinet is 71.4 °C when the running 630A, which occurs at the joints where the busbars are connected to the insulators and the circuit breaker chamber.

When the temperature of a joint rises, the metal is deformed by heat, for example, if a metal joint overheats into an expanded state, the contact surface is forced to shift, creating tiny gaps and increasing contact resistance, promoting the thermal effect.

In the simulation model, the temperature rise at the highest point of the cabinet is 51.4K. The temperature rise in other parts is even smaller, far less than the 70K specified in the national standard, which verifies the reasonableness of the switchgear design.
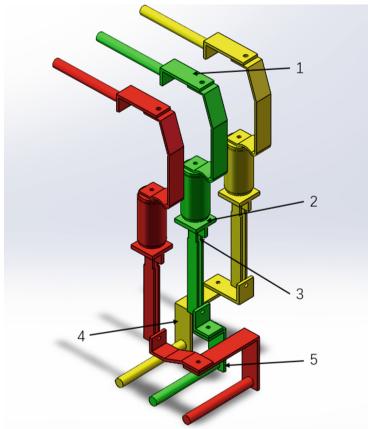
Fig. 7. Temperature detection point diagram

Structural Optimization and Improvement

Reduction of Eddy Current Losses. The appropriate optimization options have already been discussed in the previous section and will not be repeated here.

Other Optimization Methods. Several factors, such as poor contact, small busbar spacing, poor copper material, small cross-sectional area, etc cause the high-temperature rise in the busbar. There is a causal effect between lower bus temperature and current carrying capacity. Some methods can reduce the bus temperature, such as using me-chanical structures with better contact, better quality copper, and applying petroleum jelly or conductive paste to the cover to reduce contact resistance.
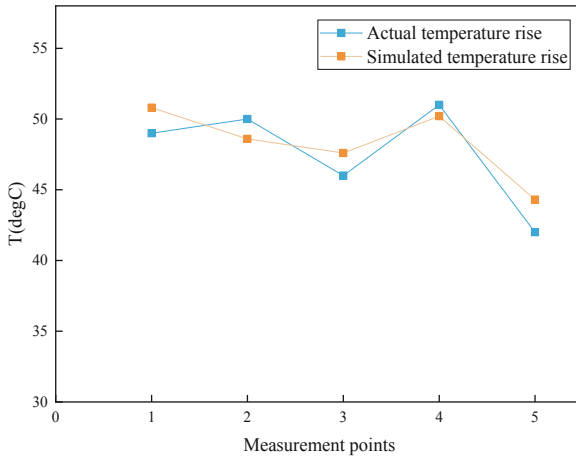
Fig. 8. Comparison of simulated and actual temperatures
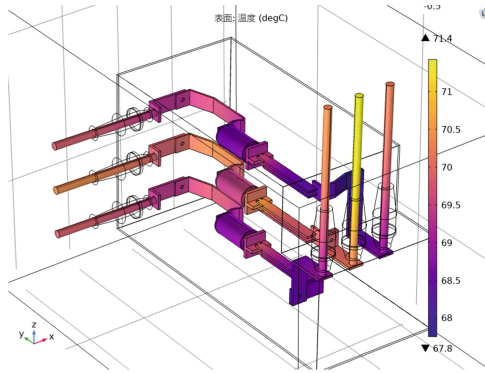
Fig. 9. Busbar temperature distribution diagram

5 Conclusion

In this paper, the electromagnetic field distribution and temperature distribution inside the new environmentally friendly switchgear are simulated based on the finite element analysis method, and the following conclusions can be drawn:

(1) Eddy current losses exist in switchgear cabinets, especially at the busbar inlet and outlet and at the bottom of the cabinet. Eddy currents can be effectively reduced by increasing the distance between the busbar and the bottom of the cabinet.

(2) According to the distribution of electric field strength, we can determine the areas where the switchgear is prone to partial discharge: the contact between the load switch and the bus bar, the connection between the bus bar and the cabinet, the corner of the bus bar, etc. Measures such as chamfering the busbars and adding

insulators at the connection between the busbars and the cabinet can be taken to avoid partial discharges.

(3) By conducting temperature tests on five temperature measurement points and comparing them with the simulation results, the errors are all within 5%. The temperature rise at the highest point of the switchgear is 51.4K after long-term operation at a high current, which is much less than the 70K specified in the national standard

.

References

1. Ahmethodzic, A., Kapetanovic, M., Gajic, Z.: Computer simulation of high-voltage SF6 circuit breakers: approach to modeling and application results. IEEE Trans. Dielectr. Electr. Insul. **18**(4), 1314–1322 (2011)
2. Yan, X., Gao, K., Zheng, Y., Li, Z., Wang, H., Jie, H., et al.: Progress of Gas mixture and alternative gas of SF_6. Power Syst. Technol. **42**(6), 1837–1844 (2018)
3. Lin, S., Li, X., Li, L.: Research progress of environmentally friendly SF_6 substitute medium in electrical equipment. High Voltage Apparat. **52**(12), 1–7 (2016)
4. Zhou, W., Zheng, Y., Yang, S., Qin, Z., Wang, B.: Research progress and trend of SF_6 alternative with environment friendly insulation Gas. High Voltage Apparat. **52**(12), 8–14 (2016)
5. Zhang, X., Tian, S., Xiao. S, Li, Y.: A review study of SF_6 substitute gases," Trans. China Electrotech. Soc. **33**(12), 2883–2893 (2018)
6. Xiao, D., Jiao, J., Yan, J.: Arc quenching characteristics analysis of environmental-friendly insulation gases. High Volt. Eng. **42**(6), 1681–1687 (2016)
7. Xiao, D.: Development prospect of gas insulation based on environmental protection. High Volt. Eng. **42**(4), 1035–1046 (2016)
8. Li, X., Zhao, H.: Review of research progress in SF_6 substitute gases. High Volt.e Eng. **42**(6), 1695–1701 (2016)
9. Li, X., Zhao, H., Murphy, A.B.: SF6-alternative gases for application in gas-insulated switchgear. J. Phys. D: Appl. Phys. **51**(15), 153001 (2018)
10. Zhang, P., Li, W., Yang, K.: Condition estimate of contacts of current-carrying conductor in GIS based on the FEM calculation of temperature field. In: 2015 3rd International Conference on Electric Power Equipment – Switching Technology (ICEPE-ST), pp. 69–73, Oct. 2015
11. Qu, J., Chong, F., Wu, G., Li, X., Wang, Q.: Application of computational fluid dynamics to predict the temperature-rise of low voltage switchgear compartment. In: 2014 IEEE 60th Holm Conference on Electrical Contacts (Holm), 2014, pp. 1–5 (2014)
12. Lü, H., Wang, L., Zheng, W., Wang, L., Lin, L.: Coupled simulation of eddy-current thermal field in medium voltage switchgear. In: 2015 3rd International Conference on Electric Power Equipment – Switching Technology (ICEPE-ST), pp. 63–68 (2015)
13. Pawar, S., Joshi, K., Andrews, L., Kale, S.: Application of computational fluid dynamics to reduce the new product development cycle time of the SF_6 gas circuit breaker. IEEE Trans. Power Delivery **27**(1), 156–163 (2012)

14. Liao, C., Ruan, J., Liu, C., Wen, W., Du, Z.: 3-D Coupled electromagnetic-fluid-thermal analysis of oil-immersed triangular wound core transformer. IEEE Trans. Magn. **50**(11), 1–4 (Nov.2014)
15. Wang, L., Zheng, W., Wang, L., Lin, J., Li, X., Jia, S.: Electromagnetic-thermal-flow field coupling simulation of 12-kV medium-voltage switchgear. IEEE Trans. Compon. Pack. Manuf. Technol. **6**(8), 1208–1220 (2016)
16. Wang, L., Wang, L., Li, X., Lin, J., Zheng, W., Jia, S.: Multi physical field simulation of medium voltage switchgear and optimal design. In: 2016 27th International Symposium on Discharges and Electrical Insulation in Vacuum (ISDEIV), pp. 1–4 (2016)
17. Hrovat, G., Hamler, A.: Coupled current and thermal problem in the motor protection switch; verification of calculated temperature with measured ones. IEEE Trans. Compon. Packag. Technol. **29**(4), 764–769 (2006)
18. Kim, J.-K., Lee, J.-Y., Wee, S.-B., Hahn, S.-C.: A novel coupled magneto-thermal-flow analysis for temperature rise prediction of power apparatus. International Conference on Electrical Machines and Systems **2008**, 585–588 (2008)
19. Ahmethodzic, A., Kapetanovic, M., Gajic, Z.: Computer simulation of high-voltage SF_6 circuit breakers: approach to modeling and application results IEEE Trans. Dielect. Electr. Insulat. **18**(4), 1314–1322 (2011)

A Method of Small Current Grounding Fault Diagnosis Based on Catastrophe Value

Lei Chen, Longhui Zhang, and Feng Liu[✉]

College of Electrical Engineering and Control Science, Nanjing Tech University,
Nanjing 211816, China
f.liu_1@hotmail.com

Abstract. The distribution network usually adopts the operation mode of ungrounded neutral point or grounded through arc suppression coil to improve the stability of the system, but under these two working modes, the output current signal of the system is weak when a single-phase grounding fault occurs, which leads to the difficulty of fault diagnosis. In order to realize the diagnosis of small current grounding fault under these two working modes and improve the accuracy of small current grounding fault diagnosis technology in distribution automation (DA) system, through the analysis of the transient characteristics of the system when grounding fault occurs, combined with the relationship between the transient zero sequence current of fault line and non-fault line and the relationship between transient zero sequence voltage and zero sequence current when grounding fault occurs, Based on the sudden change value of zero sequence voltage and zero sequence current, a small current grounding fault identification method is presented. MATLAB is used to simulate the small current grounding system model of distribution network with ungrounded neutral and grounded through arc suppression coil, and the simulation results are analyzed to verify the accuracy of the proposed discrimination method.

Keywords: distribution automation · neutral point operation mode of distribution network · small current grounding system · ground fault · MATLAB

1 Introduction

The improvement of social economy and the development of power grid technology promote the construction process of smart grid. Smart grid refers to the intelligent power grid, which is an information-based, digital and automatic power grid [1]. Distribution Automation (DA) improves power supply reliability by realizing automatic fault isolation and automatic power recovery [2]. In today's society, the development of people's life and productivity is inseparable from electricity, and power failure will bring huge losses to society. DA improves the reliability of power supply significantly.

High voltage transmission line fault identification is of great significance to ensure the safe and stable operation of power grid. The insulator surface of high-voltage equipment is easy to accumulate dirt and lead to insulation aging. Under severe conditions

such as thunderstorm, it is easy to cause power line faults, among which power failure caused by single-phase grounding fault accounts for about 80% [3, 4]. When a single-phase grounding fault occurs in a small current grounding system, the fault zero sequence current (referred to as zero current) signal is very weak, and the terminal sampling accuracy is inaccurate, which makes it difficult to judge the fault. The traditional grounding fault judgment methods based on the characteristics of steady-state zero current can only be used in systems with obvious fault zero current. Therefore, many scholars have studied the small current grounding fault judgment method. Literature [5] uses the time-frequency matrix obtained by S transformation from the reliability decision fusion to carry out fault line selection and improve the accuracy and sensitivity of line selection. Literature [6] uses the equivalent half wave injection method to inject signal waveforms into distribution network lines, and compares the injected DC signals extracted from fault lines, non-fault lines and signal generators to achieve the purpose of fault location. Literature [7] used sample data processing and ADABOOST method for comprehensive route selection, but this method requires sufficient sample data support, and data collection is difficult. Literature [8] improved the efficiency of line selection by constructing GA-BP neural network to train network parameters for fault measurement data such as wavelet packet method, active component method, group amplitude comparison method and fifth harmonic method.

Based on the analysis of the transient characteristics of single-phase grounding fault in the arc suppression coil grounded system, this paper proposes a judgment method for small current grounding fault based on zero sequence voltage (referred to as zero voltage) and zero current sudden change value. By taking the sudden change of zero current or zero voltage as the fault starting time, the method analyzes and counts the judgment method of zero sequence power of sampling points meeting the transient grounding characteristics within 20 ms before and after the starting time. The system model of neutral grounded by arc suppression coil is built using MATLAB to capture the waveform of voltage and current when grounding fault occurs in the system. The waveform is compared and analyzed to verify the correctness of the proposed grounding fault judgment method.

2 Analysis of Neutral Grounding System of Distribution Network via Arc Suppression Coil

When a ground fault occurs in the distribution network, the capacitive current of each phase of the system will flow through the fault point, and the capacitive current at the fault point will increase. At this time, if no compensation current flows through the fault point, it is easy to cause arc grounding, which will have a certain impact on the system stability [9]. Although the neutral point of the distribution network is grounded through the arc suppression coil, which can effectively prevent the generation of arc, the zero current in the system is very small at this time, and it is difficult to judge the grounding fault. When the grounding fault occurs in the small current system, the current of line n in the neutral point grounding system through the arc suppression coil is as shown in Fig. 1.
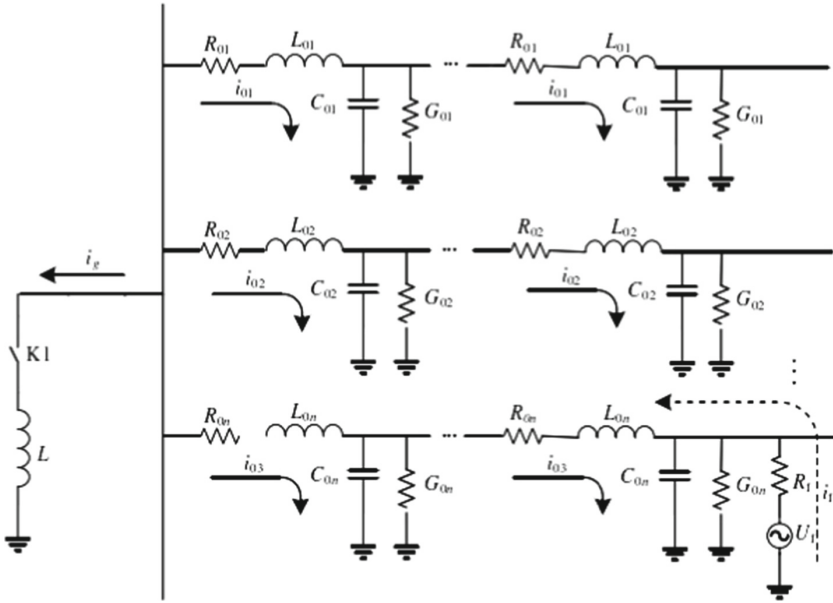
Fig. 1. Zero sequence current distribution of neutral grounding system through arc suppression coil.

It can be seen from Fig. 1 that the current flowing through the fault point has both capacitive current I_L and inductive current I_C [10]. According to Kirchhoff's current law, the current flowing through the fault point can be expressed as:

$$I_D = I_C - I_L = j(\omega C + 1/\omega L)U \tag{1}$$

Because the capacitive current is in the opposite direction to the inductive current, the inductive compensation current generated by the arc suppression coil reduces the fault zero current [11]. Only relying on the zero sequence amplitude in the steady state cannot meet the small current fault judgment under this grounding mode.

The transient process is actually a wave process, so the input zero sequence impedance Zin of the non-fault line in case of ground fault is obtained according to the wave equation and S transformation, as shown in Formula (2).

$$Z_{in} = Z_c ch\gamma S \tag{2}$$

where, $ch\gamma S = (\hat{e}\gamma S + \hat{e}(-\gamma S))/2$, Zc represents wave impedance, see Eq. (3), γ is the line propagation coefficient, as shown in Formula (4), and S is the line length.

$$Z_c = \sqrt{((R_0 + j\omega L_0)/(G_0 + j\omega C_0))} \tag{3}$$

$$\gamma = R_0 G_0 + j\omega R_0 C_0 + G_0 L_0 - \omega^2 L_0 C_0 \tag{4}$$

Since the admittance of the non fault line to the ground is approximately equal to 0, substitute (3) and (4) into Formula (2) to get:

$$Z_{in} = -j\sqrt{(L_0/C_0 - j\,R_0/(\omega C_0))}\ \cot\left(S\sqrt{(\omega^2\,L_0\,C_0 - j\omega R_0\,C_0)}\right) \tag{5}$$

3   Transient Characteristics of Small Current Grounding Fault

3.1   Distribution Characteristics of Transient Current in Small Current Grounding System

At the moment of line grounding fault, zero voltage and zero current will change suddenly. The zero current of the fault line flows from the load side to the power supply side. When the ground fault occurs, the amplitude of the first 1/2 cycle transient current is far greater than the amplitude of the steady-state current. The transient current is far greater than the steady capacitive current; the zero current of the ungrounded line and the downstream line of the fault point flows from the power supply side to the load side.

For the neutral grounding system through arc suppression coil, the zero current of the non-fault line flows from the power supply side to the load side; The zero current direction of the fault line is related to the working state of the arc suppression coil: under the over compensation state, the zero current direction is the same as that of the non-fault line; In the under compensation state, the zero current will flow from the load side to the power supply side.

3.2   Transient Process Impedance Characteristics

When the grounding fault occurs, the current includes both fundamental frequency component and high-frequency component. The transient process is dominated by high-frequency components with short duration. The transient component is mainly the transient resonance component generated between the equivalent inductance and equivalent capacitance of the system [12, 13]. In high frequency and low frequency, the influence of zero sequence resistance on zero sequence impedance is negligible, so Formula (5) can be simplified as:

$$Z_{in} = -j\sqrt{(L_0/C_0)}\ cot\ (\omega S\sqrt{(L_0\ C_0)}) \tag{6}$$

The neutral point impedance is Z, and its value is:

$$Z = j\omega L \tag{7}$$

The parallel resistance value R_f of all lines and the zero sequence admittance Y_n of fault line n can be expressed as:

$$Y_n = 1/R_f - 1/Z - 1/Z_{in} \tag{8}$$

Substitute Formula (6) and (7) into Formula (8) to get:

$$Y_n = 1/Y_n + (1/R_f + (1/\omega L - (\sqrt{(C_0)}/(\sqrt{(L_0)}\ cot\ (\omega S\sqrt{(L_0 C_0)}))) \tag{9}$$

Zero sequence impedance of fault line is:

$$Z_n = 1/Y_n = (1/R_f - j(1/(\omega L) - \sqrt{C_0}/(\sqrt{L_0} cot\ (\omega S\sqrt{(L_0 C_0)}))))$$
$$/(1/R_f^2 + (1/(\omega L) - \sqrt{C_0}/(\sqrt{L_0} cot(\omega S\sqrt{(L_0 C_0)})))^2 \tag{10}$$

When the line has series resonance, the line impedance is the minimum [14]. It can be seen from Formula (10) that when the non-fault line has series resonance, the impedance amplitude of the fault line |Zn| is approximately equal to zero, so the fault line also has series resonance [15]. Since the series resonance of each non fault line will affect the series resonance of the fault line, the amplitude frequency characteristics of the fault line will not change at the same frequency band.

4   Judgment Method of Grounding Fault in Small Current System

When the small current grounding system is grounded in the occurrence area, the slope of the zero voltage waveform is opposite to that of the zero current waveform. When the operation mode and power supply direction of the line change, the relative direction of the bus and the line changes, so adaptive adjustment is required according to the power direction of the line.

When the switch is put into forward operation for power supply, the phase voltage is consistent with the positive sequence of phase current and the same name terminal, and the zero current is consistent with the same name terminal of phase current, zero voltage and phase voltage, so as to ensure that the same name terminal of zero voltage and zero current is consistent. In case of inconsistency, the phase sequence and polarity shall be adjusted by parameters. When the line is in reverse power supply, the original power supply side of the system becomes the load side, and the original load side becomes the power supply side. Therefore, when the positive sequence current of the switch is greater than 1% of the rated value and the active power is less than 0, it is necessary to reverse the zero current sampling value, and then calculate and judge.

In the small current grounding system, most single-phase grounding characteristics are that the system zero voltage and zero current suddenly rise, and when the grounding fault occurs, the steady-state zero current is very small, compared with the transient zero current, it is relatively large. Therefore, the zero voltage sudden change value and zero current sudden change value reaching the set sudden change fixed value are used as the starting condition of the grounding criterion, and the transient process within 1/4 cycle after grounding is used as the main criterion of the grounding fault. In the case of high resistance grounding and slow change of grounding resistance, the phase relationship between zero voltage and zero current in steady state is used to judge. If the zero voltage reaches the threshold value for a certain time during the grounding process, the system can be judged to be grounded. Since the reliability of ground fault judgment is related to the sampling accuracy, in order to capture the process of transient occurrence, it is necessary to increase the sampling frequency to ensure that there are more point responses to the voltage and current values when the fault occurs.

4.1   Transient Criterion

Zero sequence voltage sudden change or zero sequence current sudden change, and the system has zero sequence voltage, the criteria for zero sequence voltage sudden change are as follows:

$$
\begin{aligned}
&||Uz_{(i)} - Uz_{(i-N)}| - |Uz_{(i-N)} - Uz_{(i-2N)}|| \\
&> 1.25||Uz_{(i-N)} - Uz_{(i-2N)}| - |Uz_{(i-2N)} - Uz_{(i-3N)}|| + U_{zsetdb}
\end{aligned}
\tag{11}
$$

$$Uz_{(i)} > 1.2Uz_{(i-N)} \tag{12}$$

Criteria for sudden change of zero sequence current are as follows:

$$\begin{aligned}
&||Iz_{(i)} - Iz_{(i-N)}| - |Iz_{(i-N)} - Iz_{(i-2N)}|| \\
&> 1.25||Iz_{(i-N)} - Iz_{(i-2N)}| - |Iz_{(i-2N)} - Iz_{(i-3N)}|| + I_{zsetdb}
\end{aligned} \tag{13}$$

Criteria for zero sequence voltage of the system are as follows:

$$U_z > U_{zset} \tag{14}$$

U_{zsetdb} represents zero voltage sudden change parameter, which is set as 3% of zero voltage rated value by default during operation; I_{zsetdb} represents zero current sudden change parameter, and the criteria to avoid positive zero sequence current sudden change are as follows: zero current is taken as reference value during normal operation, and it is set as 8‰ of zero current rated value by default during operation; U_{zset} represents zero voltage threshold value to avoid neutral point voltage deviation during normal operation, and it is greater than the minimum value of neutral point voltage when the current power grid is grounded. It is not less than 5% of zero voltage rating during field operation; I_Z and U_Z represent the current zero current and zero voltage amplitude.

The zero voltage is within the latest 1/6 cycle. If the sampling point of 1/8 cycle meets the formulas (5) and (6), it means that the system has a sudden change of zero voltage; The zero current is within the latest 1/6 cycle. If the sampling point of 1/8 cycle meets the formula (7), it means that the system has a sudden change of zero current. When the zero pressure meets Formula (5) and (6) or the zero current meets Formula (7), the sudden change signal occurs first as the starting point, and at least 20 ms within 20 ms –60 ms after the sudden change meets Formula (8), then it is judged that the system has zero pressure and zero pressure or zero current sudden change occurs.

When the direction of zero current and zero voltage transient quantity is opposite, the sampling point of 1/5 cycle forward from the judgment time of zero voltage or zero current sudden change is the single-phase grounding time, and the sampling point where the instantaneous value of zero current within 1/4 cycle after the grounding time is greater than the threshold value is the effective sampling point. When the number of effective sampling points is more than half of the 1/4 cycle sampling points, it is considered that the zero current is greater than the threshold value. At this time, the derivative product sum of zero voltage and zero current in the specific frequency band of 1/4 cycle is calculated from the time of grounding. When the sum is negative and less than -100, that is, the zero sequence average power is negative, it is judged that a single-phase grounding fault occurs at this time.

The transient process of grounding fault is complex, especially the harmonic component is rich in the transient process of arc grounding. Among the harmonic components, the third harmonic and higher harmonic are very small, and even harmonics cancel each other, so the zero current fifth harmonic component is selected as the transient criterion [16–18]. The acquired zero voltage and zero current need to be filtered as follows: after the zero voltage or zero current suddenly changes, calculate the fifth harmonic and fundamental wave of the 1/4 cycle zero current from the time of grounding. When the

amplitude of the fifth harmonic is greater than 50% of the fundamental wave, select a 100–300 Hz filter. When the amplitude of the fifth harmonic is less than 50% of the fundamental wave, use a 0–200 Hz low-pass filter.

4.2 Steady State Criterion

When zero voltage is detected in the system and formula (14) is met, the fundamental wave relative angle of zero current and zero voltage is used for grounding judgment.

$$I_z > I_{zset} \tag{15}$$

$$225° < \tan^{-1}(I_Z/U_Z) < -45° \tag{16}$$

When zero pressure meets Formula (14) and zero current meets Formula (15), start to calculate the relative angle between zero current and zero pressure. When the angle meets the formula (16) and the time exceeds 40 ms, it is judged that a single-phase grounding fault occurs at this time.

4.3 The System Has No Negative Sequence Voltage

Because there is zero voltage in the system when the line has a phase failure at the power supply side, it may be mistaken as a ground fault. Generally, the negative sequence voltage value generated by phase failure at the power supply side will not be lower than 15% of the rated voltage [19, 20]. In order to improve the accuracy of ground fault diagnosis, the negative sequence voltage lockout criterion can be added on the basis of the original ground fault diagnosis method by using the characteristics of the negative sequence voltage of the open phase at the power supply side. When using the transient criterion, judge the negative sequence voltage after the zero voltage sudden change occurs for 20 ms. If the negative sequence voltage is less than 15% of the rated value of the phase voltage, it is considered that the system has no negative sequence voltage. When using the steady state criterion, the negative sequence voltage is calculated synchronously. If the negative sequence voltage is less than 15% of the rated value of the phase voltage, it is considered that the system has no negative sequence voltage.

4.4 Action Delay Criterion

Considering that transient grounding may be caused by some special reasons in reality, in order to avoid the occurrence of ground fault in terminal judgment in this case, a certain delay criterion needs to be added to ensure the reliability of ground fault judgment. After satisfying the judgment of grounding protection, start the transient criterion. If the zero voltage is less than the setting value for more than 200 ms continuously, then the protection and startup return, and judge that it is not an internal grounding fault at this time; If the grounding conditions in the area are met, the protection will act after setting delay.

4.5 Small Current Grounding Start

When the zero voltage steady-state value is greater than the setting value, and the grounding signal in the area obtained after calculation is positive, the small current grounding starts and maintains the starting state. If the zero voltage steady state for more than 200 ms is less than the setting value or the grounding signal in the area is not positive, the state returns.

5 MATLAB Modeling and Simulation

5.1 Simulation Model Establishment

Simulink is used to build the simulation model of neutral grounding system through arc suppression coil. The system frequency is 50 Hz, mainly including transformer, transmission line, load, grounding fault, etc. There are 4 lines in the system. The sequence parameters of the line are shown in Table 1, and the system simulation model is shown in Fig. 2.

Table 1. Line sequence parameters.

Positive sequence resistance	0.192 Ω/km
Zero sequence resistance	0.741 Ω/km
Positive sequence inductive reactance	1.92×10^{-4} H/km
Zero sequence inductive reactance	8.71×10^{-4} H/km
Positive sequence capacitive reactance	1.65×10^{-6} F/km
Zero sequence capacitive reactance	5.23×10^{-7} H/km

5.2 Simulation Analysis

When the arc suppression coil is connected in the system simulation model, a single-phase grounding fault occurs on line 4. The zero voltage waveform of the system monitored by Scope10 is shown in Fig. 3. The zero current waveform monitored by Scope3 and Scope4 is compared and analyzed to obtain the zero current waveform shown in Fig. 4.

It can be seen from the waveform comparison at the first half wave of Fig. 4 and Fig. 5 that the transient zero voltage and zero current direction of Line 4 are opposite, and the transient zero voltage and zero current direction of Line 3 are the same. It can be seen from Fig. 5 that the transient zero current amplitude of Line 4 is greater than its steady-state zero current amplitude. Comparing the transient zero current of Line 4 with that of Line 3, it is found that their directions are opposite and the amplitude of transient zero current of Line 4 is greater than that of Line 3. Therefore, the judgment method is correct by comparing the relationship between the transient zero current of
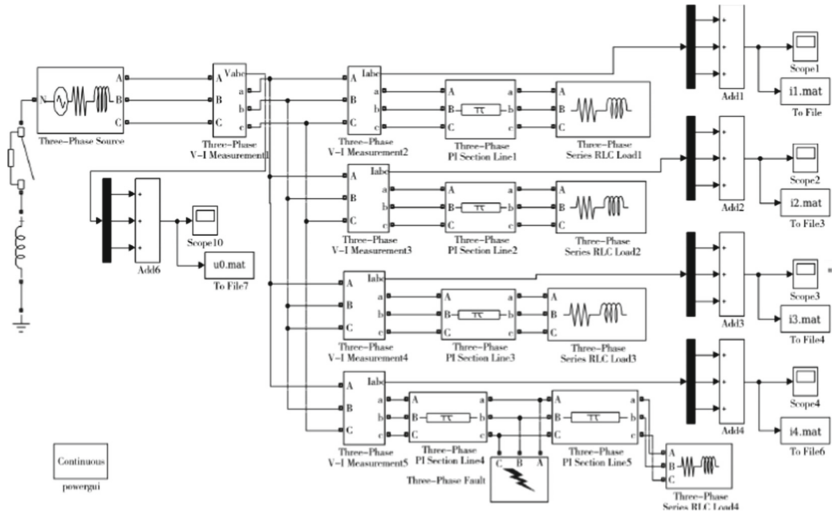
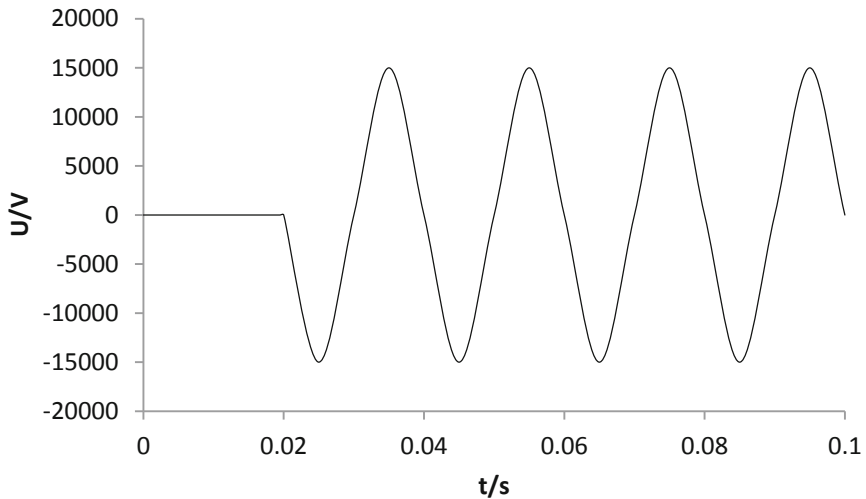**Fig. 2.** Simulation model of small current grounding system.

Fig. 3. Zero sequence voltage waveform.

the fault line and the non-fault line and taking the transient zero voltage characteristics as the auxiliary criterion.

In order to verify whether the above ground fault judgment method is also applicable to the neutral point ungrounded system of the distribution network, disconnect the access switch of the arc suppression coil, and compare the zero current waveform of Line 4 obtained under the same grounding mode at the same point to obtain the waveform shown in Fig. 5.
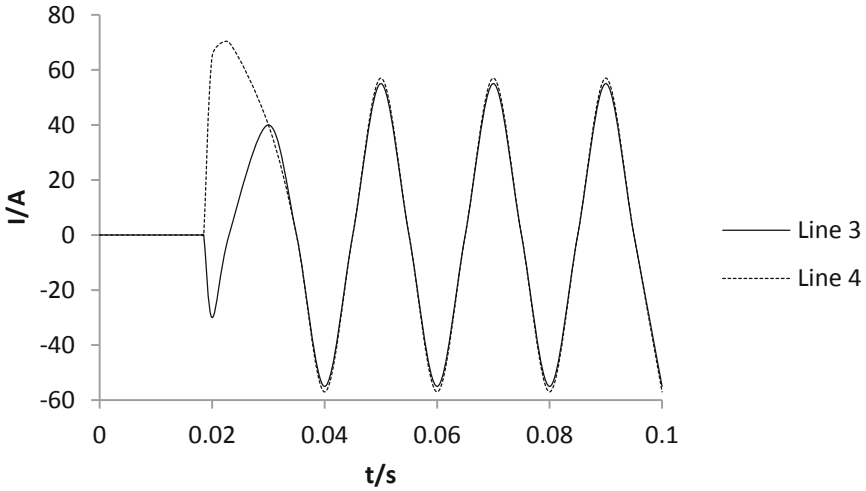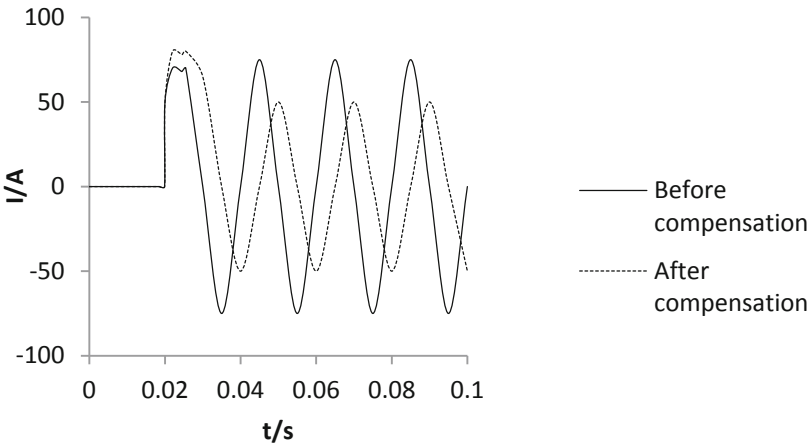
Fig. 4. Zero sequence current waveform.

Fig. 5. Comparison of zero sequence current waveform.

It can be seen from Fig. 5 that the amplitude and phase of transient zero current before and after compensation at the first half wave are basically the same, and the amplitude of steady-state zero current after compensation is smaller than that before compensation. Therefore, the grounding fault judgment method by comparing the phase relationship between the transient zero voltage and zero current at the first half wave is also applicable to the neutral ungrounded system.

In order to analyze the influence of different grounding modes on ground fault judgment, suppose that different grounding faults occur at the same location of Line 4, and the current flowing into the bus is specified as the positive direction, the data obtained by analyzing the waveform is shown in Table 2.

Table 2. Amplitude of zero sequence current under different grounding resistance.

Grounding resistance /Ω	Ground resistance fault distance /km	Line	Electric current /A
0	5	L1	−1.252
		L2	−1.345
		L3	−1.546
		L4	+ 4.148
50	5	L1	−0.948
		L2	−1.022
		L3	−1.172
		L4	+ 3.151
120	5	L1	−0.546
		L2	−0.674
		L3	−0.889
		L4	+ 2.113

It can be seen from the data in Table 2 that the change of grounding resistance only affects the magnitude of zero current amplitude, and has no effect on the direction of zero current. Comparing the zero current of the fault line with that of the non-fault line, it is found that their directions are opposite and the zero current amplitude of the fault line is equal to the sum of the zero current amplitudes of the non-fault line. Therefore, the grounding resistance has no influence on the grounding fault judgment method proposed in this paper.

6 Conclusion

The small current grounding fault judgment method proposed in this paper is not only applicable to neutral ungrounded system, but also applicable to neutral grounded system through arc suppression coil. The main conclusions of this study are as follows:

(1) When the grounding fault occurs in a small current grounding system, the zero voltage and zero current in the system will suddenly change. The characteristics of the transient zero current at the first half wave are consistent with those of the transient capacitance current, and the transient inductance current has little effect on it. By comparing the magnitude and direction of transient components of transient zero voltage and zero current, correct fault diagnosis can be achieved.

(2) The correctness of ground fault diagnosis can be improved by using the transient criterion of zero current and zero voltage and attaching the steady-state criterion. If any of the following conditions is met, ground fault will be judged: a Transient criterion: not only meet the requirements that the zero voltage and zero current of the system have sudden changes and the amplitude is greater than the set threshold

value, but also meet the requirements that the transient zero current and zero voltage have opposite directions; b. Steady state criterion: it is required to ensure that the system has continuous zero voltage and zero current and the amplitude is greater than the set threshold value, and that the steady state zero current and zero voltage are in opposite directions.

(3) In this paper, a judgment method of small current grounding fault combining transient method and steady state method is proposed, which makes up the shortage of using a single method to judge the grounding fault. When the running direction of the line changes, adaptive adjustment can be made according to the power direction, which provides an important reference value for improving the technical reliability and applicability of the temporary location of small current grounding system.

References

1. Bertolini, M., Buso, M., Greco, L.: Competition in smart distribution grids. Energy Policy **145**, 111729 (2020)
2. Kong, X., Liu, C., Shen, Y., et al.: Power supply reliability evaluation based on big data analysis for distribution networks considering uncertain factors. Sustain. Cities Soc. **63**, 102483 (2020)
3. Li, J., Zhang, G., Li, H., et al.: A review of fault location methods for small current grounding systems. IOP Conf. Ser Mater. Sci. Eng. **677**(5), 052045 (2019)
4. Xianxin, S., Hua, W.: A fault-line selection method for small-current grounded system based on deep transfer learning. Energies **15**(9), 3467 (2022)
5. Libo, L., Yang, G., Cailian, G., et al.: A new method of fault line selection for resonant grounding system based on the S-transform and credibility decision. Electr. Measur. Instrum. **56**(15), 85–90 (2019)
6. Jun, Z., Na, L., Shuguang, L.: Small current grounding fault line selection based on equivalent half wave injection method. Electr. Measur. Instrum. **57**(4), 55–60 (2020)
7. Kui, C., Xiaoguang, W., Jinbo, C., et al.: Fault line detection using sampled data processing and adaboost for small current grounding system. Proc. CSEE **34**(34), 6228–6237 (2014)
8. Siyang, X., Jianying, F., Qiang, D.: Line selection method of small current grounding fault based on GA optimized BP neural network. Electr. Measur. Instrum. **25**(3), 1–7 (2021)
9. Wang, P., Chen, B., Tian, C., et al.: A novel neutral electromagnetic hybrid flexible grounding method in distribution networks. IEEE Trans. Power Delivery **32**(3), 1350–1358 (2017)
10. Yaojing, T., Yongle, C., Jinrui, T., et al.: A Novel faulty phase selection method for single-phase-to-ground fault in distribution system based on transient current similarity measurement. Energies **14**(15), 4695 (2021)
11. Rong, H., Ge, M., Zhang, G., et al.: An Approach for detecting fault lines in a small current grounding system using fuzzy reasoning spiking neural p systems. Int. J. Comput. Commun. Control **13**(4), 521–536 (2018)
12. He, Y., Xinhui, Z., Rui, W., et al.: Faulty section location method based on dynamic time warping distance in a resonant grounding system. Energies **15**(13), 4923 (2022)
13. Yu, H., Zhang, X., Wu, W., et al.: Faulty line selection method based on comprehensive dynamic time warping distance in a flexible grounding system. Energies **15**(2), 471 (2022)
14. Li, J., Wang, G., Zeng, D., et al.: High-impedance ground faulted line-section location method for a resonant grounding system based on the zero-sequence current's declining periodic component. Int. J. Electr. Power Energy Syst. **119**, 105910 (2020)
15. Jia-Min, L., Shu-Chuan, C., Xiang, S., et al.: A single-phase-to-ground fault location method based on convolutional deep belief network. Electr. Power Syst. Res. **209**, 108044 (2022)

16. Xuewen, W., Hengxu, Z., Fang, S., et al.: Location of single phase to ground faults in distribution networks based on synchronous transients energy analysis. IEEE Trans. Smart Grid **11**(1), 774–785 (2020)
17. Li, B.: Technology of fault line selection for single-phase-to-earth fault in small current grounding system. Nonlinear Dyn. **67**(3), 2111–2122 (2012)
18. Yuanyuan, W., Yuhao, H., Xiangjun, Z., et al.: Feeder detection of single phase-earth fault using grey relation degree in resonant grounding system. IEEE Trans. Power Delivery **32**(1), 55–61 (2017)
19. Amir, F., Lauri, K., Kimmo, K.: Non-directional earth fault passage indication in isolated neutral distribution networks. Energies **13**(18), 4732 (2020)
20. Zhang, T., Haibin, Y., Zeng, P., et al.: Single phase fault diagnosis and location in active distribution network using synchronized voltage measurement. Int. J. Electr. Power Energy Syst. **117**, 105572 (2020)

Research on the Efficiency of Line Laser Removal of Tree Barriers on Transmission Lines

Fang Chunhua, Hu Tao[(✉)], Pu Ziheng, Li Peng, Wu Tian, Jiang Jinbo, Li Fang, and Zhang Yilin

College of Electrical Engineering and New Energy, China Three Gorges University, Yichang 443002, Hubei, China

taoedu96@163.com

Abstract. Tree barriers on overhead lines may lead to tripping accidents. Using the high-energy laser to remove tree barriers on transmission lines is a safe and effective new method. In this study, different types of typical trees were used as research objects for establishing ablation models, and experiments on the factors affecting the efficiency of laser tree removal were conducted. The effects of laser power, tree type, water content, and wind speed on the efficiency of laser tree removal were analyzed separately. The results showed that the ablation efficiency was negatively correlated with tree density and positively correlated with water content, wind speed, and laser power. The higher the laser power, the shorter the time required for the laser to clear the tree barrier. Trees with a water content of 50.4% are less likely to produce a charred layer that prevents the laser energy from penetrating deeper after laser burning and take less time to remove than trees with a water content of 14.2%. Wind speed has a slight effect on the efficiency of laser tree removal. The results of this study provide an essential basis for applying a laser device for clearing tree barriers.

1 Introduction

With the development of the electric power industry, the length of transmission line circuits is increasing, and a large number of brush forests have to be crossed. As the height of trees reaches within the safety range of overhead conductors, it is easy for the conductor to be struck through, thus causing tripping and blackout accidents [1–3]. During 2013–2014, according to national grid statistics, trees in the line channel are too close to the conductor and led to discharge caused by power grid blackouts, forest fires and other accidents occurred in many cases. According to the statistics of the last three years, hidden danger caused by transmission line tripping accidents in the Guangdong power grid by the tree barrier accounted for 46% of the total tripping accidents, causing a huge hidden danger to the safe operation of the line.

At present, the power sector mainly relies on manual removal of tree barriers using tools such as insulated bucket-arm trucks, telescopic ladders, and chainsaws [4, 5]. This type of clearing is highly risky in terms of safety for working at height and is not suitable for mountainous areas with poor road conditions in the field. If the power is cut off for clearing, it will cause large economic losses and affect the life of residents. For this reason, the power industry is in urgent need of a new type of efficient, safe and reliable transmission line tree barrier removal technology.

Laser technology has progressed with the development of science and technology, and compared with traditional manual removal methods of tree barriers, lasers have the advantages of noncontact, safety, and efficiency, and the application of laser barrier removal technology to transmission lines has become a research hotspot in recent years [6–8]. The interaction process between laser and material is a coupling of temperature and stress, and its extremely high energy density brings about a heating rate [9–11]. Li [12] et al. introduced the typical application of pulsed laser technology in insulator fouling cleaning and the cleaning process parameters [13]. Qi et al. conducted a study on laser deicing, and through simulation and experiment, determined a more suitable laser deicing for power industry deicing Liu [14] et al. studied the laser ablation behavior of different carbon materials and proposed the ablation mechanism for different ablation regions. The literature [15, 16] conducted a numerical modeling study on material charring and discovered the phenomena and patterns of pyrolysis, charring and ignition processes of wood under variable heat flow conditions.

Most of the above studies are theoretical mechanism studies on the application of laser technology and laser removal of foreign objects in substations, and there are few experimental studies on laser removal of tree barriers. To deeply study the efficiency of laser tree removal, this paper carries out laser tree removal experiments with different types of trees as the research object, and based on the experimental results, in-depth analysis of the influencing factors such as laser power, tree type, water content and wind speed is carried out.

2   Test Equipment and Methods

2.1   Test Equipment

The laser removal of the transmission line tree barrier device used in this test is shown in Fig. 1, consisting of an air-cooled continuous fiber laser, collimator, HD camera, head tripod, and flat plate. The output form of the device is point and line laser switching, the working distance is up to 200 m, andthe characteristics of the laser parameters are shown in Table 1.

Fig. 1. Laser removal of transmission line devices

Table 1. Laser characteristic parameters

| Item	Specification
Laser type	air-cooled fiber laser
Maximum optical power	200 W
Output mode	continuous
Aiming mode	HD camera + green light indication
Size (L × W × H)	479 mm × 589 mm × 181 mm
Power consumption	1600 W
Weight	50 kg

2.2 Test Methods and Samples

The test samples used in this paper were Paulownia, Korean pine, Osmanthus fragrans, Cinnamomum camphora and Quercus acutissima, and the list of tree samples and physical property parameters [17] are shown in Table 2.

Laser removal of tree barriers on transmission lines is applied as shown in Fig. 2. During the test, to observe the dynamic process of laser tree removal in real time, a Ti480Pro infrared camera was used to measure the temperature change of the tree surface, and the high-speed camera was used to capture the intense burning phenomenon and a dynamic process of complete ablation during laser tree removal. Considering the actual situation of flame burning, 500 frames per second was chosen for the actual shooting to meet the requirements.

Table 2. Tree physical characteristics parameters

Type	Thermal conductivity w/(m · °C)	Density kg/m^3	Specific heat capacity J/(kg · °C)
Korean Pine	0.1	456	2400
Paulownia	0.073	246	2400
Quercus acutissima	0.222	963	2400
Osmanthus fragrans	0.152	700	2400
Cinnamomum camphora	0.173	810	2400
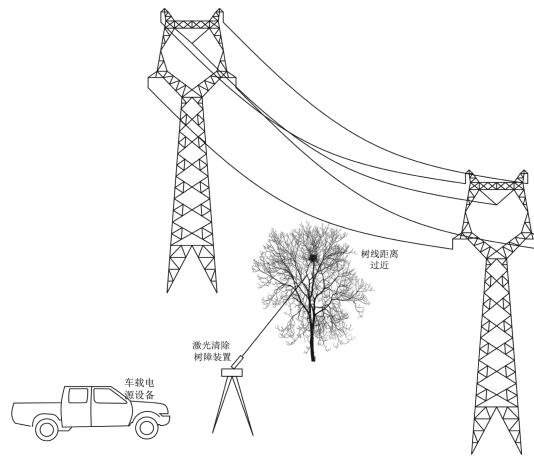
Fig. 2. Laser removal of tree barriers on transmission lines

3 Experimental Results and Discussion

3.1 Flame Distribution Pattern

In this experiment, red pine, laurel and balsam fir trees were used as test samples, and laser ablation of trees was performed in the form of a 200 W line laser during the test. To study the flame distribution, a high-speed camera was used to capture the flame screen, and then the flame area size was obtained after image processing. Figure 3 shows the flame distribution after image processing.

Figure 3(a)–(c) Fire distribution charts of Pinus koraiensis, Osmanthus fragrans and Cinnamomum camphor. The flame areas are 22.83 cm^2, 29.23 cm^2 and 49.64 cm^2 respectively by image processing. When illuminated by a laser, trees burn violently and the flame sprays out. When only considering the barrier itself, only the laser irradiation center burns violently during the process of removing the barrier and reacts quickly from the surface to the inside. No burning occurs on the trees outside the area irradiated by the laser. The laser stops transmitting and the burning stops immediately. It can be seen from the size of the flame area that the greater the density of trees, the larger the area of
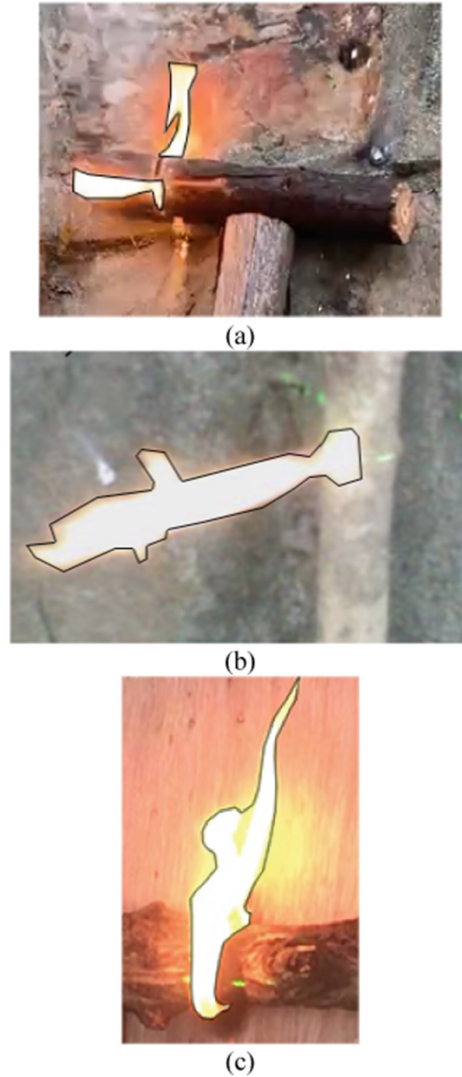
(a)

(b)

(c)

Fig. 3. Flame distribution (a) Korean pine, (b) Osmanthus fragrans, (c) Cinnamomum camphora

burning flame. However, the flame area is the area of laser action, so the larger the flame area is, the smaller the laser energy density and the longer the burning time of trees.

3.2 Effect of Laser Power on Efficiency

In this test, a 30 mm diameter laurel tree was used as the test sample object, and a line laser of 50 W, 100 W, 150 W, and 200 W was applied to the test sample until the tree was burned through.

Figure 4 shows the relationship between burn-through time and laser power. When the laser power was 50 W, the burn-through time was 37.53 s, which was the longest time; when the laser power was the peak power of 200 W, the burn-through time was 6.64 s, which was the shortest time. From Fig. 4, it can be seen that the higher the laser power is, the shorter the ablation time of trees, i.e., the higher the laser energy density is, the faster the ablation speed. According to the experimental results data, it can be found that the ablation time and laser power are not completely linear, with the increase of power, the ablation time shortening speed instead has some slowdown. This is because too high a laser power can cause the surface of the tree to heat up sharply, which results in a charring reaction. And a large part of the energy in the laser ablation process acts on the charred area, which slows the laser longitudinal ablation speed to some extent.
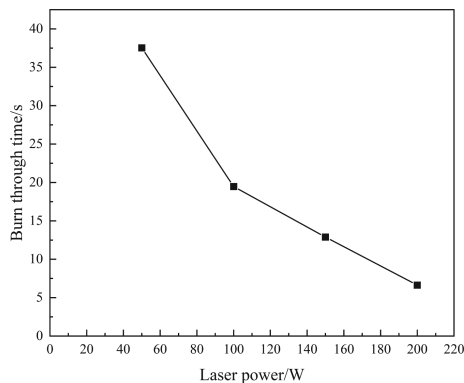

Fig. 4. Relationship between burn through time and laser power

3.3 Effect of Tree Type on Efficiency

In this test, we used 30.00 mm diameter paulownia, red pine, laurel, balsam fir and oak as the test samples. In the process of the test, we conducted ablation tests of different tree species in the form of an online laser with 200 W power, and to obtain the temperature of the trees during laser ablation in real time, we used infrared thermography for temperature measurement and a stopwatch for timing until the trees burned through. As shown in Fig. 5, the burn-through time versus tree species is shown.

As shown in Fig. 5, the longest burn-through time in the laser ablation tree test was 7.47 s for hemp oak, and the shortest time was 3.92 s for paulownia. Other conditions being equal, the higher the density of the tree, the longer the burn-through time required and the lower the maximum temperature. This is because that as the density of the trees increases, the internal defects of the trees decrease and the resistance to ablation increases.

3.4 Effect of Water Content on Efficiency

To investigate laser ablation efficiency of trees at different moisture contents, four Korean Pines with a diameter of 52.23 mm were used in this experiment to make test samples,
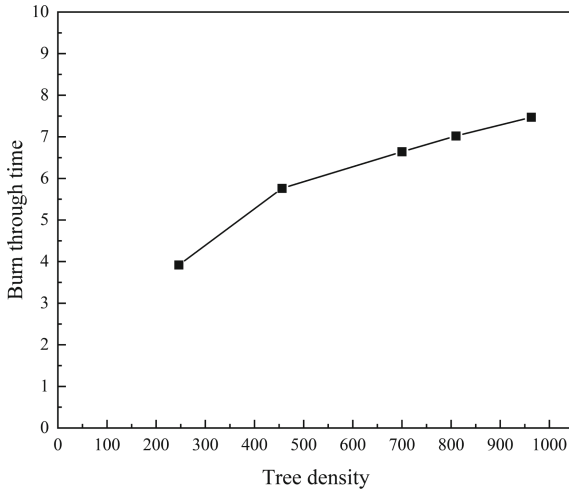
Fig. 5. Relationship between Burn through time and Tree species

and the moisture contents of the test samples were 50.4%, 43.7%, 35.1% and 14.2%, respectively, obtained by exposure to sunlight and soaking in water using the HT632 digital probe type wood moisture detector. As shown in Fig. 6, Korean pine test samples with moisture contents of 50.4%, 43.7%, 35.1%, and 14.2%, are shown.

Fig. 6. Korean pine samples with different moisture contents

In the test, four Korean pines with the same diameter and different moisture contents were irradiated with 200 W peak power in the form of a line laser until they burned through, and the temperature change of the red pines was measured with an infrared thermographic camera using stopwatch timing. During the test, the laser controller,

infrared thermal imaging camera and shooting system work simultaneously. As shown in Fig. 7, the infrared thermograms at the highest temperature of laser ablation were 50.4%, 43.7%, 35.1% and 14.2% of the Korean pine test.
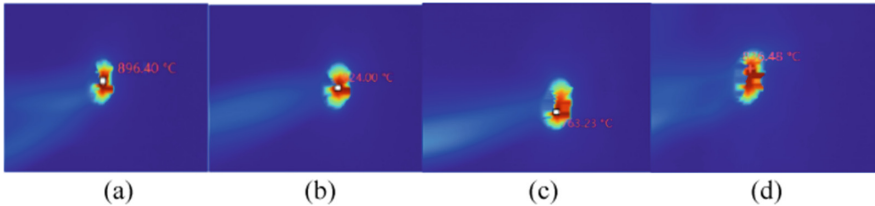

(a)   (b)   (c)   (d)

Fig. 7. Infrared thermal image at maximum temperature (a)50.4% (b)43.7% (c) 35.1% (d) 14.2%

As shown in Fig. 7, the higher the tree moisture content, the higher the maximum temperature when the line laser ablates red pine with four different moisture contents. When the laser ablates the trees, only the thermal effect in the center of the irradiation is obvious, and the temperature of the rest of the tree is basically unchanged. As seen from Fig. 8, the highest moisture content of 50.4% burned through the shortest time, 9.56 s, and the lowest moisture content of 14.2% almost dry red pine wood burned through the longest time, 16.34 s. It can be seen that the use of laser removal of tree barriers, so that the trees have the appropriate moisture content can improve the efficiency of clearing.
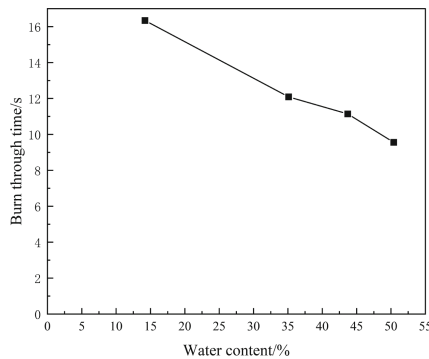

Fig. 8. Relationship between burn through time and water content

3.5   Effect of Wind Speed on Efficiency

In this test, red pine, laurel tree, and hemp oak with a diameter of 30.00 mm were used as test samples, and in the process of the test, the test of ablating tree specimens under different wind speed levels was conducted with 200 W peak power in the form of a line laser, To obtain accurate wind speed conditions, an HT625A high-precision digital anemometer was used with a three-position fan to adjust reasonable wind speed,

and an infrared thermometer was used for temperature measurement and real-time The temperature of the trees during laser burning was obtained and a stopwatch was used for timing until the trees burned through [18–20]. The burn-through times of the trees at five common wind speeds of 0.3 m/s, 1 m/s, 2 m/s, 2.5 m/s, and 3 m/s are shown in Fig. 9.
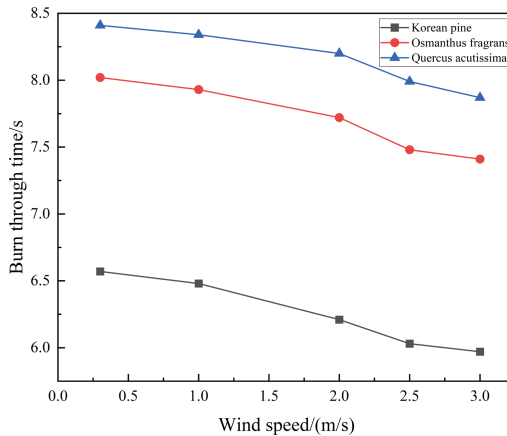

Fig. 9. Relationship between burn through time and wind speed

The time required for trees to burn through was the longest at a wind speed of 0.3 m/s, and the time required for trees to burn through was the shortest at a wind speed of 3 m/s. This shows that wind speed has a slight effect on the efficiency of laser tree clearing. This is due to the fact that when the wind blows through the laser irradiation center, the increase in air flow rate brings enough oxygen for the tree to burn violently, thus improving the clearing efficiency, although the increase in wind speed also improves heat dissipation, resulting in a slight decrease in the maximum temperature of the irradiation center, but because of the laser source of energy, the temperature effect is negligible. In general working conditions, the actual wind speed is not too large, and the wind speed has negligible effect on the efficiency of laser tree clearing.

4   Conclusion

(1)   With a peak power 200 W line laser burning through the trees, the temperature of the laser irradiation center was high, and the thermal effect was obvious only in the laser irradiation area, while the temperature in the rest of the area was kept at a lower temperature. Other conditions being the same, the higher the tree density, the larger the flame distribution area, and the longer the burn-through time required when laser ablation of different tree species was performed.

(2)   When laser ablation of trees with different water contents was performed, it was found by infrared thermography that the higher the water content of the trees, the higher the maximum temperature, and the shorter the time required for laser ablation

of trees with high water content. The lower water content of the tree ablation place is more easily charred, and most of the laser energy is blocked and absorbed by charcoal and powder.

(3) It was found that the wind speed had a low impact on the clearing efficiency under different wind speed conditions, although it only reduced the clearing time by approximately 0.5–1 s, but the wind brought sufficient oxygen for the burning of the cutting part to intensify, and did improve the clearing efficiency in general.

References

1. Zhang, W., Zhang, J., Wang, B., et al.: The research on early-warning methods of tree barriers of transmission lines based on LiDAR data. In: 2016 4th International Conference on Applied Robotics for the Power Industry (CARPI). IEEE, pp. 1–4 (2016)
2. Chen, Q., Miao, X., Jiang, H., et al.: Measurement of tree barriers in transmission line corridors based on binocular stereo vision. In: 2018 15th International Conference on Control, Automation, Robotics and Vision (ICARCV), pp. 1514–1519. IEEE (2018)
3. Fang, S., Xiaoyu, W., Haiyang, C., et al.: Research and advances in vegetation management for power line corridor monitoring. In: 2020 IEEE International Conference on Information Technology, Big Data and Artificial Intelligence (ICIBA), vol. 1, pp. 146–149. IEEE (2020)
4. Zhang, Y., Li, J., Li, C., et al.: Development of foreign matter removal robot for overhead transmission lines. J. Phys. Conf. Ser. IOP Publishing **1303**(1), 012021 (2019)
5. Zhu, A., Tu, Y., Zheng, W., et al.: Design and implementation of high-voltage transmission line inspection and foreign bodies removing robot. In: 2018 15th International Conference on Ubiquitous Robots (UR), 852–856. IEEE (2018)
6. Wang, H.Y.: Research on Foreign Matter Detection of Transmission Lines Based on Image Processing Technology. Northeast Electric Power University, Jinlin (2017)
7. Xu, X., Fang, C.H., Li, J., et al.: Analysis of ablation characteristics of the foreign matter when removing foreign matter from transmission line by laser. Photoelectron Laser **32**(06), 637–644 (2021)
8. Liu, L., Liu, X., Shan, N.: Three-dimensional simulation study on laser removal of foreign matters in high voltage transmission line. Laser Infrared **51**(10), 1286–1293 (2021)
9. Russo, R.E., Mao, X., Liu, H., et al.: Laser ablation in analytical chemistry−a review. Talanta **57**(3), 425–451 (2002)
10. Cheng, S., Geng, L., Liu, X.C., et al.: Laser ablation behavior and mechanism of C/SiC coated with ZrB2 -MoSi2 -SiC/Mo prepared by HVOF. Ceram. Int. **46**(11), 17752–17762 (2020)
11. Luan, X., Yuan, J., Wang, J., et al.: Laser ablation behavior of Cf/SiHfBCN ceramic matrix composites. J. Eur. Ceram. Soc. **36**(15), 3761–3768 (2016)
12. Li, X., Tian, J., Ma, Z., et al.: Numerical analysis and experimental study of the laser cleaning of ceramic insulator contamination. IEEE Access **10**, 49285–49296 (2022)
13. Qi, L., Zhu, X., Zhu, C., et al.: Deicing with Nd: YAG and CO_2 lasers. Opt. Eng. **49**(11), 114301 (2010)
14. Liu, Q., Zhang, L., Jiang, F., et al.: Laser ablation behaviors of SiC–ZrC coated carbon/carbon composites. Surf. Coat. Technol. **205**(17–18), 4299–4303 (2011)
15. Liu, W.P., Lv, Y.W., Wu, L.X., et al.: Numerical simulation of microwave transmission attenuation caused by laser ablation and carbonization of glass fiber reinforced plastics. Infrared Laser Eng. **50**(12), 279–285 (2021)
16. Guo, Z.F.: Study on temperature distribution and carbonization rate of wood pyrolysis process under linear rising heat flow. China University of Science and Technology 200

17. Clark, A.: Weight, volume, and physical properties of major hardwood species in the Upland-South. US Department of Agriculture, Forest Service, Southeastern Forest Experiment Station (1986)
18. Nelson, R.M., Jr.: An effective wind speed for models of fire spread. Int. J. Wildland Fire **11**(2), 153–161 (2002)
19. Kuipers, E.W., Jarvis, B., Bullman, S.J.: Combustion Efficiency of Natural Gas Flares; Effect of Wind Speed, Flow Rate and Pilots. Air & Waste Management Association, Pittsburgh (1996)
20. Valdivieso, J.P., Rivera, J.D.: Effect of wind on smoldering combustion limits of moist pine needle beds. Fire Technol. **50**(6), 1589–1605 (2014)

Study on the Interaction Characteristics of C_4F_7N/CO_2 and Its Decomposition Products with UiO-66 Based on Molecular Dynamics

Keli Gao[1], Xianglian Yan[1], Wei Liu[2], Wen Wang[1], Menglei Jin[3(✉)], Junyi Chen[3], Song Xiao[3], Yi Li[3], and Ju Tang[3]

[1] China Electric Power Research Institute, Beijing 100192, China
[2] State Grid Anhui Electric Power Company Anhui Electric Power Research Institute, Anhui 230601, China
[3] School of Electrical Engineering and Automation, Wuhan University, Hubei 430072, China
`1277407676@qq.com`

Abstract. C_4F_7N/CO_2 gas mixture is the most promising environment-friendly gas insulating medium. The selection of suitable materials for treating the C_4F_7N mixture and its decomposition products could not only keep the environment-friendly gas insulating equipment stable, but also guarantee the safety of the operation and maintenance personnel. It is necessary to study the interaction mechanism of UiO-66 with C_4F_7N and its decomposition products, which could provide a theoretical basis for the selection of adsorbents in the C_4F_7N/CO_2 gas insulating equipment. In this research, the molecular dynamics simulation was used to study the adsorption process of C_4F_7N/CO_2 gas mixture and its nine kinds of decomposition products CO, CF_4, C_2F_6, C_3F_8, C_3F_6, CF_3CN, C_2F_5CN, C_2N_2 and COF_2 in UiO-66. The adsorption configurations, adsorption capacities and isosteric heats were obtained through equal proportion competitive adsorption simulation. UiO-66 exhibits good adsorption performance for C_2F_6 and C_2N_2, with adsorption capacities of 7.25 cm^3/g, 6.97 cm^3/g, and isosteric heats of 43.46 kJ/mol, 41.87 kJ/mol, respectively. The findings suggest that UiO-66 has the potential to be used as an adsorbent in C_4F_7N/CO_2 gas insulating equipment.

Keywords: C_4F_7N/CO_2 · Decomposition products · UiO-66 · Molecular dynamics simulation

1 Introduction

As gas insulation, perfluoroisobutyronitrile (C_4F_7N) has brilliant insulating properties and low global warming potential. Despite its high liquefaction temperature (4.7 °C), it has the potential to be used in medium and low-pressure gas insulation devices after mixing with buffer gases such as CO_2 [1–3]. However, during the long-term operation of the gas-insulated switchgear, the insulating medium would decompose due to local overheating and discharge. In the cases for C_4F_7N mixtures, they would decompose

to produce toxic and corrosive gases. Some of the decomposition products may even influence the insulating properties of the mixtures. Therefore, adsorption materials are usually placed in the chamber of the switchgear to absorb these decomposition products. In this way, the gas insulation equipment could work stably much longer [4–7].

Nowadays, porous materials such as molecular sieves and activated alumina are commonly used as adsorbents in gas-insulated equipment [8, 9]. However, existing research shows that the adsorption effect of decomposition products in C_4F_7N mixture is not excellent. As one of the metal organic frameworks (MOFs), UiO-66 is a porous material with a very high internal surface area, which has high potential applications in gas storage, separation and adsorption. In this paper, performance prediction is made from the perspective of molecular dynamics simulation, and the analysis of interaction characteristics between UiO-66 and C_4F_7N/CO_2 and its decomposition products is realized by using molecular dynamics simulation, which can provide theoretical support for the treatment and detection of C_4F_7N/CO_2 gas decomposition components.

2   Molecular Dynamics Simulation

2.1   Adsorption Model

The adsorption studies were performed using the Biovia Materials Studio. Before the Grand canonical Monte Carlo (GCMC) simulations, C_4F_7N/CO_2 gas mixture and its nine kinds of decomposition products CO, CF_4, C_2F_6, C_3F_8, C_3F_6, CF_3CN, C_2F_5CN, C_2N_2 and COF_2 were geometrically optimized using Forcite code, and the electrostatic potential (EPS) charges were applied to the guest molecules. To guarantee the accuracy of the simulation and to ensure that the lengths of the three directions in space are greater than twice the cutoff radius, UiO-66 was modeled as a 2*2*2 supercell. In order to describe MOF parameters, the Universal force field was employed and geometry optimization was obtained using a forcite module to obtain structures, as shown in Fig. 1. The optimization is done to obtain stable geometry.
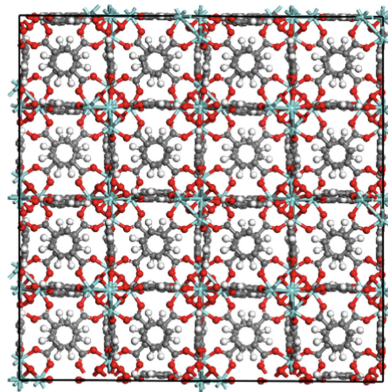

Fig. 1. Optimized UiO-66 supercell structure

2.2 GCMC Simulation

The adsorbate molecules and UiO-66 have been treated as solid structures. Ewald and atom based methods were used for electrostatic interaction and van der Waals interaction respectively. The symmetry of UiO-66 is changed to P1, which is necessary before running the sorption module. The simulation of $1*10^5$ steps was used to reach equilibrium and $1*10^6$ production steps for sampling thermodynamic properties, including the Monte Carlo steps of insertion, deletion, molecular rotation, and translation. Using the sorption module where Universal forcefield and Metropolis method were used, the fixed pressure task was applied to simulate the equal proportion competitive adsorption. The fugacity of C_4F_7N mixture and its decomposition products is set to be the same.

3   Results and Discussion

The adsorption density distribution, the minimum energy configuration, the adsorption capacity and the isosteric heats of adsorption can be obtained from the equal proportion competitive adsorption simulation.

The distribution of adsorption sites and the distribution density of adsorbate at the adsorption sites can be directly observed in the adsorption density distribution and the minimum energy configuration, as shown in Fig. 2.
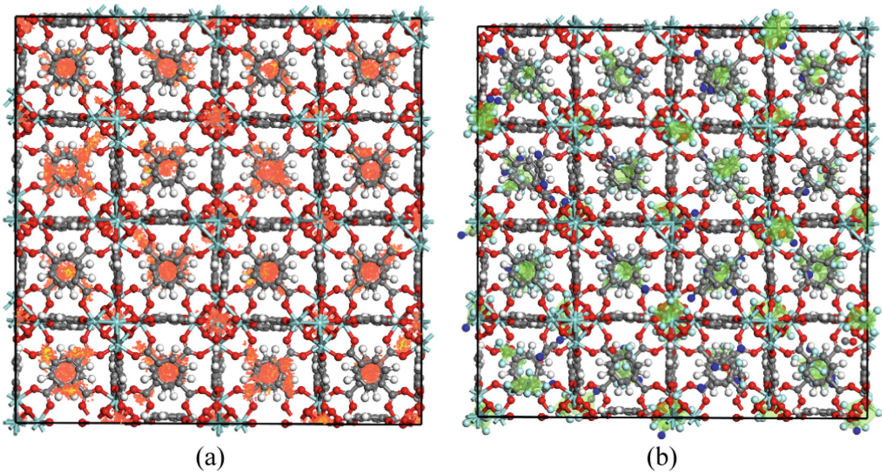

(a)   (b)

Fig. 2. (a)Adsorption density distribution and (b) minimum energy configuration of UiO-66

It can be seen from Fig. 2 that the adsorbate molecules are evenly distributed in the two main kinds of holes of UiO-66, the octahedral pore cage and the tetrahedral pore cage, which proves that the two main kinds of holes of UiO-66 have adsorption effects on the adsorbate molecules.

The adsorption capacity of equal proportion competitive adsorption simulation is depicted in Fig. 3.
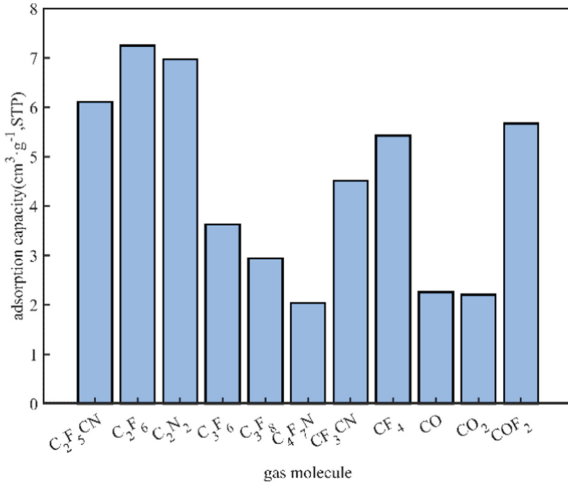
Fig. 3. Adsorption capacity of UiO-66 (298 K, 101.3 kPa)

It can be clearly seen from the figure that UiO-66 has a certain adsorption capacity for the decomposition products of C_4F_7N mixture in equal proportion competitive adsorption. C_2F_6, C_2N_2 and C_2F_5CN have higher adsorption capacity, which are 7.25 cm^3/g, 6.97 cm^3/g and 6.11 cm^3/g respectively. The adsorption capacity of C_4F_7N and CO_2 is relatively low, 2.04 cm^3/g and 2.21 cm^3/g respectively, which proves that UiO-66 will preferentially adsorb the decomposition products of C_4F_7N mixture, and has little impact on the main gas insulation medium in the equipment.

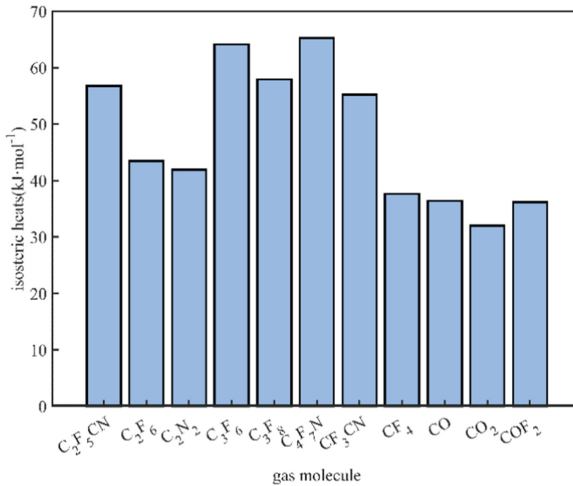The isosteric heats of equal proportion competitive adsorption simulation is depicted in Fig. 4.

Fig. 4. Isosteric heats of UiO-66 (298 K, 101.3 kPa)

The adsorption heat is 30–70 kJ/mol, indicating that it is mainly physical adsorption. Compared with the results of adsorption capacity, it is found that there are obvious differences, indicating that the adsorption process is a complex process, and the adsorption performance is not completely determined by the adsorption heat.

4 Conclusion

In this work, the equal proportion competitive adsorption simulation was conducted to assess the adsorption characteristics of UiO-66. It is found that UiO-66 has little impact on the main gas insulation medium in the equipment and has a certain adsorption capacity for the decomposition products of C_4F_7N mixture. Next, the adsorption performance of UiO-66 can be further studied through experiments and other potential adsorbents should be tested.

References

1. Li, Y., et al.: Experimental study on the partial discharge and AC breakdown properties of C_4F_7N/CO_2 mixture. High Volt. **4**(1), 12–17 (2019)
2. Gao, K., et al.: Progress of technology for environment-friendly gas insulated transmission line. Trans. China Electrotech. Soc. **35**(1), 3–20 (2020). (in Chinese)
3. Wang, Y., et al.: Research on infrared spectrum characteristics and detection technology of environmental-friendly insulating medium $C_5F_{10}O$. Vib. Spectrosc. **118**, 103336 (2022)
4. Simka, P., et al.: Decomposition of alternative gaseous insulation under partial discharge. In: Proceedings of the 20th International Symposium on High Voltage Engineering, Buenos Aires, Argentina, 28p (2017)
5. Li, Y., et al.: Influence regularity of O_2 on dielectric and decomposition properties of C_4F_7N–CO_2–O_2 gas mixture for medium-voltage equipment. High Volt. **5**(3), 256–263 (2020)
6. Wang, C., et al.: Decomposition products and formation path of C_3F_7CN/CO_2 mixture with suspended discharge. IEEE Trans. Dielectr. Electr. Insul. **26**(6), 1949–1955 (2019)
7. Yang, T., et al.: Experimental study on decomposition products of C_4F_7N/CO_2 mixture under different fault conditions. High Volt. Eng. **47**(12), 4216–4228 (2021). (in Chinese)
8. Su, Z., Zhao, Y.: Experimental investigation into effects of adsorbent on detection of SF_6 decomposition products in SF_6 equipment. High Volt. Appar. **49**(6), 26–37 (2013). (in Chinese)
9. Tang, J., et al.: Experiment and analysis of two adsorbents on the adsorption of characteristic components of SF_6 decomposition. Proc. CSEE **33**(31), 211–219 (2013). (in Chinese)

Combined Electrical and Thermal Aging Characteristics of Epoxy Resin Insulators for GIS

Wang Qing[1], Gao Jiaping[1(✉)], Su Jiahua[1], Chang Shuai[1], Xia Tianlei[1], Hao Chenyu[1], and Li Hongtao[2]

[1] State Grid Changzhou Power Supply Company, Changzhou 213000, China
962147631@qq.com
[2] State Grid Jiangsu Electric Power Co. Ltd., Electric Power Research Institute, Nanjing 211103, China

Abstract. The basin insulator is the main solid insulation component in GIS (Gas Insulated Switchgear). However, the combined stresses of thermal, electrical, and mechanical for a long time during operation may lead to the insulation failure of the insulator. It is of great significance to study the aging problem of the insulator to ensure the reliable operation of GIS. For the basis of analyzing the actual operation state of the basin insulator, an aging test platform contained multiple stresses (electrical, thermal etc.) is setup in this study. It is composed of aging chamber, AC power supply and temperature control unit. The aging temperature was controlled at 130 °C. An electric field of 5 kV/cm was applied to the surface of the epoxy resin sample. The accelerated aging test was carried out for 240 h. By means of the surface flashover test, ISPD (Isothermal Surface Potential Decay), and FTIR (Fourier Transform Infrared Spectroscopy), the performance characteristics of basin insulators with different aging degrees were studied from macroscopic and microscopic perspectives. The research results show that with the increase of aging time, the flashover voltage increases first, then decreases, then increases and decreases last with aging time. This is due to the different changes of epoxy resin at different stages of aging. The ISPD results show that the deep trap energy level increases with the aging time. The increase rate of electrical-thermal aging is slightly higher than that of thermal aging alone. The research results can provide technical support for aging state assessment of basin insulators, which have application value of practical engineering.

Keywords: Basin insulator · GIS · Electrical and Thermal Aging · Epoxy Resin

1 Introduction

GIS (Gas Insulated Switchgear) is a kind of equipment that seals a variety of electrical components in a grounded metal enclosure and connects them together. It has the advantages of compact structure, excellent insulation performance, good reliability and convenient installation, etc. It is widely used in substations of various voltage levels [1,

2]. As the main solid insulation component in GIS, the basin insulator plays a key role in supporting metal guide rod, isolating and sealing air chamber, solid insulation, etc. Its insulation life is closely related to the overall reliable operation of GIS. Meanwhile, the basin insulator failure is also one of the main causes of GIS equipment failure [3, 4].

Basin insulator is mainly made of solid epoxy resin, curing agent and Al_2O_3 filler. It has good insulation and mechanical properties. However, due to the combined effect of thermal, electrical, mechanical force in the operation process for a long time, the basin insulator will deteriorate. It is easy to induce flashover, breakdown, explosion and other failures [5, 6]. Therefore, in order to ensure the reliable operation of GIS, it is of great practical significance to study the aging issue of the basin insulator.

In this article, an electrical-thermal combined aging test platform was built. A 240 h aging test was carried out on the epoxy resin used for basin insulators. Firstly, the electrical properties such as surface flashover, resistivity and trap characteristics were tested. After that, FTIR and dielectric energy spectrum were used to further characterize the aging degree. Finally, the activation energy was calculated using dielectric energy spectrum. These results provide a basis for establishing the relationship between activation energy and aging state.

2 Experimental Details

2.1 Electrical-Thermal Aging Platform

The test was carried out in a constant temperature aging chamber. The experimental device is shown in Fig. 1 [7]. Many properties of polymers change dramatically near the glass transition temperature. Therefore, the temperature of electrical-thermal combined aging was set to the glass transition temperature of epoxy resin sample 130 °C [8].
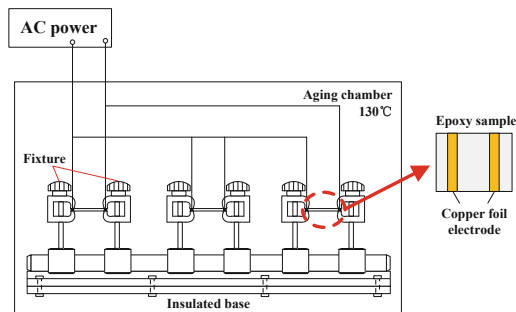

Fig. 1. Aging experiment platform

The electrical stress applied a uniform electric field to the surface through the copper foil electrode. The power supply is a high-voltage AC power supply with 50 Hz. The voltage was applied with reference to 50% of the initial flashover voltage, which was 5 kV/cm. The electrode spacing was 2 cm.

2.2 Sample Preparation

The epoxy resin samples were plates of 70 × 50 × 1 mm with the same pouring process. Before the test, the surface of the sample was wiped with anhydrous ethanol and dried at 70°C in the room temperature drying box. Two groups of samples were set: thermal aging only and electrical-thermal combined aging. The samples were taken at 30 h intervals. The aged samples were cut to square of 20 × 20 × 1 mm for subsequent testing.

3 Aging Test and Discussion

3.1 Flashover Voltage Test

The surface flashover of basin insulator is a common fault in GIS. To analyze the flashover voltage characteristics, finger electrodes are used for flashover test. The electrode spacing was 1cm. Ten flashover tests was performed for each sample. The flashover voltage data was analyzed based on weibull distribution [9]. The scale parameter was counted, which represents the flashover voltage when the cumulative failure probability is 63.2%. It can reflect the insulation performance of the material. The results are shown in Fig. 2. The flashover voltage of the epoxy sample shows an increasing - decreasing - increasing - decreasing trend with the aging time. The variation range of the electrical-thermal combined aging is larger. Because the structure of epoxy resin changes with the aging time. In the first stage, the "secondary curing" of thermal aging can further cross-link the epoxy sample under the action of thermal and the action of residual curing agent to improve the performance of the sample [10]. In the second stage, the curing agent degrades to produce free acid, at the same time, the chemical bond in the molecular chain of epoxy resin with weak connection breaks. The two reactions produce polar groups and free radicals, which reduces the performance of epoxy. In the third stage, the performance improves slightly because the curing agent basically decomposes completely and accompanies by gas volatilization. The decrease of the number of free radicals in epoxy resin leads to the weakening of the adsorption of carrier and space charge. Finally, due to the molecular chain fracture of the epoxy resin, a large number of polar groups are generated, which leads to a decline in properties and subsequent deterioration over time [11].

3.2 ISPD Test

Trap characteristics can be used as an effective characterization parameter of polymer aging [12]. The trap density and trap energy levels of epoxy samples with different aging time were measured by ISPD method [13]. The ISPD result is shown in Fig. 3. The deep trap energy level increases with aging time. The growth rate of electrical-thermal aging is slightly higher than that of thermal aging alone. The density of the deep trap is related to the aging rate. The higher the density of the deep trap, the higher the aging rate of the material and the faster the insulation performance will decline. It can be seen from the trap characteristics that the deterioration rate of the electric heating aging at 120 h is significantly faster, while the thermal aging deterioration rate gradually accelerates with the aging time. The density of the deep trap is related to the aging rate. The higher
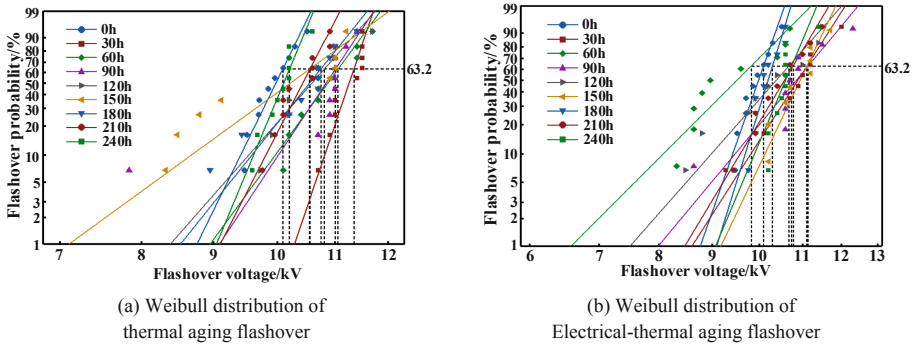
(a) Weibull distribution of
thermal aging flashover

(b) Weibull distribution of
Electrical-thermal aging flashover

Fig. 2. Flashover voltage characteristics at different aging conditions

the density of the deep trap, the higher the aging rate of the material and the faster the insulation performance will decline. It can be seen from the trap characteristics that the deterioration rate of electric heating aging for 120 h is significantly higher than that of 240 h, while the thermal aging rate gradually increases with the aging time.
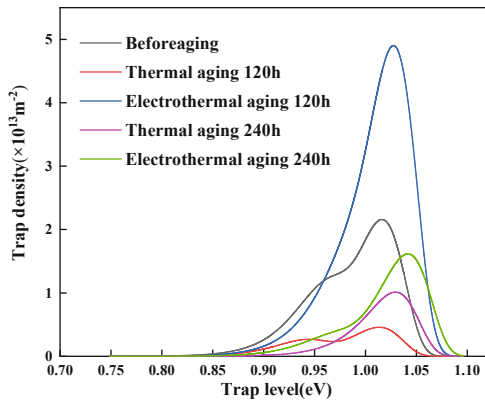

Fig. 3. Trap characteristics of epoxy samples at different aging times

3.3 FTIR Test

Fourier Transform Infrared spectroscopy is used to track and analyze the spectral information of the aging process of materials [14]. The characteristic quantity of the aging state of materials is determined by the peak value of chemical bond corresponding to the wavenumber of different functional groups. The four major groups in the epoxy were analyzed, as shown in Table 1.

Table 1. Main group of epoxy resins for basin insulators

Group	Wavenumber/cm^{-1}
C-O-C	1037
C=O	1735
CH3	2900
OH	3600

(a) FITR under thermal aging
at different aging times

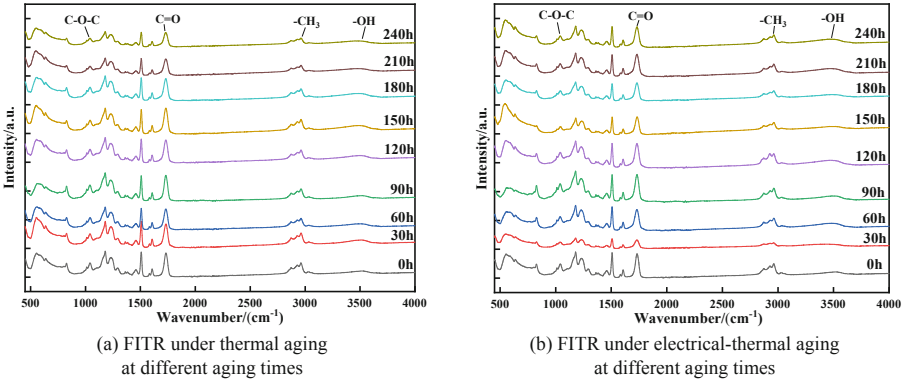(b) FITR under electrical-thermal aging
at different aging times

Fig. 4. FITR at different aging conditions

The FTIR result is shown in Fig. 4. At the early stage of aging, the water and residual small molecules in the sample volatilized, causing the decrease of hydroxyl content. After 150 h, the ester bond broke to form the hydroxyl group. The thermal oxygen reaction occurred during aging, resulting in the gradual increase of hydroxyl content [15]. However, the addition of electric field inhibited the generation of hydroxyl by the thermal oxygen reaction. Due to the instability of the free radicals in the oxidation process, the addition of an electric field can provide electrons for the free radicals to stabilize them, thus inhibiting oxidation.

4 Summary

In this paper, the combined electrical and thermal aging characteristics of epoxy resin insulators for GIS is investigated. The main conclusions are summarized as follow:

1) The flashover voltage of epoxy sample changes regularly with aging time. The deterioration degree of electrical-thermal combined aging is larger and the external deterioration is greater than the internal deterioration.
2) The higher the deep trap density, the higher the material aging rate and the faster the insulation performance decline. The effect of electric heating aging is obviously greater than that of thermal aging alone, which proves that electric stress has an accelerated effect on aging.

3) According to the FTIR results, the epoxy resin insulating materials undergo oxidation decomposition and molecular chain fracture after aging. However, there are certain differences in the changes of group peak value between thermal aging and electrical-thermal aging.

References

1. Chang, C., Chang, C.S., Jin, J.: Source classification of partial discharge for gas insulated substation using waveshape pattern recognition. IEEE Trans. Dielectr. Electr. Insul. **12**(2), 374–386 (2005)
2. Li, C., Xu, Y., Lin, C: Surface charging phenomena on HVDC spacers for compressed sf6 insulation and charge tailoring strategies. CSEE J. Power Energy Syst. **6**(1), 83–99 (2019)
3. Pearson, J.S., Farish, O., Hampton, B.F.: Partial discharge diagnostics for gas insulated substations. IEEE Trans. Dielectr. Electr. Insul. **2**(5), 893–905 (1995)
4. Lin, L., Yao, Z., Yanpeng, H.: Surface flashover patterns of GIS basin insulator under impulse voltage. Eng. Fail. Anal. **130**, 105800 (2021)
5. Bo, Q., Chunjia, G., Chengrong, L.: The influence of surface charge accumulation on flashover voltage of GIS/GIL basin insulator under various voltage stresses. Int. J. Elect. Power Energy Syst. **105**, 514–520 (2019)
6. Tong, L., Hongtao, L., Jianjun, L.: Insulation breakdown fault caused by stress crack of GIS basin-type insulator. High Volt. Apparat. **56**(2), 240–245 (2020)
7. Preetha, P., Thomas, M.J., Ranjan, R.: Electro-thermal Ageing of Epoxy Nanocomposites. IEEE Trans. Dielectr. Electr. Insul. **19**(6), 2081–2089 (2013)
8. Roggendorf, C., Schnettler, A.: Accelerated hydrothermal aging of epoxy resin based syntactic foams with polymeric microspheres. IEEE Trans. Dielectr. Electr. Insul. **19**(3), 973–980 (2012)
9. Duo, H., Chengyan, R., Fei, K.: Aging characteristics of polymeric materials by repeated surface flashovers in vacuum under microsecond pulse. IEEE Trans. Dielectr. Electr. Insul. **26**(1), 171–178 (2019)
10. Rongguo, W., Long, J., Zhonghai, X.: Thermal aging behavior of carbon fiber/epoxy composites at high temperature. Polym. Polym. Compos. **22**(3), 309–312 (2014)
11. Peng, R., Honglei, L., Yunpeng, L.: Life prediction method and application of dry type insulation equipment based on activation energy. Insulat. Mater. **54**(3), 91–97 (2021)
12. Zhonglei, L., Boxue, D., Chenlei, H.: Trap modulated charge carrier transport in polyethylene/graphene nanocomposites. Sci. Rep. **7**, 4015 (2017)
13. Sjostedt, H., Gubanski, S.M., Serdyuk, Y.V.: Charging characteristics of EPDM and silicone rubbers deduced from surface potential measurements. IEEE Trans. Dielectr. Electr. Insul. **16**(3), 696–703 (2009)
14. Benhong, O., Huan, L., Xu, Z.: The role of micro-structure changes on space charge distribution of xlpe during thermo-oxidative ageing. IEEE Trans. Dielectr. Electr. Insul. **24**(6), 3849–3859 (2017)
15. Xiaoxing, Z., Yunjian, W., Xiaoyu, C.: Theoretical study on decomposition mechanism of insulating epoxy resin cured by anhydride. Polymers **9**(8), 341 (2017)

Thermal-Pressure Effect Simulation and Protection Effect Analysis of Metal Grid Absorber Due to Internal Short-Circuit Arcing in the Switchgear

Peng Li[1,2(✉)], Yehe Gao[1,2], Chang Liu[3], Qihui Liu[1,2], Ziheng Pu[1,2], Tian Wu[1,2], and Chunhua Fang[1,2]

[1] Hubei Provincial Engineering Technology Research Center for Power Transmission Line, China Three Gorges University, Yichang 443002, Hubei, China
lipeng_ctgu@163.com
[2] College of Electrical Engineering and New Energy, China Three Gorges University, Yichang 443002, Hubei, China
[3] State Grid Handan Power Supply Company, Handan 056035, Hebei, China

Abstract. As one of the important pieces of equipment in the power system, the safe and stable operation of switchgear is crucial to the security and reliability of the power supply . However, short-circuit arcing accident in the switchgear happens occasionally, the high temperature and pressure effect produced by which seriously threatens the safety of surrounding buildings and staff. In this paper, a calculation method of arc thermal-pressure effect based on arc energy heat equivalence was proposed, and the validity of the calculation method was verified by experiments . Meanwhile, in order to reduce the harm of high temperature and high-speed airflow caused by short-circuit arcing process, the protective measures based on metal grid absorber were put forward. An equivalent mathematical model of metal grid absorber was constructed, and the influence of grid arrangement on the protection effect was analyzed. The results show that the pressure rise obtained by the arc energy heat equivalent method is in good agreement with the experimental results, and the error is small. The metal grid absorber can effectively reduce the temperature and velocity of gas in the opening. When the metal grid absorber is in-line arrangement, the maximum velocity and temperature of gas in the pressure relief opening are decreased by about 31.18% and 38.29%, respectively. The protection effect of the metal grid absorber with staggered arrangement is better, and the heat absorption efficiency is about 6.83%, which is about 2.09% higher than that of metal grid absorber with in-line arrangement.

Keywords: switchgear · short-circuit arcing · thermal-pressure effect · metal grid absorber · protection effect

1 Introduction

Switchgear is one of the important equipments to ensure the safe and stable operation of the power system [1, 2]. Switchgear is often damaged in substations, among them,

the insulation aging and overload operation caused by the switchgear failure accounted for a large proportion [3–5], these two kinds of reasons may lead to switchgear internal short-circuit arcing and other faults resulting in its explosion burned, endangering the safety of surrounding buildings and staff.

Currently for the closed container internal short-circuit arc generated by the pressure rise problem has carried out more research, Uzelac et al. [6] proposed the standard calculation method (SCM), which can directly calculate the pressure rise inside the chamber as long as the arc energy is obtained. Friberg et al. [7] proposed an improved standard calculation method (ISCM) and a pressure rise calculation method based on fluid dynamics (CFD). Li M et al. [8–10] used the MHD method to calculate the thermal-pressure effect caused by short-circuiting arcing in a closed container and analyzed the differences between different radiation models. To reduce the harm caused by arc fault, in addition to active protection measures such as grounding protection and arc protection [11, 12], passive protection methods can also be used [13], such as installing metal grid absorbers at the pressure relief openings of switchgear to protect equipment and staff safety. Iwata et al. [14, 15] found that the installation of a metal grid absorber in the pressure relief channel of switchgear can effectively reduce the airflow temperature and maximum pressure rise at the pressure relief opening. Oyvang et al. [16] analyzed the influence of metal grid absorber on temperature and pressure rise by conducting an internal arcing experiment with metal grid absorber. Anantavanich et al. [17] studied and analyzed the influence of the placement position and number of layers of the metal grid absorber on the airflow velocity and temperature inside. In general, the existing research mainly analyzes the protective effect of the metal grid absorber on the arc fault and pays less attention to the construction of the equivalent mathematical model of the metal grid absorber and its arrangement.

In this paper, the cable chamber of 7.2 kV switchgear is taken as the research object, and the calculation method of the thermal-pressure effect of internal short-circuit arcing in switchgear based on the thermal equivalence of arc energy is proposed. Meantime, the equivalent mathematical model of metal grid absorber is established. The protection effect is verified by simulation calculation, and the difference between different grid arrangements is analyzed. The research can provide a reference for numerical simulation and protection design of the thermal-pressure effect of internal short-circuit arcing in switchgear.

2 Arc Energy Thermal Equivalence Calculation Method

2.1 Calculation Method and Process

In order to study the arc thermal-pressure effect caused by short-circuiting arcing inside the switchgear, obtain the temperature-pressure rise distribution inside the compartment, and improve the computational efficiency, a calculation method of arc thermal-pressure effect based on arc energy heat equivalence of arc energy is proposed, which ignores the influence of the electromagnetic field, equates the high-temperature arc as a fixed heat source Q_{arc}, combines the air plasma physical parameters, turbulence model, radiation model, by solving the temperature-fluid field to obtain the distribution

of thermal-pressure effect inside the compartment. The Q_{arc} can be calculated below:

$$Q_{arc} = P_{arc} / V_{arc} = UI / V_{arc} \tag{1}$$

where Q_{arc} the arc equivalent heat source, P_{arc} the arc power, V_{arc} the arc volume.

This paper uses the six-band P−1 radiation model, which can calculate the radiation self-absorption effect at any point in space, and can better simulate the radiation conditions in the low-temperature region. The turbulence is described by the standard $k-\varepsilon$ model, which is suitable for most engineering flow field calculations [18, 19].

2.2 Calculation Model and Parameters

Due to the large size of the actual switchgear and high calculation cost, a scaling model with a reduction factor of volume set to 1/8 (as shown in Fig. 1) was established based on the actual size of the cable compartment of the 7.2 kV air-insulated switchgear. The size of pressure relief flap is 15 × 30 cm, and the pressure measurement point is located at #1 in Fig. 1 with coordinates (0, 10, 10), which can monitor the change of the pressure rise inside.
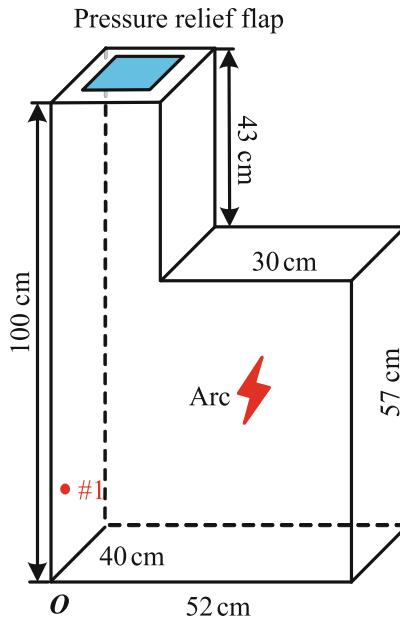

Fig. 1. Calculation model

The air plasma physical parameters, which depend on the temperature and pressure, are taken from Xi'an Jiaotong University's "Gas Discharge Plasma Database". The power of the short-circuit arcing obtained from the experiment, the law of change is shown in Fig. 2: the arc power obtained under the fully enclosed condition and the pressure relief flap opening condition is basically the same, and the error is small.
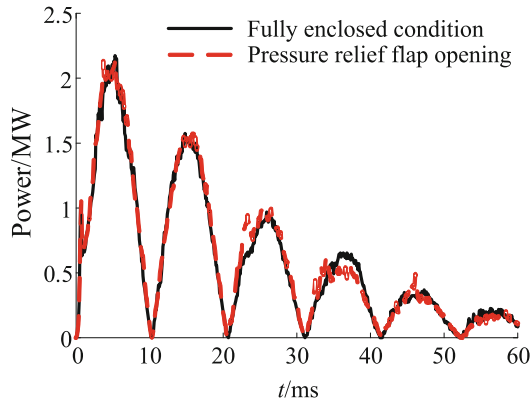
Fig. 2. Power of the short-circuit arc

2.3 Calculation Method Validation

Through the calculation of the short-circuit arcing process monitoring point #1 pressure rise change law. It can be seen in Fig. 3 that the experiment and simulation of the pressure rise change law are basically the same, fully enclosed conditions, due to the arc power oscillation down, the pressure inside is increased and then gradually saturated trend, with pressure relief flap conditions, the pressure inside rising before the pressure relief flap opening is the same as the fully enclosed model, when the arcing process to about 25 ms, the pressure relief flap open, the pressure inside drops rapidly to the ambient pressure. Therefore, the thermal equivalent of the arc energy based on the internal short circuit of the switchgear thermal-force effect calculation method proposed has good accuracy in this paper.
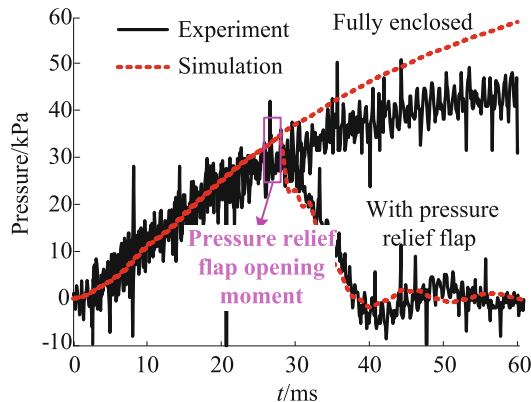

Fig. 3. Comparison between calculation and test results

3   Metal Grid Absorber Mathematical Model

3.1   Effects of Metal Grid Absorber

Metal grid absorber is a filter composed of porous plates, which is one of the methods to limit the thermal-pressure effect of short-circuit arcing inside the switchgear. When the high temperature and high-speed airflow generated by the burning arc through the metal grid absorber, it can cool the hot airflow and produce resistance, thus reducing the temperature and the gas flow velocity at the pressure relief flap. The main effects of absorber is heat energy absorption and flow resistance. Based on the tube bundle heat transfer theory [20], an equivalent mathematical model of the metal grid absorber is proposed, including the heat energy absorption model and the flow resistance model.

3.2   Calculation Method

In the simulation, the heat absorption and flow resistance of the metal grid absorber is solved by adding the source term to the corresponding conservation equation:

(1)   Modelling of heat energy absorption:

The heat energy absorption of the metal grid absorber can be equated to the energy loss in the area of the metal grid absorber, and the loss source term S_h can be added to the energy conservation equation.

$$\int S_\mathrm{h} \cdot dV = -\frac{\Delta Q}{V_\mathrm{A} \cdot \Delta t} \cdot V \tag{2}$$

where ΔQ is the total heat absorbed at each time step, V_A is the total volume of the absorber, and the minus sign represents the energy loss.

(2)   Modelling of flow resistance

The flow resistance is reflected in the pressure loss Δp caused by the frictional force F_F on the fluid in the area of the metal grid absorber, where the frictional force F_F is calculated as shown in Eq. (3):

$$F_\mathrm{F} = \int_0^{A_\mathrm{A}} \Delta p \cdot dA = \Delta p \cdot A_\mathrm{A} \tag{3}$$

where A_A is the surface area of the metal grid absorber. Since the pressure loss due to friction is reflected in the volume force, the loss source term S_f can be added to the momentum conservation equation, which is calculated as shown in Eq. (4):

$$\int S_\mathrm{f} \cdot dV = -\frac{F_\mathrm{F}}{V_\mathrm{A}} \cdot V \tag{4}$$

4   Calculation of Thermal-Pressure Effect of Short-Circuit Arc Inside Switchgear with Metal Grid Absorber

4.1   Calculation Model and Parameters

In order to study the protection effect of the metal grid absorber, a computational model was established with the installation of the metal grid absorber shown in Fig. 4.
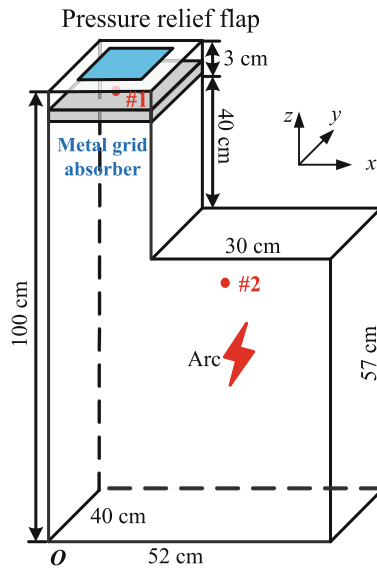

Fig. 4. Calculation model with metal grid absorber

The metal grid absorber is located 3 cm below the pressure relief flap, and its dimensions are 22 × 40 × 3.5 cm. Two monitoring points (#1 and #2) are provided inside the compartment with coordinates (11, 20, 98) and (30, 20, 50), which can monitor the changes of outlet temperature, flow rate and pressure rise inside. The calculation parameters of the metal grid absorber are shown in Table 1.

Table 1. Parameters of arc energy absorber

	In-line arrangement	Staggered arrangement
N_A (gird layer)	3	
S_A (surface area)	0.264 m^3	0.264 m^3
effective orifice area	0.108 m^3	0.108 m^3

<div align="right">(continued)</div>

	In-line arrangement	Staggered arrangement
a (transverse pitch ratio)	1.75	
b (pitch ratio)	1.25	
d (Diameter of grid strip)	0.01 m	0.01 m

4.2   Calculation Results and Analysis

According to the above model for simulation calculation, the thermal-pressure effect distribution of the short-circuit arcing process inside the cable compartment with the pressure relief flap is obtained. Among them, the flow velocity distribution of the cross-section with and without metal grid absorber (in-line arrangement) is shown in Fig. 5: when the pressure relief flap opens at 25 ms, the gas inside flows out quickly and the flow rate increases significantly. Installation of metal grid absorbers reduces the gas flow rate by approximately 30%. It can be seen that the metal grid absorber can effectively reduce the speed of high-speed airflow inside and reduce its impact effect on the outside.
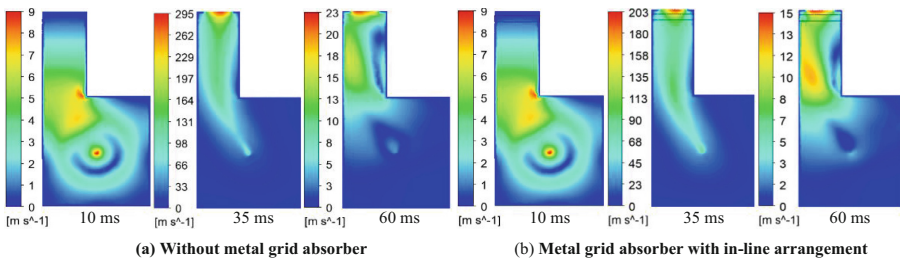

(a) Without metal grid absorber   (b) Metal grid absorber with in-line arrangement

Fig. 5. Velocity distribution of symmetrical section

When the pressure relief flap is opened, due to the airflow outward at high speed, the arc area hot gas diffusion to the outlet, the pressure relief flap section temperature distribution is shown in Fig. 6. As can be seen, the metal grid absorber can significantly reduce the temperature of the high-velocity gas ejected from the cabinet, thus weakening the thermal effect of the fault arc on the surrounding staff and buildings.

4.3   Effect of the Arrangement on the Protection Effect

In order to study the effect of metal grid absorber arrangement on the protection effect, the difference of airflow rate, temperature and pressure rise in the cabinet and pressure relief flap when the metal grid is arranged in in-line and staggered arrangement is compared and analyzed. The variation of the flow velocity at the pressure relief flap (monitoring point #1) is shown in Fig. 7(a). During the pressure relief process, the maximum flow velocity obtained for the in-line and staggered arrangements of the metal grid absorber was about 43.39% and 54.31% lower than those without the absorber. The staggered
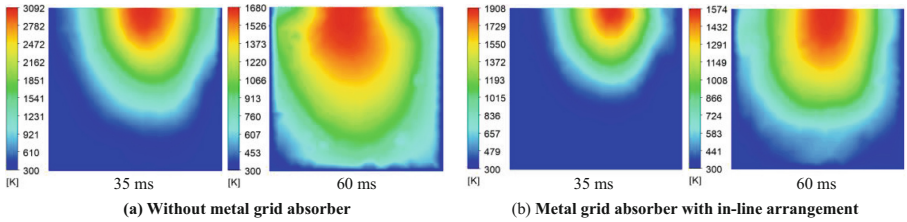
(a) Without metal grid absorber   (b) Metal grid absorber with in-line arrangement

Fig. 6. Temperature distribution of pressure relief opening cross-section

arrangement has the best flow resistance effect, and the gas flow velocity decreases by about 42.10% compared to the in-line arrangement.

As shown in Fig. 7(b), the temperature change at the pressure relief flap is influenced by the flow rate. When the flow rate inside increases, the hot airflow accelerates out, resulting in a higher outlet temperature. During pressure relief, the maximum temperature obtained for the in-line and staggered arrangement were about 5.19% and 6.40% lower than without the metal grid absorber. During the arcing process, the heat absorption efficiency of the metal grid absorber in-line and staggered arrangement is 4.74% and 6.83%, which shows that the heat absorption effect of the staggered arrangement method is better and its heat absorption efficiency is about 2.09% higher than that of the in-line arrangement.
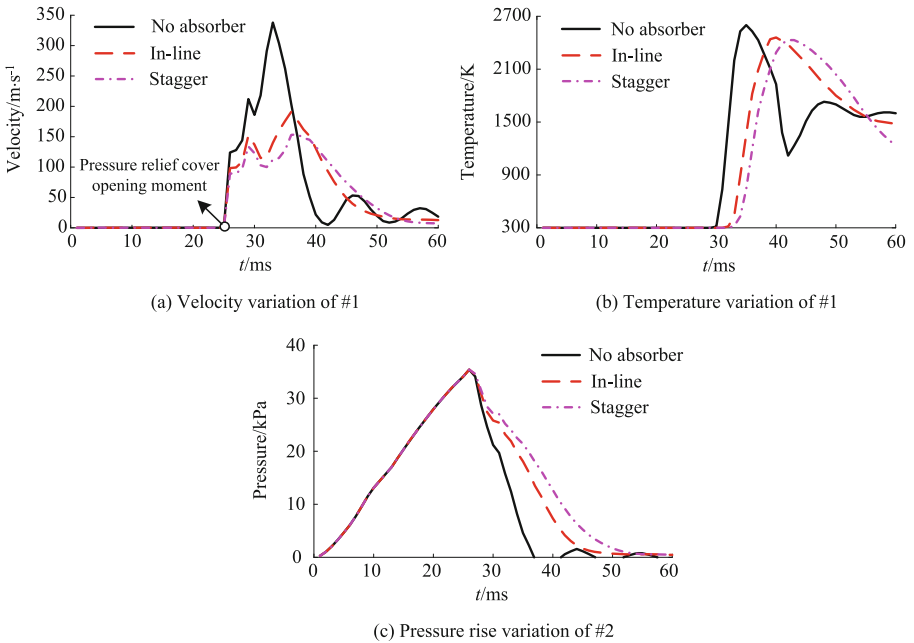

(a) Velocity variation of #1

(b) Temperature variation of #1

(c) Pressure rise variation of #2

Fig. 7. Effect of arrangement on the protection effect

As shown in Fig. 7(c), the maximum pressure rise in the model with metal grid absorber is basically the same as that without metal grid absorber in both arrangement. The metal grid absorber only slows the rate of pressure drop inside but does not affect the pressure relief process. In summary, the staggered arrangement method of high temperature and high-speed airflow protection is more effective, it is recommended that the actual use of metal grid absorber staggered arrangement to reduce the impact of the fault arc.

5   Conclusion

1) When the internal short-circuit arcing occurs in the switchgear, the pressure rise calculated by the arc energy thermal equivalence calculation method is basically consistent with the experiment results, and the error is small, which verifies the effectiveness of the calculation method.
2) The metal grid absorber can effectively reduce the temperature and flow rate of the air emitted from the pressure relief flap, which can reduce the damage to the surrounding staff and buildings. When the metal grid absorber is in-line arrangement, the maximum velocity and temperature of air at the pressure relief flap can be reduced by about 31.18% and 38.29% respectively.
3) The maximum velocity of air at the pressure relief flap can be reduced by about 19.29% compared with the in-line arrangement. The heat absorption efficiency of the metal grid absorber staggered arrangement is 6.83%, which is about 2.09% higher than that of the in-line arrangement. Therefore, it is suggested that the metal grid absorber should be arranged in staggered arrangement.

References

1. Hussain, G.A., Shafiq, M., et al.: Online condition monitoring of mv switchgear using d-dot sensor to predict arc-faults. IEEE Sensors J. **15**(12), (2015)
2. Daalder, J.E., Lillevik, O., Rein, A., et al.: Arc in SF6 MV switchgear pressure rise in equipment room. In: 10th International Conference on Electricity Distribution, pp. 37–41. Brighton, UK (1989)
3. Zhang, X., Dai, K., Niu, W., et al.: Simulation and analysis of a gas insulated switchgear explosion accident caused by a failure of high-voltage circuit breaker in a thermal power plant. J. Eng. **2019**(4), 3418–3424 (2019)
4. Straumann, U., Stoller, P.: The impact of partly liquefied SF6 on the dielectric performance of SF6-insulated switchgear. IEEE Trans. Dielectr. Electr. Insul. **26**(1), 137–145 (2019)
5. Cressault, Y., Hannachi, R., Teulet, P., et al.: Influence of metallic vapours on the properties of air thermal plasmas. Plasma Sources Sci. Technol. **17**(3), 035016 (2008)
6. Uzelac, N., Dullni, E., Kriegel, M., et al.: Application of simplified model for the calculation of the pressure rise in MV switchgear due to internal arc fault. In: 22nd International Conference on Electricity Distribution, pp. 10–13. Stockholm, Sweden (2013)
7. Friberg, G., Pietsch, G.J.: Calculation of pressure rise due to arcing faults. IEEE Trans. Power Delivery **14**(2), 365–370 (1999)

8. Rong, M., Li, M., Wu, Y., et al.: 3-D MHD modeling of internal fault arc in a closed container. IEEE Trans. Power Delivery **32**(3), 1220–1227 (2017)
9. Li, M., Zhang, J., Hu, Y., et al.: Simulation of fault arc based on different radiation models in a closed tank. Plasma Sci. Technol. **18**(05), 549–553 (2016)
10. Li, M., Wu, Y., Liu, J., et al.: Aluminum erosion due to fault arcing and its effects on temperature and pressure in a closed air vessel. IEEE Trans. Plasma Sci. **48**(10), 3487–3494 (2020)
11. Pan, B., Zhang, Y., Gui, X., et al.: Summarize on application of arc protection device in substation. IOP Conf. Ser. Mater. Sci. Eng. **677**(5), (2019)
12. Cherng, G.J., Shin, L.D., Wang, J.M., et al.: Design of a DC series arc fault detector for photovoltaic system protection. IEEE Trans. Indust. Appl. **55**(3), (2019)
13. Parsons, A., Faber, T., Metzdorf, M.A., et al.: Enhancing worker and equipment protection through passive arc-fault mitigation. IEEE Trans. Indus. Appl. **56**(3), (2020)
14. Iwata, M., Tanaka, S., Miyagi, T., et al.: Influence of perforated metal plate on pressure rise and energy flow due to internal arcing in a container with a pressure-relief opening. IEEE Trans. Power Delivery **29**(3), 1292–1300 (2014)
15. Iwata, M., Tanaka, S., Miyagi, T., et al.: CFD calculation of pressure rise and energy flow of hot gases due to short-circuit fault arc in switchgears. In: 18th International Conference on Electrical Machines and Systems (ICEMS), pp. 1390–1394. Pattaya, Thailand (2015)
16. Oyvang, T., Rondeel, W., Fjeld, E., et al.: Energy based evaluation of gas cooling related to arc faults in medium voltage switchgear. In: 22nd International Conference and Exhibition on Electricity Distribution, pp. 1–4. Stockholm, Sweden (2013)
17. Anantavanich, K., Pietsch, G., Uzelac, N., et al.: Effect of arc energy absorber in a wind turbine switch unit. IEEE Trans. Power Delivery **28**(2), 549–556 (2013)
18. Wu, Y., Li, M., Rong, M., et al.: Experimental and theoretical study of internal fault arc in a closed container. J. Phys. D Appl. Phys. **47**(50), 505204 (2014)
19. Zhou, Q., Li, H., Xu, X., et al.: Comparative study of turbulence models on highly constricted plasma cutting arc. J. Phys. D: Appl. Phys. **42**(1), (2009)
20. Stephan, P., Martin, H., Kabelac, S., et al.: VDI Heat Atlas. Springer-Verlag, Berlin Heidelberg, pp. 1076–1090 (2010)

Aging State Detection Method of Composite Insulator Based on Microwave Transmission Method

Li Zijin[1,2], Li Peng[1,2(✉)], Zhang Boming[1,2], Pu Ziheng[1,2], Wu Tian[1,2], and Fang Chunhua[1,2]

[1] Hubei Provincial Engineering Technology Research Center for Power Transmission Line, China Three Gorges University, Yichang 443002, Hubei, China
lipeng_ctgu@163.com
[2] College of Electrical Engineering and New Energy, China Three Gorges University, Yichang 443002, Hubei, China

Abstract. Composite insulators will suffer different degrees of insulation aging phenomenon due to long-term internal and external overvoltage and complex environment and other factors, which will seriously threaten the normal operation of transmission lines. In this paper, a method for detecting the aging state of composite insulators is proposed based on microwave transmission. According to the 10 kV composite insulators and its aging law, the numerical simulation models of insulators with different aging states are constructed. Through the fixed frequency scanning at different positions with the rectangular waveguide, the best-fixed frequency detection method is determined by comparing and analyzing the amplitude variation law of S_{21} (scattering parameter). Considering different degrees of aging, the detection effect of microwaves on the overall aging of composite insulators was studied by moving waveguide detection method. The results show that when the waveguide is transverse and the scanning frequency is 17.695 GHz, the detection effect of different aging states of composite insulators is the most significant. The research results are of great significance to the field of composite insulator aging state detection and evaluation.

Keywords: Composite insulators · microwave transmission method · aging detection · scattering parameter

1 Introduction

Composite insulators are widely used in power systems because of their light weight and good internal insulation performance [1–6]. Composite insulators withstand long-term internal and external overvoltage and complex natural environments. The aging of its components will lead to degradation of its insulation performance, endangering the safety of the operation of the power system [7–10]. Therefore, in order to prevent transmission line insulation failure, an effective method for detecting the aging state of composite insulators is particularly important.

At present, many achievements have been made in the aging state detection of composite insulators at home and abroad. [11] proposed a combination of multi-spectral and hyperspectral imaging technology to evaluate the aging state of insulating materials, and the quantitative detection of composite insulator aging was completed. The detection accuracy reached 83.1%. [12] experimentally analyzed the epoxy resin material based on the polarization and depolarization current method. It was found that the polarization and depolarization currents increased with the aging of the epoxy resin, which proved that the method was suitable for the aging detection of composite insulators. [13] found that the trap charges increase with the increase of service life, which reflects the aging state of composite insulators. However, in general, although the above research methods can effectively detect the aging of composite insulators, they all have certain limitations, so a fast and direct detection method is needed to improve the detection efficiency.

Microwave nondestructive testing technology is widely used in nondestructive testing research field because of its advantages of non-contact, strong penetrability and low power consumption [14]. In reference [15], the reflection effect of microwave on metal was used to verify the feasibility of microwave for detecting internal cracks in steel tubes. Reference [16] presents a method of porcelain insulator detection based on microwave nondestructive testing, which realizes the low value and zero value fault detection of porcelain insulator and has good effect in a certain frequency range. It can be seen that microwave nondestructive testing technology has achieved various research results in many fields, but the research on the aging state detection of composite insulators has not yet been carried out.

Therefore, a numerical simulation method for microwave nondestructive testing of composite insulators in aging state is proposed in this paper. The feasibility of the method is verified by analyzing the variation of the microwave transmission parameter S_{21} of composite insulators in different aging states, which provides a new idea for the detection and evaluation of the aging state of composite insulators.

2 The Principle of Theory

When the microwave is incident from the side of the composite insulator, transmission and reflection will occur at the interface of air, silicone rubber and epoxy resin. The curvature of the composite insulator is much larger than the microwave wavelength used in this paper. The insulator is simplified as a flat homogeneous medium. The model is shown in Fig. 1. The aging detection principle is analyzed by the microwave transmission model.

The principle of the microwave transmission method used in this paper is analyzed. When the microwave is incident vertically as shown in Fig. 1, the amplitude transmittance is expressed by τ_1 as shown in Formula (1):

$$\tau_1 = \frac{2\eta_1}{\eta_1 + \eta_0} \tag{1}$$

where, η_0 and η_1 represent the wave impedance of air and silicone rubber respectively. For air medium, the wave impedance is mainly determined by the air permeability μ_0
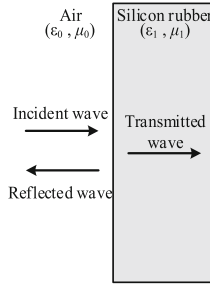
Fig. 1. Reflection and transmission of electromagnetic waves

and dielectric constant ε_0, the relationship is:

$$\eta_0 = \sqrt{\frac{\mu_0}{\varepsilon_0}} \tag{2}$$

For the silicone rubber medium, the wave impedance is related to the angular frequency ω of the incident wave, the permeability μ_1, the dielectric constant ε_1 and the conductivity σ_1 of the silicone rubber, where $\omega = 2\pi f$, f is the frequency of the incident wave. The specific relationship is as follows:

$$\eta_1 = \sqrt{\frac{j\omega\mu_1}{\sigma_1 + j\omega\varepsilon_1}} \tag{3}$$

In Formula (3), because the loss tangent of silicone rubber is very small, σ_1 is close to 0 and can be omitted, so Formula (3) can be simplified as:

$$\eta_1 = \sqrt{\frac{\mu_1}{\varepsilon_1}} \tag{4}$$

Substituting η_0 and η_1 into Formula (1), the amplitude transmittance of electromagnetic wave is:

$$\tau_1 = \frac{2}{1 + \sqrt{\frac{\mu_0\varepsilon_1}{\varepsilon_0\mu_1}}} = \frac{2}{1 + \sqrt{\frac{\varepsilon_r}{\mu_r}}} \tag{5}$$

where, μ_r and ε_r are the relative permeability and relative dielectric constant of silicone rubber, respectively. Since the silicone rubber is a non-magnetic material, and the loss tangent is small, that is, $\mu_r = 1$, which is substituted into Formula (5) and expressed in power form, the electromagnetic transmittance on the surface of the microwave silicone rubber material is obtained:

$$T_1 = \tau_1^2 = \left(\frac{2}{1 + \sqrt{\varepsilon_r}}\right)^2 \tag{6}$$

After the aging of silicone rubber, its dielectric constant will increase significantly, resulting in the change of the overall equivalent dielectric constant in the sensing area when the microwave penetrates, and the original microwave field will change accordingly. Therefore, the aging of composite insulators can be detected according to the change of microwave field.

3 Numerical Simulation Method for Microwave Non-destructive Testing of Composite Insulator Aging State

3.1 Construction of Basic Model

In this paper, based on the geometric parameters of 10 kV composite insulators, a simplified simulation model shown in Fig. 2 is established by using CST software to simulate the aging state of composite insulators detected by microwave. The composite insulator model has a total length of 150 mm and a mandrel diameter of 14 mm. The sheath thickness is 5.5 mm. Geometrical parameters of sheds #1 to #4 are shown in Table 1, where shed #1 is the actual high voltage side shaft of the composite insulator.

According to the theoretical formula of M. Rockwitz, the required frequency band is calculated. The WR-62 (11.9 to 18 GHz) rectangular waveguide in the International Electrotechnical Commission standard is selected as the detection probe. The effective cross-section size is 15.799×7.899 mm^2. When there is a large aging area, it can also meet the detection requirements.

In Fig. 2, the rectangular waveguide is placed on both sides of the composite insulator, facing its central axis. At the same time, the lift-off distance between the waveguide and the edge of shed #4 is set to 2 mm. Port excitation is provided on the back of the two waveguides as the output and receiver of the actual microwave signal source. By comparing the amplitude difference of transmission coefficient S_{21} before and after aging, the aging detection of composite insulators is realized.
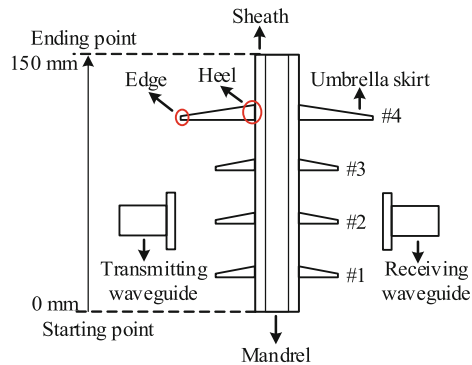
Fig. 2. Simulation model of 10 kV composite insulator

3.2 Setting of Simulation Parameters

The microwave transmission method is based on the difference in transmission level reflected by materials with different dielectric properties. Therefore, after the completion of the composite insulator model, it is necessary to set the material properties of each part. Where the waveguide and mandrel materials are ideal conductors (PEC) and Epoxy resin, respectively. For silicone rubber materials, relevant parameters need to be set according

Table 1. Geometric parameter setting of umbrella skirt #1 ~ #4

Umbrella skirt	Heel thickness /mm	Edge thickness /mm	Range of position scale x /mm
#1	6	2.2	21–27
#2			51–57
#3			81–87
#4	8		111–119

to their actual aging state. The parameters of unaging silicone rubber are shown in Table 2 below, where ε_1 and tanδ are the relative dielectric constant and dielectric loss factors, respectively. λ, c and ρ are thermal conductivity, specific heat capacity and density, respectively.

Table 2. Parameters of unaged silicone rubber

ε_1	tanδ	λ(W/(m•K))	c(J/(kg•K))	ρ(kg/m^3)
3.17	0.015	0.27	1000	1150

According to GB/Z 18890.3-2002, the relative dielectric constant of unaged silicone rubber is generally between 2.5 and 3.5. Combined with the propagation characteristics of microwave in silicone rubber, the amplitude of transmission coefficient and reflection coefficient mainly depends on the distribution of dielectric constant. Therefore, in the simulation, the permeability μ_1 of silicone rubber is set to 1, and different aging states of silicone rubber are simulated by setting different dielectric constant ε_1 and dielectric loss factor tanδ. Parameter settings for silicone rubber with different degrees of aging are given in Table 3.

Table 3. Parameter definition of different aging degree

Aging degree	ε_1	tanδ
Unaged	3.17	1.50%
Mild aging	3.91	2.63%
Moderate aging	4.65	3.75%
Severe aging	5.39	4.88%

4   Numerical Simulation

4.1   Analysis of Working Frequency

Considering that under the same lift-off distance, the detection results will vary with the change of frequency, so in order to carry out aging detection more effectively, it is necessary to select the microwave operating frequency.

A suitable detection frequency requires sufficient sensitivity to the aging phenomenon, i.e. a large ΔS_{21} (ΔS_{21} is the difference between the transmission coefficient S_{21} measured under aging and non-aging conditions) in the aging region. In order to explore the influence of working frequency on the detection effect, the following two groups of models are set up: one group is the unaged composite insulator, and the other group is based on the first group to set the shed #1 for severe aging. In the area corresponding to the umbrella skirt #1, three fixed scanning points are set, which are the bottom, middle and top of the umbrella skirt. Microwave scanning detection is performed at three positions, and the corresponding ΔS_{21} amplitude results and the relationship between the mean value and frequency of the three are shown in Fig. 3.
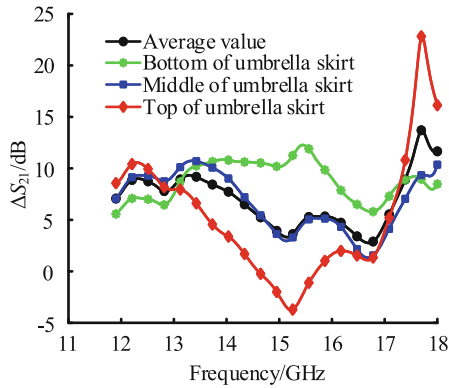
Fig. 3. ΔS_{21} amplitude at different frequencies

As can be seen from Fig. 3, when the aging shed #1 detection position changes, the relationship between ΔS_{21} and frequency will change, and the optimal detection frequency will be different. Therefore, the average value of the results corresponding to the three positions is the basis for frequency selection. When the frequency is 17.695 GHz, the mean value ΔS_{21} reaches the maximum value of 13.7037 dB, indicating that the frequency point can more effectively reflect the aging phenomenon of composite insulators in the frequency band. Therefore, this frequency is chosen as the detection frequency for subsequent studies.

4.2   Analysis of Aging Detection Effect

Composite insulators will undergo varying degrees of aging during operation. Based on the original basic model, according to the determined detection method, the overall

aging states of different aging degrees are set, and the waveguide is scanned with a step size of 3 mm to analyze the detection effect of microwave nondestructive technology on different aging states.

The composite insulator shed and sheath materials are set up as four groups of simulation models including non-aging, light aging, moderate aging and severe aging. The specific parameters of the four ageing materials are listed in Table 3. The four groups of models are scanned by moving rectangular waveguide, and the results of transmission coefficient S_{21} are shown in Fig. 4.

The area enclosed by the S_{21} curve and the horizontal axis $S_{21} = 0$ may reflect the mean amplitude of S_{21} and indirectly reflect the degree of aging of composite insulators. As the degree of aging deepens, the S_{21} curve moves downwards as a whole, and the area enclosed by it will also increase. In Fig. 4, with the deepening of the aging degree of composite insulators, the curve area increases in turn, the minimum value decreases gradually, and the amplitude change degree of the curve increases. The calculation results show that the aging degree of composite insulators can be reflected by the variation trend of the transmission coefficient S_{21} amplitude and its enclosed area, which confirms the effectiveness of this method in detecting the overall aging of insulators.
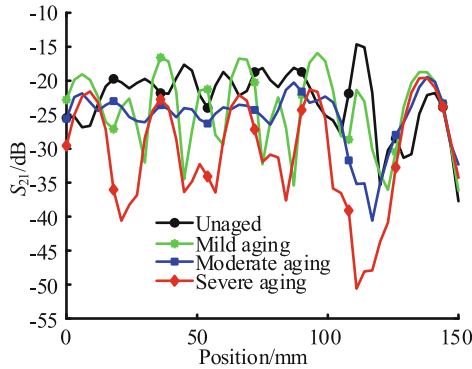
Fig. 4. S_{21} amplitude under overall aging

5   Conclusion

In this paper, a composite insulator aging detection method based on microwave transmission method is proposed. By analyzing the transmission parameter S_{21} under different aging degrees, the following conclusions are drawn:

(1) For different degrees of overall aging of 10 kV composite insulators, the detection effect is best when the microwave detection frequency is 17.695 GHz.
(2) The degree of aging can be determined by mobile scanning of composite insulators. With the deepening of the overall aging degree of composite insulators, the S_{21} curve gradually moved downward and the amplitude decreased.

References

1. Ramesh, M., Cui, L.: Impact of superficial and internal defects on electric field of composite insulators, Int. J. Electr. Power Energy Syst. **106**, 327–334 (2019)
2. Kokkinaki, O., Anglos, D.: Assessing the type and quality of high voltage composite outdoor insulators by remote laser-induced breakdown spectroscopy analysis: A feasibility study, Spectrochim. Acta Part B Atom. Spectrosc. **165**,105768. (2020)
3. Hao, Y., Pan., R.: Influence of water and defects on abnormal temperature rise of composite insulator. Eng. Fail. Anal. **135**, 106134 (2022)
4. Jiang, H., Li, B.: Aging characterization of 500-kV field-serviced silicone rubber composite insulators with self-normalized photothermal radiometry, Infrared Phys. Technol. **116**, 103763. (2021)
5. Nandi, S., Subba Reddy, B.: Understanding field failures of composite insulators, Eng. Fail. Anal. 116, 104758 (2020)
6. Abderrazzaq, M.H., Abu Jalgif, A.M.: Characterizing of corona rings applied to composite insulators. Electr. Power Syst. Res. **95**, 121–127 (2013)
7. Gao, Y., Liang, X.: Effect of electrical stress on glass fiber reinforced polymer used in high voltage composite insulator under wet environment. Compos. Sci. Technol. **155**, 151–159 (2018)
8. Liu, S., Liu, S.: Improving surface performance of silicone rubber for composite insulators by multifunctional Nano-coating. Chem. Eng. J. **451**, 138679 (2023)
9. Subba Reddy, B., Ramamurthy, P.C.: Analysis of in-service composite insulators used in overhead railway traction, Eng. Fail. Anal. **108**, 104227 (2020)
10. Ogbonna, V.E., Popoola., P.I.: A comparative study on the failure analysis of field failed high voltage composite insulator core rods and recommendation of composite insulators: a review. Eng. Fail. Anal. **138**, 106369 (2022)
11. Wang, B., et al.: Evaluation of insulator aging status based on multispectral imaging optimized by hyperspectral analysis. Meaurement **205** (2022)
12. Yuan, Z.: Evaluation of aging characteristics of composite insulators based on polarization/depolarization current method. In: 7th IEEE International Conference on High Voltage Engineering and Application, ICHVE 2020 – Proceedings (2020)
13. Ying, L., Gao, L.: The quantitative evaluation of aging state of field composite insulators based on trap characteristics and volume resistivity-temperature characteristics, J. Electr. Eng. Technol. **13**, pp. 1355–1362 (2018)
14. Yee, T.S., Shrifan, N.H.M.M.: Prospect of using machine learning-based microwave non-destructive testing technique for corrosion under insulation: a review. IEEE Access **10**, 88191–88210 (2022)
15. Sasaki, K., Katagiri, T.: Demonstration of the applicability of nondestructive microwave testing to the long-range inspection of inner-surface cracks in tubes. Mater. Trans. **58**, 692–696 (2017)
16. Pan, Z.: Non-destructive microwave testing method on porcelain suspension insulators, In: 2021 IEEE 5th Advanced Information Technology, Electronic and Automation Control Conference (IAEAC), pp. 985–988 (2021)

Magnetic Field Limit and Potential Impact of Offshore Wind Farm Submarine Cables in Ecosystems

Xiuyi Li[1], Jiahao Chen[2], Haoyu Zhan[1], Yanze Zhang[1], Xiaoyue Chen[1(✉)], and Hailiang Lu[1]

[1] College of Electrical Engineering and Automation, Wuhan University, Wuhan 430072, China
ringgle1987@126.com
[2] Guangzhou Power Supply Bureau of Guangdong Power Grid Corporation, Guangzhou 510013, China

Abstract. As an important component of offshore wind farms, submarine cables directly lay on the seabed and the magnetic field they generate may potentially have a negative impact on the eco-system, affecting the fish around, in particular. In light of this, an experiment platform was developed to expose the degree of this impact and offer a magnetic field limit. Helmholtz coils was used to generate the magnetic field and zebrafish (*Brachydanio rerio*) was chosen as the experiment sample. The behavior of fish under different magnetic fields was recorded by a wireless camera. Speed and trajectory analyses show that there is no significant difference between the experiment group and the control group ($P > 0.05$) even though the magnetic field reached 400 μT. This indicates the 100 μT magnetic field limit in the current standards may be strict. A calculation on the magnetic field distribution of typical submarine cables was carried out with finite element method and the results reveal that magnetic field falls quickly outside the cable. In most cases, it falls under 100 μT at 0.5 m from the center of the cable. Therefore, magnetic field may be an ignorable constraint in the application of submarine cables.

Keywords: Magnetic field · Submarine cable · Fish behavior · Offshore wind farm

1 Introduction

With the development of cross-sea interconnection and offshore wind power, the application of submarine cables is gradually increasing, and the electromagnetic environment problems are attracting public attention [1, 2]. The electric field of submarine cables attenuates to a small value after it passes through insulating materials. Hence, the magnetic field with strong penetration is the main influence. Before the wide practices of submarine cables, land power cables are already in mature applications, with many research focusing on the electromagnetic environment [3–5]. The electromagnetic interference of land power cables is generally associated with the way they grounded. In addition, the induced current in the sheath and armor will weaken the magnetic field.

The magnetic field on earth is classified into natural magnetic field and man-made magnetic field. The man-made magnetic field comes from the production and living activities of human beings. It is mainly embodied in the time-varying electromagnetic field of power frequency and the static magnetic field of DC, which is categorized as "extremely low frequency magnetic field". Prior to the development and application of submarine cables, studied on the biological impact of electromagnetic environment were carried out, mainly based on epidemiology, animal experiments and statistical analysis of exposure [6–8], because of the magnetic field generated by substation equipment and the overhead transmission lines.

2   Magnetic Field Limit in Current Standards

Field exposure will generate induced current in human tissues. Therefore, most international organizations and national standards propose magnetic field limits based on induced current. For power frequency of 50 Hz, when the induced current density in human tissues of any part of human body is over 100 mA/m^2, the program being responsible for nervous system excitation will undergo drastic changes and other acute reactions will occur [7]. The proposed magnetic field limits are mainly in line with the summary of research results in various fields, including epidemiological investigation, human volunteer experiments, animal experiments, cellular and molecular studies and biophysical studies.

In terms of international standards, there is no IEC standard limit of power frequency magnetic field exposure. The international Committee on Non-Ionizing Radiation (ICNIRP) first proposed the limit of power frequency electromagnetic field in the world. By studying the effects of magnetic field on humans and other animals, ICNIRP published the guidelines for limiting exposure to time-varying electric, magnetic and electromagnetic fields (below 300 GHz) in 1998 [7]. As a standard for magnetic field exposure, the guidelines take safety factors of 10 and 50 for professionals and the public. Therefore, the occupational and public exposure limits of the current density are 10 mA/m^2 and 2 mA/m^2. In consequence, the public exposure limit of power frequency magnetic induction intensity is set at 100 μT. ICNIRP guidelines are based on epidemiological, volunteer, cellular and zoological research. Nowadays, it has been recognized by many international organizations, such as the World Health Organization (WHO) and the International Labor Organization (ILO), and has become the basis in many countries. The standards of power-frequency electromagnetic field are sorted as shown in Table 1.

Although the limits of magnetic field are slightly different in many countries and various international organizations, they mainly refer to the ICNIRP standard. Therefore, the magnetic field outside the submarine cables should be limited to less than 100 μT in the case of power frequency at 50 Hz.

Table 1. Power frequency electromagnetic field exposure standards of some countries and international organizations.

Organization or country	Year	Frequency (Hz)	Occupational exposure (μT)	Public Exposure (μT)
ICNIRP: Guidelines for limiting exposure to time-varying electric, magnetic, and electromagnetic fields (up to 300 GHz)	1998	50	500(25/f)	100(5/f)
		60	420(25/f)	83(5/f)
	2010	50/60	1000	200
ACGIH: Documentation of the threshold limit values and biological exposure indices	2005	50/60	1000	/
IEEE C95.6. Standard for safety levels with respect to human expo sure to electromagnetic fields, 0–3 kHz	2002	50	2170	904
EU: Council recommendation of 12 July 1999 on the limitation of exposure of the general public to electromagnetic fields (0–300 GHz)	2004 /1999	50	500(25/f)	100(5/f)
NRPB: Restrictions on human exposure to static and time varying electromagnetic fields and radiation: Scientific basis and recommendations for the implementation of the board's statement	1993	50	1600	100(5/f)
	2004	50	500(25/f)	

Table 1. (*continued*)

Organization or country	Year	Frequency (Hz)	Occupational exposure (μT)	Public Exposure (μT)
BMU: No.1966. 26th Ordinance implementing the federal emission control act (EMF ordinance-26th bimschv) of 16 December	1996	50	/	100
ARPANSA: Radiation Health Series No. 30. Interim guidelines on limits of exposure to 50/60 Hz electric and magnetic fields	1999	50/60	500	100
China: HJ T24-1998 Technical regulations on environmental impact assessment of electromagnetic radiation produced by 500 kV ultrahigh voltage transmission and transfer power engineering	1998	40	/	100
China: GB 8702-2014 Controlling limits for electromagnetic environment	2014	50	/	100

3   Exposure Experiment of Zebrafish

3.1   Material and Method

In this experiment, Helmholtz coil was used to generate uniform magnetic field. Coil current was adjusted by voltage regulator to change the level of the magnetic field, and a water tank was set in the exposed magnetic field. Fish samples were exposed in the water tank, and their behaviors were recorded and tracked by a camera. A schematic diagram of the experiment is shown in Fig. 1(a), and experiment platform is shown in Fig. 1(b).

Zebrafish is widely used in the research field of embryology, developmental biology, genetics, molecular biology, toxicology, environmental science, experimental oncology
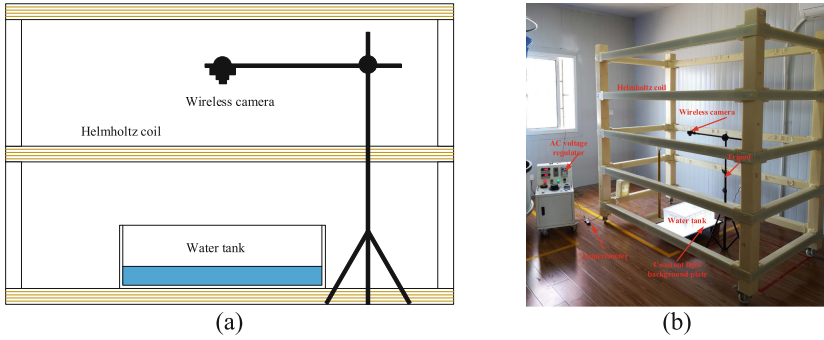
Fig. 1. (a) A schematic diagram of the experiment platform; (b) Overall setting of the experiment platform.

and immunology, and it is recommended by international organization for standardization to test fish toxicity. Therefore, zebrafish is chosen as the experimental fish. The zebrafish for experiment is at the age of 6 months. The body length is (3.2 ± 0.2) cm. They were domesticated in dechlorinated water with a water pump adding oxygen for 15 days. The temperature of the water is (28 ± 1) °C, and the photoperiod is 12 h. All zebrafish were feed once a day and stopped feeding for 24 h before experiment.

3.2 Calculation and Measurement of Magnetic Field

Before the experiment, a magnetic field calculation was carried out with finite element method. The model was built according to the real object of the Helmholtz coil used in the experiment. The result of the calculation is shown in Fig. 2(a). Besides, the magnetic field at the center and the four corners of the water tank was measured, as shown in Fig. 2(b). The comparison between the calculation results and measurement results of magnetic field under different current is shown in Fig. 2(c).
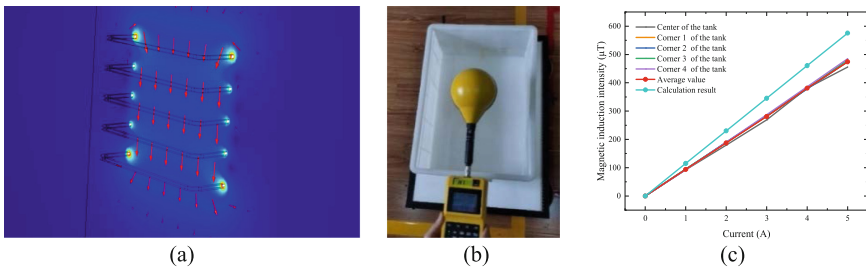
Fig. 2. (a) Magnetic field distribution; (b) Measurement of magnetic field; (c) Results of calculation and measurement under different coil current.

The measurement and calculation results are basically accordance. Magnetic distribution result shows that the magnetic field of the center area of the coil is uniform. The results of simulation and measurement show a linear trend, and the magnetic induction intensity reaches the limit of 100 µT when the current is 1 A.

3.3   Experiment Results

Four zebrafish samples were put into the tank for 10 min of exposure under different magnetic field. Every sample was exposed under the magnetic field of 0 µT, 93.92 µT, 187.5 µT, 281.0 µT, 381.3 µT and 474.4 µT. The according coil current level are 0 A, 1 A, 2 A, 3 A, 4 A respectively. The experiment started after the samples got familiar with the new circumstance and swam freely around. Tracking results of sample 1 is shown in Fig. 3. Speed of Zebrafish was statistically calculated, and its average value and variance were shown in Fig. 4.
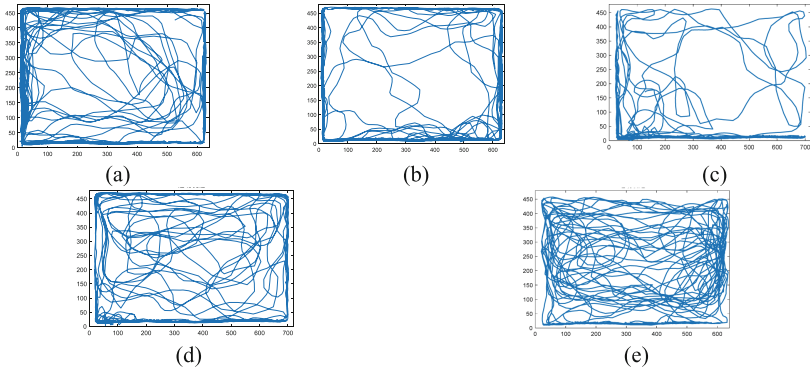
Fig. 3. Tracking results of sample 1 under different coil current levels. (a) Control group; (b) 1A; (c) 2A; (d) 3A; (e) 4A.
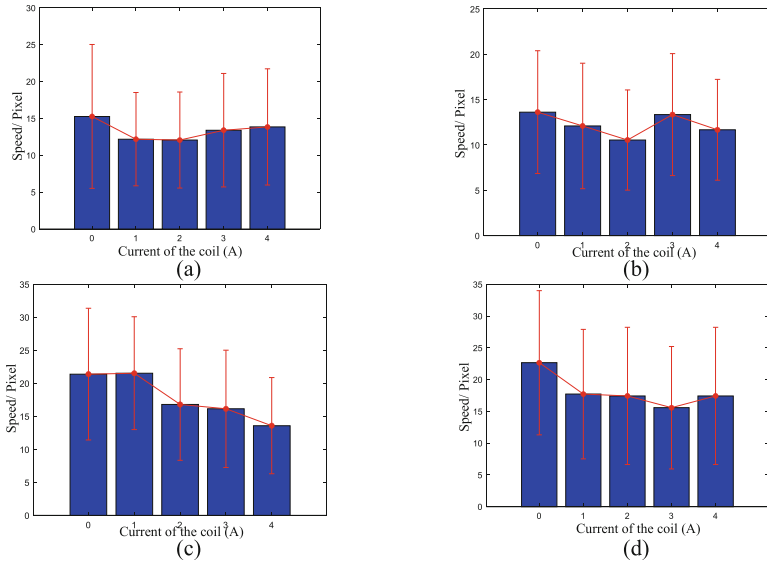
Fig. 4. Average and variance of speed under different coil current levels. (a) Sample 1; (b) Sample 2; (c) Sample 3; (d) Sample 4.

Significant test (T test) was carried out after the speed value was obtained. Firstly, a null hypothesis was proposed: There was no essential difference in the speed between the control group and the experimental group. Secondly, the probability was calculated. The test statistic is:

$$t = \frac{X_1 - X_2}{\sqrt{\frac{\sigma_{X_1}^2 + \sigma_{X_2}^2 - 2\gamma\sigma_{X_1}\sigma_{X_2}}{n-1}}} \tag{1}$$

where X_1 and X_2 are the average value of test groups. σ_1 and σ_2 are the variance of the test groups. n is the sample size. γ is the correlation coefficient of the samples.

The degree of freedom is 3 ($df = n\text{-}1 = 3$). The $t(3)_{0.05}$ value in the t value table was checked. Compare the calculated t value and the $t(3)_{0.05}$ value. If $P < 0.05$, reject the null hypothesis based on the probability that the event is unlikely to occur, or accept the null hypothesis. The t test result is listed in Table 2.

Table 2. Result of t test.

Groups	P value
Control group-1A experiment group	0.4901
Control group-2A experiment group	0.2018
Control group-3A experiment group	0.1734
Control group-4A experiment group	0.1565

It can be seen from Table 2 that the significance level of the experimental group and the control group is larger than 0.05. Therefore, it is believed that the difference between the experimental group and the control group is caused by experimental error, that is, at the magnetic induction level of 100 μT and above, there is no significant difference between the fish swimming behavior with and without a magnetic field up to 400 μT. As a result, 100 μT can be selected as the magnetic field limit, and the limit is strict.

4   Calculation of Magnetic Field Distribution of Submarine Cable

In order to find out the area of magnetic field level over 100 μT, a calculation of magnetic field distribution around submarine cables is carried out with different voltage levels and sectional areas by using finite element method. The structural geometry of the cable was taken into consideration, because the induced current in the sheath and armor may have an impact on the magnetic field distribution. Besides, the spiral winding structure of the armor was taken into consideration in the model. After a circle of winding, the induced voltage in the armor will get balanced, and the induced current in the armor is quite small [5].

The calculation covers the voltage level from 35 kV to 220 kV. Sectional areas of the cables are ranging from 50 mm^2 to 1000 mm^2. The magnetic field distribution of a
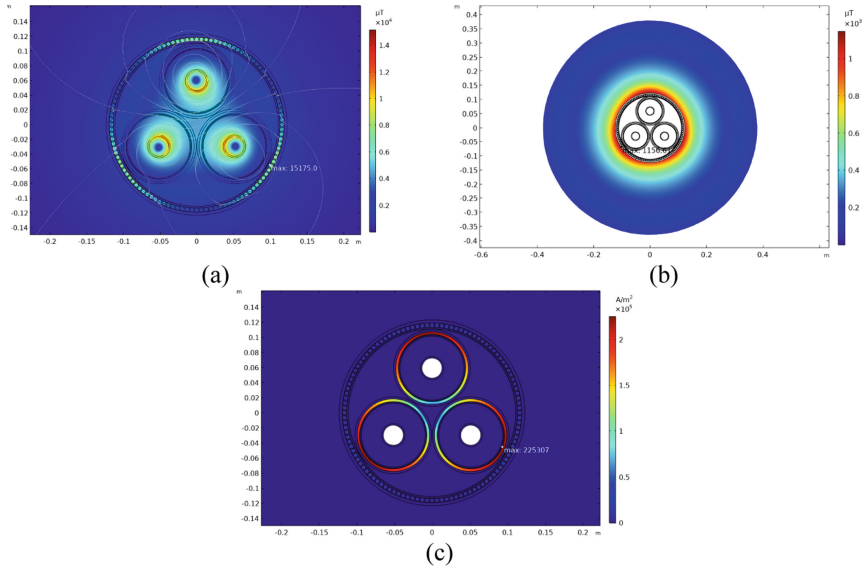
Fig. 5. Calculation results of 220 kV 1000 mm^2 three core submarine cable. (a) Magnetic field distribution; (b) Induced current density distribution; (c) Magnetic field distribution outside the cable.

220 kV 1000 mm^2 three core submarine cable is shown in Fig. 5(a). The induced current density distribution is shown in Fig. 5(b), and the magnetic field outside the cable is shown in Fig. 5(c). The outer boundary in Fig. 3(c) is 100 μT.

Calculation results of submarine cable with all voltage level and sectional area is listed in Table 3.

Table 3. Result of magnetic field calculation of different cable.

Voltage level (kV)	Sectional area (mm^2)	Rated current (A)	Capacity (MW)	External maximum magnetic induction intensity (μT)	Distance between 100 μT boundary and the cable center (m)
35	3*50	204	12	699.316	0.136
	3*120	332	20	1067.43	0.185
	3*240	470	28	1402.09	0.234
	3*500	639	39	1679.70	0.293
	3*800	753	46	1722.36	0.332
66	3*95	295	34	911.545	0.182

(*continued*)

Table 3. (*continued*)

Voltage level (kV)	Sectional area (mm^2)	Rated current (A)	Capacity (MW)	External maximum magnetic induction intensity (µT)	Distance between 100 µT boundary and the cable center (m)
	3*240	470	54	1336.00	0.245
	3*500	640	73	1610.75	0.303
	3*800	753	86	1672.46	0.344
220	3*500	644	245	1156.61	0.380
	3*1000	804	306	1302.41	0.427
	1*500 (3 phase)	769	293	1519.02	0.510
	1*1000 (3 phase)	961	366	1826.03	0.581
	1*1600 (3 phase)	1100	400	1783.96	0.621

The calculation result shows that, for three-core submarine cables, the magnetic induction intensity in the outer space is smaller than that of the single core cable. This is due to the good structural symmetry and the offsetting effect of the sheath and armor. The induced current on the armor and its loss is negligible. The induced current and loss are mainly distributed on the sheath. Although the submarine cables with different voltage levels and cross-sectional areas have different magnetic field distributions, their external magnetic induction intensities all decrease rapidly. The magnetic induction intensities of three-core cables all drop to less than 100 µT within the range of 0.5 m. The worst case is three 220 kV single core cables lay horizontally. But it also decays to less than 100 µT outside the range of 0.6 m. However, the actual laying depth of submarine cables is generally 0.5 m to 1 m, and the magnetic induction intensity above the seabed is considered to be less than the limit. Therefore, magnetic field is not an important factor to limit submarine cables application.

5   Conclusion

To reveal whether the magnetic field generated by the submarine cables in the off-shore wind farms may affect the living pattern of fish near, an experiment platform with Helmholtz coil as magnetic field generator was set. Zebrafish was chosen as the experiment sample. The trajectory and speed of 4 fish samples under different magnetic field level are obtained with the help of a camera and a tracking program. Statistical analysis shows that there is no significant difference between the fish swimming behavior with and without a magnetic field up to 400 µT. The calculation results of magnetic field distribution results of submarine cables of different voltage levels and cross-sectional

areas show that the external magnetic field falls quickly. Most of them falls lower than 100 µT in a distance of 0.5 m. In conclusion, when planning the offshore wind farms, the limit of magnetic field generated by submarine cables which may affect the living creatures nearby may not be so significant. Other limit factors should be considered prior to magnetic field, and a check the magnetic field limit after design is necessary.

References

1. Xu, L., Islam. S.: Reliability issues of offshore wind farm topology. In: International Conference on Probabilistic Methods Applied to Power Systems IEEE (2008)
2. Taormina, B., et al.: A review of potential impacts of submarine power cables on the marine environment: knowledge gaps, recommendations and future directions. Renew. Sustain. Energy Rev. **96**, 380–391 (2018)
3. Baù, M., et al.: Steady state modelling of three-core wire armoured submarine cables: power losses and ampacity estimation based on FEM and IEC. In: 2016 51st International Universities Power Engineering Conference (UPEC) IEEE, Coimbra, Portugal (2017)
4. Viafora, N., et al.: Analytical expression of equivalent transverse magnetic permeability for three-core wire armoured submarine cables. In: 2016 51st International Universities Power Engineering Conference (UPEC) (2016)
5. Bremnes, J.J.., Evenset, G., Stølan, R.: Power loss and inductance of steel armoured multi-core cable: comparison of IEC values with 2.5D FEA results and measurements. In: CIGRE Session B1–116 (2010)
6. Öhman, M.C., Sigray, P., Westerberg, H.: Offshore windmills and the effects of electromagnetic fields on fish. Ambio **36**(8), 630–633 (2007)
7. Westerberg, H., Begout-Anras. M.L.: Orientation of silver eel (Anguilla anguilla) in a disturbed geomagnetic field. In: Advances in Fish Telemetry. Proceedings of the 3rd Conference on Fish Telemetry, pp. 149–158 (2000)
8. ICNIRP, Guidelines. Guidelines for limiting exposure to time-varying electric, magnetic, and electromagnetic fields (up to 300 Ghz). Health Phys. **74**(3), 257–258(1998)

Hotspot Temperature Inversion of 110 kV Single-Core Cable Joint Based on Function Fitting

Tianhao Peng[✉], Shuoyang Zhao, and Daochun Huang

School of Electrical Engineering and Automation, Wuhan University, Wuhan 430072, China
2020302192010@whu.edu.cn

Abstract. Cable joint temperature is a key factor affecting its insulation performance and service life. To avoid direct measurement which may damage the cable joint structure, this paper adopts the method of inverting the joint hotspot temperature by surface temperature, where a fitting function and a thermal circuit are established to complete the inversion. Firstly, a transient simulation is used to obtain simulation temperature data samples of cable joint and body, not only as a comparison for inversion results, but also for constructing an inversion function connect the two variables by function fitting method. Then, a transient thermal circuit model recommended by IEC60853 is established at the cable body to calculate real-time cable body core temperature from the surface temperature. Finally, substituting the real-time cable body core temperature into the fitting function to obtain the joint hotspot temperature as inversion results. For error analysis, we compare the simulation results with the inversion, and the influence of heat dissipation changes on the inversion accuracy is studied. The research results indicate that the maximum error is controlled within 7 °C under relatively unfavorable conditions, which can meet the engineering needs.

Keywords: cable joint · hotspot · temperature field simulation · function fitting · thermal circuit model

1 Introduction

The operating and health status of power cables are directly related to the safe and stable operation of power transmission system [1–3]. Due to the complex installation process, large material dispersion, electrical stress concentration and multi-composite interface structure, the cable joint is the weakest link in the insulation of the cable system, so its fault has been high in the proportion of cable failure [4–7]. Temperature is one of the important factors affecting the insulation performance and service life of cable joints. Studies have shown that when the long-term working temperature of XLPE cable exceeds 8% of the allowable value, its life will be halved; If it exceeds 15%, only 1/4 of the cable life will be left [8]. If the temperature of the cable joint can be monitored and analyzed in real time, accidents can be effectively prevented [9–12]. Therefore, the researches on hot spot temperature inversion of medium and high voltage cable joints

are of great significance and practical value for ensuring the safe and stable operation of power cable systems.

In terms of cable joint temperature measurement, scholars have carried out a lot of research work. Yunpeng Gao [13, 14] et al. established simplified thermal circuit model of cable joint to calculate the cable core temperature. It will result in a great error because of the real structure of cable joint is complicated and hand-made process will change the structure and material parameters inevitably. Wenzhi Chang [15] et al. established a BP neural network [16] model with the surface temperature of cold shrinkable prefabs and current load as input, temperature of cable joint as output. Since the temperature of cold shrinkable prefabs cannot be measured directly, it cannot be applied to engineering practice. Gengmin Lv [17, 18] et al. measured the cable joint temperature by presetting optical fibers in the cable conductors. However, this method of implantable detection can cause harm to insulation and reduce the life of cable.

In this paper, the method of thermal circuit model and function fitting are used to calculate the hotspot temperature of cable joint, and the complete process of constructing the fitting function will be mainly introduced, in which the required data is obtained from finite element simulation. Finally, compared with the simulation results under different conditions, the error index such as SSE, MSE, MAPE, MSPE is calculated to judge the applicability of the fitting function.

In general, the inversion algorithm in this paper effectively avoids the disadvantages of implantable detection methods on cable life. Secondly, the thermal circuit model is established on conductor instead of cable joint to reduce the error caused by process of the on-site installation. Finally, the temperature field simulation based on finite element experiment software has high accuracy, so adopt this method instead of repeated temperature-rise experiment can greatly expand the training sample, thereby further improving the accuracy of the fitting function.

2 Finite Element Simulation Acquires Simulation Data Samples

Firstly, the finite element simulation software is used to establish a physical model of the cable joint, assign material parameters to each part, load the transient heat source, select the boundary conditions, and complete the transient temperature field simulation. The temperature data of the inversion point and the joint hot spot are extracted as the training sample set of the axial temperature inversion function.

2.1 Physical Model of the Cable Joint

The 110 kV cable joint and body structure are shown in Fig. 1, and the total cable length is set to 12 m.
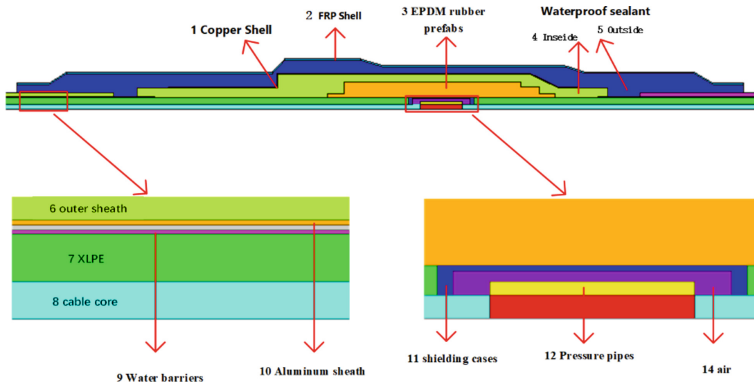
Fig. 1. Cable joint and body

The material parameters are shown in Table 1, in order to simplify the calculation, the density and specific heat capacity of the material are approximated within the allowable range of errors, and the subsequent simulation results also prove that the approximation does not affect the results.

Table 1. Material Parameters

Material	Construction	λ W/(m·K)	ρ kg/m^3	C J/(kg·K)
Copper	1,8,11,12	383	8889	390
Aluminum	10	218	2780	883
XLPE	6,7	0.29	1000	2400
Polyurethane	4	0.04	1000	1000
FRP	2	0.26	1850	535
Water belt	9	0.16	1000	2000
EPDM rubber	3	0.2	1000	1000
Bitumen	5	0.27	1000	1000

2.2 Transient Temperature Field Simulation

The outer surface of the cable and connector is adopted by the third type of boundary condition based on heat transfer theory,

$$-\lambda \frac{\partial T}{\partial n}|_\Gamma = \alpha(T - T_f)|_\Gamma \tag{1}$$

where λ is known as coefficient of thermal conductivity, α is convection heat transfer coefficient and T_f is fluid temperature. λ of different materials will be set by the Table 1,

and the ambient temperature is set to 25 °C, the α is set to $8W/(m^2 \cdot °C)$. The heat source is generated by the Joule heat of the current on the cable core, which is divided into two parts: the cable core and conductor at pressure pipe, as shown in Fig. 2, where the total resistance R_j at the pressure pipe is measured to be $5.1 \mu\Omega$.
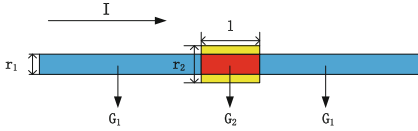
Fig. 2. Cable heat source loading
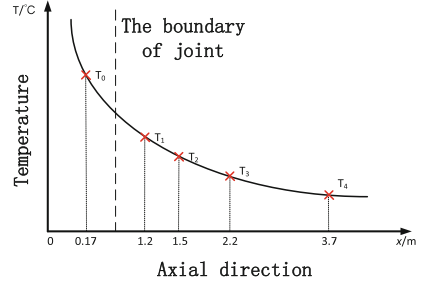
Fig. 3. Axial inversion points position

The two parts of the heat source are calculated as follows:

$$G_1 = \frac{I^2 \times \rho}{\pi^2 \times r_1^4} \tag{2}$$

$$G_2 = \frac{W_2}{V} = \frac{I^2 \times R_j}{\pi \times r_2^2 \times l} \tag{3}$$

where ρ is the copper conductor resistivity 1.75×10^{-8} $\Omega \cdot$m, l is the length of pressure pipe, $l = 0.133$ m, r_1 and r_2 are the radius of the cable core and the pressure pipe, respectively. $r_1 = 0.015$ m, $r_2 = 0.0237$ m, calculating from which $G_1 = I^2 \times 0.035$, $G_2 = I^2 \times 0.0217$.

$x = 1.2$, $x = 1.5$, $x = 2.2$ and $x = 3.7$ in cable core are preliminarily selected as inversion points, and their temperatures are represented by T_1, T_2, T_3, T_4 respectively, and the temperature at the cable joint core $x = 0.17$ is represented by T_0 as hotspot temperature. A schematic diagram of the position of the axial inversion point is shown in Fig. 3.

In order to ensure that fitting function can meet the inversion accuracy under different loads of cable, it is necessary to ensure the coverage of sample. Assuming that the maximum ampacity of the cable is 1300 A, the transient temperature field simulation of multiple steps is performed from 100 A to 1300 A as a load at 100 A intervals. The calculation time of each step is set to 50 h, and a set of transient result data is taken every 10 min, including the temperature of the 4 inversion points and the hotspot. The final temperature data sample contains 3900 sets of data, and the simulation results of the temperature field in cable joint are shown in Fig. 4.
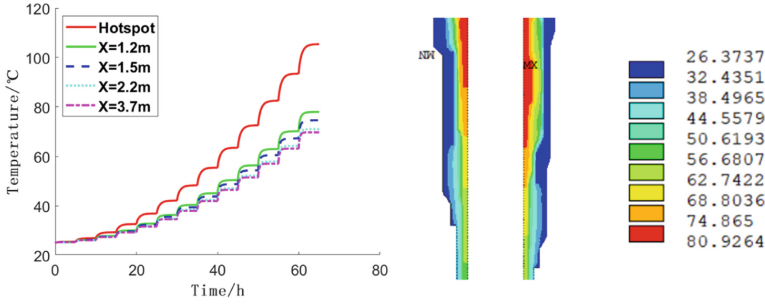
Fig. 4. Inversion points, hotspot temperature-time curves and temperature field of cable joint

3   Temperature Function Fitting

The purpose of axial temperature inversion is to find the mathematical relationship between the hotspot temperature of the cable joint as dependent variable and inversion points in the cable core as independent variables. The key to inversion lies in choosing the appropriate functional relationship and sample of temperature data to fit the coefficients in its expression. In this paper, according to the theory of infinite series, basic elementary functions and their combinations can be expanded into McLaughlin series, and can be further approximated to polynomials up to the power of m. If the number of monitoring points n is 4 and the highest power m is 4, then the hotspot temperature T_0 of cable joint can be expressed as:

$$
\begin{aligned}
T_0 =& f(T_1, T_2, T_3, T_4) \approx f_1(T_1) + f_2(T_2) + f_3(T_3) + f_4(T_4) \\
\approx& a_1 \cdot T_1^4 + a_2 \cdot T_1^3 + a_3 \cdot T_1^2 + a_4 \cdot T_1^1 + b_1 \cdot T_2^4 + b_2 \cdot T_2^3 + b_3 \cdot T_2^2 + b_4 \cdot T_2^1 \\
&+ c_1 \cdot T_3^4 + c_2 \cdot T_3^3 + c_3 \cdot T_3^2 + c_4 \cdot T_3^1 + d_1 \cdot T_4^4 + d_2 \cdot T_4^3 + d_3 \cdot T_4^2 + d_4 \cdot T_4^1 + e
\end{aligned}
\tag{4}
$$

where T_1, T_2, T_3 and T_4 represent the temperatures of four inversion points in cable core, a_i, b_i, c_i, d_i and e are coefficients of each independent variable in the polynomial. Suppose that the temperatures of each inversion point are independent of each other, the influence between them is ignored in the above equation.

Based on the 3900 sets of transient simulation temperature data obtained above, the function expressions are parametrically fitted by the Levenberg-Marquardt + Universal global optimization method with the help of the nonlinear fitting professional software 1stOpt. The coefficients of the function expression are shown in Table 2 below. After 26 iterations, the correlation coefficient R of the expression is 0.9999998, and the fitting effect is good.

Table 2. Quartic polynomial axial temperature inversion expression coefficients

a_i	value	b_i	value	c_i	value	d_i	value
a_1	−0.0000265	b_1	−0.01058	c_1	0.006803	d_1	−0.00075
a_2	0.004645	b_2	0.5562	c_2	−0.2562	d_2	−0.04354
a_3	−0.2615	b_3	−64.4683	c_3	42.2059	d_3	−11.7548
a_4	35.0993	b_4	−0.0005	c_4	0.0000091	d_4	−0.4281
e	0.00006350	-	-	-	-	-	-

4 Comparison of Inversion and Simulation Results

It is hoped that the complete inversion process in the actual engineering will be simulated to verify the accuracy of the method. That is, the temperature of the inversion points on the cable surface is obtained through sensor. Then the temperature of the inversion points in cable core is calculated by the thermal circuit model recommended by IEC60853, and finally they are brought into the axial inversion function constructed above to obtain the hotspot inversion temperature and compare with the simulation value. In order to avoid repeated temperature-rise tests, the temperature of the cable surface inversion points will be obtained by simulation experiments.

In order to determine the universality of the fitting inversion function to current fluctuations, change the load to multi-step currents 100 - 700 - 1300 - 200 - 800 - 1200 - 300 - 1100 - 400 - 1000 - 500 - 900 - 600A for a new simulation, each step current lasts 4 h, a total of 52 h.

Through this new transient temperature field simulation, extract temperature data of 4 inversion points in cable surface T_1', T_2', T_3', T_4' and hotspot T_{0s}. Using the thermal circuit model recommended by IEC-60853, calculate the temperature of the inversion point in cable core: T_1, T_2, T_3 and T_4. Then T_1, T_2, T_3 and T_4 are brought into the inversion function, then corresponding fitted inversion temperature data set T_0 of hotspot can be obtained. Comparing T_{0s} and T_0, as shown in Fig. 5 below, the maximum absolute error is about 2 °C. So the fitting is good.
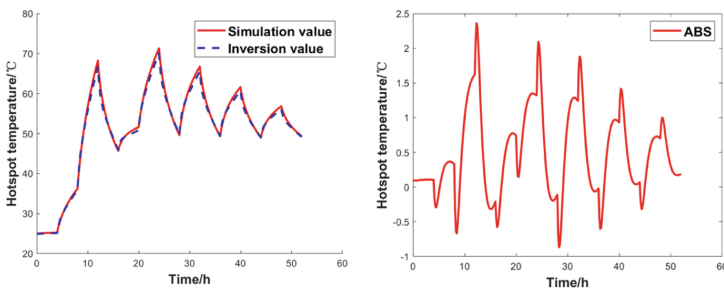
Fig. 5. Comparison of the inversion and simulation results of the fitting expression of four inversion points and the quartic polynomial

Adopt the following commonly used error index to analyze the error of the inversion results as follows Table 3.

Table 3. SSE, MSE, MAPE, MSPE Calculation formula

sum of squared error, SSE $$e_{SSE} = \sum_{i=1}^{N} (A_i - p_i)^2$$	mean squared error, $$\text{MSE } e_{MSE} = \frac{1}{N}\sqrt{\sum_{i=1}^{N} (A_i - P_i)^2}1$$
mean absolute percentage error, MAPE $$e_{MAPE} = \frac{1}{N} \sum_{i=1}^{N} \left| \frac{A_i - P_i}{A_i} \right|$$	mean square percentage error, $$\text{MSPE } e_{MSPE} = \frac{1}{N}\sqrt{\sum_{i=1}^{N} \left(\frac{A_i - P_i}{A_i}\right)^2}$$

where A_i is the test value (simulated value) of the ith test sample; P_i is the predicted value (inversion value) of the ith test sample; N is the number of predicted samples. The error calculation results are shown in Table 4, and the error is within the allowable range.

Table 4. Error index for the axial temperature inversion of the four inversion points and quartic polynomial

Error index	SSE	MSE	MAPE	MSPE
Value	196.7	0.0448	0.0107	0.0007

5   Optimize the Fitting Results

5.1   The Influence of Fitting Function's Expression

Next, cubic polynomials, quadratic polynomials and linear polynomials are used for fitting, and quadratic function fitting effect is the best judging by the error index. Comparison results shows in Fig. 6 and Table 5.
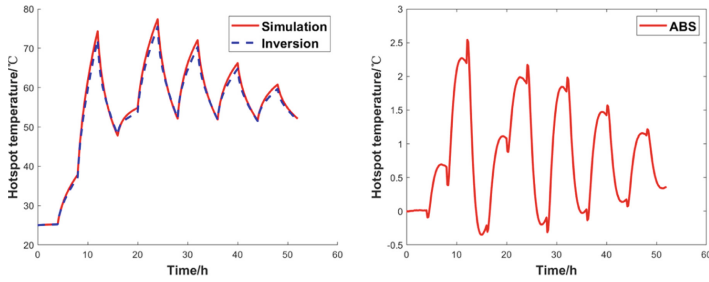
Fig. 6. The inversion result of the quadratic polynomial is used to fit the expression and the simulation result is compared with the curve

Table 5. Error of axial temperature inversion corresponding to different fitted expressions

	SSE	MSE	MAPE	MSPE
Linear	72.62	0.0272	0.0068	0.0005
Quadratic	69.98	0.0267	0.0067	0.0005
Cubic	200.5	0.0452	0.0107	0.0008
Quartic	196.7	0.0448	0.0107	0.0007

5.2 The Influence of the Number of Inversion Points

Analyzing the influence of the number of inversion points, the inversion points were 5 ($x = 1.2, x = 1.5, x = 2.2, x = 2.5, x = 3.7$), 3 ($x = 1.2, x = 2.2, x = 3.7$), and 2 ($x = 1.2, x = 2.2$), which are judged by the error index in Table 6. Results indicate that inversion works best when there are 4 inversion points, and 4 inversion points are used as follow.

Table 6. Inversion error index corresponding to the number of inversion points

	SSE	MSE	MAPE	MSPE
5 points	2870	0.1712	0.0512	0.0031
4 points	196.7	0.0448	0.0107	0.0007
3 points	221.3	0.0475	0.0114	0.0009
2 points	345.5	0.0594	0.0153	0.0011

5.3 The Influence of External Factors on the Accuracy of Inversion

The axial temperature inversion function in the previous section is obtained by the simulation without soil, mainly for tunneled or conduit cables. The actual buried environment of the cable includes the direct burial type, where the cable is surrounded by soil, whether

the function is still satisfied at this occasion needs to be verified by the simulation of cable joint in soil. Assume that the buried depth of cable is 0.8 m. Finally compare the results and find that the presence or absence of soil has a certain influence on axial temperature inversion, and the maximum error is within 6 °C.

Actual joints have a certain dispersion, so the effect of thermal conductivity of material needs to be analyzed. The joint includes five parts of prefabricated silicone rubber, air, copper shell, AB glue and FRP shell, the thermal conductivity of air and copper shell will not change theoretically, so the rest will be changed. Comparing the inversion results and simulation results, find that the error increases slightly, but doesn't exceed 3 °C.

The value of the contact resistance is related to the crimping process and has a certain dispersion, so it is necessary to analyze the influence of the value of contact resistance. After changing the value of it to double and half, comparing results and find that inversion accuracy is reduced, and the error doesn't exceed 4 °C.

The fitted temperature dataset and the validation model are that the cable is exposed to air, and the convection heat transfer coefficient is set to 8 W/(m^2·°C). Considering the influence of the external environment temperature on inversion, the convection heat transfer coefficient is set to 4 W/(m^2·°C), the transient temperature field simulation calculation and temperature inversion are re-performed. Compare the results and find that the heat dissipation environment having a certain influence on the axial temperature inversion, and the maximum error is within 5 °C.

The above analysis is a single factor change, but actual process of various factors may change, considering the most serious situation, inversion conditions are: convection heat transfer coefficient of 4 W/(m^2· °C), the thermal conductivity of prefabricated silicone rubber, AB glue and FRP shell is reduced by half, the contact resistance is doubled, and all the above influencing factors increase the hot spot temperature of the joint. The axial inversion function is obtained when the convection heat transfer coefficient is 8 W/(m^2·°C), the ambient temperature is 25 °C, and all parameters of the cable are normal. Select $x = 1.2$, $x = 1.5$, $x = 2.2$ and $x = 3.7$ as inversion points, use quadratic function for fitting, the results of axial temperature inversion are shown in the figure below, it can be seen that in the most serious case, the maximum error does not exceed 7 °C, considering that the actual load current will not fluctuate so violently, the parameters of the joint will not change too much, and the inversion result can meet the engineering error requirements. Comparison results show in Fig. 7 and Table 7.
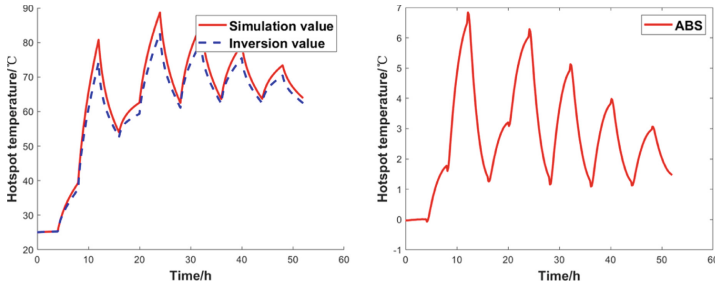
Fig. 7. Comparison curve between the inversion result and the simulation result under comprehensive influence

Table 7. Temperature inversion error index under different conditions

	SSE	MSE	MAPE	MSPE
In soil	2911	0.1724	0.0517	0.0032
1/2 Thermal conductivity	251.1	0.0506	0.0112	0.0008
Double Thermal conductivity	252.2	0.0507	0.0162	0.0011
1/2 Contact resistance	132.4	0.0368	0.0101	0.0007
Double Contact resistance	372.5	0.0617	0.0138	0.0010
1/2 Convection	923.4	0.0971	0.0224	0.0016
Combined impact	3492	0.1888	0.0417	0.0026

6 Conclusion

- (1) Based on the numerical calculation method of function fitting, the inversion algorithm of calculating the hotspot temperature of the cable joint from the cable conductor core temperature is realized; Combined with the thermal circuit model, the temperature at the cable conductor core is calculated by the measured cable conductor surface temperature, which can realize the complete inverse calculation of the hotspot temperature in cable joint from cable conductor surface temperature.
- (2) The fitting results of various occasions are compared with the finite element simulation results, and error index SSE, MSE, MAPE, MSPE are calculated. The comprehensive analysis shows that the inversion of quartic polynomial and 4 inversions points is relatively good. The inversion accuracy is also verified by simulating the changes of various conditions. Finding that even the inversion is carried out under the most unfavorable conditions, the maximum error is within 7 °C. But in practice, such unfavorable conditions would hardly occur, so the inversion accuracy is within the acceptable range.
- (3) The structure of the single-core cable joint and the body is quite different, in the process of axial temperature fitting, using a unified axial inversion function will produce errors, which need to be corrected if the further improvement of inversion accuracy is needed.

References

1. Liu, G., Lei, C., Liu, Y.: Analysis on transient error of simplified thermal circuit model for calculating conductor temperature by cable surface temperature. Power Syst. Technol. **35**(4), 212–217 (2011)
2. Liang, Y., Li, Y., Li, Y.: Calculation of the static temperature field of underground cables using heat charge simulation method. Proc. CSEE **28**(16), 128–134 (2008)
3. Chang, C.-K., Chang, H.-H., Boyanapalli, B.K.: Application of pulse sequence partial discharge based convolutional neural network in pattern recognition for underground cable joints. IEEE Trans. Dielectr. Electr. Insul. **29**(3), 1070–1078 (2022)
4. Liu, G., Wang, P., Mao, J., et al.: Simulation calculation of temperature field distribution in high voltage cable joints. High Volt. Eng. **44**(11), 3688–3698 (2018)
5. Wenzhi, C., Li, C., Su, Q.: Study on development of partial discharges at the defect caused by a needle damage to a cable joint. Trans. China Electrotech. Soc. **33**(07), 192–201+1 (2013)
6. Liu, C., Ruan, J., Huang, D.: Hot spot temperature of cable joint considering contact resistance. High Volt. Eng. **42**(11), 3634–3640 (2016)
7. Olsen, R., Anders, G.J., Holboell, J.: Modeling of dynamic transmission cable temperature considering soil-specific heat, thermal resistivity, and precipitation. IEEE Trans. Power Deliv. **28**(3), 1907–1909 (2013)
8. Gao, Z.: Study on Forecasting System of Current Carrying Capability for Power Cable in Duty. Harbin University of Science and Technology, Heilongjiang (2005)
9. Wu, R.N., Chang, C.K.: The use of partial discharges as an online monitoring system for underground cable joints. IEEE Trans. Power Deliv. 26(3), 1585–1591 (2011)
10. Douglass, D.A., Edris, A.A.: Real-time monitoring and dynamic thermal rating of power transmission circuit. IEEE Trans. Power Delivery **11**(3), 1407–1418 (1996)
11. Valdes, P.: An application of a system to monitor the conductor temperature of underground cables. IEEE Trans. Power Appar. Syst. **10**(10), 2794–2798 (1984)
12. Yang, Y., Hepburn, D.M., Zhou, C., Zhou, W., et al.: On-Line monitoring of relative dielectric losses in cross-bonded cables using sheath currents. IEEE Trans. Dielectr. Electr. Insul. **24**(5), 2677–2685 (2017)
13. Gao, Y., Tan, T., Liu, K.: Research on temperature retrieval and fault diagnosis of cable joint. High Volt. Eng. **42**(2), 535–542 (2016)
14. Zhan, Q., Xiao, W., Luo, R., et al.: The temperature monitoring of cable joint conductor based on transient thermal circuit model and inversion algorithm. Southern Power Syst. Technol. **8**(2), 83–87 (2014)
15. Chang, W., Han, X., Li, C., et al.: Experiment study on cable joint temperature measurement technology under step current. High Volt. Eng. **39**(5), 1156–1162 (2013)
16. Lei, C., Liu, G., Li, Q.: Dynamic calculation of conductor temperature of single-cable using BP neural network. High Volt. Eng. **37**(1), 184–189 (2011)
17. Lv, G., Zhang, D., Fu, C.: Split conductor in preset temperature fiber XLPE cables and accessories of the development and test. Electric Wire &Cable (05), 8–11+14 (2013)
18. Zhang, Z., Zhao, J., Rao, W., et al.: Validate test for the calculation congruity of distributed temperature sensing system. High Volt. Eng. **38**(6), 1362–1367 (2012)

A Condition Evaluation Method of Power Transformer Based on Text Mining Technology

Linghui Liu[1], Zehui Zhang[1], Quanfu Zhao[1], Xuliang Wang[2], Peijie Zhang[1], and Qingquan Li[2($\boxtimes$)]

[1] State Grid Shandong Electric Power Company Laiwu Power Supply Company, Jinan 271100, Shandong, China
[2] Shandong Provincial Key Laboratory of UHV Transmission Technology and Equipment, Shandong University, Jinan 250061, Shandong, China
`wang715586468@163.com`

Abstract. Text analysis of power transformer defect record is a challenging task because of the large number of professional words and the scarcity of labelled text data. These problems make generic models less effective in the power transformer domain. Pre-trained models can help solve these problems as they can be pre-trained on large-scale cross-domain unlabeled data, and can solve tasks in specific domains by continue training on the corpus of specific domains. We introduce the "pre-training, continue-training, fine-tuning" transfer learning approach to the field of power transformer text mining, and propose a language model based on Bidirectional Encoder Representations from Transformers (BERT) to solve the power transformer defect text classification problem. The model is first trained on the Chinese Wikipedia corpus to learn the language representation. We then continue to train the model on the power transformer corpus to learn the expertise. On this basis, this paper compares the accuracy rate, confusion matrix, differential mean F_1 (F_{1micro}) and other factors with traditional machine learning, deep learning and other methods. The case study demonstrates that our model can automatically and accurately classify the text of power transformer defect record with better classification results.

Keywords: Power Transformer · Defect Record · Text Mining · Transfer Learning · BERT

1 Introduction

After the power transformer fails, field operation and maintenance personnel record the failure phenomena in the form of words, including changes in sound, vibration, scent, color and temperature. Then, the description of failure phenomena is combined with relevant standards and guidelines to determine the cause, location and scope of failure manually for subsequent failure statistic analysis, equipment maintenance and remaining life prediction. At present, the method of artificial judgment alone is inefficient, and due to the limitation of staff knowledge reserve and experience, frequent errors occur in

the judgement of certain sub-health deficiencies. With the application of Natural Language Processing (NLP) in problem understanding, it is expected to achieve automatic classification of defect levels based on fault text analysis, provide decision reference for field workers, reduce the possibility of misjudgment, and save time.

In the development of deep learning and NLP, Krizhevsky first applied convolutional neural network (CNN) to image classification with good results [1], and Kim introduced CNN to text classification [2]. However, for long input sequences such as text, which are heavily influenced by preceding and following information, CNN cannot extract the correlation features of the preceding and following information, and the results are not very good. Some scholars have proposed recurrent neural network (RNN), which can extract relevant information before and after [3], but suffer from the problem of gradient explosion. Later on, long short term memory network (LSTM) [4] was proposed to further improve the ability to extract text features. These general models are not effective in the field of power transformer. Text classification of power transformer defect record needs to address two challenges: 1) complex classification algorithms using neural networks require large amounts of labelled data, but labelling power transformer defect record text requires expensive expertise and a lot of time. 2) The language model trained in the general field is difficult to identify the professional vocabulary in the field of power transformer.

Building a specialist electric power dictionary is a good way to address these issues [5, 6]. Extract the specialized vocabulary and let the model learn proprietary words directly. However, the method of word frequency statistics of professional vocabulary is insufficient in understanding deep semantics.

With the development of language representation technology, "pre-training, continue-training, fine-tuning" has become a promising solution to the above challenges [7]. A general model with strong representation ability is chosen to be a language representation model. The model is trained using a large corpus and target tasks in the pre-training stage to encode a significant amount of semantic knowledge; in the continue-training stage, the model will continue to train on the unlabeled corpus of a specific domain, so that the model can learn domain expertise; in the fine-tuning stage, fine-tuning the labeled data enables the model to learn how to use this semantic information to predict tags.

We introduce the transfer learning method of "pre-training, continue-training, fine-tuning" into the field of power text mining, and propose a power transformer defect record text classification model based on BERT [8]. We evaluated the classification model on the power transformer defect record text data set collected by the research group, and verified the improvement of the model performance by the "continue-training " strategy.

We have trained three other NLP models, which are based on the traditional machine learning model GBDT [9], the deep learning model CNN and BiLSTM. And they are used in power transformer defect record text classification, and compared with the model proposed in this paper.

2   Method

The BERT neural network architecture and the text classification model of the power transformer defect record based on BERT are briefly introduced in this section.

2.1 BERT

The early language representation models include ELMo [10] and OpenAI GPT [11], which are based on bidirectional LSTM and Transformer Decoder frameworks respectively. It is the BERT model that really makes language representation technology a mainstream solution. BERT takes Transformer Encoder as the skeleton, masked language model as the pretraining task, and uses Chinese Wikipedia corpus for training to get the pretraining model. Combined with the simple output layer, BERT obtained the most advanced results in 11 downstream NLP tasks, including text classification task. Figure 1 depicts the Transformer's basic structure.
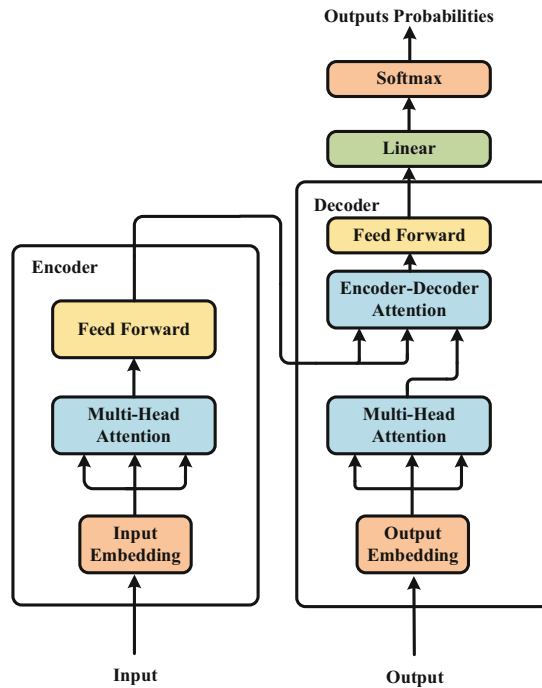
Fig. 1. Transformer

Transformer is a machine translation model first proposed by the paper Attention is All you Need [12], which outperforms the conventional RNN machine translation model. Its primary structure, which is based on the encoder-decoder framework, consists of the attention mechanism.

The encoder is made up of identical multi-layer stacks, and each layer has two sublayers: a feedforward neural network and a multi-head attention layer. The multi head attention layer is mainly used to input the relationship between words in the corpus (such as fixed collocation of words). Its external performance is the weight between words, and it can also help the model learn the dependency relationship such as grammar.

Decoder is also composed of identical multi-layer stacks, and each layer also includes two sub layers. There is also an encoder-decoder attention layer between encoder and

decoder. The encoder-decoder attention layer receives two sources of input. One is the output of the encoder, which can help the decoder focus on which position of the input sequence is worth paying attention to. The other part is the output of the results decoded by the decoder after being processed by the multi-head attention layer of the decoder. It can help the decoder take into account the noteworthy parts of the translated content when decoding. In the decoding process, decoder will output a real number vector each time step, which will be mapped to a vector called logits after passing through a full connection layer. After softmax normalization, it will be possible to determine the probability distribution of each word's appearance in the current time step.

As a deep bidirectional representation model, BERT does not predict the next character according to the previous character like other models, but uses the masked language model (MLM). MLM randomly replaces 15% of the input sequences with [MASK], and then predicts these replaced inputs through the softmax layer above the last encoder layer. Figure 2 depicts the MLM structure.
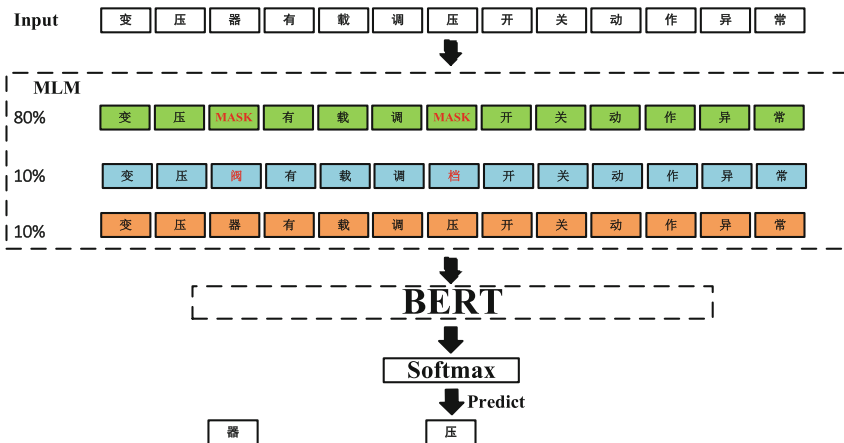
Fig. 2. Masked language model

In the process, BERT learned a lot of semantic knowledge. However, since [MASK] does not appear in the fine-tuning phase of the downstream task, this causes the model to be sensitive to [MASK] but insensitive to other inputs. To solve this problem, we adopt the strategy: when replacing the input sequence, not all [MASK], but 80% [MASK],10% other random input, and 10% original input. This strategy makes BERT sensitive to all inputs, not just [MASK], allowing the model to pick up on the representational information of any input sequence.

2.2 BERT for Power Transformer Defect Record

In this section, we will describe how to implement the text classification model of power transformer defect record based on BERT: 1) How to continue to train BERT on the corpus of the specific field of power transformer; 2) How to achieve the text classification task through the trained BERT.

Literature [6] shows that it is quite useful to customize the training model according to the domain of the target task. In order to achieve continue-training, our research group constructed a large corpus in the field of power transformer (see Sect. 3.1 for details). We continue to train the pre-training model on the corpus in the field of power transformer, and the training task is MLM mentioned above. In the process, the model learns domain expertise.

For the input power transformer defect record, we first convert each character into a N dimension vector. The N dimension vector is formed by adding the token embedding and position embedding corresponding to each character. At the first position of each input text sequence, we set a special classification mark [CLS]. The final hidden vector of the special tag [CLS] is represented as C, which is used as input to the text classification task. We represent the input embedding as E, and the final hidden vector of the nth input as T_n. Figure 3 shows the structure of power transformer defect record text classification model.
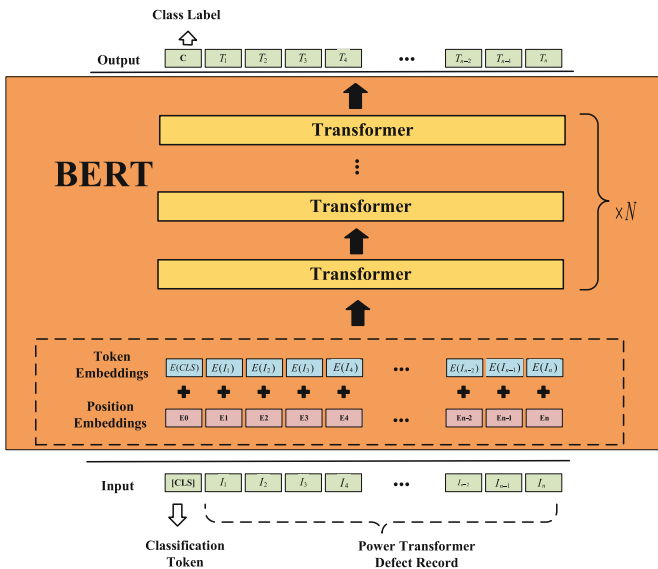
Fig. 3. Power transformer defect record text classification model based on BERT

3 Experiment

3.1 Datasets

Our research group collected three Chinese power transformer datasets for continue-training of the model: (1) Power transformer defect records, including on-site transformer fault records from a power grid company in a province of China in the past two decades; (2) About 100,000 public papers in the field of power transformers; (3) IEC and State

Grid of China standards and guidelines for power transformers. After collecting the original text, we preprocess the dataset to reduce duplication and noise. We set the number of sequence characters to range from 32 to 512. Table 1 summarizes the dataset for continue-training.

Table 1. Corpora used for continue-training

Corpus	Size
Power transformer defect record	560 KB
Articles	174 MB
Standards and guidelines	78 MB

We select on-site power transformer defect record as the research object. According to the standard: Q/GDW 1906–2013 (defect classification standard for power transmission and transformation primary equipment), we can divide transformer defect into three categories: general, serious and critical. General defects refer to the defects that are normal in nature, mild in condition and have little impact on safe operation. Serious defects refer to the defects that pose an important threat to people or equipment and can operate temporarily, but need to be handled as soon as possible. Critical defects refer to the defects that directly threaten the safe operation of equipment and require immediate treatment. Otherwise, the defects may cause equipment damage, personal injury, or fire at any time. This paper's primary objective is to build a text classification model to divide the defect degree into general, serious and critical, according to the phenomenon description in the power transformer defect record.

3.2   Software and Hardware Platform Setup

The code running environment is PyCharm and BMLCodeLab, and the hardware condition for cloud running is TeslaGPU_P4_8G. The deep learning framework is PaddlePaddle version 2.4. This paper uses sklearn's train_test_split function to divide 2435 datasets into training sets and test sets in a ratio of 0.8:0.2.

3.3   Model Performance Analysis

In order to assess the classification model, we use three indicators: accuracy, cross entropy loss and F_{1micro}. Due to the type imbalance in the dataset, the number of general defects is much larger than serious and critical defects. We use the square root of the inverse frequency to weight the cross entropy loss. At the same time, we calculate the F_1 separately according to the category, and then take the average value. It provides a good measure of categorical performance.

For the text classification model of power transformer defect record based on BERT constructed in this paper, the model parameters are set as follows: maximum sentence length is 512, learning rate is $2e^{-5}$, number of transformer layers is 12, character vector length is 768, and self-attention heads are 12.

With the training of the model, the loss value gradually decreases, while the accuracy gradually increases, and finally become stable. We input test data after the training of the model is completed, the accuracy and F_{1micro} were 0.932 and 0.918. Figure 4 displays the confusion matrix of the test data.

Number of samples

Predict
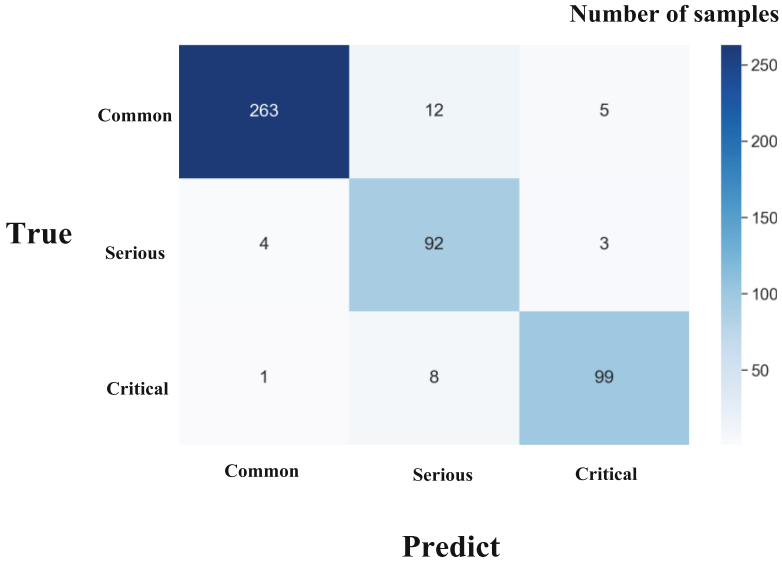
Fig. 4. Confusion matrix

For comparison experiments, we consider three different methods: a classifier based on the traditional machine learning model GBDT; a classifier based on deep learning model CNN; a classifier based on BiLSTM. The training methods are roughly the same. Firstly, we divide the defect record into words and count the word frequency. Then we set the domain vocabulary according to the word frequency. We conversely segment the defect record according to the domain vocabulary. Finally, we use word2vec to vectorize words and input them into the model for training.

At the same time, in order to verify the improvement of the model performance by the continue-training method, we also set up a classifier trained only using Wikipedia corpus. We compare the model constructed in this paper with the GBDT, CNN, LSTM model and BERT model without continue-training. Table 2 displays the performance of the five models.

Table 2. Performance comparison of different models

Model	Accuracy	F_{1Micro}
GBDT	0.811	0.775
CNN	0.881	0.855
BiLSTM	0.909	0.897
BERT without Continue-Training	0.720	0.708
BERT with Continue-Training	**0.932**	**0.918**

The traditional Chinese text classification method uses machine learning model. Table 2 shows that the accuracy and F_{1micro} of model based on GBDT are lower than other deep learning models. The accuracy of the machine learning classification model mainly depends on the quality of the word vector constructed. Due to the complexity of text structure, word vectors only extract the feature information of words, but ignore the feature information of sentence structure. The deep learning classification model further considers the sentence structure information and improves the accuracy of text classification. BiLSTM can effectively memorize the previous and subsequent information, so the classification accuracy of model based on it is higher than CNN. However, because the power transformer defect record length is generally very short, the advantages of LSTM are not obvious. Meanwhile, BiLSTM and CNN cannot dynamically encode the character vector, and their performance is lower than model based on BERT.

From the table, it is clear that the continue-training method significantly improves the performance of BERT. The original BERT pre-training material does not include the text in the field of power transformers, so its internal parameters are not capable of identifying power transformer fault description characteristics. The continue- training method adjust the parameters of BERT according to the professional power transformer corpus in the training process, its accuracy and F_{1micro} are higher.

4   Conclusion

In this paper, we present a transfer learning technique of "pre-training, continue-training, fine-tuning" into the field of power transformer text mining to address the issue of data cost in power transformer defect record text classification, and propose a power transformer defect record text classification model based on BERT. We also verify that the continue-training method improves the performance of the generic model in a specific domain. We train three other popular and advanced text classification models. The classification accuracy and F_{1micro} of the model constructed in this paper are higher than existing models.

The defect record text classification is only a small step towards realizing the state evaluation based on power transformer text data mining. With the development of intelligent power grid and AI technology, the next step is to use NLP technology to achieve the match of fault content and guidelines, and build the knowledge map in power transformer field.

References

1. Krizhevsky, A., Sutskever, I., Hinton, G.E.: Imagenet classification with deep convolutional neural networks. Commun. ACM. **60**, 84 (2017)
2. Kim, Y.: Convolutional Neural Networks for Sentence Classification. Eprint Arxiv (2014)
3. Williams, R.J., Zipser, D.: A learning algorithm for continually running fully recurrent neural networks. Neural Comput. **1**, 270 (1989)
4. Graves A.: Long short-term memory. Supervised sequence labelling with recurrent neural networks **37** (2012)
5. Loughran, T., McDonald, B.: When is a liability not a liability? Textual analysis, dictionaries, and 10-Ks. J. Finan. **66**, 35 (2011)
6. Araci, D.: Finbert: Financial sentiment analysis with pre-trained language models. arXiv preprint arXiv:1908.10063 (2019)
7. Gururangan, S., et al.: Don't stop pretraining: adapt language models to domains and tasks. arXiv preprint arXiv:2004.10964 (2020)
8. Devlin, J., Chang, M., Lee, K., Toutanova, K.: Bert: Pre-training of deep bidirectional transformers for language understanding. arXiv preprint arXiv:1810.04805 (2018)
9. Friedman, J.H.: Greedy function approximation: a gradient boosting machine. Ann. Stat. 1189 (2001)
10. Peters, M.E., et al.: Deep contextualized word representations. In: Proceedings of NAACL, vol. (2018)
11. Radford, A., Narasimhan, K., Salimans, T., Sutskever, I.: Improving language understanding with unsupervised learning (2018)
12. Vaswani, A., et al.: Attention is all you need. In: Advances in Neural Information Processing Systems, vol. 30 (2017)

Research on the Operation Reliability of Beidou Chip Considering the Electric Field of Transmission Line Tower

Yiming Wang[✉] and Daochun Huang

School of Electrical Engineering and Automation, Wuhan University, Wuhan, China
2020302191661@whu.edu.cn

Abstract. Beidou chip plays an important role in monitoring overhead transmission line tower deformation and galloping [2], but the corona discharge, caused by large electric field on the surface of transmission line tower and nearby the Beidou chip, have an impact on the operational reliability of Beidou chip. It is of great significance to get an accurate calculation, which is important to the chip safety and monitoring equipment operation reliability. According to the actual 500 kV tower parameters, the finite element simulation model of electrostatic field is established. Based on the finite element method, the electric field strength of the tower and the chip surface is computed. Based on the simulation results, the effects of installation position and protective materials on the electric field are discussed. By changing the parameters of the box and the arrays, shapes, and spacing of the aperture, the electric field strength distribution under different conditions is obtained. Research results show that when the box is made of glass fiber reinforced plastic (GRP) and the aperture array is designed as 4×4, with a total area of 800 mm^2, the electric field strength on the chip surface is about 471.7 V/m. This design can provide some guidance for the reliable operation of Beidou chip and the normal operation of transmission line monitoring.

Keywords: tower · Beidou chip

1 Introduction

Beidou system has been widely used in power system due to its advantages of wide coverage, high-precision positioning, and high security [1]. For example, the Beidou positioning system can be used in the time synchronization of power systems and disaster prevention and monitoring of power systems [2]. It can also play an important role in the maintenance and monitoring of power systems due to its unique trait of high-precision positionings, such as transmission line icing monitoring [3] and transmission line tower foundation displacement monitoring [4]. The influence of electromagnetic interference of transmission lines on the quality and positioning accuracy of Beidou deformation monitoring data has been studied by scholars [5], however, there are few studies on the reliable operation of Beidou chips in power frequency electric fields. Based on modeling and simulation, the electric field distribution near 500 kV overhead transmission line

towers and the electric field strength distribution cloud diagram on the chip surface is obtained.

There are many methods to calculate the power frequency electric field, such as the charge simulation method and finite element method [6]. Due to the power frequency electric field of the transmission line conforms to the quasi-static field model, the calculation of electric field strength on the chip surface is simplified to electrostatic field calculation and the finite element method is used to compute the electric field distribution.

The refined model of 500 kV double circuit negative phase sequence tower on one tower is established, and a board with a chip is installed in the proper position at the tower body. Based on the finite element method, the electric field strength at the tower base and on the surface of the chip is obtained.

In order to meet the needs of ventilation, power supply, and communication, it is inevitable to open holes in the shielding body [7]. Since the GNSS antenna needs to receive signals, the shielding box cannot be used to load the chip. However, after testing, the factors that affect the shielding effectiveness of the shielding box will also affect the electric field strength in the ordinary box. The number, shape and interval of the aperture will have effect on the electric field in the box. By comparing and analyzing the above factors, this paper proposes a practicable design that has the minimum electric field strength for the same aperture area.

2 Simulation Model

2.1 Description of Tower Model

According to the actual 500 kV tower parameters, the finite element simulation model of electrostatic field is built. Since the chip is installed at the tower body position, the calculation accuracy of the part above the base has little effect on the study results. In order to simplify the simulation calculation, the model below 6.7 m of the tower is finely modeled, while the part above 6.7 m is just modeled with a solid block. Considering the actual situation, the model is simplified as follows.

(1) For the lower part of the tower, the connection between the angle steel is simplified in the actual modeling. And the angle steel is simplified into a rectangular structure. The above reasonable simplification will not affect the electrical calculation results.

(2) According to the references, the effect of insulators on the electric field strength distribution declines with increasing distance from the insulators. Therefore, insulators are omitted.

(3) According to the references, the end effect and sag effect of the conductor are omitted, and the conductors are approximately considered as infinite smooth cylinder parallel to the ground [8]. The length of the conductor is set to 100 m, the vertical distance between the conductor and the crossarm is set to 4.5 m, and the equivalent radius of the conductor is set to 250 mm.

The final model is established as Fig. 1.
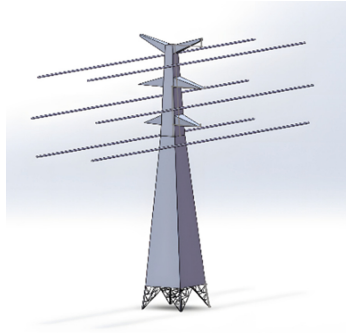
Fig. 1. Modeling diagram of the whole tower

2.2 Beidou Chip and Outer Box

Based on the given drawing of Beidou chip, a PCB board with the chip is established. The rest of the electrical components on the PCB board are omitted. The chip is also simplified to a square structure. The PCB board is installed in the middle of the box and appress the inner wall of the box. The size of the box is 100 mm × 80 mm × 24 mm and the thickness is set to 2 mm. The size of the PCB board is set to 71.1 mm × 45.7 mm × 1.6 mm.

3   Simulation Results and Analysis

3.1   Simulation of Tower

Calculation of electric field on tower surface. Import the model into the simulation software to calculate the electric field strength on the tower surface. The hexahedral element solid122 and the surface element surf154 are used to mesh the model. Since the tower is equipotential and only the electric field strength of the surface of tower needs to be obtained, the surf154 is used to mesh the surface of the tower. The solid122 is used to mesh the remaining entity parts. In order to give consideration to both calculation accuracy and calculation speed, a double-layer air pack is established. The mesh accuracy is gradually reduced from the tower model, inner air pack, and external air pack to optimize the transition and change of mesh size, and reduce the number of elements to save calculation time.

The tower is of double circuit negative phase sequence. The left circuit is ABC from top to bottom, and the other is CBA from top to bottom. The potential of each phase of the conductor surface is applied according to the phase order and the difference of phase angle is 120°.

Considering the highest operating phase voltage, the applied voltage U_m is set to 450 kV.

Grounded towers loaded with zero potential. All solid models are surrounded by air bodies, zero potential is applied to the ground and outer air boundaries. The size of the truncated boundary is set to 120 m × 120 m × 120 m, and the calculation accuracy for the lower part of the tower meets the requirements.

Result analysis. The electric field strength obtained at each moment is the instantaneous value and the electric field is loaded according to the initial phase of phase A as 0°, take 60° as the step to analyze the electric field strength on the surface of tower. Due to the structural symmetry of the tower, take $\omega t = 120°$, $\omega t = 180°$, $\omega t = 240°$ as the reference, calculate the electric field strength on the surface of the tower respectively. The electric field strength distribution cloud atlases are as follows.
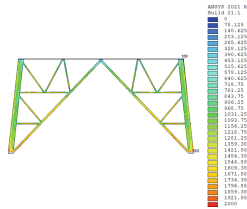
Fig. 2. The electric field strength distribution in the lower part of the tower, measured at $\omega t = 120°$
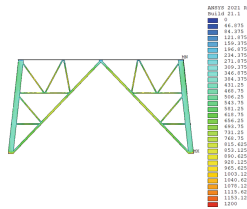
Fig. 3. The electric field strength distribution in the lower part of the tower, measured at $\omega t = 180°$
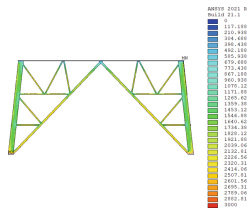
Fig. 4. The electric field strength distribution in the lower part of the tower, measured at $\omega t = 240°$

It can be seen from Figs. 2, 3, and 4 that the electric field distributions of the angle steel junctions at 4.2 m above the ground and at the edge of the tower are more stable and almost at the lowest level. Therefore, this point can be considered as the best location for chip installation.

3.2 Simulation of the Electric Field on the Surface of Chip

Comparison of electric field under different material of the outer box. Since the GNSS antenna needs to receive signals, the ordinary box is used instead of the shielding box. The material of the ordinary box is usually plastic and GRP. The relative dielectric

constant of weak polar plastic is between 2.5 and 3.5, and the relative dielectric constant of GRP is between 3.5 and 4.8. Give material properties to the box respectively and install the box with chip on the best installation point mentioned above. The electric field distribution on the chip surface under two conditions is shown in Figs. 5 and 6.
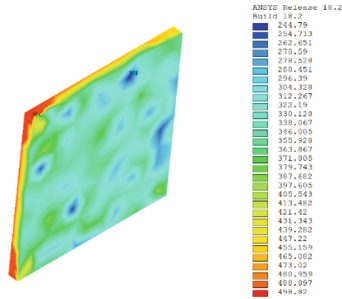
Fig. 5. Electric field distribution when the box is made of GRP
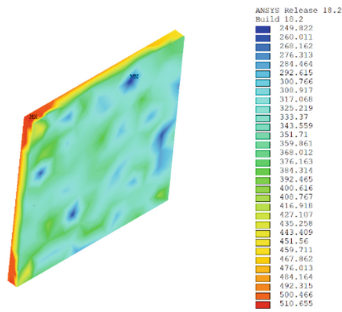
Fig. 6. Electric field distribution when the box is made of plastic

It can be seen that under the power frequency electric field, when the box is made of glass fiber reinforced plastic, the internal electric field strength is lower.

Comparison of electric field strength under different aperture designs. The area and shape of the aperture, the incident angle of the plane wave, and the number of aperture arrays all affect the shielding effectiveness in the cavity [9]. Although the box is not a shielded box, it is found after simulation that the above factors will also affect the electric field strength in the ordinary box. Under the condition that the aperture area is 800 mm^2, five kinds of different aperture designs are discussed and their maximum electric field strength is obtained in this paper. The results are shown in the following Table (Table 1).

Table 1. Different aperture designs while keeping the total area the same

No	Shape	Number	Size (mm)	Interval (mm)	E (V/m)
1	Circle	4×4	R = 3.99	20	471.7
2	Circle	2×2	R = 7.08	20	485.7
3	Circle	4×4	R = 3.99	15	481.6
4	Square	4×4	L = 7.07	20	481.8
5	Rectangle	4×4	A = 12.5 B = 4	20	481.0

R represents the radius of circular aperture. L represents the side length of square aperture. A and B represent the length and width of the rectangular aperture respectively. Comparing No. 1 and No. 2, it can be found that the more the apertures are, the smaller the electric field strength is. Comparing No. 1 and No. 3, it can be found that the greater the aperture interval is, the smaller the electric field strength is. Comparing No. 1, No. 4, and No. 5, it can be found that the electric field strength under the circular aperture is the smallest compared with the rectangle and square. Therefore, when designing the box, the number of apertures and the interval between apertures should be appropriately increased and the apertures should be designed to circular form to reduce the electric field strength. The maximum electric field strength appears on the side close to the aperture. Therefore, the Beidou chip should be installed as far away from the aperture as possible.

4   Conclusion

In this paper, the electric field strength of 500 kV tower and box surface and chip under different box designs are studied. The following conclusions were drawn from the results:

1. The electric field strength obtained at each moment is the instantaneous value and the electric field distributions of the angle steels surface will change with time change. However, by observing the electric field distribution at the three reference times, it can be found that the electric field strength of the angle steel junctions at 4.2 m above the ground always stays at the lowest level. Therefore, this point can be considered as the best location for chip installation.
2. The maximum electric field strength on the chip surface will change with the change of the box. By comparing five different box designs, we can find that we can increase the number of aperture arrays, increase the aperture interval, reduce the distance between Beidou chip and aperture, and use circular apertures to reduce the electric field strength on the chip surface.

References

1. Wang, H.C., Wanyan, S.P., Yu, J.: Study on Beidou satellite system application in power industry. Shandong Electric Power **48**(07), 8–12(2021)

2. Kuang, X.F.: Beidou navigation and positioning technology and its application in electric power system. Modern Ind. Econ. Info. **11**(10), 140–141(2021)
3. Yang, H.L., Si, X.D., Liang, S.B., et al.: Research on the application of Beidou navigation and positioning system in monitoring the icing of overhead transmission lines. Electron. Compon. Info. Technol. **5**(03), 94–95 (2021)
4. Feng, Z.Q., Hu, D.H., Yao, Y., et al.: Monitor displacement of tower base of transmission lines by beidou precise positioning technology. Hubei Electric Power **41**(11), 15–19 (2017)
5. Feng, Z.Q., Zhang, Y.D., Hu, D.H.: Influence analysis of transmission line electromagnetic interference on BDS data quality and accuracy. Bull. Surv. Mapp. (10), 94–97(2021)
6. Cheng, N., Wen, X.S., Lan, L., et al.: Accurate calculation of three-dimensional power frequency electromagnetic field for space crossed transmission line. High Voltage Eng. **37**(07), 1752–1759 (2011)
7. Wang, L.P., Gao, Y.G., Sheng, Y.M., et al.: Analysis of shielding effectiveness of rectangular cavity of loaded PCB with aperture by transmission line method. Chin. J. Radio Sci. **23**(04), 740–744 (2008)
8. Huang, D.C., Ruan, J.J., Yu, S.F., et al.: Calculation of power frequency electric field strength of ultrahigh voltage compact transmission lines. High Voltage Eng. **32**(07), 69–71 (2006)
9. Peng, Q., Zhou, D.F., Hou, D.T., et al.: Shielding effectiveness analysis of rectangular cavity with aperture by modification and expansion of transmission line method. High Power Laser and Particle Beams **25**(09), 2355–2362 (2013)

Mechanical Characteristics Simulation of UHV Insulating Pull Rod: Considering Anisotropic Composite Cylindrical Shell

Wei Yang[1], Bingyue Yan[1], Ruitao Ma[2], Zhicheng Wu[2(✉)], Qiaogen Zhang[2], and Yuxiao Zhao[2]

[1] Beijing Smart Energy Research Institute, Beijing 102209, China
[2] Xi'an Jiaotong University, Xi'an 710049, China
z_c_wu@163.com

Abstract. As the main mechanical transmission device of GIS circuit breaker, the insulating pull rod needs to have good performance in insulation performance and mechanical strength. At present, the research on the failure mechanism of aramid composite insulating pull rod still needs to be explored. In this paper, we have considered the stability of cylindrical shell which is made of orthotropic material and analyzed the stress and buckling instability characteristics of ultra-high voltage hollow tubular insulating pull rod under different loads by using finite element method, and investigated the effects of model size and angle offset of composite laminates on mechanical properties. The results show that the stress distribution of the pull rod is uneven under tension and compression loads, and different thickness, diameter and end connection conditions will affect the buckling critical load. The stress distribution of each layer in the multi-layer shell structure is different, and the maximum stress on the outer surface is more than twice that on the inner surface. This paper expounds the mechanical failure mechanism of UHV insulating pull rod, which provides a reference for its fault diagnosis and operation maintenance.

Keywords: Insulating pull rod · Aramid fiber · Anisotropic materials · Buckling

1 Introduction

GIS (Gas Insulator Switchgear) is one of the most important SF_6 gas insulated equipment. Compared with the traditional open power distribution device, it occupies a small area and has less maintenance work due to the sealing of components. It is widely used in the power system [1, 2]. Among them, SF_6 circuit breaker is an important equipment, and there are high requirements for its opening and closing speed in ultra-high voltage equipment. Therefore, as the transmission device of GIS circuit breaker, the insulating pull rod plays the role of insulation and operation breaking, and needs to withstand a large switching over-voltage impact and mechanical loads such as compression, bending and stretching. Therefore, it needs to have good bending, compression and torsion resistance at the same time with good insulation performance [3].

Fiber reinforced epoxy resin materials are used to produce insulating pull rods. The applied fiber materials include glass fiber, polyester fiber and aramid fiber. Among them, aramid fiber (PPTA) has low density, high tensile strength and high bending strength compared with traditional glass fiber materials, as well as good insulation properties and thermal stability [7], Meanwhile, polyester fiber has good wettability with epoxy resin. Therefore, aramid fiber and polyester fiber mixed materials are generally used in production to impregnate with epoxy resin, which improves the bonding performance of fiber materials and epoxy resin while ensuring the axial mechanical strength. The aramid composite insulated pull rod is made into a slender hollow tube structure, which has the advantages of high strength and light weight, reducing the operating power of the mechanism and ensuring the switching speed.

Although the current UHV grade insulating pull rod accounts for a small proportion of all insulating pull rods, it plays an irreplaceable role in the power system. With the increase of the voltage level of equipment and the trend of equipment miniaturization in the future, the application of UHV insulating pull rods will further increase [4–6], Therefore, it is very necessary to study the failure causes of insulating pull rod. However, according to statistics, in actual operation practice, UHV aramid insulating pull rod has a high failure rate [8]. At the same time, due to insufficient investigation on the actual working condition and stress of insulating pull rod, manufacturers generally only focus on the tensile strength of the pull rod, ignoring the compression load when closing in actual operation and lack of investigation on buckling instability [9]. Therefore, through finite element simulation, we investigated the stress distribution of insulating pull rod under tensile and compressive loads, and analyzed the relationship between the maximum principal strain and the thickness of the rod; The influence of different geometric conditions on the buckling critical load of pull rod is also analyzed; Finally, the stress distribution of each layer in the composite multilayer shell structure with 8 layers is investigated. Through the simulation research in this paper, we have summarized the influence of various factors on the mechanical properties of insulated pull rod, and have a clearer understanding of its stress distribution and instability characteristics during operation, which provides a reference for the design and failure diagnosis of insulating pull rod, and is of great significance for the safe operation and fault detection of ultra-high voltage equipment.

2   Simulation Model and Parameter Settings

The simulation object is an ultra-high voltage aramid composite hollow tubular insulated pull rod. The length of the pull rod can be estimated by Eq. 1, which is an empirical formula used to calculate the creepage distance along the surface of the insulated pull rod.

$$L = K_3 K_4 \frac{U}{E_\tau} \tag{1}$$

where K_3 and K_4 represent the electric field non-uniformity coefficient and safety coefficient near the pull rod, and the values are 2.0 and 1.8. $E\tau$ is the allowable tangential electric field strength on the surface of insulating parts, which is 10 kV/mm; U is the

lightning impulse voltage. For 1100 kV equipment, U is 2400 kV. After the above formula is calculated and a certain margin is reserved, the length of the simulation model is taken as 800 mm. The initial thickness of the model is set as 5 mm, The inner radius R_2 and outer radius R_1 of the circular tube are set to 18 mm and 23 mm, and the two ends of the pull rod are sleeved with aluminum metal connectors for connecting the mechanism and the circuit breaker. In the simulation, it is assumed that the material of aramid composite pipe is uniform, smooth and free of defects. The adhesion model in the simulation is used to set the two ends of the pull rod and the metal joint to be bonded all the time, and the direction of load application is parallel to the axis.
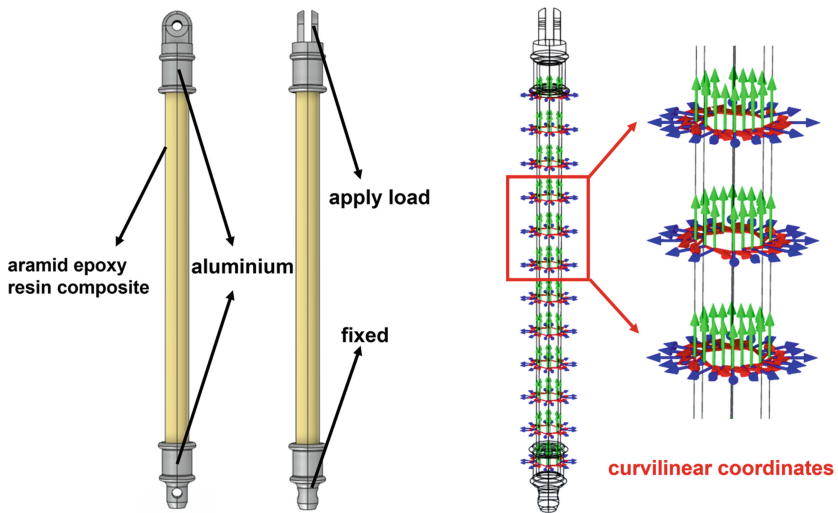
Fig. 1. Model and coordinate system.

In order to analyze the hollow cylinder structure, a curvilinear coordinate as shown on the right side of Fig. 1 is established for the stress analysis and calculation of the tubular composite part based on the tubular structure. The first axis direction is the circumferential direction of the tube, and the second axis is the axial direction of the tube. Since it is assumed in the simulation that the fiber reinforced material used in the tie rod is orthotropic, and its anisotropy parameters are difficult to be directly measured under the tubular structure, the orthotropic parameters of similar materials shown in Table 1 are used for qualitative analysis.

Table 1. Material parameters

Material type	Parameter	Value	Unit
Aramid reinforced epoxy resin composite pipe	Young's modulus (E_1, E_2, E_3)	(6, 29, 6)	GPa
	Shear modulus (G_{12}, G_{23}, G_{13})	(3.85, 5, 5)	
	Poisson's ratio (υ_{12}, υ_{23}, υ_{13})	(0.4, 0.31, 0.3)	1
Aluminum joint	Young's modulus E	72	GPa
	Poisson's ratio υ	0.33	GPa

In the solid mechanics simulation, the load application position and model boundary conditions are shown in Fig. 1. One end of the pull rod is fixed, and the other end is set boundary conditions with free or fixed x and y direction displacement. The connection between the metal joint and the pull rod uses the bonding mode in contact connection.

Considering that the aramid fiber in the aramid insulating rod has a high crystallinity on its surface and is inert in chemical properties, it is difficult to form a firm interface with the epoxy resin, resulting in insufficient infiltration performance with epoxy resin [12, 13]. Therefore, manufacturers generally use aramid filament fiber and polyester fiber together as reinforcement materials to reduce the proportion of aramid. Aramid fiber is used in the axial direction to ensure the mechanical strength, and polyester fiber is used in the circumferential direction to improve the wettability with the epoxy resin [14], which results in the difference in mechanical strength in these two directions. The pull rod is composed of two kinds of fibers interwoven by warp and weft, which are wound on the winding machine, then soaked with epoxy resin through vacuum pressure impregnation process. It can be regarded as a multi-layer shell structure.

In the simulation of exploring the stress on different layers of composite multilayer shells, the model used is an 8-layer laminated structure. The stress distribution simulation under static load and the comparison of the difference of stress on the layers under buckling are carried out for this structure. The structure model is shown in Fig. 2.
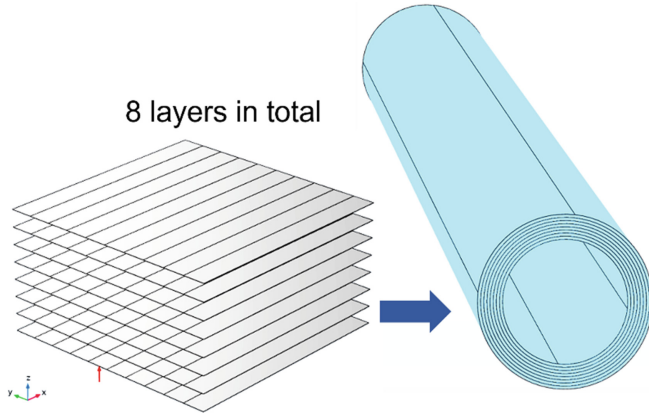
Fig. 2. Multilayer shell structure of insulating pull rod

3 Simulation Analysis and Results

3.1 Stress Analysis Under Static Load

Set the outer radius R_1 of the pull rod as 23 mm, and set the range of the inner radius R_2 as 15 to 21 mm to change the thickness. Apply 100 kN tensile load and compression load respectively for static structural mechanics analysis. The stress distribution results of the pull rod are shown in Fig. 3 ($R_2 = 18$ mm). Under this simulation condition, the average stress, peak stress and maximum principal strain on the pull rod under various conditions are counted, and the results are shown in Fig. 4. At the same time, we selected two sections parallel to the pipe axis on the inner and outer surfaces as references to observe the axial distribution of stress along the surface of the pull rod. The results are shown in Fig. 5.
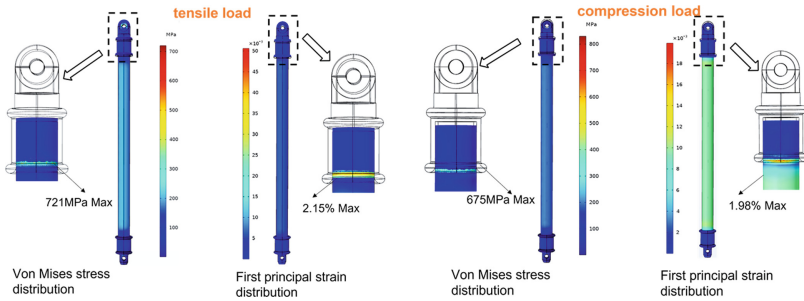
Fig. 3. Stress and strain distribution of pull rod under tensile load and compression load (100 kN)
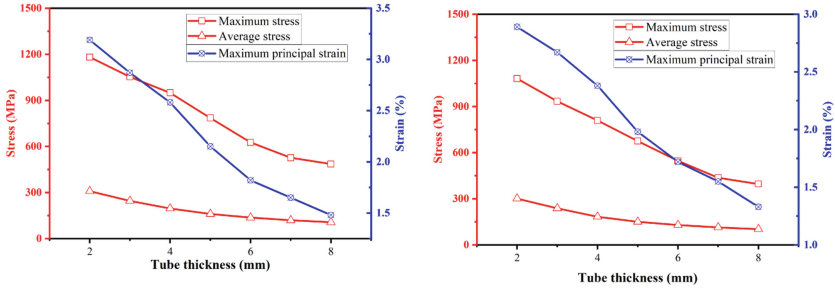
Fig. 4. The stress and strain of the rod under tension and compression when the thickness changes
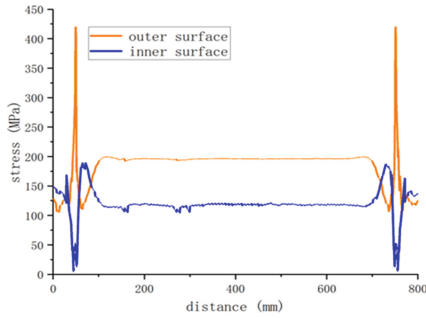
Fig. 5. Axial stress distribution

The results in Fig. 3 show that the stress distribution on the pipe is uneven when the pull rod is stressed, especially at the position where the metal joint is connected. There is a large stress concentration which is easy to cause mechanical property damage at this position. Therefore, the connection position between the pull rod and the metal joint is a weak position in the structure, which should be focused in the design and production process to avoid defects.

According to the results in Fig. 4, the average stress, maximum stress and principal strain in the structure increase with the decrease of the thickness of the pull rod, which has a negative effect on the mechanical properties of the structure. Therefore, the appropriate thickness should be selected while taking into account the weight. It can be seen from Fig. 5 that the stress distribution on the axis of the inner and outer surfaces suddenly increases at the edge of the joint. At the same time, the stress amplitude of the inner and outer surfaces of the pull rod is greatly different. The stress on the outer surface is higher and the stress concentration at the joint is more intense, so the outer surface of the pull rod is more vulnerable to damage.

3.2 Buckling Analysis

Insulating pull rod is a slender tubular structure. When the compression load is higher than a certain threshold, it will suddenly bend and lose its stability, that is, buckling [10, 11]. This failure is different from material strength failure because the structure

will return to the original state after unloading. The rod is easy to bend due to slight disturbance when the load reaches the critical buckling load, so it is necessary to analyze the buckling characteristics of the rod under compression.

Equation (2) is often used in engineering design to estimate the strength of pull rod instability.

$$F_{cr} = \frac{\pi^2 EI}{(uL)^2} \tag{2}$$

where F_{cr} is the critical buckling load, E is the axial Young's modulus, L is the length, u is the length factor, the value of u is related to the constraints on both ends of the pull bar, and the value is 0.5 when both ends are fixed. The value of u is 1 when both ends are hinged and when one end is fixed and one end is free, the value is 2. I is the cross-section inertia moment of the pull rod, which can be calculated by Eq. (3). Where D and d are outer and inner diameters of the pull rod.

$$I = \frac{\pi}{64} \left(D^4 - d^4 \right) \tag{3}$$

When analyzing the influence of geometric structure on the critical buckling load, two factors are considered. Firstly, considering the effect of thickness, the outer diameter R_1 is set to 23 mm while the inner diameter R_2 is changed. The relationship between critical buckling load and thickness under both end conditions (fixing both ends or one end) is shown in Fig. 7. When R_2 is 18 mm, the buckling modes at each end condition are shown in Fig. 6. Secondly, when considering the influence of the outer diameter, the thickness is fixed to 5 mm. The relationship between the outer diameter of the pull rod and the critical load for buckling is shown in Fig. 7.
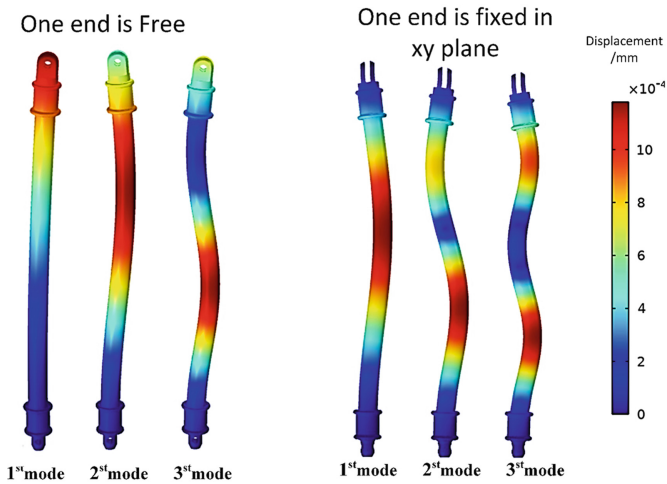
Fig. 6. Buckling modes at each end condition
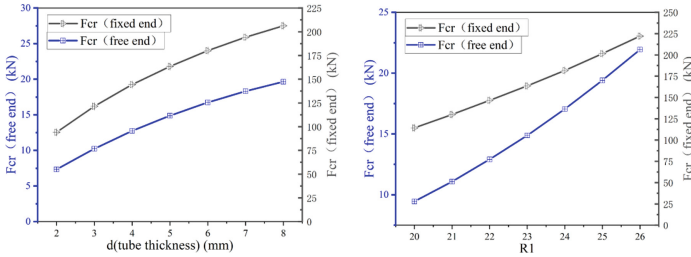
Fig. 7. Influence of thickness and outer diameter on buckling critical load

From the results of Fig. 6, it can be seen that when horizontal restraint is added at one end, the critical buckling load is more than ten times higher than when one end is free, so the restraint conditions at the end have an important influence on the structural stability. The lower free degree at both ends of the pull rod is, the higher the critical buckling load will be. In addition, with the increase of thickness and outer diameter, the critical load of instability increases continuously. Therefore, in engineering application, the compressive capacity and the weight of pull rod should be considered comprehensively so as to reduce the weight on the premise of guaranteeing high critical buckling load.

3.3   Analysis of Composite Multilayer Shells

In order to explore the difference of stress on different layers, the multi-layer shell structure is used to analyze the stress distribution on different layers under static load and buckling.

The multilayer shell model is 800 mm long and 5 mm thick (8×0.625 mm/layer), with an outer radius of 23 mm. In the simulation, an eight layers structure is used for analysis. The bottom is fixed, and an axial 100 KN compression load is applied on the top. The main direction of the material is axial. When the laying angle of each layer is 0°, the stress distribution of each layer under 100 kN compression load is shown in Fig. 8 (from left to right, it is the outer layer to the inner layer).
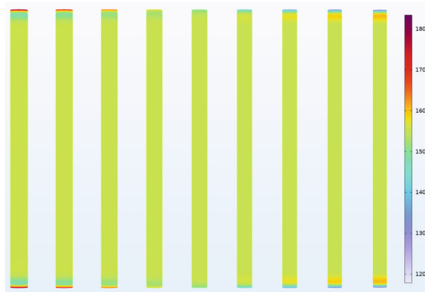
Fig. 8. Stress distribution on each layer under 100 kN compression load
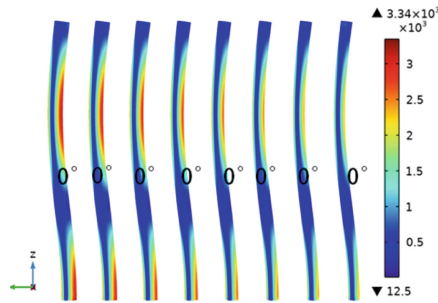
Fig. 9. Stress distribution on each layer when the rod buckles (fixed at both ends)

The stress on the layer closer to the outer surface is greater. The maximum value is located at the bottom of the shell and the stress concentration on the outer wall is most obvious while the middle layer is uniform.

The Fig. 9 shows the stress distribution on each layer when the insulating pull rod buckles (fixed at both ends). It can be seen that the stress on the layer closer to the outer surface will be greater, which means that the mechanical properties of the outer layer have an important impact on the buckling instability of the pull rod. Cracks or breaks generated by compression load will first occur on the outer surface after the buckling occurs.

4   Conclusion

This study investigates the geometrical influence on the stress distribution and buckling characteristics of insulating pull rod under different load and ends condition. The difference of stress distribution on different layers of composite laminated tubes is also analyzed.

Stress distribution on the pipe is uneven when pull rod is stressed. The connection position between the pull rod and the metal joint is a weak position in the structure which is vulnerable to damage. Average stress, maximum stress and maximum principal strain in the structure increase with the decrease of the thickness of the pull rod.

Restraint conditions at the end have an important influence on the structural stability. The lower free degree at both ends of the pull rod is, the higher the critical buckling load will be. The critical load of instability increases with the increase of thickness and outer diameter.

In multi-layer shell structures, the stress on the outer layer is greater when the pull rod is compressed or buckled. The stress distribution in the middle layer is relatively uniform and the outermost layer is vulnerable to damage.

References

1. Yi, L., Tang, J., Cheng, P., et al.: The transition mechanism of surface charge accumulation dominating way in DC GIS/GIL. Transactions of China Electrotechnical Society **34**(23), 5039–5048 (2019)
2. Wang, F., Liang, F., Zhong, L., et al.: Active charge dissipation method for surface charge on the surface of DC GIS/GIL insulator based on short-time X-ray irradiation. Trans. China Electrotech. Soc. **35**(14), 3147–3151 (2020)
3. Ning, M., Hou, M.: Research and development of aramid insulation pull rod. Sci. Technol. Innov. Herald **13**(19), 52–53 (2016)
4. Wang, R., Hou, M., Xie, R., Zhang, Z., Chen, X.: Research on high-voltage insulated pull rod. Insulators Surge Arresters **2015**(3), 13–15 (2015)
5. Zhang, S., Yao, N., Wu, J., Zhang, G.: Mechanical properties of glass fiber reinforced epoxy resin composites. Electr. Mater. **2016**(1), 11–14 (2016)
6. Hou, Y., Zhang, J., Hou, G., Chen, R., Wu, M.: Study on the formulation of epoxy resin for high-performance aramid insulated pull rod. Thermosetting Resin **33**(6), 27–30 (2018)
7. Equipment management department of State Grid Corporation of China: GIS insulation pull rod technology and fault case analysis [M]. China water resources and Hydropower Press, Beijing, China (2021)
8. Cui, B., Wang, N., Wang, C., Peng, Z., Chen, Y., Cheng, P.: Quality control for basin insulator used in gas insulated metal enclosed switchgear of ultra high voltage. High Voltage Eng. **40**(12), 3888–3894 (2014)
9. Chen, Y., Zhang, P., Cui, B., Wang, N., Wu, L., Liu, Y.: Application status of insulation tie rod for UHV GIS circuit breaker. High Voltage Technol. **45**(09), 2699–2706 (2019)
10. Liu, H.: Mechanics of materials 1st edn [M]. Higher Education Press, Beijing, China, Beijing (2017)
11. Wang, H., Chen, Y., Wu, Z., Zhang, P., Liao, W., Peng, Z.: Dynamic performance simulation test of circuit breaker insulation pull rod. J. Electr. Technol. **36**(S1), 311–320 (2021)
12. Wang, L., Wang, H.: Discussion of quality problems in 550 kV GIS disconnector insulating pull rod. Insulating Mater. **46**(1), 63–65 (2013)
13. Chen, C., Zhang, J., Zhao, M., Li, J.: Typical insulation fault cases and cause analysis of GIS. Electric Porcelain Arrester **2013**(6), 7–10 (2013)
14. Pan, Z., Gao, N., Li, C., et al.: Effect of aramid fiber surface state on mechanical properties of epoxy resin composites. Insulating Mater. **51**(7), 15–21 (2018)

Author Index